

Lesław Gołębiowski
Damian Mazur
Editors

Analysis and Simulation of Electrical and Computer Systems

Lecture Notes in Electrical Engineering

Volume 324

Board of Series editors

Leopoldo Angrisani, Napoli, Italy
Marco Arteaga, Coyoacán, México
Samarjit Chakraborty, München, Germany
Jiming Chen, Hangzhou, P.R. China
Tan Kay Chen, Singapore, Singapore
Rüdiger Dillmann, Karlsruhe, Germany
Haibin Duan, Beijing, China
Gianluigi Ferrari, Parma, Italy
Manuel Ferre, Madrid, Spain
Sandra Hirche, München, Germany
Faryar Jabbari, Irvine, USA
Janusz Kacprzyk, Warsaw, Poland
Alaa Khamis, New Cairo City, Egypt
Torsten Kroeger, Stanford, USA
Tan Cher Ming, Singapore, Singapore
Wolfgang Minker, Ulm, Germany
Pradeep Misra, Dayton, USA
Sebastian Möller, Berlin, Germany
Subhas Mukhopadhyay, Palmerston, New Zealand
Cun-Zheng Ning, Tempe, USA
Toyoaki Nishida, Sakyo-ku, Japan
Bijaya Ketan Panigrahi, New Delhi, India
Federica Pascucci, Roma, Italy
Tariq Samad, Minneapolis, USA
Gan Woon Seng, Nanyang Avenue, Singapore
Germano Veiga, Porto, Portugal
Haitao Wu, Beijing, China
Junjie James Zhang, Charlotte, USA

About this Series

“Lecture Notes in Electrical Engineering (LNEE)” is a book series which reports the latest research and developments in Electrical Engineering, namely:

- Communication, Networks, and Information Theory
- Computer Engineering
- Signal, Image, Speech and Information Processing
- Circuits and Systems
- Bioengineering

LNEE publishes authored monographs and contributed volumes which present cutting edge research information as well as new perspectives on classical fields, while maintaining Springer’s high standards of academic excellence. Also considered for publication are lecture materials, proceedings, and other related materials of exceptionally high quality and interest. The subject matter should be original and timely, reporting the latest research and developments in all areas of electrical engineering.

The audience for the books in LNEE consists of advanced level students, researchers, and industry professionals working at the forefront of their fields. Much like Springer’s other Lecture Notes series, LNEE will be distributed through Springer’s print and electronic publishing channels.

More information about this series at <http://www.springer.com/series/7818>

Lesław Gołębiowski · Damian Mazur
Editors

Analysis and Simulation of Electrical and Computer Systems

 Springer

Editors

Lesław Gołębiowski
Damian Mazur
Department of Electrical and Computer
Engineering Fundamentals
Rzeszów University of Technology
Rzeszów
Poland

ISSN 1876-1100

ISBN 978-3-319-11247-3

DOI 10.1007/978-3-319-11248-0

ISSN 1876-1119 (electronic)

ISBN 978-3-319-11248-0 (eBook)

Library of Congress Control Number: 2014954098

Springer Cham Heidelberg New York Dordrecht London

© Springer International Publishing Switzerland 2015

This work is subject to copyright. All rights are reserved by the Publisher, whether the whole or part of the material is concerned, specifically the rights of translation, reprinting, reuse of illustrations, recitation, broadcasting, reproduction on microfilms or in any other physical way, and transmission or information storage and retrieval, electronic adaptation, computer software, or by similar or dissimilar methodology now known or hereafter developed. Exempted from this legal reservation are brief excerpts in connection with reviews or scholarly analysis or material supplied specifically for the purpose of being entered and executed on a computer system, for exclusive use by the purchaser of the work. Duplication of this publication or parts thereof is permitted only under the provisions of the Copyright Law of the Publisher's location, in its current version, and permission for use must always be obtained from Springer. Permissions for use may be obtained through RightsLink at the Copyright Clearance Center. Violations are liable to prosecution under the respective Copyright Law.

The use of general descriptive names, registered names, trademarks, service marks, etc. in this publication does not imply, even in the absence of a specific statement, that such names are exempt from the relevant protective laws and regulations and therefore free for general use.

While the advice and information in this book are believed to be true and accurate at the date of publication, neither the authors nor the editors nor the publisher can accept any legal responsibility for any errors or omissions that may be made. The publisher makes no warranty, express or implied, with respect to the material contained herein.

Printed on acid-free paper

Springer is part of Springer Science+Business Media (www.springer.com)

Foreword

The XI Scientific Conference Selected Issues of Electrical Engineering and Electronics (WZEE) was held in Rzeszów and Czarna, Poland on September 27–30, 2013.

The main aim of the Conference was to provide academia and industry to discuss and present the latest technological advantages and research results, and to integrate the new interdisciplinary scientific circle in the field of electrical engineering, electronics, and mechatronics.

The historical seminar devoted to the memory of Prof. Roman Dzięślewski, one of the founders of the Polish electrical engineering, took place on the first day of the Conference.

The Conference was organized by the Rzeszów Division of Polish Association of Theoretical and Applied Electrical Engineering (PTETiS) in cooperation with Rzeszów University of Technology, the Faculty of Electrical and Computer Engineering and Rzeszów University, the Faculty of Mathematics and Natural Sciences. The Polish Association of Theoretical and Applied Electrical Engineering is a nonprofit organization devoted to promoting research and publications in the field of electrical engineering.

The Conference attracted more than 100 participants. Over a 100 papers were presented both in oral and poster sessions. The presented papers covered a wide range of topics:

- Mathematical models of electronics components and systems,
- Methods and tools for the modeling and simulation of selected electrical systems,
- New solutions in the field of construction, technology, and metrology of electrical engineering,
- Processing, optimization, and signal processing,
- Automation and control of electrical machines,
- Methods of calculation of electromagnetic fields,
- Impact of electromagnetic fields on organisms and the environment,
- New developments in the field of electrical engineering, electronics, and related fields,

- Protection of devices against electromagnetic surge,
- Practical implementations of systems, components, and their applications.

Based on a strict peer review process 35 papers were selected for this publication.

We cordially thank all participants, authors, reviewers and organizers for making The XI WZEE Conference a success!

The Organizing Committee of The XI WZEE Conference

Contents

Hierarchical Control of Four-Leg Three-Level Grid-Connected Converter for RES	1
M.P. Kazmierkowski, M. Sędlak, S. Stynski and M. Malinowski	
Model of Hybrid Active Power Filter in the Frequency Domain.	15
Dawid Buła and Marian Pasko	
Analysis of Resonance Phenomena in Series <i>RLC</i> Circuit with Supercapacitor.	27
Janusz Walczak and Agnieszka Jakubowska	
Study the Quality of Global Neural Model with Regard to the Local Models of Dynamic Complex System.	35
G. Drałus	
Transient Analysis of Interstitial Microwave Hyperthermia Using Multi-slot Coaxial Antenna.	63
Piotr Gas	
Impulse Responses of Generalized First Order LTV Sections.	73
Anna Piwowar and Janusz Walczak	
On Some Inequalities for Fourier Coefficients	81
Piotr Lorenc, Damian Słota, Marcin Szczygieł, Jacek Uryga and Roman Wituła	
On the Three, Five and Other Periodic Orbits of Some Polynomials	91
Roman Wituła, Edyta Hetmaniok, Damian Słota, Tomasz Trawiński and Wojciech Kołton	

Examination of Chaos Occurring in Selected Branched Kinematic Chains of Robot Manipulators	109
Tomasz Trawiński, Wojciech Kołton, Edyta Hetmaniok, Damian Słota and Roman Wituła	
An Estimation of the Geothermal Energy Sources for Generating Electricity	127
Roman Szostek	
Thermal Coupling Analysis of the Permanent Magnet Synchronous Generator	135
Lesław Gołębiowski, Marek Gołębiowski and Damian Mazur	
Universal High Speed Induction Motor Driver	149
Tomasz Binkowski	
Improvement of Immunity of Adjustable AC Drives with Induction Motors on Voltage Sags	163
Z. Głowacz and H. Krawiec	
Investigation of End Winding Proximity Losses in a High-Speed PM Machine	171
Adrian Młot, Mariusz Korkosz and Marian Łukaniszyn	
Modeling of the Squirrel-Cage Induction Motor Having Symmetrically Distributed Groups of Broken Cage Bars	187
Damian Krawczyk	
Analysis of Established Thermal Conditions for Magnetorheological Clutch for Different Loading Conditions	197
Zbigniew Pilch	
An Analytical Model of an Electrical Machine with Internal Permanent Magnets	215
Tomasz Drabek, Andrzej Matras and Jerzy Skwarczyński	
Modeling of Repetitive Ignitions in Switching Devices: Case Studies on Vacuum Circuit Breaker and GIS Disconnecter	241
Marcin Szewczyk, Tomasz Kuczek, Piotr Oramus and Wojciech Piasecki	
The Use of Statistical Signatures to Detect Anomalies in Computer Network	251
Marek Bolanowski and Andrzej Paszkiewicz	

Wireless Networks Environment and Complex Networks 261
 Franciszek Grabowski, Andrzej Paszkiewicz and Marek Bolanowski

Network Anomaly Detection Based on the Statistical Self-similarity Factor 271
 Paweł Dymora and Mirosław Mazurek

Analysis of Static Characteristics of a Switched Reluctance Motor 289
 B. Jankowski, D. Kapelski, M. Karbowski, M. Przybylski and B. Ślusarek

Robust Integral Sliding Mode Tracking Control of a Servo Drives with Reference Trajectory Generator 305
 Stefan Brock

Dynamic Modeling of the Skin Effect in Rotor Bars with Optimized Ladder Networks 315
 C. Schmülling and A. Conradi

Using BALSAs Environment for the Asynchronous Microprocessor Design 321
 Dariusz Stachańczyk

Random Dynamical Systems of the First Order 329
 J. Walczak and S. Mazurkiewicz

Analysis of the Distribution of Air Flow Rate Through Stator End Winding of Turbo Generator 337
 K. Zhao and C. Kreischer

Two-Directional Two-Pole Single Phase Line Start Permanent Magnet Synchronous Motor 343
 M. Gwoździewicz

Overhead Lines in Power System with Wind Power Plants and Photovoltaic Power Plants 349
 M. Zeńczak

An Analysis of a Brushless DC Motor with a Cup-Rotor 365
 M.P. Ciurys, I. Dudzikowski and G. Bogusz

Description of the Cross Saturation in an IPMSM for Electric Vehicles Using Bicubic Splines 377
 Patrick Seibt and André Fischer

Method for Diagnosing the Vacuum Conditions Using Pulses Voltage Generator	383
W. Chmielak and Z. Pochanke	
The Group and Individual Connection to the Rail System Modelling in a Lightning Discharge Analysis	393
Zofia Wróbel	
Gearless Pedaling Electric Driven Tricycle	411
K. Zawirski, K. Nowopolski, B. Wicher, D. Janiszewski, B. Fabiański and K. Siembab	
Calculations of Conjugated Fields in the Ferromagnetic Medium.	423
Robert Pękala, Tadeusz Kwater and Bogdan Kwiatkowski	

Hierarchical Control of Four-Leg Three-Level Grid-Connected Converter for RES

M.P. Kazmierkowski, M. Sędlak, S. Stynski and M. Malinowski

Abstract Operation of the four-leg three-level flying capacitor Grid-Connected Converter (GCC) for renewable energy source (RES) is presented in this paper. The GCC with proposed hierarchical control method enables operation in presence of electrical grid disturbances by switching all legs separately to stand-alone or grid-connected mode of operation, allowing energy transfer between them. Four-leg flying capacitor GCC with described control method may be treated as DC micro-grid supplied from three independent AC sources and RES. Therefore, the hierarchical control allows for effective power management of such system. The paper describes developed control system as well as presents simulation and experimental results measured on the 10 kVA laboratory converter.

1 Introduction

The paper presents four-leg three-level Flying Capacitor Converter (FCC) used as a Grid-Connected Converter (GCC) interfacing Renewable Energy Source (RES) with four wire electrical grid (low voltage grid) or asymmetrical three-phase load in stand-alone mode of operation. Usually, low power RES, e.g. small wind turbine or photovoltaic panels, are connected through three-phase converter and an additional Δ/Y transformer [1]. However, the mentioned transformer is large, heavy, increases costs and causes additional losses. It can be eliminated by application of four-leg converter (Fig. 1) [2, 3], which gives possibility to precise control of neutral

M.P. Kazmierkowski (✉) · M. Sędlak · S. Stynski · M. Malinowski
Institute of Control and Industrial Electronics, Warsaw University of Technology,
Warsaw, Poland
e-mail: mpk@isep.pw.edu.pl

S. Stynski
e-mail: stynskis@isep.pw.edu.pl

M. Malinowski
e-mail: malin@isep.pw.edu.pl

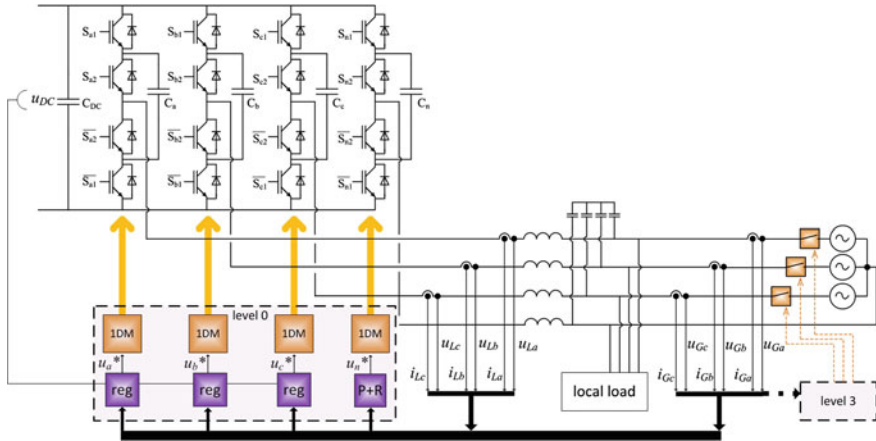


Fig. 1 Grid-connected flying capacitor converter with proposed control method

current. Moreover, such converter may be treated as three independent single-phase converters. Additional advantages can be achieved when three-level converter topology is used (e.g. lower voltage on single switch, lower total harmonic distortion (THD), reduction of passive components) [4].

Main requirements for the mentioned GCC besides of connecting RES to the grid are as follows:

- uninterruptable power supply for local load in all phases,
- symmetrical and sinusoidal grid currents at rectifier or inverter operation,
- operation at distorted grid voltage,
- operation at failure in phases by switching all legs separately to stand-alone or grid-connected mode,
- active filtering of higher harmonics in grid current caused by nonlinear load.

2 Power Flow Control

Four-leg FCC with described below control method may be treat as DC micro-grid supplied from three independent AC sources and RES. Therefore, very popular in last few years, hierarchical control [5] can be adapted to make power management of such system (Fig. 2). This section describes each level of hierarchical structure. Level 0 includes one dimensional modulator (1DM) which permits to treat each leg as independent single-phase converter in contrast to other modulation methods. This level contains also current and voltage control loops. Level 1 is responding for the grid currents symmetrization, level 2 observes converter currents for keep them and DC voltage on the proper level. Finally, level 3 includes grid monitoring block which decides about grid-connected/stand-alone mode of operation of each converter phase.

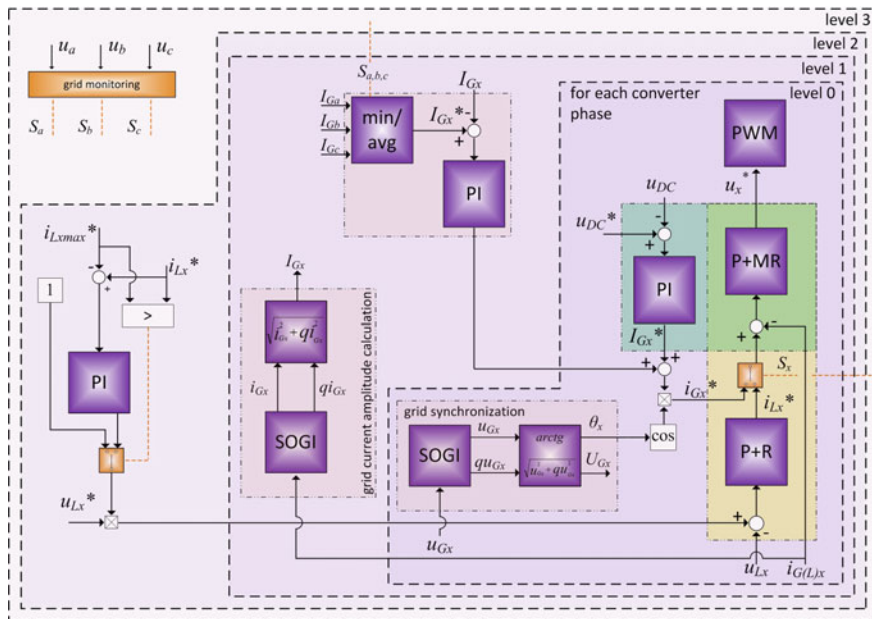


Fig. 2 Proposed hierarchical power flow control in four-leg FCC interfacing RES with grid

2.1 Level 0

2.1.1 Control Method

The four-leg converter with proposed control method enables work in association of electrical grid disturbances (e.g. sags/dips and overvoltages) by switching all legs separately to stand-alone or grid connected mode of operation, what allows for energy transfer between them. The presented method (Fig. 1) in natural $abcn$ reference frame is based on the proportional resonant (P + R) controllers described in [6, 7]. The structure of P + R controller is composed of proportional gain and resonant integrator. The transfer function contains double imaginary pole adjusted to the fundamental grid frequency ω , what allows tracking input phase-angle without any error. Proportional multi resonant (P + MR) controller has additional resonant part for each harmonic frequency that should be reduce e.g. $5\omega, 7\omega, 11\omega, 13\omega$, and so on. Full control scheme is composed of several control loops for each phase:

- current control loops in $abcn$ coordinate system (green),
- phase voltage loops only in stand-alone mode of operation (yellow),
- common outer DC-link control loop (blue).

The control scheme consists of only one P + R controller and one P + MR controller per phase in stand-alone mode of operation (yellow and green in Fig. 2) as well as one P + MR controller per phase in grid-connected operation mode (green). Commanded DC-link voltage U_{DC}^* is compared with measured value U_{DC} and delivered to PI controller which produces reference current amplitude I_x^* . This signal after multiplication by $\cos \theta$ gives i_{Gx}^* , which is compared with measured current $i_{G(L)x}$. Result is delivered to P + MR controller and then output goes to the modulator. Presented control is able to switch each converter phase to grid-connected or stand-alone mode of operation independently to other converter phases. This gives possibility to transfer energy in both directions at the same time (e.g. two phases are working in grid-connected mode and one phase is working in stand-alone mode or one phase is working in grid-connected mode and two others are working in stand-alone mode supplying only the local load). For harmonic elimination and grid currents symmetrization, closed control loop of active filter was used. Measurement of grid current i_{Gx} guarantees that this current is controlled and kept it in good condition. Such modifications permit to feed nonlinear local load with nearly sinusoidal current taking from the grid.

2.1.2 Grid Synchronization

When three-phase converter is treated as three independent single-phase units, conventional methods of grid synchronization for three-phase converter cannot be used. Any lack of phase is visible as a distortion in grid angle calculated for all phases. Therefore, each phase should have independent single-phase grid synchronization algorithm. Regenerated phase also should be all the time synchronized with other phases. For solve this problem, in proposed solution each phase has independent SOGI-QSG (second order general integrator quadrature signal generator) algorithm (Fig. 2) [8] for generation of virtual $\alpha\beta$ coordinates, which permit to calculate angle, frequency and voltage amplitude of each phase.

All calculated angles and voltage amplitudes are transferred to the grid monitoring block, which decides which converter leg should be connected/disconnected to the grid.

2.2 Level 1

Level 1 is responsible for the grid currents symmetrization. Therefore, amplitude of each phase current is calculated (Fig. 2). Next, average or minimal value of the grid currents amplitudes is compared with each grid current amplitude, and error is delivered to PI controller which output is added to signal given to the current controller.

2.3 Level 2

Level 2 (Fig. 2) is important in mixed mode of operation when there is not enough energy from RES to supply lacking phase for local load. Level 2 observes converter currents i_{Lx} and keeps them and DC voltage on the proper level. When the reference current for the leg which is in grid-connected mode is too high—the reference voltage for the leg in stand-alone mode is reduced to decrease energy consumption.

2.4 Level 3

Finally, level 3 contains grid monitoring block, which decides about grid-connected/stand-alone mode of operation of each leg. Voltage amplitudes, frequencies and angles are monitored on-line, and should meet following conditions:

- voltage amplitudes in range $\pm 10\%$ of nominal value,
- frequency in the range 49.5–50.5 Hz,
- phase angle of converter leg is synchronized with angle of the grid.

If all above mentioned conditions are met the proper leg can be connected to the grid.

3 Simulation and Experimental Results

3.1 Simulation Model and Results

For study the operation of the four-leg three-level FCC the simulation model has been built in the *Synopsys Saber Designer* software. The grid was modeled as three independent sinusoidal voltage sources u_{Ga} , u_{Gb} , u_{Gc} . Each phase of grid can be connected to, or disconnected from, the converter by switches S_a , S_b , S_c . The control method and modulation was implemented using the MAST language. Parameters of simulation, according to the simplified model shown in Fig. 3, are presented in Table 1.

Simulation studies include various types of load, from linear to nonlinear according to Fig. 3b. The following selected results are presented in this paper:

- grid-connected operating mode with symmetrical grid voltage and asymmetrical nonlinear local load,
- mixed mode—grid without one phase voltage, without RES, one leg in stand-alone operating mode, two legs in grid-connected operating mode, asymmetrical nonlinear local load,

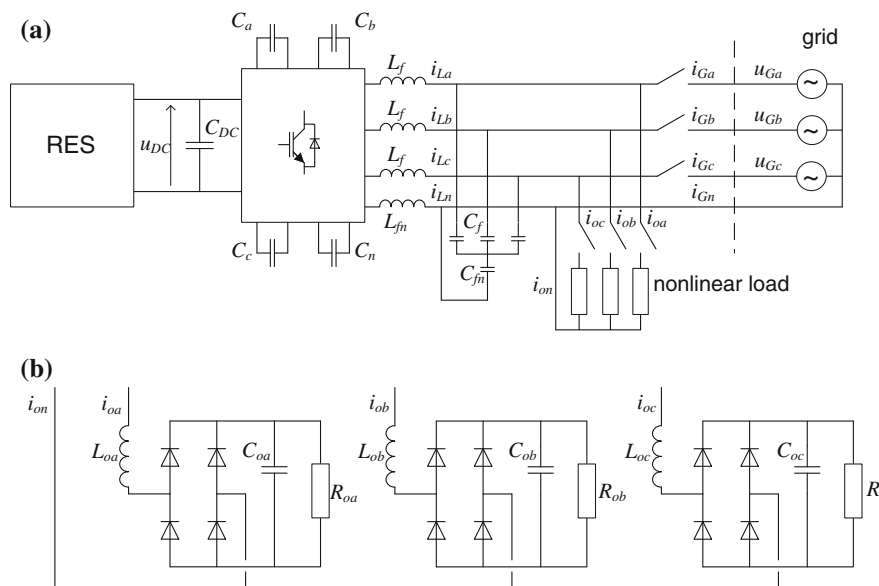


Fig. 3 Three-phase four-leg three-level FCC (a) and nonlinear load (b)

Table 1 Simulation parameters

Parameter	Value		
DC voltage	U_{DC}	700	V
Phase rms voltage	U_{Gx}	230	V
Switching frequency	f_s	16	kHz
Filter inductance	L_f	2.1	mH
filter capacitor	C_f	15	uF
Neutral leg filter inductance	L_{fn}	0.7	mH
Neutral leg filter capacitor	C_{fn}	5	uF
DC capacitor	C_{DC}	1	mF
Flying capacitor	C_x	0.2	mF

- mixed mode—grid without two phase voltages, without RES, two legs in stand-alone operating mode, one leg in grid-connected operating mode, asymmetrical nonlinear local load.

Simulation studies for the following configurations with only linear resistive local load without APF function:

- stand-alone operating mode with symmetrical and asymmetrical load,
- grid-connected operating mode,

- mixed modes—grid without one or two phase voltages with or without RES, was discussed and shown in [6].

Figure 4a presents grid-connected mode of operation with asymmetrical nonlinear local load presented in Fig. 3b, where $L_o = 2$ mH, $R_{oa} = 15$ Ω , $R_{ob} = R_{oc} = 45$ Ω , $C_{oa} = 200$ μ F, $C_{ob} = 25$ μ F and $C_{oc} = 10$ μ F. Figure 4b shows the same configuration with additional active filtering function, which gives reduction of current THD from above 80 % in phase a to the value below 5 %. It should be noted that change of current measurement's point gives only decrease of THD to about 10 % in this case; therefore addition of resonant part of controller for each harmonic up to 11th is necessary to reach acceptable current distortion, i.e. about 5 %. However, the most interesting—mixed—modes of operation are shown in Figs. 5 and 6. When appears failure of one or two grid phases, the four-leg converter delivers uninterruptable power supply to three-phase local loads, substituting lacking grid phase from the RES. If there is lack of some grid phases as well as there is no energy or not enough from the RES, the four-leg converter still shows ability to uninterruptable supply three-phase local load, because converter legs still connected to the grid are working in rectifier mode. In such case energy is transferred from legs working in grid-connected mode to other working in stand-alone mode of operation. Figure 5 presents situation where appears lack of phase 3 and there is no energy from the RES. Energy flows from two other grid phases to DC and then to the load in phase 3. Figure 6 shows similar case—lack of two grid phases—2 and 3 without energy from RES. In both situations local load in all phases is supplied. It is worth to mention that in two last cases current of grid-connected or neutral leg may reach high values, therefore it is necessary to limit current in each leg up to nominal level or oversize the converter. It is especially important for the neutral leg.

3.2 Experimental Setup and Results

Laboratory setup corresponding with simulation model was built. It consists of four-leg three-level flying capacitor converter (FCC). As a control unit dSPACE platform based on DS1005 card was used. Configuration permits to measure all converter and grid currents and phase voltages, and also DC and FC voltages. The RES was simulated with Huettinger TruPlasma DC power supply. Main parameters of experiment are presented in Table 2.

Next figures present experimental results in grid-connected and mixed mode of operation. Figure 7 presents grid currents in grid-connected mode of operation with nonlinear local load and without RES. Next, Fig. 8 presents similar situation after one grid phase break down. Two other phases supply DC side and lacking phase for local load. Figure 9 presents grid currents without active filtering. Figure 10

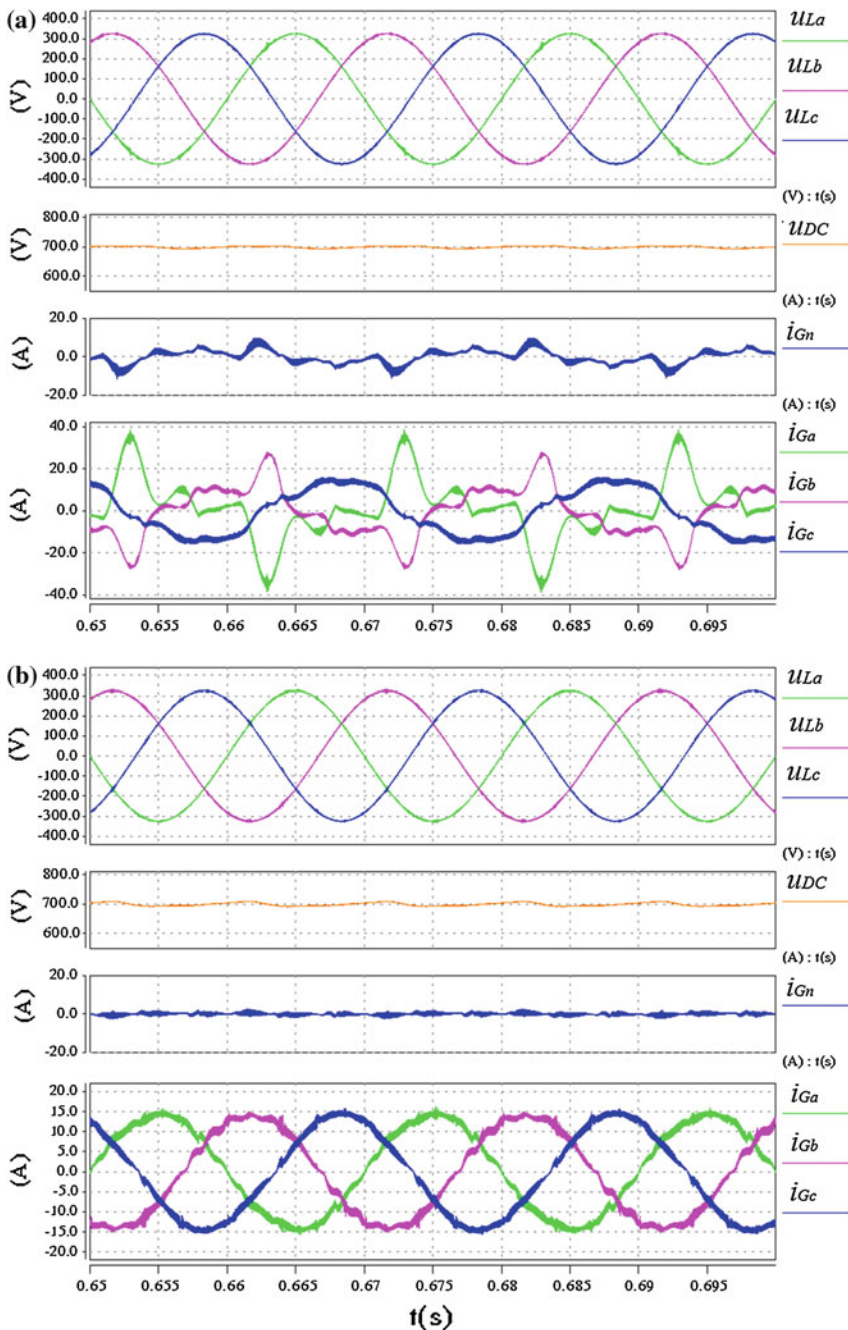


Fig. 4 Grid-connected operation mode without (a) and with (b) active filtering. From the top load voltages u_{La} , u_{Lb} , u_{Lc} , DC-link voltage u_{DC} , neutral current i_{Gn} , grid currents i_{Ga} , i_{Gb} , i_{Gc} , ($R_{oa} = 15 \Omega$, $R_{ob} = R_{oc} = 45 \Omega$, $L_{oa} = L_{ob} = L_{oc} = 2$ mH, $C_{oa} = 200 \mu\text{F}$, $C_{ob} = 25 \mu\text{F}$ and $C_{oc} = 10 \mu\text{F}$)

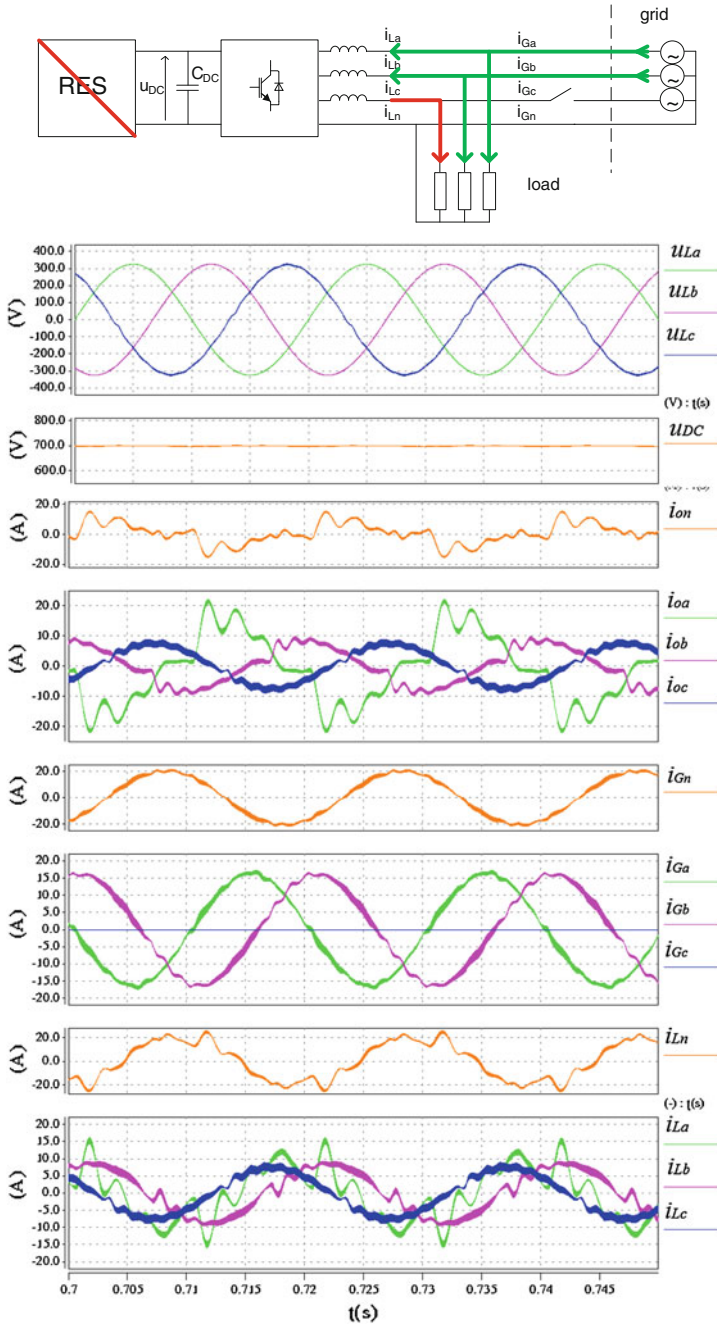


Fig. 5 Mixed mode, grid without one phase and without RES. From the *top* load voltages u_{La} , u_{Lb} , u_{Lc} , DC-link voltage U_{DC} , load neutral current i_{on} , load currents i_{oa} , i_{ob} , i_{oc} , grid neutral current i_{Gn} , grid currents i_{Ga} , i_{Gb} , i_{Gc} , converter neutral current i_{Ln} , converter currents i_{La} , i_{Lb} , i_{Lc} **a** ($R_{oa} = 25 \Omega$, $R_{ob} = R_{oc} = 45 \Omega$, $L_{oa} = L_{ob} = L_{oc} = 2 \text{ mH}$, $C_{oa} = 25 \mu\text{F}$, $C_{ob} = 25 \mu\text{F}$, $C_{oc} = 10 \mu\text{F}$) **b** ($R_{oa} = 25 \Omega$, $R_{ob} = 55 \Omega$, $R_{oc} = 45 \Omega$, $L_{oa} = L_{ob} = L_{oc} = 2 \text{ mH}$, $C_{oa} = 75 \mu\text{F}$, $C_{ob} = 25 \mu\text{F}$ and $C_{oc} = 10 \mu\text{F}$)

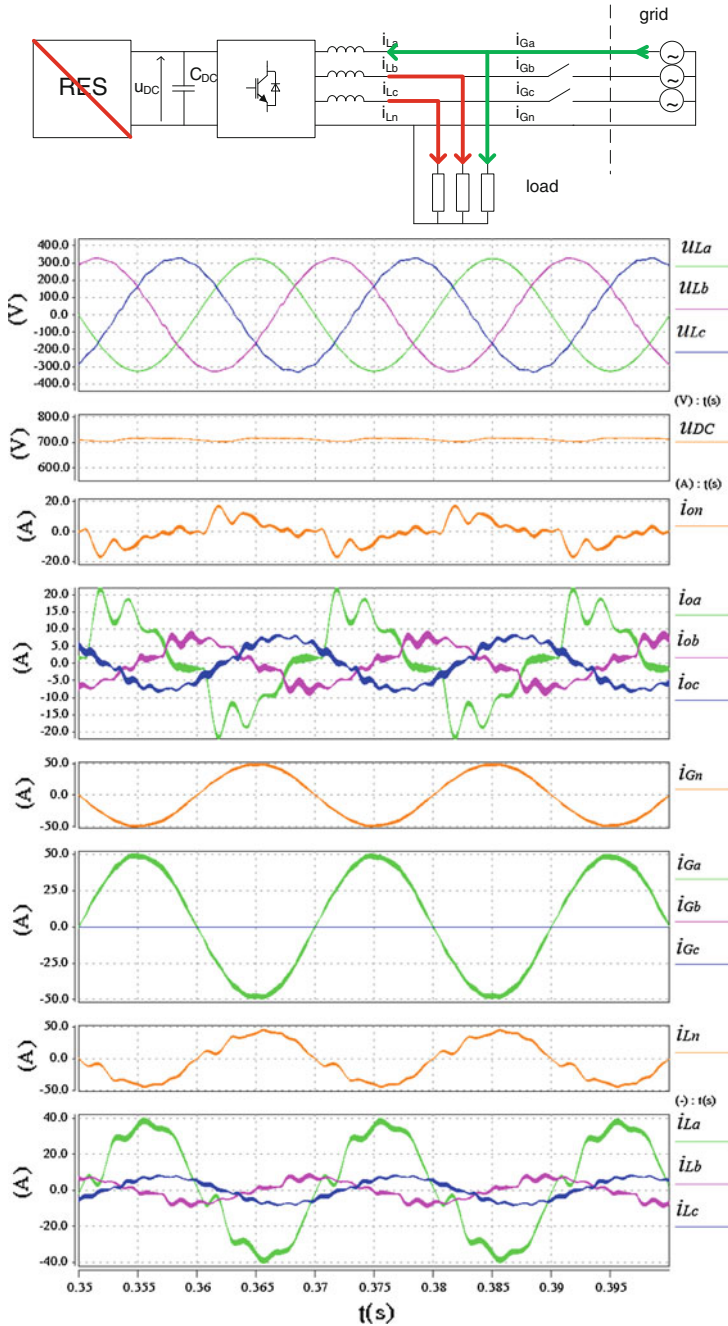


Fig. 6 Mixed mode, grid without two phases and without RES. From the *top* load voltages u_{La} , u_{Lb} , u_{Lc} , DC-link voltage U_{DC} , load neutral current i_{on} , load currents i_{oa} , i_{ob} , i_{oc} , grid neutral current i_{Gn} , grid currents i_{Ga} , i_{Gb} , i_{Gc} , converter neutral current i_{Ln} , converter currents i_{La} , i_{Lb} , i_{Lc} **a** ($R_{oa} = 25 \Omega$, $R_{ob} = R_{oc} = 45 \Omega$, $L_{oa} = L_{ob} = L_{oc} = 2 \text{ mH}$, $C_{oa} = 25 \mu\text{F}$, $C_{ob} = 25 \mu\text{F}$, $C_{oc} = 10 \mu\text{F}$) **b** ($R_{oa} = 25 \Omega$, $R_{ob} = 55 \Omega$, $R_{oc} = 45 \Omega$, $L_{oa} = L_{ob} = L_{oc} = 2 \text{ mH}$, $C_{oa} = 75 \mu\text{F}$, $C_{ob} = 25 \mu\text{F}$ and $C_{oc} = 10 \mu\text{F}$)

Table 2 Experiment parameters

Parameter		Value	
DC voltage	U_{DC}	350	V
Phase rms voltage	U_{Gx}	115	V
Switching frequency	f_s	16	kHz
Filter inductance	L_f	2.1	mH
Filter capacitor	C_f	2.9	uF
Neutral leg filter inductance	L_{fn}	2.1	mH
Neutral leg filter capacitor	C_{fn}	2.9	uF
DC capacitor	C_{DC}	1.4	mF
Flying capacitor	C_x	0.25	mF

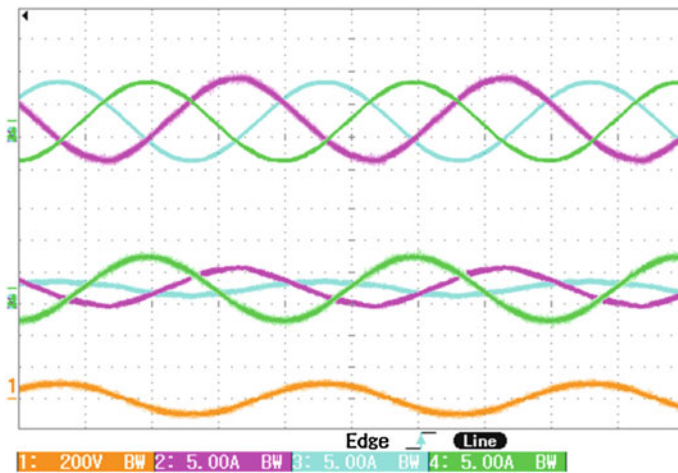


Fig. 7 Grid-connected mode of operation without RES: *top* 2, 3, 4—grid currents of L1, L2, L3 phases; *bottom* 2, 3, 4—converter currents; 1—voltage on local load in L2 phase

presents the same configuration but with active filtering and current symmetrization. Figure 11 shows transient from grid-connected to mixed mode of operation in situation when one phase of the grid disappear and there is no energy from RES. Energy is taken from two phases and given to the local load in lacking phase. Voltage of this phase is regenerated in less than one grid period.

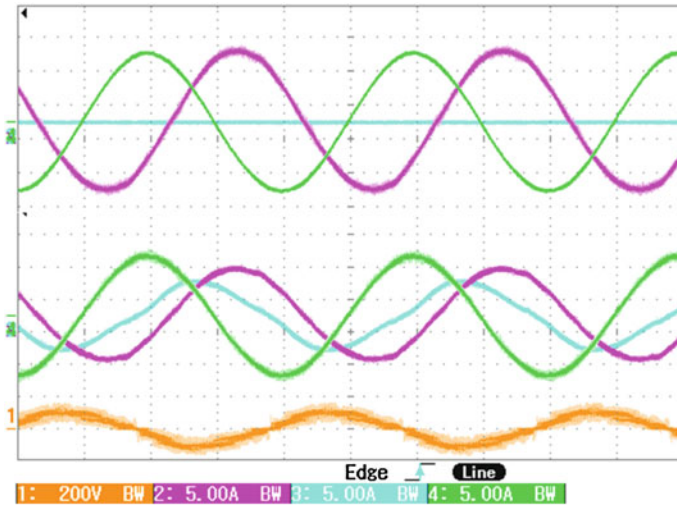


Fig. 8 Mixed mode of operation without RES and without L2 phase in the grid: *top* 2, 3, 4—grid currents of L1, L2, L3 phases; *bottom* 2, 3, 4—converter currents; 1—voltage on local load in L2 phase

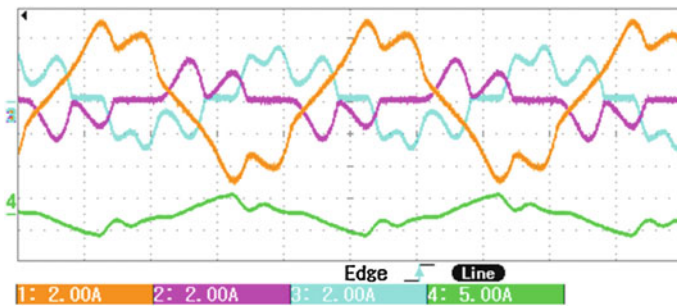


Fig. 9 Grid-connected mode of operation without active filtering: 1—DC voltage, 2, 3, 4—grid currents of phase L1, L2 and L3

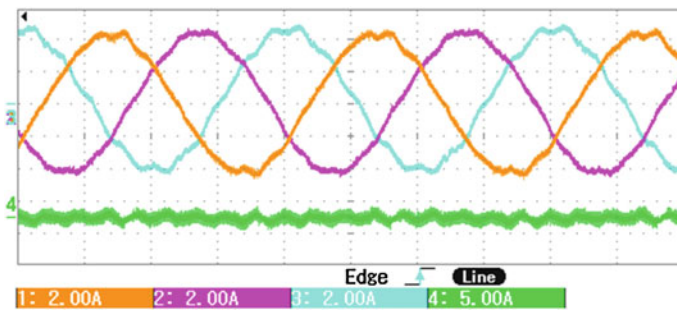


Fig. 10 Grid-connected mode of operation with active filtering and currents symmetrization: 1—DC voltage, 2, 3, 4—grid currents of phase L1, L2 and L3

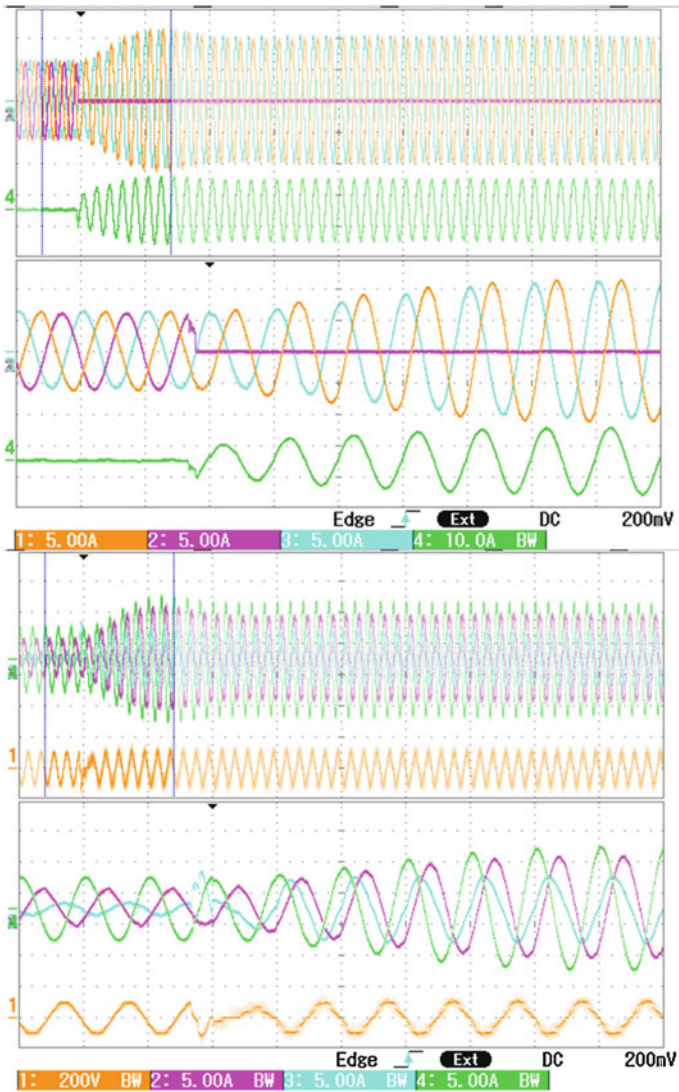


Fig. 11 Transient from grid-connected to mixed mode of operation without L2 phase and without RES: *top* 1, 2, 3—grid currents of phases L1, L2 and L3, 4—grid neutral current; *bottom* 1—L3voltage on local load in L2 phase; 2, 3, 4—converter currents of phases L1, L2 and L3

4 Conclusions

The paper presents four-leg three-level flying capacitor converter (FCC) interfacing renewable energy sources (RES) with the grid. Among important features of the proposed solution is elimination of Δ/Y transformer typically used with

three-leg converters, what provides higher efficiency, and reduction of size, weight and cost.

Moreover, the proposed control applied to four-legs three-level FCC with voltage oriented control (VOC) in natural coordinates based on proportional-resonant controllers allows to:

- uninterruptable power supply for local loads in all phases,
- symmetrical and sinusoidal grid currents at rectifier/inverter operation,
- operation at distorted grid voltage,
- operation at failure in phases by switching all legs separately to stand-alone or grid-connected mode,
- active filtering of nonlinear load.

The presented simulation and experimental results have proven good performance and verified validity of the proposed solution in different modes of operation.

Acknowledgments Described problems are the parts of the project number N N510 673540 “Transformer-less four-leg three-level converter for renewable energy systems” and sponsored by the National Science Centre.

References

1. Milczarek A, Malinowski M (2012) Monitoring and control algorithms applied to small wind turbine with grid-connected/stand-alone mode of operation. *Przeład Elektrotechniczny* 12a: 18–23
2. Benysek G, Kazmierkowski MP, Popczyk J, Strzelecki R (2011) Power electronic systems as a crucial part of Smart Grid infrastructure—a survey, *Bull Polish Acad Sci Techn Sci* 59(4): 455–473
3. Ali SM, Kazmierkowski MP (1998) Current regulation of four-leg PWM-VSI. In: *Proceedings IEEE IECON* vol. 3, pp. 1853–1858
4. Sedlak M, Stynski S, Kazmierkowski MP, Malinowski M (2012) Three-level four-leg flying capacitor converter for renewable energy sources. *Przeład Elektrotechniczny* 12a:6–11
5. Guerrero JM, Vasquez JC, Matas J, Garcia de Vicuña L, Castilla M (2011) Hierarchical control of droop-controlled AC and DC microgrids—a general approach toward standardization. *IEEE Trans Ind Electron* 58(1):158–172
6. Sedlak M, Stynski S, Kazmierkowski MP, Malinowski M (2013a) Control of three-level four-leg flying capacitor converter with active filtering function for RES. In: *2013 8th International Conference and Exhibition on Ecological Vehicles and Renewable Energies (EVER)*, pp. 1, 7, 27–30 March 2013
7. Sedlak M, Stynski S, Kazmierkowski MP, Malinowski M (2013b) Power management in four-leg converter interfacing RES with the Grid. In: *15th Conference on Power Electronics and Application*, 2013, September 2013
8. Rodriguez P, Luna A, Candela I, Teodorescu R, Blaabjerg F (2008) Grid synchronization of power converters using multiple second order generalized integrators. In: *34th Annual Conference of IEEE Industrial Electronics IECON 2008*, pp. 755, 760, 10–13 Nov 2008

Model of Hybrid Active Power Filter in the Frequency Domain

Dawid Buła and Marian Pasko

Abstract A model of the hybrid active power filter in the frequency domain has been presented in the paper. Control algorithm for detecting current harmonics uses method with Park transformation in this case. The derivation of the frequency model for this method and its application to the analyzed hybrid active power filter have been shown. The presented model allows the assessment of the impact of system parameters on the filtration characteristics of the analyzed hybrid filter.

1 Introduction

Application of an active power filter [1–4] is one of methods for reducing harmonics in three-phase power lines. Regardless of the type and configuration of the system, it is necessary to determine currents or voltages harmonics based on their measurements. These can be selected harmonics, fundamental frequency components or all of the higher harmonics. There are many methods of determining harmonics [2–5], from which the most popular are methods in the frequency domain based on the Fourier transform i.e. DFT, FFT, and their variations. Another popular group of methods are time-domain methods, which can include the analyzed method with Park transformation or a method based on p-q instantaneous power theory [1].

In contrast to the frequency methods, time-domain methods are characterized by their lower computational complexity. This allows implementation of the control algorithm in a real system without the need to use controllers with high computational power.

D. Buła (✉) · M. Pasko
Silesian University of Technology, Gliwice, Poland
e-mail: dawid.bula@polsl.pl

M. Pasko
e-mail: marian.pasko@polsl.pl

In some cases, information about control method in the frequency domain is needed. For example in hybrid active power filters where passive harmonic filters are used and the filtration characteristics of whole hybrid filter should be determined. This helps in the selection of system parameters and assessing their impact on the frequency characteristics [6–9].

The paper shows the derivation of the frequency model for harmonic detection method using Park transformation [10] and an example for use of the derived model for the analysis of hybrid power filter control algorithm in the configuration with a single harmonic passive filter [6, 11].

2 Park Transformation

The transformation from the three-phase 1-2-3 system to the d-q-0 system, also known as Park transformation, was presented for the first time by R. H. Park in 1929 [10]. This conversion is very often used in the theory of electrical machines and allows to treat quantities related to the rotor as constant in time. It is based on the transformation of the natural 1-2-3 orthogonal system to the d-q-0 system rotating with angular frequency ω_0 . Park transformation for currents can be written as:

$$\begin{bmatrix} i_d \\ i_q \\ i_0 \end{bmatrix} = \sqrt{\frac{2}{3}} \begin{bmatrix} \cos(\omega_0 t) & \cos(\omega_0 t - 2\pi/3) & \cos(\omega_0 t + 2\pi/3) \\ \sin(\omega_0 t) & \sin(\omega_0 t - 2\pi/3) & \sin(\omega_0 t + 2\pi/3) \\ \sqrt{2}/2 & \sqrt{2}/2 & \sqrt{2}/2 \end{bmatrix} \begin{bmatrix} i_1 \\ i_2 \\ i_3 \end{bmatrix}. \quad (1)$$

This form is rarely used, and the most commonly used is form with intermediate orthogonal transformation to the α - β system (Clarke transformation) which, for three-wire network is:

$$\begin{bmatrix} i_\alpha \\ i_\beta \end{bmatrix} = \sqrt{\frac{2}{3}} \begin{bmatrix} 1 & -1/2 & -1/2 \\ 0 & \sqrt{3}/2 & -\sqrt{3}/2 \end{bmatrix} \begin{bmatrix} i_1 \\ i_2 \\ i_3 \end{bmatrix}, \quad (2)$$

$$\begin{bmatrix} i_d \\ i_q \end{bmatrix} = \begin{bmatrix} \cos(\omega_0 t) & \sin(\omega_0 t) \\ -\sin(\omega_0 t) & \cos(\omega_0 t) \end{bmatrix} \begin{bmatrix} i_\alpha \\ i_\beta \end{bmatrix}. \quad (3)$$

The transformation of the 1-2-3 natural system to d-q system, rotating with angular frequency ω_0 system causes that variables of the synchronous angular frequency ω_0 are constant over time. This allows the detection of the selected harmonic.

To filter the fundamental frequency components of the symmetrical three-phase currents, DC components from d-q currents should be removed as it has been shown in the block diagram in Fig. 1. Result of the shown transformations are higher harmonics of currents ($i_{1,2,3(\text{hh})}$). In a similar way one can achieve detection of selected harmonic components and their positive and negative components in the case of an unsymmetrical system.

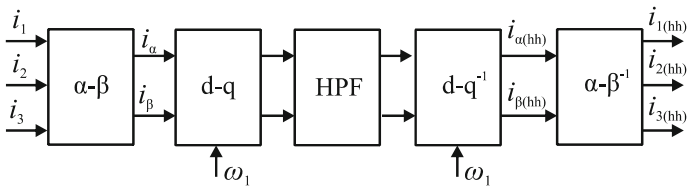


Fig. 1 Block diagram of the algorithm of detecting the higher harmonic

3 Model in Frequency Domain

The transformation of algorithm shown in Fig. 1 to the frequency domain has been performed in the α - β system (Fig. 2). High-pass filter (HPF) at the diagram in Fig. 1 (the same for both components) in this case is represented by the impulse response function $k(t)$, while the searched transfer function is designated as $G(j\omega)$.

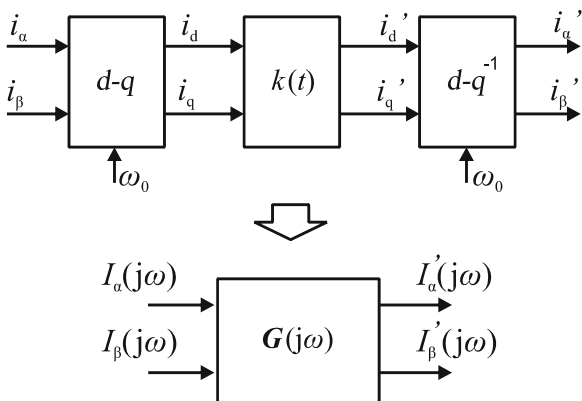
The relationship between input and output values in d-q rotating coordinates can be written as:

$$\begin{bmatrix} i'_d \\ i'_q \end{bmatrix} = \int_{-\infty}^{\infty} \left(k(t - \tau) \begin{bmatrix} i_d \\ i_q \end{bmatrix} \right) d\tau, \tag{4}$$

which after applying the Fourier transform to both sides of the equation, and next using theorem of convolution in time domain, gives:

$$\mathcal{F} \left\{ \begin{bmatrix} i'_d \\ i'_q \end{bmatrix} \right\} = K(j\omega) \mathcal{F} \left\{ \begin{bmatrix} i_d \\ i_q \end{bmatrix} \right\}, \tag{5}$$

Fig. 2 Model in frequency domain



where: $K(j\omega) = N(j\omega)/D(j\omega)$ —frequency transfer function of the applied signal filters (with the same parameters). $N(j\omega)$ and $D(j\omega)$ are polynomials in this case, the degree of the numerator is less than or equal to the degree of the denominator.

After applying the transformation to the α - β system, Eq. (5) takes the form:

$$\begin{aligned} D(j\omega)\mathcal{F}\left\{\begin{bmatrix} \cos(\omega_0 t) & \sin(\omega_0 t) \\ -\sin(\omega_0 t) & \cos(\omega_0 t) \end{bmatrix}\begin{bmatrix} i_\alpha' \\ i_\beta' \end{bmatrix}\right\} = \\ = N(j\omega)\mathcal{F}\left\{\begin{bmatrix} \cos(\omega_0 t) & \sin(\omega_0 t) \\ -\sin(\omega_0 t) & \cos(\omega_0 t) \end{bmatrix}\begin{bmatrix} i_\alpha \\ i_\beta \end{bmatrix}\right\}. \end{aligned} \quad (6)$$

Then using the relationship [6, 8, 9]:

$$\begin{aligned} \frac{d^n}{dt^n} \left(\begin{bmatrix} \cos(\omega_0 t) & \sin(\omega_0 t) \\ -\sin(\omega_0 t) & \cos(\omega_0 t) \end{bmatrix} \begin{bmatrix} i_\alpha' \\ i_\beta' \end{bmatrix} \right) \\ = \begin{bmatrix} \cos(\omega_0 t) & \sin(\omega_0 t) \\ -\sin(\omega_0 t) & \cos(\omega_0 t) \end{bmatrix} \left(\begin{bmatrix} \frac{d}{dt} & \omega_0 \\ -\omega_0 & \frac{d}{dt} \end{bmatrix}^n \begin{bmatrix} i_\alpha' \\ i_\beta' \end{bmatrix} \right), \end{aligned} \quad (7)$$

and the derivative transform theorem, while bearing in mind that $N(j\omega)$ and $D(j\omega)$ are polynomials, Eq. (6) can be converted to the form:

$$\mathbf{D}(\lambda) \left|_{\lambda=\begin{bmatrix} j\omega & \omega_0 \\ -\omega_0 & j\omega \end{bmatrix}} \mathcal{F}\left\{\begin{bmatrix} i_\alpha' \\ i_\beta' \end{bmatrix}\right\}\right. = \mathbf{N}(\lambda) \left|_{\lambda=\begin{bmatrix} j\omega & \omega_0 \\ -\omega_0 & j\omega \end{bmatrix}} \mathcal{F}\left\{\begin{bmatrix} i_\alpha \\ i_\beta \end{bmatrix}\right\}\right. . \quad (8)$$

The searched transfer function can be so written as:

$$\mathbf{G}(j\omega) = \mathbf{N}(\lambda)^{-1}\mathbf{D}(\lambda), \lambda = \begin{bmatrix} j\omega & \omega_0 \\ -\omega_0 & j\omega \end{bmatrix}. \quad (9)$$

In this form it is not possible to obtain independent characteristics for α and β components. However, in case of the filters described in the form of transfer function of a rational function, the transfer function $G(j\omega)$ can be expressed as [8, 9]:

$$\mathbf{G}(j\omega) = \begin{bmatrix} a(j\omega) & b(j\omega) \\ -b(j\omega) & a(j\omega) \end{bmatrix}, \quad (10)$$

which after transformation into symmetrical components:

$$\begin{bmatrix} I^+(j\omega) \\ I^-(j\omega) \end{bmatrix} = \begin{bmatrix} a(j\omega) - jb(j\omega) & 0 \\ 0 & a(j\omega) + jb(j\omega) \end{bmatrix} \begin{bmatrix} I^+(j\omega) \\ I^-(j\omega) \end{bmatrix}, \quad (11)$$

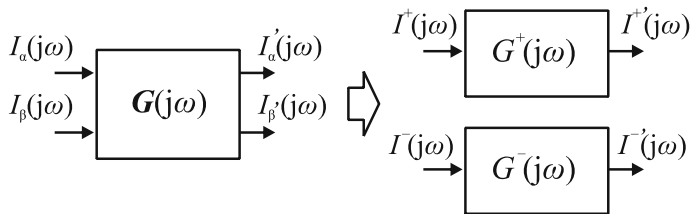


Fig. 3 Transforming model to the symmetrical components

gives independent transfer functions for positive and negative sequences:

$$\begin{aligned} \mathbf{G}^{+,-}(j\omega) &= \begin{bmatrix} G^+(j\omega) & 0 \\ 0 & G^-(j\omega) \end{bmatrix} \\ &= \frac{1}{2} \begin{bmatrix} 1 & j \\ 1 & -j \end{bmatrix} \mathbf{G}(j\omega) \begin{bmatrix} 1 & 1 \\ j & -j \end{bmatrix}. \end{aligned} \quad (12)$$

In this way, two separate transfer functions describing the analyzed system in the frequency domain (Fig. 3) have been obtained.

For example, using high-pass first order signal filters with ω_c cutoff angular frequency described by transfer function:

$$K_{\text{HPF}}(j\omega) = \frac{j\omega}{j\omega + \omega_c}, \quad (13)$$

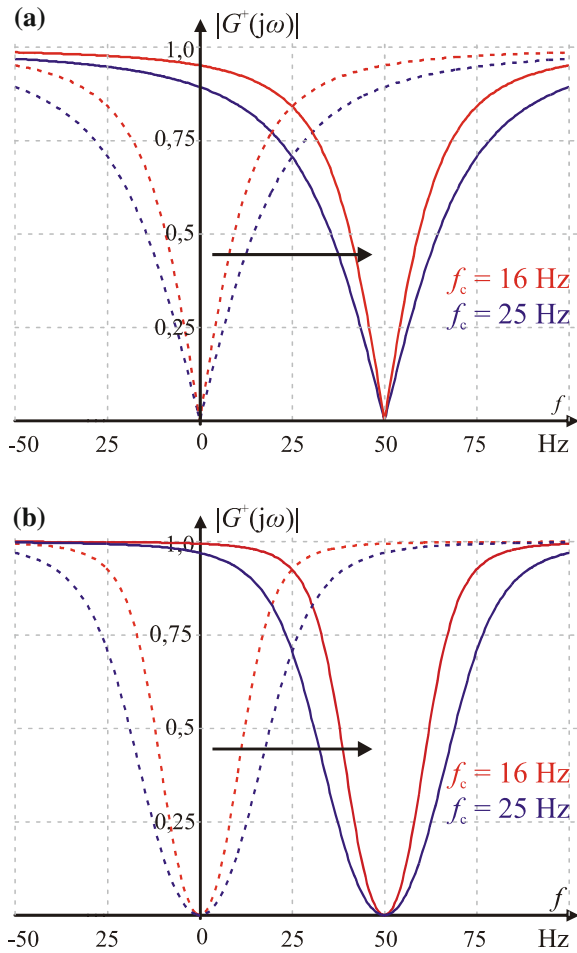
we obtain the following transfer functions:

$$G^+(j\omega) = \frac{j\omega - j\omega_0}{j\omega - j\omega_0 + \omega_c} = K_{\text{HPF}}(j\omega - j\omega_0), \quad (14)$$

$$G^-(j\omega) = \frac{j\omega + j\omega_0}{j\omega + j\omega_0 + \omega_c} = K_{\text{HPF}}(j\omega + j\omega_0). \quad (15)$$

As an effect of components filtration which are the result of Park transformation (and inverse transform), we obtain a shift in the frequency of the used signal filters characteristics. In case of positive components, the shift occurs in the positive direction by the value of ω_0 angular frequency. For negative components, shift takes place in the negative direction. Sample frequency responses of resultant transfer functions $G_1^+(j\omega)$ for first and second order low pass filters have been shown in Fig. 4.

Fig. 4 Resultant transfer functions frequency responses $G_1^+(j\omega)$ for filters: **a** first order **b** Butterworth second order



4 Application of the Frequency Model for Hybrid Power Filter Analysis

Hybrid power filters combine active power filter with traditional passive filters. This connection allows to take advantages from both solutions, usually by improving the properties of the filter in relation to the passive filters and by reducing the required power rate of the active part [1, 4, 6, 8]. Depending on the connection method and applied systems, hybrid filters are used in order to reduce currents and voltages harmonics and to compensate reactive power. One of the possible configurations of hybrid system is a series connection of parallel passive filter with a shunt active power filter (Fig. 5). The configuration with passive part reduced to the 7th harmonic filter has been used in this case [6, 8]. Diagram of the control algorithm for

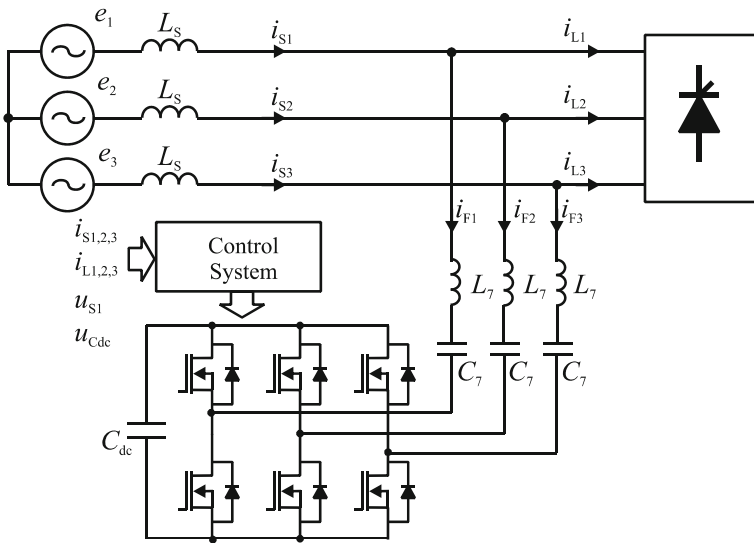


Fig. 5 Hybrid power filter with single tuned passive filter

this solution is shown in Fig. 6. In order to determine high harmonics of source currents the discussed method with d-q synchronous reference frame has been used. The upper branch of the shown control algorithm is responsible for determining higher harmonics of the source currents, as in the case of usual control of hybrid filter [1, 9]. Lower branch is responsible for determining voltage at the output of the filter which is necessary to reduce the selected harmonic current (5th and 11th in this case). In order to reduce other harmonics (e.g. 13th, 17th) additional similar branches should be connected to the lower branch of the algorithm. In the paper a simplified version of the algorithm without the part responsible for regulating the u_{DC} has been presented. The obtained voltages $v_{1,2,3(ref)}$ give rise for determining control signals of the of hybrid filter transistors.

Based on the schema of the analyzed system (Fig. 5), and the diagram of its control (Fig. 6) it is possible to create a frequency model according to the previous derivations. This model has been shown in Fig. 7.

However, the relationship between source currents and load currents can be described by the equation:

$$\begin{aligned} \begin{bmatrix} I_{S\alpha}(j\omega) \\ I_{S\beta}(j\omega) \end{bmatrix} &= [Z_F(j\omega)\mathbf{1}_2 + Z_S(j\omega)\mathbf{1}_2 + K\mathbf{G}_1(j\omega)]^{-1} \\ &\times \left[Z_F(j\omega)\mathbf{1}_2 - \sum_{h=5,11,13} \mathbf{G}_h(j\omega)\mathbf{Z}_{Fh} \right] \begin{bmatrix} I_{L\alpha}(j\omega) \\ I_{L\beta}(j\omega) \end{bmatrix}, \end{aligned} \quad (16)$$

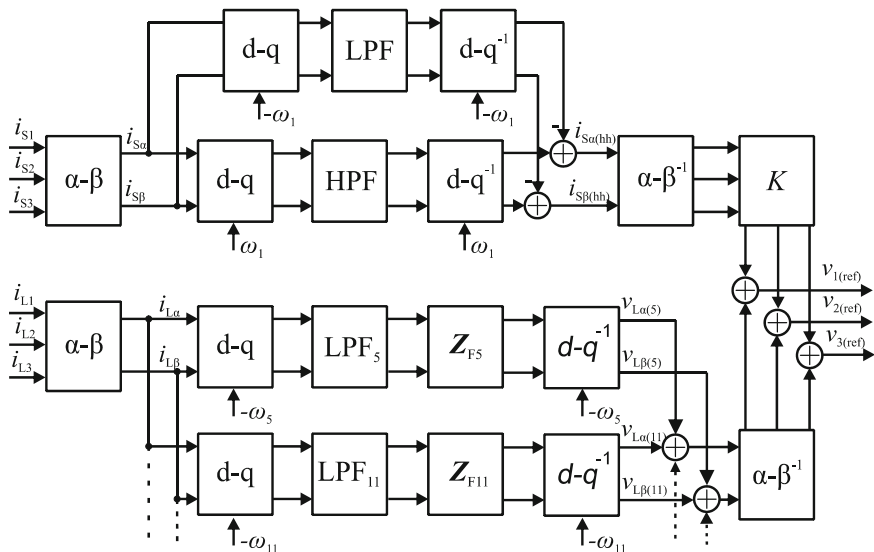


Fig. 6 Diagram of control algorithm of the analyzed hybrid power filter

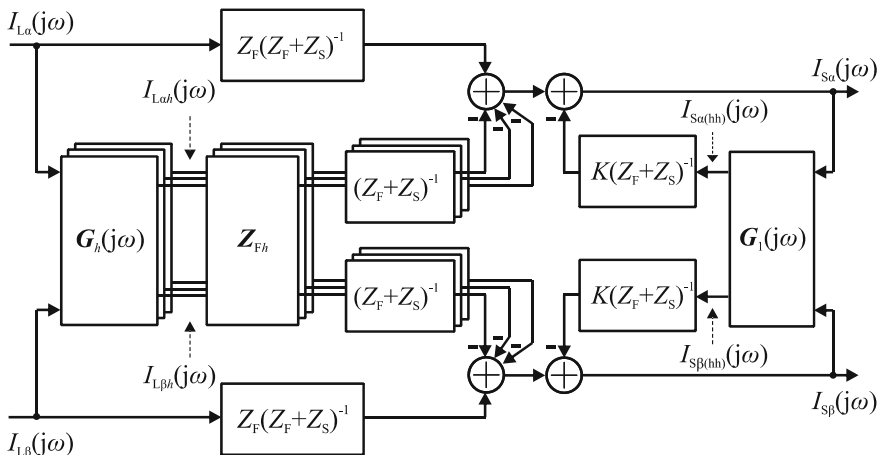


Fig. 7 Frequency model of the analyzed hybrid power filter

where: $\mathbf{1}_2$ - 2x2 identity matrix, $Z_F(j\omega)$ —passive filter impedance, $Z_S(j\omega)$ —source impedance, K —hybrid filter gain.

The remaining quantities in Eq. (16) are associated with the Park transformation and the used signal filters:

$$\mathbf{G}_1(j\omega) = \mathbf{G}'(j\omega) - \mathbf{G}''(j\omega). \quad (17)$$

$\mathbf{G}'(j\omega)$ —matrix connected with Park transformation and high pass filter (HPF):

$$\mathbf{G}'(j\omega) = \mathbf{D}_{\text{HPF}}^{-1}(\lambda') \mathbf{N}_{\text{HPF}}(\lambda'), \lambda' = \begin{bmatrix} j\omega & \omega_1 \\ -\omega_1 & j\omega \end{bmatrix}, \quad (18)$$

$$K_{\text{LPF}}(j\omega) = \frac{N_{\text{HPF}}(j\omega)}{D_{\text{HPF}}(j\omega)}. \quad (19)$$

$\mathbf{G}''(j\omega)$ —matrix corresponding with Park transformation and low pass filter (LPF) (used for computation negative components of source currents):

$$\mathbf{G}''(j\omega) = \mathbf{D}_{\text{LPF}}^{-1}(\lambda'') \mathbf{N}_{\text{LPF}}(\lambda''), \lambda'' = \begin{bmatrix} j\omega & -\omega_1 \\ \omega_1 & j\omega \end{bmatrix} \quad (20)$$

$$K_{\text{LPF}}(j\omega) = \frac{N_{\text{LPF}}(j\omega)}{D_{\text{LPF}}(j\omega)}. \quad (21)$$

$\mathbf{G}_h(j\omega)$ —matrixes related to Park transformation and low pass filters (LPF_{*h*}):

$$\mathbf{G}_h(j\omega) = \mathbf{D}_{\text{LPF}_h}^{-1}(\lambda_h) \mathbf{N}_{\text{LPF}_h}(\lambda_h), \lambda_h = \begin{bmatrix} j\omega & \omega_h \\ -\omega_h & j\omega \end{bmatrix}, \quad (22)$$

$$K_{\text{LPF}_h}(j\omega) = \frac{N_{\text{LPF}_h}(j\omega)}{D_{\text{LPF}_h}(j\omega)}. \quad (23)$$

\mathbf{Z}_{Fh} —matrix related to passive filter impedance for *h*-harmonic:

$$\mathbf{Z}_{Fh} = \begin{bmatrix} \text{Re}\{Z_F(j\omega_h)\} & -\text{Im}\{Z_F(j\omega_h)\} \\ \text{Im}\{Z_F(j\omega_h)\} & \text{Re}\{Z_F(j\omega_h)\} \end{bmatrix} \quad (24)$$

Similarly as in the derivation (10)–(13), it is possible to transform relation (16) to symmetrical components which allows to determine independent frequency responses for positive and negative components. An example of frequency responses has been shown in Fig. 8. It was assumed that all signal filters are first order with cut-off frequency of 25 Hz.

Figure 9 shows the effect of a different cut-off frequency of signal filters on frequency response. First-order filters have been assumed in this case. Characteristics are much more selective for the filtered harmonics for signal filters with lower cut-off frequency. It allows to obtain better filtering properties of the hybrid system. Unfortunately, reducing the cut-off frequency of filters causes deterioration of the

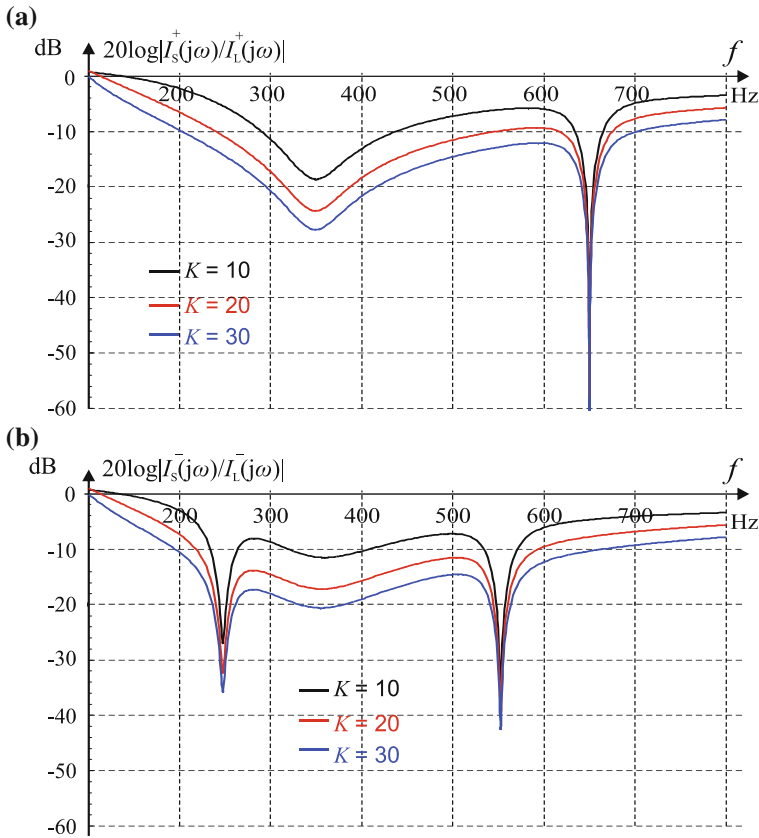


Fig. 8 Frequency responses of the analyzed hybrid filter for different value of K gain

system dynamic properties by extending the time transients [3, 6, 7]. Therefore it is necessary to compromise and to use in real applications signal filters with cut-off frequency in the range (10–20) Hz.

5 Summary

The paper presents a frequency model derivation of method for determining harmonics in three-phase systems. The analyzed method uses the Park transformation and is implemented in the time domain, however, the obtained model in frequency domain allows to analyze the frequency characteristics of the system in which it is used.

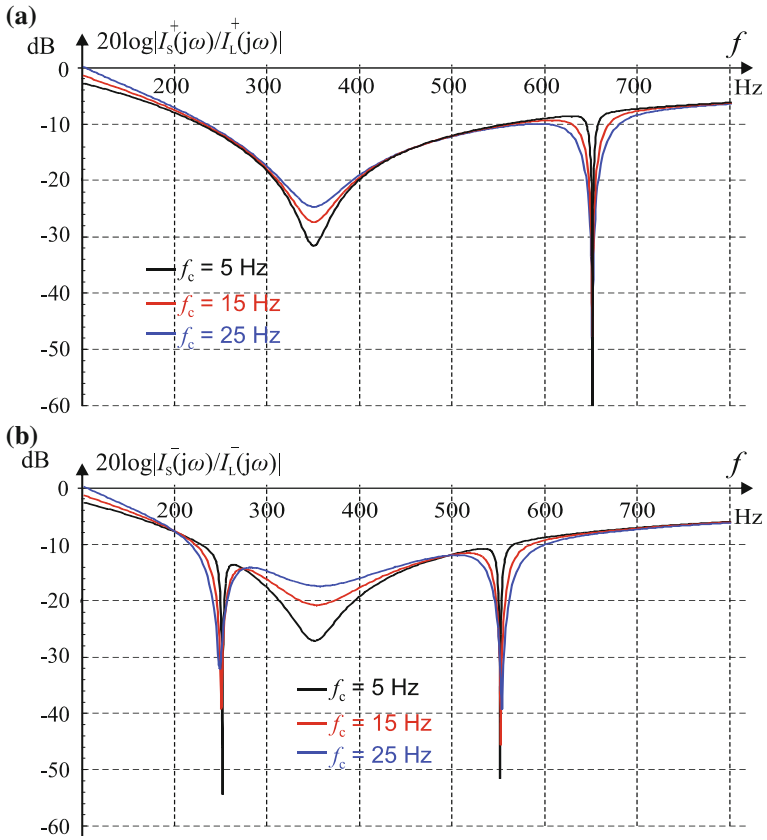


Fig. 9 Frequency responses of the analyzed hybrid filter for different cut-off frequency of signal filters ($K = 20$)

Hybrid active power filter in configuration with single tuned passive harmonic filter has been used as an example. Based on the derived model, it was possible to obtain a harmonic filtration characteristics of the analyzed hybrid filter, separately for positive and negative components. This allows for assessment of the system parameters impact on properties of the analyzed filter.

References

1. Akagi H, Watanabe EH, Aredes M (2007) Instantaneous power theory and applications to power conditioning. Wiley-IEEE Press, Hoboken
2. Asiminoaei L, Blaabjerg F, Hansen S (2007) Detection is key—Harmonic detection methods for active power filter applications. IEEE Ind Appl Mag 13:22–33

3. Buła D, Pasko M (2011) Dynamical properties of hybrid power filter with single tuned passive filter. *Przeгляд Elektrotechniczny* 1:91–95
4. Bhattacharya S, Divan DJ (1995) Synchronous frame based controller implementation for a hybrid series active filter system. *IEEE/IAS Conf Rec* 2531–2540
5. Bollen MHJ, Gu IYH (2006) *Signal processing of power quality disturbances*. Wiley/IEEE Press, Piscataway
6. Buła D (2011) Hybrid active power filters. Ph.D. thesis (in Polish). Gliwice Silesian University of Technology Digital Library. <http://delibra.bg.polsl.pl>
7. Pasko M, Maciążek M, Buła D (2008) Significance of signal filters in control system of Active Power Filters. *Przeгляд Elektrotechniczny*, 6:101–104
8. Peng FZ, Akagi H, Nabae A (1993) Compensation characteristics of the combined system of shunt passive and series active filters. *IEEE Trans Ind Appl* 29(1):144–152
9. Strzelecki R, Supronowicz H (1998) Filtration of harmonics in AC power networks (in Polish). Adam Marszałek publishing, Toruń
10. Park RH (1929) Two reaction theory of synchronous machines. *AIEE Trans* 48:716–730
11. Tangtheerajaronwong W, Hatada T, Wada K, Akagi H (2007) Design and performance of a transformerless shunt hybrid filter integrated into a three-phase diode rectifier. *IEEE Trans Power Electron* 22(5):1882–1889

Analysis of Resonance Phenomena in Series RLC Circuit with Supercapacitor

Janusz Walczak and Agnieszka Jakubowska

Abstract The article concerns an analysis of phase and magnitude resonance conditions for a series RLC circuit with supercapacitor. Supercapacitor behavior differs from classic dielectric capacitors, therefore their mathematical models are more complicated, using, in particular, fractional calculus. Simple, fractional—order model has been taken into analysis and simulations. Results have been verified experimentally. Proper selection of the resonance circuit parameters R , L , R_S and C determines either phase or magnitude resonance.

1 Introduction

Supercapacitors are a modern product of electrical engineering. For many years supercapacitor significance in industry has been spreading and gaining new areas of applications: hybrid and electric vehicle drives, power electronic converters, power saving energy systems, renewable energy, such as wind and photovoltaic power, low power devices, e.g. in UPS systems of electronic devices as well as many others [1–3]. They are characterized by very large capacitance compared to traditional electrolytic capacitors. Besides that, short charging and discharging time is their next important advantage, what determines their use as a high-power density electric energy resources. Specific structure of supercapacitors, the working conditions, and their behavior caused the necessity of new circuit models introduction for these elements. There are several kinds of models, e.g. using extended equivalent RC branches [1, 3–6] and based on artificial neural networks (ANN) [7]. Supercapacitors are often modeled using fractional integral and differential calculus methods [8–13]. There are a number of fractional order supercapacitor models.

J. Walczak (✉) · A. Jakubowska
Faculty of Electrical Engineering, Silesian University of Technology, Gliwice, Poland
e-mail: janusz.walczak@polsl.pl

A. Jakubowska
e-mail: agnieszka.jakubowska@polsl.pl

Some of them result from the observation of their dynamic processes, while the other have their origin in frequency characteristics studies. They differ from one another in complexity and accuracy of supercapacitor dynamic and frequency characteristics description. The basic model has been proposed by Westerlund and Ekstam [12]. Impedance of this model is defined as:

$$Z(j\omega) = R_s + \frac{1}{(j\omega)^\alpha C}, \quad (1)$$

where: R_s —equivalent series internal resistance (ESR), C —nominal capacitance, α —fractional order of the system.

These models should take into consideration the whole spectrum of phenomena occurring in supercapacitors, such as phase and magnitude resonance occurrence possibility and conditions, e.g. in series connection of RLC elements. Works [14–16] are devoted to the analysis of resonance phenomena in circuits with supercapacitors and in circuits containing both fractional order capacitance C_α and inductance L_β . Appropriately choosing the parameters α and β , in this circuit a positive or negative resistance, “clear” inductance or capacitance, short-circuit or free oscillation state can be obtained. This article is a development of the paper [16] and concerns an analysis of the phase and magnitude resonance effect in a series RLC circuit with supercapacitor. It includes the implementation of the fractional order model (1) and the experimental verification of the obtained results.

2 Model of the Series Resonance Circuit

Model of analyzed series RLC circuit is shown in Fig. 1:

Model from Fig. 1 takes into account the voltage source $u_s(t)$, which includes both constant component u_0 polarizing the supercapacitor, and the alternating component $u(t)$ of adjustable frequency. Therefore the voltage source $u_s(t)$ of the RLC circuit can be represented by relation:

$$u_s(t) = u_0 + u(t) = u_0 + \sqrt{2}|u| \sin(\omega t + \phi). \quad (2)$$

The analysis has been performed using the simple Westerlund–Ekstam model, given by formula (1). By adopting the above model, the total impedance of the series RLC circuit $Z(j\omega)$, seen from the source terminals, is given by the relation:

$$\begin{aligned} Z(j\omega) &= R + j\omega L + \frac{1}{(j\omega)^\alpha C} \\ &= R + \frac{1}{\omega^\alpha C} \cos\left(\frac{\alpha\pi}{2}\right) + j\left(\omega L - \frac{1}{\omega^\alpha C} \sin\left(\frac{\alpha\pi}{2}\right)\right), \end{aligned} \quad (3)$$

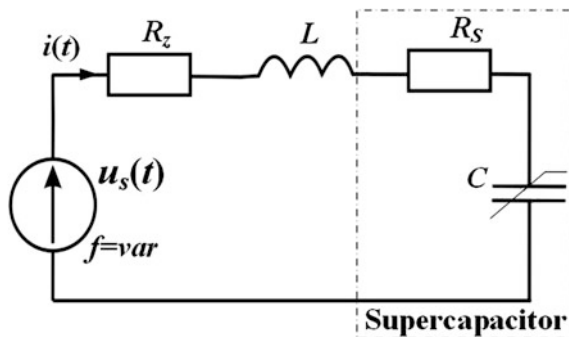


Fig. 1 Series RLC circuit with supercapacitor

where:

$$R = R_z + R_s. \tag{4}$$

The impedance module and phase of the series RLC circuit with supercapacitor are given as:

$$|Z(j\omega)| = \sqrt{R^2 + (\omega L)^2 + \frac{1}{\omega^\alpha C} \left(\frac{1}{\omega^\alpha C} + 2R \cos\left(\frac{\alpha\pi}{2}\right) - 2\omega L \sin\left(\frac{\alpha\pi}{2}\right) \right)}, \tag{5}$$

and:

$$\varphi(\omega) = \arctg \frac{\omega L - \frac{1}{\omega^\alpha C} \sin\left(\frac{\alpha\pi}{2}\right)}{R + \frac{1}{\omega^\alpha C} \cos\left(\frac{\alpha\pi}{2}\right)}. \tag{6}$$

Derived relations for impedance of the series RLC circuit with supercapacitor have been simulated and illustrated in graphs in Figs. 2 and 3.

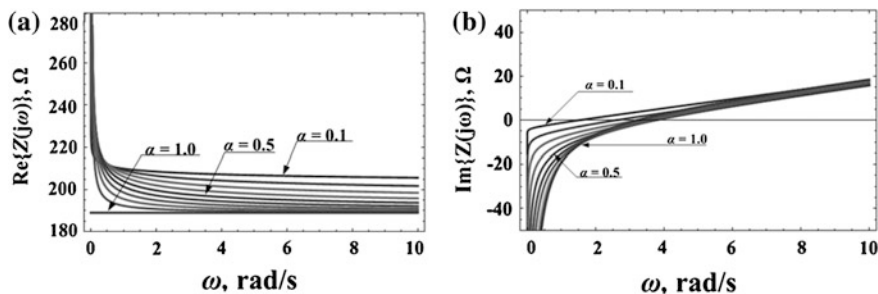


Fig. 2 Graph of the function based on the formula (3) for $\alpha \in (0, 1) >$: **a** $\text{Re}\{Z(j\omega)\}$, **b** $\text{Im}\{Z(j\omega)\}$

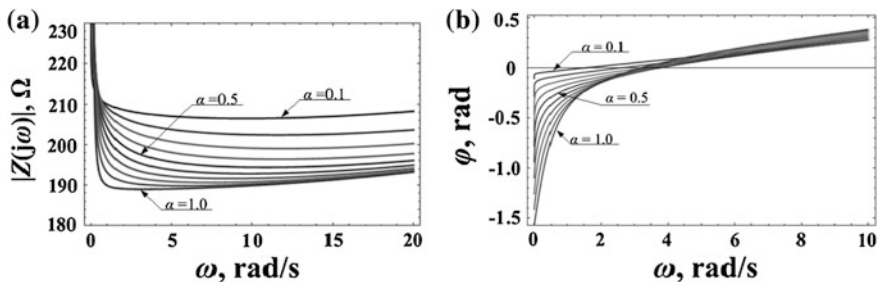
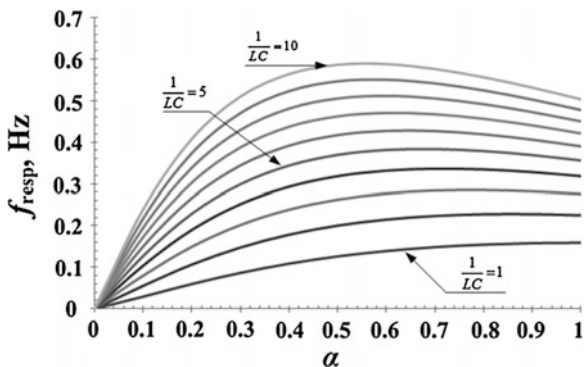


Fig. 3 Graph of the function based on the formula (5) and (6) for $\alpha \in (0, 1)$ **a** $|Z(j\omega)|$, **b** $\varphi(\omega)$, when $R_Z = 0$

Fig. 4 Graph of the function $f_{\text{resp}}(L, C, \alpha)$



Simulations were conducted for real parameters of the series RLC circuit: inductance $L = 2.07$ H, series resistance $R_Z = 143 \Omega$, and Panasonic supercapacitor with a nominal capacity $C = 0.047$ F and internal series resistance $R_S = 46 \Omega$ determined experimentally [17].

The phase resonance frequency for the discussed RLC circuit is determined from the general resonance condition $\text{Im}\{Z(j\omega)\} = 0$. It shall be:

$$f_{\text{resp}} = \frac{1}{2\pi} \sqrt{[\alpha + 1]} \left(\frac{1}{LC} \right) \sin\left(\frac{\alpha\pi}{2}\right). \quad (7)$$

The second phase resonance condition $\text{Im}\{Y(j\omega)\} = 0$ in the discussed circuit is also fulfilled for the same resonance frequency, as defined by formula (7). Analysis of the Eq. (7) indicates that when $\alpha < 1$, the phase resonance frequency f_{resp} is smaller than the phase resonance frequency of a classic series RLC circuit $f_{\text{res}} = (2\pi)^{-1} (\sqrt{LC})^{-1}$. The dependence of phase resonance frequency for different values of L , C and α is shown in Fig. 4.

The RMS value of current flowing in the series RLC branch with supercapacitor from Fig. 1, can be written as:

$$|I(j\omega)| = \frac{|U_0|}{\sqrt{R^2 + (\omega L)^2 + \frac{1}{\omega^2 C} \left(\frac{1}{\omega^2 C} + 2R \cos\left(\frac{\alpha\pi}{2}\right) - 2\omega L \sin\left(\frac{\alpha\pi}{2}\right) \right)}}. \quad (8)$$

The magnitude resonance condition for supplying circuit with a voltage source $|U_0|$:

$$\frac{\partial |I(j\omega)|}{\partial \omega} = 0, \quad (9)$$

provides the following equation:

$$\omega^{2(1+\alpha)}L^2C^2 + \omega^{1+\alpha}LC(\alpha - 1) \sin\left(\frac{\alpha\pi}{2}\right) - \omega^\alpha RC\alpha \cos\left(\frac{\alpha\pi}{2}\right) - \alpha = 0. \quad (10)$$

Equation (10) can be solved analytically if the series resistance in the circuit $R = 0$. Then the magnitude resonance frequency takes the form:

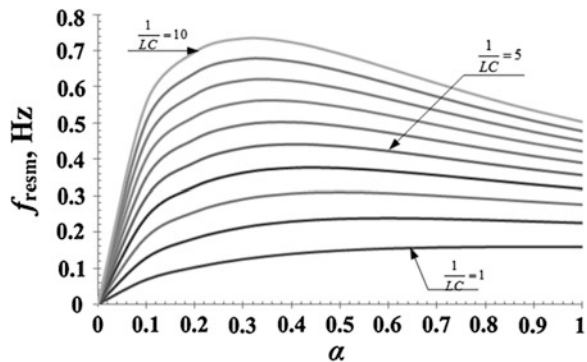
$$f_{resm} = \frac{1}{2\pi} \sqrt{[1 + \alpha] \frac{\sin\left(\frac{\alpha\pi}{2}\right)(1 - \alpha) + \sqrt{\sin^2\left(\frac{\alpha\pi}{2}\right)(\alpha - 1)^2 + 4\alpha}}{2LC}}. \quad (11)$$

In a particular case, for $\alpha = 1$, formula (11) takes the form:

$$f_{resm} = \frac{1}{2\pi} \frac{1}{\sqrt{LC}}, \quad (12)$$

which corresponds to the phase and magnitude resonance frequency of a classic series RLC circuit. The dependence of magnitude resonance frequency for different parameter values of L , C and α (for $R = 0$) are presented in Fig. 5.

Fig. 5 Graph of the function $f_{resm}(L, C, \alpha)$



In general case, for $R \neq 0$, formula (10) can be solved numerically for specified circuit parameters: R , L , C and known value of α . The simulation results for selected parameter values: $L = 2.07$ H, $R = 189 \Omega$, $C = 0.047$ F allow to conclude that the magnitude resonance in the analyzed circuit exists only when $\alpha = 1$. Last section of the article presents experimental studies and results of the resonance effect in a series RLC circuit with supercapacitor, which have been conducted to verify the results of theoretical and simulation analysis.

3 Experimental Results

Model of the experimental system for studying the resonance phenomenon in a series RLC circuit with supercapacitor from Fig. 1 is presented in Fig. 6.

Function generator served as a voltage source. The offset voltage was taken into account to polarize positively the supercapacitor with voltage $u_0 = 2.93$ V. Circuit parameters were selected the same as in the above simulations. Waveforms of voltages across the inductor and the supercapacitor, and current flowing in the circuit have been recorded. Measurements have been conducted for a wide range of frequency. Exemplary waveforms of these quantities are shown in Fig. 7.

Based on measurements, the current RMS value frequency characteristics has been determined and shown in Fig. 8.

No explicit maximum of RMS current value has been observed. The fractional order of used Panasonic supercapacitor has been approximately $\alpha \approx 0.35$. For this parameter α value, Eq. (10) shows that there is no magnitude resonance in this circuit. It can be noticed from the obtained characteristics, that the resonance phenomena in the series RLC circuit with supercapacitor differs from those in a classic series RLC circuit.

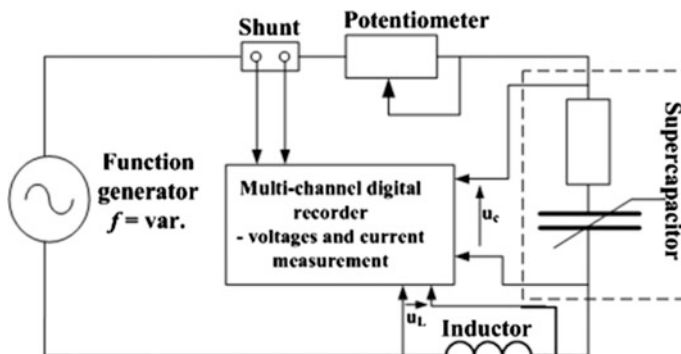


Fig. 6 Scheme of the experimental system for testing the resonance effect in a series RLC circuit with supercapacitor

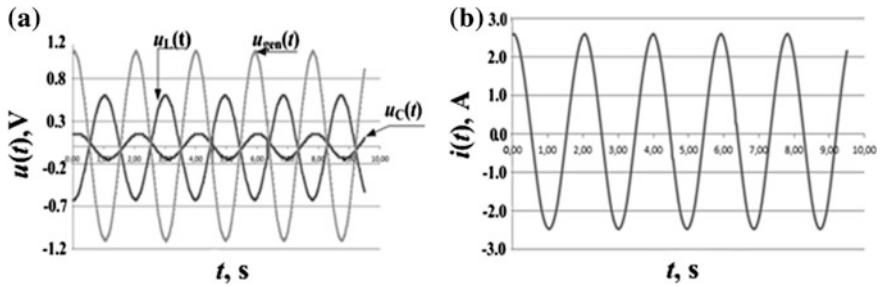
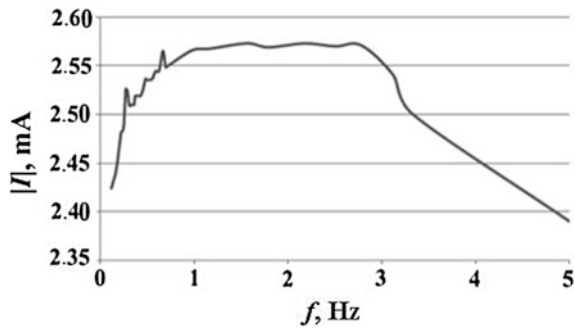


Fig. 7 Waveforms of **a** voltages across the generator $u_{gen}(t)$, inductor $u_L(t)$ and supercapacitor $u_C(t)$, and **b** current $i(t)$, in the considered series *RLC* circuit, for $f = 0.5$ Hz

Fig. 8 Obtained current RMS value characteristics in the considered series *RLC* circuit



4 Conclusion

The article presents results of the analysis of resonance phenomena in a simple series *RLC* circuit with supercapacitor. Basic fractional order mathematical model, firstly proposed by Westerlund and Ekstam, has been taken into calculations and simulations. The analysis shows that there are two resonance frequencies—phase and magnitude resonance frequency. Phase resonance frequency depends on three parameters: the inductance L , the capacitance C and fractional order of the supercapacitor α . Magnitude resonance frequency depends on the same parameters, but its determination requires numerical solution of nonlinear Eq. (10). When neglecting the resistance in the circuit, it is possible to obtain a closed solution of Eq. (10) (see formula (11)). For parameter $\alpha = 1$, all derived relations reduce to well-known formulas for a classic series *RLC* circuit. Performed experimental studies confirmed the theoretical and simulation analysis of the resonance phenomena in a simple series *RLC* circuit with supercapacitor.

References

1. Zhang Y (2009) Study of supercapacitor in the application of power electronics. *J WSEAS Trans CAS* 8(6):508–517
2. Juda Z (2008) Supercapacitors application in energy recovery system of an electric vehicle. *Tech J* 6:191–199 (Cracow University of Technology Publisher) (in Polish)
3. Kotz R, Carlen M (2000) Principles and applications of electrochemical capacitors. *Electrochimica Acta* 45:2483–2489 (Elsevier)
4. Wang Y (2008) Modeling of ultracapacitor short—term and long—term dynamic behavior—MS thesis, The University of Akron
5. Buller S, Karden E (2002) Modeling of dynamic behavior of supercapacitors using impedance spectroscopy. *IEEE Trans Indus Appl* 38(6):1622–1626
6. Shi L, Crow ML (2008) Comparison of ultracapacitor electric circuit models. In: Proceedings of IEEE power and energy society general meeting, Pittsburgh, USA, pp 1–6
7. Marie-Francoise J-N, Gualous H, Berthon A (2006) Supercapacitor thermal- and electrical-behaviour modeling using ANN. In: IEE Proceedings -Electric Power Applications, vol 153, No 2
8. Wang Y, Hartley T, Lorenzo C, Adams J (2010) Modeling ultracapacitors as fractional—order systems, new trends in nanotechnology and fractional calculus applications, USA, pp 257–262. Springer, Netherlands
9. Martin R, Quintana J, Ramos A, Nuez I (2008) Modeling electrochemical double layer capacitor, from classical to fractional impedance. In: The 14th IEEE medditeranean electrotechnical conference, Ajaccio, 4–7 May, pp 61–66
10. Dzieliński A, Sarwas G, Sierociuk D (2011) Comparison and validation of integer and fractional order ultracapacitor models. *Advances in Difference Equations*, Springer Open Journal (2011)
11. Sarwas G (2008) Modeling supercapacitors using fractional calculus, Institute of Electrotechnics Works, Issue 239, pp 17–28 (2008) (in Polish)
12. Westerlund S, Ekstam L (1994) Capacitor theory. *IEEE Trans Dielectr Electr Insul* 1 (5):826–839
13. Dzieliński A, Sierociuk D, Sarwas G (2009) Ultracapacitor parameters identification based on fractional order model. In: Proceedings of European control conference 2009, Budapest, Hungary, ECC'2009, 23–26 August 2009
14. Radwan AG, Salama KN (2011) Passive and active elements using fractional $L_{\beta}C_{\alpha}$ circuit. *IEEE Trans CAS* 58(10):2388–2397
15. Walczak J, Jakubowska A (2013) Phase resonance in series $RL_{\beta}C_{\alpha}$ circuit. In: Krivoklatu RK (ed) CPEE—AMTEE 2013, Czech Republic, part III—4, 4–6 Sept 2013
16. Walczak J, Jakubowska A (2013) Phase resonance in RLC circuit with ultracapacitor, XXXVI IC—SPETO, 22–25 May 2013, Ustroń, pp 47–48
17. Panasonic: Passive Components—Electric Double Layer Capacitor. <http://industrial.panasonic.com/EECS0HD473H>

Study the Quality of Global Neural Model with Regard to the Local Models of Dynamic Complex System

G. Draluś

Abstract In this paper a dynamic neural global model with regard to local models of dynamic complex systems is discussed. A dynamic complex system which consists of two nonlinear discrete time sub-systems is considered. As a global model with regard to local models multilayer neural networks in a dynamic structure with TDL are used. The global model with regard local models is composed of two simple models and two local models. One way to take account of local models in the global model is an appropriate definition of a synthetic quality criterion. The criterion of the whole model. That criterion contains coefficients which define the participation of the quality criteria of the global model and local models. The contribution of this work is study of the influence these coefficients on the global model quality. The influence is examined for a special learning algorithm for dynamic complex neural networks.

1 Introduction

Complex system is a wide term which can concern a different nature (technical, economical, others). We can take into consideration interactions between units of the system, large dimensionality, a large number of interacting entities or unusual behavior.

The concept of a complex system, we need to narrow down to the field of technical. So, the complex system means a dynamic input-output complex system. In a such complex system can be distinguished elementary objects, which have inputs and outputs. It can be also pointed out connections between these objects, that means, outputs of some objects are inputs of another object. A number of examples of such complex systems can be found in chemical industry, for example chemical process of sulphuric acid production [1] or ammonium nitrite process production [2].

G. Draluś (✉)

Department of Electrical and Computer Engineering Fundamentals,
Rzeszow University of Technology, Rzeszow, Poland
e-mail: gregor@prz.edu.pl

Mathematical methods allow us to model simple plants. However, modeling of dynamic complex systems is a very important and difficult problem so far has not been well enough solved. In complex systems, we do not have to deal with particular simple plants, but with dynamic or static simple plants which are interconnected into the complex system. Additionally, there exist numerous interactions between units of the complex system. One of the basic problems is taking into consideration the quality of the system model as a whole and providing a suitable approximation quality of particular subsystems.

Neural networks are investigated in an application to the identification and modeling complex process exhibiting nonlinearities and typical disturbances. Neural networks offer a flexible structure that can map arbitrary nonlinear functions, making them ideally suited for the modeling and control of complex, nonlinear systems [3]. They are particularly appropriate for multivariable applications, where they can readily characterize the interactions between different inputs and outputs. A further benefit is that the neural architecture is inherently parallel, and can be applied to real time implementations.

Actually, neural networks have many applications in modeling and control of systems. By ability to approximate nonlinear functions neural networks can be used for modeling and identification of simple and dynamic objects [4]. Models of simple objects that are part of a complex system are inadequate to modern science. Accurate and detailed models of complex systems are strongly expected today. One of the tools that is suitable for modeling of complex systems are just the neural networks [2, 5–7].

In this paper, a global neural model with regard to local models for modeling of dynamic complex systems is discussed. Multilayer neural network as a global model are used. The global model with regard to local model should take into account quality local models. So, adequate complex neural model should be built. The complex neural model is non-typical multilayer feedforward neural networks. In the global neural model can be indicated parts of the model which are adequate to the simple plants in the complex system. Also local models should be built.

The global neural model with regard to local models integrates two approaches to the modeling of complex systems. A local approach, where each element of complex system is separately modeled after decomposition of the complex system [8]. As well as, a global approach, in which a complex system is modeled as a whole [9].

2 Modeling of Dynamic Complex Systems

2.1 Description of Dynamic Complex Systems

An overwhelming majority objects in the real world are complex systems. The complex systems can be in various structures. An important case of complex system is a serial complex system (e.g. series connection of each unit of the complex system). There are known methods of modeling of dynamic simple objects. One of

them is the series-parallel model of identification [7]. The idea of the series-parallel model of identification of simple dynamic objects is developed in this paper for identification and modeling of complex dynamic systems.

In the series-parallel model, the present and past input signals and output signals are transmitted via tapped delay lines (TDL) into the input of the model. Using TDL allows us to build dynamic models. In the series-parallel model there is no feedback from the model, but from the object. In this case as a model the multilayer feed-forward neural networks can be used. What's more, multilayer neural networks can be learned according to the static backpropagation learning algorithms. We say that the model is in a learning mode. After the learning stage, if errors of modeling are sufficiently small, the feedback loop from the output object is switched to a feedback loop from the output of the model. Therefore, the series-parallel model is becoming the parallel model, with feedback loop from the output of the model. By such switching of the feedback loop, the dynamics of the model is obtained.

2.2 A Global Model Taking into Account Local Models

Let's consider a complex system which consists of R simple objects. (see Fig. 1). A global model of the complex system also consists of R simple models, denoted as $M_1..M_R$. A structure of global model corresponds to the structure of the complex system. In that model a previous simple model output is an input to the next simple model. However, a global model with regard to local models also includes local models. Thus, each simple object of the complex system has a suitable local model. The output of the simple object P_r is the input to the next local model M_{r+1} .

For such models special back propagation leaning algorithms should be developed. As a model a feedforward multilayer neural network with TDL is used.

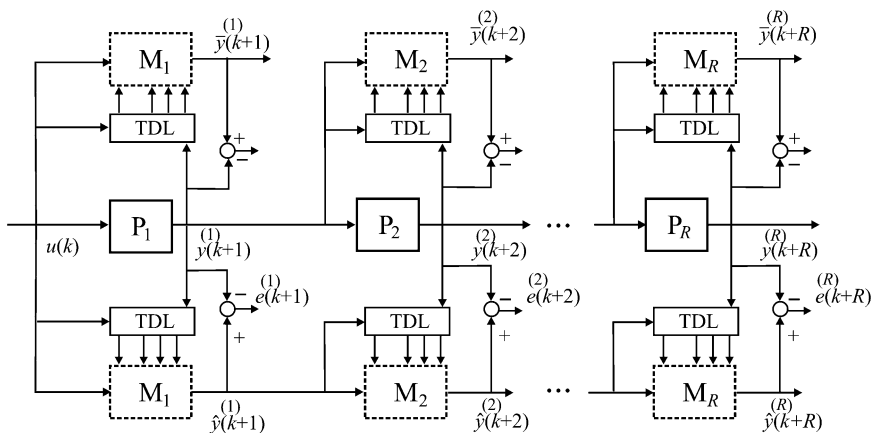


Fig. 1 A dynamic complex system and their dynamic global model with regard to local models using TDL

The complex dynamic global model consists of dynamic simple models, connected in series, like the complex system. Physically the simple model M_r and the local model M_r is the same model. They only differ in the input signals and way of learning. Local models will be used to build a global model taking into account the quality of local models.

In the global model with regard to local models, for each the r -th dynamic local model is defined a local quality criterion as the difference between the output $\bar{y}^{(r)}$ of the r -th local model and the output $y_j^{(r)}$ of the r -th simple object respectively, for all K ($k = 1, 2, \dots, K$) discrete time samples:

$$Q_d^{(r)}(\mathbf{w}^{(r)}) = \frac{1}{2} \sum_{k=1}^K \sum_{j=1}^{J_r} \left(\bar{y}_j^{(r)}(k+r) - y_j^{(r)}(k+r) \right)^2 \quad (1)$$

where: J_r is the number of outputs of the r -th simple object, $\mathbf{w}^{(r)}$ is the set of parameters of the r -th simple model and local model.

In the global approach, a global quality criterion is based on the difference between the output $\hat{y}^{(R)}$ of the last simple model M_R of the global model and the output $y^{(R)}$ of the last simple object P_R :

$$Q_G(\mathbf{W}) = \frac{1}{2} \sum_{k=1}^K \sum_{j=1}^{J_R} \left(\hat{y}_j^{(R)}(k+R) - y_j^{(R)}(k+R) \right)^2 \quad (2)$$

On the basis quality criterions $Q_d^{(r)}$ of local models and the global quality criterion Q_G was formulated a synthetic quality criterion of the global model with regard to the quality of local models:

$$Q_s(\mathbf{W}) = \alpha_0 Q_G(\mathbf{W}) + \sum_{r=1}^R \alpha_r \left(\bar{y}_j^{(r)}(k+r) - y_j^{(r)}(k+r) \right)^2 \quad (3)$$

where: R —number of parts of complex model, $\mathbf{W} = [\mathbf{w}^{(1)}, \mathbf{w}^{(2)}, \dots, \mathbf{w}^{(R)}]$ is the set of parameters (weights) of the global model divided into subsets of simple models and local models, $\alpha_r \in [0, 1]$ and $\sum_{r=1}^R \alpha_r = 1$ are weighted coefficients for the local models, α_0 is weighting coefficient of the global model, such that $0 \leq \alpha_0 \leq 1$.

2.3 Motivation

The weighting factors α_r determine an individual participation of the quality criteria $Q_d^{(r)}$ of local models in the synthetic quality criterion (3), while the weighting factor α_0 determines the participation the global quality index Q_G in the synthetic quality criterion (3).

The investigation of influence of these coefficients on the quality of the global model of a dynamic complex system is discussed. The investigation is performed on a complex system which is composed from two nonlinear dynamic simple plants (discreet time system).

The synthetic quality criterion Q_s is used to develop learning algorithms for complex neural models. Learning algorithms allow us to obtain the desired parameters of the complex neural model. The criterion Q_s contains weighting factors α , which determine the influence of local models quality and the global model quality on the final quality of the model. Now the question is, how to properly select the weighting factors α .

In case when complex system consists of two simple objects the synthetic criterion contains three elements, as follow:

$$Q_s(\mathbf{W}) = \alpha_0 \left(\hat{y}_j^{(2)}(k+2) - y_j^{(2)}(k+2) \right)^2 + \alpha_1 \left(\bar{y}_j^{(1)}(k+1) - y_j^{(1)}(k+1) \right)^2 + \alpha_2 \left(\bar{y}_j^{(2)}(k+2) - y_j^{(2)}(k+2) \right)^2 \quad (4)$$

The formula (4) contains two factors α_1 and α_2 for local models and one factor α_0 for the global model. For which the weighting factors α can be obtained an optimal global model? For which the weighting factors α can be obtained an appropriate quality of local models in the global model? How local models quality influence on the global model quality?

If should we select $\alpha_1 = 0.5$ and $\alpha_2 = 0.5$ e.g. and also which would mean an equal influence of both local models in the formula (4). What is the value of the factor α_0 should we choose, for example, whether you choose the factor α_0 equal to 0.5 or any other value.

The study is carried out in a such way that for determined neural architecture of the global model and under the same initial conditions, in constant amount of learning steps in each particular case we conduct a parameter model selection of coefficient for changing α_1 and α_2 participation in the global criterion (4), ranging from 0.001 to 0.999 (as per formula $\alpha_1 + \alpha_2 = 1$) for three case of the factor α_0 e.g. for: $\alpha_0 = 1$, $\alpha_0 = 0.5$, and $\alpha_0 = 0.1$.

2.4 A Complex Backpropagation Learning Algorithm for the Global Model with Regard to Local Models for Dynamic Complex System

To develop the learning algorithm for multilayer neural networks, of which dynamic global model with regard to local models is constructed, it was necessary to modify and adapt one of a gradient back propagation algorithms [10]. In this modification have to be considered that, the complex model consists of a static neural networks with tapped delay lines and feedback loop from the complex

system under the learning stage and feedback loop from the complex model when the model works. Additionally, it must be consider a quality of local models.

By minimize the synthetic quality criterion (3), a gradient learning algorithm can be developed. The change of the global model parameters e.g. the weights of neural networks as were achieved by gradient computation as the following:

$$\Delta w_{ji} = -\eta \frac{\partial Q_s(\mathbf{W})}{\partial w_{ji}} \quad (5)$$

where the factor η is a learning rate.

A new gradient algorithm can be adapted to the selected algorithm with the variable learning rate, which may be many times faster. Thus, on the basis of the calculation of the gradient of the formula (5) and the RPROP algorithm [11] was created a new neural network learning algorithm for a dynamic complex global model taking into account the local models called DGLM-RPROP learning algorithm.

This new algorithm can be used to find global model parameters including local models. The global model is composed of multilayer neural networks and delay lines, and creates a dynamic structure.

The DGLM-RPROP algorithm allow us calculate change of the weights in particular layers of the neural network:

- in output layer:

$$\begin{aligned} \Delta w_{ji}^{(R),M} = & -\eta_{ji}^p \sum_{k=1}^K f'(z_j^{M,k+R}) \left(a_0 \left(\hat{y}_j^{(R)}(k+R) - y_j^{(R)}(k+R) \right) \right. \\ & \left. + a_R \left(\bar{y}_j^{(R)}(k+R) - y_j^{(R)}(k+R) \right) \right) \hat{u}_i^{M-1}(k+R-1) \end{aligned} \quad (6)$$

- in hidden layers:

$$\Delta w_{ji}^{(r),m} = -\eta_{ji}^p \sum_{k=1}^K f'(z_j^{m,k+r}) \sum_{l=1}^{I_{m+1}} \delta_l^{(r),m+1,k+r} w_{lj}^{(r),m+1} \hat{u}_i^{m-1}(k+r-1) \quad (7)$$

- in *additional* (or ‘binding’) hidden layers, e.g. output layers of simple models in the global complex model:

$$\Delta w_{ji}^{(r),m} = -\eta_{ji}^p \sum_{k=1}^K f'(z_j^{m,k+r}) \left(\sum_{l=1}^{I_{m+1}} \delta_l^{(r+1),m+1,k+r} w_{lj}^{(r+1),m+1} \right. \\ \left. + a_r \left(\bar{y}_j^{(r)}(k+r) - y_j^{(r)}(k+r) \right) \right) \hat{u}_i^{m-1}(k+r-1) \quad (8)$$

where: η^p is an adaptive learning rate at the p -th epoch of learning, m is a number of layer of a neural network, $z_j^{m,k}$ is the input signal of activation function f of j -th neuron, $\hat{u}_j^{m,k}$ is the output signal of j -th neuron for k -th sample.

The adaptive learning rate η^p at p -th epoch of learning is calculated as follow:

$$\eta_{ji}^p = \begin{cases} \min\left(a \cdot \eta_{ji}^{(p-1)}, \eta_{\max}^p\right) & \text{for } S_{ji}^p \cdot S_{ji}^{(p-1)} > 0 \\ \max\left(b \cdot \eta_{ji}^{(p-1)}, \eta_{\min}^p\right) & \text{for } S_{ji}^p \cdot S_{ji}^{(p-1)} < 0 \\ \eta_{ji}^{(p-1)} & \text{for } S_{ji}^p \cdot S_{ji}^{(p-1)} = 0 \end{cases} \quad (9)$$

where: $S_{ji}^p = \frac{\partial Q_s(\mathbf{W}(p))}{\partial w_{ji}}$; $a = 1.2$; $b = 0.5$; $\eta_{\max} = 50$; $\eta_{\min} = 10^{-6}$.

3 Simulation Study

3.1 Complex Dynamic System and Dynamic Neural Model

To the simulation a dynamic nonlinear complex system which consists of two dynamic nonlinear simple objects connected in series was used. Both simple objects (denotes as P_1 and P_2 , see Fig. 2) of the complex system are described by the second-order nonlinear difference equations.

The output of the first simple object P_1 is described by the following non-linear difference equation:

$$y^{(1)}(k+1) = f_1\left(y^{(1)}(k), y^{(1)}(k-1), y^{(1)}(k-2), u(k), u(k-1)\right) \quad (10)$$

The output of the second simple object P_2 is described by the following non-linear formula:

$$y^{(2)}(k+2) = f_2\left(y^{(2)}(k+1), y^{(2)}(k), y^{(2)}(k-1), y^{(1)}(k+1), y^{(1)}(k)\right) \quad (11)$$

The nonlinear functions f_1 in formula (10) of the first simple object P_1 is given by the following formula [6]:

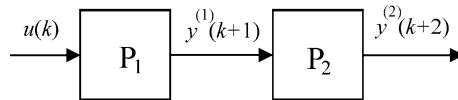


Fig. 2 A two-parts dynamic (discrete time) complex system

$$f_1(x_1, x_2, x_3, x_4, x_5) = \frac{x_1 x_2 x_3 x_5 (x_3 - 1) + x_4}{1 + x_2^2 + x_3^2} \quad (12)$$

The second nonlinear functions f_2 in formula (11) is given by the formula:

$$f_2(v_1, v_2, v_3, v_4, v_5) = \frac{v_2 v_3 v_5 (v_1 - 1) + v_4}{1 + 2v_1^2} \quad (13)$$

As a global model of the considered complex system given by formulas (10) and (11) the 6-layer feedforward neural network with TDL was used (see Fig. 3).

The neural network has the following structure: one external input, 5 inputs neurons; 20 neurons in the first hidden layer; 10 neurons in the second hidden layer; 1 neuron in the third layer called “binding” layer; 20 and 10 neurons in the fourth and the fifth layer, respectively; 1 linear neuron in the sixth (output) layer of the complex model (shortly, 1(5)-20-10-1(5)-20-10-1). The left part of the global model is the first simple model (see Fig. 3) and is also the first local model. The right part of the global model is the second simple model and it is also the second local model. Neurons in the third layer and the sixth layer have linear transfer functions. Neurons in layer number: 1, 2, 4 and 5 have hyperbolic tangent transfer functions.

In the complex neural model (see Fig. 3) there exist non typical hidden layers called ‘binding’ hidden layers. The ‘binding’ layer is the layer which connects simple models in the complex model. The output of this layer is suitable to the output of the suitable simple object. In this model the ‘binding’ hidden layer is the

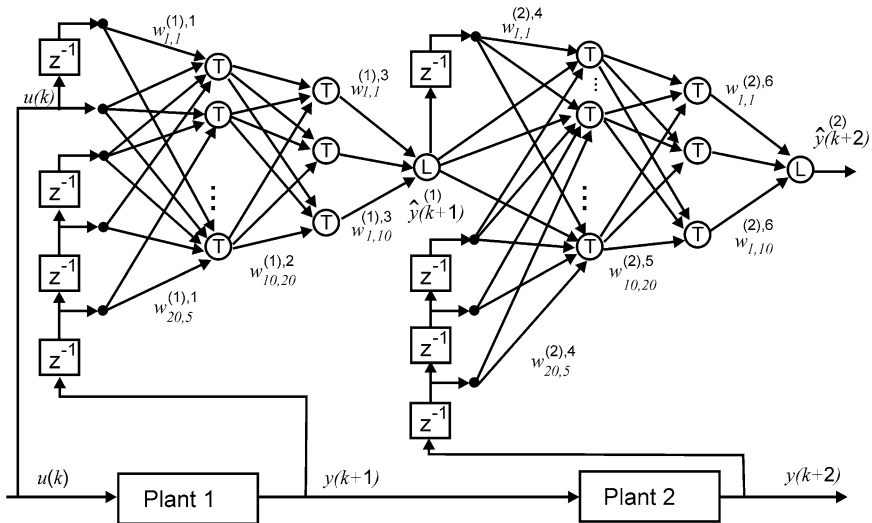


Fig. 3 The neural network as the global model of the complex system (series-parallel model in learning mode)

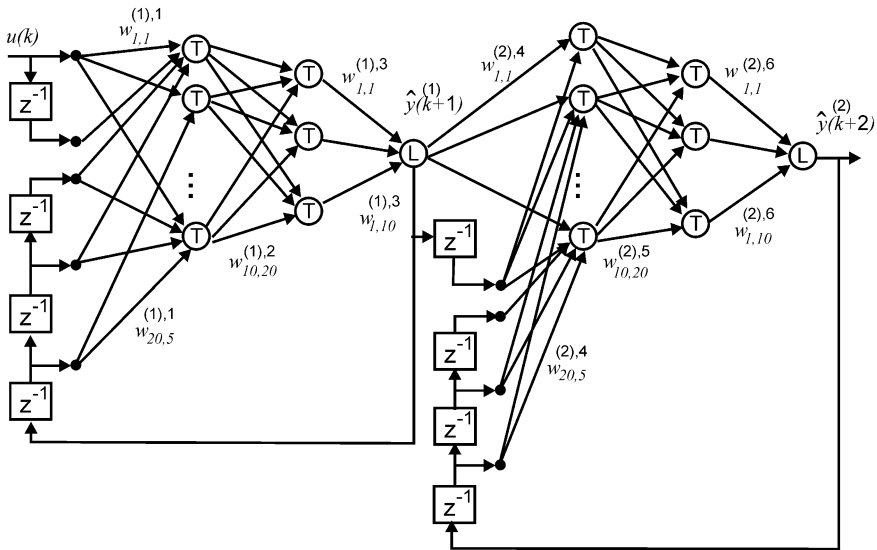


Fig. 4 The neural network as the global model of the complex system (the parallel model in the work mode)

third layer (as such 1(5)). The architecture of the model in the learning mode allows us to use the complex learning algorithms for the multilayer neural networks.

At the end of the learning process (when the model parameters have been adjusted) the global model is switched from the learning mode to the work mode. In the learning model the neural model is the series-parallel model (see Fig. 3). In the work mode the neural model is the parallel model (see Fig. 4). The neural model uses one delay elements in the external input line and three delay elements in the output line. In such kind of architecture, the model inputs depend on the neural model delayed values. This architecture of the model allows us to approximate the true dynamic of the complex system.

3.2 Data and Results of Simulation

For the purpose of simulations, the training data were random uniformly distributed in the interval $[-1, 1]$ according to Nguyen-Widrow rule [10], and contain 101 points. Initial weights were randomly generated and were the same for all simulations. The preparation of training data using past samples of input and output signals must be done using TDL.

For simulation study the DGLM-RPROP learning algorithms was used. The global model with take into account local models was trained for 500 epochs. For the complex system and the global model the test signal is given by the following formula:

$$\begin{aligned} u(k) &= \sin(2\pi k/250) && \text{for } k \leq 250 \\ u(k) &= 0.8 \sin(2\pi k/250) + 0.2 \sin(2\pi k/25) && \text{for } 250 < k \leq 500 \end{aligned} \quad (14)$$

The results of the simulations are presented in numerical and graphic form for both the learning mode and the work mode of the neural model also for the training data and the test data.

Simulations were performed for three selected values of factor α_0 , that is, for factors: $\alpha_0 = 0.1$, $\alpha_0 = 0.5$, $\alpha_0 = 1$. Simulations were carried out so that, for fixed value of factor α_0 , the other two factors (i.e. α_1 and α_2) from Eq. (4) varied according to the following formula $\alpha_1 + \alpha_2 = 1$.

In order to additional and independent assessment of model quality an additional performance index, called relative percentage error (called RPE) was defined for r -th local model:

$$\text{RPE}^{(r)} = \frac{\sum_{k=1}^K |\bar{y}^{(r)}(k) - y^{(r)}(k)|}{\sum_{k=1}^K |y^{(r)}(k)|} \cdot 100 \% \quad (15)$$

The performance indices $Q_d^{(1)}$ and $Q_d^{(2)}$, the global performance index Q_G and the synthetic quality criterion Q_s after 500 epochs of learning for DGLM-RPROP algorithm for the training data for the series-parallel model and for the parallel model are shown in Table 1, for factor $\alpha_0 = 1$. In Table 2 are shown the performance indices for the training data for series-parallel model, and the parallel model, for factor $\alpha_0 = 0.5$. For factor $\alpha_0 = 0.1$, the performance indices for the training data are shown in Table 3.

Table 1 Values of performance indices for the training data for factor $\alpha_0 = 1$

α_1	$Q_d^{(1)}$	$Q_d^{(2)}$	Q_G	Q_s	$Q_d^{(1)}$	$Q_d^{(2)}$	Q_G	Q_s
	Series-parallel model				Parallel model			
0.001	606	3.58	2.56	6.75	356	8.15	8.94	17.4
0.01	0.0549	0.0584	0.0426	0.106	0.0662	0.138	0.241	0.384
0.1	0.0311	0.0115	0.00675	0.0203	0.0390	0.0129	0.0112	0.0267
0.2	0.0344	0.0134	0.0107	0.0283	0.0389	0.0147	0.0147	0.0343
0.3	0.0264	0.0123	0.00709	0.0263	0.0334	0.0150	0.0124	0.0329
0.4	0.0242	0.00941	0.00758	0.0229	0.0286	0.00958	0.0109	0.0281
0.5	0.0182	0.0117	0.00515	0.0201	0.0180	0.0122	0.00712	0.0222
0.6	0.0221	0.0138	0.00932	0.0281	0.0240	0.0145	0.0107	0.0309
0.7	0.0224	0.0124	0.00572	0.0247	0.0276	0.0135	0.0101	0.0335
0.8	0.0249	0.0185	0.00881	0.0324	0.0261	0.0195	0.0103	0.0350
0.9	0.0190	0.0135	0.00434	0.0228	0.0212	0.0148	0.00642	0.0270
0.99	0.0166	0.0170	0.00566	0.0223	0.0195	0.0186	0.00783	0.0273
0.999	0.0184	0.0157	0.00728	0.0257	0.0212	0.0185	0.0108	0.0320

Table 2 Values of performance indices for the training data for factor $\alpha_0 = 0.5$

α_1	$Q_d^{(1)}$	$Q_d^{(2)}$	Q_G	Q_s	$Q_d^{(1)}$	$Q_d^{(2)}$	Q_G	Q_s
	Series-parallel model				Parallel model			
0.001	508	2.17	6.58	5.97	528	3.65	27.4	17.90
0.01	0.0356	0.00756	0.0109	0.0133	0.0367	0.00988	0.0165	0.0184
0.1	0.0378	0.00700	0.0131	0.0166	0.0407	0.00904	0.0162	0.0203
0.2	0.0201	0.00666	0.00676	0.0127	0.0200	0.00656	0.00761	0.0130
0.3	0.0220	0.00861	0.00958	0.0174	0.0226	0.00926	0.00990	0.0182
0.4	0.0223	0.0105	0.00876	0.0196	0.0222	0.0120	0.0103	0.0212
0.5	0.0139	0.00623	0.00522	0.0127	0.0150	0.00710	0.00904	0.0160
0.6	0.0176	0.00690	0.00522	0.0159	0.0175	0.00739	0.00711	0.0170
0.7	0.0159	0.00967	0.00781	0.0179	0.0153	0.0102	0.00874	0.0181
0.8	0.0159	0.0129	0.00638	0.0185	0.0174	0.0147	0.00898	0.0213
0.9	0.0276	0.0158	0.0109	0.0318	0.0302	0.0167	0.0131	0.0354
0.99	0.0232	0.0149	0.00926	0.0278	0.0259	0.0150	0.00898	0.0304
0.999	0.0165	0.0131	0.00548	0.0193	0.0180	0.0135	0.00642	0.0212

Table 3 Values of performance indices for the training data for factor $\alpha_0 = 0.1$

α_1	$Q_d^{(1)}$	$Q_d^{(2)}$	Q_G	Q_s	$Q_d^{(1)}$	$Q_d^{(2)}$	Q_G	Q_s
	Series-parallel model				Parallel model			
0.001	0.0250	0.00471	0.00970	0.00570	0.0257	0.00600	0.0121	0.00723
0.01	0.0269	0.00426	0.0138	0.00587	0.0264	0.00496	0.0155	0.00669
0.1	0.0140	0.00384	0.00855	0.00571	0.0131	0.00466	0.00812	0.00632
0.2	0.0151	0.00348	0.0104	0.00684	0.0183	0.00505	0.0129	0.00898
0.3	0.0145	0.00351	0.00765	0.00758	0.0167	0.00485	0.00936	0.00936
0.4	0.0178	0.00478	0.0125	0.0112	0.0181	0.00641	0.0138	0.0125
0.5	0.0175	0.00444	0.0132	0.0127	0.0199	0.00705	0.0156	0.0150
0.6	0.0163	0.00495	0.0131	0.0131	0.0172	0.00553	0.0126	0.0138
0.7	0.0186	0.00483	0.0124	0.0157	0.0200	0.00728	0.0157	0.0177
0.8	0.0234	0.00730	0.0166	0.0218	0.0263	0.00903	0.0205	0.0249
0.9	0.0105	0.00470	0.00971	0.0107	0.0121	0.00528	0.00850	0.0123
0.99	0.0172	0.0112	0.00971	0.0181	0.0196	0.0117	0.0114	0.0207
0.999	0.0152	0.0159	0.00815	0.0160	0.0146	0.0174	0.0105	0.0157

The quality criteria $Q_d^{(1)}$ and $Q_d^{(2)}$ of local models the global quality criterion Q_G and he synthetic quality criterion Q_s after 500 epochs of learning for DGLM-RPROP algorithm for the test data for the series-parallel model and for the parallel model are shown in Table 4, for the factor $\alpha_0 = 1$. In Table 5 are shown the performance indices for the test data for the factor $\alpha_0 = 0.5$. For the factor $\alpha_0 = 0.1$, the performance indices for the test data are shown in Table 6.

The RPE indices after 500 epochs of learning for DGLM-RPROP algorithm for the training data for the series-parallel model and for the parallel model are shown in Table 7 for the factor $\alpha_0 = 1$, for the factor $\alpha_0 = 0.5$ in Table 8. For factor $\alpha_0 = 0.1$, the RPE indices for the training data are shown in Table 9.

Table 4 Values of performance indices for the test data for factor $\alpha_0 = 1$

α_1	$Q_d^{(1)}$	$Q_d^{(2)}$	Q_G	Q_s	$Q_d^{(1)}$	$Q_d^{(2)}$	Q_G	Q_s
	Series-parallel model				Parallel model			
0.001	379	7.06	29.6	40.4	349	51.9	35.8	91.1
0.01	9.72	1.83	9.25	11.2	12.9	1.55	7.68	9.34
0.1	4.73	0.167	1.75	2.38	4.03	0.181	0.822	1.39
0.2	2.31	0.285	1.36	2.06	1.26	0.639	0.212	1.06
0.3	6.37	0.185	2.30	4.34	2.79	0.370	0.388	1.48
0.4	2.21	0.0396	0.721	1.63	1.34	0.122	0.216	0.826
0.5	0.872	0.017	0.245	0.735	0.654	0.0965	0.106	0.482
0.6	1.62	0.0351	0.616	1.61	0.771	0.0568	0.227	0.712
0.7	2.58	0.245	1.86	3.74	1.47	0.0969	0.837	1.89
0.8	9.76	0.472	3.33	11.2	7.41	0.681	0.970	7.04
0.9	1.34	0.589	1.42	2.73	0.977	0.258	0.620	1.52
0.99	2.18	0.164	0.839	3.00	1.10	0.123	0.272	1.36
0.999	1.53	0.201	0.434	1.96	1.05	0.161	0.225	1.27

Table 5 Values of performance indices for the test data for factor $\alpha_0 = 0.5$

α_1	$Q_d^{(1)}$	$Q_d^{(2)}$	Q_G	Q_s	$Q_d^{(1)}$	$Q_d^{(2)}$	Q_G	Q_s
	Series-parallel model				Parallel model			
0.001	1760	15.8	92.5	63.8	63.8	7.74	128	75.0
0.01	1.88	0.194	0.494	0.458	0.458	0.338	0.200	0.448
0.1	3.60	0.301	0.658	0.961	0.961	0.302	0.408	0.770
0.2	3.81	0.432	1.19	1.70	1.70	0.276	0.532	0.926
0.3	3.72	0.273	1.13	1.87	1.87	0.214	0.249	0.639
0.4	2.43	0.142	1.54	1.83	1.83	0.0715	0.400	0.695
0.5	2.69	0.0770	0.677	1.72	1.72	0.0810	0.250	0.847
0.6	2.08	0.273	0.598	1.65	1.65	0.237	0.166	0.750
0.7	2.38	0.110	0.980	2.19	2.19	0.0873	0.334	0.825
0.8	2.48	0.163	0.867	2.45	2.45	0.118	0.295	1.21
0.9	1.64	0.190	0.613	1.80	1.80	0.149	0.290	1.01
0.99	7.36	0.152	1.26	7.92	7.92	0.240	0.538	4.43
0.999	2.64	0.0970	1.05	3.16	3.16	0.0448	0.418	1.54

The RPE indices for the test data for the series-parallel model and for the parallel model are shown in Table 10 for the factor $\alpha_0 = 1$. For the factor $\alpha_0 = 0.5$ the RPE indices are shown in Table 11 and for factor $\alpha_0 = 0.1$ in Table 12.

Table 6 Values of performance indices for the test data for factor $\alpha_0 = 0.1$

α_1	$Q_d^{(1)}$	$Q_d^{(2)}$	Q_G	Q_s	$Q_d^{(1)}$	$Q_d^{(2)}$	Q_G	Q_s
	Series-parallel model				Parallel model			
0.001	4.73	0.132	0.132	0.275	3.23	0.299	0.467	0.349
0.01	3.69	0.183	0.183	0.398	1.86	0.0747	0.498	0.142
0.1	1.34	0.252	0.252	0.401	0.639	0.152	0.162	0.217
0.2	2.48	0.500	0.500	0.976	2.40	0.317	0.852	0.819
0.3	2.53	0.379	0.379	1.11	1.65	0.193	0.325	0.664
0.4	1.74	0.0680	0.0680	0.763	0.856	0.0747	0.0786	0.395
0.5	1.15	0.317	0.317	0.788	0.826	0.210	0.381	0.556
0.6	1.41	0.294	0.294	1.03	0.959	0.158	0.290	0.668
0.7	1.55	0.343	0.343	1.23	0.841	0.237	0.223	0.682
0.8	1.84	0.489	0.489	1.67	0.928	0.306	0.466	0.850
0.9	4.64	0.375	0.375	4.33	2.48	0.211	0.423	2.30
0.99	0.922	0.137	0.137	0.955	0.603	0.0678	0.202	0.618
0.999	2.25	0.0845	0.0845	2.32	1.24	0.129	0.286	1.27

Table 7 RPE indices values for the training data for factor $\alpha_0 = 1$

α_1	RPE ⁽¹⁾	RPE ⁽²⁾	RPE _G ⁽²⁾	RPE ⁽¹⁾	RPE ⁽²⁾	RPE _G ⁽²⁾
	Series-parallel model			Parallel model		
0.001	570	37.6	37.5	411	62.1	72.5
0.01	13.1	5.76	5.15	15.3	8.87	11.5
0.1	3.35	2.62	1.99	3.83	2.75	2.72
0.2	3.96	2.92	2.45	4.21	3.12	2.93
0.3	3.35	1.96	2.69	3.86	2.91	2.73
0.4	3.22	2.34	2.07	3.39	2.45	2.66
0.5	2.89	2.83	1.82	2.86	2.88	2.12
0.6	3.14	2.71	2.32	3.29	2.74	2.51
0.7	3.12	2.72	1.65	3.50	2.83	2.44
0.8	3.26	3.33	2.26	3.22	3.42	2.54
0.9	2.93	3.01	1.55	3.04	3.10	1.93
0.99	2.79	3.28	1.87	3.00	3.37	2.15
0.999	2.78	3.14	2.11	3.03	3.29	2.60

Table 8 RPE indices values for the training data for factor $\alpha_0 = 0.5$

α_1	RPE ⁽¹⁾	RPE ⁽²⁾	RPE _G ⁽²⁾	RPE ⁽¹⁾	RPE ⁽²⁾	RPE _G ⁽²⁾
	Series-parallel model			Parallel model		
0.001	511	33.3	59.3	583	47.5	134
0.01	3.84	2.18	2.65	3.92	2.52	3.19
0.1	4.11	2.16	2.77	4.24	2.37	3.18
0.2	3.04	2.05	1.98	2.88	2.06	2.13
0.3	3.07	2.33	2.42	3.09	2.36	2.52
0.4	2.93	2.35	2.21	2.98	2.46	2.52
0.5	2.36	1.94	1.74	2.46	2.05	2.33
0.6	2.81	2.19	1.72	2.72	2.31	2.03
0.7	2.55	2.38	2.17	2.45	2.41	2.28
0.8	2.59	2.71	1.97	2.82	2.89	2.39
0.9	3.40	3.25	2.63	3.61	3.33	2.95
0.99	3.03	2.95	2.42	3.27	2.98	2.39
0.999	2.63	2.86	1.79	2.77	2.88	1.93

Table 9 RPE indices values for the training data for factor $\alpha_0 = 0.1$

α_1	RPE ⁽¹⁾	RPE ⁽²⁾	RPE _G ⁽²⁾	RPE ⁽¹⁾	RPE ⁽²⁾	RPE _G ⁽²⁾
	Series-parallel model			Parallel model		
0.001	3.20	3.20	2.42	3.26	1.85	2.76
0.01	3.31	3.31	2.90	3.26	1.68	3.12
0.1	2.47	2.47	2.32	2.36	1.64	2.21
0.2	2.44	2.44	2.38	2.73	1.70	2.73
0.3	2.44	2.44	2.12	2.69	1.64	2.42
0.4	2.74	2.74	2.86	2.77	1.91	3.01
0.5	2.75	2.75	2.66	2.91	2.00	2.85
0.6	2.55	2.55	2.81	2.63	1.87	2.71
0.7	2.73	2.73	2.68	2.82	2.06	2.96
0.8	3.02	3.02	3.19	3.32	2.31	3.54
0.9	2.11	2.11	2.02	2.30	1.74	2.26
0.99	2.66	2.66	2.50	3.02	2.60	2.45
0.999	2.60	2.60	2.13	2.52	3.44	2.58

Table 10 RPE indices values for the test data for factor $\alpha_0 = 1$

α_1	RPE ⁽¹⁾	RPE ⁽²⁾	RPE _G ⁽²⁾	RPE ⁽¹⁾	RPE ⁽²⁾	RPE _G ⁽²⁾
	Series-parallel model			Parallel model		
0.001	555	25.4	62.7	571	65.2	76.3
0.01	23.5	16.2	32.8	28.1	14.9	30.4
0.1	15.8	4.52	15.2	14.5	4.50	10.9
0.2	11.6	7.23	14.2	9.03	6.18	9.55
0.3	18.5	5.11	16.7	13.1	7.18	7.60
0.4	10.0	2.25	9.78	8.00	3.96	5.35
0.5	7.97	3.99	5.64	7.08	3.90	3.84
0.6	9.97	2.46	9.39	7.22	2.77	5.28
0.7	11.1	6.65	16.2	8.61	3.81	10.8
0.8	21.0	8.85	20.3	18.9	9.74	12.3
0.9	8.56	8.34	15.8	7.26	6.08	10.5
0.99	10.1	5.30	10.8	7.56	4.65	6.55
0.999	8.45	5.91	8.34	7.25	5.27	6.10

Table 11 RPE indices values for the test data for factor $\alpha_0 = 0.5$

α_1	RPE ⁽¹⁾	RPE ⁽²⁾	RPE _G ⁽²⁾	RPE ⁽¹⁾	RPE ⁽²⁾	RPE _G ⁽²⁾
	Series-parallel model			Parallel model		
0.001	386	49.7	108	552	31.5	133
0.01	11.3	5.65	8.33	9.83	7.74	5.10
0.1	15.0	7.09	8.98	13.5	6.90	6.77
0.2	14.5	8.61	12.8	11.6	7.07	8.90
0.3	12.3	7.20	10.7	7.92	6.12	5.74
0.4	11.3	5.10	13.5	8.15	3.41	7.35
0.5	12.2	3.48	9.23	9.34	3.58	5.77
0.6	11.3	6.64	9.06	8.11	6.41	5.40
0.7	11.3	4.11	11.6	7.50	3.79	6.62
0.8	11.9	5.19	10.9	9.00	4.12	6.03
0.9	9.58	5.75	9.92	7.56	4.93	6.45
0.99	17.4	5.14	13.2	14.0	5.53	8.65
0.999	9.97	3.82	12.4	7.52	2.64	8.13

Table 12 RPE indices values for the test data for factor $\alpha_0 = 0.1$

α_1	RPE ⁽¹⁾	RPE ⁽²⁾	RPE _G ⁽²⁾	RPE ⁽¹⁾	RPE ⁽²⁾	RPE _G ⁽²⁾
	Series-parallel model			Parallel model		
0.001	14.7	4.86	14.2	13.5	5.64	8.84
0.01	15.9	4.44	16.9	11.6	3.64	9.29
0.1	9.42	6.21	6.48	6.73	4.90	4.29
0.2	12.5	8.15	11.2	12.7	7.13	9.87
0.3	11.2	7.55	9.29	9.50	5.53	6.01
0.4	9.40	3.16	5.71	6.90	3.41	3.25
0.5	8.24	7.30	9.37	7.05	5.74	7.64
0.6	8.87	6.46	9.91	7.40	4.61	6.34
0.7	9.96	7.92	7.73	7.79	6.43	5.52
0.8	9.80	7.55	13.2	7.13	6.48	8.70
0.9	15.1	7.26	13.6	11.6	6.11	8.19
0.99	7.78	4.50	8.12	6.21	3.12	5.52
0.999	12.4	3.66	10.9	9.38	4.41	6.41

3.3 Analysis of an Influence of Factor α_0 on the Quality of the Model

The increase of factor α_0 means the increase of participation of the global quality criterion Q_G in the synthetic quality criterion Q_s .

3.3.1 Analysis for the Training Data

The increase in factor α_0 generally results in an increase in values of the quality criterion $Q_d^{(1)}$, for the most values of factor α_1 in the series-parallel model. Similarly, in the parallel model, the increase in the value of factor α_0 results in an increase quality criterion $Q_d^{(1)}$, but with some exceptions (see Fig. 5).

In the series-parallel model, the increase in factor α_0 results in an increase in values of the quality criterion $Q_d^{(2)}$. This can be seen more clearly. Similarly, in the parallel model, the increase in factor α_0 results in an increase quality criterion $Q_d^{(2)}$, also more clearly (see Fig. 6).

It is difficult to assess the influence of factor α_0 on the quality criterion Q_G . The quality criterion Q_G values depends on both the value of factor α_0 and also the value of factor α_1 . However, in the series-parallel model, the quality criterion Q_G reaches the lowest values for factor $\alpha_0 = 1$, and reaches the higher values for factor $\alpha_0 = 0.1$ (see Fig. 7). In the parallel model, is also difficult to point clearly the influence of factor α_0 on the quality criterion Q_G . For the most values of α_1 the criterion Q_G reaches the lowest values for factor $\alpha_0 = 0.5$ (see Fig. 7).

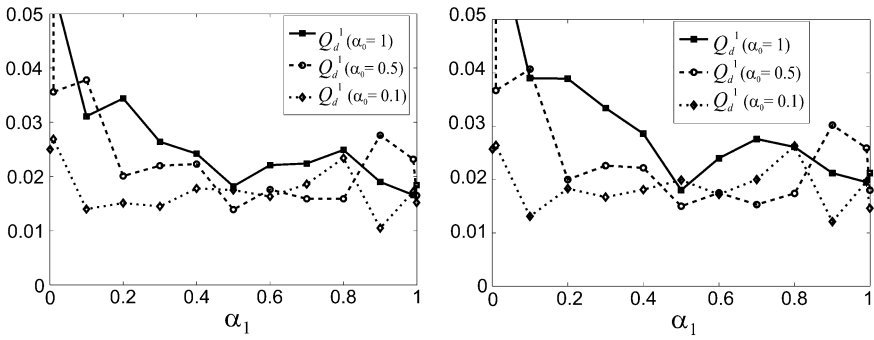


Fig. 5 Performance index $Q_d^{(1)}$ for the training data in the series-parallel model (the left chart) and the parallel model (the right chart)

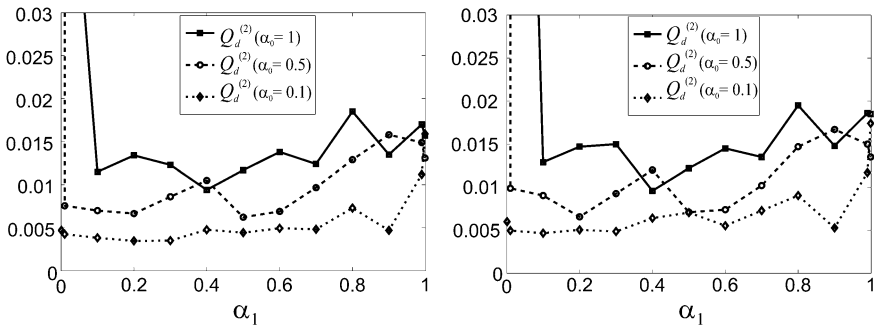


Fig. 6 Performance index $Q_d^{(2)}$ for the training data in the series-parallel model (the left chart) and in the parallel model (the right chart)

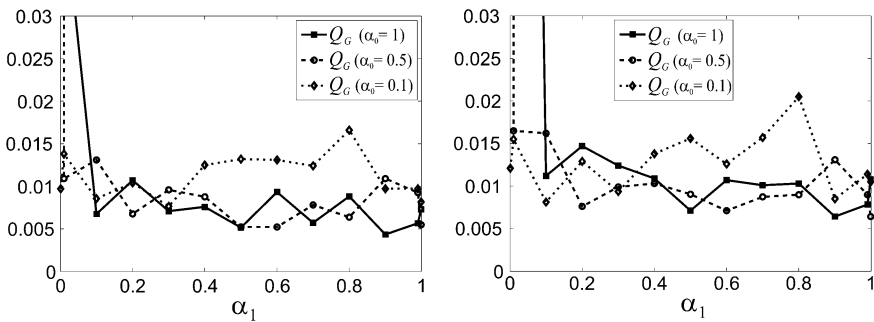


Fig. 7 Performance index Q_G for the training data in the series-parallel model (the left chart) and in the parallel model (the right chart)

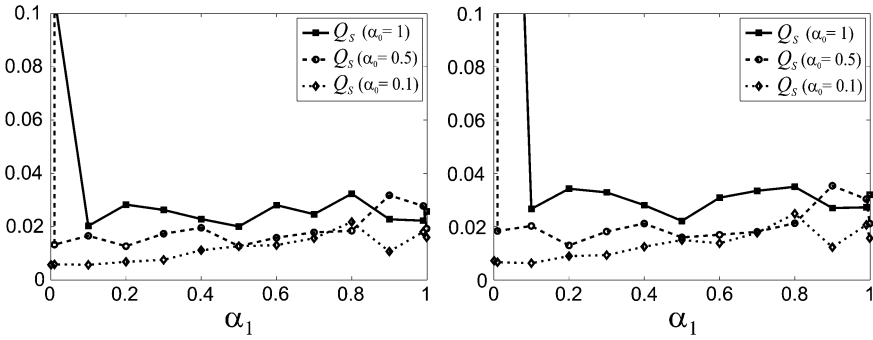


Fig. 8 Performance index Q_s for the training data in the series-parallel model (*the left chart*) and in the parallel model (*the right chart*)

In the series-parallel model, the increase in factor α_0 causes an increase in values of the quality criterion Q_s (unlike the indices $Q_d^{(1)}$ and $Q_d^{(2)}$, see Fig. 8). Similarly, in the parallel model, the increase in factor α_0 causes an increase quality criterion Q_s (see Fig. 8).

3.3.2 Analysis for the Test Data

The increase in factor α_0 generally results in an increase in values of the quality criterion $Q_d^{(1)}$, for the most values of factor α_1 in the series-parallel model but with some exceptions (see Fig. 9). Similarly, in the parallel model, the increase in the value of factor α_0 results in an increase the quality criterion $Q_d^{(1)}$ but also with some exceptions, see Fig. 9). For example, for factor $\alpha_1 = 0.5$ the quality criterion $Q_d^{(1)}$ achieves the lowest values for factor $\alpha_0 = 1$ both in the series-parallel and the

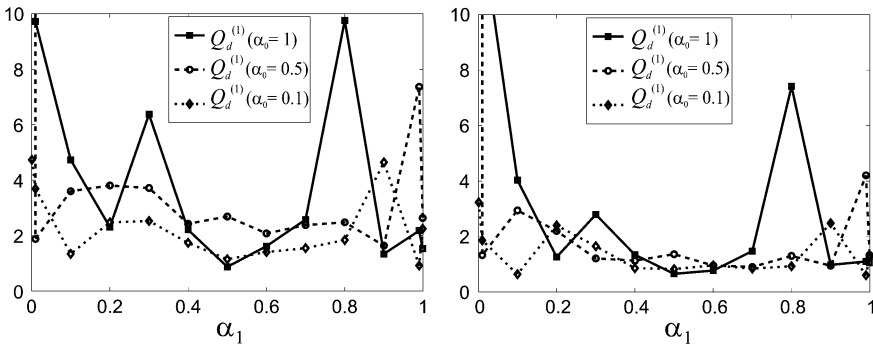


Fig. 9 Performance index $Q_d^{(1)}$ for the test data in the series-parallel model (*the left chart*) and in the parallel model (*the right chart*)

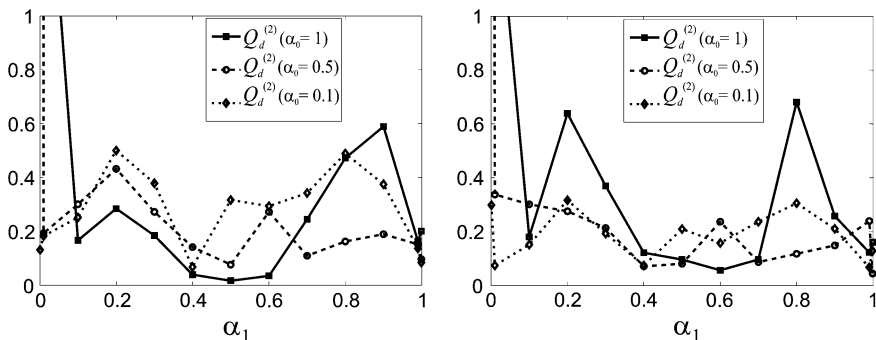


Fig. 10 Performance index $Q_d^{(2)}$ for the test data in the series-parallel model (the left chart) and in the parallel model (the right chart)

parallel model. For the test data there are large hesitation quality criterion $Q_d^{(1)}$. Level values of the quality criterion $Q_d^{(1)}$ for the test data is about two order higher than that for the training data.

In the series-parallel model the increase in factor α_0 causes an decrease in values of the quality criterion $Q_d^{(2)}$, but only in terms of factor α_1 from 0.1 to 0.7 (see Fig. 10). For small and large values of factor α_1 (that is $\alpha_1 = 0.01$, $\alpha_1 = 0.99$) the increase in factor α_0 causes an increase in values of the quality criterion $Q_d^{(2)}$. In the parallel model, the increase in factor α_0 has a variable effect on the quality criterion $Q_d^{(2)}$, and also depends on the values of α_1 factor (see Fig. 10). Level values of the quality criterion $Q_d^{(2)}$ for the test data is about one order higher than that for the training data. For the test data there are large hesitation quality criterion $Q_d^{(2)}$.

In the series-parallel model, the increase in factor α_0 results in an increase in values of the quality criterion Q_G , but with some exceptions, for example, for factor $\alpha_1 = 0.5$, (see Fig. 11). In the parallel model, the increase in factor α_0 has a variable effect on the quality criterion Q_G (see Fig. 11). However, for factor $\alpha_0 = 1$, the quality criterion Q_G mostly reaches the larger values than in other cases of the factor α_0 . Level values of the quality criterion Q_G for the test data is about two orders higher than that of the training data in the series-parallel model. However in the parallel model level values of quality criterion Q_G for the test data is about one order higher than that for the training data.

The increase in factor α_0 results in an increase in values of the quality criterion Q_s , in the series-parallel model but with a few exceptions (see Fig. 12). Similarly, in the parallel model, the increase in the value of factor α_0 results in an increase of the quality criterion Q_s but also with a few exceptions (see Fig. 12). Level values of the quality criterion Q_s for the test data is about two orders higher than that of the training data.

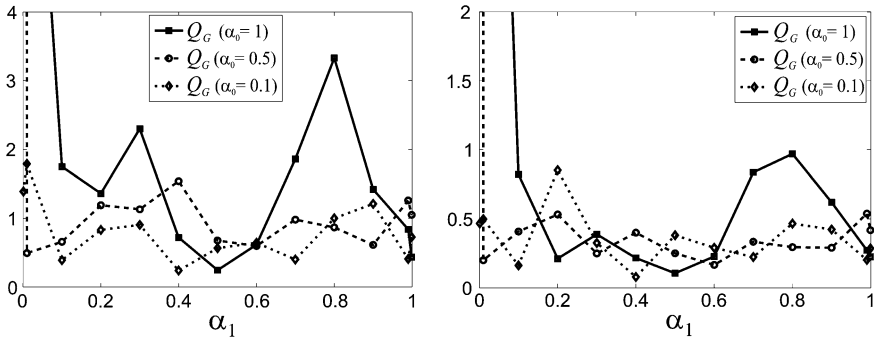


Fig. 11 Performance index Q_G for the test data in the series-parallel model (*the left chart*) and in the parallel model (*the right chart*)

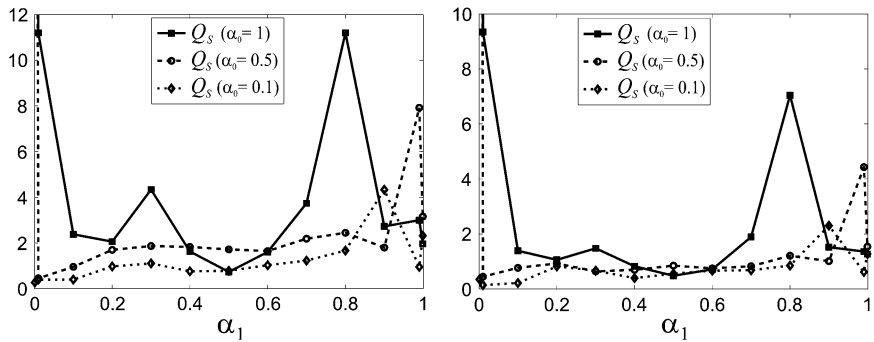


Fig. 12 Performance index Q_S for the test data in the series-parallel model (*the left chart*) and in the parallel model (*the right chart*)

3.4 Analysis of an Influence of Factor α_1 on the Quality of the Model

The weighting factors α_1 and α_2 determine an individual participation of the quality criteria $Q_d^{(r)}$ of local models in the synthetic quality criterion (4). For simplicity of analysis, the influence of factors α_1 and α_2 will be only refer to the factor α_1 , but we must remember that $\alpha_1 + \alpha_2 = 1$.

3.4.1 Analysis for the Training Data

Analyzing obtained in simulations results it can be stated that the increase of factor α_1 causes an oscillating decrease in the value of the of quality index $Q_d^{(1)}$ of the first local model in the series-parallel model. The index $Q_d^{(1)}$ reaches the minimum for

the maximum value of factor $\alpha_1 = 0.999$ for factor $\alpha_0 = 1$, but for factor $\alpha_0 = 0.1$ the index $Q_d^{(1)}$ reaches the minimum for factor $\alpha_1 = 0.99$ (see Fig. 5). Similarly, in the parallel model, the increase of factor α_1 causes an oscillating decrease in the index $Q_d^{(1)}$.

The increase of factor α_1 causes an oscillating increase in the value of the local quality criterion $Q_d^{(2)}$ in both the series-parallel model, and in the parallel model (see Fig. 6). However, for small values of factor α_1 ($\alpha_1 = 0.01$), and for factors $\alpha_0 = 1$ and $\alpha_0 = 0.5$ the quality index $Q_d^{(2)}$ reaches high values, and falls off quickly.

In both the series-parallel model, and in the parallel model, the increase of factor α_1 causes an oscillating decrease in the value of the global quality criterion Q_G (see Fig. 7). However, there is an exception for factor $\alpha_0 = 0.1$ while the increase of factor α_1 causes an oscillating decrease and increase of the index Q_G .

Influence of factor α_1 on the synthetic quality criterion Q_s must be considered individually for each value of factor α_0 . In both the series-parallel model, and in the parallel model, In the case of factor $\alpha_0 = 1$, the increase of factor α_1 causes a rapid decrease in the value of the synthetic quality criterion Q_s , and then an oscillating decrease in values of the index Q_s (see Fig. 8). In case of factor $\alpha_0 = 0.5$, the increase of factor α_1 causes a rapid decrease in the value of the synthetic quality criterion Q_s , and then an oscillating increase in the value of the index Q_s (see Fig. 8).

3.4.2 Analysis for the Test Data

The increase of factor α_1 causes an oscillating course of the quality index $Q_d^{(1)}$ in the series-parallel model. The index $Q_d^{(1)}$ reaches the global minimum at the point $\alpha_1 = 0.5$ for factor $\alpha_0 = 1$, at the point $\alpha_1 = 0.9$ for factor $\alpha_0 = 0.5$, at the point $\alpha_1 = 0.99$ for factor $\alpha_0 = 0.1$. Similarly, in the parallel model, the increase of factor α_1 causes an oscillating course of the index $Q_d^{(1)}$.

The increase of factor α_1 causes an oscillating course of the quality index $Q_d^{(2)}$ in the series-parallel model. The index $Q_d^{(2)}$ reaches the global minimum at the point $\alpha_1 = 0.5$ for factor $\alpha_0 = 1$, at the point $\alpha_1 = 0.5$ for factor $\alpha_0 = 0.5$, at the point $\alpha_1 = 0.4$ for factor $\alpha_0 = 0.1$. Similarly, in the parallel model, the increase of factor α_1 causes an oscillating course of the index $Q_d^{(2)}$. The index $Q_d^{(2)}$ reaches the global minimum at the point $\alpha_1 = 0.6$ for factor $\alpha_0 = 1$, at the point $\alpha_1 = 0.4$ for factor $\alpha_0 = 0.5$, at the point $\alpha_1 = 0.99$ for factor $\alpha_0 = 0.1$. This means that the quality criterion $Q_d^{(2)}$ reaches a global minimum in the middle of the range of factor α_1 .

In the series-parallel model, the increase of factor α_1 causes an oscillating course of the quality index Q_G . The index Q_G reaches the global minimum at the point $\alpha_1 = 0.5$ for factor $\alpha_0 = 1$, at the point $\alpha_1 = 0.6$ for factor $\alpha_0 = 0.5$, at the point

$\alpha_1 = 0.4$ for factor $\alpha_0 = 0.1$. Similarly, in the parallel model, the increase of factor α_1 causes an oscillating course of the index Q_G .

In the series-parallel model, the increase of factor α_1 causes an oscillating course of the quality index Q_s for factor $\alpha_0 = 1$, and an increase of the index Q_s for factors $\alpha_0 = 0.5$ and $\alpha_0 = 0.1$. Similarly, in the parallel model, an increase of factor α_1 causes an oscillating increase of the index Q_s . The index Q_s reaches the global minimum at the point $\alpha_1 = 0.5$ for factor $\alpha_0 = 1$, at the point $\alpha_1 = 0.01$ for factor $\alpha_0 = 0.5$, and at the point $\alpha_1 = 0.01$ for factor $\alpha_0 = 0.1$.

3.5 Analysis of an Influence of Factor α_0 and Factor α_1 on the Quality of the Mode—The RPE Index

3.5.1 Analysis for the Training Data

For the training data, in the series-parallel model the increase in factor α_0 causes an increase in index $RPE^{(1)}$ of the first local model, but with some exceptions (see Fig. 13). Similarly, in the parallel model, the increase in factor α_0 causes an increase in the index $RPE^{(1)}$ but also with some exceptions (see Fig. 13).

In the series-parallel model the increase of the factor α_1 causes an oscillating decrease in the index $RPE^{(1)}$ only for factor $\alpha_0=1$ (see Fig. 13). For factors $\alpha_0 = 0.5$ and $\alpha_0 = 0.1$, the increase of factor α_1 causes an oscillating course of the index $RPE^{(1)}$. In the parallel model the increase of factor α_1 causes an oscillating course of the index $RPE^{(1)}$ (see Fig. 13). The index $RPE^{(1)}$ reaches the global minimum at the point $\alpha_1 = 0.999$ when factor $\alpha_0 = 1$, at the point $\alpha_1 = 0.5$ when factor $\alpha_0 = 0.5$, and at the point $\alpha_1 = 0.9$ when factor $\alpha_0 = 0.1$. The level of errors determined by the index $RPE^{(1)}$ in the series-parallel model is the same as in the parallel model.

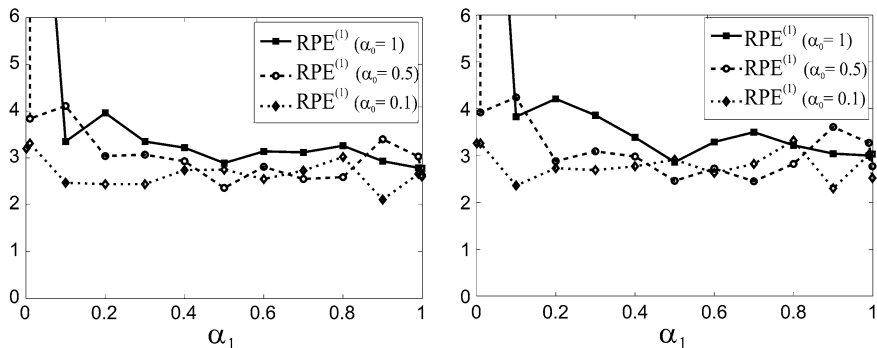


Fig. 13 The $RPE^{(1)}$ index for the training data in the series-parallel model (the left chart) and in the parallel model (the right chart)

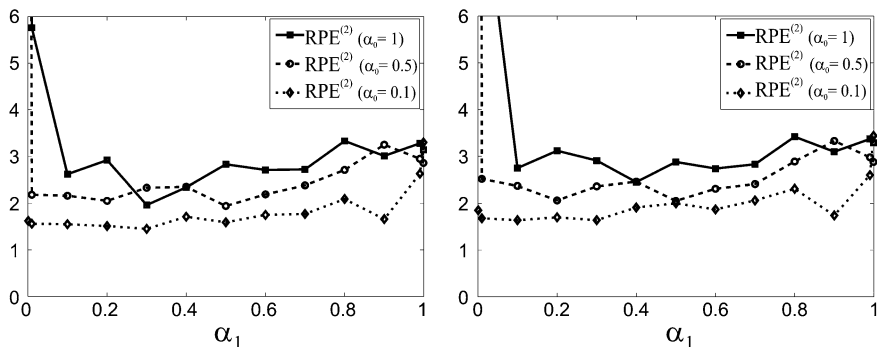


Fig. 14 The $RPE^{(2)}$ index for the training data in the series-parallel model (*the left chart*) and in the parallel model (*the right chart*)

In both the series-parallel model and in the parallel model, the increase in factor α_0 causes an increase in the index $RPE^{(2)}$ of the second local model, but only with three exceptions (see Fig. 14). In both the series-parallel model, and in the parallel model, in case of factors $\alpha_0 = 1$ and $\alpha_0 = 0.5$, the increase of the factor α_1 causes a rapid decrease in the index $RPE^{(2)}$, and then on oscillating increase in the value of the index $RPE^{(2)}$ (see Fig. 14). In the case of factor $\alpha_0 = 0.1$, the increase of factor α_1 causes an oscillating increase in the index $RPE^{(2)}$.

The index $RPE_G^{(2)}$ determines the quality of the global model based on the formula (15) and based on the global model output $\hat{y}^{(2)}$ and the output of the complex system $y^{(2)}$.

It is difficult to assess the influence of factor α_0 on the index $RPE_G^{(2)}$. The index $RPE_G^{(2)}$ strong depends on both the values of factor α_0 and factor α_1 . In both the series-parallel model and the parallel model, for small values of factor α_1 , the index $RPE_G^{(2)}$ reaches lowest values when factor $\alpha_0 = 0.1$ (see Fig. 15). However, for

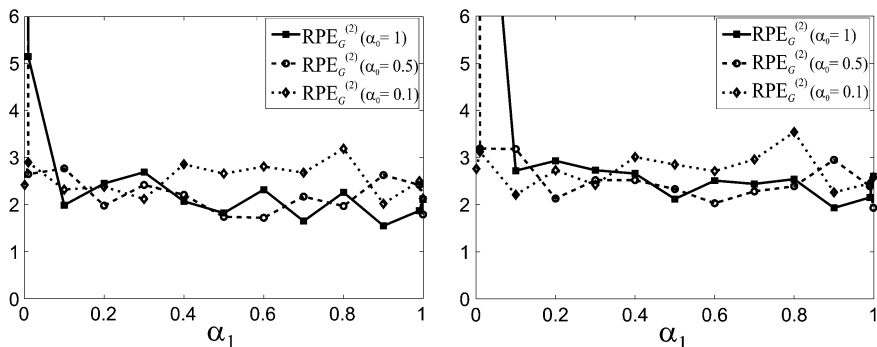


Fig. 15 The $RPE_G^{(2)}$ index for the training data in the series-parallel model (*the left chart*) and in the parallel model (*the right chart*)

values of factor α_1 larger than 0.4, the index $RPE_G^{(2)}$ reaches lowest values when factors $\alpha_0 = 1$ or $\alpha_0 = 0.5$. In both models the increase of factor α_1 causes an oscillating decrease in the index $RPE_G^{(2)}$. However, the index $RPE_G^{(2)}$ reaches the global minimum at the point $\alpha_1 = 0.9$ when factor $\alpha_0 = 1$.

3.5.2 Analysis for the Test Data

For the test data, in the series-parallel model the increase in factor α_0 causes an increase in the index $RPE^{(1)}$ but with some exceptions (see Fig. 16). Similarly, in the parallel model, the increase in factor α_0 causes a increase in index $RPE^{(1)}$ but with a few exceptions. In the series-parallel model the increase of factor α_1 causes an oscillating decrease in the index $RPE^{(1)}$. In the parallel model, the increase of factor α_1 also causes an oscillating course of the index $RPE^{(1)}$ (see Fig. 16). The level of errors determined by the index $RPE^{(1)}$ in the series-parallel model is higher than in the parallel model, for the test data. But, in both models the values of the index $RPE^{(1)}$ for the test data are about three times higher than for the training data.

In the series-parallel model the increase in factor α_0 causes a decrease in index $RPE^{(2)}$ when factor α_1 is in the range from 0.1 to 0.6. (see Fig. 17). In the parallel model, the it is difficult to assess the impact of factor α_0 on the index $RPE^{(2)}$ (see Fig. 17).

For the test data, in both the series-parallel model and in the parallel model the increase of factor α_1 causes an oscillating course of the index $RPE^{(2)}$. The index $RPE^{(2)}$ reaches the minimum in the middle range of the value of factor α_1 . In both models the values of the index $RPE^{(2)}$ for the test data are about two times higher than for the training data.

For the test data, in the series-parallel model the increase in factor α_0 causes an increase in index $RPE_G^{(2)}$ but with some exceptions (see Fig. 18). Similarly, in the parallel model, the increase in factor α_0 usually causes an increase in index $RPE_G^{(2)}$

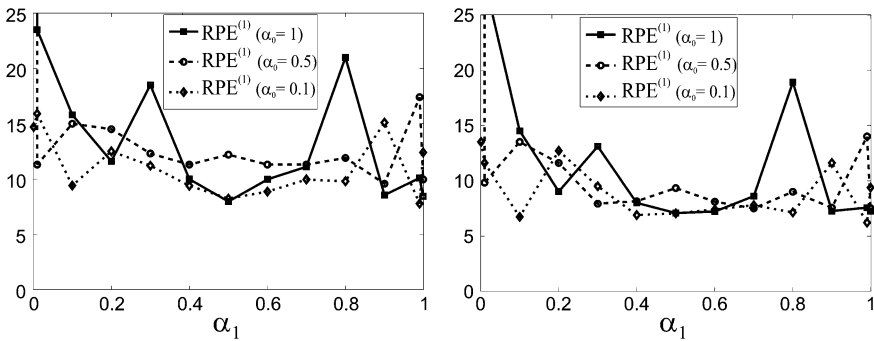


Fig. 16 The $RPE^{(1)}$ index for the test data in the series-parallel model (the left chart) and in the parallel model (the right chart)

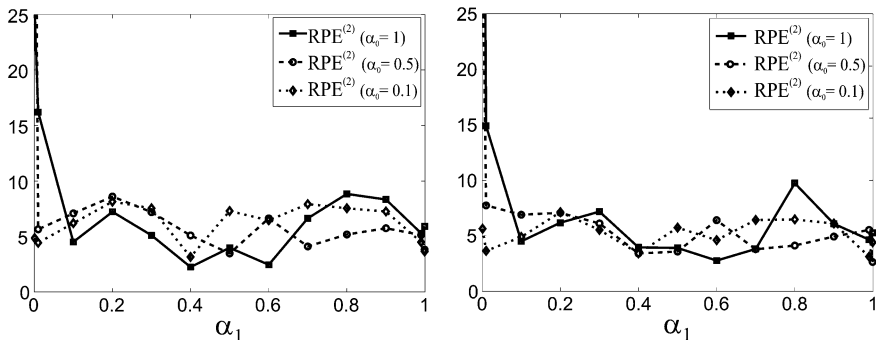


Fig. 17 The $RPE^{(2)}$ index for the test data in the series-parallel model (*the left chart*) and in the parallel model (*the right chart*)

(see Fig. 18). In both the series-parallel model and in the parallel model the increase of the factor α_1 causes an oscillating course of the index $RPE_G^{(2)}$. The index $RPE_G^{(2)}$ reaches its minimum in the middle range of the value of factor α_1 .

The level of errors determined by the index $RPE_G^{(2)}$ in the series-parallel model is somewhat higher than in the parallel model for the test data. In the series-parallel model the values of the index $RPE_G^{(2)}$ for the test data are about four times higher than for the training data. However, in the series-parallel model the values of the index $RPE_G^{(2)}$ for the test data are about two times higher than for the training data.

For the training data, for factor $\alpha_0 = 1$, the index $RPE_G^{(2)}$ usually is smaller than the index $RPE^{(2)}$ both in the series-parallel model and in the parallel model. For factor $\alpha_0 = 0.5$, the index $RPE_G^{(2)}$ is smaller than the index $RPE^{(2)}$ in both models but for values of factor α_1 larger than 0.5. For factor $\alpha_0 = 0.1$, the index $RPE_G^{(2)}$ is usually bigger than the index $RPE^{(2)}$ in both models.

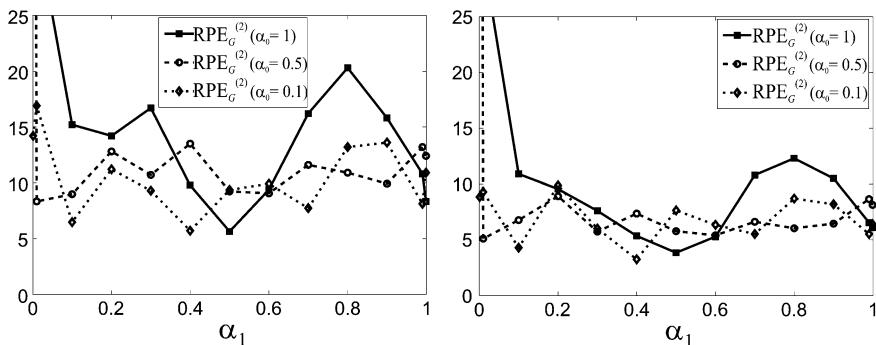


Fig. 18 The $RPE_G^{(2)}$ index for the test data in the series-parallel model (*the left chart*) and in the parallel model (*the right chart*)

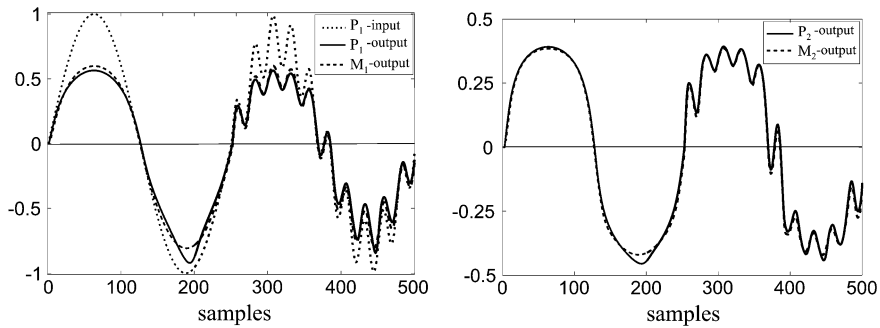


Fig. 19 The first simple object (P_1) and first simple model (M_1) outputs (*the left chart*) and second simple object (P_2) and second simple model (M_2) outputs (*the right chart*) for the test data

For the test data, the index $RPE_G^{(2)}$ usually is bigger than the index $RPE^{(2)}$ both in the series-parallel model and in the parallel model.

In Fig. 19 are shown the output signals of first simple plant and simple model, and the output signals of second simple plant and simple model for the training data for factors: $\alpha_0 = 1$, $\alpha_1 = 0.5$ and $\alpha_2 = 0.5$.

4 Conclusions

The global model with regard to quality local models of the dynamic complex system was presented. The dynamic complex system which consists of two non-linear discrete time sub-systems was considered. Multilayer neural networks were introduced as a models of the complex systems. The influence of factors α of the synthetic quality criterion on the models quality was investigated. The results of the investigation were shown for the new learning algorithm (i.e. DGLM-RPROP algorithm), and both the training and the test data.

One of the important conclusions is that the quality of the series-parallel model is on the same level as the parallel model both for the training data and for the test data. This fact confirms the assumption of this method of modeling that when the model parameters are good enough, it is allowed to switch the feedback loop form the object to the model output, so that the model is parallel, with little threat to the stability of the model.

The results of the simulation show relationships in the complex model, what is the quality of the global model and quality of the local models as a function of the factors α . Results of simulations show sufficiently the influence of the factor α_0 , and separately factors α_1 and α_2 on the global model quality as well as on local models quality. Knowing the results, e.g. how α_0 and α_1 coefficients influence on the quality of the model can be consciously selected values of factors α_0 , α_1 and α_2 , to obtain the model good enough and/or to obtain local models good enough. Under that conscious

selection we may better control the learning process. Thus, we may faster and more certainly achieve the required quality of the global model and local models.

This algorithms and architecture of the global neural models allow us to adjust the parameters of the global model effectively. The presented approach of modeling is useful for computer control systems of complex systems.

References

1. Osowski S (2007) Modeling and simulation of dynamic systems and processes. Warsaw University of Technology Publishing House, Warsaw
2. Drałus G, Świątek J (2009) Static and dynamic complex models: comparison and application to chemical systems. *Kybernetes: Int J Syst Cybern Emerald* 38(7/8):1198–1215
3. Hunt KJ, Sbarbaro D, Zbikowski R, Gawthrop PJ (1992) Neural networks for control systems: a survey. *Automatica* 28(8):s.1083–s.1112
4. Hornik K (1989) Multilayer feedforward networks are universal approximators. *Neural Networks* 2:359–366
5. Dahleh MA, Venkatesh S (1997) System Identification of Complex Systems; Problem Formulation and Results. *IEEE Proc* 3:2441–2446
6. Drapała J, Świątek J (2006) Modeling of dynamic complex systems by neural networks. In: Proceedings of 18th international conference on systems engineering, Coventry University, England, pp 109–112
7. Narendra KS, Parthasarathy K (1990) Identification and control of dynamic systems using neural network. *IEEE Trans Neural Networks* 1(1):4–27
8. Drałus G (2004) Modeling of dynamic nonlinear complex systems using neural networks. In: Proceedings of the 15th “International Conference on Systems Science”, Oficyna Wydawnicza Politechniki Wrocławskiej, Wrocław, vol III, pp 87–96
9. Drałus G (2012) Complex neural models of dynamic complex systems: study of the global quality criterion and results, human: computer systems interaction, AISC 99, Part II. Springer, Berlin, pp 477–495; (ISSN 1867–5662)
10. Gupta MM, Jin L, Homma N (2003) Static and Dynamic Neural Networks: From Fundamentals to Advanced Theory. IEEE Press, Wiley- Interscience, A John Wiley & Sons, Inc
11. Riedmiller M, Braun H (1992) RPROP—a fast adaptive learning algorithm. Technical Report, University Karlsruhe

Transient Analysis of Interstitial Microwave Hyperthermia Using Multi-slot Coaxial Antenna

Piotr Gas

Abstract This paper outlines the impact of the number of air gaps appearing in the microwave antenna structure on the transient temperature distribution in the human tissue. From the mathematical point of view this problem can be described by coupling the wave equation in sinusoidal steady-state and the bioheat transfer equation in transient form with the adequate boundary-initial conditions. Moreover, the Cole–Cole model has been used to evaluate the complex relative permittivity of the human tissues for the antenna operating frequency of 2.45 GHz. At the stage of numerical realization the finite element method has been applied. The computational results in case of the 2D analysis of single-, double- and triple-slot antennas are presented and compared to each other for several tissues typically treated during interstitial microwave hyperthermia.

1 Introduction

The attempts to use heat in medicine have been well known since the ancient times but their popularity has been observed in recent years due to the rapid technological development [1]. Nowadays most of the hyperthermia techniques with high frequency needle electrodes, small antennas, external coils as well as ferromagnetic rods, seeds or fluids are using electromagnetic fields to heat up pathological tissues [2]. Among other microwaves can induce heat in the biological structures and thereby have a significant part in their healing process. Heat transfer phenomenon proceeding in the living tissues is very important subject during such treatment. Hyperthermia uses differences in normal and tumor cells resistance of high-temperature. Research shows that the temperature between 40 and 45 °C can cause the destruction of the malignant cells and thus tumor thermonecrosis while not affect the surrounding healthy tissues [3]. Higher temperatures lead to thermo ablation and

P. Gas (✉)

AGH University of Science and Technology, Krakow, Poland
e-mail: piotr.gas@agh.edu.pl

permanent damage of healthy and diseased cells [4]. This is the reason why thermal therapy has become a prevalent technique for cancer treatment.

Maintaining the desired temperature throughout the whole treatment lasting even tens of minutes is still an extremely problematical and challenging scientific mission. In recent time, more and more publications related to hyperthermia appear and scientists are looking for new techniques to improve the efficacy and safety of thermal therapy [5, 6]. The clinical studies have shown increase in the effectiveness of hyperthermia combined with other cancer treatments such as radiotherapy, chemotherapy, immunotherapy and gene therapy, which are increasingly replacing traditional surgery [3]. High hopes are associated with the use of nanotechnology in hyperthermia treatment and targeting magnetic nanoparticles in places of interest [7]. Such attempts can be found today in many scientific works.

Interstitial microwave hyperthermia is an invasive medical procedure that involves inserting the coaxial antenna directly into the place of sickness and inducing thermonecrosis in the malignant tissues at the distance of 1–2 cm from the applicator. This makes possible the healing of inaccessible tumors located deeply in the human body, with diameter not exceeding 5 cm [8]. Depending on the tumor type and its degree of progress the application time usually varies between 30 and 60 min [9]. Effective treatment with this method requires knowledge of the electromagnetic field and temperature distributions inside the tissue induced by the multi-slot coaxial antenna. To get these distributions the construction and operation of the microwave antenna as well as the electro-thermal parameters of biological tissues need to be known. The number of the air gaps in the microwave antenna structure seems to have significant influence on the amount of energy absorbed by the conductive medium as it is shown in this paper. The considered 2D model makes it possible to predict easily the transient temperature distributions in the target area for different human tissues usually cured with this method [2].

2 Model Foundations

In general one can consider the multi-slot coaxial antenna comprising a central conductor, a dielectric, an outer conductor and a plastic catheter inside the surrounding human tissue for interstitial hyperthermia treatment as it shown in following Fig. 1.

For simplification, a 2D axisymmetric model in the cylindrical coordinate system (r, φ, z) is under consideration. The antenna is relatively thin—its diameter is less than 2 mm, and the dimensions of the individual elements can be found in the literature [10]. The air gaps are coaxial and have the same size $d_1 = d_2 = d_3 = d = 1$ mm. They are all positioned in the outer conductor at the following levels: $z_1 = 16.0$, $z_2 = 21.2$, and $z_3 = 26.4$ mm, respectively. The distances between the slots are constant, namely $l_1 = l_2 = l = 4.2$ mm.

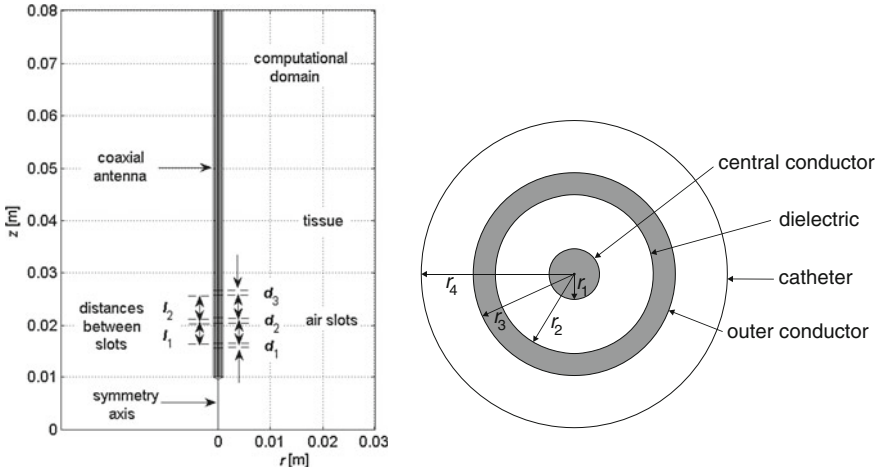


Fig. 1 The general model of the multi-slot coaxial antenna inserted into the human tissue (*left*) and its cross section (*right*) taking into account the individual antenna elements

From mathematical point of view the interstitial microwave hyperthermia with multi-slot coaxial antenna is a complex issue, the numerical analysis of which requires solving two partially dependent equations, namely the wave equation in TM mode and the bioheat equation in non-stationary case with the appropriate boundary-initial conditions. The basic formula governing the electromagnetic field in the present case was derived from Maxwell's equations taking into account the material dependencies for the uniform, linear, isotropic media. The wave equation with respect to the complex vector of the magnetic field intensity \mathbf{H} is governed by

$$\nabla \times [\underline{\epsilon}_r^{-1} \nabla \times \mathbf{H}] - \epsilon_0 \mu_0 \mu_r \omega^2 \mathbf{H} = 0 \tag{1}$$

where ϵ_0 and μ_0 denote the electric and magnetic constants, respectively, μ_r is the relative permeability of the medium, and ω —the radial frequency of the electromagnetic field (rad s^{-1}). Moreover, $\underline{\epsilon}_r$ represents the frequency-dependent complex relative permittivity, which for the dielectric antenna components is defined as

$$\underline{\epsilon}_r(\omega) = \epsilon'_r - j\epsilon''_r = \epsilon_r - j \frac{\sigma}{\omega \epsilon_0} \tag{2}$$

In above equation ϵ_r is the dielectric constant, σ —the electrical conductivity (S m^{-1}) and j means the imaginary unit. Biological structures due to water content can be regarded as dispersive conductive media in which typical dielectric relaxation processes occur. Therefore in tissues $\underline{\epsilon}_r$ is approximated by the Cole–Cole model [11].

$$\underline{\varepsilon}_r(\omega) = \varepsilon_\infty + \frac{\varepsilon_s - \varepsilon_\infty}{1 + (j\omega\tau_0)^{1-\alpha}} - j \frac{\sigma_s}{\omega\varepsilon_0} \quad (3)$$

where ε_∞ denotes the infinite limit of relative permittivity, ε_s —the static limit of relative permittivity, α —the Cole–Cole parameter, τ_0 —the relaxation time constant (ps) and σ_s —the static conductivity of the material (S m^{-1}).

The multi-slot coaxial antenna uses transverse magnetic (TM) wave, therefore there are no electromagnetic field changes in the azimuthal direction and the following expressions may be adopted: $\mathbf{H} = H_\varphi \mathbf{e}_\varphi$ and $\mathbf{E} = E_r \mathbf{e}_r + E_z \mathbf{e}_z$, where \mathbf{e}_r , \mathbf{e}_φ , \mathbf{e}_z denote the versors in the cylindrical coordinate system. Finally, the wave equation in 2D axisymmetric TM model is solved on the φ -component of the magnetic field strength in the following way

$$\nabla \times [\underline{\varepsilon}_r^{-1} \nabla \times H_\varphi] - \varepsilon_0 \mu_0 \mu_r \omega^2 H_\varphi = 0 \quad (4)$$

In the simulation some boundary conditions have to be assumed, which are thoroughly described in paper [11]. The attention should be paid to the port boundary condition at the dielectric input where the excitation magnetic field $H_{\varphi 0}$ is set as

$$H_{\varphi 0} = \frac{1}{Zr} \sqrt{\frac{Z P_{\text{in}}}{\pi \ln(r_2/r_1)}} \quad (5)$$

where P_{in} is to the microwave input power elevation at the feed point, while r_1 and r_2 are respectively the inner and outer radii of the dielectric. What is more, Z denotes the dielectric wave impedance according to the equation

$$Z = \sqrt{\frac{\mu_0}{\varepsilon_0 \varepsilon'_r}} = \frac{120\pi}{\sqrt{\varepsilon'_r}} \quad (6)$$

Heat transfer in living organism structures is a complicated process involving multiple complex mechanisms. Temperature deposited inside the human body is determined through the electric field generated by the microwave antenna and the physical parameters of the tissue. Transient temperature field in biological tissues is well described by the bioheat equation specified by Pennes [12] as follows

$$\rho C \frac{\partial T}{\partial t} + \nabla \cdot (-\lambda \nabla T) = \rho_b C_b \omega_b (T_b - T) + Q_{\text{ext}} + Q_{\text{met}} \quad (7)$$

where t denotes the time (s), T —the tissue temperature (K), λ —the tissue thermal conductivity (W (m K)^{-1}), ρ —the tissue density (kg m^{-3}), C —the tissue specific heat (J (kg K)^{-1}). What is important, the quantities related to blood are marked with

Table 1 Fitting parameters for the Cole–Cole model and thermal conductivity for various human tissues at the frequency of 2.45 GHz [11, 13]

Tissue	ϵ_{∞}	ϵ_s	τ_0 (ps)	α	σ_s (S m ⁻¹)	λ (W(m K) ⁻¹)
Brain	4.0	32	7.958	0.1	0.02	0.51
Breast	2.5	3	17.680	0.1	0.01	0.33
Kidney	4.0	47	7.958	0.1	0.05	0.53
Liver	4.0	39	8.842	0.1	0.02	0.52
Lung	2.5	18	7.958	0.1	0.03	0.39

the subscript “b” as in ω_b , which is the blood perfusion rate (s⁻¹). The Pennes model is the most commonly used one in numerical simulations because of its accuracy and simplicity. It takes into account both the heat generated by the metabolic cell processes Q_{met} (W m⁻³) as well as the energy generated by the microwave antenna $Q_{\text{ext}} = 0.5 \sigma |\mathbf{E}|^2$ (W m⁻³) where $|\mathbf{E}|$ is modulus of electric field. For simplification, the computational domain is limited only to the part of the same tissue. Therefore at the outer edge of the tissue the adiabatic boundary condition describing thermal insulation is used

$$\mathbf{n} \cdot (-\lambda \nabla T) = 0 \quad (8)$$

The initial temperature field is known as the normal temperature of the human body, namely $T = T_0 = 37$ °C.

For this study, it has been assumed that the microwave applicator is operating at $f = 2.45$ GHz with input power set to $P_{\text{in}} = 1$ W. The electric properties of the individual antenna elements have been taken from [10]. What is more, the electro-thermal parameters for various human tissues have been gathered in Table 1 according to [11, 13]. The blood parameters occurring in the Pennes equation have been considered at the following levels: $T_b = 310.15$ K, $\rho_b = 1020$ kg m⁻³, $C_b = 3640$ J (kg K)⁻¹ and $\omega_b = 0.004$ s⁻¹. It is worth mentioning that the tissue’s metabolic heat generation could be omitted since it is much smaller than the external heat source $Q_{\text{met}} \ll Q_{\text{ext}}$.

Summing up, the main Eqs. (4) and (7) were solved with the finite element method in the whole computational domain.

3 Simulation Results

At the outset, it should be emphasized that all the results have been computed for different active slot configurations and various tissues under the same boundary-initial and working antenna conditions. Figure 2 summarizes the predictions of

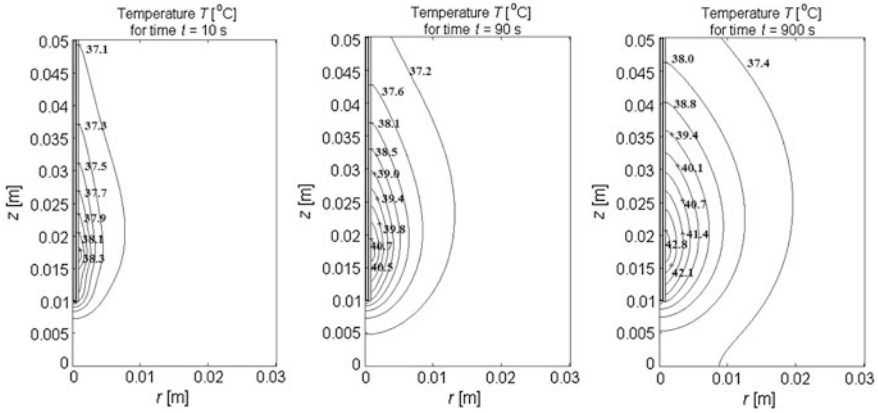


Fig. 2 Isothermal lines inside the human liver tissue for the single-coaxial antenna for different moments of time (all for $f = 2.45$ GHz and $P_{in} = 1$ W)

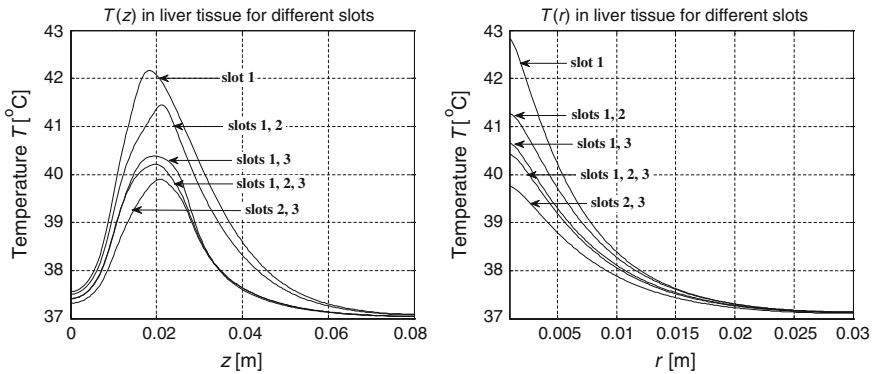


Fig. 3 Temperature distributions in the human liver tissue along the paths $r = 2.5$ mm (left) and $z = 16$ mm (right) for the coaxial antennas in steady-state

temperature elevations within the liver tissue derived from the single-slot microwave antenna for three sampled moments of time. The following figure illustrates the comparison of temperature distributions inside the liver tissue in the steady-state along two paths defined as $z = 16$ mm (level of the first slot) and $r = 2.5$ mm (parallel to the symmetry axis) between antennas with one, two and three air gaps (Fig. 3). Time dependent variations of temperature in the case of antennas with

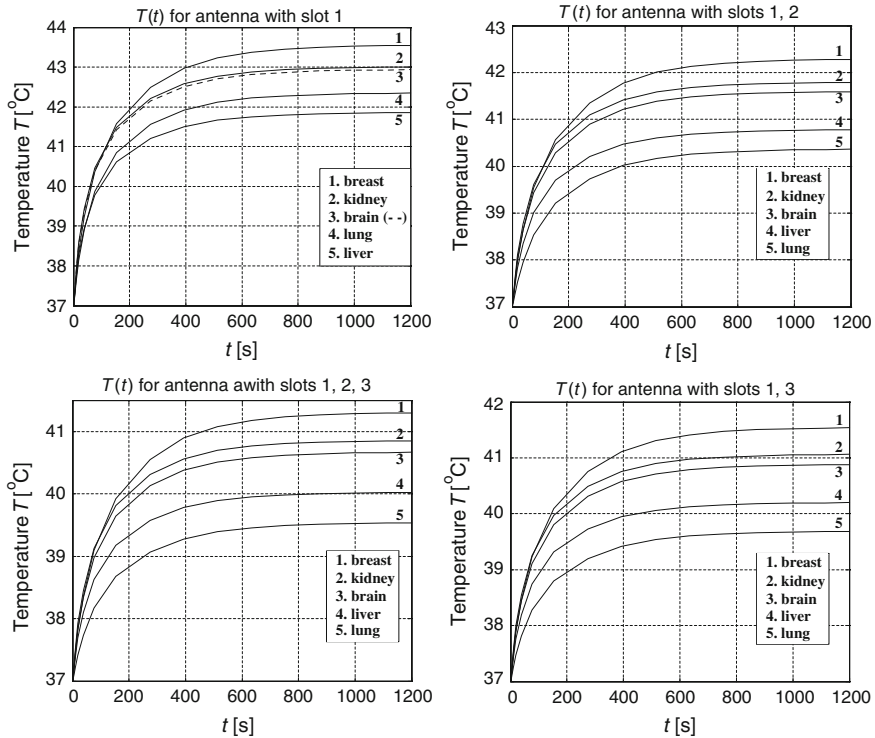


Fig. 4 Examples of transient temperature distributions for various human tissues at point $r = 2.5$ mm and $z = 16$ mm for the coaxial antennas with different active slots

different number of active slots inserted into various human tissues and can be seen in Fig. 4. As the point of observation the intersection of the predefined paths has been chosen ($r = 2.5$, $z = 16$ mm).

Table 2 summarizes the simulation results and compares the presented models in the case of the single-, double- and triple-slot antennas. Three observation points lying at the height of each of the air gaps within 2.5 mm from the antenna’s symmetry axis are considered. T denotes the temperature in the steady-state, and t —the time after which the temperature reaches a steady-state with a tolerance of 1 %. The highest temperatures and the lowest times for each model are shown in bold.

Table 2 Quantitative comparison between models

No. of slot	Tissue	Points of observation (all for $r = 2.5$ mm and z as below)		
		$z_1 = 16.0$ mm	$z_2 = 21.2$ mm	$z_3 = 26.4$ mm
1	Brain	$t = 776.8$ s, $T = 42.9$ °C	$t = 791.5$ s, $T = 42.9$ °C	$t = 828.9$ s, $T = 41.7$ °C
	Breast	$t = 824.7$ s, $T = 43.6$ °C	$t = 836.6$ s, $T = 43.7$ °C	$t = 869.1$ s, $T = 42.2$ °C
	Kidney	$t = 770.9$ s, $T = 43.0$ °C	$t = 781.9$ s, $T = 43.1$ °C	$t = 823.9$ s, $T = 41.8$ °C
	Liver	$t = 783.2$ s, $T = 41.9$ °C	$t = 795.6$ s, $T = 41.9$ °C	$t = 831.0$ s, $T = 41.0$ °C
	Lung	$t = 802.8$ s, $T = 42.3$ °C	$t = 828.6$ s, $T = 42.0$ °C	$t = 857.5$ s, $T = 41.0$ °C
1, 2	Brain	$t = 806.0$ s, $T = 41.6$ °C	$t = 783.8$ s, $T = 42.4$ °C	$t = 822.5$ s, $T = 41.2$ °C
	Breast	$t = 843.9$ s, $T = 42.3$ °C	$t = 834.5$ s, $T = 43.1$ °C	$t = 872.7$ s, $T = 41.6$ °C
	Kidney	$t = 798.0$ s, $T = 41.8$ °C	$t = 778.9$ s, $T = 42.6$ °C	$t = 822.5$ s, $T = 41.2$ °C
	Liver	$t = 812.3$ s, $T = 40.8$ °C	$t = 792.2$ s, $T = 41.4$ °C	$t = 829.4$ s, $T = 40.5$ °C
	Lung	$t = 851.8$ s, $T = 40.4$ °C	$t = 831.8$ s, $T = 41.2$ °C	$t = 850.0$ s, $T = 40.7$ °C
1, 3	Brain	$t = 794.4$ s, $T = 40.9$ °C	$t = 789.3$ s, $T = 41.1$ °C	$t = 815.8$ s, $T = 40.2$ °C
	Breast	$t = 834.4$ s, $T = 41.6$ °C	$t = 832.1$ s, $T = 41.8$ °C	$t = 863.9$ s, $T = 40.5$ °C
	Kidney	$t = 787.8$ s, $T = 41.1$ °C	$t = 776.2$ s, $T = 41.3$ °C	$t = 813.5$ s, $T = 40.3$ °C
	Liver	$t = 801.4$ s, $T = 40.2$ °C	$t = 793.6$ s, $T = 40.3$ °C	$t = 820.3$ s, $T = 39.7$ °C
	Lung	$t = 851.5$ s, $T = 39.7$ °C	$t = 859.6$ s, $T = 39.6$ °C	$t = 829.8$ s, $T = 40.0$ °C
2, 3	Brain	$t = 812.6$ s, $T = 39.9$ °C	$t = 789.1$ s, $T = 40.5$ °C	$t = 812.2$ s, $T = 39.8$ °C
	Breast	$t = 846.5$ s, $T = 40.4$ °C	$t = 829.4$ s, $T = 41.1$ °C	$t = 857.4$ s, $T = 40.1$ °C
	Kidney	$t = 800.7$ s, $T = 40.0$ °C	$t = 771.8$ s, $T = 40.7$ °C	$t = 811.1$ s, $T = 39.9$ °C
	Liver	$t = 817.2$ s, $T = 39.4$ °C	$t = 793.3$ s, $T = 39.9$ °C	$t = 815.3$ s, $T = 39.4$ °C
	Lung	$t = 860.0$ s, $T = 39.1$ °C	$t = 849.5$ s, $T = 39.3$ °C	$t = 837.5$ s, $T = 39.5$ °C
1, 2, 3	Brain	$t = 799.4$ s, $T = 40.7$ °C	$t = 793.8$ s, $T = 40.1$ °C	$t = 826.5$ s, $T = 39.9$ °C
	Breast	$t = 837.7$ s, $T = 41.3$ °C	$t = 833.4$ s, $T = 41.6$ °C	$t = 871.4$ s, $T = 40.2$ °C
	Kidney	$t = 789.6$ s, $T = 40.9$ °C	$t = 782.5$ s, $T = 41.0$ °C	$t = 824.0$ s, $T = 40.0$ °C
	Liver	$t = 805.3$ s, $T = 40.0$ °C	$t = 798.2$ s, $T = 40.1$ °C	$t = 831.9$ s, $T = 39.5$ °C
	Lung	$t = 854.4$ s, $T = 39.6$ °C	$t = 871.3$ s, $T = 39.6$ °C	$t = 847.1$ s, $T = 39.6$ °C

4 Conclusions

The dynamics of the heating and the highly non-uniform temperature distribution are among the main contributors to the risk for side effects associated with hyperthermia. It is therefore essential to determine the temperature elevations in treated tissues including their variation over time. In this work, the emphasis is placed on estimating the transient temperature distributions for the numerical model of interstitial microwave hyperthermia with a multi-slot coaxial antenna. The simulations have been performed for different configurations of active air gaps and various human tissues usually cured with this method. In line with the expectations, the temperature in the target tissue decreases rapidly with the distance from the microwave applicator. The highest temperatures were obtained with the single-slot antenna. The lowest ones occurred for the antenna with slots 2 and 3. What is more,

under the same conditions, the lowest and the highest temperatures appeared in the lung and breast tissues, respectively. The average time to reach a steady-state temperature is about 800 s. The fastest temperature has been fixed in the kidney tissue and the most significant values of the temperature in a steady-state were obtained in the breast tissue at the height of the second slot, regardless of the model. Of course, in any of the analysed cases, the temperature values can be easily enlarged by raising the level of the antenna's total microwave input power. The numerical approach presented in this paper can have a significant impact on the actual treatment of tumors.

References

1. Gas P (2011) Essential facts on the history of hyperthermia and their connections with electromedicine. *Przeł Elektrotechniczny* 87(12b):37–40 (2011)
2. Baronzio GF, Hager ED (2006) *Hyperthermia in cancer treatment: a primer*. Landes Bioscience and Springer Science + Business Media, New York
3. McPhee SJ, Papadakis MA, Rabow MW (2013) *Current medical diagnosis and treatment 2013*, 52nd edn. The McGraw-Hill, New York (2013)
4. Ryan TP, Turner PF, Hamilton B (2010) Interstitial microwave transition from hyperthermia to ablation: historical perspectives and current trends in thermal therapy. *Int J Hypertherm* 26(5):415–433
5. Kurgan E, Gas P (2011) Treatment of tumors located in the human thigh using RF hyperthermia. *Przeł Elektrotechniczny* 87(12b):103–106
6. Gas P (2012) Tissue temperature distributions for different frequencies derived from interstitial microwave hyperthermia. *Przeł Elektrotechniczny* 88(12b):131–134
7. Miaskowski A, Sawicki B (2013) Magnetic fluid hyperthermia modeling based on phantom measurements and realistic breast model. *IEEE Trans Biomed Eng* 60(7):1806–1813
8. Siauve N, Lormel C (2012) Interstitial microwave hyperthermia treatment investigations. *J Phys Conf Ser* 395(1):1–8
9. Ito K, Saito K (2011) Development of microwave antennas for thermal therapy. *Curr Pharm Des* 17(22):2360–2366
10. Keangin P, Rattanadecho P, Wessapan T (2011) An analysis of heat transfer in liver tissue during microwave ablation using single and double slot antenna. *Int Commun Heat Mass Transfer* 38(6):757–766
11. Peyman A, Holden S, Gabriel C (2005) Measurement of the dielectric properties of biological tissues in vivo at microwave frequencies. *Mobile Telecommunications and Health Research Programme, RUM 3, Final Report* (2005)
12. Pennes HH (1998) Analysis of tissue and arterial blood temperatures in the resting human forearm. *J Appl Physiol* 85(1):5–34
13. McIntosh RL, Anderson V (2010) A comprehensive tissue properties database provided for the thermal assessment of a human at rest. *Biophys Rev Lett* 5(3):129–151

Impulse Responses of Generalized First Order LTV Sections

Anna Piwowar and Janusz Walczak

Abstract In this article, the model of the first order parametric section linear time varying (LTV) has been described. The parameter of the section under examination is non-periodically variable. These sections are the elementary blocks constituting more complex systems of parametric filters. The method aiming to determinate the impulse response of the LTV section has been presented. The results have been illustrated by an example.

1 Introduction

The synthesis and properties analysis of stationary universal linear time invariant (LTI) sections described by the ordinary differential equations with constant coefficients is well known [1]. The Laplace calculation method is most often used for the synthesis of such filters.

The parametric sections also referred to as LTV sections are systems with time varying coefficients. The time-varying systems are described by the ordinary differential equations with coefficients variable in time. The analysis and synthesis of such sections is difficult because the definition of the Laplace transform in the classical sense is pointless in this case. In the time domain parametric systems can be described in two different ways [3, 5, 8]. The first of them consist in using the linear ordinary differential equations with the variable coefficients being the time functions (compare to (2)). The analytical solution to these equations, even to the simplest ones, is a very complex mathematical problem [5, 6]. The second parametric system description method is based on the usage of the parametric convolution equation, which can be defined in different ways [4, 8]. In this article

A. Piwowar (✉) · J. Walczak
Silesian University of Technology, Gliwice, Poland
e-mail: Anna.Piwowar@polsl.pl

J. Walczak
e-mail: Janusz.Walczak@polsl.pl

the definition of parametric convolution given by Zadeh [8] is used, which is expressed by:

$$y(t) = \int_0^t h(t, \tau)x(\tau)d\tau, \tag{1}$$

where: $h(t, \tau)$ —impulse response of the system.

In this article the LTV system analysis method with non-periodically varying parameters is presented. This method enables the determination of dynamic characteristics of the nonstationary system i.e. impulse response, step response.

2 Model of the First Order LTV Section

The single input single output (SISO) transmission models of the LTV class (Fig. 1) are described using the P operation, which is the relation between input $x(t)$ and output $y(t)$ signals of the system [3].

These signals belong to signal spaces defined in different ways. For the parametric systems in the time domain, the state equations or parametric convolution equations are the P-operation. The transmission description making use of the convolution (1) enables the determination of the system response to any excitation $x(t)$ providing the $h(t, \tau)$ function is known. In this article the analysis method in time domain has been shown, which includes the impulse response $h(t, \tau)$ and $y(t)$ first order LTV low pass filter response described by the differential equation:

$$y'(t) + \omega(t)y(t) = x(t), \tag{2}$$

where: $\omega(t)$ —the parametric function interpreted as time varying angular frequency.

It can be proved that any non-periodical function with limited energy describing the time variable system parameter (Fig. 2) can be approximated by the series [2]:

$$\omega(t) = \omega_g + \sum_{\substack{k=-N \\ k \neq 0}}^{k=N} C_k e^{-p_k t}, \quad \omega_g > 0, C_k, p_k \in \mathbb{C}, \tag{3}$$

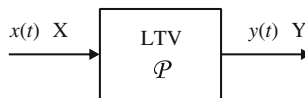


Fig. 1 The transmission model of LTV class SISO system

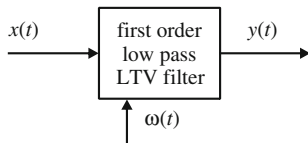


Fig. 2 Model of low pass first order LTV section

thus:

$$C_k = |C_k|e^{j\psi_k} = A_k + jB_k, \quad C_k = C_{-k}^*, \quad (4)$$

$$p_k = \gamma_k + j\omega_k, \quad p_k = p_{-k}^*. \quad (5)$$

For the assumptions (3) the parametric functions fulfill the condition:

$$\lim_{t \rightarrow \infty} \omega(t) = \omega_g > 0. \quad (6)$$

If the above condition is fulfilled and the considered parametric sections are stable [5], after sufficiently long time the LTV sections are equivalent to the stationary low pass sections with angular frequency ω_g . These sections become classical low pass LTI filters. The Eq. (3), which express the time-variable parameter, can be converted to the form:

$$\omega(t) = \omega_g + \sum_{k=1}^{k=N} e^{-\gamma_k t} (A_k \cos(\omega_k t) + B_k \sin(\omega_k t)), \quad (7)$$

where:

$$A_k = 2|C_k| \cos \psi_k, \quad (8)$$

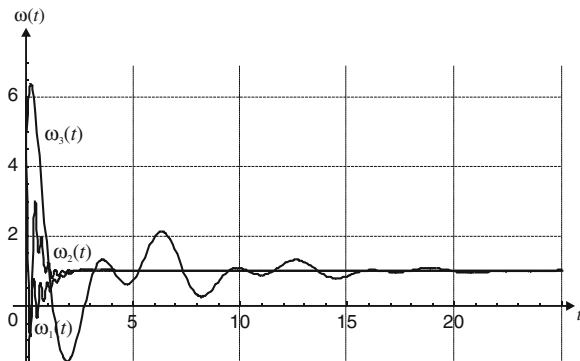
$$B_k = -2|C_k| \sin \psi_k. \quad (9)$$

The examples of parametric function waveforms described by the Eq. (7) are presented in Fig. 3.

3 Analysis of Generalized First Order LTV Section

The article [7] is devoted to the analysis of a particular case of the first order parametric section (for $N = 1$) with the parameter variable accordingly to Eq. (7). This work is continues the LTV system examination and is devoted to the generalized LTV section with a parameter being any limited energy function described by the Eq. (7) (Fig. 3). The examination of parametric systems in the time domain

Fig. 3 Parametric functions waveforms



consists in the analysis of parametric differential equations describing their models. For the zero initial condition, the solution to Eq. (2) is given by the equation [6]:

$$y(t) = \int_0^t e^{-(\alpha(t)-\alpha(\tau))} x(\tau) d\tau, \quad (10)$$

where:

$$\alpha(t) = \int_0^t \omega(\tau) d\tau. \quad (11)$$

Taking into consideration the Eq. (7) into formulae (10), (11), one can obtain the relation determining the section model in the convolution form, whereas the function $\alpha(t)$ is expressed as:

$$\alpha(t) = \sum_{k=1}^N (D_{1k} \cos(\omega_k t) + D_{2k} \sin(\omega_k t)) e^{-\gamma_k t} + \omega_g t - D_0, \quad (12)$$

where:

$$D_{1k} = \frac{-A_k \gamma_k - B_k \omega_k}{\gamma_k^2 + \omega_k^2}, \quad (13)$$

$$D_{2k} = \frac{A_k \omega_k - B_k \gamma_k}{\gamma_k^2 + \omega_k^2}, \quad (14)$$

$$D_0 = \sum_{k=1}^N D_{1k}. \quad (15)$$

After comparing the Eqs. (1) to (10) and taking into consideration the formula (12), one can obtain the impulse response equation of the analyzed section in a closed form:

$$\begin{aligned}
 h(t, \tau) = \exp(-\omega_g(t - \tau)) & \exp\left(\sum_{k=1}^N D_{1k}(\cos(\omega_k \tau) - \cos(\omega_k t))\exp(\gamma_k(t - \tau))\right) \\
 & \exp\left(\sum_{k=1}^N D_{2k}(\sin(\omega_k \tau) - \sin(\omega_k t))\exp(\gamma_k(t - \tau))\right).
 \end{aligned}
 \tag{16}$$

Based on the knowledge of impulse response (16) and the relation (1), one can determine the parametric system response to any excitation $x(t)$. The results obtained this way describe a complete transmission model of the generalised first order parametric section with a variable coefficient described by formula (7).

4 Example

The low pass LTV first order filter presented in Fig. 2 has been analyzed for three different parameter $\omega(t)$ variability behaviours. The waveform of time varying cut-off angular frequency of the system has been shown in Fig. 3.

The impulse responses $h(t, \tau)$ of the analyzed systems determined on the base of the formula (16) have been presented in Figs. 4, 5, 6. On the contrary to classical stationary sections, the impulse responses of parametric section are functions of two variables t —time, and τ —moment of application of the excitation in the Diracc impulse form to the input of the system. The variable τ is treated as a system parameter. The exemplar 2D diagrams are sections of the surface described by function $h(t, \tau)$ for particular moments τ .

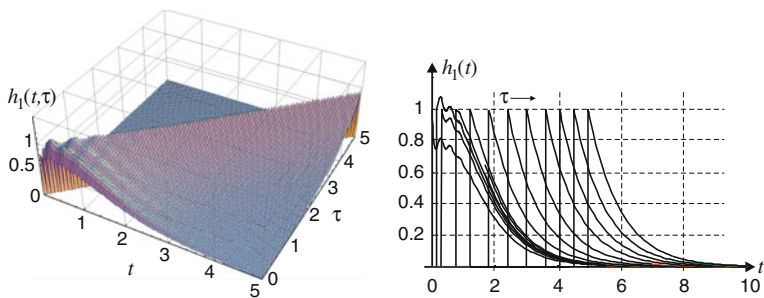


Fig. 4 The impulse response of first order LTV filter with variable parameter $\omega_1(t)$

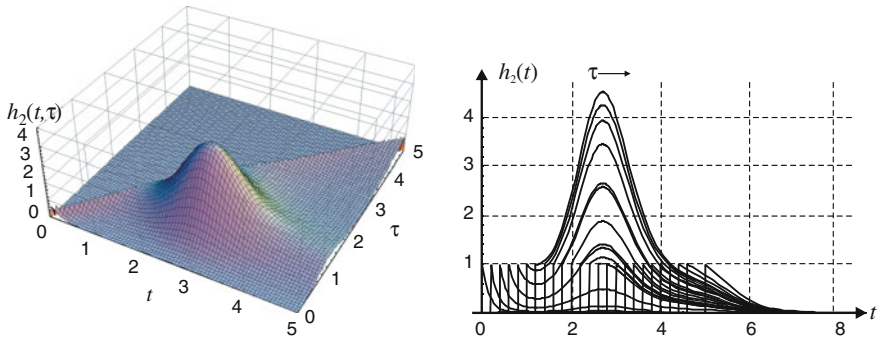


Fig. 5 The impulse response of first order LTV filter with variable parameter $\omega_2(t)$

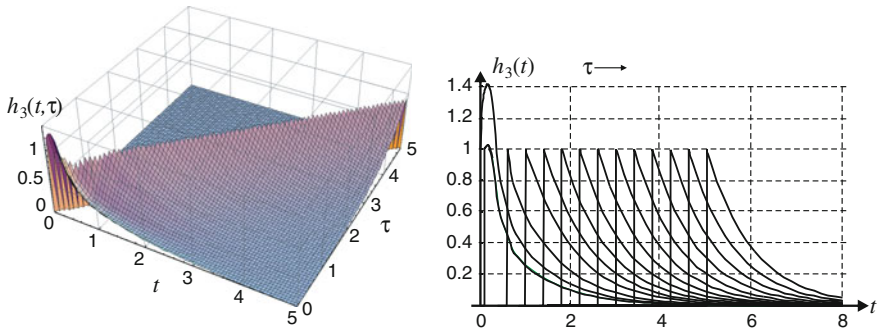


Fig. 6 The impulse response of first order LTV filter with variable parameter $\omega_3(t)$

5 Conclusion

The proposed analytical model of the first order generalised parametric low-pass section with a non periodically variable parameter enables the determination of the system response to any excitation with finite average power and limited energy.

On the contrary to classical stationary sections, the impulse responses of parametric sections are functions of two variables—time, and moment of application of the excitation to the input of the system. Changing parameters has an impact on the shape of the impulse response.

In the stationary state, the sections with variable parameters are equivalent to stationary sections. The advantage of the proposed approach is the possibility to improve the dynamic properties by the proper choice of the parametric function.

References

1. Chen WK (1995) The circuits and filters handbook. IEEE Press, New York
2. Clement PR (1963) On completeness of basis function used for signal analysis. *SIAM Rev* 5 (2):167–172
3. Descoer CA, Vidyasager M (1995) Feedback systems: input-output properites. Academic Press, New York
4. D'Angelo H (1970) Linear time-varying systems. Analysis and synthesis. Allyn and Bacon Inc, Boston
5. Piwowar A (2011) Analysis of parametric systems consist in the first and he second order sections, Ph.D. thesis, Gliwice
6. Polyanin AD, Zaitsev VF (2003) Handbook of exact solutions for ordinary differential equations, 2nd edn. Chapman & Hall/CRC, Boca Raton
7. Walczak J, Piwowar A (2011) Generalised transmission model of first order parametric section. In: Proceedings of the conferences AMTEE, Klatovy, Czech Republic, wrzesień 2011, pp III-9-III-10
8. Zadeh LA (1961) Time-varying networks I. *Proc IRE* 49(20):1488–1503

On Some Inequalities for Fourier Coefficients

Piotr Lorenc, Damian Słota, Marcin Szczygieł, Jacek Uryga and Roman Witula

Abstract The main aim of this paper is to present the improved version of results from paper [1]. All of these concern the certain inequalities of global type for Fourier coefficients and their applications to trigonometric integral inequalities. Also some proofs omitted in [3] are added in this paper.

1 Introduction

In the classical monograph by Zygmund [3] (see also [2]) the order of magnitude of Fourier coefficients of an integrable function $g : [0, 2\pi] \rightarrow \mathbb{R}$ with the aid of the modulus continuity of function g is given

$$\left(\int_0^{2\pi} g(x) \cos(nx) dx \right)^2 + \left(\int_0^{2\pi} g(x) \sin(nx) dx \right)^2 \leq \left(\frac{1}{2} \int_0^{2\pi} \left| g(x) - g\left(x + \frac{\pi}{n}\right) \right| dx \right)^2.$$

Aim of this paper is to receive an optimal bounding constant for the cases of

$$g : [0, 2\pi] \rightarrow [-1, 1] \quad \text{and} \quad g : [0, 2\pi] \rightarrow [0, 1].$$

P. Lorenc · D. Słota · J. Uryga · R. Witula (✉)
Institute of Mathematics, Silesian University of Technology,
Kaszubska 23, 44-100 Gliwice, Poland
e-mail: roman.witula@polsl.pl

M. Szczygieł
Department of Mechatronics, Silesian University of Technology,
Akademicka 10A, 44-100 Gliwice, Poland

Moreover, a discussion of optimal cases and some applications to trigonometric inequalities are presented here. We note that the given in this paper inequalities are stronger than the respective inequalities deduced from the above Zygmund's inequality.

2 Main Result

The following result is the generalization of Theorem 1 from [1].

Theorem 1 *Let $g \in L^1_{\mathbb{R}}([0, 2\pi])$, $|g| \leq 1$. Then the following inequalities hold true*

$$\left| \int_0^{\xi} g(x) \sin(nx) dx \right| \leq \frac{2}{n} \left\lceil \frac{n\xi}{\pi} \right\rceil, \quad (1)$$

$$\left| \int_0^{\xi} g(x) \cos(nx) dx \right| \leq \frac{2}{n} \left\lceil \frac{n\xi}{\pi} \right\rceil, \quad (2)$$

$$\left| \int_0^{\xi} |g(x)| \sin(nx) dx \right| \leq \frac{2}{n} \left\lceil \frac{n\xi}{2\pi} \right\rceil, \quad (3)$$

$$\left| \int_0^{\xi} |g(x)| \cos(nx) dx \right| \leq \frac{2}{n} \left\lceil \frac{n\xi}{2\pi} \right\rceil, \quad (4)$$

for every $n \in \mathbb{N}$ and $\xi \in (0, \infty)$.

Remark 1 From (1)–(4) the following estimation of the order of magnitude of the Fourier coefficients of an integrable function $g : [0, 2\pi] \rightarrow \mathbb{R}$, $|g| \leq 1$ can be obtained

$$\begin{aligned} \left(\int_0^{\xi} g(x) \cos(nx) dx \right)^2 + \left(\int_0^{\xi} g(x) \sin(nx) dx \right)^2 &\leq \frac{8}{n^2} \left\lceil \frac{n\xi}{\pi} \right\rceil^2, \\ \left(\int_0^{\xi} |g(x)| \cos(nx) dx \right)^2 + \left(\int_0^{\xi} |g(x)| \sin(nx) dx \right)^2 &\leq \frac{8}{n^2} \left\lceil \frac{n\xi}{2\pi} \right\rceil^2. \end{aligned}$$

Both inequalities are better than Zygmund's result from Introduction. Simultaneously we think that the best estimation will be obtained by replacing in both inequalities multiplier 8 by 4.

Remark 2 Proof of Theorem 1 runs in the similar way as proof of Theorem 1 from [1].

Let us present the following result.

Theorem 2 *Let $g \in L^1_{\mathbb{R}}([0, 2\pi])$, $|g| \leq 1$. Then, for every $n \in \mathbb{N}$, the following inequalities hold true*

$$\left(\int_0^{2\pi} g(x) \cos(nx) dx \right)^2 + \left(\int_0^{2\pi} g(x) \sin(nx) dx \right)^2 \leq 16 \quad (5)$$

and

$$\left(\int_0^{2\pi} |g(x)| \cos(nx) dx \right)^2 + \left(\int_0^{2\pi} |g(x)| \sin(nx) dx \right)^2 \leq 4. \quad (6)$$

If the equality sign is established in (5) then

$$|g(x)| = 1 \quad (7)$$

for almost all $x \in [0, 2\pi]$. Moreover, if the condition (7) is satisfied then from (6), for $n = 1$ we get

$$\left(\int_A \sin x dx \right)^2 + \left(\int_A \cos x dx \right)^2 \leq 4, \quad (8)$$

where $A := \{x \in [0, 2\pi]; g(x) = 1\}$. Hence, it follows that (8) holds for every measurable subset A of $[0, 2\pi]$.

If the condition (7) is satisfied then there is the equality sign in (5) for $n = 1$ iff there is the equality sign in (8).

Corollary 1 *If $g \in L_{\mathbb{C}}([0, 2\pi])$, $|g| \leq 1$, then, for every $n \in \mathbb{N}$, the following inequality holds*

$$\left| \int_0^{2\pi} g(x) \cos(nx) dx \right|^2 + \left| \int_0^{2\pi} g(x) \sin(nx) dx \right|^2 \leq 32. \quad (9)$$

Corollary 2 *Let A be a Lebesgue measurable subset of $[0, \pi]$ (or $A \subset [\pi, 2\pi]$, respectively). Then the following inequality holds*

$$\left(\int_A \sin x dx\right)^2 + \left(\int_A \cos x dx\right)^2 \leq 4 \left|\int_A \sin x dx\right|. \quad (10)$$

Moreover if $A \subset [0, \pi]$ then we have

$$\left(2 \int_{[0, \frac{\pi}{2}] \cap A} \sin x dx + \int_{A'_s} \sin x dx\right)^2 + \left(\int_{A'_s} \cos x dx\right)^2 \leq 4, \quad (11)$$

where $A_s := \{x \in A : \pi - x \in A\}$ and $A'_s := A \setminus A_s$.

On the other hand, if $A \subset [\pi/2, 3\pi/2]$ then we have

$$\left(\int_A \sin x dx\right)^2 + \left(\int_A \cos x dx\right)^2 \leq -4 \int_A \cos x dx, \quad (12)$$

We think that both inequalities (10) and (12) can be strengthened to the one's with multiplier 4 replaced by 2. It seems that there will be the optimal inequalities, which results from the following discussion.

So if $A = [x, z]$ then (10) with multiplier 4 replaced by 2 is equivalent to inequality

$$\begin{aligned} (\cos x - \cos z)^2 + (\sin x - \sin z)^2 &\leq 2|\cos x - \cos z|, \\ 2 - 2\cos(x - z) &\leq 4 \sin \frac{x+z}{2} \sin \frac{|x-z|}{2}, \\ 4 \sin^2 \left(\frac{x-z}{2}\right) &\leq 4 \sin \frac{x+z}{2} \sin \frac{|x-z|}{2}, \end{aligned}$$

which implies

$$\sin \frac{|x-z|}{2} \leq \sin \frac{x+z}{2} \quad (13)$$

for every $x, z \in [0, \pi]$. This inequality really holds since we have

$$\begin{cases} \sin \frac{x+z}{2} + \sin \frac{x-z}{2} = 2 \sin \frac{x}{2} \cos \frac{z}{2} \geq 0, \\ \sin \frac{x+z}{2} + \sin \frac{z-x}{2} = 2 \sin \frac{z}{2} \cos \frac{x}{2} \geq 0, \end{cases}$$

i.e.,

$$\sin \frac{x+z}{2} = \begin{cases} 2 \sin \frac{x}{2} \cos \frac{z}{2} + \sin \frac{z-x}{2} \geq \sin \frac{z-x}{2}, \\ 2 \sin \frac{z}{2} \cos \frac{x}{2} + \sin \frac{x-z}{2} \geq \sin \frac{x-z}{2}, \end{cases}$$

which generates (13).

Proof of Theorem 2 First the proof of (5) and (6) will be presented. To this aim let us put

$$c_s = c_s(f) = \int_0^{2\pi} f(t) \sin(nt + s) dt,$$

$$d_s = d_s(f) = \int_0^{2\pi} f(t) \cos(nt + s) dt,$$

for $s \in \mathbb{R}$ and $f \in L^1_{\mathbb{R}}([0, 2\pi])$, $|f| \leq 1$ and $n \in \mathbb{N}$. Moreover, let $c = c_0(f)$, $d = d_0(f)$. Next fix $n \in \mathbb{N}$ and a respective $f \in L^1_{\mathbb{R}}([0, 2\pi])$. Then it follows that

$$\begin{cases} c_s = c \cos s + d \sin s \\ d_s = d \cos s - c \sin s \end{cases} \quad (14)$$

for $s \in \mathbb{R}$. This clearly forces

$$c_s^2 + d_s^2 = c^2 + d^2 \quad (15)$$

Now observe that

$$d_s \pm c_s = \int_0^{2\pi} f(t) [\cos(nt + s) \pm \sin(nt + s)] dt$$

$$= \sqrt{2} \int_0^{2\pi} f(t) \cos\left(nt + s \mp \frac{\pi}{4}\right) dt,$$

which implies

$$|d_s \pm c_s| \leq \sqrt{2} \int_0^{2\pi} \left| \cos\left(nt + s \mp \frac{\pi}{4}\right) \right| dt = \sqrt{2} \int_0^{2\pi} |\cos nt| dt = 4\sqrt{2}. \quad (16)$$

But we have

$$\max\{|d_s + c_s|, |d_s - c_s|\} = |c_s| + |d_s| \quad (17)$$

and it is possible to choose a value of s in such a way that $c_s = d_s$ (by (14) it follows either $s = 0$ if $c = d$ or $\cot s = \frac{c+d}{d-c}$ if $c \neq d$). For these value of s , by (16) and (17), we deduce that

$$|c_s| \leq 2\sqrt{2} \quad \text{and} \quad |d_s| \leq 2\sqrt{2}, \quad (18)$$

i.e. by (15)

$$c^2 + d^2 \leq 16. \quad (19)$$

Let $g \in L^1_{\mathbb{R}}([0, 2\pi])$, $|g| \leq 1$. Then the function

$$f(x) := 2|g(x)| - 1$$

belongs to $L^1_{\mathbb{R}}([0, 2\pi])$ as well, $|f| \leq 1$, $c(f) = 2c(|g|)$ and $d(f) = 2d(|g|)$ which by (19) implies

$$4(c^2(|g|) + d^2(|g|)) = c^2(f) + d^2(f) \leq 16,$$

i.e.

$$c^2(|g|) + d^2(|g|) \leq 4$$

which finishes the proof of (5) and (6).

Our next goal is to prove that if the equality sign is established in (5), then (7) holds. To this aim let us suppose that $f \in L^1_{\mathbb{R}}([0, 2\pi])$, $|f| \leq 1$. Put

$$A := \{x \in [0, 2\pi] : |f(x)| < 1\}.$$

Assume that $l(A) > 0$. Then there exists $\delta \in (0, 1)$ such that

$$A_\delta := \{x \in A : |f(x)| \leq 1 - \delta\} \quad \text{and} \quad l(A_\delta) > 0$$

(since $l(A_\delta) \rightarrow l(A)$ when $\delta \rightarrow 0^+$). There is no loss of generality in assuming that the restriction $\sin nx|_{A_\delta}$ has the constant sign. Now, a new function will be defined

$$h_\gamma(x) := \begin{cases} f(x) + \gamma, & \text{for } x \in A_\delta \\ f(x), & \text{for } x \in [0, 2\pi] \setminus A_\delta, \end{cases}$$

where $\gamma \in (-\delta, \delta)$. Clearly we have

$$h_\gamma([0, 2\pi]) \subset [-1, 1] \quad \text{and} \quad h_\gamma \in L^1_{\mathbb{R}}[0, 2\pi].$$

Furthermore, the following identity holds

$$\begin{aligned} & \left(\int_0^{2\pi} h_\gamma(x) \sin x \, dx \right)^2 + \left(\int_0^{2\pi} h_\gamma(x) \cos x \, dx \right)^2 \\ &= \left(\int_0^{2\pi} f(x) \sin x \, dx \right)^2 + \left(\int_0^{2\pi} f(x) \cos x \, dx \right)^2 \\ &+ 2\gamma \left[\left(\int_{A_\delta} \sin x \, dx \right) \int_0^{2\pi} f(x) \sin x \, dx + \left(\int_{A_\delta} \cos x \, dx \right) \int_0^{2\pi} f(x) \cos x \, dx \right] \\ &+ \gamma^2 \left(\left(\int_{A_\delta} \sin x \, dx \right)^2 + \left(\int_{A_\delta} \cos x \, dx \right)^2 \right). \end{aligned}$$

Hence, if we set

$$M = \left(\int_{A_\delta} \sin x \, dx \right) \int_0^{2\pi} f(x) \sin x \, dx + \left(\int_{A_\delta} \cos x \, dx \right) \int_0^{2\pi} f(x) \cos x \, dx$$

and

$$\gamma = \begin{cases} 2^{-1}\delta, & \text{for } M > 0, \\ -2^{-1}\delta, & \text{for } M < 0, \end{cases}$$

then we deduce that maximum of the following expression

$$\left(\int_0^{2\pi} g(x) \sin x \, dx \right)^2 + \left(\int_0^{2\pi} g(x) \cos x \, dx \right)^2, \quad (g \in L^1_{\mathbb{R}}([0, 2\pi]), \quad |g| \leq 1),$$

is obtained iff $|g(x)| = 1$ almost everywhere on $[0, 2\pi]$.

Suppose that $g \in L^1_{\mathbb{R}}([0, 2\pi])$, $|g| = 1$ almost everywhere on $[0, 2\pi]$. Set

$$A = \{x \in [0, 2\pi] : g(x) = 1\}.$$

Then we have

$$\begin{aligned}
 & \left(\int_0^{2\pi} g(x) \sin x \, dx \right)^2 + \left(\int_0^{2\pi} g(x) \cos x \, dx \right)^2 \\
 &= \left(\int_A \sin x \, dx - \int_{[0,2\pi] \setminus A} \sin x \, dx \right)^2 + \left(\int_A \cos x \, dx - \int_{[0,2\pi] \setminus A} \cos x \, dx \right)^2 \\
 &= \left(2 \int_A \sin x \, dx \right)^2 + \left(2 \int_A \cos x \, dx \right)^2 = 4 \left[\left(\int_A \sin x \, dx \right)^2 + \left(\int_A \cos x \, dx \right)^2 \right],
 \end{aligned}$$

which by (5) implies (8). \square

Proof of Corollary 2 Suppose that A and B are some Lebesgue measurable subsets of $[0, 2\pi]$ and let $A \subset B$. From (8) for $A := B \setminus A$ we obtain

$$\left(\int_B \sin x \, dx - \int_A \sin x \, dx \right)^2 + \left(\int_B \cos x \, dx - \int_A \cos x \, dx \right)^2 \leq 4.$$

Hence for $B = [0, \pi]$ or $[\pi, 2\pi]$ we get (10), while for $B = [\frac{\pi}{2}, \frac{3}{2}\pi]$ the inequality (12) follows.

On the other hand, if $B := [0, \pi]$ and $A := A_s \cup A'_s$, where $A_s := \{x \in A : \pi - x \in A\}$ and $A'_s := A \setminus A_s$ then

$$\int_{A'_s} \cos x \, dx = 0,$$

$A_s \cap A'_s = \emptyset$ and

$$\int_{A_s} \sin x \, dx = 2 \int_{[0, \frac{\pi}{2}] \cap A_s} \sin x \, dx,$$

which implies (11). \square

References

1. Uryga J, Wituła R (2012) On some inequalities of global type for the Fourier coefficients, *Materiały XV Jubileuszowego Sympozjum „Podstawowe Problemy Energoelektroniki, Elektromechaniki i Mechatroniki”*, PPEEm 2012, Gliwice 2012, pp 208–209
2. Vretblad A (2005) *Fourier analysis and its applications*. Springer, Berlin
3. Zygmund A (2005) *Trigonometric series*, vol I. Cambridge University Press, Cambridge

On the Three, Five and Other Periodic Orbits of Some Polynomials

Roman Wituła, Edyta Hetmaniok, Damian Słota, Tomasz Trawiński and Wojciech Kolton

Abstract In the paper all three and five periodic orbits of certain (known and a bit less known) quadratic and cubic polynomials as well as polynomials of order greater than 4 are generated. Other periodic orbits are also discussed here. The basic polynomials considered in this paper are the minimal polynomials of $2 \cos \frac{2\pi}{2n-1}$ or $2 \sin \frac{2\pi}{2n-1}$ for every $n = 4, 5, 6, 7, 8$. The concept of n -periodic trigonometric orbits is introduced. Also generalizations of Benedetto identities are presented.

1 Organization of the Paper

The paper is divided into three main sections completed by references and one table. The sections are:

1. *Introduction* where besides the ideas and notations used in the paper also the investigated polynomials are introduced. Background of the paper subject-matter is presented too.
2. *The first set of trigonometric type polynomials* where the periodic orbits of two first special polynomials $s_w(x)$ and $t_w(x)$ are discussed. Moreover, some generalizations of Benedetto identities (see [1]) connected with the periodic orbits of polynomials (over fields of characteristic zero) are introduced.
3. *Amazing cubic polynomials* $-3x + \frac{1}{w^2}x^3$, i.e. polynomials $wT_3(\frac{x}{w})$ where $w \in \mathbb{R} \setminus \{0\}$ and T_3 is the third Chebyshev polynomial of the first kind (especially see [2–6] for the basic informations on Chebyshev polynomials). The section is

R. Wituła (✉) · E. Hetmaniok · D. Słota
Institute of Mathematics, Silesian University of Technology, Gliwice, Poland
e-mail: roman.witula@polsl.pl

T. Trawiński · W. Kolton
Department of Mechatronics, Faculty of Electrical Engineering, Silesian University of Technology, Gliwice, Poland

devoted to discussing the periodic orbits of these polynomials. Indeed it is known (see [7]) that if $p \in \mathbb{N}$ is a prime number then we seek the finite elements of periodic orbits of polynomial T_p in the set of solutions of equation

$$T_{p^n}(x) = x, \quad x \in \mathbb{R}, \quad n \in \mathbb{N}.$$

However we still do not know, but we suppose, that all these solutions are of the form $x = \cos\left(\frac{kr\pi}{p}\right)$, $(kr, p) = 1$, $0 \leq i \leq p - 1$. Polynomial $T_3(x)$ seems to confirm this hypothesis. Moreover, we present in this section some Benedetto type identities and the general form of cubic polynomials satisfying some characteristic equalities connected with elements of 3-periodic orbits of T_3 .

Presented paper constitutes the continuation of a discussion started in paper [8]. On its basis the paper [9] has also been prepared in which, among others, the new families of Chebyshev polynomials are generated. Next, paper [10] of the engineering nature is an effect of common interdisciplinary research in the subject of chaos theory.

2 Introduction

In the paper we intend to discuss the periodic orbits of certain basic quadratic and cubic polynomials. The main rôle in discussion will be played by the following polynomials (see [11–15], we note that all presented below polynomials are minimal polynomials of its roots):

$$p(\mathbb{X}) = \mathbb{X}^3 - 3\mathbb{X} + 1 = \prod_{k=0}^2 (\mathbb{X} - c(2^k \beta)),$$

$$q(\mathbb{X}) = \mathbb{X}^3 + \mathbb{X}^2 - 2\mathbb{X} - 1 = \prod_{k=0}^2 (\mathbb{X} - c(2^k \alpha)),$$

$$ps(\mathbb{X}) := \mathbb{X}^3 - 3\mathbb{X} + \sqrt{3} = \prod_{k=0}^2 (\mathbb{X} - (-1)^k s(2^k \beta)),$$

$$qs(\mathbb{X}) := \mathbb{X}^3 - \sqrt{7}\mathbb{X}^2 + \sqrt{7} = \prod_{k=0}^2 (\mathbb{X} - s(2^k \alpha)),$$

$$qs_2(\mathbb{X}) := -q(2 - \mathbb{X}) = \mathbb{X}^3 - 7\mathbb{X}^2 + 14\mathbb{X} - 7 = \prod_{k=0}^2 (\mathbb{X} - s^2(2^k \alpha)),$$

$$\begin{aligned} P_1(\mathbb{X}) &:= \mathbb{X}^3 + \frac{1 - \sqrt{13}}{2}\mathbb{X}^2 - \mathbb{X} + \frac{\sqrt{13} - 3}{2} \\ &= (\mathbb{X} - c(\delta))(\mathbb{X} - c(3\delta))(\mathbb{X} - c(4\delta)), \end{aligned}$$

$$\begin{aligned}
P_2(\mathbb{X}) &:= \mathbb{X}^3 + \frac{1 + \sqrt{13}}{2} \mathbb{X}^2 - \mathbb{X} + \frac{\sqrt{13} + 3}{2} \\
&= (\mathbb{X} - c(2\delta))(\mathbb{X} - c(5\delta))(\mathbb{X} - c(6\delta)), \\
P(\mathbb{X}) &:= P_1(\mathbb{X})P_2(\mathbb{X}) = \mathbb{X}^6 + \mathbb{X}^5 - 5\mathbb{X}^4 - 4\mathbb{X}^3 + 6\mathbb{X}^2 + 3\mathbb{X} - 1, \\
Q(\mathbb{X}) &:= \mathbb{X}^5 + \mathbb{X}^4 - 4\mathbb{X}^3 - 3\mathbb{X}^2 + 3\mathbb{X} + 1 = \prod_{k=0}^4 (\mathbb{X} - c(2^k\gamma)), \\
R(\mathbb{X}) &:= \mathbb{X}^4 - \mathbb{X}^3 - 4\mathbb{X}^2 + 4\mathbb{X} + 1 = \prod_{k=0}^3 (\mathbb{X} - c(2^k\varepsilon)),
\end{aligned}$$

where the notation given below is used

$$\begin{aligned}
\alpha &:= \frac{2\pi}{7}, & \beta &:= \frac{2\pi}{9}, & \gamma &:= \frac{2\pi}{11}, & \delta &:= \frac{2\pi}{13}, & \varepsilon &:= \frac{2\pi}{15}, \\
c(x) &:= 2 \cos(x) & \text{and} & & s(x) &:= 2 \sin(x),
\end{aligned}$$

and which will be applied throughout the entire paper. In this connection we obtain the following form of the known trigonometric identities

$$\begin{aligned}
c(2x) &= c^2(x) - 2 = 2 - s^2(x), \\
s(2x) &= s(x)c(x), \\
s(x) \prod_{k=0}^{N-1} c(2^k x) &= s(2^N x).
\end{aligned}$$

Remark 1 Polynomial $qs_2(\mathbb{X})$ is called the Johannes Kepler polynomial (see [5], vol III). We have $\mathbb{X}qs_2(\mathbb{X}) = 2T_7(\mathbb{X}/2)$ where $T_7(\mathbb{X})$ is the seventh Chebyshev polynomial of the first kind.

Moreover we will use the notation $-A := \{-a : a \in A\}$ for every nonempty $A \subset \mathbb{R}$.

We know [16, 17] that if \mathbb{K} is an algebraically closed field of zero characteristic and f is a non-linear polynomial over \mathbb{K} , then f has in \mathbb{K} the cycles of all length with at most one exception. Moreover, the exceptional case may occur only when f is linearly conjugated to the polynomial $\mathbb{X}^2 - \mathbb{X}$ (we say that polynomials f and g are *linearly conjugated* if $f(a\mathbb{X} + b) = ag(\mathbb{X}) + b$ for some $a, b \in \mathbb{K}$, $a \neq 0$). In this exceptional case f does not possess any cycles of length 2.

Cases of the cycles of polynomials over algebraically closed fields of positive characteristics have been discussed by Pezda in papers [18, 19].

Certainly, the problem of analytic description of such orbits in specific cases (especially over complex field) is still interesting for us. It turned out that there exist several particular quadratic and cubic polynomials, in case of which the analysis of their orbits is especially interesting because it is connected, among others, with

determination of new sequences of integers (associated with the length of appropriate orbits of given polynomials) and new sequences of “modified” Chebyshev polynomials possessing the intriguing properties. It seems that obtained results are worth to be popularized for the sake of their accessibility and creativity. This paper is a substantial supplement of papers [8, 9].

We say that n -periodic real orbit $\{x_1, x_2, \dots, x_n\}$ of a polynomial $p \in \mathbb{R}[x]$ possesses *the trigonometric form* if there exist $\alpha_1, \alpha_2, \dots, \alpha_n \in [0, 2\pi)$ such that $x_i = c(\alpha_i)$ for every $i = 1, 2, \dots, n$. In particular, if there exist $\alpha \in (0, 2\pi)$ and $k \in \mathbb{N}$ such that $x_i = c(k^i \alpha)$ for every $i = 1, 2, \dots, n$, then orbit $\{x_1, x_2, \dots, x_n\}$ will be called the *n -periodic trigonometric orbit*.

Remark 2 In paper [20] the authors have proven that a real analytic function, whose Maclaurin series expansion is $\sum_{n=0}^{\infty} a_n x^n$, behaves chaotically whenever the following condition holds

$$a_2^2 - a_1 a_3 > 0. \tag{1}$$

It can be easily observed that all the polynomials presented in this section, and simultaneously all ones discussed in this paper, satisfy condition (1), i.e. they are chaotic [21–24].

3 The First Set of Trigonometric Type Polynomials

In this section polynomials

$$s_w(x) := -\frac{1}{w}x^2 - x + 2w$$

and

$$t_w(x) := s_w(x) - w$$

will be considered. We will present all their 2, 3 and 4-periodic orbits and discuss their rôle in construction of the cubic polynomials possessing the same 3-periodic orbits. We will also present generalizations of the Benedetto identities [1].

Theorem 1 *We have*

$$\begin{aligned} s_w(2w \cos x) &= -2w \cos x - 2w \cos 2x, \\ s_w(2w \cos(k\beta)) &= 2w \cos(4k\beta), \end{aligned} \tag{2}$$

$$t_w(2w \cos(k\alpha)) = 2w \cos(4k\alpha), \tag{3}$$

for every $k = 1, 2, 4$, $x \in \mathbb{R}$ and $w \in \mathbb{C} \setminus \{0\}$.

Proof We note that

$$t_1 \circ t_1 \circ t_1(x) - x = -(x^2 + 2x - 1)(q(x))^2$$

and

$$t_w \circ t_w \circ t_w\left(\frac{x}{w}\right) = w(t_1 \circ t_1 \circ t_1(x)).$$

□

Corollary 1 *Sets*

$$\{wc(\beta), wc(2\beta), wc(4\beta)\} \quad \text{and} \quad \{wc(\alpha), wc(2\alpha), wc(4\alpha)\}$$

are the 3-periodic orbits of polynomials s_w and t_w , respectively. In case of t_w the last set is the only 3-periodic orbit of this map. From Sharkovsky's Theorem [25–28] we get that both s_w and t_w possess periodic orbits of any finite cardinality.

Remark 3 Since

$$s_1 \circ s_1 \circ s_1(x) - x = -(x^2 + 2x - 2)p(x)(x^3 + 2x^2 - 3x - 5),$$

it could be easily deduced that there exists only one more additional 3-periodic orbit of $s_w(x)$:

$$\{wx_1, wx_2, wx_3\}$$

(more precisely, $wx_1 \xrightarrow{s_w} wx_2 \xrightarrow{s_w} wx_3 \xrightarrow{s_w} wx_1$) where $x_1 = -2.3772\dots$, $x_2 = -1.27389\dots$ and $x_3 = 1.65109\dots$ are the roots (all real) of polynomial $x^3 + 2x^2 - 3x - 5$. Observe that the orbit $\{x_1, x_2, x_3\}$ cannot be of the shape $\{c(\alpha_1), c(\alpha_2), c(\alpha_3)\}$ for some $\alpha_1, \alpha_2, \alpha_3 \in [0, 2\pi)$, i.e. this orbit does not possess the trigonometric form.

Remark 4 Numbers $(-1 \pm \sqrt{3})w$ are the only fixed points of s_w , while numbers $(-1 \pm \sqrt{2})w$ are the only fixed points of t_w .

Remark 5 Sets $\{c(\frac{\pi}{4}), c(\frac{3}{4}\pi)\} = \{\pm\sqrt{2}\}$ and $\{\sqrt{2}s(\frac{\pi}{12}), -\sqrt{2}c(\frac{\pi}{12})\} = \{-1 \pm \sqrt{3}\}$ are the only 2-periodic orbits of $s_1(x)$. Sets $\{\pm s(\frac{\pi}{6})\} = \{\pm 1\}$ and $\{-1 \pm \sqrt{2}\}$ are the only 2-periodic orbits of $t_1(x)$.

Moreover, $s_1(x)$ possesses three 4-periodic orbits (all omitted here since none is of the trigonometric form), whereas $t_1(x)$ possesses only one real 4-periodic orbit $\{-1.26799, -0.0960418, 0.66019, 1.08682\}$ and two complex 4-periodic orbits.

Remark 6 (The Benedetto type identities [1]) We have

$$\begin{aligned} \prod_{k=0}^2 (c(2^k \beta) + s_1(c(2^k \beta))) &= \prod_{k=0}^2 (c(2^k \beta) + c(2^{k+2} \beta)) = \prod_{k=0}^2 (-c(2^{k+1} \beta)) = 1, \\ \prod_{k=0}^2 (c(2^k \alpha) + t_1(c(2^k \alpha))) &= \prod_{k=0}^2 (c(2^k \alpha) + c(2^{k+2} \alpha)) \\ &= \prod_{k=0}^2 (-1 - c(2^{k+1} \alpha)) = q(-1) = 1. \end{aligned}$$

3.1 Generalization of the Benedetto Type Identities

If complex roots of the following complex polynomial

$$F(x) = x^3 + ax^2 + bx + c = \prod_{i=1}^3 (x - x_i)$$

form the 3-periodic orbit of some polynomial $G(x)$ then we have

$$\prod_{i=1}^3 (x_i + G(x_i)) = \prod_{i=1}^3 (-a - x_i) = F(-a) = c - ab.$$

Similarly, if complex roots of the following quartic complex polynomial

$$\tilde{F}(x) = x^4 + ax^3 + bx^2 + cx + d = \prod_{i=1}^4 (x - x_i)$$

form the 4-periodic orbit of some polynomial $\tilde{G}(x)$ then we have

$$\prod_{i=1}^4 (x_i + \tilde{G}(x_i) + \tilde{G}^2(x_i)) = \prod_{i=1}^4 (-a - x_i) = \tilde{F}(-a) = ba^2 - ca + d.$$

3.2 Properties (2) and (3) for Cubic Polynomials

Now we describe all the cubic polynomials possessing properties (2) and (3).

Theorem 2 Let $r(x) := x^3 + ax^2 + bx + c$, $a, b, c \in \mathbb{C}$.

(a) If

$$r(2w \cos(k\beta)) = 2w \cos(4k\beta), \quad (4)$$

for every $k = 1, 2, 4$, where $w \in \mathbb{C} \setminus \{0\}$, then $a = -\frac{1}{w}$, $b = -3w^2 - 1$ and $c = w^3 + 2w$, i.e.

$$r(x) = w^3 p\left(\frac{x}{w}\right) + s_w(x).$$

Moreover, $r(x)$ is the only polynomial satisfying condition (4). Hence, the set

$$\{wc(\beta), wc(2\beta), wc(4\beta)\}$$

is a 3-periodic orbit of $r(x)$ and, in consequence, polynomial $r(x)$ possesses n -elements periodic orbits for every $n \in \mathbb{N}$. We note that for $w = 1$ we obtain

$$r(x) = p(x) + s_1(x) = x^3 - x^2 - 4x + 3.$$

(b) If

$$r(2w \cos(k\alpha)) = 2w \cos(4k\alpha), \quad (5)$$

for every $k = 1, 2, 4$, then $a = w - \frac{1}{w}$, $b = -2w^2 - 1$ and $c = w^3 + w$, i.e.

$$r(x) = w^3 q\left(\frac{x}{w}\right) + t_w(x).$$

Furthermore, $r(x)$ is the only polynomial satisfying condition (5). The set

$$\{wc(\alpha), wc(2\alpha), wc(4\alpha)\}$$

is a 3-periodic orbit of $r(x)$ and $r(x)$ possesses periodic orbits of any finite cardinality. In case of $w = 1$ we get

$$r(x) = q(x) + t_1(x) = p(x) - 1 = x^3 - 3x.$$

Proof Only the case of $w = 1$ will be discussed here.

(a) From (4) we get

$$\sum_{k=0}^2 r(c(2^k \beta)) = \sum_{k=0}^2 c(2^k \beta),$$

which by definition of $p(x)$ implies

$$-3 + a \sum_{k=0}^2 c^2(2^k \beta) + 3c = 0,$$

i.e.,

$$a \left(6 + \sum_{k=0}^2 c(2^k \beta) \right) + 3(c - 1) = 0,$$

$$2a + c = 1.$$

Moreover,

$$\begin{aligned} (c(\beta))^3 + a(c(\beta))^2 + b(c(\beta)) + c &= c(4\beta) = -c(\beta) - c(2\beta) \\ &= -c(\beta) - c^2(\beta) + 2. \end{aligned}$$

Hence, by

$$\begin{aligned} 3c(\beta) - 1 + (a + 1)c^2(\beta) + (b + 1)c(\beta) + c - 2 &= 0, \\ (a + 1)c^2(\beta) + (b + 4)c(\beta) + c - 3 &= 0, \end{aligned}$$

which, in view of the fact that $p(x)$ is the minimal polynomial of its roots, means that

$$\begin{aligned} a + 1 = b + 4 = c - 3 &= 0, \\ a = -1, \quad b = -4 \quad \text{and} \quad c &= 3. \end{aligned}$$

(b), (c), (d) Proofs run similarly like in case (a). □

4 Amazing Cubic Polynomial $-3x + \frac{1}{w^2}x^3$

Title polynomial

$$f_w(x) := -3x + \frac{1}{w^2}x^3,$$

where $w \in \mathbb{C} \setminus \{0\}$, is the rescaled third Chebyshev polynomial of the first kind $T_3(x)$ (more precisely, we have $f_w(x) = wT_3(\frac{x}{w})$) and it has a periodic orbits for every $n \in \mathbb{N}$. All of them have trigonometric periodic form (we note that $f_w([-2|w|, 2|w|]) = [-2|w|, 2|w|]$ for every $w \in \mathbb{R}$ and, what is very attractive, also $f_w([-2w, 2w]) = [-2w, 2w]$ for every $w \in \mathbb{C}$). Moreover these orbits could be deduced from the discussion of sets of the form

$$\mathfrak{C}_{r,n} = \left\{ \cos\left(3^k \frac{\pi r}{n}\right) : k = 0, 1, \dots \right\}$$

and

$$\mathfrak{S}_{r,n} = \left\{ (-1)^k \sin\left(3^k \frac{\pi r}{n}\right) : k = 0, 1, \dots \right\},$$

where $n \in \mathbb{N}$, $n \geq 4$, $(n, 3r) = 1$. It is the consequence of identities (6) and (7) given below.

Theorem 3 *The following identities hold true*

$$f_w(\pm 2w \cos x) = \pm 2w \cos 3x, \quad (6)$$

$$f_w(\pm 2w \sin x) = \mp 2w \sin 3x, \quad (7)$$

where either upper signs or lower signs, respectively, are considered.

Hence (and from the form of compositions of f_w) we get that sets

$$\begin{aligned} C(w; \alpha) &:= \{wc(\alpha), wc(2\alpha), wc(4\alpha)\}, C(-w; \alpha), \\ C_1(w; \delta) &:= \{wc(\delta), wc(3\delta), wc(4\delta)\}, C_1(-w; \delta), \\ C_2(w; \delta) &:= \{wc(2\delta), wc(5\delta), wc(6\delta)\}, \\ C_2(-w; \delta), &\left(\text{we remember that } \delta = \frac{2\pi}{13} \right) \\ S(w; \alpha) &:= \{ws(\alpha), ws(2\alpha), ws(4\alpha)\}, S(-w; \alpha) \end{aligned}$$

are all 3-periodic orbits of f_w ,

$$\begin{aligned}
C(w; \gamma) &:= \{wc(2^k\gamma) : k = 0, 1, \dots, 4\}, C(-w; \gamma), \\
S(w; \gamma) &:= \{ws(2^k\gamma) : k = 0, 1, \dots, 4\}, \\
S(-w; \gamma) &\left(\text{we remember that } \gamma = \frac{2\pi}{11} \right)
\end{aligned}$$

are the 5-periodic orbits of f_w ,

$$S_1^\pm(w; \delta) := \{\pm ws(\delta), \pm ws(3\delta), \pm ws(4\delta)\}$$

and

$$S_2^\pm(w; \delta) := \{\pm ws(2\delta), \pm ws(5\delta), \pm ws(6\delta)\}$$

are the 6-periodic orbits of f_w . It is obvious that $f_w(x)$ possesses the n -periodic orbits for every $n \in \mathbb{N}$. The only fixed points of f_w are 0 and $\pm 2w$.

The only 2-periodic orbits of f_w are sets

$$\{-\sqrt{2}w, \sqrt{2}w\} = \left\{ wc\left(\frac{\pi}{4}\right), wc\left(\frac{3}{4}\pi\right) \right\}, \{\varphi w, -\varphi^{-1}w\} = \left\{ wc\left(\frac{\pi}{5}\right), wc\left(\frac{3}{5}\pi\right) \right\}$$

and

$$\{-\varphi w, \varphi^{-1}w\} = \left\{ ws\left(\frac{\pi}{5}\right), -ws\left(\frac{3}{5}\pi\right) \right\},$$

where φ denotes the golden ratio (see [29]), i.e. $\varphi = \frac{1}{2}(1 + \sqrt{5})$. Moreover, all 4-periodic orbits of f_w can be found in Table 1.

We have

$$\cos\left(3^m \frac{r\pi}{n}\right) = \cos\left(\frac{r\pi}{n}\right) \Leftrightarrow \sin\left(\frac{3^m + 1}{2} \cdot \frac{r\pi}{n}\right) \sin\left(\frac{3^m - 1}{2} \cdot \frac{r\pi}{n}\right) = 0,$$

which implies easily that the 7-periodic orbits of $f(x) := f_1(x)$ can be found among sets of the form $2\mathfrak{C}_{r,547}$ and $2\mathfrak{C}_{r,1093}$, whereas the 13-periodic orbits of $f(x)$ can be found among sets of the form $2\mathfrak{C}_{r,398581}$ and $2\mathfrak{C}_{r,797161}$. All four numbers n in last notation of $\mathfrak{C}_{r,n}$ are primes and the sets $2\mathfrak{C}_{r,n}$ can be considered in these cases as “singular”.

Proof Relations (6) and (7) follow from the known trigonometric identities

$$\cos 3x = -3 \cos x + 4 \cos^3 x \quad \text{and} \quad \sin 3x = 3 \sin x - 4 \sin^3 x. \quad \square$$

Table 1 Periodic orbits of polynomial $f(x) = x^3 - 3x$

$$A_1\left(w; \frac{\pi}{10}\right) := \left\{ wc\left(\frac{\pi}{10}\right), wc\left(\frac{3\pi}{10}\right), wc\left(\frac{9\pi}{10}\right), wc\left(\frac{27\pi}{10}\right) \right\}$$

$$= \left\{ \pm wc\left(\frac{\pi}{10}\right), \pm wc\left(\frac{3\pi}{10}\right) \right\} = \left\{ \pm w\sqrt{\frac{1}{2}(5 + \sqrt{5})}, \pm w\sqrt{\frac{1}{2}(5 - \sqrt{5})} \right\},$$

(elements of $A_1(1; \frac{\pi}{10})$ are the roots of polynomial $x^4 - 5x^2 + 5$)

$$A_2\left(w; \frac{\pi}{8}\right) := \left\{ wc\left(\frac{\pi}{8}\right), wc\left(\frac{3\pi}{8}\right), wc\left(\frac{9\pi}{8}\right), wc\left(\frac{27\pi}{8}\right) \right\}$$

$$= \left\{ \pm wc\left(\frac{\pi}{8}\right), \pm wc\left(\frac{3\pi}{8}\right) \right\} = \left\{ \pm w\sqrt{2 + \sqrt{2}}, \pm w\sqrt{2 - \sqrt{2}} \right\},$$

(elements of $A_2(1; \frac{\pi}{8})$ are the roots of polynomial $x^4 - 4x^2 + 2$)

$$A_3\left(w; \frac{\pi}{20}\right) := \left\{ wc\left(\frac{\pi}{20}\right), wc\left(\frac{3\pi}{20}\right), wc\left(\frac{9\pi}{20}\right) = ws\left(\frac{\pi}{20}\right), wc\left(\frac{13\pi}{20}\right) = -ws\left(\frac{3\pi}{20}\right) \right\}$$

$$= \left\{ w\sqrt{2 + \frac{1}{2}\sqrt{10 \pm 2\sqrt{5}}}, \pm w\sqrt{2 - \frac{1}{2}\sqrt{10 \pm 2\sqrt{5}}} \right\},$$

$$A_4\left(w; \frac{7\pi}{20}\right) := \left\{ wc\left(\frac{7\pi}{20}\right), wc\left(\frac{19\pi}{20}\right), wc\left(\frac{17\pi}{20}\right), wc\left(\frac{11\pi}{20}\right) \right\} = -A_3\left(w; \frac{\pi}{20}\right),$$

(elements of set $A_3(w; \frac{\pi}{20}) \cup A_4(w; \frac{7\pi}{20})$ are the roots of polynomial $x^8 - 8x^6 + 19x^4 - 12x^2 + 1$)

$$A_5\left(w; \frac{\pi}{40}\right) := \left\{ wc\left(\frac{\pi}{40}\right), wc\left(\frac{3\pi}{40}\right), wc\left(\frac{9\pi}{40}\right), wc\left(\frac{27\pi}{40}\right) = -ws\left(\frac{7\pi}{40}\right) \right\}$$

$$= \left\{ w\sqrt{2 + \sqrt{2 + \frac{1}{2}\sqrt{10 \pm 2\sqrt{5}}}}, \pm w\sqrt{2 \pm \sqrt{2 - \frac{1}{2}\sqrt{10 \pm 2\sqrt{5}}}} \right\},$$

$$A_6\left(w; \frac{7\pi}{40}\right) := \left\{ wc\left(\frac{7\pi}{40}\right), wc\left(\frac{21\pi}{40}\right) = -ws\left(\frac{\pi}{40}\right), \right.$$

$$wc\left(\frac{17\pi}{40}\right) = ws\left(\frac{3\pi}{40}\right), wc\left(\frac{29\pi}{40}\right) = -ws\left(\frac{9\pi}{40}\right) \left. \right\} =$$

$$= \left\{ -w\sqrt{2 - \sqrt{2 \pm \frac{1}{2}\sqrt{10 \pm 2\sqrt{5}}}}, w\sqrt{2 \pm \sqrt{2 \mp \frac{1}{2}\sqrt{10 - 2\sqrt{5}}}} \right\},$$

$$A_7\left(w; \frac{11\pi}{40}\right) := \left\{ wc\left(\frac{11\pi}{40}\right), wc\left(\frac{33\pi}{40}\right), wc\left(\frac{19\pi}{40}\right), wc\left(\frac{33\pi}{40}\right) \right\} = -A_6\left(w; \frac{7\pi}{40}\right),$$

$$A_8\left(w; \frac{13\pi}{40}\right) := \left\{ wc\left(\frac{13\pi}{40}\right), wc\left(\frac{39\pi}{40}\right), wc\left(\frac{37\pi}{40}\right), wc\left(\frac{31\pi}{40}\right) \right\} = -A_5\left(w; \frac{\pi}{40}\right),$$

(elements of set $A_5(w; \frac{\pi}{40}) \cup A_6(w; \frac{7\pi}{40}) \cup A_7(w; \frac{11\pi}{40}) \cup A_8(w; \frac{13\pi}{40})$ are the roots of polynomial $x^{16} - 16x^{14} + 104x^{12} - 352x^{10} + 659x^8 - 664x^6 + 316x^4 - 48x^2 + 1$)

$$A_9\left(w; \frac{\pi}{41}\right) := \left\{ wc\left(\frac{\pi}{41}\right), wc\left(\frac{3\pi}{41}\right), wc\left(\frac{9\pi}{41}\right), wc\left(\frac{27\pi}{41}\right) = -wc\left(\frac{14\pi}{41}\right) \right\},$$

$$A_{10}\left(w; \frac{2\pi}{41}\right) := \left\{ wc\left(\frac{2\pi}{41}\right), wc\left(\frac{6\pi}{41}\right), wc\left(\frac{18\pi}{41}\right), wc\left(\frac{54\pi}{41}\right) = -wc\left(\frac{13\pi}{41}\right) \right\},$$

$$A_{11}\left(w; \frac{4\pi}{41}\right) := \left\{ wc\left(\frac{4\pi}{41}\right), wc\left(\frac{12\pi}{41}\right), wc\left(\frac{36\pi}{41}\right) = -wc\left(\frac{5\pi}{41}\right), -wc\left(\frac{15\pi}{41}\right) \right\},$$

$$A_{12}\left(w; \frac{7\pi}{41}\right) := \left\{ wc\left(\frac{7\pi}{41}\right), wc\left(\frac{21\pi}{41}\right) = -wc\left(\frac{20\pi}{41}\right) = -ws\left(\frac{\pi}{82}\right), \right.$$

$$wc\left(\frac{19\pi}{41}\right) = ws\left(\frac{3\pi}{82}\right), wc\left(\frac{57\pi}{41}\right) = -wc\left(\frac{16\pi}{41}\right) \left. \right\},$$

$$A_{13}\left(w; \frac{8\pi}{41}\right) := \left\{ wc\left(\frac{8\pi}{41}\right), wc\left(\frac{24\pi}{41}\right) = -wc\left(\frac{17\pi}{41}\right), wc\left(\frac{10\pi}{41}\right), -wc\left(\frac{11\pi}{41}\right) \right\}$$

(continued)

Table 1 (continued)

(elements of set $A_9(w; \frac{\pi}{41}) \cup A_{10}(w; \frac{2\pi}{41}) \cup \dots \cup A_{13}(w; \frac{8\pi}{41})$ are the roots of polynomial $T(x) := x^{20} - x^{19} - 19x^{18} + 18x^{17} + 153x^{16} - 136x^{15} - 680x^{14} + 560x^{13} + 1820x^{12} - 1365x^{11} - 3003x^{10} + 2002x^9 + 3003x^8 - 1716x^7 - 1716x^6 + 792x^5 + 495x^4 - 165x^3 - 55x^2 + 10x + 1$).
The other five orbits are created by sets
$-A_9(w; \frac{\pi}{14}), -A_{10}(w; \frac{2\pi}{41}), -A_{11}(w; \frac{4\pi}{41}), -A_{12}(w; \frac{7\pi}{41}), -A_{13}(w; \frac{8\pi}{14})$.
Elements of these sets are roots of polynomial $T(-x)$.

In the next step of the proof we replace in discussion polynomial $f_w(x)$ by equivalent and simple polynomial $f_1(x) = f(x) = -3x + x^3$. The following decomposition can be obtained

$$f \circ f \circ f(x) - x = -x(x + 2)(x - 2)q(x)q(-x)qs_2(x^2)P(x)P(-x),$$

which, by definitions of $q(x)$, $qs_2(x)$ and $P(x)$, implies the form of all 3-periodic orbits of $f(x)$ and then of $f_w(x)$ after multiplying by w the respective elements of periodic orbits of $f(x)$.

Form of the presented above 5-periodic and 6-periodic orbits of $f_w(x)$ can be obtained from the discussion of sets $\mathfrak{C}_{r,n}$ and $\mathfrak{S}_{r,n}$. For example, we have

$$c(\gamma) \xrightarrow{f} c(3\gamma) \xrightarrow{f} c(2\gamma) \xrightarrow{f} c(5\gamma) \xrightarrow{f} c(4\gamma) \xrightarrow{f} c(\gamma),$$

$$s(\delta) \xrightarrow{f} -s(3\delta) \xrightarrow{f} -s(4\delta) \xrightarrow{f} -s(\delta) \xrightarrow{f} s(3\delta) \xrightarrow{f} s(4\delta) \xrightarrow{f} s(\delta).$$

Whereas, the remarks about the n -periodic orbits for $n = 7$ and $n = 13$ result from the fact that numbers

$$\frac{3^7 - 1}{2} = 1093, \quad \frac{3^7 + 1}{4} = 547, \quad \frac{3^{13} - 1}{2} = 797161 \quad \text{and} \quad \frac{3^{13} + 1}{4} = 398581$$

are all primes.

Remark 7 We have

$$f(f(x)) = f(x)((f(x))^2 - 3)$$

and

$$(f(x))^2 - 3 = (x^3 - 3x)^2 - 3 = -ps(-x)ps(x) = \prod_{k=0}^2 (x - s(2^k\beta))(x + s(2^k\beta)).$$

We note that since f possesses 3-periodic orbit, the polynomial $f(f(x)) = f^2(x)$ is strictly turbulent which means that there exist the disjoint closed subintervals I_0 and I_1 of $[-2, 2]$ such that $I_0 \cup I_1 \subset f^2(I_0) \cap f^2(I_1)$ (see [26]).

Problem 1 Authors of this paper do not know actually whether each periodic orbit of $f(x)$ is of the form $\mathfrak{C}_{r,n}$ or $\mathfrak{S}_{r,n}$ for some $r, n \in \mathbb{N}$, however we have almost obsessive conviction about this. Discussion of the numerical form of polynomial $f^n(x) - x$ indicates that answer to this problem can be positive.

Of course, generalizing our considerations for the other Chebyshev polynomials $T_n(x)$, more precisely for the scaled polynomials $\Omega_n(x) := 2T_n(\frac{x}{2})$ (see [6]), we are asking whether the only possible periodic orbits of these polynomials are of the form

$$\left\{ c \left(\frac{n^k r \pi}{N} \right) : k = 0, 1, \dots, l, \text{ where } (nr, N) = 1 \text{ and } \cos \left(\frac{n^l r \pi}{N} \right) = \cos \left(\frac{r \pi}{N} \right) \right\}?$$

Let us notice, for example, that from identity $T_{mn}(x) = T_m \circ T_n(x)$ it results that

$$T_{3m}(\mathfrak{C}_{1,7}) = T_m(\mathfrak{C}_{1,7})$$

and that $\mathfrak{C}_{1,7}$ is the 3-elements orbit of polynomials $T_5(x)$ and $T_9(x)$.

Partial answer to the posed problems can be found in paper [7, Lemma 2], where it has been proven that if $p \in \mathbb{N}$ is a prime number and $w \in \mathbb{R} \setminus \{0\}$, then all the periodic orbits of $wT_p(\frac{x}{w})$ are among the solutions of equations

$$x = wT_{p^n} \left(\frac{x}{w} \right), \quad x \in \mathbb{R}, \quad n \in \mathbb{N}.$$

In other words, for the respective $\lambda \in \mathbb{R}$, $\varphi \in [0, 2\pi)$, the periodic solutions are among

$$\frac{\lambda}{w} \cos \varphi = T_{p^n} \left(\frac{\lambda}{w} \cos \varphi \right),$$

which for the case $|\frac{\lambda}{w}| \leq 1$ implies that

$$\cos \psi = \cos(p^n \psi),$$

where $\cos \psi := \frac{\lambda}{w} \cos \varphi$.

Remark 8 The map $f_w|_{[-2w, 2w]}$ is transitive (see [30, 31]). In case of this map it follows from the fact that the sequence $\{w c(3^n x \pi)\}_{n=0}^\infty$ is dense in $[-2w, 2w]$ for almost all $x \in \mathbb{R}$. Proof of this fact results from the uniform distribution of sequence $\{3^n x\}_{n=1}^\infty$ for almost all $x \in \mathbb{R}$ (see [32]). In consequence the map $f_w|_{[-2w, 2w]}$ is chaotic in the sense of Devaney (see [21, 31]).

Remark 9 (Benedetto type identities [1]) We have

$$\begin{aligned} \prod_{k=0}^2 (s(2^k \alpha) + f(s(2^k \alpha))) &= \prod_{k=0}^2 (s(2^k \alpha) + s(2^{k+2} \alpha)) \\ &= \prod_{k=0}^2 (\sqrt{7} - s(2^{k+1} \alpha)) = qs(\sqrt{7}) = \sqrt{7}, \\ \prod_{k=0}^2 (c(3^k \delta) + f(c(3^k \delta))) &= (c(\delta) + c(3\delta))(c(3\delta) + c(4\delta))(c(4\delta) + c(\delta)) \\ &= \prod_{k=0}^2 \left(\frac{\sqrt{13} - 1}{2} - c(3^k \delta) \right) = P_1 \left(\frac{\sqrt{13} - 1}{2} \right) = -1, \\ \prod_{k=0}^2 (c(3^k \cdot 2\delta) + f(c(3^k \cdot 2\delta))) &= (c(2\delta) + c(6\delta))(c(6\delta) + c(5\delta))(c(5\delta) + c(2\delta)) \\ &= \prod_{k=0}^2 \left(-\frac{\sqrt{13} + 1}{2} - c(3^k \cdot 2\delta) \right) \\ &= P_2 \left(-\frac{\sqrt{13} + 1}{2} \right) = \sqrt{13} + 2, \\ \prod_{k=0}^3 (c(3^k \frac{\pi}{8}) + f(c(3^k \frac{\pi}{8})) + f^2(c(3^k \frac{\pi}{8}))) &= \prod_{k=0}^3 c(3^k \frac{\pi}{8}) = 2, \\ \prod_{k=0}^3 (c(3^k \frac{\pi}{10}) + f(c(3^k \frac{\pi}{10})) + f^2(c(3^k \frac{\pi}{10}))) &= \prod_{k=0}^3 c(3^k \frac{\pi}{10}) = 5, \\ \prod_{k=0}^4 (c(2^k \gamma) + f(c(2^k \gamma)) + f^2(c(2^k \gamma)) + f^3(c(2^k \gamma))) & \\ &= \prod_{k=0}^4 (-1 - c(2^k \gamma)) = Q(-1) = -1. \end{aligned}$$

4.1 Properties (6) and (7) for the General Cubic Polynomials

At the end of Sect. 4 we present the description of all cubic polynomials satisfying properties (6) and (7) for the fixed argument x equal to a , d and $2d$, respectively.

Theorem 4 Let us put $r(x) = (1 + \frac{1}{w^2})x^3 + ax^2 + bx + c$, where $a, b, c, w \in \mathbb{C}$, $w \neq 0$.

(a) *If*

$$r(ws(2^k\alpha)) = ws(2^{k+2}\alpha), \quad (8)$$

for every $k = 0, 1, 2$, *then*

$$r(x) = \left(1 + \frac{1}{w^2}\right)x^3 - \sqrt{7}wx^2 - 3x + \sqrt{7}w^3 = w^3qs\left(\frac{x}{w}\right) + f_w(x).$$

Moreover, polynomial $r(x)$ *is the only cubic complex polynomial which satisfies condition* (8).

(b) *If*

$$r(wc(2^k\alpha)) = wc(2^{k+2}\alpha), \quad (9)$$

for every $k = 0, 1, 2$, *then*

$$r(x) = \left(1 + \frac{1}{w^2}\right)x^3 - 3(1 + w^2)x + \sqrt{3}w^3 = w^3ps\left(\frac{x}{w}\right) + f_w(x).$$

Similarly like above, polynomial $r(x)$ *is the only cubic complex polynomial which satisfies condition* (9).

(c) *If*

$$r(wc(3^k\delta)) = wc(3^{k+1}\delta), \quad (10)$$

for $k \in \mathbb{N} \cup \{0\}$, *then*

$$r(x) = w^3P_1\left(\frac{x}{w}\right) + f_w(x).$$

Moreover, polynomial $r(x)$ *is the only cubic complex polynomial which satisfies condition* (10) *and it possesses cyclic orbits of any finite cardinality.*

(d) *If*

$$r(wc(3^k2\delta)) = wc(3^{k+1}2\delta), \quad (11)$$

for $k \in \mathbb{N} \cup \{0\}$, *then*

$$r(x) = w^3P_2\left(\frac{x}{w}\right) + f_w(x).$$

Moreover, polynomial $r(x)$ is the only cubic complex polynomial which satisfies condition (11) and it possesses the cyclic orbits of any finite cardinality.

Problem 2 Does the reduction of conditions (8)–(11) to the form $r(A) = A$ for sets $A = \{ws(\alpha), ws(2\alpha), ws(4\alpha)\}$, $\{wc(\alpha), wc(2\alpha), wc(4\alpha)\}$, $\{wc(\delta), wc(3\delta), wc(9\delta)\}$, $\{wc(2\delta), wc(6\delta), wc(18\delta)\}$ change the final description of respective polynomials $r(x)$?

References

1. Benedetto R (2001) An elementary product identity in polynomial dynamics. *Am Math Mon* 108:860–864
2. Mason JC, Handscomb DC (2003) Chebyshev polynomials. Chapman & Hall/CRC, Boca Raton
3. Rivlin TJ (1990) Chebyshev polynomials from approximation theory to algebra and number theory. Wiley, New York
4. Paszkowski S (1975) Numerical applications of Chebyshev polynomials and series. PWN, Warsaw (in Polish)
5. Wituła R, Complex numbers, polynomials and partial fraction decomposition, vols I and II. Wydawnictwo Politechniki Śląskiej (2010) (in Polish)
6. Wituła R, Słota D (2006) On modified Chebyshev polynomials. *J Math Anal Appl* 324:321–343
7. Tričković SB, Stanković MS (2004) On periodic solutions of a certain difference equation. *Fibonacci Q* 42:300–305
8. Wituła R, Słota D (2009) Fixed and periodic points of polynomials generated by minimal polynomials of $2 \cos(\pi/n)$. *Int J Bifur Chaos Appl Sci Eng* 19:3005–3016
9. Hetmaniok E, Lorenc P, Słota D, Wituła R (in press) Periodic orbits of boundary logistic map and new kind of modified Chebyshev polynomials. In: Monograph on the occasion of 100th birthday anniversary of Zygmunt Zahorski, R. Wituła, D. Słota, W. Hołubowski (eds.), Wyd. Pol. Śl., Gliwice.
10. Trawiński T, Kołton W, Hetmaniok E, Słota D, Wituła R (2013) Analysis of Chaotic phenomena occurring in chosen branched kinematic chains of robot manipulators. In: *Wybrane Zagadnienia Elektrotechniki i Elektroniki*, pp 1–8. Czarna
11. Wituła R (2011) Formulae for sums of unimodular complex numbers. WPKJS, Gliwice (in Polish)
12. Wituła R, Słota D (2009) Decomposition of certain symmetric functions of powers of cosine and sine functions. *Int J Pure Appl Math* 50:1–12
13. Wituła R, Słota D (2007) New Ramanujan-type formulas and quasi-fibonacci numbers of order 7. *J Integer Seq* 10 (Article 07.5.6)
14. Wituła R, Słota D (2007) Quasi-fibonacci numbers of order 11. *J Integer Seq* 10 (Article 07.8.5)
15. Wituła R, Słota D (2010) Quasi-fibonacci numbers of order 13 on the occasion of the thirteenth international conference on fibonacci numbers and their applications. *Congr Numer* 201:89–107
16. Baker IN (1960) The existence of fixpoints of entire functions. *Math Z* 73:280–284
17. Baker IN (1964) Fixpoints of polynomials and rational functions. *J London Math Soc* 39:615–622
18. Pezda T (1994) Cycles of polynomials in algebraically closed fields of positive characteristic. *Colloq Math* 67:187–195
19. Pezda T (1996) Cycles of polynomials in algebraically closed fields of positive characteristic II. *Colloq Math* 71:23–30

20. Hacibekiroğlu G, Çağlar M, Polatoğlu Y (2009) The higher order Schwarzian derivative: its applications for chaotic behavior and new invariant sufficient condition of Chaos. *Nonlinear Anal Real World Appl* 10:1270–1275
21. Devaney RL (1989) *An introduction to chaotic dynamical systems*. Addison-Wesley, Boston
22. Gulick D (2012) *Encounters with Chaos and fractals*. CRC Press, Boca Raton
23. Kwietniak D, Oprocha P (2008) Chaos theory from the mathematical viewpoint. *Mat Stosow* 9:1–45 (in Polish)
24. Li TY, Yorke JA (1975) Period three implies Chaos. *Am Math Mon* 82:985–992
25. Ciesielski K, Pogoda Z (2008) On ordering the natural numbers or the Sharkovski theorem. *Am Math Mon* 115:159–165
26. Du BS (2007) A simple proof of Sharkovsky's theorem revisited. *Am Math Mon* 114:152–155
27. Elaydi SN (2005) *An introduction to difference equations*. Springer, New York
28. Misiurewicz M (1997) Remarks on Sharkovsky's theorem. *Am Math Mon* 104:846–847
29. Dunlap R (2006) *The golden ratio and fibonacci numbers*. World Scientific, Singapore
30. Hsu C-H, Li M-C (2002) Transitivity implies period six: a simple proof. *Am Math Mon* 109:840–843
31. Vellekoop M, Berglund R (1994) On intervals, transitivity = Chaos. *Am Math Mon* 101:353–355
32. Kuipers L, Niederreiter H (1974) *Uniform Distribution of Sequences*. Wiley, New York

Examination of Chaos Occurring in Selected Branched Kinematic Chains of Robot Manipulators

Tomasz Trawiński, Wojciech Kołton, Edyta Hetmaniok,
Damian Słota and Roman Witula

Abstract The article focuses on analysis of possible chaotic behavior of chosen kinematic chains of branched robot manipulators. The branched kinematic chain of robot manipulators, analyzed in this paper, consists of one main link (so-called—bough) and multiple links which may be collected into separate branches. Such kinematic chains of robots are kinematically similar for example to top part of human body (trunk and hands). In the article the method for mathematical model formulation of branched kinematic chains is presented. The result of numerical calculation of angular speed and angular displacements of joints are presented and shows their possible chaotic behavior. Finally, the part of mathematical equations responsible (in author's opinion) for vibration transfer between links are presented.

1 Introduction

Intensive development of robotics makes robots enter almost all areas of modern widely understood industry and medicine. Kinematic chains of these robots differ significantly depending on their application, but the dominant feature of the

T. Trawiński (✉) · W. Kołton
Faculty of Electrical Engineering, Department of Mechatronics, Silesian University
of Technology, Gliwice, Poland
e-mail: tomasz.trawinski@polsl.pl

W. Kołton
e-mail: wojciech.kolton@polsl.pl

E. Hetmaniok · D. Słota · R. Witula
Institute of Mathematics, Silesian University of Technology, Gliwice, Poland
e-mail: edyta.hetmaniok@polsl.pl

D. Słota
e-mail: damian.slota@polsl.pl

R. Witula
e-mail: roman.witula@polsl.pl

industrial robot manipulators are their single, serial kinematic chains. In the designs of industrial robot manipulators also are used parallel kinematic chains, such as Stewart platform. In contrast to the robots which are commonly used in the industry, an interesting feature of the robots used in medicine, especially currently developed robots assisted surgery (telesurgery) [1], is the use of several robots with serial open kinematic chains placed on a common shared basis [2]. The manipulators of such robots can be considered and analyzed as branched systems—branched manipulators. In these robots manipulators, each of the individual branches performs a surgical instrument. The class of such robots include: the da Vinci surgical robot, ZEUS, NeuroArm, MicroSurge and many others [3, 4].

A separate class of miniature devices, that can be classified into a group of miniature branched manipulators, are the modern heads positioning systems of mass storage devices—hard disk drives [5–7]. In these systems, the main rotating member (the so-called E-block) is embedded by additional branches—miniature manipulators that move sliders and heads above the surface of storage media [6]. In such complex structures of kinematic chains of branched manipulators may occur the transfer of the oscillations between the working links.

This article provides some examples of the structure of branched kinematic chains of robot manipulators, which have been formulated by the dynamics equation and in particular matrices of inertia. The structures of the inertia matrix after inversion, in which the matrix elements responsible, according to the authors opinion, for the internal positive feedback are indicated, conducive to the transmission of vibrations between the links.

2 Structure of Branched Kinematic Chains

Through the branched kinematic chain robot manipulator we understand the complex kinematic structure consisted of the bough and of the branches. By bough we understand the complex kinematic pair of rigid links (including the base) connected by a rotary joint [5]. For branch we understand the set of kinematic pairs combined together with help of rotary or prismatic joints, which establish the individual open kinematic chains. The whole kinematic chain, consisting of bough and branches of the whole manipulator, will be called by tree of branched manipulator. A typical role that plays each individual branch is positioning and orientation of a single object (the miniature cutters, the laparoscope tip [4], and the heads that read and write data [7]). However, given the division of the tasks of positioning and orientation of the tool in three-dimensional space into two separate tasks: positioning—for which a single manipulator is responsible, orientation—for which a gripper system is responsible, the total number of degrees of freedom of the single branch may be limited to three degrees of freedom. The general structure of the trees of the branched manipulator can be divided according to the spatial configuration of the joints and links in several groups, namely:

- vertical configuration—individual branches are placed one above the other—it can be concluded that the joints and branches links (at initial state) are cut by common vertical plane,
- horizontal configuration—individual branches are located next to each other—it can be concluded that the joints and branches links (at initial state) are cut by common horizontal plane,
- mixed configuration—each group branches are cut by horizontal or by vertical planes.

Figure 1 shows, in depictive way, the structures of trees of branched manipulators, wherein, due to the transparency of the drawings the branches number of degrees of freedom is limited and the joints are marked by marks “x” denoting the rotary or prismatic joints.

In the following analysis, we assume the following form a single branches the kinematic chain, which is composed of three rotary joints with mutually perpendicular axes of rotation. So an example of a branch which meets these assumptions is shown in Fig. 2.

3 Dynamic Matrix Formulation for Branched Kinematic Chains

To formulate the equations of dynamics was used Denavit-Hartenberg notation, with her help was found relationships describing the position and orientation of centre of masses of the individual links of manipulator’s tree. This made it possible to find the Jacobian matrices of centers of masses of links and determine the form of the kinetic energy of the branched manipulator. Figure 3 shows the described kinematic chain of branched manipulator belonging to the vertical configuration.

Described kinematic chain, presented in Fig. 3, allows the formulation of a homogeneous transformation matrix associated with the centers of masses and centers of introduced coordinate systems—associated with links of manipulator tree. The general form of the elementary homogeneous transformation matrix in Denavit-Hartenberg notation is well known and can be found for example in [7]. For presented in Fig. 3 manipulator tree we obtain the following two sets of homogeneous transformation matrix associated with the coordinate system associated with the tree links and associated with centers of masses of tree links. To calculate the Jacobian matrix of centers of masses, which show the relationships between the joint velocities and linear velocity vector and angular velocity vector of the center of gravity, it is necessary to calculate the homogeneous transformation matrix of every centers of masses, which represents its position and orientation expressed in base coordinate system. In the present case we are dealing with seven centers of masses (three for each branch and one for the bough), and therefore the

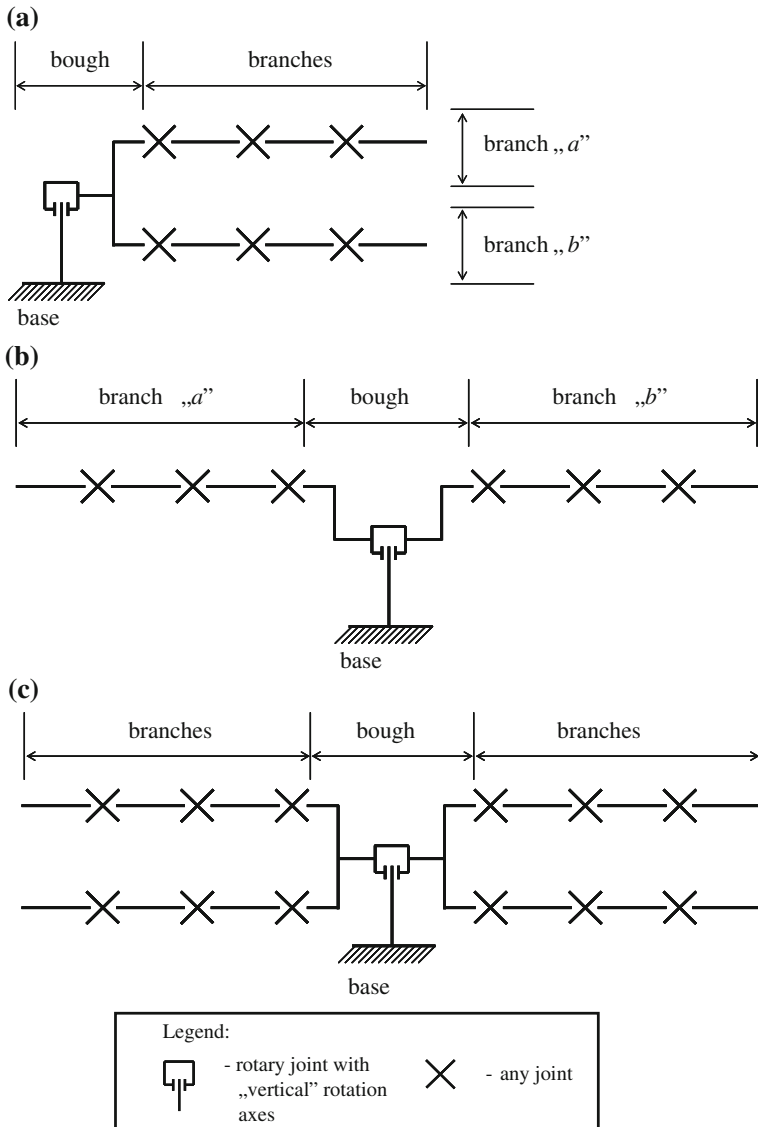


Fig. 1 Structures of trees of branched manipulators: **a** Vertical configuration, **b** Horizontal configuration, **c** Mixed configuration

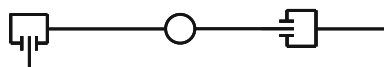


Fig. 2 Exemplary branch consisted with three rotary joint with mutually perpendicular rotation axes

where s_1, c_1 —abbreviate notation of sine and cosine function of ϑ_1 angle; s_{1gi}, c_{1gi} —abbreviated notation of sine and cosine function of the sum of ϑ_1 and ϑ_{gi} angles; a_i, a_{cgi} —denoting length of the “ i -th” link or position of “ gi ” mass centers (with respect to local coordinate system), respectively; d_{gi}, d_{cgi} —denoting “ gi ” links offsets and offsets of “ gi ” mass centers respectively, the sign “ \pm ” became “ $+$ ” for “ a ” branch, sign “ \times ” denotes unimportant elements of chosen matrix.

Based on formulated homogeneous transformation matrices (1)–(4), it is possible to define Jacobian matrices of centers of masses for manipulator tree. They depict the relationship between linear velocity vectors and angular velocity vectors of centers of masses and relevant links in function with the joint velocity vector. Jacobian matrices for bough and branches $g \in \{a, b\}$ are as follows:

$$\mathbf{J}_{c1} = \begin{bmatrix} \mathbf{S}(\mathbf{z}_0)(\mathbf{o}_{c1} - \mathbf{o}_0) & \mathbf{0} & \mathbf{0} & \mathbf{0} \\ \mathbf{z}_0 & \mathbf{0} & \mathbf{0} & \mathbf{0} \end{bmatrix}, \quad (5)$$

$$\mathbf{J}_{cg2} = \begin{bmatrix} \mathbf{S}(\mathbf{z}_0)(\mathbf{o}_{cg2} - \mathbf{o}_0) & \mathbf{S}(\mathbf{z}_{g1})(\mathbf{o}_{cg2} - \mathbf{o}_{g1}) & \mathbf{0} & \mathbf{0} \\ \mathbf{z}_0 & \mathbf{z}_{g1} & \mathbf{0} & \mathbf{0} \end{bmatrix}, \quad (6)$$

$$\mathbf{J}_{cg3} = \begin{bmatrix} \mathbf{S}(\mathbf{z}_0)(\mathbf{o}_{cg3} - \mathbf{o}_0) & \cdots & \mathbf{S}(\mathbf{z}_{g2})(\mathbf{o}_{cg3} - \mathbf{o}_{g2}) & \mathbf{0} \\ \mathbf{z}_0 & \cdots & \mathbf{z}_{g2} & \mathbf{0} \end{bmatrix}, \quad (7)$$

$$\mathbf{J}_{cg4} = \begin{bmatrix} \mathbf{S}(\mathbf{z}_0)(\mathbf{o}_{cg4} - \mathbf{o}_0) & \cdots & \cdots & \mathbf{S}(\mathbf{z}_{g3})(\mathbf{o}_{cg4} - \mathbf{o}_{g3}) \\ \mathbf{z}_0 & \cdots & \cdots & \mathbf{z}_{g3} \end{bmatrix}, \quad (8)$$

with \mathbf{o}_{gi} —denoting coordinates of origin of coordinate system fixed with tree links; \mathbf{o}_{cgi} —denoting coordinates of mass centers; $\mathbf{S}(\mathbf{z}_i)$ —denoting skew symmetric matrix build from versor \mathbf{z}_i .

Appearing in Eqs. (5)–(8) the coordinates of center of masses \mathbf{o}_{cgi} , the origins of coordinate systems of \mathbf{o}_{gi} , the versors axis \mathbf{z}_i are found in the defined homogeneous transformation matrices (1)–(4), which can be written in a general way, namely:

$$\mathbf{o}_{c1} = \mathbf{T}_0^{c1}(1 : 3, 4), \quad (9)$$

$$\mathbf{o}_{cgi} = \mathbf{T}_0^{cgi}(1 : 3, 4), \quad (10)$$

$$\mathbf{z}_{gi} = \mathbf{T}_0^{gi}(1 : 3, 3) \quad (11)$$

The total kinetic energy of the manipulator tree can be represented as the sum of the components of kinematic energy associated with the center of masses of the bough and the sums of the kinetic energy of mass centers of individual branches. The form of the total kinetic energy of the manipulator tree, formulated utilizing previously calculated Jacobian matrices and homogeneous transformation matrices, has the form:

$$\begin{aligned}
 E_k = & \frac{1}{2} \dot{\mathbf{q}}_0^T (m_{c1} \mathbf{J}_{vc1}^T \mathbf{J}_{vc1} + \mathbf{J}_{\omega c1}^T \mathbf{R}_{c1} \mathbf{I}_{c1} \mathbf{R}_{c1}^T \mathbf{J}_{\omega c1}) \dot{\mathbf{q}}_0 \\
 & + \frac{1}{2} \sum_g \dot{\mathbf{q}}_g^T \sum_{s=2}^n (m_{cgs} \mathbf{J}_{vcgs}^T \mathbf{J}_{vcgs} + \mathbf{J}_{\omega cgs}^T \mathbf{R}_{cgs} \mathbf{I}_{cgs} \mathbf{R}_{cgs}^T \mathbf{J}_{\omega cgs}) \dot{\mathbf{q}}_g
 \end{aligned}
 \tag{12}$$

where $g \in \{a, b\}$, n —sum of bough and branches numbers of degrees of freedom (DoF); \mathbf{J}_{vc1} , \mathbf{J}_{vcgs} —Jacobian matrices of linear velocity of center of masses; $\mathbf{J}_{\omega c1}$, $\mathbf{J}_{\omega cgs}$ —Jacobian matrices of angular velocity of center of masses; \mathbf{R}_{c1} , \mathbf{R}_{cgs} —the orientation matrices included in homogenous transformation matrices (1)–(4)—every first 3×3 submatrices. Vectors representing the joint velocities have the following form:

$$\begin{aligned}
 \dot{\mathbf{q}}_0 &= [[\dot{q}_1], [0, 0, \dots, 0]]^T \\
 \dot{\mathbf{q}}_a &= [[\dot{q}_1], [\dot{q}_{a2}, \dot{q}_{a3}, \dots, \dot{q}_{an}]]^T \\
 \dot{\mathbf{q}}_b &= [[\dot{q}_1], [\dot{q}_{b2}, \dot{q}_{b3}, \dots, \dot{q}_{bn}]]^T \\
 &\vdots
 \end{aligned}
 \tag{13}$$

Expressions appearing in the kinetic energy Eq. (12) in parentheses specify the form of the inertia matrix \mathbf{D} of manipulator’s tree. This matrix can be represented as an array of block matrices with the following structure presented in Fig. 4.

In the presented structure of the inertia matrix, for every isolated block matrices (submatrices) it is possible to identify its physical meanings. This can be interpreted physically as follows:

- one element k_{11} of bough self inertia matrix \mathbf{k} —a matrix that can be expressed directly by means of the elements of the Jacobian matrices and elements of orientation matrices in the form of:

Fig. 4 Block structure of inertia matrix \mathbf{D} formulated for manipulator tree presented in Fig. 3

\mathbf{k}	\mathbf{a}_k	\mathbf{b}_k
	\mathbf{a}	$\mathbf{0}$
		\mathbf{b}

sym

$$\begin{aligned}
k_{11} = & m_{c1} \sum_{i=1}^3 J_{vc1_i1}^2 \\
& + I_{zc1} \left(\sum_{i=1}^3 J_{\omega c1_i1} r_{c1_i3} \right)^2 \\
& + \sum_{g \in \{a,b\}} \sum_{s=2}^n m_{cgs} \sum_{i=1}^3 J_{vcgs_i1}^2 \\
& + \sum_{g \in \{a,b\}} \sum_{s=2}^n I_{zgs} \left(\sum_{i=1}^3 J_{\omega cgs_i1} r_{cgs_i3} \right)^2
\end{aligned} \tag{14}$$

where m_{ci} , m_{cgi} —masses of links, $g \in \{a, b\}$; I_{zci} , I_{zgs} —mass moments of inertia of links; J_{vc1_i1} , J_{vcgs_i1} , $J_{\omega c1_i1}$, $J_{\omega cgs_i1}$ —elements of Jacobian matrices; r_{c1_i3} , r_{cgs_i3} —elements of orientation matrices (every first 3×3 submatrices of Eq. (1)–(4)).

- nine-elements, symmetric and square matrix of self inertia of branches a and b :
 - diagonal elements of sub-matrices a and b :

$$a_{k-1,k-1} = \sum_{s=2}^n \left(m_{cas} \sum_{i=1}^3 J_{vcas_ik}^2 + I_{zas} \left(\sum_{i=1}^3 J_{\omega cas_ik} r_{cas_i3} \right)^2 \right) \tag{15}$$

$$b_{k-1,k-1} = \sum_{s=2}^n \left(m_{cbs} \sum_{i=1}^3 J_{vcbs_ik}^2 + I_{zbs} \left(\sum_{i=1}^3 J_{\omega cbs_ik} r_{cbs_i3} \right)^2 \right) \tag{16}$$

where $k \geq 2 \wedge k \leq \text{sum DoF numbers of bough and one branch}$.

- off-diagonal elements of sub-matrices a and b :

$$a_{w,k} = \sum_{s=2}^n \left(m_{cas} \sum_{i=1}^3 \prod_{j \in \{w,k\}} J_{vcas_ij} + I_{zas} \prod_{j \in \{w,k\}} \sum_{i=1}^3 J_{\omega cas_ij} r_{cas_i3} \right) \tag{17}$$

$$b_{w,k} = \sum_{s=2}^n \left(m_{cbs} \sum_{i=1}^3 \prod_{j \in \{w,k\}} J_{vcbs_ij} + I_{zbs} \prod_{j \in \{w,k\}} \sum_{i=1}^3 J_{\omega cbs_ij} r_{cbs_i3} \right) \tag{18}$$

where $k > 2$, $w \geq 2$.

- three-elements, rectangular matrix of mutual coupling inertia matrix between bough and chosen branch links:

Fig. 5 Block structure of inertia matrix D formulated for manipulator tree presented in Fig. 1b

b	b_k^T	0
b_k	k	a_k
0	a_k^T	a

$$a_{k(w,k-1)} = \sum_{s=2}^n \left(m_{cas} \sum_{i=1}^3 \prod_{j \in \{w,k\}} J_{vcas_ij} + I_{zas} \prod_{j \in \{w,k\}} \sum_{i=1}^3 J_{ocas_ij} r_{cas_i3} \right) \quad (19)$$

$$b_{k(w,k-1)} = \sum_{s=2}^n \left(m_{cbs} \sum_{i=1}^3 \prod_{j \in \{w,k\}} J_{vcbs_ij} + I_{zbs} \prod_{j \in \{w,k\}} \sum_{i=1}^3 J_{ocbs_ij} r_{cbs_i3} \right) \quad (20)$$

In a similar manner elements of the inertia matrix can be formulated for the branched kinematic chains presented in Fig. 1b, c. These matrices may arise by moving columns and rows in the matrix presented in Fig. 4, so in the case of a horizontal configuration structure of inertia matrix shall be as presented in Fig. 5.

However, the matrix of inertia (for a mixed configuration) will have the following block structure, shown in Fig. 6.

Fig. 6 Block structure of inertia matrix D formulated for manipulator tree presented in Fig. 1c

d	0	d_k^T	0	0
0	b	b_k^T	0	0
d_k	b_k	k	a_k	c_k
0	0	a_k^T	a	0
0	0	c_k^T	0	c

4 Dynamic Equation in Canonical Form

The equations for the dynamics of the manipulator branched tree can be presented in the canonical form that is convenient in the process of integration of differential equations. For branched manipulator kinematic structure, presented in Fig. 1a (for vertical configuration), these equations will have the general form, in which there is an inverse block matrix of inertia (the first matrix on the right side of the equal sign) [5, 8]:

$$\begin{aligned} \begin{bmatrix} \ddot{q}_1 \\ \ddot{q}_a \\ \ddot{q}_b \end{bmatrix} &= \begin{bmatrix} k_1 & -k_1 a_k a^{-1} & -k_1 b_k b^{-1} \\ & a_1 & a^{-1} a_k^T k_1 b_k b^{-1} \\ sym & & b_1 \end{bmatrix} \begin{Bmatrix} \tau_1 \\ \tau_a \\ \tau_b \end{Bmatrix} - \\ &- \begin{bmatrix} B_1 & 0 & 0 \\ 0 & B_a & 0 \\ 0 & 0 & B_b \end{bmatrix} \begin{bmatrix} \dot{q}_1 \\ \dot{q}_a \\ \dot{q}_b \end{bmatrix} - \begin{bmatrix} G_1 \\ G_a \\ G_b \end{bmatrix} \end{aligned} \quad (21)$$

where q_1, q_a, q_b —vectors of joints angular displacements, single and double points above vectors of joint angular displacements denoting angular speed and angular acceleration; τ_1, τ_a, τ_b —vectors of driving torque; B_1, B_a, B_b —diagonal matrices of joints dumping; G_1, G_a, G_b —vector of gravitational torque.

Occurring in matrix (21) the inverted matrices k_1, a_1, b_1 are expressed by the following relationships:

$$\begin{aligned} k_1 &= (k - a_k a^{-1} a_k^T - b_k b^{-1} b_k^T)^{-1}, \\ a_1 &= (a - a_k^T (k_1^{-1} + a_k a^{-1} a_k^T)^{-1} a_k)^{-1}, \\ b_1 &= (b - b_k^T (k_1^{-1} + b_k b^{-1} b_k^T)^{-1} b_k)^{-1}. \end{aligned} \quad (22)$$

Vector components of gravitational torque G_i (bough and branches), which are present in matrix (21) depend on the spatial configuration of the whole manipulator tree versus the coordinate system associated with the ground. This article assumes that the axis z_0 of the base coordinate is tangent (parallel) to the equipotential lines of the gravitational field of the earth. This corresponds to a situation in which the tree of robot manipulator is suspended on the operating table (in the case of surgical robot), so kinematic chain presented in Fig. 3 is rotated by the angle $\vartheta_0 = -\pi/2$. Vectors of gravitational torques are calculated using previously formulated homogeneous transformation matrices of mass centers (Eqs. (1)–(4)), namely:

$$G_i = g \frac{\partial \sum_i T_{0(1,4)}^{ci} m_{ci}}{\partial q_i}, \quad (23)$$

where g —acceleration constant due to gravity, $i \in \{1, a2, a3, a4, b2, b3, b4\}$.

5 Simulation Studies of Vibrations in Branched Kinematic Chains

In simulation studies, the following parameters of the model of branches of manipulator tree were chosen: weight— $m_1 = 10$ kg, $m_{a2,b2} = 4$ kg, $m_{a3,a4,b3,b4} = 2$ kg, mass moments of inertia— $I_1 = 0.1$ kg·m², $I_{a2,a3,b2,b3} = 0.05$ kg·m², $I_{a4,b4} = 0.005$ kg·m², the length of the links— $a_1 = 1$ m, $a_{a2,b2} = 0.5$ m, position of centers of masses of the links— $a_{c1} = -0.1$ m, $a_{ca2,cb2} = 0.25$ m, $a_{ca3,cb3} = 0$ m, $d_{ca4,cb4} = 0.05$ m. Simulation studies were performed in MATLAB/Simulink with the following adopted initial conditions: $\omega_i = 0$ rad/s, $\vartheta_{a3,b3} = -\pi/2$ rad, the rest of the initial variables of angular displacements $\vartheta_i = 0$ rad. Damping coefficients were assumed in the same way for all joints equals $B_i = 0.1$ N·m·s/rad. The simulation calculations used the ode45 integration method. Figs. 7, 8 and 9 show the Poincare sections of the trajectories of speed v . angular displacement in joint of bough and the first joint of branches, strobed at time intervals corresponding to the period of driving torque. The driving torque was applied to first joint of branch a . The amplitude of sinusoidal driving torque was $\tau_{ea2} = 4$ N·m and the frequency was $f_{a2} = 1$ Hz. From the analysis of Fig. 8 it results that the trajectory of the first link of branch a tends to elliptical like attractor [9], furthermore the first link of branch b also tends to elliptical attractor (Fig. 9). However, the trajectory of bough seeks to shape resembling an isosceles triangle (Fig. 7). In contrast, the quite different characters take on the trajectories for driving first joint of a branch at frequency $f_{a2} = 0.7325$ Hz and amplitude $\tau_{ea2} = 0.25$ N·m (Figs. 10, 11 and 12). The waveforms trajectory of the first joints of branches a and b resemble the shape of deformed conchoid or Pascal snails [10–12] (Figs. 11 and 12), wherein, in the upper part of the trajectory shown in Fig. 11, it is delaminated as well the lower part of the trajectory presented in Fig. 12. This proves to double or even to fourfold periods of

Fig. 7 Trajectories of speed versus angular displacement of bough

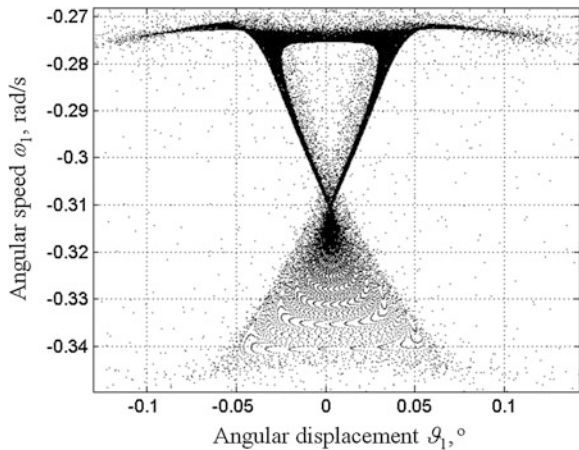


Fig. 8 Trajectories of speed versus angular displacement of branch *a*

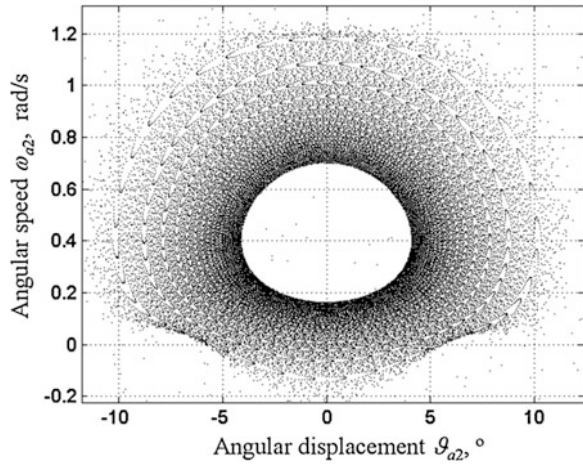


Fig. 9 Trajectories of speed versus angular displacement of branch *b*

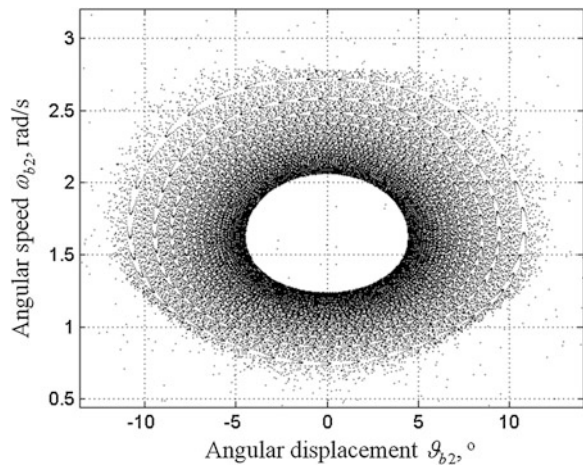


Fig. 10 Trajectories of speed versus angular displacement of bough

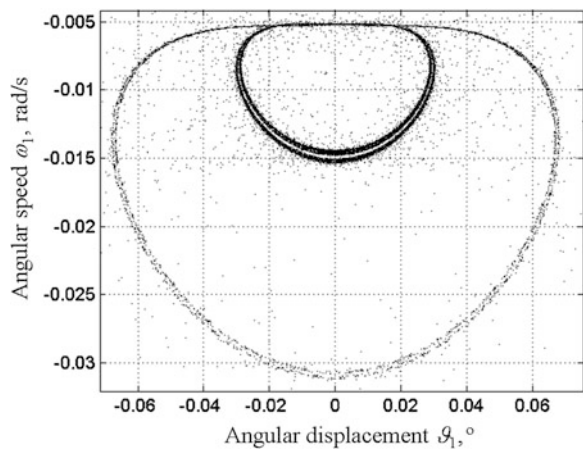


Fig. 11 Trajectories of speed versus angular displacement of branch *a*

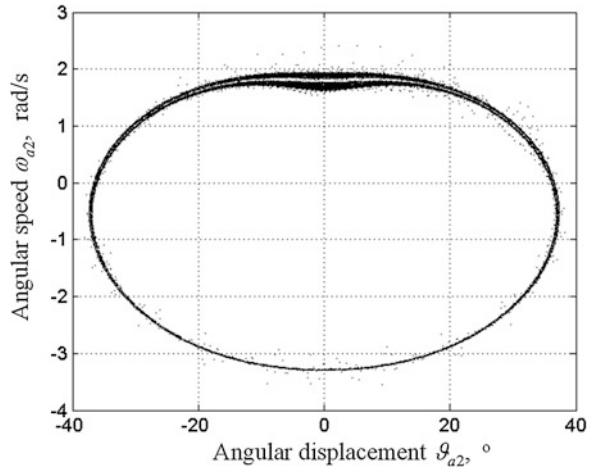
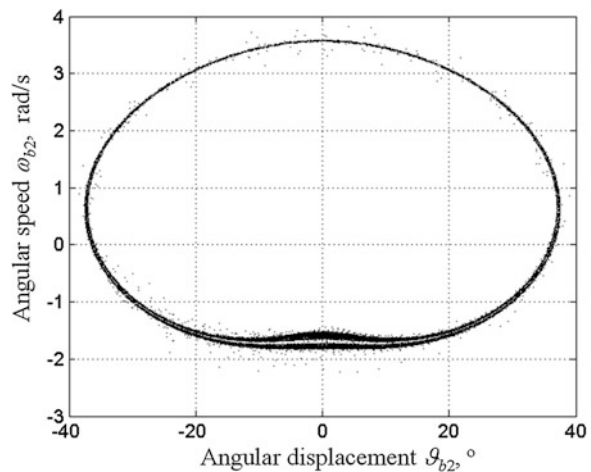


Fig. 12 Trajectories of speed versus angular displacement of branch *b*



trajectory. The waveforms in Figs. 10, 11 and 12 show the evolution in time of the branched manipulator trajectory in the interval of 25,000–55,000 s.

The further evolution of the system in time results in conversion of a trajectory to form presented in Figs. 13, 14 and 15. The trajectories of the first joint of branches are divided into two loops, mutually intertwined. Presented waveforms show the evolution over time in the interval from 95,000 to 1,05,000 s.

In the analysis of these waveforms it can be seen the striving to generate motion in branch joints (in this case in branch *b*), in branch which are not subject to external forcing, but as result of motion in the other branches (which are subjected to external driving torque—in this case, in the first joint of branch *a*). It can be concluded that the motion of branch is synchronized. In order to demonstrate that components of Eq. (21) are responsible for foster mutual synchronization

Fig. 13 Trajectories of speed versus angular displacement of bough

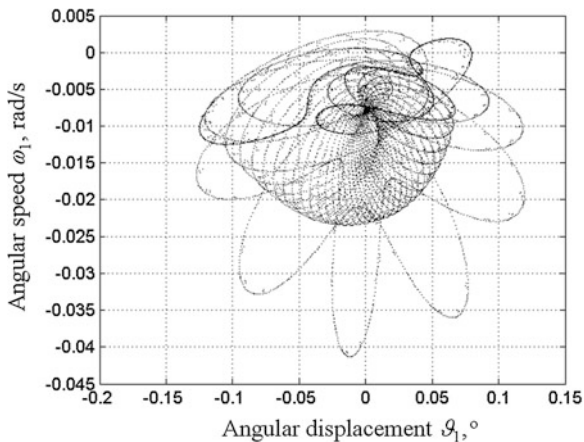


Fig. 14 Trajectories of speed versus angular displacement of branch *a*

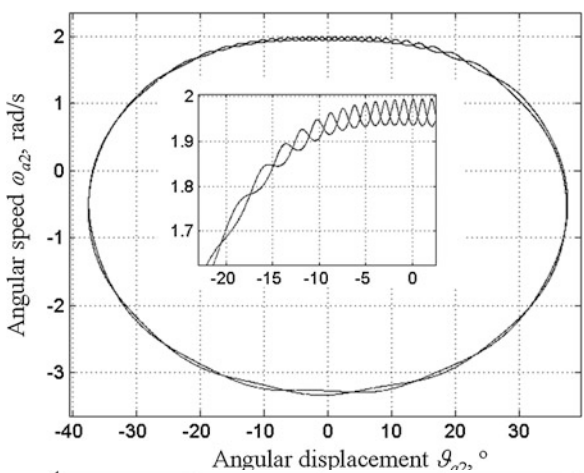
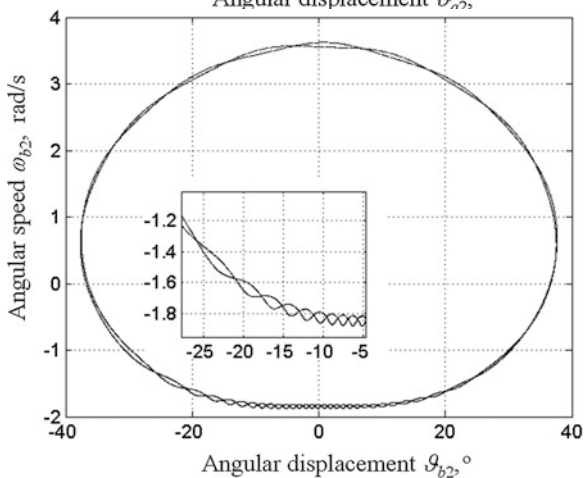


Fig. 15 Trajectories of speed versus angular displacement of branch *b*



(couplings between branches and the transmission of vibrations), assume that the bough is brake, so $\omega_1 = 0$ rad/s, and $\tau_{e1} = 0$ N·m.

In such conditions Eq. (21) may be transformed to the following two models:

- the first model—in which there is a component present in the matrix of inertia block, having the form:

$$\mathbf{a}^{-1} \mathbf{a}_k^T \mathbf{k}_1 \mathbf{b}_k \mathbf{b}^{-1} \quad (24)$$

- the second model—in which above mentioned component is eliminated.

Mathematical model of branched manipulator takes, after simplification, the following matrix form:

- the first model:

$$\begin{aligned} \ddot{\mathbf{q}}_a &= \mathbf{k}_1 \mathbf{a}_k \mathbf{a}^{-1} \mathbf{G}_1 + \mathbf{a}_1 (\tau_a - \mathbf{B}_a \dot{\mathbf{q}}_a - \mathbf{G}_a) \\ &\quad - \mathbf{a}^{-1} \mathbf{a}_k^T \mathbf{k}_1 \mathbf{b}_k \mathbf{b}^{-1} (\mathbf{B}_b \dot{\mathbf{q}}_b + \mathbf{G}_b) \\ \ddot{\mathbf{q}}_b &= \mathbf{k}_1 \mathbf{b}_k \mathbf{b}^{-1} \mathbf{G}_1 - \mathbf{b}_1 (\mathbf{B}_b \dot{\mathbf{q}}_b + \mathbf{G}_b) + (\mathbf{a}^{-1} \mathbf{a}_k^T \mathbf{k}_1 \mathbf{b}_k \mathbf{b}^{-1})^T \tau_a \\ &\quad - (\mathbf{a}^{-1} \mathbf{a}_k^T \mathbf{k}_1 \mathbf{b}_k \mathbf{b}^{-1})^T (\mathbf{B}_a \dot{\mathbf{q}}_a + \mathbf{G}_a) \end{aligned} \quad (25)$$

- the second model:

$$\begin{aligned} \ddot{\mathbf{q}}_a &= \mathbf{k}_1 \mathbf{a}_k \mathbf{a}^{-1} \mathbf{G}_1 + \mathbf{a}_1 (\tau_a - \mathbf{B}_a \dot{\mathbf{q}}_a - \mathbf{G}_a) \\ \ddot{\mathbf{q}}_b &= \mathbf{k}_1 \mathbf{b}_k \mathbf{b}^{-1} \mathbf{G}_1 - \mathbf{b}_1 (\mathbf{B}_b \dot{\mathbf{q}}_b + \mathbf{G}_b) \end{aligned} \quad (26)$$

In Figs. 16 and 17 the Poincare sections is presented for motion trajectories related with branches a and b , obtained results came from solving the second model represented by Eq. (26). In the first joint of branch a the sinusoidal driving torque was applied with frequency $f_{a2} = 0.5$ Hz and amplitude $\tau_{ea2} = 1$ mN·m (bough joint was stopped). Presented in Figs. 16 and 17 the trajectories are not synchronized, vibration has all the time an accidental character and the synchronization does not occur.

Figures 18 and 19 show the trajectories of motion joints of the first branch a and b , as in the above case—joint of bough was stopped, and the first joint were applied this same time curve of torque, as in the case above. Even a cursory analysis of the trajectory of motion in the joints of the first branch of it time evolution reveals a similar nature during the motion; the trajectories converge to a point—the socket type attracting attractor.

Fig. 16 Trajectories of speed versus angular displacement of branch *a*

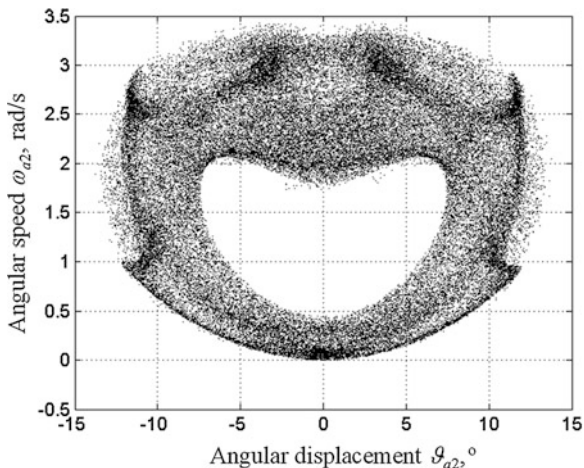


Fig. 17 Trajectories of speed versus angular displacement of branch *b*

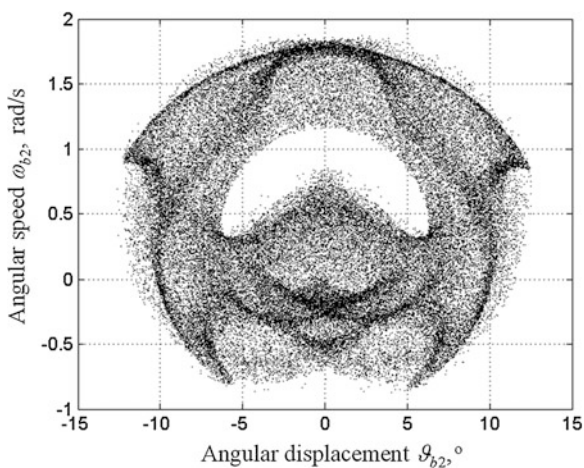


Fig. 18 Trajectories of speed versus angular displacement of branch *a*

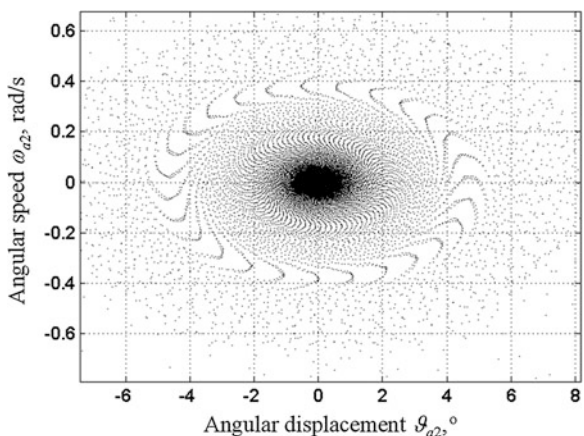
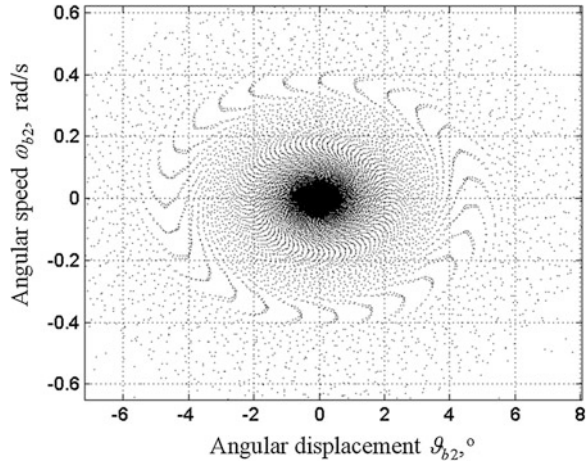


Fig. 19 Trajectories of speed versus angular displacement of branch b



6 Summary

The inverted inertia matrix block structure for the manipulator tree reveals (to a much greater extent than the block matrices shown in Figs. 4, 5 and 6) the elements responsible for the internal dynamic coupling between his links. Submatrix associated with internal dynamic couplings can be classified into three groups:

1. submatrix responsible for a “negative” feedback dynamic:

$$-\mathbf{k}_1 \mathbf{a}_k \mathbf{a}^{-1}, \tag{27}$$

2. submatrix responsible for a “positive” feedback dynamic:

$$\mathbf{a}^{-1} \mathbf{a}_k^T \mathbf{k}_1 \mathbf{b}_k \mathbf{b}^{-1}, \tag{28}$$

3. matrix elements \mathbf{g}_1 (for $g \in \{a, b, \dots\}$)—located outside the main diagonal—are responsible for a dynamic coupling between the individual members within the branch.

Analysis of the structure of matrix (28) shows that the components responsible for the excitation of movement in the joint branch b are the elements of matrix \mathbf{b}_1 . The elements of matrix (22) can be written as:

$$\mathbf{b}_1 = (\mathbf{b} - \mathbf{b}_k^T (\mathbf{k} - \mathbf{a}_k \mathbf{a}^{-1} \mathbf{a}_k^T)^{-1} \mathbf{b}_k)^{-1}. \tag{29}$$

They depend on the matrix elements of branch a or an matrices \mathbf{a}_k and \mathbf{a} . Sets in motion branch a change the parameters of mentioned matrices, which in turn causes the changes in the parameters \mathbf{b}_1 matrices. A similar change will tend to be element \mathbf{k}_1 . Hence the conclusion that the reason for motion the first joint of branch b by the

action of the first branch joint a under driving torque are elements \mathbf{b}_1 and \mathbf{k}_1 , responsible for coupling in this model. Joints are not intended to synchronize motion between branches, generated motion have definitely a random character. Taking into account in the model type of block sub-matrix:

$$\mathbf{a}^{-1}\mathbf{a}_k^T\mathbf{k}_k\mathbf{b}_k\mathbf{b}^{-1}, \quad (30)$$

results in a synchronization between the links branches a and b . This phenomenon is well illustrated in Figs. 18 and 19.

Presentation of the inverse matrices of inertia in the form of a block is a convenient tool to analyze the impact of its components on the dynamic properties, including the term of components involved in the transmission of vibrations between links of manipulator branched tree. This allowed the determination of the role of the matrix elements .

References

1. Butner SE, Ghodoussi M (2003) Transforming a surgical robot for human telesurgery. *IEEE Trans Robot Autom* 19(5):818–824
2. Lai F, Howe RD (2000) Evaluating control modes for constrained robotic surgery. *Proceedings of IEEE international conference on robotics and automation*, vol 1, San Francisco, pp 603–609
3. Beasley RA (2012) Medical robots: current systems and research directions. *J Robot* 2012:1–14
4. Dwivedi J, Mahgoub I (2012) Robotic surgery—a review on recent advances in surgical robotic systems. *2012 Florida conference on recent advances in robotics*, pp 1–7
5. Trawiński T (2010) Modeling of driving lay-out of mass storage head positioning system. *Wydawnictwo Politechniki Śląskiej, Gliwice* (in polish)
6. Trawiński T, Kluszczyński K (2012) Drive system of magnetic disk as mechatronic systems—overview of research issues and perspectives for further development. *Przegląd Elektrotechniczny R. 88 NR 10b/2012:7–10* (electrical review)
7. Trawiński T (2011) Kinematic chains of branched head positioning system of hard disk drives. *Przegląd Elektrotechniczny R. 87 NR 3/2011:204–207* (electrical review)
8. Słota D, Trawiński T, Witula R (2011) Inversion of dynamic matrices of HDD head positioning system. *Appl Math Model* 35(3):1497–1505
9. Szemplińska-Stupnicka W (2012) Chaos, bifurcations and fractals around us, *Oficyna Wydawnicza Politechniki Warszawskiej, Warszawa* (in polish)
10. Gulik D (2012) *Encounters with chaos and fractals*. CRC Press, Boca Raton
11. Devaney RL (1989) *An introduction to chaotic dynamical systems*, Addison-Wesley, Reading
12. Witula R, Słota D (2009) Fixed and periodic points of polynomials generated by minimal polynomials of $2\cos(\pi/n)$. *Int J Bifurcat Chaos* 19:3005–3016

An Estimation of the Geothermal Energy Sources for Generating Electricity

Roman Szostek

Abstract The purpose of the paper is to estimate the power of a geothermal source when the energy is obtained by means of a heat exchanger. It has been assumed that the temperature of the rocks at large distances from the heat exchanger is the same regardless of the direction and that the exchanger is sphere-shaped. Owing to this it is possible to estimate the power of the system without having to study the dynamics of the heat propagation in the rocks. The system has been analysed in steady state. The model and all the calculations are the author's results.

1 Introduction

It is expected that the source of the thermal energy inside the Earth is mainly different kinds of radioactive disintegration [1]. The current exploitation methods of the energy make use of the water of above 65 °C that is in deep rock crevices. A closed circulation is forced where the water carries heat from the inside of the Earth up to the surface. The energy obtained may be used to warm buildings, produce electricity or in technological processes [2].

Making use of the water that is in direct contact with rocks is chiefly responsible for the failures in the geothermal heating systems as the rocks dissolve in water. That sort of water may show high chemical aggression. Besides, there occurs precipitation of minerals in the pipes, exchangers, valves and pumps of the system, which considerably increases the cost of its exploitation and is responsible for its breakdowns. That is why such systems have a limited energy efficiency since they can tap thermal energy only from relatively small depths at which water filled crevices can be found.

An alternative, at present prospective source of renewable energy is the heat contained in waterproof rocks, mainly in granites that are found at a depth below 5,000 m.

R. Szostek (✉)
Rzeszow University of Technology, Rzeszow, Poland
e-mail: rszostek@prz.rzeszow.pl

The rock temperature at that depth may reach even 300 °C. Owing to sealed heat exchangers placed at a great depth under the surface of the Earth it will be possible to acquire great amounts of energy via water fed from the surface which will have no direct contact with rocks. The water may circulate in a closed system and it may be treated before use. The nowadays applied technologies allow drilling down to 6,000 m, with holes of a few meters in diameter that will enable the fitting in of effective heat exchangers.

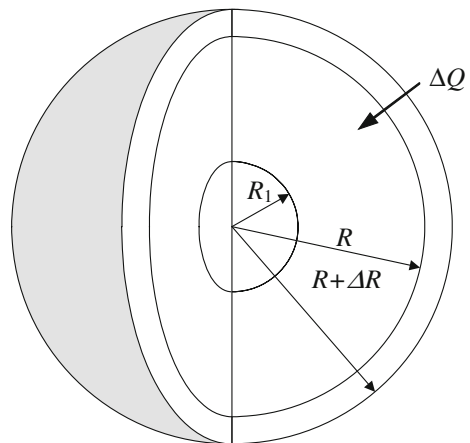
The installations for acquiring energy at great depths will undoubtedly be expensive. Therefore, it seems advisable to make models of the whole system and then perform a simulation of their operation to minimize possible losses resulting from faulty installations.

2 Model and Its Analysis

Let us assume that an exchanger, closely fitted into the rocks, has been put at a great depth under the Earth. It is sphere-shaped, of radius R_1 . The water flow is controlled in such a way that the rocks directly at the exchanger have a temperature of $T(R_1)$, constant in time. To make things simpler, let us assume that the temperature at a distance $R_2 \gg R_1$ from the centre of the exchanger is the same in any direction of the exchanger and is $T(R_2) > T(R_1)$. It is these distant hot rocks that are the source of thermal energy. The situation is presented in Fig. 1.

An operating heat exchanger cools the rocks in its environment. Heat reaches the exchanger through a thick layer of rocks. In steady state, the temperature of the rocks at any point is steady in time t . Thus, heat ΔQ flowing towards the exchanger through each sphere will be steady in time t . It follows from the law of conservation of energy that the flowing heat ΔQ will not depend on the radius R of the sphere. Consequently we have

Fig. 1 Exchanger of radius R_1 placed in rocks



$$\Delta Q(R, t) = \text{const}(R, t) = \Delta Q \quad (1)$$

The heat flowing through the sphere within the Δt time interval is

$$\Delta Q = c_p \frac{S(R) \cdot [T(R + \Delta R) - T(R)]}{\Delta R} \cdot \Delta t \quad (2)$$

where:

- $S(R)$ sphere surface of radius R ,
- $T(R)$ temperature at distance R from the centre of the exchanger,
- $c_p \left[\frac{W \cdot m}{m^2 \cdot s \cdot K} \right]$ thermal conductivity for rocks (rocks are assumed to be homogenous).

Then the power of the system is

$$M = \frac{\Delta Q}{\Delta t} = 4\pi c_p \cdot R^2 \frac{[T(R + \Delta R) - T(R)]}{\Delta R} = \text{const}(R, t) \quad (3)$$

If $\Delta t \rightarrow 0$, then, based on (3), we obtain

$$M = 4\pi c_p \cdot R^2 \frac{dT(R)}{dR} \quad (4)$$

$$4\pi c_p \cdot dT(R) = M \cdot \frac{1}{R^2} dR \quad (5)$$

$$4\pi c_p \cdot \int_{T(R_1)}^{T(R)} dT(R) = M \cdot \int_{R_1}^R \frac{1}{R^2} dR \quad (6)$$

$$4\pi c_p \cdot [T(R) - T(R_1)] = M \cdot \left[\frac{1}{R_1} - \frac{1}{R} \right] \quad (7)$$

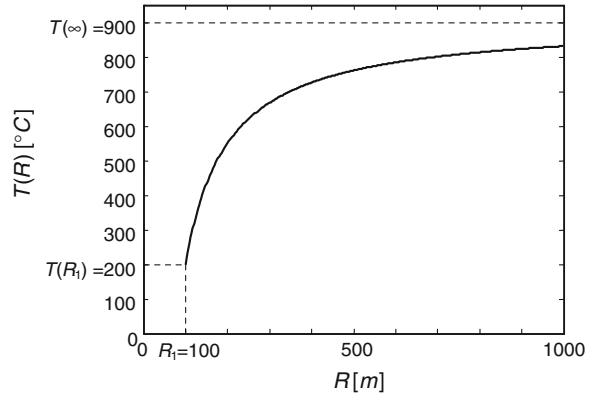
Finally, we arrive at

$$T(R) = \frac{M}{4\pi c_p} \cdot \left[\frac{1}{R_1} - \frac{1}{R} \right] + T(R_1) \quad (8)$$

Within the $R_2 \gg R_1$ distance from the centre of the exchanger the rock temperature is steady and is $T(R_2)$. Based on this boundary condition and Eq. (8) it is possible to determine the power of the system, M , after the substitutions of $T(R) = T(R_2)$ and $R = R_2$ in (8). Then, we obtain

$$M = \frac{4\pi c_p \cdot [T(R_2) - T(R_1)]}{\frac{1}{R_1} - \frac{1}{R_2}} \quad (9)$$

Fig. 2 Exchanger of radius R_1 placed in rocks



After putting (9) into (8) we obtain

$$T(R) = \frac{T(R_2) - T(R_1)}{\frac{1}{R_1} - \frac{1}{R_2}} \cdot \left[\frac{1}{R_1} - \frac{1}{R} \right] + T(R_1) \quad (10)$$

Thus, the temperature distribution for the rocks, $T(R)$, does not depend on the thermal conductivity for rocks c_p . An example of the $T(R)$ temperature graph is shown in Fig. 2.

As $R_2 \gg R_1$, then, based on (9), it can be assumed that

$$M \cong 4\pi c_p [T(R_2) - T(R_1)] \cdot R_1 \quad (11)$$

Hence, it follows that the power M of the system is proportional to the radius R_1 of the exchanger.

$$M \sim R_1 \quad (12)$$

3 Estimation of the Geothermal Source Power

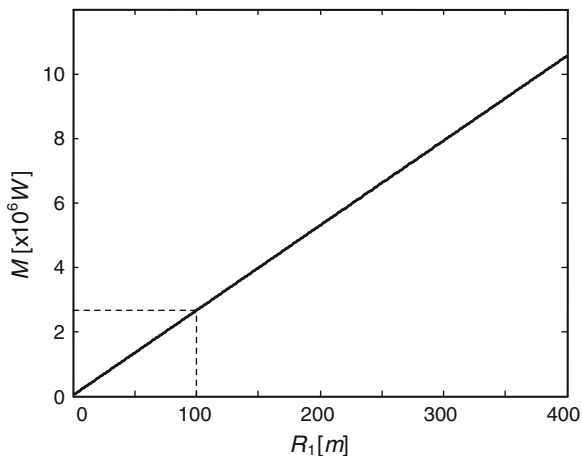
Let us assume that the thermal conductivity of rocks (sandstone, quartzite, granite, anhydrite) is

$$c_p \cong 3 \frac{W \cdot m}{m^2 \cdot ^{\circ}K} \quad (13)$$

the temperature of the rocks at a large distance from the exchanger is

$$T(R_2) = 900 \text{ } ^{\circ}C \quad (14)$$

Fig. 3 Dependence of the power of the system on radius R_1



and the temperature of the rocks at the exchanger is stabilized to

$$T(R_1) = 200 \text{ }^\circ\text{C} \quad (15)$$

Then, based on (11), the power of the system is

$$M \cong 12\pi[900 - 200] \cdot R_1 = 26376 \cdot R_1 [\text{W}] \quad (16)$$

The power of the system for the adopted values is shown in Fig. 3.

Thus, in order to obtain 2, 6 MW, it is necessary to use an exchanger with at least a 100 m radius.

4 Model with the Heat Exchanger

The following presents an analysis of the heat flow, taking into account thermal conductivity heat exchanger $c_h [\frac{\text{W}}{\text{m}^2 \cdot \text{K}}]$. The inner radius of the exchanger is R_0 , the external R_1 . ($R_0 \approx R_1$). The situation is presented in Fig. 4.

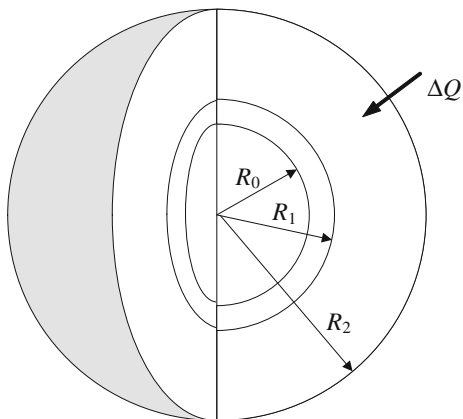
In analogy to Eq. 3 we have in heat exchanger environment

$$M_h = \frac{\Delta Q_h}{\Delta t} = 4\pi c_h \cdot R_1^2 [T(R_1) - T(R_0)] \quad (17)$$

so we have

$$T(R_1) = \frac{\Delta Q_h}{\Delta t} \cdot \frac{1}{4\pi c_h \cdot R_1^2} + T(R_0) \quad (18)$$

Fig. 4 Model with the heat exchanger



After inserting to 11 we have

$$\frac{\Delta Q}{\Delta t} = 4\pi c_p \cdot [T(R_1) - \frac{\Delta Q_h}{\Delta t} \cdot \frac{1}{4\pi c_h \cdot R_1^2} - T(R_0)]R_1 \quad (19)$$

Because in steady state we have

$$\frac{\Delta Q}{\Delta t} = \frac{\Delta Q_h}{\Delta t} \quad (20)$$

so the Eq. 11 takes the form

$$M_h \cong \frac{4\pi c_p [T(R_2) - T(R_1)] \cdot R_1}{1 + \frac{c_p}{c_h} \cdot \frac{1}{R_1}} \quad (21)$$

Since if R_1 is large, then

$$\frac{c_p}{c_h} \cdot \frac{1}{R_1} \rightarrow 0 \quad (22)$$

thus thermal conductivity of heat exchanger does not affect the power of the system.

5 Conclusions

In [3] are shown the solution of the equation of heat to the central symmetry of the system for different boundary conditions. This equation is a model of transient processes in the system, which is analyzed in this paper. Since these solutions have a complex form, so it is difficult to estimate on the basis of the method of analysis

power of the system. Presented in the paper steady state analysis allows the estimation of geothermal power source analytical methods.

In [4] and [5] presented information on the energy stored in hot rocks and the prospect of obtained the energy in the future. The recovery of energy from deep hot rock involves the need to resolve a number of technical problems [6] and modeling of differential equations [7]. In the [8] and [9] presented finite element method and system applicable to the calculation of Matlab.

The power of a geothermal source of energy depends, in steady state, on the radius of an exchanger in a linear way. That explains why it is essential to apply relatively large exchangers in order to acquire considerable powers.

A k -enlargement of the radius of the exchanger results in a k^2 -enlargement of its surface. It might seem that the power of the system should be proportional to the exchanger surface. However, it follows from the analysis of the adopted model, that the power of the system is not proportional to the surface of the exchanger but to its radius. This is due to the effect of large rock layers which form a barrier for the inflowing heat.

The model under investigation assumes that the rock temperature is the same irrespective of the direction. In fact, high temperatures will occur in the rocks situated below the exchanger, from where heat energy will flow. The rocks located above the exchanger will not be a source of energy. Thus, the power of a real system will be lower than that estimated by means of the model under consideration. That is why the power presented by Eq. (11) must be treated as the upper estimation of the power that is attainable in a real system

References

1. Franciszek L (2012) Calculus with an introduction to differential equations (Rachunek różniczkowy i całkowy ze wstępem do równań różniczkowych), PWN, Poland, Warszawa
2. Jamróz D, Niedoba T (2014) Application of observational tunnels method to select set of features sufficient to identify a type of coal. *Physicochemical Probl Mineral Process* 50 (1):185–202
3. Polyanin AD (2002) Handbook of linear partial differential equations for engineers and scientists. Chapman & Hall/CRC, Boca Raton
4. Kozłowski RH, Żakiewicz BM (2010) Large capacity energy from Geo—Plutonic formation for power plants with zero CO₂ emissions. *J Achievements Mater Manuf Eng* 43(2):790–795
5. Kozłowski RH (2011) Geothermic power plants of high capacity—how far? *J Achievements Mater Manuf Eng* 49(2):573–576
6. Szostek K (2008) Control for pneumatic cylinder by changing air pressure supply parameters. *Pneumatyka*, nr. 1, s 72–77. ISSN 1426-6644
7. Szostek K, Węsierski Ł (2009) Model of pneumatic parallel drive. *Transactions of the Universities of Kosice* 3, ISSN 1335-2334 (2009)
8. Bogacz R, Noga S (2012) Free transverse vibration analysis of a toothed gear. *Arch Appl Mech* 82:1159–1168. doi:10.1007/s00419-012-0608-6
9. Noga S (2010) Free transverse vibration analysis of an elastically connected annular and circular double-membrane compound system. *J Sound Vib* 329:1507–1522

Thermal Coupling Analysis of the Permanent Magnet Synchronous Generator

Lesław Gołębiowski, Marek Gołębiowski and Damian Mazur

Abstract The construction and thermal analysis of the 2 KW generator designed for a small wind power station with vertical axis of rotation was presented in this article. The analysis is required in order to determine temperature distribution inside the machine to avoid magnets demagnetization and insulation damage. The presented thermal analysis of synchronous generator prototype was made using Computational Fluid Dynamics (CFD) Ansys Fluent analysis. In order to determine losses at the machine components Ansys Maxwell system was used. The analysis was made for three variants of the air flow speed around the generator frame. The lowest speed corresponds to the conditions of air flow during the study at the test stand, while higher speeds simulate the normal generator operation.

1 Introduction

The electromagnetic analysis plays the main role in the process of designing electric generators. New constructional solutions, high demands imposed on designed machines, application of new materials and attainment of higher efficiency have oriented research at thermal problems. A large number of publications are dedicated to the thermal problems. Nevertheless a small number of them is devoted to the electric generators as well as not many of them make use of the Computational Fluid Dynamics (CFD) method for thermal analysis of the generator [1–6]. The losses generated by windings, magnets and other components of generators have an influence on their efficiency assessment.

L. Gołębiowski (✉) · M. Gołębiowski · D. Mazur
Rzeszow University of Technology, Rzeszow, Poland
e-mail: golebiye@prz.edu.pl

M. Gołębiowski
e-mail: yegolebi@prz.edu.pl

D. Mazur
e-mail: mazur@prz.edu.pl

The thermal analysis is required to determine a temperature distribution inside a generator because too high temperature may cause magnets to demagnetize as well as to damage winding insulation. There are two distinct methods among thermal methods applied to electric machines.

The first method is so-called the Thermal Scheme method and the other one is the numerical method. The numerical method is also divided into thermal calculations with the use of the Computational Fluid Dynamics (CFD) and the Finite Element Method (FEM) based on setting values of heat transfer coefficients. The thermal analysis that is based on the numerical fluid mechanics is more precise and enables to study complex flow processes.

The presented thermal analysis of three-phase synchronous generator prototype was performed with the aid of the computerized fluid mechanics by the Ansys-Fluent computational scheme. The losses for each machine component have been determined by using the Ansys Maxwell computational tool.

2 Description of the Generator Structure and the Computational Model of Losses

The Ansys Maxwell software is applied to analyse electromagnetic phenomena. It allows to design and analyse 2D and 3D models based on the Maxwell equations. This software provides a lot of capability to model electric machines with the use of the RMxpert system library which was used to make a computational model of the generator analysed. The generator prototype has 34 magnets in the rotor corresponding to 17 pairs of poles. The magnetic circuit data of the stator and rotor are gathered in Table 1 while the generator rating are gathered in Table 2.

In the analyzed model the rotor was modelled as a steel pipe on which the N38SH fixed magnets were mounted. The CAD model of the generator analyzed with disks is shown in the Fig. 1.

For the preliminary loss analysis the Maxwell system with the use of the Magnetostatic computational solver was used. Applying of this solver can deliver good results for the winding. To evaluate better losses results for other parts of the generator steady-state solver for harmonic current excitation needs to be used.

The computed loss values are shown in Table 3. The loss values obtained from the rotor and the stator are much lower than the coil losses. The losses generated in

Table 1 Magnetic circuit data

		Stator	Rotor
D_z	Outside diameter	209 mm	140 mm
D_w	Inside diameter	137 mm	111 mm
Q	Number of grooves	36	–
g	Air-gap	1.5 mm	
D_l	Length of generator pack	150 mm	

Table 2 Generator rating

P_N	Rated power	2,000 W
U_n	Rated voltage	230/400 V
I_n	Rated current	2.89 A
N	Rated speed	176.5 rpm

Fig. 1 CAD model of the analyzed generator

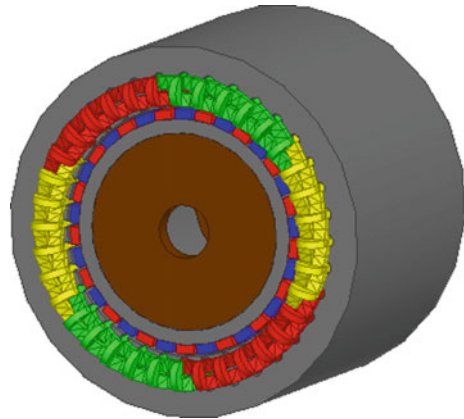


Table 3 Loss values computed by the Maxwell system

	Losses (W)
Stator	2.499E-14
Rotor	5.14E-15
Disks 2x	4.14E-17
Shaft	3.38E-17
Frame	1.92E-18
Winding	74.48863
Magnets	4.43E-08

the coils decide then how heat is propagated in the generator. The loss resistance values are shown in the Fig. 2 while the magnetic induction distribution of the studied generator is shown in the Fig. 3.

3 CFD Computational Model—Numerical Fluid Mechanics

The Ansys program allows integrating various computational environments such as FLUENT, Maxwell, Thermal, Structural and so on. The ANSYS FLUENT program was used for thermal analysis. This program enables to model fluid flow around a

Fig. 2 Winding loss resistance values

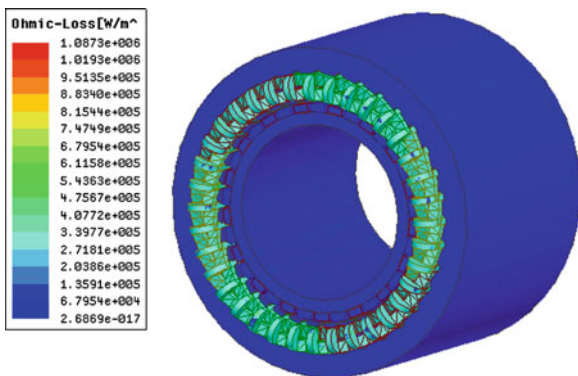
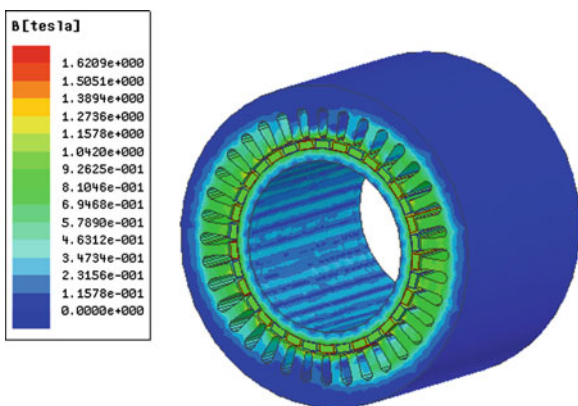


Fig. 3 Magnetic induction distribution



body. The CFD analysis requires making its own computational model to which the losses computed by the Maxwell software will be introduced. The CFD model is shown in the Fig. 4.

The generator frame ambient air was modeled in the form of cylinder 600 mm in diameter and 1,500 mm in length. Apart from the outer air flow the entrapped air inside the electric machine was taken into account in the model.

This air is able to circle inside the machine towards coils and air-gap between the rotor and the stator. A very precise mesh is required for the CFD analyses. The Ansys Workbench program was used for the mesh generation. The mesh of the whole model including the area surrounding the generator consists of 8,917,767 elements and 15,945,598 nodes. The mesh of the total model is shown in the Fig. 5. The generator view is shown in the Fig. 6 while the Fig. 7 depicts a fragment of the generator inner model.

Fig. 4 CFD analytical model

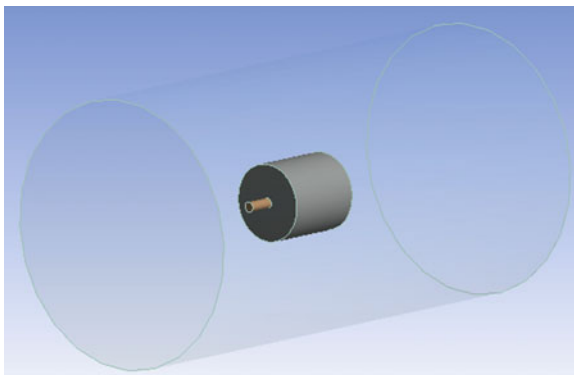


Fig. 5 Mesh of the CFD computational model

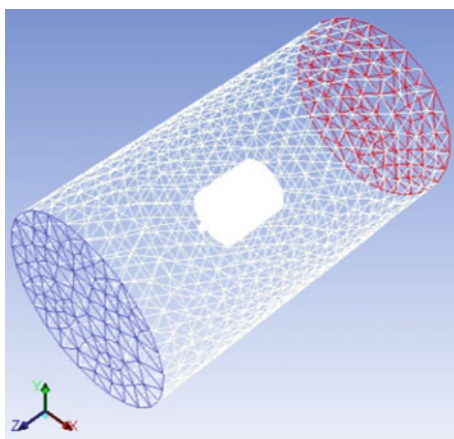
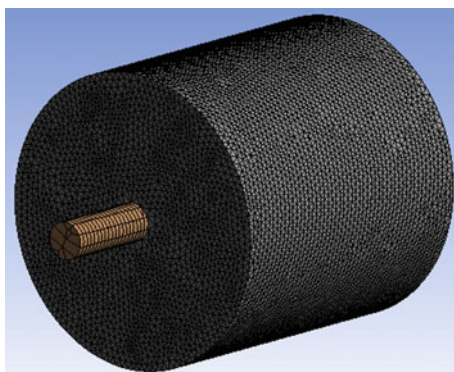


Fig. 6 Mesh of the generator model



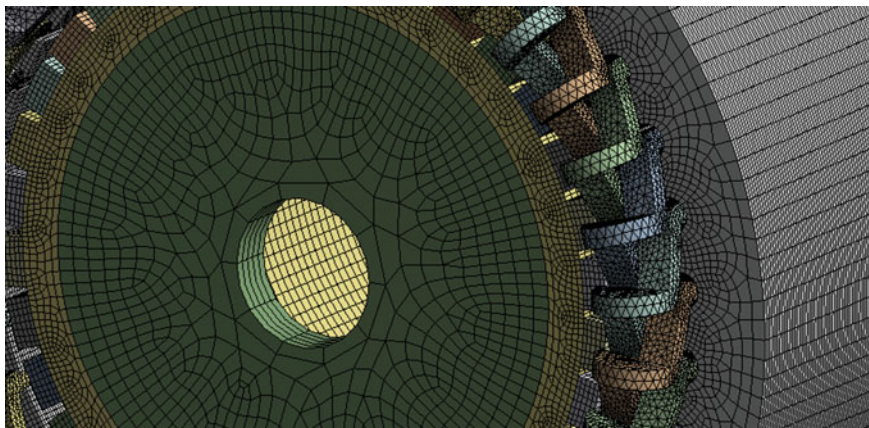


Fig. 7 Mesh of the generator inner fragment

4 Material Data Assumed for Calculations

Material properties for different generator parts have been given in Table 4.

5 Boundary Conditions

The following boundary conditions were used to make calculations with the use of the ANSYS FLUENT program:

- *working pressure* 101325 Pa
- *inlet speed* 0.2; 2.5; 5 m/s
- *viscosity* 1.8421 kg/(m·s)
- *density* 1.225 kg/m³
- *type of turbulence model* *k-ε* (RNG)
- *ambient temperature* 300 K

Table 4 Material properties for thermal model

	Material	Density (kg/m ³)	Specific heat (J/kg-K)	Thermal conductivity (w/m-K)
Winding	Copper	8,978	381	387.6
Shaft + 2x disks	Steel	8,030	502.48	16.27
Frame	Aluminium	2,719	871	202.4
Stator and rotor	Carbon electrical steel	7,872	448	45
Magnets	N38SH	7,500	460	6.4

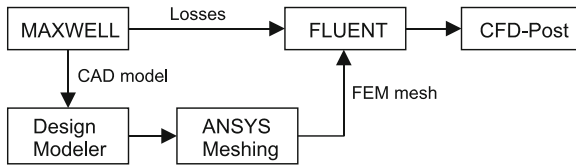


Fig. 8 Computational algorithm of the thermal analysis within the ANSYS computational system. Design Modeler is responsible for geometry preparation, Ansys meshing—mesh construction, Maxwell—electromagnetic analysis—loss determination, Ansys FLUENT—solver, CFD-post—postprocessor

The CFD analysis was carried out for three variants of the inflow velocities onto the generator frame. The lowest speed corresponds to the air flow round conditions during examination on a stand while higher speeds simulate the generator operation under service conditions. The very essential element to obtain correct results provides the right input values such as: turbulent kinetic energy and turbulent energy dissipation.

The program based on the wind inlet value, turbulence intensity and hydraulic diameter value computes the turbulent kinetic energy and the turbulent energy dissipation values [7].

The values assumed to make calculations are as follows:

- turbulence intensity—0.5 %
- hydraulic diameter—0.23 m = the studied object diameter—in our case it is a frame diameter

The reduced computational algorithm of the thermal analysis is shown in the Fig. 8.

6 Results of Calculations

The Ansys program allows integrating various moduli including CFD-Post environment. The CFD-Post is a postprocessor that provides possibility to review Ansys Fluent results. The Fig. 9 depicts temperature distribution for a temperature distribution of the 3D model for the inflow speed 0.2 m/s.

From the thermal analysis for three different inflow speeds temperature values were specified for the individual elements of the electric machine. The Figs. 10, 11 and 12 show temperature diagrams of the machine elements. Their maximum values were assumed as temperature values and determined by a sampling method.

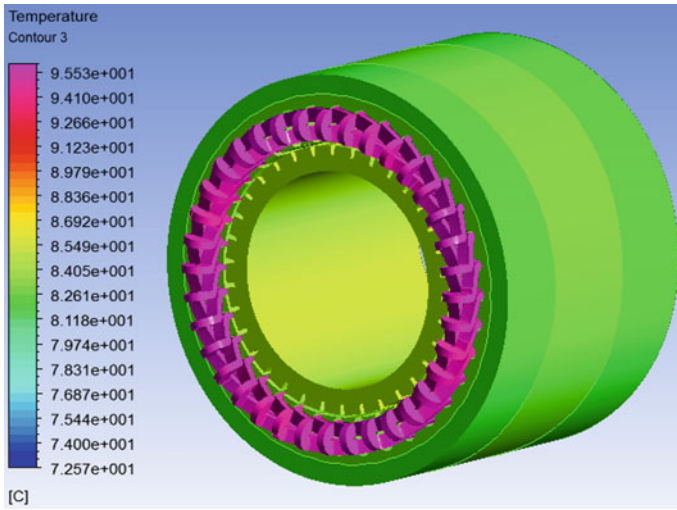


Fig. 9 Temperature distribution of the 3D model for the inflow speed 0.2 m/s

Fig. 10 Diagram of the machine element temperatures for the air inflow speed 0.2 m/s

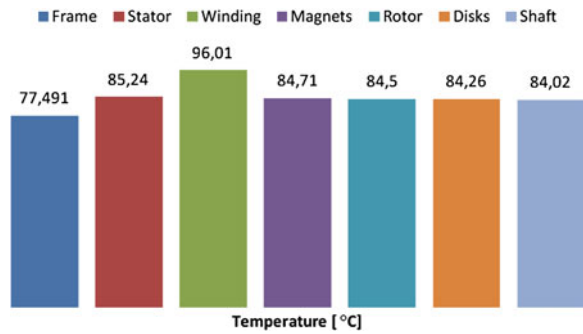


Fig. 11 Diagram of the machine element temperatures for the air inflow speed 2.5 m/s

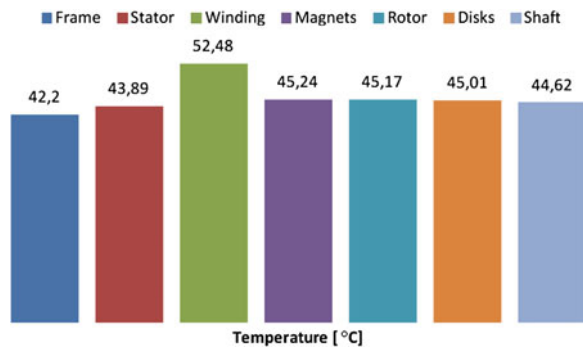
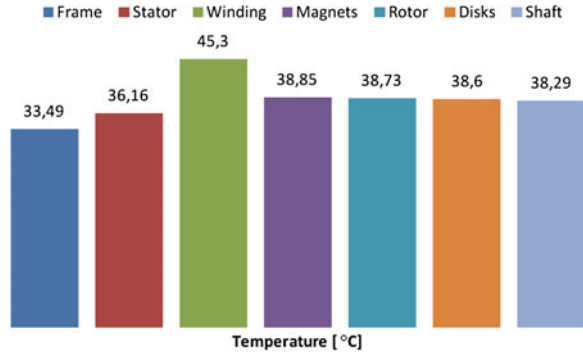


Fig. 12 Diagram of the machine element temperatures for the air inflow speed 5.0 m/s

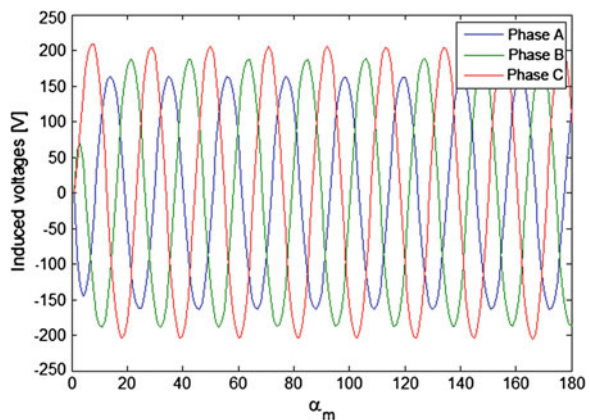


7 Thermal Analysis of the Diagnostic Cases

Thermal analysis was also carried out for two diagnostic cases. The analysis of the diagnostic cases covers the analysis of the generator with winding asymmetry and also with short circuit of one of the generator winding. The winding asymmetry was simulated by giving different number of conductors in coils for every phase. Characteristics of the induced voltages and currents with winding asymmetry versus the angle of rotor position (mechanical angle) were presented in the Figs. 13 and 14. The temperature distribution of the machine for winding asymmetry was presented in the Fig. 15.

The calculations for the second case are carried out for the short circuit in one of the winding phases. The short circuit was simulated by low value of the equivalent resistance in one of the winding phases. Characteristics of the current versus the angle of rotor rotation (mechanical angle) was presented in the Fig. 16. The temperature distribution of the machine with the short circuit in one of the winding phases was presented in the Fig. 17.

Fig. 13 Characteristics of the induced voltages values versus the angle of rotor rotation (*mechanical angle*) for winding asymmetry



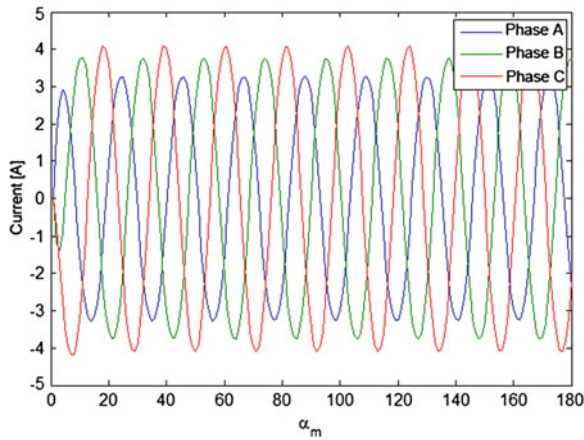


Fig. 14 Characteristics of the current values versus the angle of rotor rotation (*mechanical angle*) for winding asymmetry

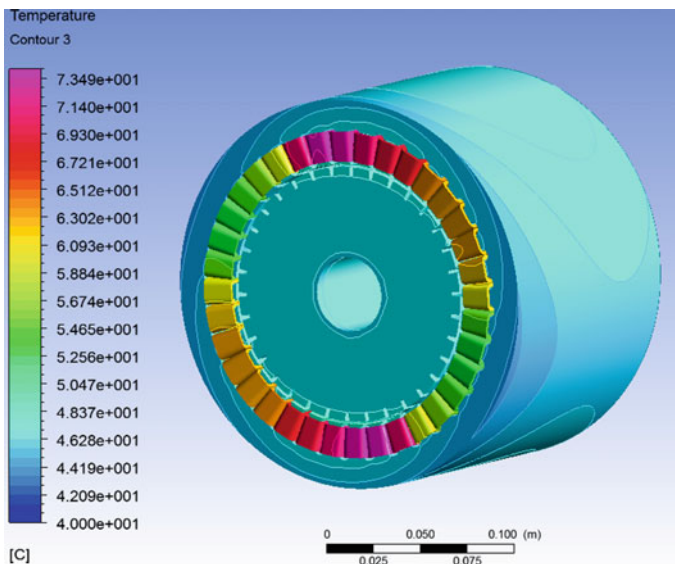


Fig. 15 The temperature distribution of the machine for winding asymmetry

8 Experimental Investigation of the Generator

Measurement experiment was conducted to evaluate the temperature of the frame generator using of the thermo-graphic camera (Fig. 18). The image of the frame generator taken by camera is presented in the Fig. 19.

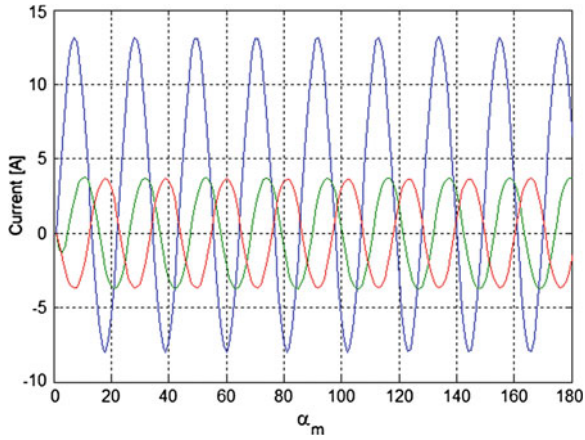


Fig. 16 Characteristics of the current values versus the angle of rotor rotation (*mechanical angle*) with the short circuit in one of the winding phases

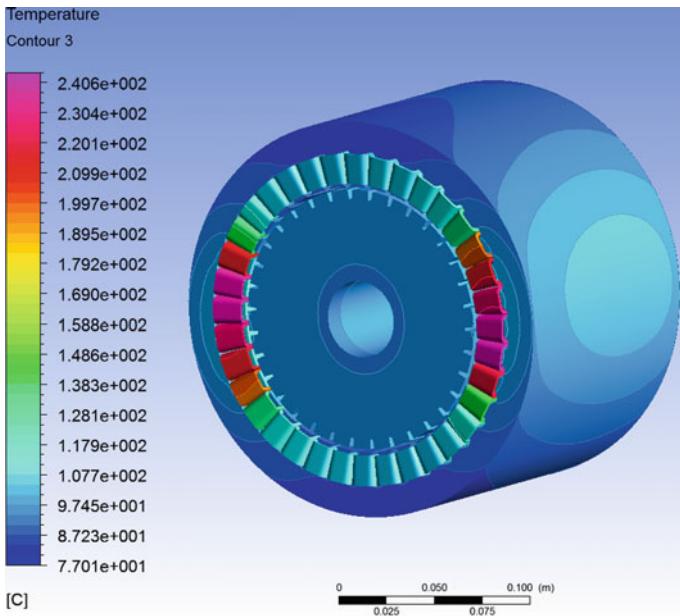


Fig. 17 The temperature distribution of the machine with the short circuit in one of the winding phases



Fig. 18 View of the test rig with the 2 kW generator

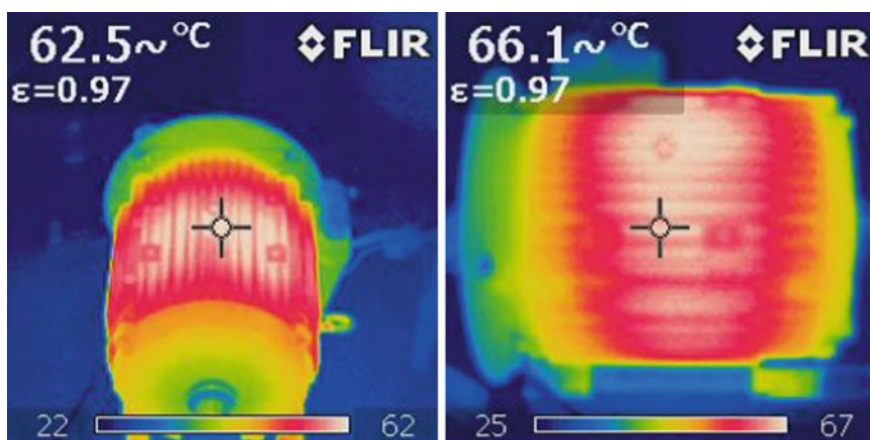


Fig. 19 The temperature distribution of the frame generator (*the image taken by thermographic camera*)

9 Conclusions

The Ansys Fluent analysis allows specifying temperature distribution of the machine elements without having to determine heat exchange coefficients. Difference of temperatures between the warmest element and the coolest element depends on the air inflow speed and is about 19 °C for the flow round 0.2 m/s and decreases to 12 °C for the speed 5 m/s. Under normal operating conditions the generator is flown round by air and its temperature is much lower than temperature under laboratory conditions at the inflow speed 0.2 m/s. Information about the magnet

temperatures allows to assess the magnet operation properly preventing from exceeding temperatures at which they lose magnetic properties. An advantage of the CFD method is its accuracy. The correct computational results are practically limited just by requirements concerning a hardware capacity. A disadvantage of the numerical computations is the fact that it requires a considerable experience in the problems that make use of the numerical fluid mechanics as well as the right division of the model into finite elements. The Ansys software provides a lot of capability for model formation as well as performing all types of coupled analyses. Due to this type of analyses models can be already optimized at the stage of designing in order to increase their efficiency.

The Magnetostatic solver was used in the presented analysis. The next stage in the thermal analysis will be making calculations with the aid of the Ansys Maxwell computational system within the transient solver which enables to determine the time function losses and later temperature distribution.

Preliminary measurements performed with a use of thermographic camera delivered similar values of the temperature as they were evaluated by analytical software.

References

1. Yangsoo L, Hahn S-Y, Kauh SK (2000) Thermal analysis of induction motor with forced cooling channels. *IEEE Trans Magn* 36(4):1398–1402
2. Staton D, Boglietti A, Cavagnino A (2003) Solving the more difficult aspects of electric motor thermal analysis. *IEEE International Electric Machines and Drives Conference, IEMDC'03*, vol 2, pp 747–755. 1–4 June 2003
3. Mezani S, Takorabet N, Laporte B (2005) A combined electromagnetic and thermal analysis of induction motors. *IEEE Trans Magn* 41(5):1572–1575
4. Okoro OI (2005) Steady and transient states thermal analysis of a 7.5-kW squirrel-cage induction machine at rated-load operation. *IEEE Trans Energy Convers* 20(4):730–736
5. Boglietti A, Cavagnino A, Pastorelli M, Staton D, Vagati A (2006) Thermal analysis of induction and synchronous reluctance motors. *IEEE Trans Ind Appl* 42(3):675–680
6. Incropera FP, DeWitt DP, Bergman TL, Lavine AS (2006) *Fundamentals of heat and mass transfer*, 6th edn. Hoboken, Wiley, pp 6–8
7. Fluent Inc (2006) *Fluent 6.3 user's guide*. Lebanon, USA

Universal High Speed Induction Motor Driver

Tomasz Binkowski

Abstract The article describes the concept of a universal driver of three branches voltage inverter supply three-phase or two-phase induction motors. It shows the assumptions of driver and describes the identification process of engine type based on an analysis of the changes of spatial vector output currents. The whole article closes the presentation of selected research results of universal driver held for two- and three-phase high-speed motor.

1 Introduction

Electric drives with inductive engines are getting wider use in the industry, appliances and cordless power tools. This situation arises primarily from the reliability of this type of engines and higher efficiency compared to drives with commutation. In addition, increasing the frequency of induction motors work is associated with a reduction of the overall dimensions of the engine. This, on the other hand, leads to a reduction in the cost of production [1]. The universality of inductive motors drive forces needs to develop electronic drivers whose functionality depends mainly on the number of stages of induction motor and its tasks. The most used engines are two- and three-phase induction motors. Tasks are primarily the current control and the speed control. Number of phases of the motor supply determines the type of inverter, and how our control strategy implements the modulation waveforms. Power control and speed control tasks are the control algorithms.

The article is about a universal induction motor driver. Its versatility is automatic to use two-phase motors and three-phase. Assuming that both the two-phase motors and three-phase, are powered via a three branches voltage inverter. Power inverter topology limits the control strategy of supported engines for variants with

T. Binkowski (✉)
University of Technology, Rzeszow, Poland
e-mail: tbinkow@prz.edu.pl

three-phase three-wire induction motor and two-phase motors with derived common point. The power electronic switches of inverter are turned on as a result of the implementation of pulse width modulation (PWM) resulting from the comparison between the carrier wave and modulation waves. Set modulation function waves can be represented in different coordinate systems and realized by the natural or vector modulation. The advantages and disadvantages of vector and natural modulation are shown in many publications [2–5].

Inductive motor control algorithms depend on the established tasks of electric drives. The primary and main task is to control the current. It requires precise measurement of load current in all phases of the load or the current of DC-link. The versatility of the machine requires a driver to distinguish situations described above. Current control is carried out by the controller based on the reference value that originates from a move further regulatory parameters governing the degrees expected from electric drive. It may be speed, acceleration, and even spurt controllers. These controls require in addition the reference value of current value of controlled quantity. In the case of speed controller it is the value of the measured speed for example by speed sensor or approximate value. The value of the approximate speed may be the result of calculations or observers estimated the value of the output current control [5–7]. The number of options presented must be configurable in the driver.

Given the number of possible job configuration, driver control device must have the appropriate computing power coupled with large hardware resources. Therefore, to implement the universal driver for induction motors the programmable device FPGA of EP3C40 type is used.

2 Driver Concept

2.1 Configuration Parameters and Assumptions

Universal driver for induction motors has been limited to the choice of the appropriate configuration options. These options are summarized in Table 1. The configuration parameters are set by the driver operator and reflect the expected driver tasks.

Working with the motor drive variants of two- or three-phase power, speed measured or observed are determined automatically. In the case of incorrect determination of configuration, automatic driver corrects it to the correct value. This situation takes place for example if operator configures the driver to work with speed control and with speed measurement when the speed sensor is not connected or is damaged.

Taking into account the automatic work of the driver, in addition to the established configuration parameters, it realizes other functions arising from the assumptions.

Table 1 The configuration parameters

Parameter	Description
Sc	Speed control
Sm	Speed measurement
Pn	Automatic identification of a number of phases
Sd	Spin direction
As	Additional security automation
Ci	Automatic identification of the point of current measurement
Sp	Type of speed controller

These features make the maintenance work of the drive in the case of a temporary power outage or shut it in a secure way.

Additional features implemented by the driver:

- weight of swirling energy recovery;
- the measurement of active current component;
- decreasing the value of the error fixed speed proportional control;
- reducing the sensitivity of speed controller on small errors;
- safe start;
- safe shutdown;
- expandable.

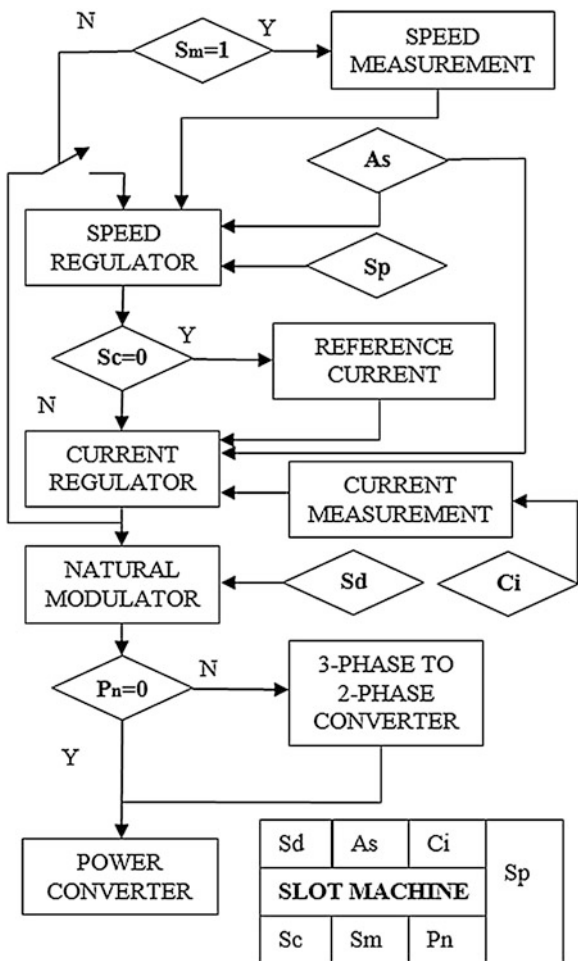
2.2 Flowchart of the Driver

General block diagram of a generic driver for induction motors is shown in Fig. 1. It takes into account the functional blocks, performing the functions of the driver and the connection between them, with an indication of the impact of configuration parameters.

Driver parameter $S_m = 1$ (speed measurement) decides to join the block measuring signal to the speed regulator, entered from the external port. In case of $S_m = 0$, the information about current speed the speed controller approximates via an internal feedback from the output signal current regulator. Automatic identification of a number of phases takes place as a result of the procedure implementation described in Chap. “[Transient Analysis of Interstitial Microwave Hyperthermia using Multi-Slot Coaxial Antenna](#)”. After identification of the receiver type in the case of a three-phase motor the parameter P_n is set to zero. The value of the parameter $P_n = 1$ corresponds to the two-phase machine.

If case of need to change the direction of the motor spin the engine is set up S_d parameter ($S_d = 0$ for clockwise or $S_d = 1$ for unclockwise). The change of the direction of spin is performed by replacing the appropriate control signals for the different branches of the inverter voltage depending on the value of the parameter P_n .

Fig. 1 Block diagram of the universal driver for induction motors



In many applications, such as driver in kitchen appliances, this parameter is not used in relation to the nature of the load.

Additional security automation (As) is a parameter determining joined network actions to special driver safety procedures. They prevent dropping information by regulators as a result of the disappearance of the supply voltage, the power supporting during temporary/casual voltage drop, or inserting the inertia to the work of proportional controls. Further information regarding the operation of these procedures are described in the publication [1].

$$i\left(\frac{\pi}{2}\right) = I_m \sin\left(\frac{\pi}{2} - \varphi\right) = I_m \cos \varphi \tag{1}$$

Specifically, the universal driver implements scalar control induction motors. Vector control is the future option and will not be considered in the current publication.

One of the most important factors determining the correct operation of the drive is the correct current measurement. It is assumed that the error term which is the input signal power regulator is calculated relatively to the component of the active current component of a load. Therefore, depending on the parameter C_i another measurement strategy is activated. The value of the parameter C_i depends on the identification of a number of measurement points. This identification is based on the observation of two measurement signals.

In case of the three output currents in the system there are two non-zero measurement signals on the basis of which the currents spatial vector is calculated and its active component in the references related to the voltages. In case of measurement of DC-link current an information about the active component is latched in discrete moments of passing through maximum voltage in each phase (1). This procedure is described in paper [1].

Depending on the driver application, it is possible to determine the type of speed controller. For applications, in which the value of the speed is not important, it is enough to use proportional controls. This reduces the controller transfer function, which can result in a reduction of parasitic oscillation of the entire drive system. For applications that require conducting a drive after drive preset trajectory, it is necessary to use the regulator with proportional and integral terms. A change in the type of speed control can be achieved by setting up the appropriate parameter Sp . For $Sp = 0$ the proportional control algorithm is made and for $Sp = 1$ an algorithm with integrator.

3 Structure of the Modulator Block

Automatic load detection in induction motors driver puts the modulator block between the parts of driver which controls the two-phase or three-phase motor. In case of diagnosis of three-phase load natural modulation is conducted. As a result of the implementation of the natural three-phase modulation algorithm three signals are produced (u_{sk} , where $k = -1, 0, 1$) that control the three branches of the inverter. The waves of a modulating function describes pattern (2). Using the same inverter unit for two-phase and three-phase motor, connector topology forces the three control signals usage, as in case of a three-phase motor. Natural modulator remains in the same configuration, therefore, the modulation functions must be changed in relation to the number of phases [8, 9].

$$u_{sk}(t) = \cos\left(\omega t + k\frac{2\pi}{3}\right). \quad (2)$$

One way to transform three sine functions shifted relatively to each other symmetrically about $1/3$ of the full angle to the three functions modulating waveforms of the two-phase inverter powered by three-branches inverter is converting data patterns by Eqs. (3), (4) and (5).

$$u_{AM} = u_{\alpha} + u_0 \quad (3)$$

$$u_{BM} = u_{\beta} + u_0 \quad (4)$$

$$u_{CM} = u_0 = -\frac{1}{2}(u_{\alpha} + u_{\beta}) \quad (5)$$

where u_{AM} and u_{BM} -modulating function for the two branches of the inverter, which connects the winding engine with converter, and u_{CM} is a function which describes the modulation process for branch of the inverter which is connected to a common point.

These equations require an earlier natural coordinate system transformation (ABC) to the stationary coordinate system α - β in accordance with the model (6) and (7).

$$u_{\alpha} = u_A \quad (6)$$

$$u_{\beta} = \frac{1}{\sqrt{3}}u_{BC} \quad (7)$$

The waveforms of modulating functions for two-phase load and three branches of the inverter are shown in Fig. 2. Figure 3 shows the result of simulation of two-phase load output currents supplied from the three-branch inverter. A block diagram of a portion of the driver responsible for the modulation process of the driver is shown in Fig. 4.

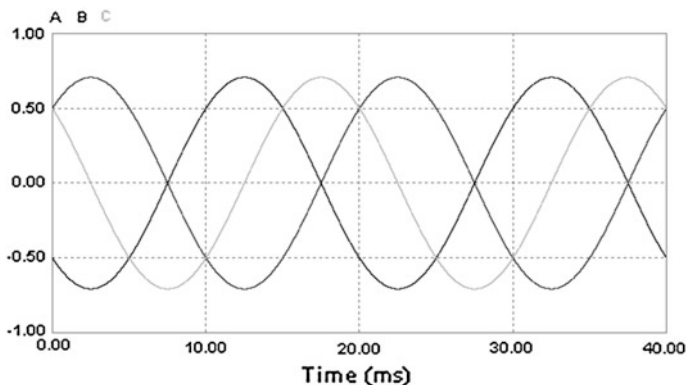


Fig. 2 Modulation signals waveforms of A, B, C inverter branches for two phase load

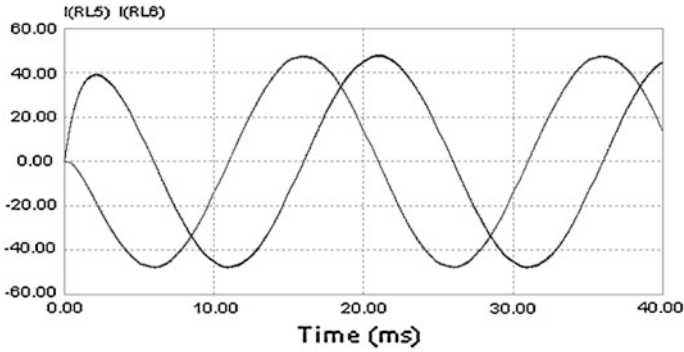
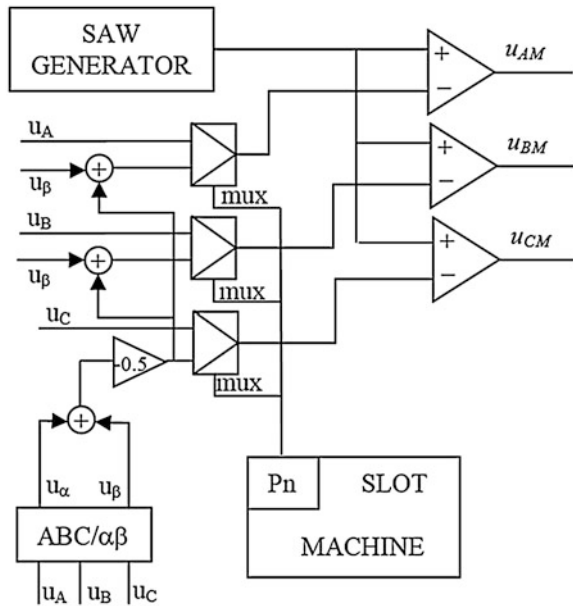


Fig. 3 Output currents of two phase load connected with three branches voltage inverter

Fig. 4 Block diagram of the natural modulator with switching system between three- and two-phase motor



4 Structure of Regulator Block

The induction motor drive regulation process in case of established uses, for example kitchen appliances and electric equipment's must satisfy two fundamental requirements. The first of them and most important is the full control of motor currents. Second requirement is the motor speed control or voltage control. When motor exceeds current limit the switches in an power converter can be destroyed. Such a situation forces usage of regulator with the error integration with output

value limitation. In many cases the motor speed isn't very important. Such a situation implicates the usage of master regulator of voltage without the integral. In the experimental researches the controller with integral in voltage regulator was tested. In the final drive the integral in voltage regulator was removed. Regulator settings were accepted as a heuristic data. The gain of current regulator was less than unity value and its integral constant was 2–3 times of time constant in voltage pulses of DC-link. A gain of voltage regulator was taken from 20 to 40 values. Among the main assumptions of elaborated drive is a drive cost minimization. This economical criterion causes in a mechanical and electrical sensors limitation and causes in a DC-link capacitance limitation. In the considered drive the voltage/speed sensor of motor can be eliminated by the internal feedback (Fig. 5).

If in the regulation process the speed value is unknown, the accuracy of speed regulation is saddled with error. This is insignificant in considered fields of usage. Failure situations were serviced by proper block with regulator tracking, which detects situations when the regulator works in a saturation range. When regulator is saturated longer than set value, the motor drive is stopped.

Figure 3 shows the block diagram of considered structure of voltage and current regulator. The output regulator value m is scaled in the range 0–1. As a result of this scaling the regulator output is equal to the voltages gain of inverter. Based on m value the controller calculates the frequency of voltages supplied motor. The value of voltages frequency is the result of assumed scalar control strategy which the constant u/f value is keeping. Taking into account the motor resistance, u/f characteristic is modified by proper shift in discrete points. It is a result of different values of voltage drop of motor resistances in relation to the voltage vector at different voltage frequencies. In the control algorithm the characteristic $u = f(f)$ has different directivity factors in different frequency ranges. Assumed frequency range was divided into three parts. In the first part the supply voltage is equal zero. This range begins at zero frequency and ends at the frequency when begins a rotation of the motor [1, 5]. The second part of characteristic refers to the start-up process. It was calculated based on motor measurement in the saturation boundary. The

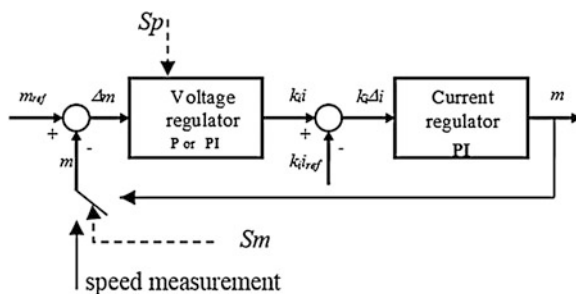


Fig. 5 Block diagram of drive regulator; m_{ref} —voltage reference, m —value of inverter gain, Δm —voltage error, $k_i i_{ref}$ —scaled current, $k_i i$ —current set value, $k_i \Delta i$ —current error, S_p —speed control parameter, S_m —speed measurement parameter

limitation of current in this range is bigger than limitation in the range of normal drive work (third part of characteristic). In the second part of u-f characteristic the assumed current limitation and motor operation in saturation increase a torque in dynamical part of motor operation. The third part of considered characteristic refers to the normal motor operation. In this range it was assumed that motor is not in the start-up state and the frequency changes are a consequence of regulator operation. In this part the u-f characteristic is most steep and current limitation is smaller than limitation in second part [1, 5].

The control values in the two-stage regulator are motor speed and motor torque. These quantities are indirectly controlled. The speed control is realized indirectly by motor voltages control. The motor torque control is realized using current controller. In order to torque control the current controller must control only the current active component. The value of active component of motor current is measured by current sampler synchronization in the moment when supply voltages are crossing the zero value. In relation to the active inverter state measured current is equal with their active component and their value is proportional to the torque value. Then the measured current is converted to the digital form. This process is characterized by transient state, which in case of sampling five times per period can provide the bad work of drive. The proper current measurement cannot be provided in transient state of measured current. In the elaborated controller the measure is synchronized with carrier wave. The active current measurement is proper only when the voltages crossing zero value and carrier wave achieve extreme values. In real motor operation these two events practically take place in different moments.

5 Main Machine Driver

Universal induction motors driver implements control tasks connected to an inverter motor according to the given parameters and the identification of the motor, and security from no typical situations. One of the developed driver assumptions is loading the control electronics of the drive circuit from DC-link. This assumption forces the development of safe work procedures in cases of unusual operation and when connecting it to the power supply voltage. A solution based on the dependence of voltage values on a DC-link circuit capacitor was adopted. It is assumed that the power control circuits are working correctly when a voltage is greater than the value U_{c0} . When the circuit voltage is insufficient for proper supply unit operation, the inverter does not have the ability to produce voltages in the motor winding. It was also assumed that during normal operation of an intermediate circuit voltage drive may vary in terms of the value of the U_{cmin} do U_{cmax} . In normal operation area the scalar control regulators are used. In a situation where the DC-link voltage is in the range of U_{c0} to U_{cmin} , the output value of the regulator is resized proportionally to the value of the voltage of the DC-link. As a consequence of the erroneous exclusion of drive, or loss of supply voltage a motor is stopped through the drive controllers. Momentary loss of input voltage in this situation may

not always end by stopping the engine, because the energy needed to obtain correct operation of electronic regulatory circuits is supplied with an DC-link capacitor, in addition supplied as a result of the work of the engine in generator mode. If the voltage of power supply is proper on the input terminals, the drive automatically will return to normal operation. Connections between the work of regulators with voltage in DC-link are shown in Fig. 6. There are three slave slots. The first of them (slot 1) depending on the value of the voltage in a DC-link sets the value of the speed restrictions, indirectly affecting the reduction of excess voltage on the DC-link capacitors. The machine at the same time, adjusts the speed reference value in order to bring the engine to a halt in case of disconnection from the inverter supply voltage.

This machine may also limit the impact of ripple voltage in a DC-link through parallel correction (Δu) of the output value of a controller by static electricity regulator amendment saved in ROM memory.

The second slot (slot 2) switches the current limitation between two parametrically set values depending on the relationship between the expected frequency of operation of the engine, and the reference frequency. Third slot, represented by a block of delay, stops the drive, depending on the state of controller output and the measurement of currents. Its main task is to identify the status of a short circuit of the engine and disconnecting it from the power supply as a consequence. These machines work during the driver operation with electrical motor as compared to the entire electric drive configuration initialization. Driver initialization phase takes the configuration depending on the static parameters of the automatic identification and measurement points and number of phases of the induction motor.

The correct selection of the measuring points shall be decided by the rough rules described in Sect. 2. Identification of induction motor phase is carried out through the observation of the behavior of the currents space vector. The basis for proper identification is to check the scope changes of the space vector with three phase

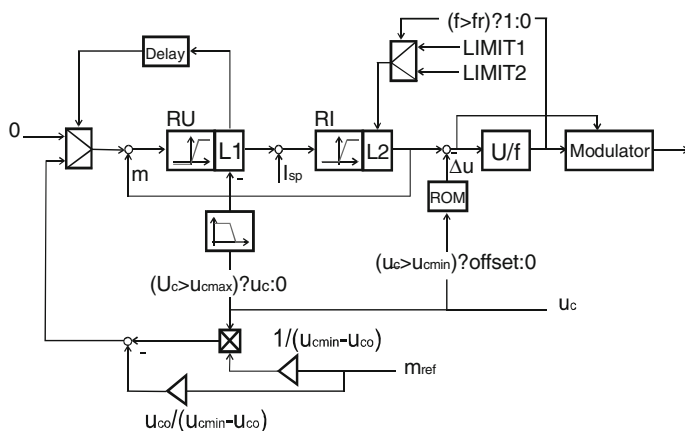


Fig. 6 Relation between drive regulators and DC-link voltage (U_c)

natural modulation process. If the space vector module within the generated six active inverter states causing the rising trajectory of a circular field is fixed—in accordance with the model (8)—then the natural three-phase modulation algorithm is run. If minor changes of the space vector currents are observed, it may indicate a three-phase load asymmetry, in accordance with the formula (9). In this case, the three phase modulation algorithm is activated and can optionally be turned on the corrector of vector trajectory. This module provides a future option, and its operation is described in [10]. The condition of the identification of the two phases of the load is given in Eq. (10).

$$\sqrt{i_A^2 + \frac{1}{3}(i_B - i_C)^2} = const \tag{8}$$

$$I_{asym} \leq \Delta \sqrt{i_A^2 + \frac{1}{3}(i_B - i_C)^2} \leq I_{2ph} \tag{9}$$

$$\Delta \sqrt{i_A^2 + \frac{1}{3}(i_B - i_C)^2} \geq I_{2ph} \tag{10}$$

In Eqs. (8), (9) and (10) the symbols are introduced: i_A, B, C —the current values for load currents, I_{asym} —adopted maximum value of the space vector currents changes for three phase modulation, I_{2ph} —the value of the space vector currents changes in the case of connecting the two-phase motor, Δ —the symbol of the vector space currents calculated with respect to the previous measuring point. Graphical interpretation of number of the load phases identification is shown in Fig. 7.

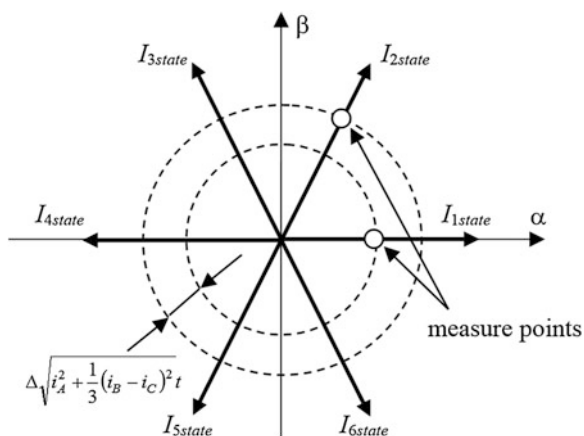


Fig. 7 Graphical interpretation of number of phases identification

6 Laboratory Investigations

Laboratory investigations of a universal induction motors driver have been carried out by implementing the algorithm in the programmable device FPGA EP3C40 embedded in base tab DBM_C3XX. This driver has been connected by a fiber interface with the three-branches inverter, (power to 5 kW), which is connected to the three-phase or two-phase induction motors. These engines were high speed motors intended to be installed in equipment or kitchen appliances.

The identification and implementation of the given configuration parameters were carried out successfully. In Fig. 8 is show an example of a three-phase motor currents. Figure 9 shows the waveforms of currents flowing in a two-phase load. In addition, there is the efficiency of the power converter for three-phase and two-phase motor variant. The results of the measurements are shown in Fig. 10.

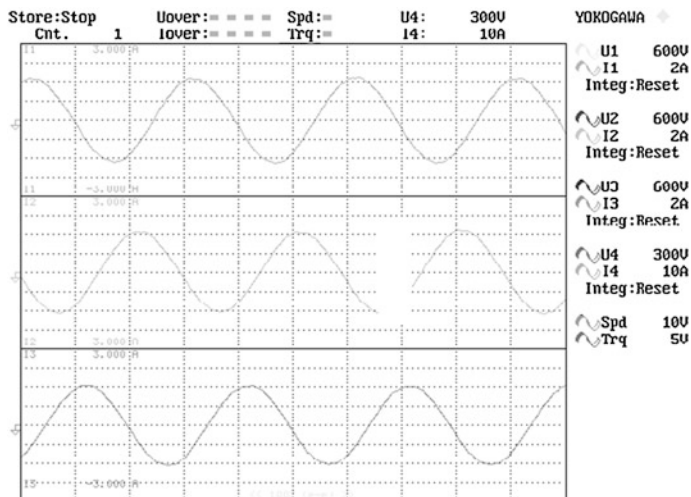


Fig. 8 Output currents in case of three phase motor

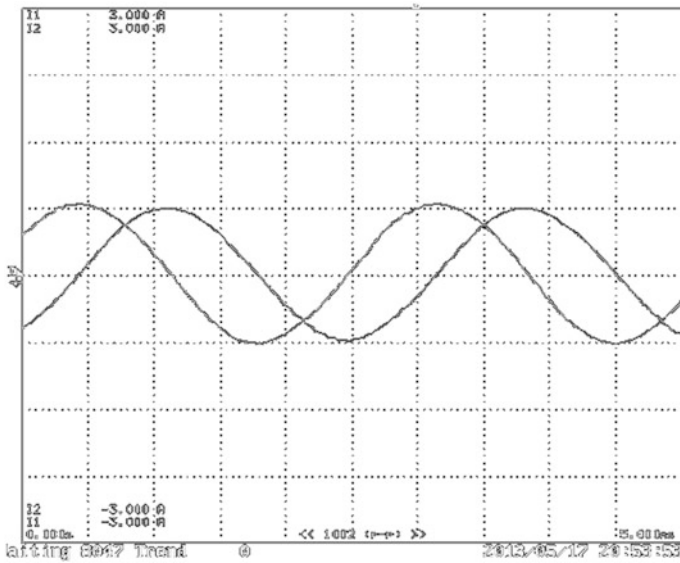
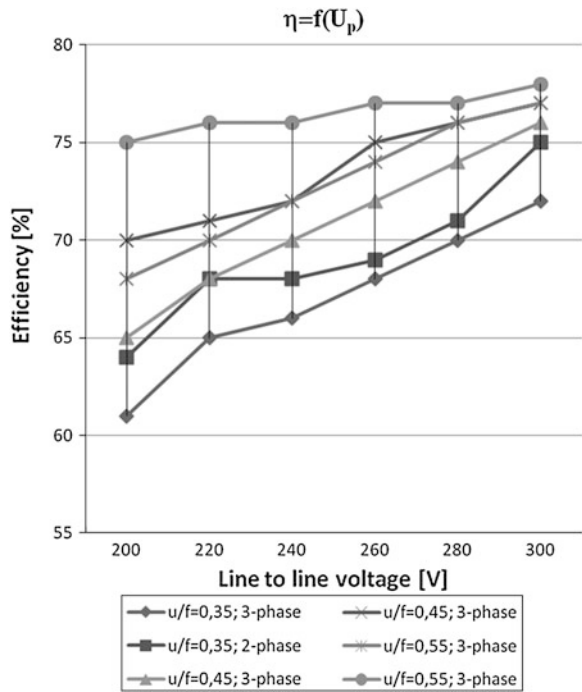


Fig. 9 Output currents in case of two phase motor

Fig. 10 Relation between efficiency and line-to line voltage for different values of u/f constant



7 Conclusion

The developed universal driver for induction motors may have wide application, especially in the field of electric drives of small power, where a large precision control isn't expected. After the extension of its functionality it can also be used in case of BLDC motors. The versatility of the concept and the hardware platform gives the ability to use other than natural methods of modulation and control algorithms, including acting in other than the natural reference systems. Additional features and algorithms are planned to be implemented in future versions of the driver.

References

1. Binkowski T, Buczek K (2011) Control of high speed drive in kitchen appliances. *Electrical review*, R 87 NR 8/2011, pp 2–7 (in Polish)
2. Marino R, Tomei P, Verelli CM (2010) Induction motor control design. *Advances in industrial control*. Springer, London
3. Xiaofang S, Binbin B, Shijie L, Ruilan Z (2011) Optimal Space vector modulation control for three-phase inverter. Springer, Heidelberg, pp 609–616
4. Ranganathan VT (1997) Space vector pulsewidth modulation—a status review. Springer, India
5. Binkowski T, Buczek K (2009) High speed induction motor drive, *Technical news*, vol 12, Lviv
6. Niasar AH, Moghbelli H, Yavari M (2012) Sensorless speed control of hysteresis motor based on model reference adaptive system and Luenberger observer techniques. Springer, Heidelberg, pp 455–464
7. Yongchang Z, Zhengming Z (2008) Speed sensorless control for three-level inverter-fed induction motors using an extended Luenberger observer. *IEEE Vehicle Power and Propulsion Conference (VPPC)*, pp 3–5
8. Binkowski T (2010) Control of 2-phase high speed induction motor, *MiS-6 Koscielisko*, o W PTETiS, Polish Section IEEE (in Polish)
9. Pirog S (2006) *Power electronics*. Cracow, Poland (in Polish)
10. Binkowski T (2012) Correction of space vector trajectory base on fuzzy logic. *Electronics*, vol 12, str 35–38 (in Polish)

Improvement of Immunity of Adjustable AC Drives with Induction Motors on Voltage Sags

Z. Głowacz and H. Krawiec

Abstract This paper presents a proposal to modify the induction motor vector control system in order to provide the required torque and the reference speed of drives during voltage sags. Based on the simulations, the immunity improvement of adjustable AC drives with induction motors on voltage sags has been confirmed.

1 Introduction

Voltage sags are considered one of the most important problems in the field of power quality. They are a threat to vulnerable machines and power supply voltage disturbances can lead to very high costs associated with downtime of industrial plants [1–4].

Voltage sags have a short, abrupt decrease in the effective value of voltage at a given point in the network, after which in a short time, the voltage increases to a value before the sag.

Previous solutions presented in the available literature [5–7], involving the improvement of immunity of adjustable AC drives with induction motors against voltage sags mainly focus on power electronics—improved immunity through the expansion of power supply or expansion of the inverter.

Assessing the impact of regulation and control methods:

- scalar-controlled (V/Hz),
- rotor-field-oriented (RFO),
- direct-torque-controlled (DTC)

on the behavior of the drive system with an induction motor during voltage sags is presented in [7].

Z. Głowacz (✉) · H. Krawiec
AGH University of Science and Technology, Department of Power Electronics
and Energy Control Systems, Cracow, Poland
e-mail: glowacz@agh.edu.pl

H. Krawiec
e-mail: hkr@agh.edu.pl

2 Drive System

Drive system (Fig. 1) consists of:

- the net in which the voltage sag occurs, (70 %, 0.5 s),
- voltage inverter VSI (diode bridge, indirect LC circuit, inverter),
- the converter control system, V/f control or vector control in coordinates in relation to the rotor flux vector [1],
- an induction motor, J (moment of inertia), k (elasticity),
- implementing the technology requirements the speed and the load torque.

The following cases of power were considered:

- directly from the network—including the voltage sag (70 %, 0.5 s) between time 10.0–10.5 s,
- by inverter VSI, with higher capacity in the intermediate circuit, so as to ensure in the case of voltage (70 %, 0.5 s), linear reduction u_C voltage in the range of 0.1 s of the drive controlled by V/f,
- by inverter VSI, with higher capacity in the intermediate circuit, so as to ensure in the case of voltage sag (70 %, 0.5 s) linear reduction voltage u_C for 0.1 s of the drive system with vector-controlled coordinate related of the rotor flux vector [8].

The necessary torque $T_e = T_N$ and the required motor speed $\omega = \omega_N$ can be achieved by supplying a reduced voltage induction motor, with a higher frequency of about 5 %, consequently the current rises to about 80 %, and the rotor flux is 0.6 of the nominal value at nominal conditions (400 V, 50 Hz) (Fig. 2).

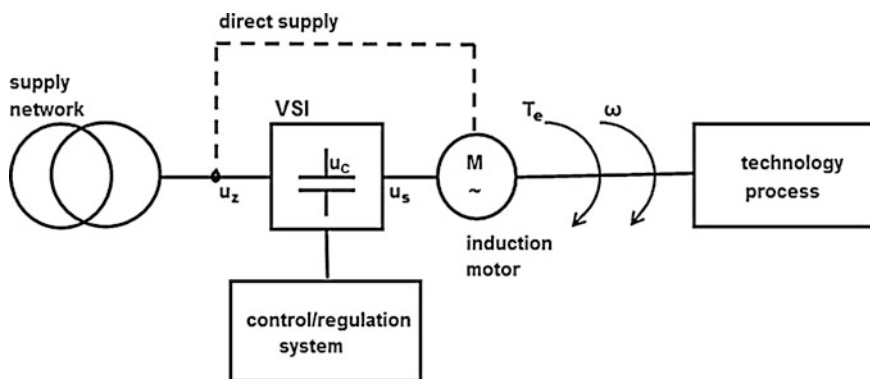


Fig. 1 Adjustable AC drive with a frequency inverter VSI

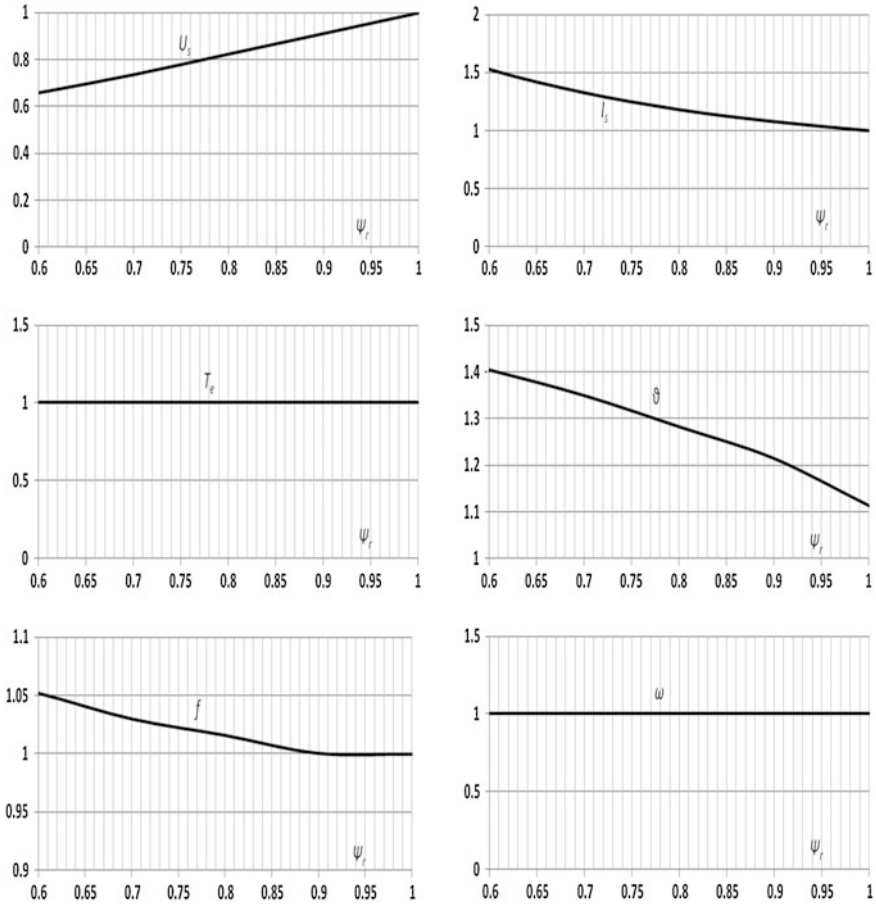


Fig. 2 Changing the amplitude/frequency of the supply voltage to sustain the T_N and ω_N in the steady state

3 Analysis of Simulation Results

The simulation was performed using MATLAB from the available SIMULINK library.

Below are the results of the simulations with the direct connection of the cage induction motor at the power supply net.

Relative units referenced to the rated three-phase induction motor: 15 kW, 400 V, 1460 rpm were used (Fig. 3).

When the voltage sag occurs the current fluctuations are nearly fivefold and fluctuations of torque nearly threefold—reduced turnover of 12 % (Fig. 4).

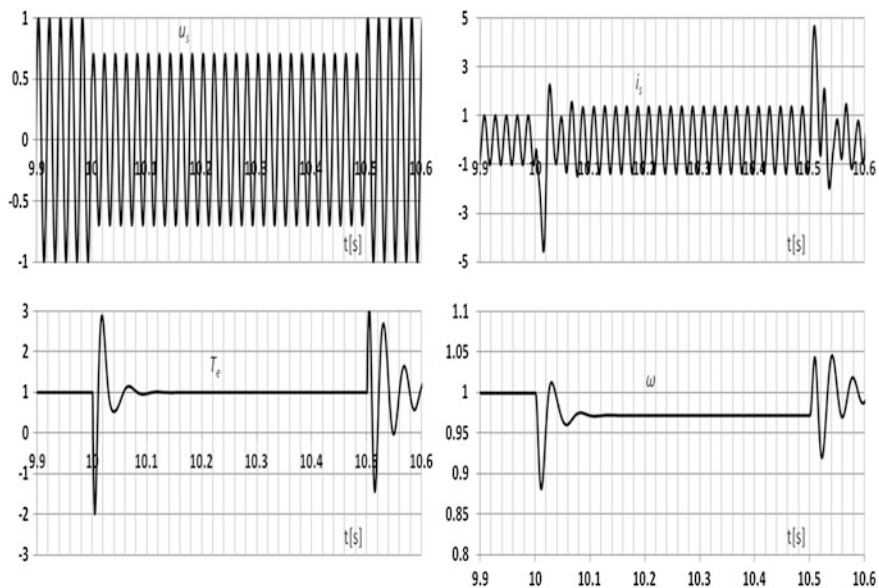


Fig. 3 Simulation of the drive system with the induction motor connected directly to the network during the voltage sag (70 %, 0.5 s)

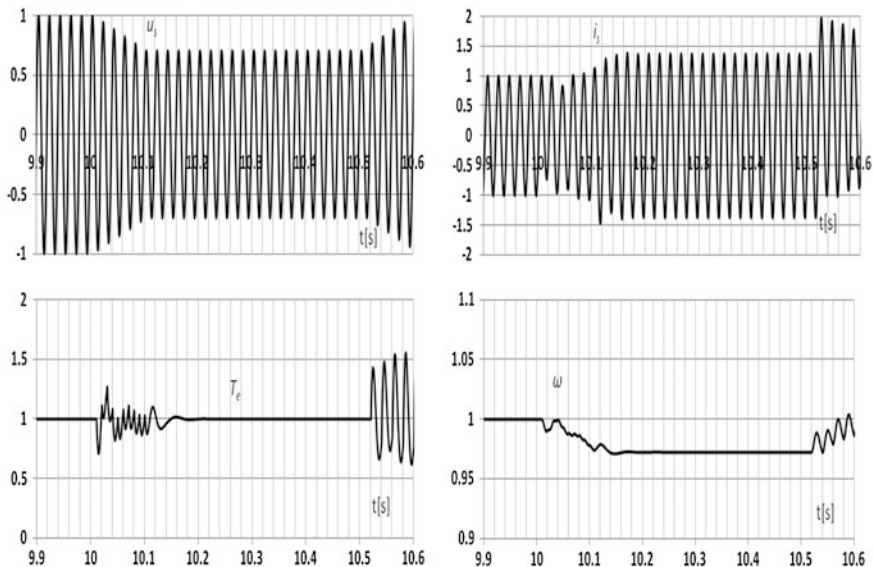


Fig. 4 Simulation of the drive system with the induction motor supplied with the VSI (U/f) during the voltage sag (70 %, 0.5 s)

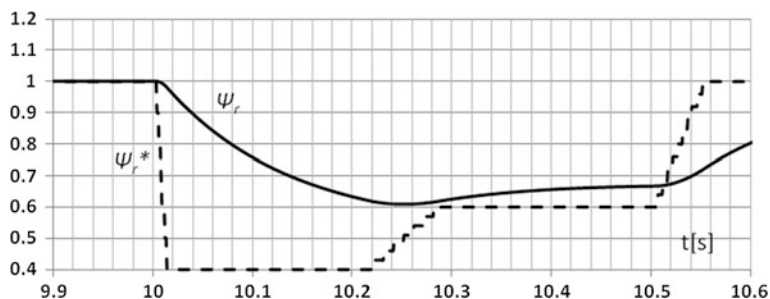


Fig. 5 Reference value and actual value of rotor flux during the voltage sag (70 %, 0.5 s)

Voltage sag immunity of drive systems can be significantly improved by increasing the capacity in the intermediate circuit in order to ensure that the u_C linear voltage is reduced to 70 % for 0.1 s in case of a voltage sag.

During the voltage sag the current is doubled, fluctuations of torque 60 %—there is a reduction of speed by only a few percent.

In summary, there has been a significant improvement in system dynamics, reduced turnover by 3 % may allow the technological process to continue in a limited way.

By analogy to the DC drive it is proposed the motor flux be reduced as a function of the supply voltage (Fig. 5).

In order to be able to have a flow of energy and manipulate drive control, the SEM must be smaller than the voltage to frequency converter.

The proposed method is—in case of a voltage sag—regulated reduction of the motor flux, which can reduce the SEM enabling effortless adjustment of the current (Fig. 6).

At a reduced rotor magnetic flux in order to provide the required torque and to maintain the selected reference speed, it is necessary to increase the corresponding component of the stator current.

The voltage sag causes the increase of currents (up to 50 %), small variations of torque—consequently virtually constant speed.

In this case another frequency of voltage and a more favorable setting current vector I_s and rotor flux vector Ψ_r occurs.

In Fig. 7 there are waveforms of stator currents I_s and rotor fluxes Ψ_r as well as rotor angles ν between the current vector I_s and rotor flux vector Ψ_r during the voltage sag (70 % of 0.5 s), for the three different kinds of supply:

- D* direct supply from the network,
- L* linear decrease of the amplitude of the output voltage,
- R* adjustable output power (weakening of the motor flux).

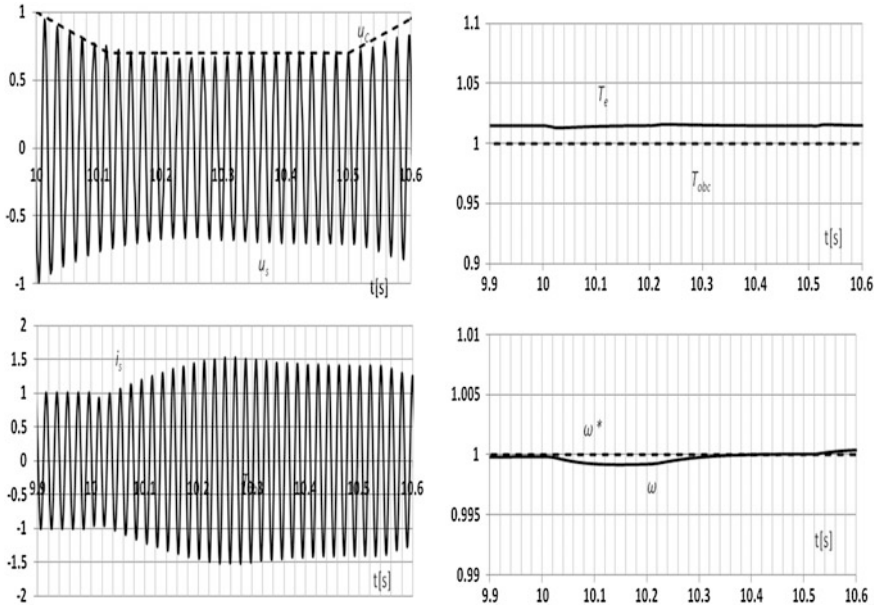


Fig. 6 Simulation of the drive system with induction motor supplied from VSI with the rotor flux control during the voltage sag (70 %, 0.5 s)

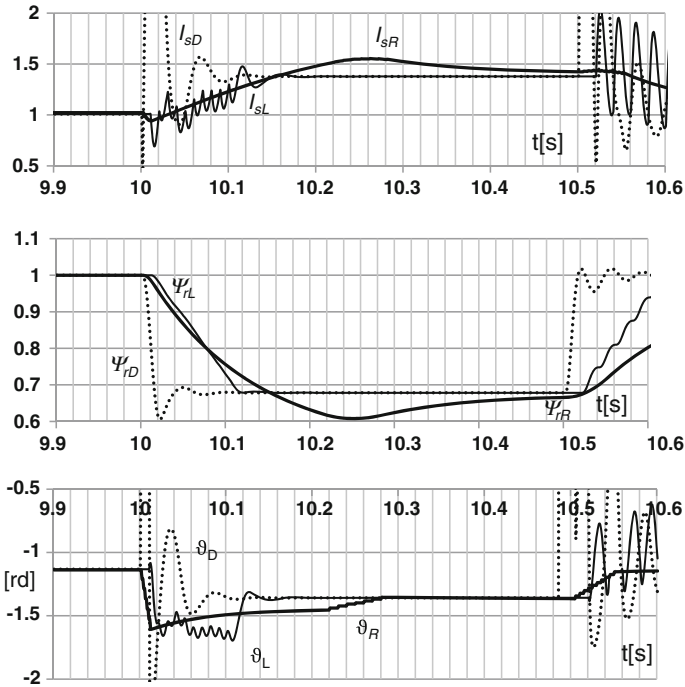


Fig. 7 Comparison of stator currents I_s , rotor fluxes Ψ_r and the angles ν between the current vector I_s and rotor flux vector Ψ_r —for the three cases of the supply

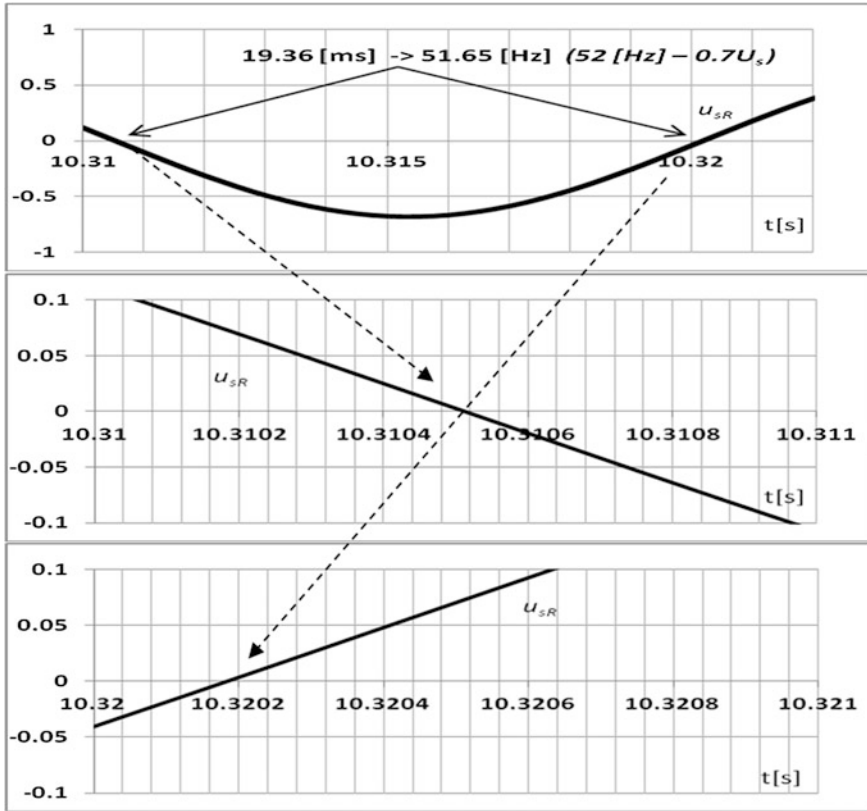


Fig. 8 Determination of the period (frequency) of the voltage u_{sR}

4 Discussion and Conclusions

Carried out simulations confirm the effectiveness of the proposed method to improve the immunity of controlled AC drives with induction motors against voltage sags (Fig. 8).

The presented method can be used to improve the immunity of drive systems with synchronous motor against voltage sags.

It is proposed to use the PID regulator of motor flux which monitors voltage sags.

It is likely that a control system, an algorithm based on the weakening of the motor flux can be developed in the future for convenient, practical use.

Acknowledgments The work was carried out under the project KIC CIPOWER.

References

1. Gieras J, Gieras I (1998) Electrical energy utilization. Publishing House Adam Marszałek, Cracow
2. Gołębiowski L, Gołębiowski M, Mazur D (2011) Unscented Kalman filter in rotor diagnostic testing of the asynchronous motor. *Przeгляд Elektrotechniczny* 87(8):48–52
3. Matulka J, Barlik R, Nowak M, Rąbkowski J (2010) Properties of PWM current source converter with active damping control of the input circuits. *Przeгляд Elektrotechniczny* 86 (4):258–265 (in Polish)
4. Rafał K, Kaźmierkowski M (2012) Power quality enhancement in distribution network—control scheme of STATCOM with energy storage system. *Przeгляд Elektrotechniczny* 88 (12a):1–5 (in Polish)
5. Collins E, Mansoor A (1997) Effects of voltage sags on AC motor drives. In: Proceedings of the IEEE Textile, Film, and Fiber Industry Conference, Greenville SC, May 1997
6. Hanzelka Z (2013) The quality of electric power supply. AGH University of Science and Technology Press, Cracow (in Polish)
7. Petronijević M, Jeftenić B, Mitrović N, Kostić V (Dec. 2006) Voltage sag drop in speed minimization in modern adjustable speed drives. *Ser. Electr. Energ.* 16:231–337
8. Böcker J (2009) *Geregelte Drehstromantriebe*. Universität Paderborn, New York

Investigation of End Winding Proximity Losses in a High-Speed PM Machine

Adrian Młot, Mariusz Korkosz and Marian Łukaniszyn

Abstract This paper presents three- and two-dimensional finite element analyses (2D, 3D FEA) of the proximity losses in brushless AC permanent magnet motor with concentrated windings operating at high speed. The proximity effect only occurs if the examined conductor is penetrated by an external magnetic field, which is caused by adjacent conductor currents. To reduce the proximity effect several alternative winding layouts including rectangular wires are used. The calculated results of the eddy current losses within end-winding regions are significant and must be considered in the design of stator windings. 3D calculations are compared with 2D ones to show the behaviour of the eddy-current into the conductors and also compared with respect to the power loss and AC resistance. The calculations are in a good agreement with measurements on a prototype high-speed motor.

1 Introduction

This paper focuses on the AC copper loss caused by circulating current effects within multi-strand concentrated windings in a high speed permanent magnet (PM) AC brushless motor. There are two different phenomena that lead to additional AC losses. The first one is the skin effect which is a tendency for high-frequency currents to flow on the surface of a conductor, which can be mitigated through the

A. Młot (✉) · M. Łukaniszyn

The Faculty of Electrical Engineering, Automatic Control and Informatics,
Opole University of Technology, Opole, Poland
e-mail: a.mlot@po.opole.pl

M. Łukaniszyn

e-mail: m.lukaniszyn@po.opole.pl

M. Korkosz

The Faculty of Electrical and Computer Engineering, Rzeszów University of Technology,
Rzeszów, Poland
e-mail: mkosz@prz.edu.pl

© Springer International Publishing Switzerland 2015

L. Gołębiowski and D. Mazur (eds.), *Analysis and Simulation of Electrical and Computer Systems*, Lecture Notes in Electrical Engineering 324,
DOI 10.1007/978-3-319-11248-0_14

use of smaller conductor strands. The second one is the proximity effect in windings which is caused by the presence of AC magnetic fields that are generated by adjacent conductors or external sources in high-frequency AC motor [1–12]. In most winding designs, the losses increase toward the air-gap due to the skin and proximity effects. Since the air-gap region has worse cooling than the other parts of the coils, additional losses close to the air-gap can cause extremely high temperatures in the copper [2, 3]. Heat generated by a high-speed machine must be known to accurately predict an amount of the proximity effect. Heat flow in the motor winding is present in the axial, radial and circumferential directions [13–15]. The axial conduction provides a flow path for heat dissipated in the end-windings and in the coil sides. Dissipated heat from the end-winding enters the slot via the conductors. As the end-winding reaches the slot, heat starts to flow into the stator core, therefore the end-winding effect must be taken into account which provides reliable information of copper loss amount. Heat is also dissipated in the coil sides due to resistive losses. As the hot spot temperature is crucial for the determination of the maximum output power, it is decisive to calculate the loss in detail. The proximity effect can be significantly reduced with an appropriate arrangement of conductors and can be minimised by locating the conductors towards the rear of the slot and by minimizing height in the radial direction of the parallel conductor bundle forming each turn [1–3, 10–12]. The skin and proximity effects are well-known current-displacement effects within electrical machines, transformers and inductors. Less attention has been paid to considering proximity effects in the end-region of these electrical devices.

This paper extends the author's previous research [1] to give some insight into the AC loss generated in the end-winding of a high speed traction motor. A segmented stator topology used in the motor design allows for various winding layouts to be analysed using a simplified approach [1]. They have used the most common numerical approach employing a 2D FE analysis, which allows an accurate representation of the winding and magnetic circuit cross-section. Nevertheless, the two-dimensional approach omits the end-winding effect on the stator and rotor cores, therefore the whole amount of eddy current losses within conductors are incompletely known. Furthermore, in papers [2, 3] authors have presented copper loss prediction in power inductor using 2D and 3D FEA for the active-length and end-winding regions. The obtained results have shown that to account for the end-winding effect when using results from 2D FEA a correction should be introduced to account for the true path length of AC circulating currents within the conductors. Additionally, the presented results clearly demonstrate that the high frequency AC copper loss varies with temperature in a different manner depending on the DC winding resistance. Accurate prediction of power loss distribution within an electrical device is highly desirable as it allows for thermal behavior to be evaluated at the early design stage.

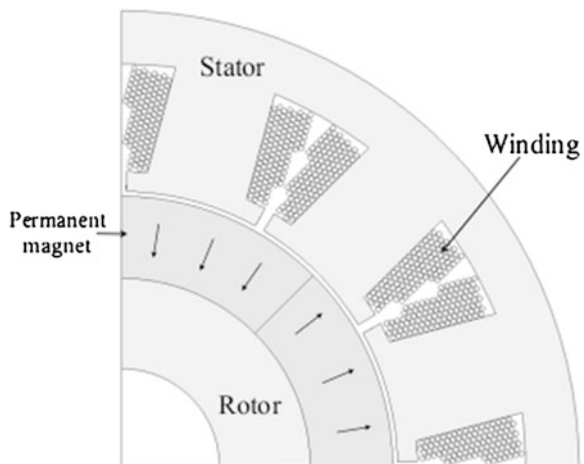
In this paper, the authors investigate the end-region proximity loss generated in machines operating at high speeds. The winding used in the presented machine can suffer from significant bundle-level proximity losses. The AC copper loss predictions including the end-winding are compared with data from more conventional

two-dimensional approaches where the active length only is accounted for. The discrepancies between the results are presented and discussed. This paper also includes experimental validation of the theoretical findings. Also, several winding structures are analyzed and compared with respect to the loss and AC resistance. Depending on a winding structure, the amount of winding losses and ratio of AC to DC loss within end-winding under high frequencies have a tendency to be higher or lower with respect to the standard winding, and that is also affected by a connection of conductors.

2 High-Speed PM Motor Prototype

The research has been applied to the design of a highly efficient (97 % peak efficiency) and compact (2 kW/kg continuous rated) water jacket cooled PM motor designed for a large vehicle application. Additionally, the prototype motor was designed to operate at high frequency up to 800 Hz in order for minimize the overall system weight. The motor comprises 8 poles and 12 slots with a two-layer concentrated winding, Fig. 1. The segmented stator core is cooled via an outer water jacket and the laminated stator segments are made of 0.35 mm silicon iron. These kinds of drives are tested by several companies to evaluate benefits of the hybrid electric drive technology, e.g. reduced mass/volume/weight; improved efficiency; fault tolerance; improved acceleration. In the original design, a high copper packing factor is realized through the use of a multi-stranded parallel winding. The standard winding is made of seven strands of sixteen parallel conductors wound uniformly around the tooth with a 50 % copper fill factor.

Fig. 1 Cross section of the AC motor used in the investigation



3 Experimental Validation

To evaluate the AC copper loss within the analyzed machine a simplified approach has been adopted utilizing the segmented stator topology. The segmented stator allows for simple and inexpensive winding test before a complete prototype motor is built [1]. Two further stator segments were placed on each side to replicate the true slot profile and the influence of the rotor was assumed to be negligible, Fig. 2. To understand the behavior of circulating eddy-currents in the solid conductors along active length and in the end-winding regions the mutual coupling between phases which affect the proximity loss is not taken into account.

Figure 3 presents the three-teeth test rig including an AC and/or DC power supply, a thermally insulated test chamber emulating adiabatic boundary condition, thermocouples and the tooth assembly. To improve the thermal path between the single-tooth with wound coil and aluminum cold plate, the aluminum plate and external core surfaces were impregnated with a high thermal conductivity liquid. An external coolant circuit is used to maintain the temperature of the cold plate at a fixed temperature of 20 °C.

The first DC test required energizing the winding from the experimental bench with a DC current of 40 A. In the next test the winding was energized with ac sinusoidal current of RMS 40 A at 400 Hz. In both tests input voltage, current,

Fig. 2 Three-tooth sector of the stator with standard wound coil and cold plate

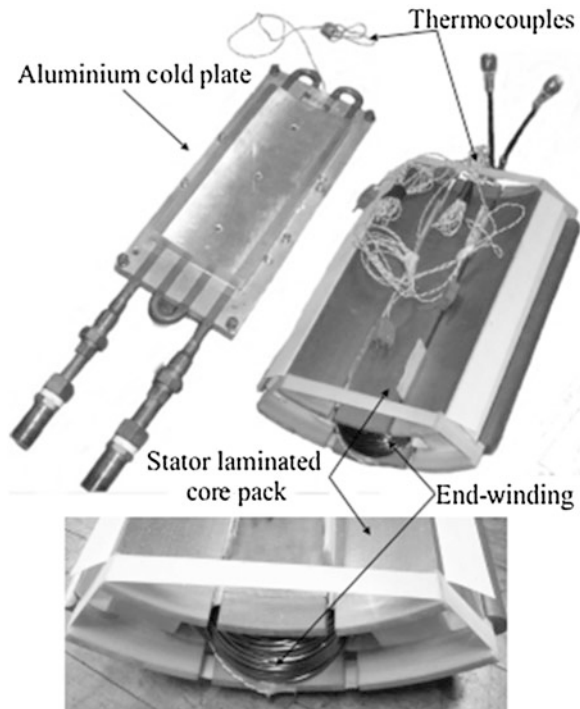
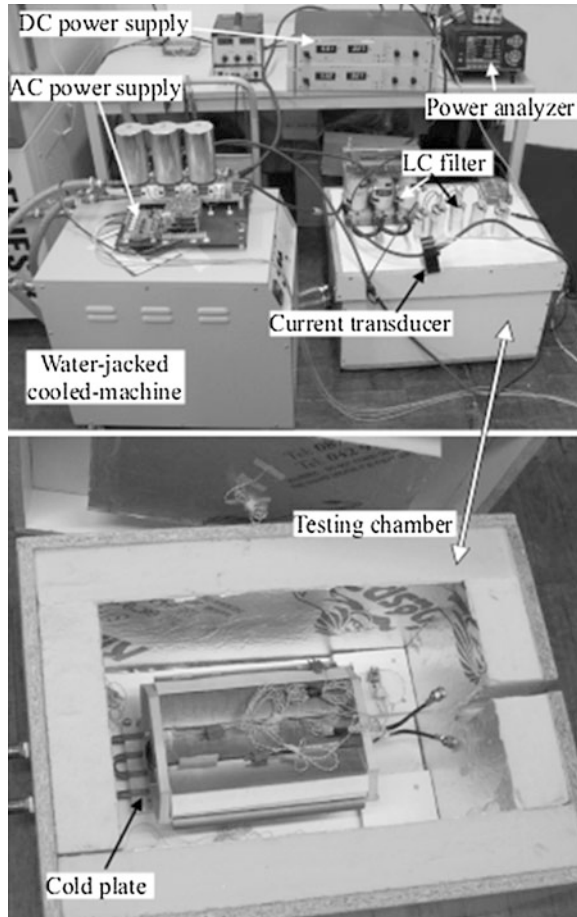


Fig. 3 Experimental setup for a three-teeth thermal test

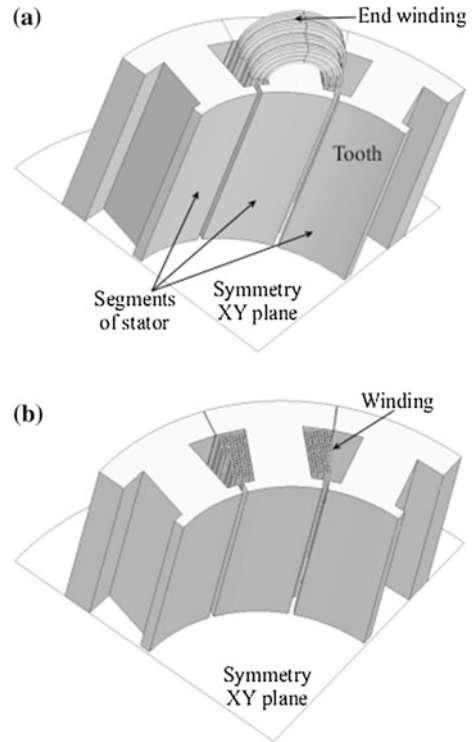


power and temperature at various points in the chamber and in the winding are monitored continuously.

4 Finite Element Analysis

The theoretical investigation of the AC copper loss within the winding according to the Joule law, loss has been carried out using a 3D FEA with steady state AC magnetic application in the harmonic state for a given frequency (sinusoidal steady state). The magnetic field results from the presence of time varying electric currents. This application takes into account the current induced in the conducting regions called eddy currents within solid conductors. It also considers the skin and proximity effects in the conducting regions.

Fig. 4 Three-tooth sector of the machine with wound coil used in the investigation: 3D (a) and 2D (b) model of standard round conductor



Due to the relatively short active-length of the presented models, the contribution of the conductors forming the end-winding will be significant. In the analysis and discussion of the loss distribution within the solid conductors, both 2D (within active-length only) and 3D FE methods are used, see Fig. 4. The end-winding region for the motor 3D FE model with standard round conductors is shown in Fig. 4a, whereas Fig. 4b depicts the 2D FE model of investigate motor, in which the proximity and skin effects in end-winding region are totally omitted.

The discretization mesh within the cross-section is the same for both 2D and 3D models and the same for both calculation methods assuming a constant winding reference temperature, set arbitrarily to 20 °C. Due to the symmetry, the study domain for FE stator models can be limited to half (the symmetry in the XY plane).

5 AC Copper Loss Results

The stator's winding is represented as separate solid conductors linked together via an external circuit and energized from a sinusoidal current source. Figure 5 presents three physical winding arrangements for DC and AC power loss investigations. Different numbers of turns and the equivalence between the winding versions are

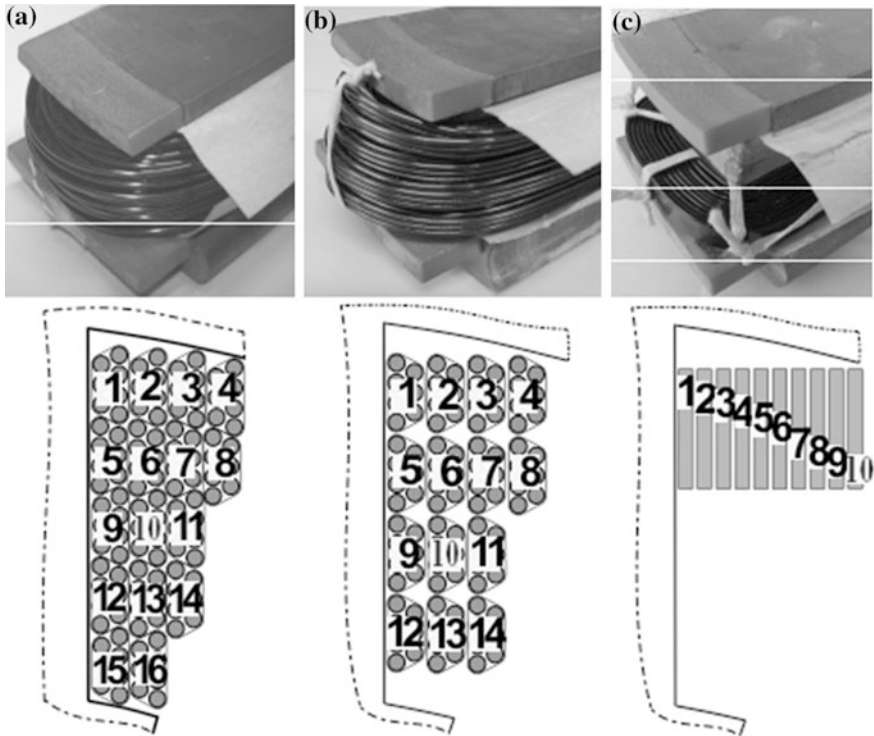


Fig. 5 The experimental winding layouts: 16 turns in 7-strands of parallel conductors (a), 14 turns in 7-strands of parallel conductors precisely defined (b) and 10 turns in series rectangular conductors (c)

presented to demonstrate various phenomena of proximity effects. The baseline configuration, winding version I, is representative of mush winding comprising 7 parallel conductor strands with 16 turns series random wound onto the tooth ‘in hand’ (50 % copper fill factor). The second winding arrangement was manufactured using 14 turns with 7 parallel conductor strand (44 % copper fill factor), where the location of conductors is precisely defined by banding them in the defined position in the slot. This allows the arrangements of conductors in the slots for winding version II to be accurately reproduced in the FE model. The third winding version comprised 10 turns of a rectangular conductors connected in series with 6.7 % copper fill factor. Again for winding III the distribution of the conductors could be accurately represented in the FE model.

Position of each conductor placed into the slot is shown by labels, Fig. 5. The rectangular windings layouts described by version III located on the rear slot can be expected to decrease the ac losses in the machine [1].

Table 1 compares experimental results with FEM calculation of total loss including iron loss (P_{Fe}) and copper loss (P_{Cu}) for the winding version I under DC

Table 1 Theoretical prediction of R_{ac}/R_{dc} and total power loss measurement with FEA prediction at 400 Hz and 40 Arms

Winding version		I	II	III
Copper fill factor		50 %	44 %	6.7 %
R_{ac}/R_{dc} (3D FEA prediction)		–	2.1	1.8
R_{ac}/R_{dc} (2D FEA prediction)		–	2.2	1.8
Power loss ($P_{Cu} + P_{Fe}$)	Measurements	54.4 W	61.5 W	38.5 W
	3D FEA	–	68 W	47 W
	2D FEA	–	44.3 W	42.3 W

(57 °C) and AC (76 °C) current supply at 400 Hz, winding version II at average temperature working for copper equal to 50 °C under DC and 88 °C under AC at 400 Hz, and average temperature working for winding version III was equal to 49 °C under DC and 71 °C under AC current supply at 400 Hz.

Winding version I to FEA was not taken into account because of the difficulty to allocate accurately the conductor strands in the slot. In fact, Table 1 and Fig. 7 shows that the 3D FEA prediction obtained with winding version II is more consistent with the experimental results than the 2D FEA prediction. However, the 2D FEA prediction is in better agreement with measured values in case of winding version III. This happened because the difference between the FE model and physical coil. Semicircular profile of end-winding in all cases of FE models was used as presented in Fig. 4a. In fact, end-winding for the prototype of winding version III is closer banded to stator core. An accurate reproduction of the arrangement of conductors in the slot in the FE model is always a challenge. And prediction of the impact of eddy-current from end-winding region on the laminated steel-sheet can be less insignificant, and total loss prediction can be calculated less accurately.

Figures 6, 7 show experimental and numerical results of DC and AC power losses for both winding versions II and III. FE calculation of power losses consist of copper and iron losses only.

Figure 7 demonstrates the AC copper loss effects at high speed operation for two versions of winding arrangements in respect to the power loss.

Eddy-current calculations are realized at high range of rotor speed and calculated for 40 RMS current representing 40 % of maximal thermal rating of the stator core. The copper power loss within the solid conductors is determined from the Joule loss:

$$P_{Cu} = \iiint_V \mathbf{E} \cdot \mathbf{J} dV = \rho \iiint_V \mathbf{J}^2 dV = l\rho \iint_S J^2 dS \quad (1)$$

Fig. 6 Measurements and FE calculation of power loss for different dc current: winding version II (a), winding version III (b)

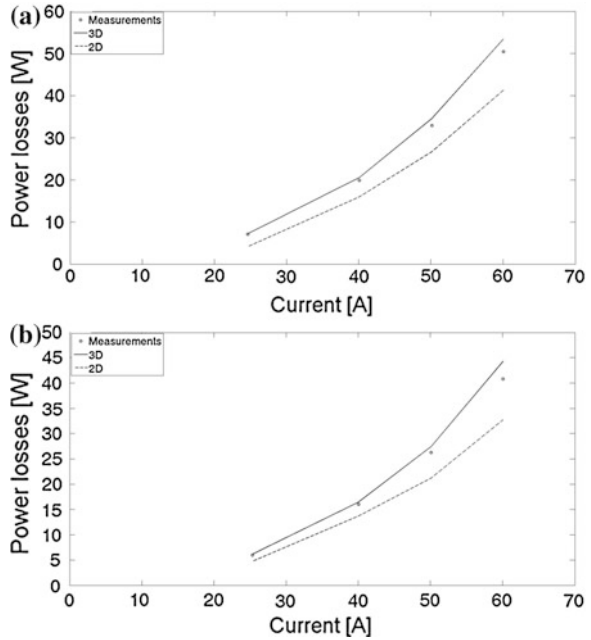
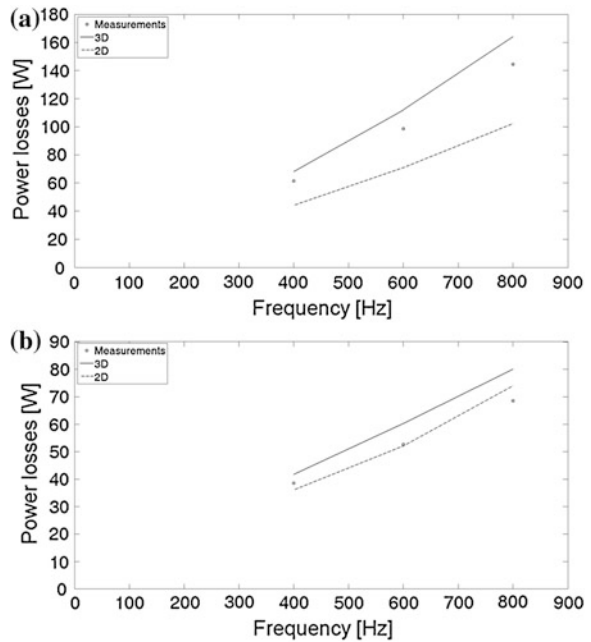


Fig. 7 Measurements and FE calculation of power loss versus frequency for $I_{rms} = 40$ A: winding version II (a), winding version III (b)



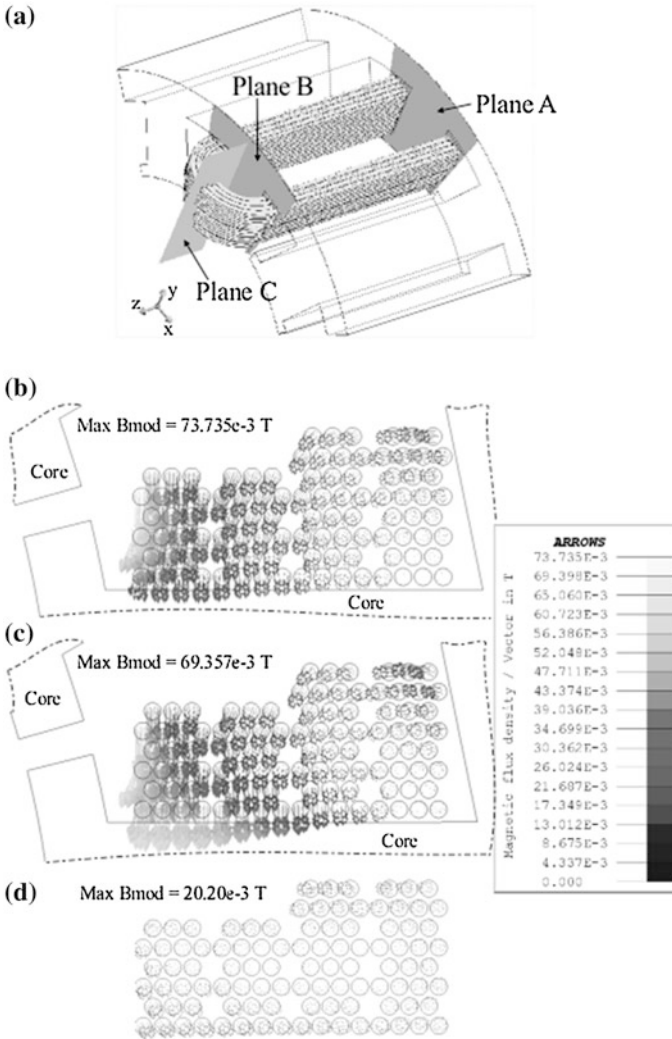
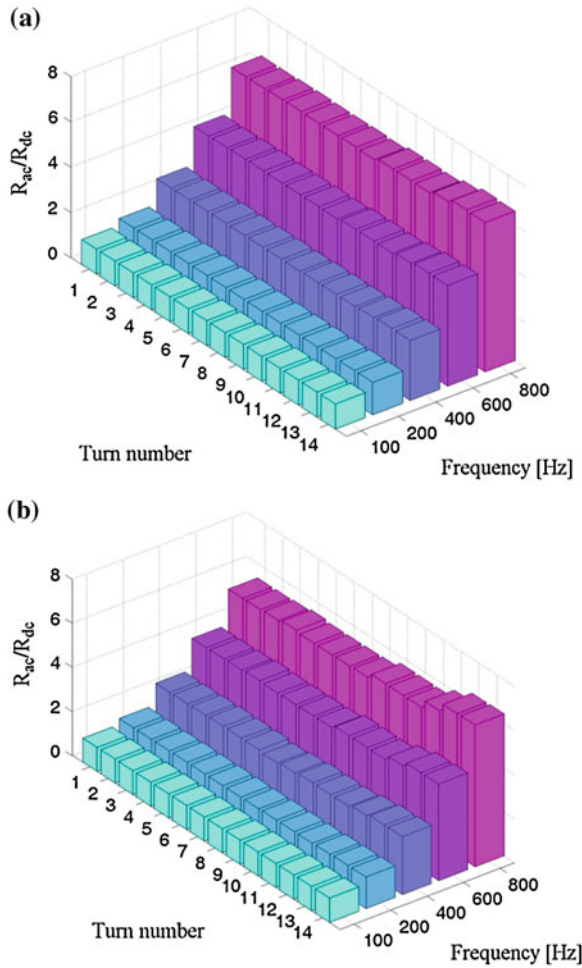


Fig. 8 3D calculation of the magnetic flux density in the motor winding version II at 40 Arms and 800 Hz: cut planes (a), in the half of active length—plane A (b), the end of the active length—plane B (c) and end-winding—plane C (d). The legend of magnetic flux density for each plane is the same

where \mathbf{E} is the electric field strength, \mathbf{J} is the current density within the conductors, ρ is the resistivity of copper ($0.1564 \times 10^{-7} \Omega \cdot \text{m}$ at 20°C) and l is the active length of the conductors. From (1), an equivalent bulk value of the winding AC resistance is found:

Fig. 9 R_{ac}/R_{dc} ratio versus conductor number at $I_{rms} = 40$ A for a winding version II at 20 C (a) 2D model, (b) 3D model



$$R_{ac} = P_{Cu}/i_{rms}^2 \tag{2}$$

where i_{rms} is the RMS current.

This bulk value of resistance (2) determines the increase of resistance under AC excitation as compared to DC operation. The ratio of the equivalent AC resistance to the ideal DC value R_{ac}/R_{dc} is a commonly used figure of merit to assess high frequency effects.

The end-winding region is exposed to the flux patterns that are different from these within the winding active length. As a consequence of this, the loss distribution for the end active regions of the winding differs too. Moreover, the end-winding region is usually where the greatest ‘hot-spot’ temperatures occur as a result of relatively poor heat transfer from the end-winding to the surrounding

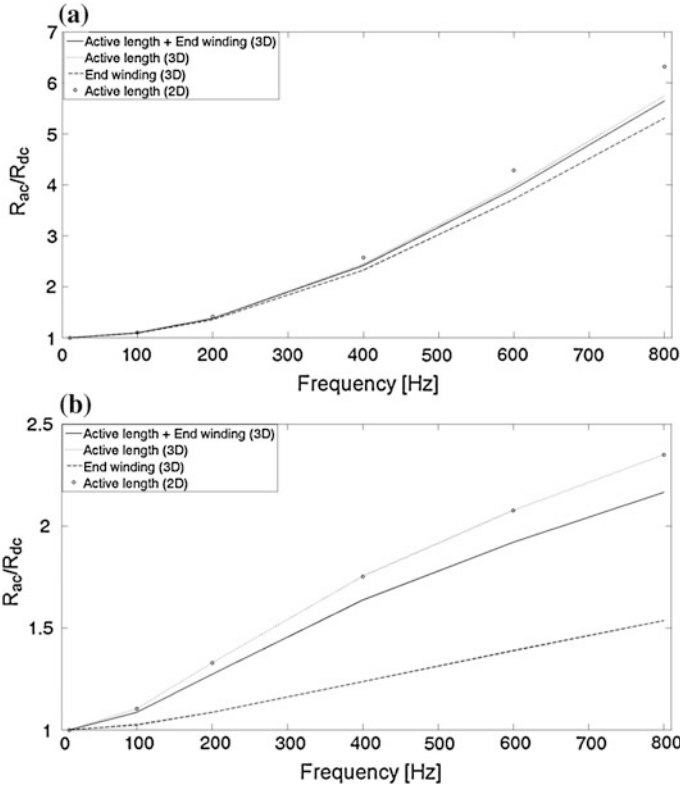


Fig. 10 Comparison of R_{ac}/R_{dc} ratio for different regions and calculation method for $I_{rms} = 40$ A: winding version II (a), winding version III (b) at constant copper temperature $20\text{ }^{\circ}\text{C}$

environment. To illustrate the behavior of the proximity losses the distribution of the magnetic flux obtained from the planes (see Fig. 8a) causes eddy-currents as illustrated in Figs. 8b–d for winding version II at 40 Arms and $f_e = 800$ Hz. The average temperature of winding is increased to $152\text{ }^{\circ}\text{C}$ and that value was considered in FEA (Fig. 8b–d). Parts (b–c) show the vector of magnetic flux from the planes A and B in the middle and the end of active-length. Part (d) shows the vector of magnetic flux density from the plane C on the top of end-winding. In the planes A and B there can be observed an increased density of magnetic flux within the conductors close to the tooth opening. This leads to elevated proximity losses in these conductors. The magnetic flux obtained from the plane B indicates higher values due to a higher flux linkage than observed in the plane A. In the plane C, higher flux densities can be seen for the conductors placed near the stator core than for the others.

Figure 9 presents the ratio of the equivalent AC to DC resistance for the separate conductors of the winding version II, obtained from both 2D and 3D FEAs. The localized losses concentration (resistance ratio) for the model including end-

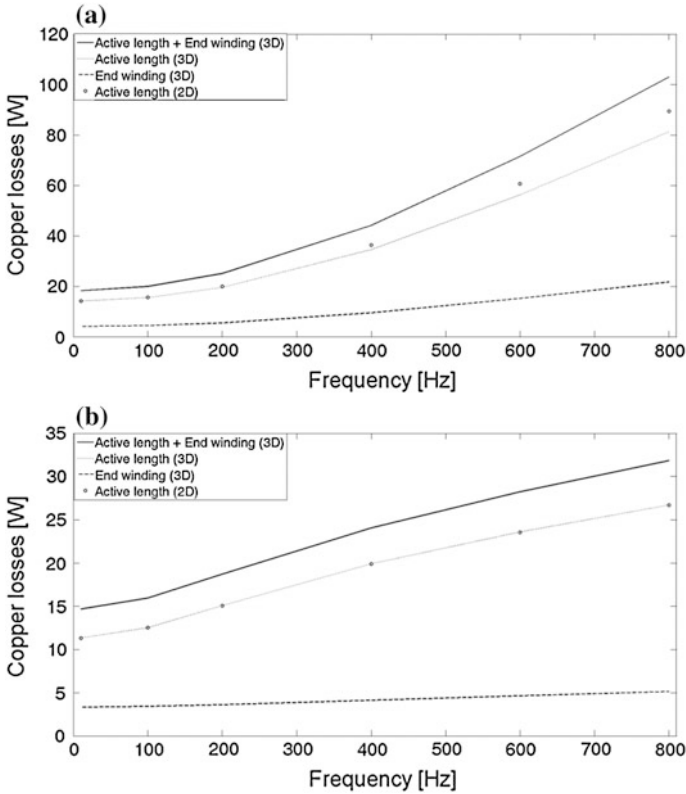


Fig. 11 Variation winding loss versus frequency at $I_{rms} = 40$ A: winding version II (a), and winding version III (b) at constant copper temperature 20 °C

winding regions in turns 9–14 is particularly visible at high excitation frequencies with relatively high magnetic flux as seen from planes A and B. The highest eddy-currents are induced close to the open slot, in particular within strands 13–14. Additionally, there can be seen slightly increasing copper losses in the strand 1 in the corner of a rear slot (Fig. 9b).

Since the copper fills the slot and the wires are very close to each other, the proximity effect can be prominent. The half of the slot filled by copper close to slot opening has large amount of proximity loss (Figs. 8, 9), therefore the winding versions I, II and III were designed with the conductors placed in the rear slot in order to reduce proximity loss.

The diameter of each conductor within the strand for winding versions I and II is low and equal to 1.6 mm. The skin effect can be insignificant since the diameter of copper is low and lower than proximity loss within conductors [1]. These two effects also strictly depend on a shape of the strands.

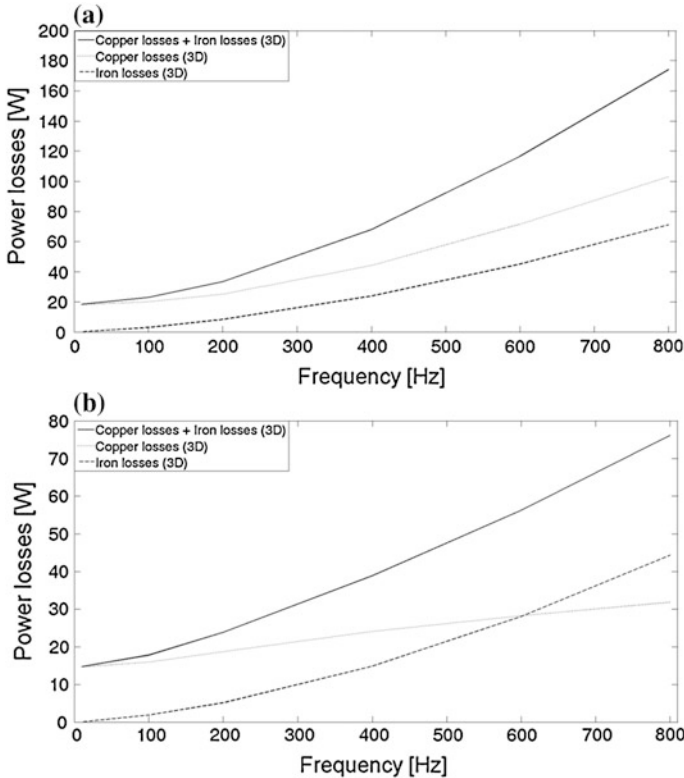


Fig. 12 3D calculation of power losses versus frequency for $I_{rms} = 40$ A: winding version II (a), and winding version III (b) at constant copper temperature 20 °C

Results of the ratio of the equivalent AC to DC resistance versus frequency are depicted in Fig. 10 for various calculation methods. The resistance ratio for rectangular conductors (dimension of each bar conductor is 1.5×3 mm) obtained from the 3D models within both active-length and end-winding regions is approx. 3 times lower relative to version II for the highest frequency range. According to 3D FEA, the proximity effect for the end-winding region is 5.4 % (version II) lower than that predicted within the active-length, and 32 % lower relative to version III.

Figure 11 shows distribution of copper power loss in the active and end winding regions. At frequencies higher than 100 Hz, power losses are rapidly growing. The profile of losses at high frequencies for version III is decreasing exponentially, and that phenomenon is opposite to winding version II. Copper losses generated by winding version II produce a higher temperature because more conductors are placed close to the slot opening where more flux linkages are crossing the slot opening region. In the machine with round conductor winding, the total copper losses in the active length obtained from 2D FE calculations are higher than from the 3D FE calculations. A different behaviour of the proximity loss is demonstrated

from bar conductor layouts where the 2D FE results of total proximity loss are lower than for 3D FE calculation.

Figure 12 shows the standard round winding (version II) compared to the designed bar conductors which can significantly reduce the copper loss. Also, the amounts of iron and copper losses are demonstrated.

6 Conclusions

New generations of high-speed PM machines can result in significant amounts of AC losses in the stator windings. An analysis of the AC proximity effects has been carried out using 3D FEA and has accounted for both the active length and end-winding regions. To demonstrate the inaccuracies that can occur when the end-winding effects are neglected, 2D calculations have been performed. Unsurprisingly, 3D calculations give more accurate knowledge of a total copper loss amount produced in high-speed motor and it can be concluded that this loss analysis method has to be taken into account. Three winding versions have been considered. The calculated 3D total copper losses in the standard round winding at a 800 Hz machine have been compared with those for the designed bar conductors, The latter ones have been found to be significantly lower due to the conductors placed aloof from the opened slots. The end-winding loss within the investigated winding layouts has been found some 20 % lower than the loss produced within the active-length regions.

Experimental verification and calculation results for DC and AC excitations present a good study of the proximity effect in the end-turn, with a good agreement. In particular measurements and 3D FEA predictions obtained with winding version II are very close to each other. However, the 2D FEA prediction is in a better agreement with measured values in case of winding version III, which may result from incorrect 3D modeling of end-windings. It can be preliminary concluded that influence of a shape of end-windings on power losses at high frequencies may be remarkable, the statement to be magnified by the forthcoming results of our current research work.

References

1. Mellor PH, Wrobel R, McNeill N (2006) Investigation of proximity losses in a high speed brushless permanent magnet motor. Proceedings of 41st IAS industry applications conference, IEEE conference publication, vol 3, pp 1514–1518
2. Wrobel R, Mlot A, Mellor PH (2010) Investigation of end-winding proximity losses in electromagnetic devices. Proceedings of 21st international conference on electrical machines, IEEE conference publications, pp 1–6
3. Wrobel R, Mlot A, Mellor PH (2011) Contribution of end-winding proximity losses to temperature variation in electromagnetic devices. *IEEE Trans Indus Electr* 58(2):848–857

4. Reddy PB, Jahns TM, Bohn TP (2009) Transposition effects on bundle proximity losses in high-speed PM machine. IEEE energy conversion congress and exposition. IEEE conference publications, pp 1919–1926
5. Iwasaki S, Deodhar RP, Liu Y, Pride A, Zhu ZQ, Bremner JJ (2009) Influence of PWM on the proximity loss in permanent-magnet brushless AC machines. IEEE Trans Indus Appl 45 (4):1359–1367
6. Evans PD, Chew WM (1991) Reduction of proximity losses in coupled inductors. IEE Proc B Electr Power Appl 138(2):51–58
7. Reddy PB, Zhu ZQ, Han S-H, Jahns TM (2008) Strand-level proximity losses in PM machines designed for high-speed operation. Proceedings of 18th international conference on electrical machines, IEEE conference publications, pp 1–6
8. Reddy PB, Jahns TM, Bohn TP (2010) Modeling and analysis of proximity losses in high-speed surface permanent magnet machines with concentrated winding. Energy conversion congress and exposition, IEEE conference publication, pp 996–1003
9. Moreau O, Popiel L, Pages JL (1998) Proximity losses computation with a 2D complex permeability modelling. IEEE Trans Magn 34(5):3616–3619
10. Spang M, Albach M (2008) Optimized winding layout for minimized proximity losses in coils with rod cores. IEEE Trans Magn 44(7):1815–1821
11. Phung A-T, Meunier G, Chadebec O, Margueron X, Keradec JP (2007) High frequency proximity losses determination for rectangular cross-section conductors. IEEE Trans Magn 43:1213–1216
12. Murgatroyd PN (1989) Calculation of proximity losses in multistranded conductor bunches. IEE Proc A IET J Mag 136:115–120
13. Weili L, Feng Z, Liming C (1998) Calculation of rotor ventilation and heat for turbo-generator radial and tangential air-cooling system. International conference on power system technology, IEEE conference publication, vol 2, pp 130–1033
14. Weili L, Chai F, Fen Z (2008) Study on eddy current loss and heat-transfer character of stator winding in synchronous generator. International conference on electrical machines and systems, IEEE conference publications, pp 479–484
15. Lin R, Haavisto A, Arkkio A (2010) Analysis of Eddy-current loss in end shield and frame of a large induction machine. IEEE Trans Magn 46(3):942–948

Modeling of the Squirrel-Cage Induction Motor Having Symmetrically Distributed Groups of Broken Cage Bars

Damian Krawczyk

Abstract This paper deals with the topic of modeling of the squirrel-cage induction motor, in which the rotor cage bars are broken. Consideration is given to the special nature of distribution of the broken bars in the cage. Namely the distribution of broken bars on the circumference of the rotor is symmetrical and in particular it is considered the case as the number of groups of broken bars is equal to the number of motor poles. This type of rotor asymmetry occurs in the induction motors synchronized by reluctance torque. There is a universal model that allows analysis of both monoharmonic and poliharmonic phenomena presented. The paper also includes the results of simulation and qualitative conclusions from these studies.

1 Introduction

The issue of broken cage rotor bars in the squirrel-cage induction motors is considered primarily in relation to the diagnostics investigations of this type of electrical machines [1]. This is particularly important in the case of high power electric motors, where the occurrence of this type of failure can lead to very serious economic effects and also to danger of people and equipment safety. Diagnostic methods are based on the analysis of measurable waveforms such as the phase currents, which frequency spectrum may contain information about rotor failure involving the lack of continuity of one or more bars of the cage rotor. In general, any number of randomly distributed bars of the cage rotor can be broken what makes the investigations quite complex.

A special group of induction motors for which the subject of broken rotor bars seems to be interesting are the induction motors synchronized by reluctance torque. This interest stems from the need of qualitative analysis of main physical phe-

D. Krawczyk (✉)

Faculty of Electrical Engineering, Chair of Mechatronics,
Silesian University of Technology, Gliwice, Poland
e-mail: damian.krawczyk@polsl.pl

nomena determining the basic performance and parameters of this type of motor. It is especially important from start-up analysis point of view because for some design solutions it is difficult or even impossible to start up and reach the synchronous velocity of the rotor.

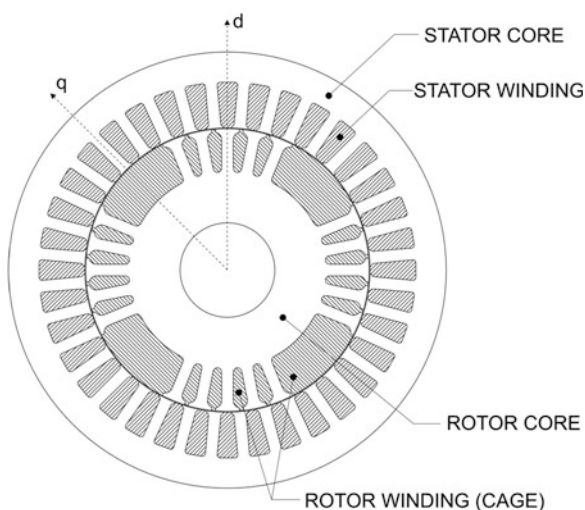
1.1 The Induction Motor Synchronized by Reluctance Torque

The induction motors synchronized by reluctance torque are interesting cost-effective solutions for constant speed applications. Such motors have some advantages of both induction motors and synchronous (reluctance) motors. An example of four-pole induction motor synchronized by reluctance torque is presented in Fig. 1.

The main advantage of the motors having the construction shown in Fig. 1 is ease of their manufacturing. It results from the fact that these motors are manufactured using the technology for the standard squirrel-cage induction motors. The stator of the motor is identical to the one used in the standard induction motor, whereas the rotor is manufactured by changing the shape of the rotor lamination. Namely, a number of small teeth along to the rotor circumference is removed to make “big teeth”. Each “big tooth” is composed of a number of the small teeth. Next all the slots (small and big) of the rotor are filled by liquid aluminium to form asymmetrical starting cage. The number of removed small teeth influences both magnetic asymmetry of the rotor (synchronous reluctance torque) and electric asymmetry of the starting cage (asynchronous torque) of the motor.

During designing the asynchronous motors synchronized by reluctance torque two main aims are to be reached:

Fig. 1 The cross-section of four-pole asynchronous motor synchronized by reluctance torque



- Reluctance (steady-state) torque should be as high as possible,
- Starting up properties should be very good (torque T_e vs. velocity n curve should be as close as possible to the curve of the symmetrical induction motor).

In this paper the second aim will be considered.

1.2 The Structure Decomposition of the Induction Motor Synchronized by Reluctance Torque

From qualitative point of view it is very convenient to use a heuristic approach to analyze the phenomena related to the asymmetrical design of the cage. Such an approach is illustrated in Fig. 2 [2–4].

The decomposition of the induction motor synchronized by reluctance torque is based on artificial division of the motor into three motors mechanically coupled to each other (in other words, placed on a common shaft) with distinct operating characteristics: the first one (marked as R) determines the average value of reluctance torque, while the other two (marked with symbols As1 and As2) have a dominant influence on motor start-up properties. The motor R is “purely” reluctance (the rotor has no windings). The induction motor As1 is an induction motor with a cage rotor consisting of four large rods (the number of rods is equal to the number of poles) and the induction motor As2 is an induction motor with a cage having symmetrically distributed four (generally equal to the number of poles) groups consisting of small bars (spaced by pole pitch) with a span of the groups of bars smaller than the pole pitch.

In this paper the motor As2 as presented in Fig. 3 will be investigated in more detail.

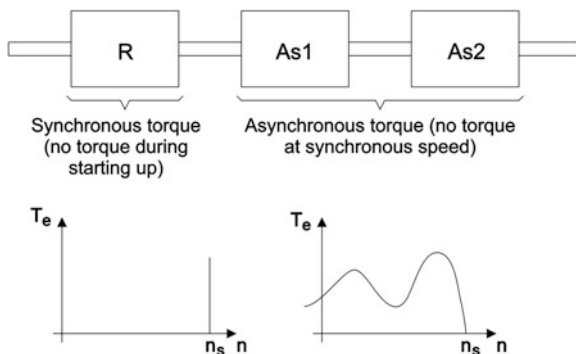
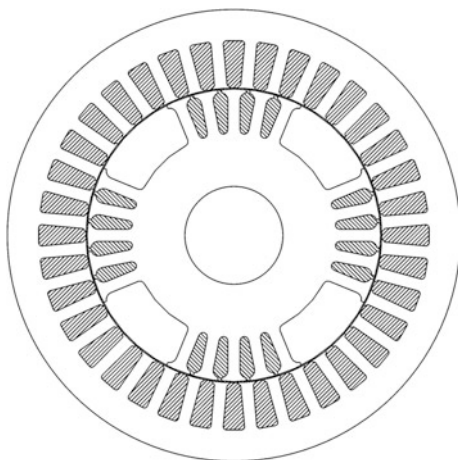


Fig. 2 The structure decomposition of the induction motor synchronized by reluctance torque into three separate motors (*R* reluctance motor, *As1* induction motor having a number of big rotor bars equal to the number of poles, *As2* induction motor having symmetrically distributed groups of broken small bars)

Fig. 3 The induction motor As2 (having symmetrically distributed groups of broken small bars)



2 The Mathematical Model of the Induction Motor

2.1 The Symmetrical Machine

The general mathematical model of the squirrel-cage induction motor given in the machine coordinates is composed of the following equations [5, 6]:

$$\begin{aligned} \begin{bmatrix} [u_s] \\ [0] \end{bmatrix} &= \begin{bmatrix} [R_s] & [0] \\ [0] & [R_r] \end{bmatrix} \begin{bmatrix} [i_s] \\ [i_r] \end{bmatrix} + \begin{bmatrix} [L_{\sigma s}] & [0] \\ [0] & [L_{\sigma r}] \end{bmatrix} \frac{d}{dt} \begin{bmatrix} [i_s] \\ [i_r] \end{bmatrix} \\ &+ \frac{d}{dt} \left\{ \begin{bmatrix} [M_{ss}] & [M_{sr}(\vartheta)] \\ [M_{rs}(\vartheta)] & [M_{rr}] \end{bmatrix} \begin{bmatrix} [i_s] \\ [i_r] \end{bmatrix} \right\} \end{aligned} \quad (1)$$

$$J \frac{d\omega_m}{dt} = [i_s]^T \frac{d}{d\vartheta} [M_{sr}(\vartheta)] [i_r] - T_m \quad (2)$$

$$\omega_m = \frac{d\vartheta}{dt} \quad (3)$$

where: $[R_s]$, $[R_r]$ —windings resistance matrices for the stator and the rotor respectively; $[L_{\sigma s}]$, $[L_{\sigma r}]$ —leakage inductance matrices for the stator and the rotor respectively; $[M_{ss}]$, $[M_{rr}]$ —main inductance matrices for the stator and the rotor respectively; $[M_{sr}(\vartheta)]$, $[M_{rs}(\vartheta)]$ —mutual inductance matrices for the stator-rotor and the rotor-stator respectively; ϑ —the angle between the rotor and the stator; $[u_s]$ —the stator supply voltage vector; $[i_s]$, $[i_r]$ —the stator and rotor currents vectors respectively; T_e —the electromagnetic torque; J —the mass inertia; T_m —the mechanical load torque.

After transforming the Eqs. (1–3) to $\alpha\beta$ coordinates which makes the model easier to handle, the model is as follows:

$$\begin{aligned} \frac{d}{dt} \begin{bmatrix} [i_s^{\alpha\beta}] \\ [i_r^{\alpha\beta}] \end{bmatrix} &= \left(\begin{bmatrix} [L_{\sigma s}^{\alpha\beta}] & [0] \\ [0] & [L_{\sigma r}^{\alpha\beta}] \end{bmatrix} + \begin{bmatrix} [M_{ss}^{\alpha\beta}] & [M_{sr}^{\alpha\beta}(\vartheta)] \\ [M_{sr}^{\alpha\beta}(\vartheta)]^T & [M_{rr}^{\alpha\beta}] \end{bmatrix} \right)^{-1} \\ &\times \left(\begin{bmatrix} [u_s^{\alpha\beta}] \\ [0] \end{bmatrix} - \left(\begin{bmatrix} [R_s^{\alpha\beta}] & [0] \\ [0] & [R_r^{\alpha\beta}] \end{bmatrix} + \frac{d}{dt} \begin{bmatrix} [M_{ss}^{\alpha\beta}] & [M_{sr}^{\alpha\beta}(\vartheta)] \\ [M_{sr}^{\alpha\beta}(\vartheta)]^T & [M_{rr}^{\alpha\beta}] \end{bmatrix} \right) \begin{bmatrix} [i_s^{\alpha\beta}] \\ [i_r^{\alpha\beta}] \end{bmatrix} \right) \end{aligned} \quad (4)$$

$$\frac{d}{dt} \omega_m = \frac{1}{J} \left(\left([i_s^{\alpha\beta}]^T \frac{d}{d\vartheta} [M_{sr}^{\alpha\beta}(\vartheta)] [i_r^{\alpha\beta}] \right) - T_m \right) \quad (5)$$

$$\omega_m = \frac{d\vartheta}{dt} \quad (6)$$

In general the Eq. (4) comprises $3 + Q_r$ equations but usually quite many of them can be neglected as ones giving solutions equal to zero [6]. So it is possible to reduce significantly the complexity of the model before its implementation.

2.2 The Asymmetrical Machine

The mathematical model of the induction motor As2 as in Fig. 3 can be derived from the standard model given by the Eqs. (4–6). The only modification which has to be done is to find a new form for the rotor resistance matrix $[R_r]$. To find the form the general structure of the motor As2 rotor cage (an example is presented in Fig. 4) should be considered.

A broken bar can be included in the resistance matrix by assuming very high increase of its resistance (of up to a thousand times) thereby it is as follows:

$$R_{prk} = k_{pr} R_{pr} \quad (7)$$

where: R_{pr} —the resistance of non broken (original) bar, k_{pr} —the coefficient of the bar resistance increase (in simulations it was equal to 1000).

Such an approach leads to the representation of the rotor resistance matrix in the form of the following sum:

$$[R_r] = [R_{rs}] + [\Delta R_{pr}] \quad (8)$$

where: $[R_{rs}]$ —the symmetrical rotor resistance matrix; $[\Delta R_{pr}]$ —the rotor resistance increase matrix;

Thus, to obtain the modified form of the mathematical model of the As2 motor, it is necessary to determine the general form of $[\Delta R_{pr}]$ matrix in the $\alpha\beta$ coordinates which can be derived from the following formula:

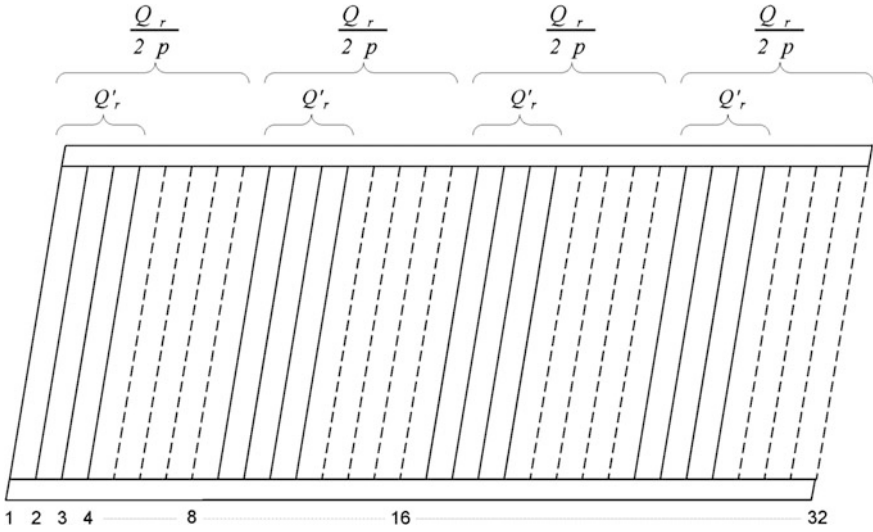


Fig. 4 The structure of the induction motor As2 rotor cage (the number of slots for the original induction motor $Q_r = 32$, the number of pole-pairs $p = 2$, the number of non broken bars per a group of small bars $Q'_r = 4$)

$$\left[\Delta R_{pr}^{\alpha\beta} \right] = [K_r] [\Delta R_{pr}] [K_r]^T \tag{9}$$

where: $[K_r]$ —the transformation matrix.

It turns out that this matrix has a predefined structure and its components change in a regular way depending on the degree of asymmetry (the number of broken bars). In Fig. 5 there is a general structure (fulfillment) of the matrix presented—the gray cells designate non-zero elements. For the symmetrical squirrel-cage induction motors the rotor resistance matrix transformed to $\alpha\beta$ coordinates system is a diagonal matrix. From Fig. 5 it results that the matrix $\left[\Delta R_{pr}^{\alpha\beta} \right]$ is not a diagonal one. Therefore there are additional linkages between the equations in the set (3) causing activation of equations which give solutions equal to zero in the fully symmetrical case (the standard squirrel-cage induction motor).

All the components of the matrix $\left[\Delta R_{pr}^{\alpha\beta} \right]$ can be categorized into specific groups (A, B, C, D, E, F) of components having similar properties as it is presented in Fig. 6.

As an example, the detailed formula for the elements designated as B is given by the following formula:

	$\alpha\beta 1$	$\alpha\beta 2$	$\alpha\beta 3$	$\alpha\beta 4$	$\alpha\beta 5$	$\alpha\beta 6$	$\alpha\beta 7$	$\alpha\beta 8$	$\alpha\beta 9$	$\alpha\beta 10$	$\alpha\beta 11$	$\alpha\beta 12$	$\alpha\beta 13$	0p	0
$\alpha\beta 1$															
$\alpha\beta 2$															
$\alpha\beta 3$															
$\alpha\beta 4$															
$\alpha\beta 5$															
$\alpha\beta 6$															
$\alpha\beta 7$															
$\alpha\beta 8$															
$\alpha\beta 9$															
$\alpha\beta 10$															
$\alpha\beta 11$															
$\alpha\beta 12$															
$\alpha\beta 13$															
0p															
0															

Fig. 5 The general structure of the rotor resistance matrix $[AR_{pr}^{\alpha\beta}]$

$$\begin{aligned}
 B(m_1, m_2) = a_1 & \left[(\cos(m_1 + m_2)\alpha_r - \cos m_1\alpha_r - \cos m_2\alpha_r + 1) \sum_{h=Q'_r}^{\frac{Q_r}{2p}-1} \cos(m_1 + m_2)h\alpha_r \right. \\
 & \left. + (\sin(m_1 + m_2)\alpha_r - \sin m_1\alpha_r - \sin m_2\alpha_r) \sum_{h=Q'_r}^{\frac{Q_r}{2p}-1} \sin(m_1 + m_2)h\alpha_r \right] \\
 + a_2 & \left[(\cos(m_1 - m_2)\alpha_r - \cos m_1\alpha_r - \cos m_2\alpha_r + 1) \sum_{h=Q'_r}^{\frac{Q_r}{2p}-1} \cos(m_1 - m_2)h\alpha_r \right. \\
 & \left. + (\sin(m_1 - m_2)\alpha_r - \sin m_1\alpha_r + \sin m_2\alpha_r) \sum_{h=Q'_r}^{\frac{Q_r}{2p}-1} \sin(m_1 - m_2)h\alpha_r \right]
 \end{aligned} \tag{10}$$

where: $a_1 = 2p$ for $m_1 + m_2 = 2 bp$; $a_1 = 0$ for $m_1 + m_2 \neq 2 bp$; $a_2 = 2p$ for $m_1 - m_2 = 2 bp$; $a_2 = 0$ for $m_1 - m_2 \neq 2 bp$; $b = 1, 2, 3, \dots$

	$\alpha 1$	$\beta 1$	$\alpha 2$	$\beta 2$	$\alpha 3$	$\beta 3$	$\alpha 4$	$\beta 4$	$0p$	0
$\alpha 1$	$A1(1)$	$C(1)$	0	0	$B(1,3)$	$E(1,3)$	0	0	0	0
$\beta 1$	$C(1)$	$A2(1)$	0	0	$E(1,3)$	$D(1,3)$	0	0	0	0
$\alpha 2$	0	0	$A1(2)$	$C(2)$	0	0	$B(2,4)$	$E(2,4)$	0	0
$\beta 2$	0	0	$C(2)$	$A2(2)$	0	0	$E(2,4)$	$D(2,4)$	0	0
$\alpha 3$	$B(3,1)$	$E(3,1)$	0	0	$A1(3)$	$C(3)$	0	0	0	0
$\beta 3$	$E(3,1)$	$D(3,1)$	0	0	$C(3)$	$A2(3)$	0	0	0	0
$\alpha 4$	0	0	$B(4,2)$	$E(4,2)$	0	0	$A1(4)$	$C(4)$	$F1(4)$	0
$\beta 4$	0	0	$E(4,2)$	$D(4,2)$	0	0	$C(4)$	$A2(4)$	$F2(4)$	0
...
...
$0p$	0	0	0	0	0	0	$F1(4)$	$F2(4)$	$A3$	0
0	0	0	0	0	0	0	0	0	0	0

Fig. 6 The detail structure of the rotor resistance matrix $\left[\Delta R_{pr}^{\alpha\beta} \right]$

3 Implementation of the Mathematical Model for the As2 Motor

The mathematical model given by the Eqs. (4–6) and (9) was implemented in Matlab Simulink environment for a chosen motor ($Q_r = 32$) for different numbers of non broken bars Q'_r in the rotor. There is the mechanical characteristic torque T_e versus rotational velocity n for different numbers ($Q'_r = 8, 5, 4$ and 3) of non broken bars per a group of bars presented in Fig. 7.

At the mechanical characteristic it can be noticed that the decline in the value of the electromagnetic torque is greater if the value of the parameter Q'_r is smaller

Fig. 7 Motor torque T_e versus rotor rotational velocity n for different numbers ($Q'_r = 8, 5, 4$ and 3) of non broken rotor bars

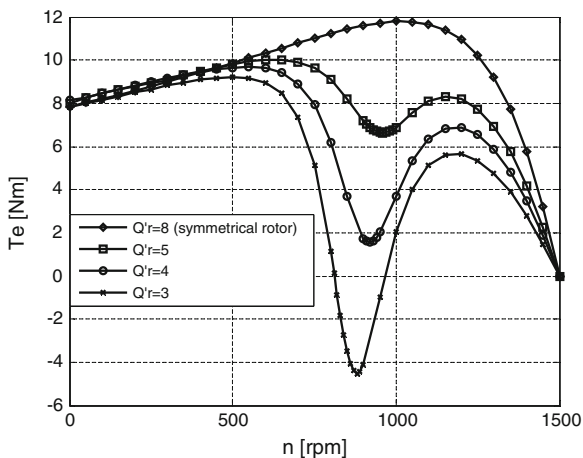


Fig. 8 The steady state stator current waveform for constant rotational velocity $n = 200$ rpm and for $Q'_r = 4$

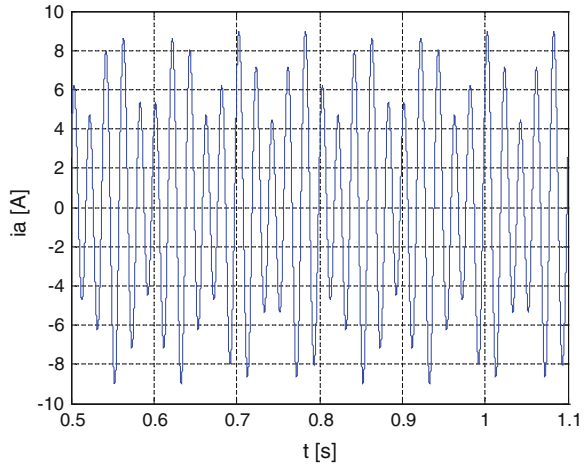
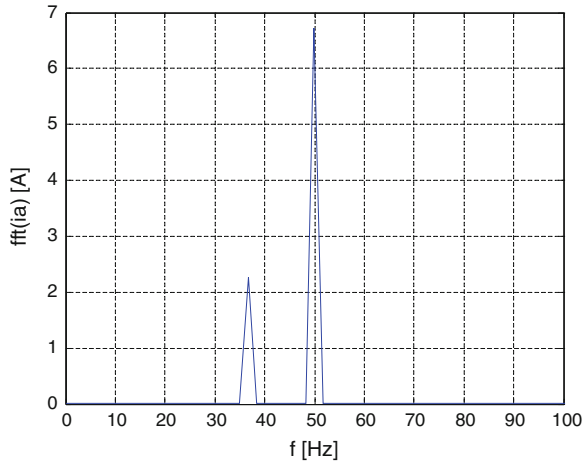


Fig. 9 The harmonic spectrum of the stator current waveform from Fig. 8



(the degree of asymmetry is bigger). This decrease occurs in the neighborhood of the point corresponding to half of the synchronous speed.

The explanation of this phenomena can be based on the analysis of the stator current at steady state. The stator current waveform at constant speed $n = 200$ rpm and for $Q'_r = 4$ is presented in Fig. 8. Although the motor is supplied from sinusoidal voltage source the current is non sinusoidal.

It results from the presence in the current not only the basic harmonic of the net frequency (50 Hz) but also the additional harmonic which frequency is dependent on the rotor velocity. Both the harmonics are presented in Fig. 9.

The stator current harmonic of the net frequency is called positive sequence component and is responsible for generating the main circular magnetic field rotating in the same direction as the rotor. The stator current harmonic which

frequency changes proportionally to the rotor velocity is called negative sequence component and it generates the circular magnetic field which rotates in the direction opposite to the rotation rotor.

The presented above phenomenon is known as Görge's effect. It was observed only in the biggest salient-pole synchronous motors until now. The effect reveals itself during start up of the motor causing some problems. It sometimes is even impossible to reach the synchronous speed.

4 Summary

The presented model resulting from a heuristic method of decomposition structure is a good tool for qualitative research and allows to formulate general guidelines for the design of the induction motors synchronized by reluctance torque. It will also be useful in the development of the more detailed analysis of Görge's phenomenon, using more precise in quantitative sense numerical methods e.g. finite element method.

References

1. Nandi S, Toliyat HA, Li X (2005) Condition monitoring and fault diagnosis of electrical motors-a review. *IEEE Trans Energy Convers* 20(4):719–729
2. Krawczyk D, Kluszczyński K (2008) Simplified circuit analysis of starting up properties of the induction motor synchronized by reluctance torque. *AutSim 2008*, Wismar, Germany
3. Krawczyk D (2006) A circuit model for starting up performance modelling of the induction motor synchronized by the reluctance torque. *Międzynarodowe XV Sympozjum Mikromaszyny i Serwosystemy*, 17–21.09.2006, Polska, Sopicowo
4. Krawczyk D (2005) Analysis of chosen phenomena during starting up of the induction motor synchronized by reluctance torque. In: *Proceedings of the XLI international symposium on electrical machines*, Poland, Opole-Jarnołtówek, 14–17 June 2005, pp. s.634–639
5. Krause PC (1986) *Analysis of electric machinery*. McGraw-Hill, New York
6. Kluszczyński K, Miksiewicz R (1993) *Momenty pasożytnicze w indukcyjnych silnikach klatkowych*. Prace Sekcji Maszyn Elektrycznych i Transformatorów Komitetu Elektrotechniki PAN, PTETiS Warszawa-Gliwice 1993

Analysis of Established Thermal Conditions for Magnetorheological Clutch for Different Loading Conditions

Zbigniew Pilch

Abstract This paper presents the results of simulation studies of thermal conditions controllable magnetorheological fluid clutch. In the first part, the construction of a prototype clutch, the CAD model and the results of measurements of the time for a variety of power clutch, realized on the test bench. An analysis of power losses in the clutch for the different states of operation. Describes the boundary conditions for finite element calculations for steady state operation of thermal coupling. Subsequently, the results of simulations carried out in the FEMM 4.2. The work summarized statement of the simulation results and the conclusions.

1 Introduction

Magneto-Rheological (MR) fluids have been known for at least 50 years. MR fluid consists of small particles of ferromagnetic material suspended (immersed) in dispersion fluid (organic solvent, oils, water). When external magnetic field is applied, the fluid is subjected to strong magnetic polarization. Its viscosity may be increased until it solidifies completely if the magnetic field is strong enough. If shear stress in the fluid does not exceed yield strength $\tau_0(B)$, then fluid does not flow and it behaves as an elastic material. Thanks to this feature MR fluid is applied in brakes [1], dampers and clutches [2, 3], cylindrical MR transmission driven by SMA spring [4]. In these devices MR fluid is introduced between moving parts. The test structures are also used where other materials SMART type [2].

On the base of the magnetic field distributions and catalogue values of yield share stress in magneto-rheological fluids clutching torque values were determined. Figure 1 shows two characteristics for two types of magneto-rheological fluids—MRF-122EG and MRF-140CG [5, 6]. One of the major limitations to the application of MR fluid is the maximum operating temperature. For the three available

Z. Pilch (✉)

Department of Mechatronic, Faculty of Electrical Engineering, Silesian University of Technology, 44100 Gliwice, Poland
e-mail: zbigniew.pilch@polsl.pl

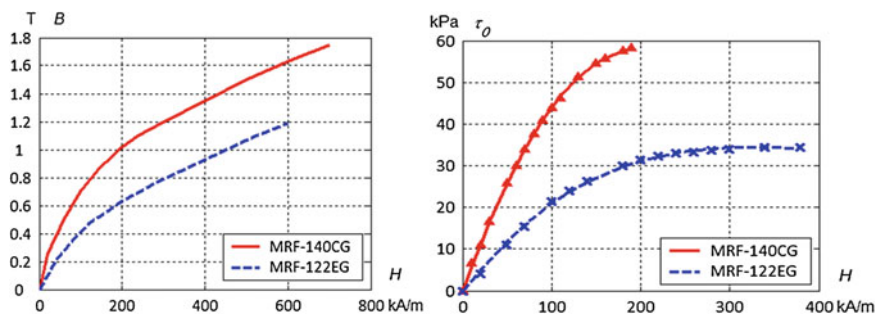


Fig. 1 Magnetization curves of different magnetorheological fluid types (*figure left*). Yield share stress versus magnetic field intensity $\tau_o(H)$ for different magnetorheological (*figure right*) [7, 8]

MRF-122EG fluid, MRF-132DG and MRF-140CG manufacturer claims it at 130 °C (403 K). Flash point for this liquid is above 150 °C (423 K) [7].

These temperature limits for the MR fluid can be a barrier to their use. This applies in particular to devices in which there are heat sources that can lead to overheating of the liquid. This effect causes a permanent loss fluid parameters.

• Proposal of coupling construction

For the proposed structure of the magnetorheological clutch magnetic field models were made [8]. The models were different for the sake of number, thickness and diameter of discs. MR fluids have been also successfully used in design of electrically controlled clutches, where rotational torque and speed may be controlled smoothly and the devices are not mechanically complex [9, 10]. Research conducted in Faculty of Electrical Engineering on Silesian University of Technology within the framework of the project “An electrically controlled magnetorheological multi-plate clutch with permanent magnet for smoothly controlled torque.” (project No. N N510 355337, financed since 2009–2011) [8, 9].

Magnetic field which changes viscosity of MR fluid is generated by the coil carrying the current I and the permanent magnet. Thanks two sources of magnetic field (coil and permanent magnet) the clutch generated clutching torque $T_C(I = 0)$ without necessity supplying the coil. The current I flowing the coil can decrease clutching torque $T_C(I-)$ or increase $T_C(I+)$. A quantity disc was determined on the basis of electromagnetic calculations.

The possible functions which multidiscs magnetorheological clutch can fulfil: dynamometrical function (for example in the screwdriver), safeties clutch, for half-active elimination of rotary vibrations, and for the system of the soft start-up.

The Fig. 2 shows test bench for multidisc clutch and view of real object.

The basic components of the measurement stand are:

- geared motor SKh71X-4C/XC40-7 production BESEL SA power of 0.55 kW. Maximum speed on the gearbox output is 186 rpm;
- investigated magnetorheological clutch;

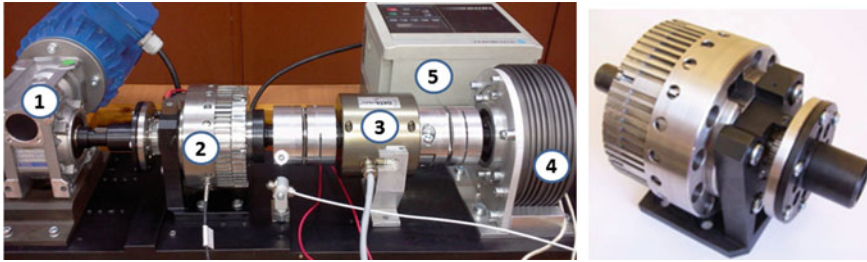


Fig. 2 View of test bench for the MR fluid clutch (number 2) and real object [8]

- torque meter DATAFLEX—20/22 production KTR;
- electromagnetic break with powder VER-30H-20-6 production FUMO Ostrzeszów;
- Inverter.

Figure 3 shows the characteristics of the clutch engaging torque coil and permanent magnet—blue curve with markers (Δ). This system has been called a hybrid system excitation electromagnetic field. The red curve with markers (*) is the torque characteristics of the clutch coupling of the coil only (no permanent magnets).

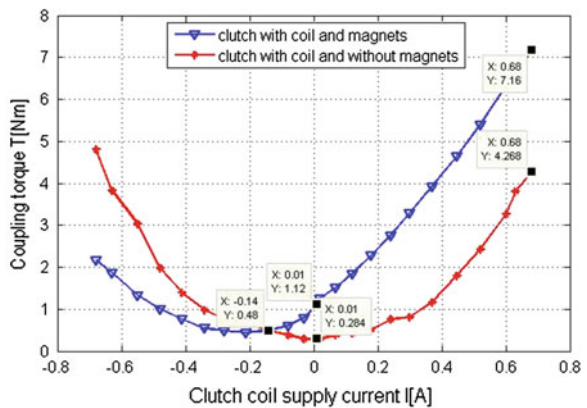
These characteristics relate to the coupling of a liquid MRF-140CG.

The graph also indicates the characteristic points (date cursors). For example, a point described as X:0.68, Y:7.16 means that it is worth the moment $T_s = 7.16$ N m corresponding to the clutch coil supply current equal to $I = 0.68$ A.

• **Operating states of clutch:**

Status controllable operating parameters in a working drive system can be described by the parameters of the transmitted power and the difference in the power supplied and developed by the clutch.

Fig. 3 Coupling torque characteristics for coupling with the coil and the magnet and the coil coupling only [8]



As defined in [11], referred to as a clutch drive system machine for connecting shafts and the torque transmission without changing its magnitude and direction. The coupling member consists of an active (drive), and a passive member (driven) and the connector. The coupling spacer is analyzed Magnetic Fluid and its parameters change due to changes in the electromagnetic field allows you to control the value of the torque capacity.

In the further considerations the following notation is:

- size associated with active coupling member are indexed number 1. These values are the mechanical power input (P_{m1}), the rotational speed of the active member (n_1), the torque acting on the active element (T_1).
- size associated with passive coupling member are indexed number 2. These values are: mechanical output power (P_{m2}) speed passive member (n_2), the torque acting on the passive element (T_2).

Size, which is related closely to the measure of loss of transmitted power is slipping s . In general, the amount of slip is calculated from the formula (1) or (2):

$$s = \frac{n_1 - n_2}{\max(n_1, n_2)} \quad (1)$$

$$s = \frac{|n_1 - n_2|}{\max(n_1, n_2)} \quad (2)$$

where:

n_1 —speed active member clutch rpm,

n_2 —speed passive coupling member rpm.

The controllable clutches slip value calculated from Eq. (1) has a value in the range $-1 \leq s \leq 1$ and the slip value is calculated according to Eq. (2) in the range $0 \leq s \leq 1$. For example, counting the slip of Eq. (1) are possible cases:

$$n_1 > 0, n_2 = 0 \Rightarrow s = 1 \quad (3a)$$

$$n_1 > 0, n_1 > n_2 > 0 \Rightarrow 1 > s > 0 \quad (3b)$$

$$n_1 > 0, n_2 = n_1 \Rightarrow s = 0 \quad (3c)$$

$$n_1 = 0, n_2 > n_1 \Rightarrow s = -1. \quad (3d)$$

$$n_1 > 0, n_2 > n_1 \Rightarrow 0 > s > -1 \quad (3e)$$

The image presented on the bench three states can be realized coupling load dependencies described (3a, c). This allows for a built-in measuring system for electromagnetic brake powder smoothly adjustable braking torque values.

Status operating parameters, which can be described by (3d, e) are possible if the passive side of the clutch there is a pattern of high-value mass moment of inertia. In

this case, inhibition of the active member or a stop may mean that the passive coupling part has a higher rotational speed than the active member ($n_2 > n_1$). This status will be short-lived state due to the thermal motion of the driven parts.

• **Analysis of the sources of heat in the clutch**

Thermal power dissipated in the clutch is the result of running various kinds of effects which are dependent on the state. This state is described in the input and output values for the member of the active and passive coupling, as described above. Sources of heat generation in the clutch coupling indicated in Fig. 4a and the power flow diagram form in the clutch in Fig. 4b.

Figure 4 indicates:

- P_{m1} —mechanical power delivered to the entrance of the clutch,
- P_{m2} —mechanical power output derived from the coupling,
- P_{fri11} —power lost to friction in the bearing of one ingredient,
- P_{fri12} —power lost to friction in the bearings of the two active,
- P_{fri2} —power lost to friction in the bearings of the passive,
- P_{el} —electrical power supplied to the clutch coil,
- P_{slip} —lost power as a result of slip between the part of the active and passive part of the clutch

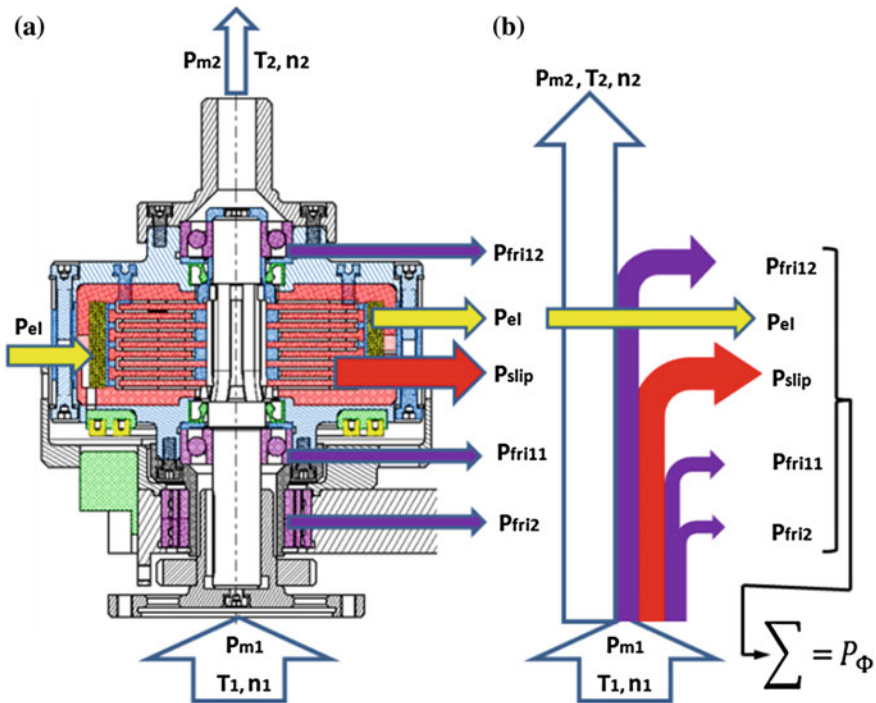


Fig. 4 The flow of power and thermal power sources in the clutch

Subsequently, determined by analysis, measuring the minimum and maximum values of the individual components of power.

- Mechanical power supplied and derived from the coupling can be calculated from Eq. (4):

$$P_{m1(2)} = \begin{cases} P_{m1(2)min} = \frac{T_{1(2)min} \cdot n_{1(2)min}}{9554} \\ P_{m1(2)max} = \frac{T_{1(2)max} \cdot n_{1(2)max}}{9554} \end{cases} \quad (4)$$

where:

$P_{m1(2)}$ —mechanical power supplied to the clutch or mechanical power derived from the coupling,

$T_{1(2)min}$ —minimum torque acting on the member active or passive element coupling

$T_{1(2)max}$ —maximum torque acting on the member active or passive element coupling

$n_{1(2)min}$ —minimum speed active member or member of passive coupling ($n_{1(2)min} = 0$ rpm)

$n_{1(2)max}$ —the maximum speed of the active member or member of passive coupling ($n_{1(2)min} = 186$ rpm).

The bearing system of the active part of the shaft consists of two bearings BE 7202. These bearings work when the slip $s \neq 0$. For $s = 0$, the slip rotational speed n_2 passive member is equal to the rotational speed n_1 of the active member, means that the track speeds of both the external and internal bearings are equal.

Power related to the friction in the bearing system was determined by measuring the friction in the system the moment the clutch bearing.

As shown in [10], friction bearings and seals for the active parts of the coupling are $T_{fri11} + T_{fri12} = T_{fri1} = 0.078$ N m.

Power associated with friction in the bearings of the active systems calculate the formula:

$$P_{fri1} = \begin{cases} P_{fri1min} = 0 & \text{for } s = 0 \\ P_{fri1max} = \frac{T_{fri1max} \cdot n_{1max}}{9554} & \text{for } s = 1 \end{cases} \quad (5)$$

Thus, the slip $s = 0$ is the minimum power 0 W and the slip $s = 1$ maximum power $P_{fri1max} = 1.52$ W.

For the passive measured torque friction bearing system of two low-profile series 30BNR 19HV1 V measuring $30 \times 47 \times 9$ $T_{fri2} = 0.024$ N m.

Power associated with friction in the bearings of the passive systems calculate the formula:

$$P_{fri2} = \begin{cases} P_{fri2min} = 0 & \text{for } s = 1 \\ P_{fri2max} = \frac{T_{fri2max} \cdot I_{2max}^2}{9554} & \text{for } s = 0 \end{cases} \quad (6)$$

Thus, the slip $s = 1$ is the minimum power 0 W and the slip $s = 0$ $P_{fri2max}$ maximum power = 0.47 W.

- Electrical power supplied to the clutch coil

The clutch used with a toroidal coil with 702 recipes of copper wire with a diameter of 0.315 mm. Measured resistance of the coil is the same $R_{CS} = 44.9 \Omega$. Resistance of the coil circuit (wires, brushes and slip rings, and coil) of 58.7 Ω .

Electric power P_{el} supply coil clutch calculate from the relation:

$$P_{el} = \begin{cases} P_{elmin} = R_{CS} \cdot I_{min}^2 \\ P_{elmax} = R_{CS} \cdot I_{max}^2 \end{cases} \quad (7)$$

where:

R_{CS} —clutch coil resistance $R_{CS} = 44.9 \Omega$,

$I_{min (max)}$ —clutch coil supply current $I_{min} = 0A$, $I_{max} = 0.68 A$

Thus, the minimum electric power is $P_{elmin} = 0 W$ (for $I_{min} = 0 A$) and maximum power $P_{elmax} = 20.8 W$. This power is the total power supplied to the power of coils. This power is independent of the actual value of the slip s .

Because the total loop resistance of the coil is 58.7 Ω , this means that 76.5% ($(44.9/58.7) \cdot 100$) of the power is dissipated within the clutch in the form of heat.

- Power associated with slip s between the part of the active and passive coupling:

Power dissipation during clutch operation is the result of the occurrence of slip between the member active and passive coupling. It is the power associated with overcoming internal friction between particles of magnetorheological fluid and the friction between the liquid molecules and the surfaces of the elements of active and passive coupling of the MR fluid. Furthermore, there are power losses due to friction in bearings and seals the system.

Total flow of mechanical power and electrical power supplied shown in Fig. 4 can be written as:

$$P_{m2} = P_{m1} - P_{fri2} - P_{fri1} - P_{slip} \quad (8)$$

Thermal power, which is created in the clutch is the difference between mechanical power brought to the clutch and the power derived. Additionally, you should still take into account the electrical power supplied to the clutch coil.

$$P_{\Phi} = (P_{m1} - P_{m2}) + P_{el} \quad (9)$$

Equation (8) after the transformation takes the form:

$$P_{slip} = P_{m1} - P_{m2} - P_{fri2} - P_{fri1} \tag{10}$$

Power dissipation in the slip (internal impacts associated with MR fluid molecules) will be dependent on the value of the slip s , consider three cases:

– **the case for $s = 1$**

For $s = 1$ we have: $n_1 \neq 0; n_2 = 0; P_{m2} = 0; P_{fri2} = 0$ Power flow diagram is shown in the Fig. 5

Power dissipation in slip write the equation:

$$P_{slip} = P_{m1} - P_{fri1} \tag{11}$$

– **the case for $s = 0$**

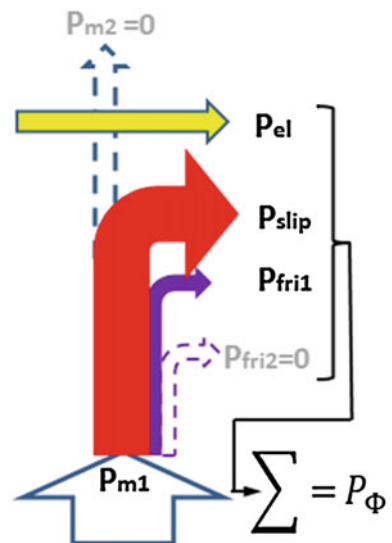
For $s = 0$ we have: $n_1 \neq 0; n_2 = n_1; P_{slip} = 0; P_{fri1} = 0$

Power flow diagram shown in Fig. 6.

Power dissipation of the slip is equal to 0, which write the equation:

$$\begin{aligned} P_{slip} = P_{m1} - P_{m2} - P_{fri2} - P_{fri1} &= 0 \\ \text{for } P_{fri1} &= 0 \\ P_{m1} - P_{m2} &= P_{fri2} \end{aligned} \tag{12}$$

Fig. 5 The flow of power for slip $s = 1$



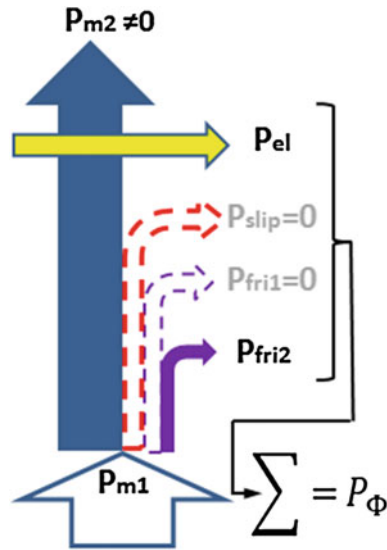


Fig. 6 The flow of power for slip $s = 0$

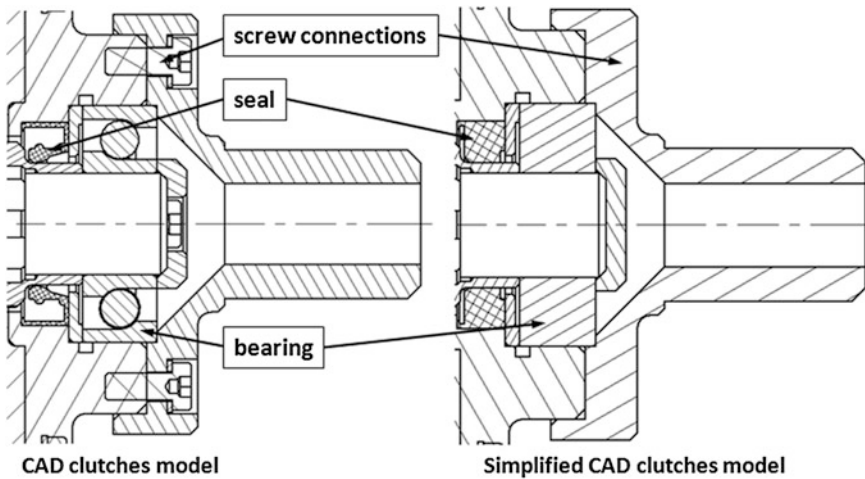


Fig. 7 CAD model and simplified CAD clutches model

–the case for $0 < s < 1$

For $0 < s < 1$ we have: $n_1 \neq 0; n_2 \neq n_1; n_2 \neq 0; P_{slip} \neq 0; P_{fri1} \neq 0; P_{fri2} \neq 0$

Power flow diagram correspond to the drawing 4b, and writing mathematical equivalent of Eq. (10).

- 3D geometric model of the clutch

Thermal calculations using finite element method are associated with the preparation of the computational model. For complex geometric objects are commonly used to simplify the geometry, which allows you to generate a smaller number of finite elements. Simplify the geometry and the preparation of the calculation model should not have a material impact on the results and their compliance with the real state of the thermal unit. During the formulation of the calculation model, the following assumptions:

- The actual coupling model created in Autodesk Inventor modified to simplify the geometry. An example of this type of treatment is shown in Fig. 7, where the ball bearings with raceways and the rolling elements have been replaced by solid rings. Same was in the case of seals and bolts.
- The calculations were carried out for axisymmetric thermal coupling model, the drawing together with their assigned areas of media types are shown in Fig. 8.

Clutch the axisymmetric model shown in Fig. 8.

Table 1 summarizes the basic parameters for the thermal clutch used in construction materials. In addition given the parameters of the air [6].

For air additionally assumed convective heat transfer coefficient $h = 7.9 \text{ W/m}^2 \text{ K}$ [12].

Simulation was carried out for a fixed heat issues (steady-state heat), for different operating conditions the coupling (slip values s are different). Heat outputs for each sub-set of the Eqs. (14) ÷ (16):

Thermal power associated with friction in the bearing of the active systems calculate the formula:

$$\dot{q}_{fril} = \frac{P_{fril}}{\pi \cdot b_{b1} \cdot (r_{b1a}^2 - r_{b1i}^2)} \tag{13}$$

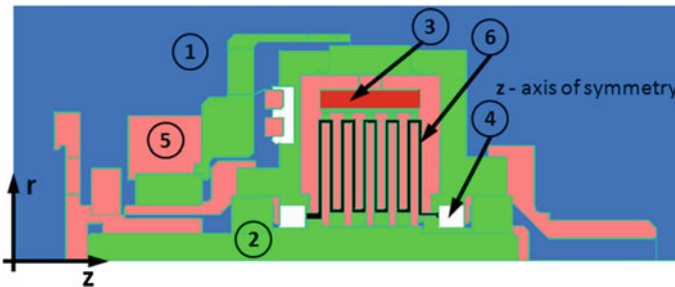


Fig. 8 Axi-symmetric model of the clutch (colors represent types of materials and numbers in the circles corresponding with number in Table 1)

Table 1 The basic thermal parameters of structural materials used in the construction of the clutch MR

	Area	Expansion coefficient 1/K [5]	Thermal conductivity W/m K	Specific heat J/kg K	Mass density kg/m ³
1	Air [6]	3.43e-3	0.0257	1,005	1.205
2	stainless steel	1.44e-5	16.26	502.1	8027.2
3	copper	1.66e-5	386	380	8,954
4	plastic	1.10e-4	0.25	1,260	1,014
5	carbon steel	1.34e-5	54	465	7,833
6	MR fluid	6.00e-4	0.8	680	3,640 [7]

where:

- P_{fri1} —power lost to friction in the bearings for the active part of the clutch
- r_{b1a} —bearing outer radius of the active clutch ($r_{b1a} = 17.5$ mm)
- r_{b1i} —inner radius of the active clutch bearings ($r_{b1i} = 7.5$ mm)
- b_{b1} —the width of the active clutch bearings ($b_{b1} = 11$ mm)

Thermal power associated with friction in the bearings of reactive systems calculate the relation:

$$\dot{q}_{fri2} = \frac{P_{fri2}}{\pi \cdot b_{b2} \cdot (r_{b2a}^2 - r_{b2i}^2)} \tag{14}$$

where:

- P_{fri2} —power lost to friction in the bearings for the passive coupling
- r_{b2a} —bearing outer radius of the active clutch ($r_{b2a} = 23.5$ mm)
- r_{b2i} —inner radius of the active clutch bearings ($r_{b2i} = 15$ mm)
- b_{b2} —the width of the active clutch bearings ($b_{b2} = 18$ mm)

Separate heat output volume of the coil is calculated as the heat flux density in the coil volume of the formula [13]:

$$\dot{q}_{el} = \frac{P_{el}}{\pi \cdot b_{cs} \cdot (r_{cz}^2 - r_{cw}^2)} \tag{15}$$

where:

- P_{el} —electrical power supplied to the clutch coil
- r_{cz} —outer radius of the clutch coil ($r_{cz} = 46$ mm)
- r_{cw} —inner radius of the clutch coil ($r_{cw} = 41$ mm)
- b_{cs} —clutch coil width ($b_{cs} = 27$ mm)

Table 2 Parameter areas where there are power losses

	Area	Volume [m ³]	Heat power [W]		Volumetric heat \dot{q} [W/m ³]
			s = 0	s = 1	
1	Coil	3.69e-5	s = 0	16.16	4.38e+5
			s = 1	16.16	4.38e+5
2	MR fluid	4.58e-5	s = 0	0	0
			s = 1	157.0	3.43e+6
3	Bearing of the driving part	8.64e-6	s = 0	0	0
			s = 1	1.52	1.76e+5
4	Bearing of the driven parts	1.85e-5	s = 0	0.47	2.54e+4
			s = 1	0	0

The heat output separated in the volume of the liquid MR is calculated as:

$$\dot{q}_{slip} = \frac{P_{slip}}{V_{MR}} \tag{16}$$

where:

- P_{slip} —the power dissipated in friction in the volume of magnetorheological fluid
- V_{MR} —volume of magnetorheological fluid in the clutch ($V_{MR} = 4.58e-5 \text{ m}^3$)—the size determined from the CAD model

Table 2 summarizes the basic information about the geometry and thermal power assigned to areas where there is loss of power.

- A fragment of a spatial model clutch limited to the identified sources of volumetric heat with the maximum heat values assigned to them are shown in Fig. 9.
- **Axi-symmetric thermal model of the clutch**

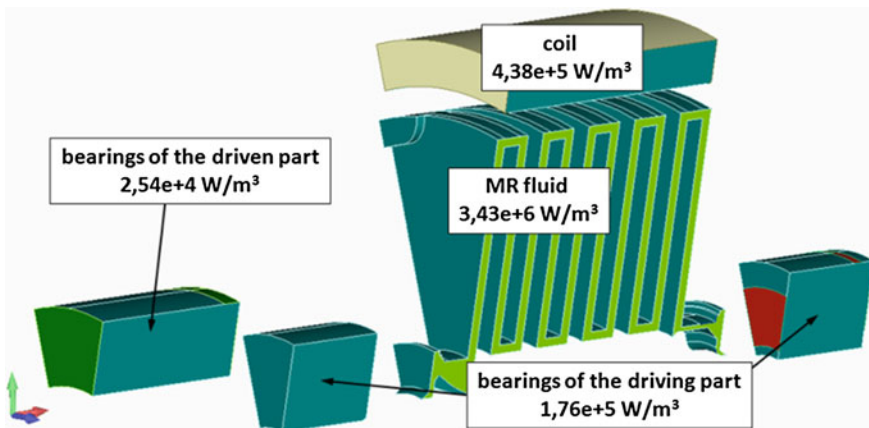


Fig. 9 A sources of thermal energy in the coupling model

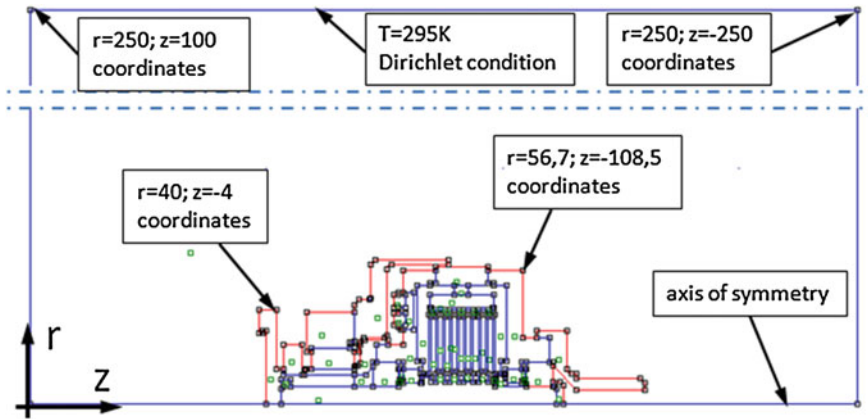


Fig. 10 Boundary conditions for the calculation model

On the basis of the calculation model was developed axisymmetric model clutch in the FEMM 4.2. Model takes into account of heat conduction between the coupling and convection to the environment.

In Fig. 10 shows a drawing of marking the boundary conditions adopted for the calculation model.

2 Simulations Results

The simulation was performed for the various operating states of the clutch, which determine the occurrence in the clutch at the different location and the heat source. The results are presented below in Figs. 11–14 in the form of colored maps and charts of temperature distribution of the temperature distribution along the four selected sections. Locating segments along which shows the temperature distribution shown in Fig. 11. For example, section describes the points A and B indicated by the solid line in green. The same type of line used in graphs 12–14.

- The temperature in clutch volume for long-term supply with a nominal value of coil current— $s = 0$, $n1 = 0$, $n2 = 0$, the heating coil (heat source defined in Table 1).
- The temperature in clutch volume for long-term operation of clutch slip $s = 0$, $n1 = 186$ rpm, $n2 = 186$ rpm (heat source defined in Table 1).
- The temperature in clutch volume for long-term operation of clutch slip $s = 1$, $n1 = 186$ rpm, $n2 = 0$ rpm (heat source defined in Table 1).

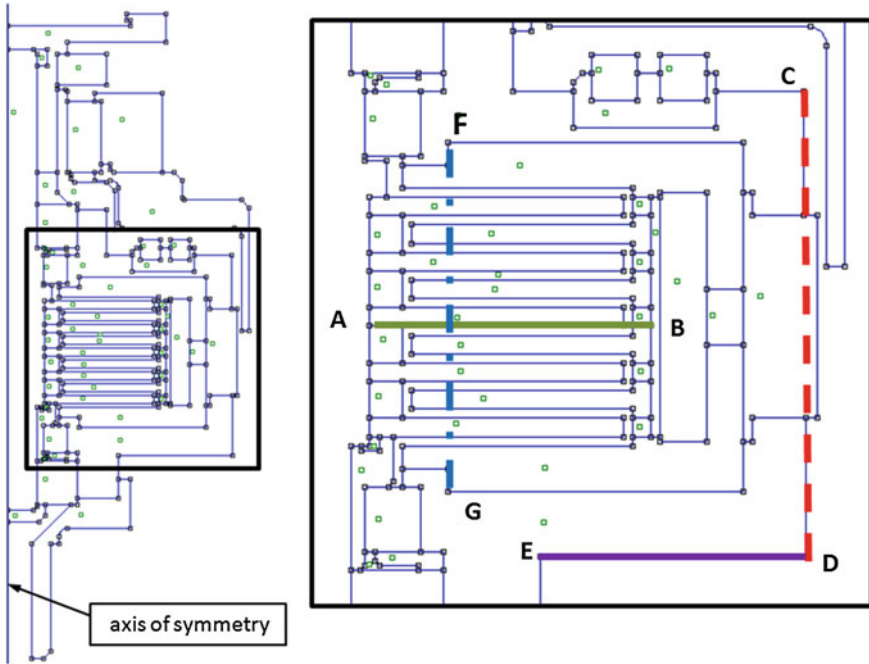


Fig. 11 Location of sections along which the temperature distribution is shown in the coupling

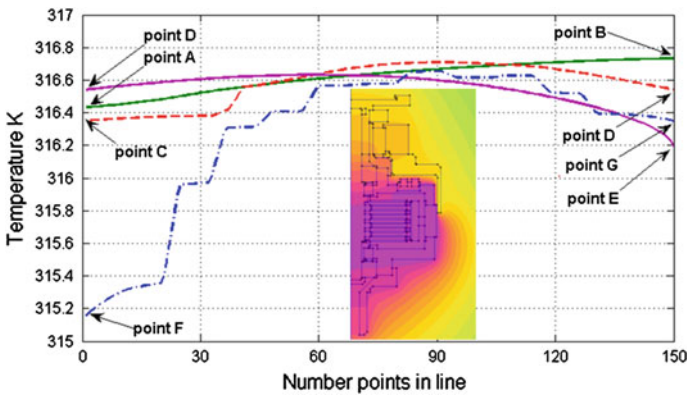


Fig. 12 Temperature distribution along the segments AB, CD, DE and FG

Figure 15 shows the results of computer simulations carried out for the parameters: $s = 1,500 \geq n1 \geq 0$ rpm, $n2 = 0$ rpm, the coupling torque of $7.5 \text{ Nm} \geq T \geq 0 \text{ Nm}$.

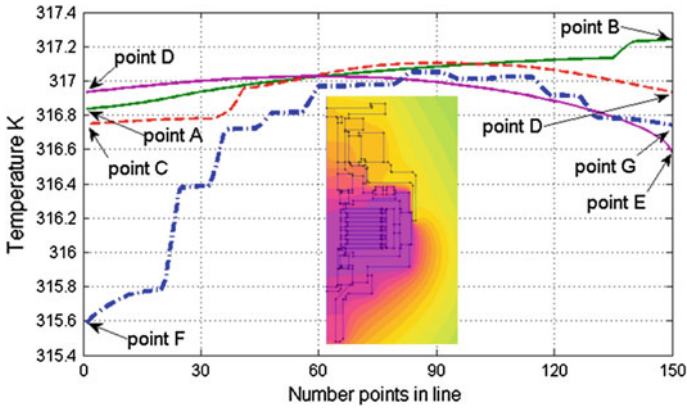


Fig. 13 Temperature distribution along the segments AB, CD, DE and FG

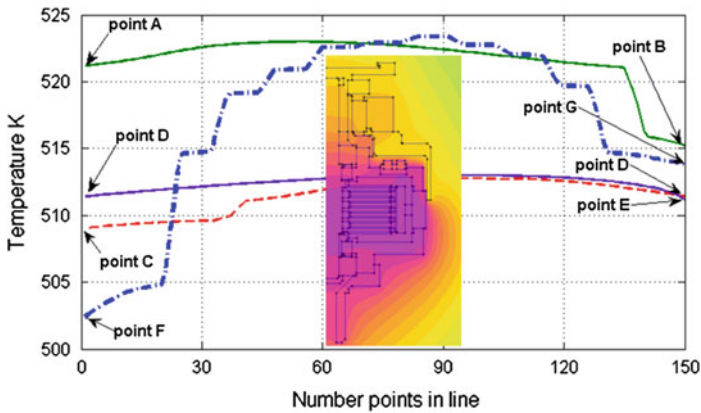
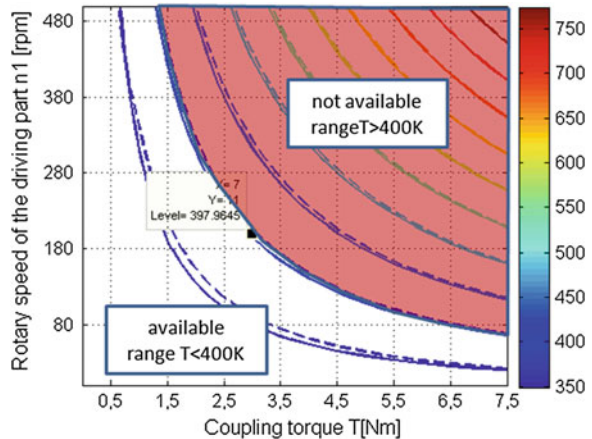


Fig. 14 Temperature distribution along the segments AB, CD, DE and FG

Fig. 15 Available and not available operation range for clutch



In accordance with data published by the manufacturer of the liquid [7] data, the maximum temperature of the fluid is 130 °C (403 K). It was assumed that the temperature in the steady state of the internal volume of the fluid coupling can not exceed 400 K. Figure 15 contains isolines of temperature distribution for the structure of the coupling coil and the permanent magnet (isolines dashed line) and the coupling coil without permanent magnet (isolines drawn with a continuous line).

3 Summary

The study calculated and obtained on the basis of their results allow for formulated the following conclusions:

Long-term heat influence zone MR fluid as a result of current flow through the coil can lead to an increase in temperature of the fluid above the temperature of the liquid limit (provided by the manufacturer around 403 K). It can therefore be considered as the state of operating parameters for safe.

Long term operation of clutch slip $s = 0$ and the maximum power supplied to the clutch makes clutch temperature MR fluid are only slightly increased relative to the thermal effects resulting from the current flow through the coil. It can therefore be considered as the state of operating parameters for safe.

Long term operation of clutch slip $s = 1$ and the maximum, brought to clutch strength, can lead to an increase in temperature that exceeds not only the loss of temperature of liquids, but also to the ignition temperature (Fig. 14). The temperature of the MR fluid zone reaches about 522 K, and the ignition temperature of liquid provided by the manufacturer is approximately 423 K. It can therefore be considered as the status of the clutch to be dangerous.

Developed a thermal model can be the basis for further analysis of the state operating parameters, involving the determination of the limits between the transmitted torque and slip ($0 < s < 1$) so that it can be long-term work with the data parameters.

The simulation results presented in Fig. 15 allows the tolerable range long life clutch can slip $s = 1$.

The use of permanent magnet excitation in the system of the magnetic field makes the thermal power generated in the clutch volume is smaller. This means that the coupling of hybrid excitation magnetic field is achieved higher, the permissible operating parameters.

Perform calculations for transient heat will help to determine the timing between the clutch thermal loading conditions and acceptable working time.

References

1. Benetti M, Dragoni E (2006) Nonlinear magnetic analysis of multi-plate magnetorheological brakes and clutches. In: Proceedings of the COMSOL users conference, Milano
2. Jędrzycka C (2007) FE analysis of electromagnetic field coupled with fluid dynamics in a MR clutch. *COMPEL* 26(4):1028–1036
3. Yuliang S, Shaopu Y, Cunzhi P (2005) Experimental research of magneto-rheological fluid clutch. In: IEEE international conference on vehicular electronics and safety, pp 104–107
4. Huang J, Chen X, Zhong L (2013) Analysis and testing of MR shear transmission driven by SMA spring. *Adv Mater Sci Eng* 2013:6. Article ID 307207. <http://www.hindawi.com/journals/amse/aip/307207/>
5. Internet page. http://www.engineeringtoolbox.com/linear-expansion-coefficients-d_95.html
6. Internet page. http://www.engineeringtoolbox.com/air-properties-d_156.html
7. Bulletins of Lord Corporation. www.lord.com
8. Scientific work sponsored from means of science in years 2009–2011 as research grant NN510 355337
9. Kielan P, Kowol P, Pilch Z (2011) Conception of the electronic controlled magneto-rheological clutch. *Elect Rev* 87(3):93–95
10. Pilch Z, Kowol P, Kielan P (2011) Wielotarczowe sprzęgło magneto-reologiczne o płynnie regulowanej wartości przenoszonego momentu. *KOMEL'2011, Ryto, Zeszyty Problemowe Nr 90 2/2011 ISSN 0239-3646* (in Polish)
11. Skoć A, Spalek J, Markusik S (2008) *Podstawy konstrukcji maszyn. tom 2, trybologia, elementy podatne, wały i osie, łożyska, sprzęgła i hamulce, Part 2.* WNT. ISBN 978-83-204-3405-7 (in Polish)
12. Internet page. http://www.engineeringtoolbox.com/convective-heat-transfer-d_430.html,
13. Hou YF, Tian ZZ, Wang NN (2010) The steady-state and transient temperature field of a magnetorheological fluid transmission device. In: International conference on computer, mechatronics, control and electronic engineering (CMCE), pp 149–153

An Analytical Model of an Electrical Machine with Internal Permanent Magnets

Tomasz Drabek, Andrzej Matras and Jerzy Skwarczyński

Abstract This paper presents an analytical model of the electrical machine with permanent magnets submerged in ferromagnetic of rotor. This model has been prepared as a circuit model of electrical machine. The model takes into account a strong, local saturation of the magnetic circuit of the rotor. In the bibliography lacks a comprehensive development, enabling a transparent transition from the geometrical dimensions of the machine to a model useful to simulate its dynamic states. This mathematical formalism can be created only as a circuit model. Created a model not to be competitive against the finite element method. It allow to understand the interrelationship between design parameters and their effect on the properties and parameters of the machine. The verification of the model related to electromotive force induced in the various circuits of the armature. Verification of the parameters of the armature is planned in the future.

1 Current Knowledge and Destination of the Model

The literature on brushless permanent magnet machines is very extensive. A vast majority of studies are based on FEM calculations due to the nonlinearity of the medium. A number of valuable works on the theory and design of machines with permanent magnets can be found in the literature, e.g. [1, 2]. Some of them also

T. Drabek (✉) · A. Matras · J. Skwarczyński
Department of Power Electronics and Energy Control Systems, Faculty of Electrical Engineering, Automatics, Computer Science and Biomedical Engineering, AGH University of Science and Technology, Krakow, Poland
e-mail: drabek@agh.edu.pl

A. Matras
e-mail: matras@agh.edu.pl

J. Skwarczyński
e-mail: jskw@agh.edu.pl

cover the design optimization problems, taking into account the properties of the machine in transient states. The results are subjected to partial verification, such as [3]. However, the applied calculation methods are generally formulated as fragmented (in that also field) models with a number of simplifying assumptions. As a result, it is often difficult to assess the extent to which the particular, frequently very important, effects and interactions and dependences have been taken into account. There is no system development, allowing for a transparent transition from the geometrical parameters to the model simulating dynamic states of the drive. Such a mathematical formalism can be created only for a circuit model.

The applicability of circuit models of electrical machinery seems to be obvious. They give a general picture of the relationship between the specific design and properties of the machine and reduce the computation time, all of which in the case of field methods depends on the applied structure. However, the applied circuit models often did not provide the required accuracy of the results.

In circuit structure models of electrical machines, e.g. in brushless permanent magnet machines, the fluxes coupled with circuitry are determined on the basis of a radial component of induction in the air gap between the rotor and the stator, also called “main gap”. In machines with additional structural gaps within the rotor core the presence of these gaps is known to have a significant influence on the field distribution in the “main gap” between the rotor and the stator. This is true when the interior interstices are completely or partly filled with magnets, and also when they only form a “flux barrier”.

The field in the “main gap” cannot be accurately determined with analytical techniques. A similar method of determining the gap with analytical methods is proposed in this paper. The accuracy of this approach should not be controlled locally, but at the level of flux passing through the individual teeth of the armature. In the authors’ opinion the degree of discretization of the machine’s cross section is sufficient to provide the peripheral description. This model is an attempt at generalization of the semi-analytical approach presented in [4].

2 Basic Assumptions and Model Structure

Operation of machines with internal magnets in the rotor core is possible thanks to the non-linear intensifying magnetization characteristics of steel. For this reason, attempts to create a mathematical model of such machines based on a linear model of the magnetic circuit are inherently wrong. However, one can extract only those fragments of the machine, whose nonlinearity largely determines operation of the machine, and try to reduce the need to account for the saturation only to those vital parts. These are ferromagnetic bridges closing spaces filled with magnets and they are necessary for structural reasons.

Figure 1 shows a cross section of one pair of poles in a model representing an internal magnet in which the magnetic power in the iron of the rotor are not used

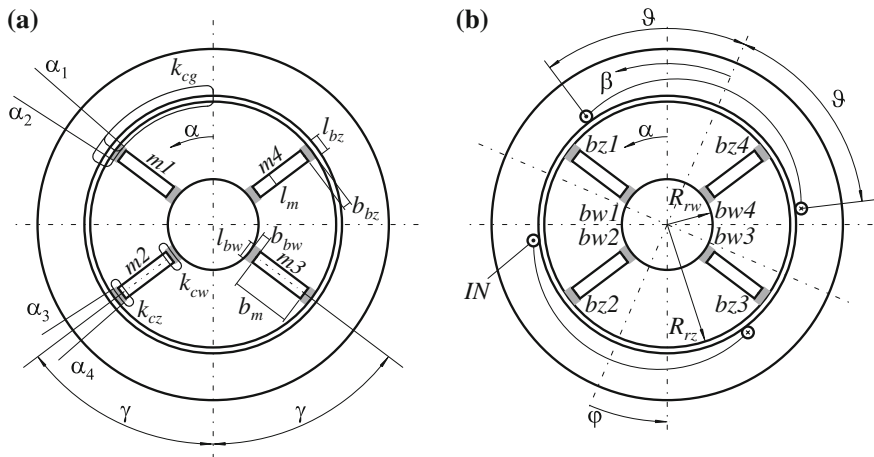


Fig. 1 The cross-section of one pair of poles of assumed machine model: **a** without armature, **b** with armature and ferromagnetic bridges

until the desired field distribution in the gap is obtained.¹ The rotor model has four radial gaps $m1$ – $m4$, symmetrically arranged in pairs, and filled with magnets. The angle between the radial axes of two adjacent gaps is $\pi/2 < 2\gamma < \pi$, another gap between the plates is $(\pi - 2\gamma)$, etc.—Fig. 1a. The gaps are closed both from the main gap between the stator and the rotor, and from the shaft with narrow ferromagnetic bridges—the shaded rectangles in Fig. 1b, denoted as bz_1 – bz_4 (“external” bridges) and bw_1 – bw_4 (“internal” bridges). The surfaces of cross section of these fragments are generally much smaller than the remaining cross-sectional areas. The small dimensions of bridges cause that they are easily saturated.

The external radius of rotor R_{rz} is half of the rotor’s actual diameter; the radius of the internal bore dimension R_{rw} results from the size of magnets and is not determined by the radius of the shaft.

The stator is equipped with a typical symmetrical windings distributed on the perimeter, the number of pole pairs is equal to the number of pole pairs of the rotor. The model was based on the following assumptions:

- magnetic permeability of cores, except for ferromagnetic bridges closing the internal spaces (dark rectangles $l_{bz} \times b_{bz}$ and $l_{bw} \times b_{bw}$ in Fig. 1), is infinitely great,
- four internal gaps of the rotor are filled with air or permanent magnets,
- stator windings and magnetic circuit are symmetrical,
- the outer surface of the rotor is a smooth cylinder with radius R_{rz} ,
- the air gap between the stator and the rotor (“main” air gap) satisfies the condition $\delta(\alpha) \ll R_{sw}$, where R_{sw} is the inner radius of the stator,

¹ Without further assumptions this model cannot be used for mapping systems where magnets in each of the four internal spaces of the rotor need to be separated into at least two parts, or for modifying their peripheral size (thickness).

- paths of flow integration k_{cz}, k_{cw} include a trace the border inner surface of cracks and bridges—Fig. 1a,
- path integral k_{cg} :
 - exceeds the “main” air gap along the radius with coordinates $\alpha = 0$ and $0 < \alpha < 2\pi$,
 - exceeds the “external” magnetic bridges in accordance with the predicted course of magnetic pole lines,
 - extend in the closure of the stator and rotor core, as in Fig. 1a.

By assuming very high magnetic permeability of yokes in practice one can omit the magnetic tension in these yokes making the field in the gap, magnets and bridges independent of the course and length of the force lines in the core. Magnetic tensions in the magnets, bridges and gaps are calculated along the projected shape of force lines in cylindrical coordinates.

3 Determining Magnetic Field in Air Gaps

Adopted rules for the description of the magnetic circuit model with internal rotor gaps include both gaps filled with magnets and cases where the gaps are filled with air and only winding of the stator generates the field.² Magnetic field passing through the main gap to the rotor, is closed by the bridges and inner rotor gaps between the bridges. The flux distribution into these three parallel roads (for each gap) is governed by the Ampere’s circuital law and Gauss’s law for magnetism. Writing the Ampere’s law for the path of integration k_{cz} , closing through the inner gap l_m and bridge b_z between the gap and the “main” gap δ , the curvilinear integral can be separated into three components of magnetic tension: in internal gap in unsaturated parts of the core and in the “external” bridge:

$$\int_{l_m} \overline{H}_{\delta w} \overline{dl} + \int_{l_{Fe}} \overline{H}_{Fe} \overline{dl} + \int_{l_b} \overline{H}_b \overline{dl} = 0 \quad (1)$$

If we ignore the magnetic tension of unsaturated parts of the core in (1), as being much lower than other components, the absolute magnetic tension value of the gap in the rotor $U_{\delta w}$ and bridge U_{b_z} must be equal. A similar conclusion applies to the “internal” bridges:

$$|U_{\delta w}| = |U_{b_z}| = |U_{b_w}| \quad (2)$$

² Magnets determine an operating point of the bridges on the saturated part of the magnetization characteristics, hindering the examination of the impact of stator windings on the value and orientation of field strength in bridges, therefore the field produced by the stator only should be analyzed separately.

The magnetic tension in an “external” bridge can be expressed as a product of replacement field strength in bridge H_{bz} and the representative length of bridge l_{bz} :

$$\int_{l_b} \overline{H}_b \overline{dl} = H_{bz} \cdot l_{bz} \tag{3}$$

Accounting for (2), the left side of (1) can be written in the following form for gaps of width l_m , which are small in comparison to the spread b_m (Fig. 1b):

$$-H_{\delta w} l_m + H_{bz} l_{bz} = 0 \tag{4}$$

where:

$H_{\delta w}$ the average field strength in the gap along segment l_m of paths of integration k_{cz} and k_{cw} .

For a path of integration k_{cw} , closing through the inner gap l_m and “internal” bridge, analogous relationships are obtained:

$$H_{\delta w} l_m = H_{bw} l_{bw} \tag{5}$$

If the internal gaps of rotor contain permanent magnets, the field strength in the Eqs. (4) and (5) becomes field strength in the magnet, and hence:

$$H_{bz} l_{bz} = H_m l_m \tag{6}$$

and:

$$H_{bw} l_{bw} = H_m l_m \tag{7}$$

where:

H_m the average field strength in the magnet along the segment l_m of the integration path k_{cz} and k_{cw} .

Vectors H_{bz} and H_m are positive if their direction is in line with the direction of the angular coordinate of a cylindrical coordinate system. In fact, the direction of vectors H_{bz} and H_m should be equal³ and opposite to the orientation of the polarization vector of the magnet. To provide the symmetry and bipolarity of field, the magnet polarization vectors $m3$ and $m4$ should be equal to the vector of magnets polarization $m1$ and $m2$, though oppositely oriented.

³ In a magnet, the positive values of magnetic flux density correspond to the negative field strength as far as demagnetization characteristic is concerned.

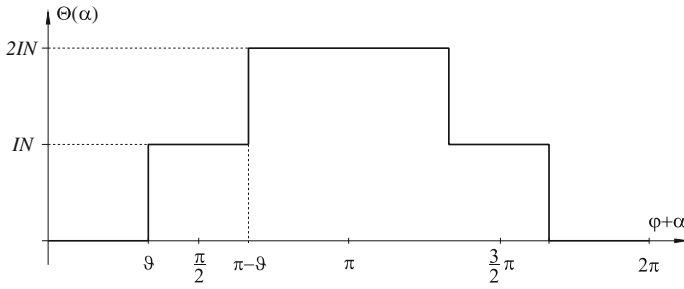


Fig. 2 Ampere-turns function of armature windings

The existence of a tangential component of field strength in outer bridges (between the inner gaps and the “main” gap) is important when calculating the field distribution in the “main” gap. Therefore, using the Ampere’s law for a path of integration k_{cg} passing the gap between the rotor and stator along the radius $\alpha = 0$ and $0 < \alpha < 2\pi$, we get the following equation:

$$H_g(0) \delta_z(0) - H_g(\alpha) \delta_z(\alpha) - U_{bz}(\alpha) = \Theta(\alpha) \tag{8}$$

where:

- $H_g(\alpha)$ field strength in the main gap;
- $\delta_z(\alpha)$ width of the replacement gap (for main gap only);
- $\Theta(\alpha)$ ampere-turns covered by path of integration k_{cg} (Fig. 2);
- $U_{bz}(\alpha)$ magnetic tension resulting from the transition of integration path k_{cg} through “external” bridges—the sign “minus” in the Eq. (8) refers to the positive sign of vector H_{bz} .

Magnetic tension of individual bridges, regardless the position of the rotor with respect to the stator, must meet the conditions resulting from the assumed symmetry of the windings and magnetic circuits and infinite magnetic permeability of cores beyond the bridges: $U_{bz1} = -U_{bz3}$, $U_{bz2} = -U_{bz4}$.⁴ This ensures compliance with the condition of symmetry of the field $B(\alpha) = -B(\alpha + \pi)$. An example of the functional sequence $U_{bz}(\alpha)$ is shown in Fig. 3, for $U_{bz1} > U_{bz2} > 0$.

⁴ Magnetic connection bridge $U_b = \int_{l_b} \overline{H}_b \overline{dl}$. The positive direction of the vectors is consistent with the orientation of cylindrical coordinates. In the bridges bz_1, bz_2 vector intensity $+\overline{H}_b$ is oriented oppositely to vector $+\overline{dl}$, whereas tensions in bridges bz_3, bz_4 are equal to tensions in bz_1 and bz_2 (distant by an angle of π) respectively and oppositely directed, due to the condition of symmetry. Negative magnetic tension of bridges bz_1 and bz_2 for positive H_b was included in the Eq. (6).

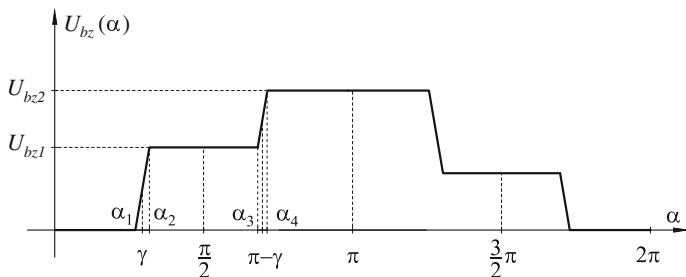


Fig. 3 Magnetic tensions of “external” magnetic rotor bridges

On the basis of (8) the gap field distribution can be represented by the formula:

$$\begin{aligned}
 B_g(\alpha) &= \frac{\mu_o}{\delta_z(\alpha)} \{ H_g(0)\delta_z(0) - U_{bz}(\alpha)\Theta(\alpha) \} \\
 &= A(\alpha) \{ H_g(0)\delta_z(0) - U_{bz}(\alpha)\Theta(\alpha) \}
 \end{aligned}
 \tag{9}$$

The unitary permeance of the air gap (FJPM) should consider opening slots on the side of stator and magnetic bridges, which in a state of deep saturation will act as zones between the pole pieces separated by stumps of an additional pole. The replacement gap will be similar to the classic commutator machine. The function FJPM can be determined as in [5] or [6]. According to [6]:

$$A(\alpha) = \mu_0 \cdot H_1(\alpha)
 \tag{10}$$

where:

$H_1(\alpha)$ the value of a radial component of the magnetic field strength vector on the circle located in the middle of the air gap, measured with unit magnetic scalar tension between the borders of the air gap, i.e. between unsaturated parts of ferromagnetic stator and rotor

The unknown magnetic tension $H_g(0) \cdot \delta_z(0)$ can be determined from the Gauss’s law for magnetism:

$$R_s l_{Fe} \int_0^{2\pi} B_g(\alpha) d\alpha = 0
 \tag{11}$$

Assuming initially⁵ that the replacement air gap $\delta_z(\alpha)$ is constant and equal to δ_z and performing integration by (11) the following is obtained:

⁵ The adoption of a fixed gap between the rotor and stator is not a prerequisite for the applicability of the proposed description.

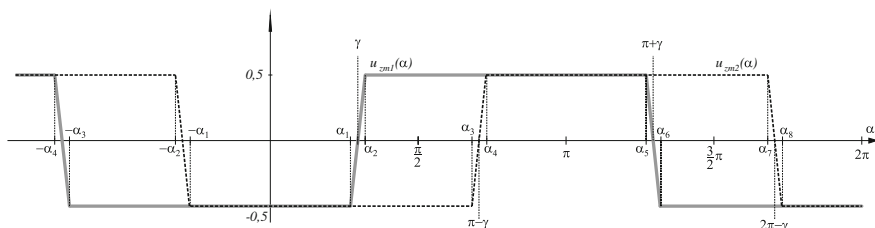


Fig. 4 Components of a distribution function of magnetic tensions in “external” bridges

$$H_g(0)\delta_z(0) = \frac{1}{2\pi} \int_0^{2\pi} \Theta(\alpha) d\alpha + \frac{1}{2\pi} \int_0^{2\pi} U_{bz}(\alpha) d\alpha \quad (12)$$

Magnetic tension means that $H_g(0) \cdot \delta_z(0)$ is a sum of the average function $\Theta(\alpha)$ and $U_{bz}(\alpha)$. The function $U_{bz}(\alpha)$ can be expressed as a sum of two functions:

$$\begin{aligned} U_{bz}(\alpha) &= U_{bz1}(\alpha) + U_{bz2}(\alpha) = U_{bz1} \left(\frac{1}{2} + u_{zm1}(\alpha) \right) + U_{bz2} \left(\frac{1}{2} + u_{zm2}(\alpha) \right) \\ &= \frac{1}{2}(U_{bz1} + U_{bz2}) + U_{bz1} \cdot u_{zm1}(\alpha) + U_{bz2} \cdot u_{zm2}(\alpha) = U_{bsr} + U_{bz2m}(\alpha) \end{aligned} \quad (13)$$

Functions $u_{zm1}(\alpha)$ and $u_{zm2}(\alpha)$ are shown in Fig. 4. The angle γ is the location of the inner radial gap axis (Fig. 1a).

The average value of function $U_{bz}(\alpha)$ is:

$$\frac{1}{2\pi} \int_0^{2\pi} U_{bz}(\alpha) d\alpha = U_{sr} = \frac{1}{2}(U_{bz1} + U_{bz2}) \quad (14)$$

Because of its dependence on rotor position φ , function $\Theta(\alpha, \varphi)$ is most conveniently represented as a Fourier series:

$$\Theta(\alpha) = \Theta_{sr} + \sum_{\rho=1,3,5,\dots}^{\infty} \Theta_{m\rho} \cos(\rho(\alpha + \phi)) = \Theta_{sr} + \Theta_{zm}(\alpha) \quad (15)$$

Harmonic amplitudes $\Theta_{m\rho}$ are calculated for a specific winding (or a windings system) and the current value of the electric current in this winding.

Field distribution in the air gap can now be represented by the formula:

$$B_g(\alpha) = -\frac{\mu_0}{\delta_z} \{ U_{bz2m}(\alpha) + \Theta_{zm}(\alpha) \} \quad (16)$$

The specific locations of the rotor: $\phi = 0, \pi$ and $\phi = \frac{1}{2}\pi, \frac{3}{2}\pi$ magnetic tensions U_{bz1}, U_{bz2} must ensure zeroing of a flux passing through the “main” gap in the angular intervals: (α_1, α_4) for $\phi = 0, \pi$ and $(-\alpha_1, \alpha_1)$ for $\phi = \frac{1}{2}\pi, \frac{3}{2}\pi$. These fluxes are:

$$\Phi_{s(\alpha_1, \alpha_4)} = l_{Fe}R_{sw} \int_{\alpha_1}^{\alpha_4} B_g(\alpha) d\alpha = -l_{Fe}R_{sw} \frac{\mu_o}{\delta_z} \left\{ \int_{\alpha_1}^{\alpha_4} U_{bz1}(\alpha) d\alpha + \int_{\alpha_1}^{\alpha_4} \Theta_{zm}(\alpha) d\alpha \right\} \quad (17)$$

$$\Phi_{s(-\alpha_1, \alpha_1)} = l_{Fe}R_{sw} \int_{-\alpha_1}^{\alpha_1} B_g(\alpha) d\alpha = -l_{Fe}R_{sw} \frac{\mu_o}{\delta_z} \left\{ \int_{-\alpha_1}^{\alpha_1} U_{bz1}(\alpha) d\alpha + \int_{-\alpha_1}^{\alpha_1} \Theta_{zm}(\alpha) d\alpha \right\} \quad (18)$$

The calculation of definite integrals leads to the results:
for $\phi = 0, \pi$:

$$\Phi_{s(\alpha_1, \alpha_4)} = -l_{Fe}R_{sw} \frac{\mu_o}{\delta_z} \left\{ U_{bz1} \frac{1}{2}(\alpha_4 - \alpha_2) - U_{bz2} \frac{1}{2}(\alpha_3 - \alpha_1) \right\} = 0 \quad (19)$$

for $\phi = \frac{1}{2}\pi, \frac{3}{2}\pi$:

$$\Phi_{s(-\alpha_1, \alpha_1)} = l_{Fe}R_{sw} \frac{\mu_o}{\delta_z} (U_{bz1}\alpha_1 + U_{bz2}\alpha_1) = 0 \quad (20)$$

In both cases, the definite integral from a function of Ampere-turns equals to zero. In the first case the following must occur: $U_{bz1} = U_{bz2}$ (because $(\alpha_4 - \alpha_2) \approx (\alpha_3 - \alpha_1)$), and in the second one: $U_{bz1} = -U_{bz2}$. The condition $U_{bz1} = U_{bz2}$ also applies to the induced magnet fields, since the axis of the field in this case should be such as induced by the stator in position $\phi = 0, \pi$.

For any position of the rotor the parameters U_{bz1} and U_{bz2} can be determined using the Gauss’s law for magnetism twice:

- covering the surface of the stator inner space contained between the angles $(-\alpha_1, \alpha_1)$, the inner surface of the rotor with the same interval and the inner layers of the rotor and bridges, with adjacent surfaces,
- the surface of the stator comprising an inner space contained between the angles α_1, α_4 , the inner surface of the rotor with the same interval and the inner layers of the rotor and bridges, with adjacent surfaces.

For magnetic fluxes passing through the surface of limiting these spaces the following equation should be satisfied:

$$\Phi_s + \Phi_{bz} + \Phi_{bw} + \Phi_m = 0 \quad (21)$$

where:

- Φ_s flux passes through the corresponding piece of inner surface of the stator;
- Φ_{bz} flux passes through “external” ferromagnetic bridges;
- Φ_{bw} flux passes through “internal” ferromagnetic bridges;
- Φ_m flux passes through inner surfaces of rotor gaps S_m .

Calculating magnetic fluxes, the orientation of normal vector to the surface “outside” the zone enclosed in the area was assumed.

The balance of fluxes passing through a surface covering the space between angles can be represented by the equation:

$$\Phi_{s(-\alpha_1, \alpha_1)} + \Phi_{(bz1, bz4)} + \Phi_{(bw1, bw4)} + \Phi_{(m1, m4)} = 0 \quad (22)$$

The magnetic flux $\Phi_{s(-\alpha_1, \alpha_1)}$, passing through the inner surface of the stator, bounded angles $-\alpha_1, \alpha_1$, can be calculated from the equation:

$$\begin{aligned} \Phi_{s(-\alpha_1, \alpha_1)} &= l_{Fe} R_{sw} \int_{-\alpha_1}^{\alpha_1} B_g(\alpha) d\alpha = -l_{Fe} R_{sw} \frac{\mu_o}{\delta_z} \left\{ \int_{-\alpha_1}^{\alpha_1} U_{zm}(\alpha) d\alpha + \int_{-\alpha_1}^{\alpha_1} \Theta_{zm}(\alpha) d\alpha \right\} \\ &= -l_{Fe} R_{sw} \frac{\mu_o}{\delta_z} \left\{ U_{b1} \int_{-\alpha_1}^{\alpha_1} u_{1zm}(\alpha) d\alpha + U_{b2} \int_{-\alpha_1}^{\alpha_1} u_{2zm}(\alpha) d\alpha + \int_{-\alpha_1}^{\alpha_1} \Theta_{zm}(\alpha) d\alpha \right\} \\ &= -l_{Fe} R_{sw} \frac{\mu_o}{\delta_z} \left\{ -(U_{b1} + U_{b2})\alpha_1 + 2 \sum_{\rho=1,3,5\dots}^{\infty} \Theta_{m\rho} \frac{\sin\rho\alpha_1}{\rho} \cos\rho\phi \right\} \end{aligned} \quad (23)$$

Flux $\Phi_{(bz1, bz4)}$ through the “external” ferromagnetic bridges bz_1, bz_4 , located between the angles α_1, α_2 and $(-\alpha_2), (-\alpha_1)$ is:

$$\Phi_{(bz1, bz4)} \approx l_{Fe} b_{bz} (B_{bz1} - B_{bz4}) = l_{Fe} b_{bz} (B_{bz1} + B_{bz2}) \quad (24)$$

Flux $\Phi_{(bw1, bw4)}$ through the “internal” ferromagnetic bridges bw_1, bw_4 , located between the angles α_1, α_2 and $(-\alpha_2), (-\alpha_1)$ is:

$$\Phi_{(bw1, bw4)} \approx l_{Fe} b_{bw} (B_{bw1} - B_{bw4}) = l_{Fe} b_{bw} (B_{bw1} + B_{bw2}) \quad (25)$$

It can be judged from equal magnetic tensions in bridges (“internal” and “external”) that identical average value of the field strength can be assumed in these bridges; as a consequence the same substitute length and flux density: $B_{bz1} = B_{bw1}$, $B_{bz2} = B_{bw2}$ are obtained:

$$\Phi_{(bz1, bz4)} + \Phi_{(bw1, bw4)} \approx l_{Fe} (b_{bz} + b_{bw}) (B_{bz1} + B_{bz2}) = l_{Fe} b_{bc} (B_{bz1} + B_{bz2}) \quad (26)$$

The symbol b_{bc} denotes the total width of bridges: $b_{bc} = b_{bz} + b_{bw}$.

Flux $\Phi_{(m1, m4)}$ through the inner surfaces S_m of the rotor gaps $m1$, $m4$ between the bridges situated between the angles α_1 , α_2 and $(-\alpha_2)$, $(-\alpha_1)$:

$$\begin{aligned} \Phi_{(m1, m4)} &= \int_{S_m} B_{\delta w1} ds_m + \int_{S_m} B_{\delta w4} ds_m l_{Fe} b_m (B_{\delta w1} - B_{\delta w4}) \\ &= l_{Fe} b_m \frac{\mu_o}{l_m} (H_{bz1} l_{bz1} + H_{bz2} l_{bz2}) \end{aligned} \quad (27)$$

When the internal gaps of the rotor are filled with permanent magnets, the magnetic flux will be further labeled as “*”. The flux $\Phi_{(m1, m4)}^*$ is:

$$\Phi_{(m1, m4)}^* = l_{Fe} b_m (B_{\delta w1} - B_{\delta w4}) = l_{Fe} b_m (B_{\delta w1} + B_{\delta w2}) = l_{Fe} b_m (B_{m1} + B_{m2}) \quad (28)$$

In the neodymium permanent magnet, magnetic flux density B_m is related to the magnetic field strength H_m which in practice has a linear demagnetization characteristics:

$$B_m = B_r + \mu_m H_m \quad (29)$$

where: $\mu_m = B_r / (-H_c) = \mu_o \cdot \mu_{mr} > 0$ and $H_c < H_m \leq 0$ and $H_c < 0$.

By substituting Eq. (29) in (28) the following formula is obtained:

$$\begin{aligned} \Phi_{(m1, m4)} &= l_{Fe} b_m (B_{r1} + B_{r2}) + l_{Fe} b_m \mu_m (H_{m1} + H_{m2}) \\ &= l_{Fe} 2b_m B_r + l_{Fe} b_m \frac{\mu_m}{l_m} (H_{bz1} l_{bz1} + H_{bz2} l_{bz2}) \end{aligned} \quad (30)$$

The comparison of (30) with (27) brings about the formula:

$$\Phi_{(m1, m4)}^* = l_{Fe} 2b_m B_r + \frac{\mu_m}{\mu_o} \Phi_{(m1, m4)} = l_{Fe} b_m (B_{r1} + B_{r2}) + \mu_{mr} \Phi_{(m1, m4)} \quad (31)$$

Equation (30) is the more general form of equation for magnetic flux and it will be used further in this paper.

After introducing the expression for the magnetic fluxes to the Eq. (22) and taking into account that: $H_{bz1} \cdot l_{bz1} = U_{bz1}$, $H_{bz2} \cdot l_{bz2} = U_{bz2}$ and $B_{r1} = B_{r2} = B_r$, then we get:

$$\begin{aligned}
 & -2 \frac{b_m}{b_{bc}} B_r + 2 \frac{\mu_o R_{sw}}{b_{bc} \delta_z} \sum_{\rho=1,3,5,\dots}^{\infty} \Theta_{m\rho} \frac{\sin \rho \alpha_1}{\rho} \cos \rho \phi + -\frac{\mu_o}{b_{bc}} \left\{ \alpha_1 \frac{R_{sw}}{\delta_z} + \mu_{mr} \frac{b_m}{l_m} \right\} H_{bz1} l_{bz1} \\
 & -\frac{\mu_o}{b_{bc}} \left\{ \alpha_1 \frac{R_{sw}}{\delta_z} + \mu_{mr} \frac{b_m}{l_m} \right\} H_{bz2} l_{bz2} = B_{bz1}(H_{bz1}) + B_{bz2}(H_{bz2})
 \end{aligned} \tag{32}$$

If the internal gaps of the rotor do not have magnets, we assume in (32) that: $B_r = 0$ and $\mu_{mr} = 1$.

The balance of magnetic fluxes to the surface covering the space between the angles is expressed by the equation:

$$\Phi_{s(\alpha_1, \alpha_4)} + \Phi_{(bz1, bz2)} + \Phi_{(bw1, bw2)} + \Phi_{(m1, m2)}^* = 0 \tag{33}$$

The magnetic flux $\Phi_{s(\alpha_1, \alpha_4)}$ passing through the inner surface of the stator, limited by angles α_1, α_4 is:

$$\begin{aligned}
 \Phi_{s(\alpha_1, \alpha_4)} &= l_{Fe} R_{sw} \int_{\alpha_1}^{\alpha_4} B_g(\alpha) d\alpha = -l_{Fe} R_{sw} \frac{\mu_o}{\delta_z} \left\{ \int_{\alpha_1}^{\alpha_4} U_{zm}(\alpha) d\alpha + \int_{\alpha_1}^{\alpha_4} \Theta_{zm}(\alpha) d\alpha \right\} \\
 &= -l_{Fe} R_{sw} \frac{\mu_o}{\delta_z} \left\{ U_{b1} \int_{\alpha_1}^{\alpha_4} u_{1zm}(\alpha) d\alpha + U_{b2} \int_{\alpha_1}^{\alpha_4} u_{2zm}(\alpha) d\alpha + \int_{\alpha_1}^{\alpha_4} \Theta_{zm}(\alpha) d\alpha \right\} \\
 &= -l_{Fe} R_{sw} \frac{\mu_o}{\delta_z} \left\{ \begin{aligned} & \frac{1}{2} U_{b1} (\alpha_4 - \alpha_2) - \frac{1}{2} U_{b2} (\alpha_3 - \alpha_1) \\ & -2 \sum_{\rho=1,3,5,\dots}^{\infty} \Theta_{m\rho} \frac{\sin \rho \frac{\pi}{2}}{\rho} \sin \rho \frac{1}{2} (\alpha_4 - \alpha_1) \sin \rho \phi \end{aligned} \right\}
 \end{aligned} \tag{34}$$

The magnetic flux $\Phi_{(bz1, bz2)}$ passing through the “external” ferromagnetic bridges bz_1, bz_2 , situated between angles α_1, α_2 and α_3, α_4 , is:

$$\Phi_{(bz1, bz2)} \approx l_{Fe} b_{bz} (B_{bz2} - B_{bz1}) = l_{Fe} b_{bz} (B_{bz2} - B_{bz1}) \tag{35}$$

The magnetic flux $\Phi_{(bw1, bw2)}$ passing through the “internal” ferromagnetic bridges $bw1, bw2$, situated between the angles α_1, α_2 and α_3, α_4 , is:

$$\Phi_{(bw1, bw2)} \approx l_{Fe} b_{bw} (B_{bw2} - B_{bw1}) = l_{Fe} b_{bw} (B_{bw2} - B_{bw1}) \tag{36}$$

On the basis of above assumptions, the sum of (35) and (36) can be written as:

$$\Phi_{(bz1, bz2)} + \Phi_{(bw1, bw2)} \approx l_{Fe} (b_{bz} + b_{bw}) (B_{bz2} - B_{bz1}) = l_{Fe} b_{bc} (B_{bz2} - B_{bz1}) \tag{37}$$

The magnetic flux $\Phi_{(m1, m2)}^*$ passing through the surface S_m of the rotor’s inner gaps $m1$ and $m2$, is:

$$\begin{aligned} \Phi_{(m1, m2)}^* &= \int_{S_m} \bar{B}_{\delta w1} \bar{d}s_m + \int_{S_m} \bar{B}_{\delta w2} \bar{d}s_m \approx l_{Fe} b_m (B_{\delta w2} - B_{\delta w1}) \\ &= l_{Fe} b_m (B_{m2} - B_{m1}) \\ &= l_{Fe} b_m (B_{r2} - B_{r1}) + \mu_m l_{Fe} b_m (H_{m2} - H_{m1}) = l_{Fe} b_m \frac{\mu_m}{l_m} (H_{bz2} l_{bz2} - H_{bz1} l_{bz1}) \end{aligned} \tag{38}$$

If the magnetic field is produced only by the winding, it must assumed on the right side of (38) that $\mu_m = \mu_o$.

After introducing the expressions for the magnetic fluxes to the Eq. (33), assuming that $H_{bz1} \cdot l_{bz1} = U_{bz1}$ and $H_{bz2} \cdot l_{bz2} = U_{bz2}$ and finally arranging Eq. (33), we get the following form of Eq. (39):

$$\begin{aligned} 2R_{sw} \frac{\mu_o}{b_{bc} \delta_z} \sum_{\rho=1,3,5...}^{\infty} \Theta_{m\rho} \frac{\sin \rho \frac{\pi}{2}}{\rho} \sin \rho \frac{1}{2} (\alpha_4 - \alpha_1) \sin \rho \phi - \frac{\mu_o}{b_{bc}} \left\{ \frac{1}{2} (\alpha_4 - \alpha_2) \frac{R_{sw}}{\delta_z} + \mu_{mr} \frac{b_m}{l_m} \right\} H_{b1} l_{bz1} \\ + \frac{\mu_o}{b_{bc}} \left\{ \frac{1}{2} (\alpha_3 - \alpha_1) \frac{R_{sw}}{\delta_z} + \mu_{mr} \frac{b_m}{l_m} \right\} H_{b2} l_{bz2} = B_{b1} (H_{b1}) - B_{b2} (H_{b2}) \end{aligned} \tag{39}$$

Equations (34) and (39) form a system of equations, defining the point of work of bridges. To solve this system it may be advantageous to add them and subtract. In this way a new system of equations is obtained. After ordering it assumes the following form:

$$\begin{aligned}
& -\frac{b_m}{b_{bc}}B_r + \frac{\mu_o R_{sw}}{b_{bc} 2\delta_z} \cdot \sum_{\rho=1,3,5,\dots}^{\infty} \Theta_{m\rho} \frac{2}{\rho} \left\{ [\sin \rho\alpha_1] \cos \rho\phi + \left[\sin \rho\frac{\pi}{2} \sin \rho\frac{1}{2}(\alpha_4 - \alpha_1) \right] \sin \rho\phi \right\} \\
& - \frac{\mu_o}{b_{bc}} \left\{ \left(\alpha_1 + \frac{1}{2}(\alpha_4 - \alpha_2) \right) \frac{R_{sw}}{2\delta_z} + \mu_{mr} \frac{b_m}{l_m} \right\} H_{bz1} l_{bz1} - \frac{\mu_o R_{sw}}{b_{bc} 2\delta_z} \left(\alpha_1 - \frac{1}{2}(\alpha_3 - \alpha_1) \right) H_{bz2} l_{bz2} \\
& = B_{bz1}(H_{bz1})
\end{aligned} \tag{40}$$

$$\begin{aligned}
& -\frac{b_m}{b_{bc}}B_r + \frac{\mu_o R_{sw}}{b_{bc} \delta_z} \cdot \sum_{\rho=1,3,5,\dots}^{\infty} \Theta_{m\rho} \frac{1}{\rho} \left\{ [\sin \rho\alpha_1] \cos \rho\phi - \left[\sin \rho\frac{\pi}{2} \sin \rho\frac{1}{2}(\alpha_4 - \alpha_1) \right] \sin \rho\phi \right\} \\
& - \frac{\mu_o}{b_{bc}} \left\{ \left(\alpha_1 - \frac{1}{2}(\alpha_4 - \alpha_2) \right) \frac{R_{sw}}{2\delta_z} \right\} H_{bz1} l_{bz1} - \frac{\mu_o}{b_{bc}} \left\{ \left(\alpha_1 + \frac{1}{2}(\alpha_3 - \alpha_1) \right) \frac{R_{sw}}{2\delta_z} + \mu_{mr} \frac{b_m}{l_m} \right\} H_{bz2} l_{bz2} \\
& = B_{bz2}(H_{bz2})
\end{aligned} \tag{41}$$

Since $(\alpha_4 - \alpha_2) \approx (\alpha_3 - \alpha_1)$, the system (40), (41) can be written in a more illustrative manner:

$$-W_m + W_{s1} - c_1 H_{bz1} - c_2 H_{bz2} = B_{bz1}(H_{bz1}) \tag{42}$$

$$-W_m + W_{s2} - c_2 H_{bz1} - c_1 H_{bz2} = B_{bz2}(H_{bz2}) \tag{43}$$

where:

$$W_m = \frac{b_m}{b_{bc}}B_r \tag{44}$$

$$W_{s1} = \frac{\mu_o R_{sw}}{b_{bc} 2\delta_z} \cdot \sum_{\rho=1,3,5,\dots}^{\infty} \Theta_{m\rho} \frac{2}{\rho} \left\{ [\sin \rho\alpha_1] \cos \rho\phi + \left[\sin \rho\frac{\pi}{2} \sin \rho\frac{1}{2}(\alpha_4 - \alpha_1) \right] \sin \rho\phi \right\} \tag{45}$$

$$W_{s2} = \frac{\mu_o R_{sw}}{b_{bc} 2\delta_z} \cdot \sum_{\rho=1,3,5,\dots}^{\infty} \Theta_{m\rho} \frac{2}{\rho} \left\{ [\sin \rho\alpha_1] \cos \rho\phi - \left[\sin \rho\frac{\pi}{2} \sin \rho\frac{1}{2}(\alpha_4 - \alpha_1) \right] \sin \rho\phi \right\} \tag{46}$$

$$c_1 = \frac{\mu_o}{b_{bc}} \left\{ \left(\alpha_1 + \frac{1}{2}(\alpha_4 - \alpha_2) \right) \frac{R_{sw}}{2\delta_z} + \mu_{mr} \frac{b_m}{l_m} \right\} l_{bz1} \tag{47}$$

$$c_2 = \frac{\mu_o R_{sw}}{b_{bc} 2\delta_z} \left(\alpha_1 - \frac{1}{2}(\alpha_3 - \alpha_1) \right) l_{bz2} \tag{48}$$

The system of equations defining the operating point of bridges (Eqs. 40 and 41), refers to a two-pole machine. For a number of pole pairs p_b the indicators summing up the series are $\rho = p_b, 3p_b, 5p_b, 7p_b, \dots$. In contrast, the dimensions and angles referring to the cross-sectional geometry are actual values.

If the magnetic field is excited only by permanent magnets, the $W_{s1} = W_{s2} = 0$; if the required equality $U_{bz1} = U_{bz2}$ is to be met, then $H_{bz1} = H_{bz2} = H_{bz}$ should hold true. H_{bz} value can be obtained from Eq. (40) or (41), optionally (42) or (43):

$$-\frac{b_m}{b_{bc}}B_r - \frac{\mu_o}{b_{bc}}\left\{\alpha_1\frac{R_{sw}}{\delta_z} + \mu_{mr}\frac{b_m}{l_m}\right\}H_{bz}l_{bz} = B_{bz}(H_{bz}) \tag{49}$$

Typically, permanent magnets introduce the operating point of bridges to the nearly-saturated zone. In this range, the magnetization characteristics can be approximated by a straight line:

$$B_{bz} = B_{bo} + \mu_b H_{bz} \tag{50}$$

Then the magnetic tension of the bridge takes the form:

$$H_{bz}l_{bz} = -\frac{l_m}{\mu_o}\frac{B_r + \frac{b_{bc}}{b_m}B_{bo}}{\frac{\alpha_1 R_{sw} l_m}{b_m \delta_z} + \mu_{mr} + \mu_{br}\frac{l_m}{l_b}\frac{b_{bc}}{b_m}} \tag{51}$$

The field strength of the magnet is:

$$H_m = \frac{H_{bz}l_{bz}}{l_m} = -\frac{1}{\mu_o}\frac{B_r + \frac{b_{bc}}{b_m}B_{bo}}{\frac{\alpha_1 R_{sw} l_m}{b_m \delta_z} + \mu_{mr} + \mu_{br}\frac{l_m}{l_b}\frac{b_{bc}}{b_m}} \tag{52}$$

It should be noted, that to obtain a positive sense of vector H_m requires a negative sense of vector B_r and polarization vector, whereas induction B_{bo} is a value at which a straight line approximating the characteristics of rotor's steel magnetization cuts the vertical axis (axis of induction). According to (16) and (13), the field distribution in the air gap can now be represented by the formula:

$$\begin{aligned} B_g(\alpha) &= -\frac{\mu_o}{\delta_z}U_{bz m}(\alpha) \\ &= -\frac{\mu_o}{\delta_z}U_{bz}(u_{zm1}(\alpha) + u_{zm2}(\alpha)) = B_{gmax}(u_{zm1}(\alpha) + u_{zm2}(\alpha)) \end{aligned} \tag{53}$$

The maximum value of induction in the air gap B_{gmax} can be found on the rotor axis ($\alpha = 0$) and equals to:

$$\begin{aligned}
 B_{g\max} &= B_g(0) = -\frac{\mu_o}{\delta_z} U_{bzm}(0) = -\frac{\mu_o}{\delta_z} (-H_m l_m) \\
 &= -\frac{l_m}{\delta_z} \frac{B_r + \frac{b_{bc}}{b_m} B_{bo}}{\frac{\alpha_1 R_{sw} l_m}{b_m \delta_z} + \mu_{mr} + \mu_{br} \frac{l_m b_{bc}}{l_b b_m}}
 \end{aligned} \tag{54}$$

Without bridges ($b_{bc} = 0$) it will be:

$$B_g(0) = -\frac{l_m}{\delta_z} \frac{B_r}{\frac{\alpha_1 R_{sw} l_m}{b_m \delta_z} + \mu_{mr}} \tag{55}$$

It would be advantageous to replace the waveform of function $u_{zm}(\alpha)$ assumed in Figs. 3 and 4 as a straight line, with a cosine section. This provides, among others, the continuity of the derivative. Assuming the same conditions in all “external” bridges when only permanent magnets excite to field, the following assumptions were made $(\alpha_2 - \alpha_1) = (\alpha_4 - \alpha_3) = 2\kappa$. Functions $u_{zm1}(\alpha)$, $u_{zm2}(\alpha)$, presented as a Fourier series, now have the form:

$$u_{zm1}(\alpha) = \sum_{\rho=1,3,5\dots}^{\infty} U_{m\rho} \sin \rho(\alpha - \gamma) \tag{56}$$

$$u_{zm2}(\alpha) = \sum_{\rho=1,3,5\dots}^{\infty} U_{m\rho} \sin \rho(\alpha - (\pi - \gamma)) \tag{57}$$

$$U_{m\rho} = \frac{2\pi p_b}{\rho} \frac{\cos \rho \kappa}{\pi^2 - (2\rho \kappa)^2} \tag{58}$$

The sum of both functions (56), (57) can be represented by the formula:

$$u_{zm1}(\alpha) + u_{zm2}(\alpha) = -\sum_{\rho=1,3,5\dots}^{\infty} 2U_{m\rho} \sin \rho \gamma \cos \rho \alpha = \sum_{\rho=1,3,5\dots}^{\infty} U_{w\rho} \cos \rho \alpha \tag{59}$$

$$U_{w\rho} = -2 U_{m\rho} \sin \rho \gamma \tag{60}$$

According to (53) and (59), the distribution of the magnetic field caused by magnets, has the final form:

$$B_g(\alpha) = \sum_{\rho=1,3,5\dots}^{\infty} B_{m\rho} \cos \rho \alpha \tag{61}$$

$$B_{m\rho} = -\frac{4\pi p_b}{\rho} \frac{\sin \rho \gamma \cos \rho \kappa}{\pi^2 - (2\rho \kappa)^2} B_{g\max} \tag{62}$$

Magnetic flux coming from this field, coupled to a single coil with a span of $2\vartheta_c$ angle, and placed on a surface of the stator (circle at the air gap/stator border) can be calculated from the following formula:

$$\begin{aligned}\psi_c(\phi) &= z_c R_{sw} l_{Fe} \int_{(\xi_c - \vartheta_c)}^{(\xi_c + \vartheta_c)} B_g(\beta) d\beta = z_c R_{sw} l_{Fe} \sum_{\rho=1,3,5\dots}^{\infty} \int_{(\xi_c - \vartheta_c)}^{(\xi_c + \vartheta_c)} B_{m\rho} \cos \rho(\beta - \phi) d\beta \\ &= 2z_c R_{sw} l_{Fe} \sum_{\rho=1,3,5\dots}^{\infty} B_{m\rho} \frac{1}{\rho} \sin \rho\vartheta_c \cos \rho(\phi - \xi_c)\end{aligned}\quad (63)$$

where:

z_c number of turns of coil;

ξ_c position of coil axis.

While the rotor rotates, the changing magnetic flux (coupled with the coil) induces voltage which can be calculated from the below formula:

$$\begin{aligned}e_c(t) &= -\frac{d}{dt}\psi_c = 2\omega z_c R_{sw} l_{Fe} \sum_{\rho=1,3,5\dots}^{\infty} B_{m\rho} \sin \rho\vartheta_c \sin \rho(\phi - \xi_c) \\ &= \sum_{\rho=1,3,5\dots}^{\infty} E_{c\rho} \sin \rho(\omega t - \xi_c)\end{aligned}\quad (64)$$

$$E_{c\rho} = 2\omega z_c R_{sw} l_{Fe} B_{m\rho} \sin \rho\vartheta_c \quad (65)$$

4 Comparison of Measurements and Calculations

The object of the test was a four-pole synchronous machine with permanent magnets, arranged in the rotor core, as shown in Fig. 5.

The stator is equipped with a symmetrical three-phase winding, single-layer, slots without skew. Additionally, for the purpose of measurements, two six-turn measuring coils, covering 1 and 8 stator teeth are installed in the machine. The cross sections of the coil sides are negligibly small as compared to other dimensions of the machine.

The first step of the verification of the model was focused on the unloaded stator voltage waveforms. Figure 6 shows the recorded waveform phase EMF and the waveform created as a sum of respectively shifted and multiplied, recorded EMF-waveforms from a tooth-coil. All waveforms recorded as a function of time are

Fig. 5 The cross-section of one pole of the rotor

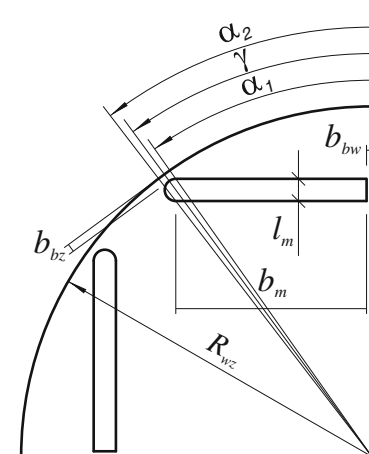
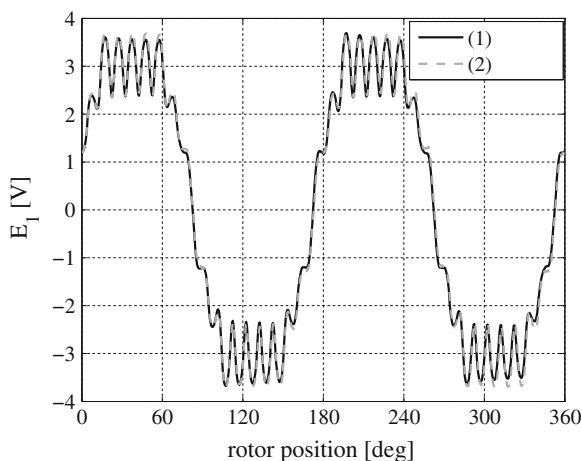


Fig. 6 EMF in the winding of one phase—waveform registered (1), the waveform obtained by summing up registered tooth-coils EMF (2)



shown as a function of the rotor position angle, expressed in degrees. The rotational speed of the rotor during the measurements was $\omega = 61.3 \text{ s}^{-1}$.

A large alternating component of EMF in phase is the result of changes in magnetic flux when passing successive stator teeth on the “external” magnetic bridges. A quick change of the radial component of the induction place in these parts of the magnetic circuit of the rotor. The existence of teeth in the stator exposes these changes, resulting in a large derivative of the flux in the tooth as shown in Fig. 7. This plot illustrates the recorded waveform of EMF tooth-coil and the integral of this EMF.

The high content of higher harmonics and at the same time full transparency EMF waveforms in the present case makes them particularly useful in the verification process. As the filtering effect of higher harmonics is expected to increase,

Fig. 7 Recorded waveform EMF of tooth-coil and integral of EMF

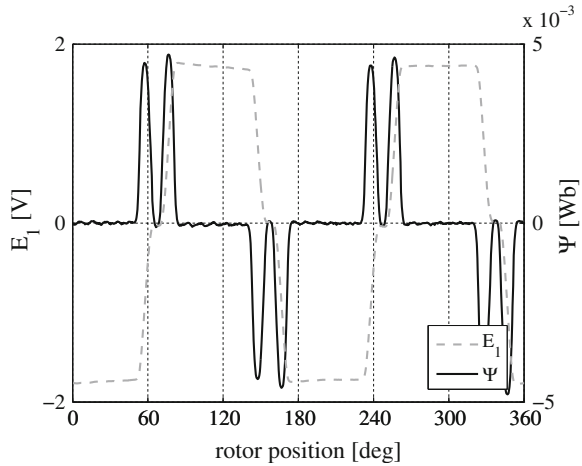
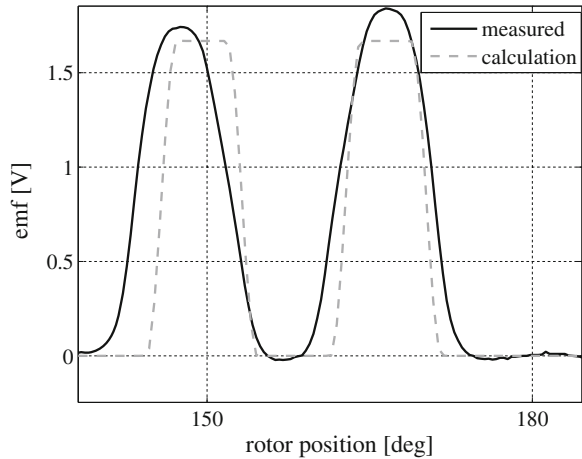


Fig. 8 EMF in the tooth-coil



decision was made to compare the calculated and measured EMF single coils, instead of only EMF phase winding. To calculate these waveforms it was enough to take into account the slotting of the stator in the average value of the substitute air gap: $\delta_z = \delta \cdot k_{Cs} = const.$ The following design parameters were assumed in the calculations: $p_b = 2$, $R_{sw} = 67$ mm, $l_{Fe} = 100$ mm, $\delta = 0.75$ mm, $k_{Cs} = 1.134$, $l_m = 4$ mm, $b_m = 35$ mm, $B_r = 1.12$ T, $H_C = -8.92e^5$ A/m, $z_{c1z} = z_{c8z} = 6$, $v_{c1z} = 3.75^\circ$, $v_{c8z} = 38.75^\circ$.

Parameters of substitute bridges have a major impact on the simulated waveforms. Initially, these parameters were assumed as in Fig. 5: $\alpha_1 = 35.1^\circ$, $\alpha_2 = 37.95^\circ$, $\gamma = 0.5 \cdot (\alpha_1 + \alpha_2)$, $\kappa = 0.5 \cdot (\alpha_2 - \alpha_1)$, $b_{bz} = 2$ mm, $l_{bz} = 2\kappa \cdot (R_{sw} - \delta)$, $b_{bw} = 1$ mm, $l_{bw} = l_m$.

Fig. 9 EMF in a coil around eight teeth

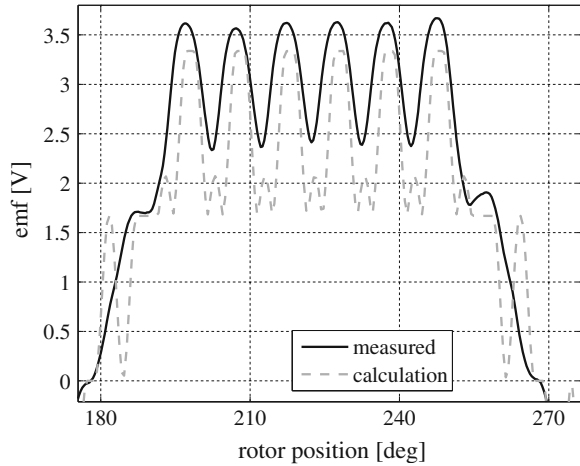
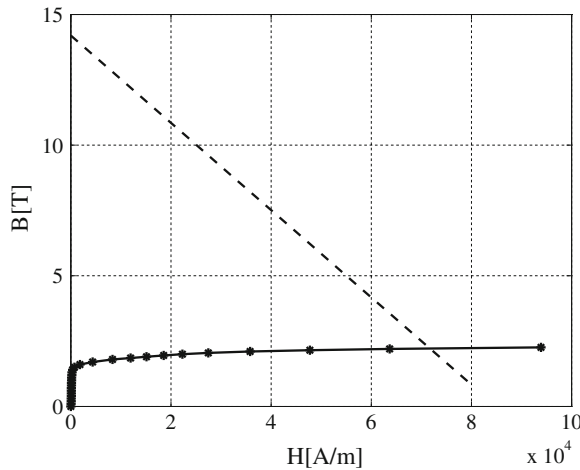


Fig. 10 Determination of the operating point of the bridge



As expected, the direct use of dimensions of cross-section could not produce any satisfactory results. Figures 8 and 9 show the EMF waveforms in coils and calculated ones, using above bridge parameters.

The causes of differences between the curves should be sought primarily in the predetermined length of the “external” bridge l_{bz} and the corresponding values of angle κ . Sensitivity induced by EMF in the coils on the “external” bridges parameters κ, γ, b_{bz} is relatively high. This allows one to easily find out the similarity of calculated and recorded waveforms. Figure 10 shows a graphic solution of Eq. (49). Figures 11 and 12 illustrate EMF-waveforms induced in coils: recorded and calculated, for: $\alpha_1 = 30.8^\circ, \alpha_2 = 40.6^\circ, b_{bc} = 2.8$ mm.

Fig. 11 EMF in the tooth-coil

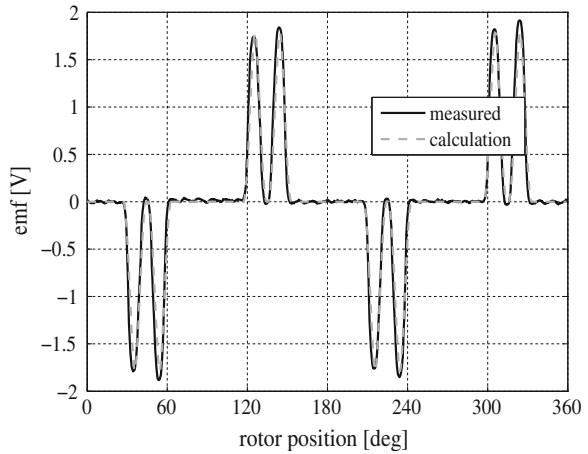
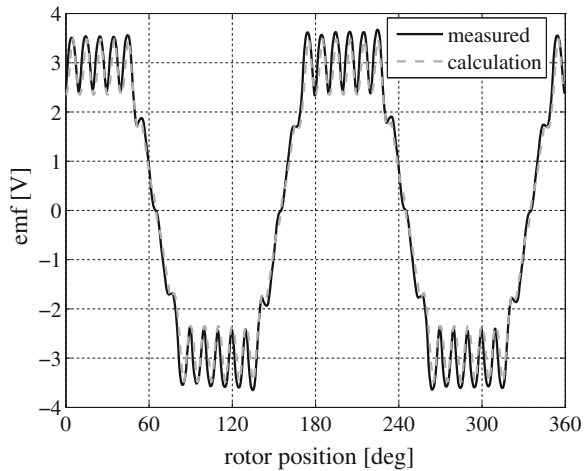


Fig. 12 EMF in a coil around eight teeth



5 Conclusions

Verification calculations based on the proposed model prove the applicability of this method as a support when designing a magnetic circuit for a machine with internal magnets. Of course, this method is not competitive in relation to MES in terms of accuracy of the results, but it seems that it allows you to easier understand the interrelationship between design parameters and their impact on the induced voltages. For a full evaluation of the model it is necessary to verify the effects on waveforms of the machine's armature. It is expected to be done in further studies.

Supplement 1

An important, but controversial assumption of the proposed model is to introduce the concept of magnetic bridges. Magnetic bridges are fragments of the rotor, where the magnetic field H_b is constant and dependent on the dimension l_b . It was assumed that the product of these two values is constant and equal to magnetic tension of the magnet $H_m \cdot l_m$. For comparison's sake, the real situation versus the model calculations were determined using the FEM 2D field distribution in the machine cross section with only permanent magnet excitation. Figures 13 and 14 shows:

- field distribution on the axis of the “internal” bridge—Fig. 13. Position of magnet on the x-axis corresponds to the interval 0–4 mm (see Fig. 5),
- distribution of the tangential component of the field strength on a piece of a circle containing centers of the “external” magnetic bridges, for four different positions of the stator tooth, to the bridge—Fig. 14. “External” bridge predicted position is within the range 35°–38°.

As a result of integration for magnetic tension fragments of the magnetic circuit the following is obtained: for “internal” bridge: $U_{bw} = 540$ A, for “external” bridge: 548 A. Magnetic tension of permanent magnet is $U_m = 552$ A, the field strength $H_m = 13.2e^4$ A/m. Magnetic tensions are therefore similar, but the distribution of the magnetic field strength depends on the shape of the edges of a constriction of the magnetic circuit, that creates the bridge.

The graphs and values allow us to assess the level of approximation to reality and the importance of the assumptions. It would be unacceptable if the purpose of the calculations was mapping of the fields in the machine's cross section. However, the degree of discretization of space is limited to a single slot of the stator, and the

Fig. 13 Field distribution on the axis of the internal bridge (FEM)

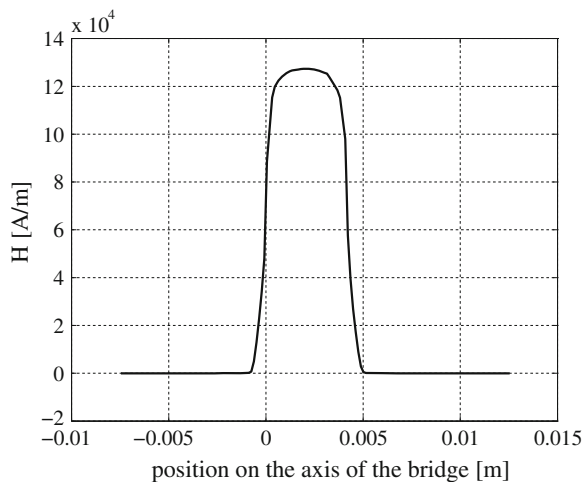


Fig. 14 Distributions of the tangential component of the field strength on a piece of a circle containing centers of the external magnetic bridges

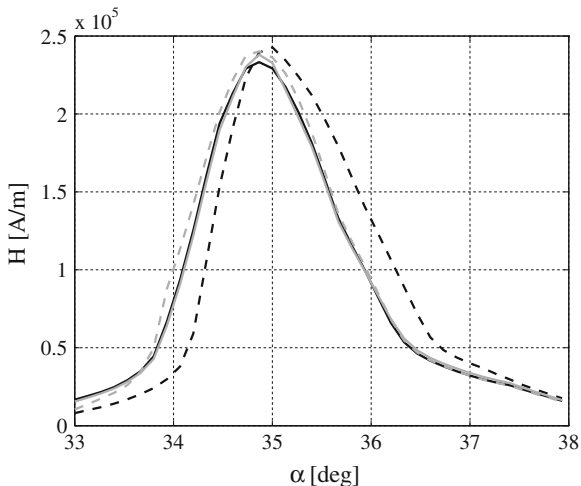
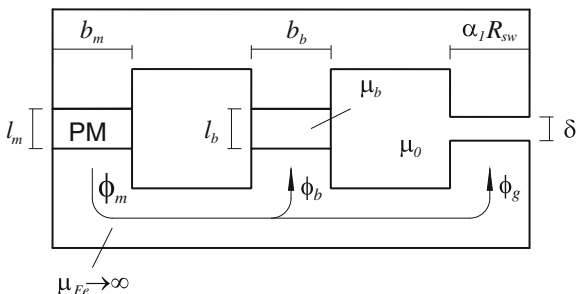


Fig. 15 Analyzed magnetic circuit



comparison value is the average value of induction in the teeth. So it seems, that the problem boils down to the choice of criteria for the selection of H_b field strength and length l_b bridges, especially the “external” ones, and establish the position of the radial axis of the magnet (angle γ). In this study, the major criterion was to make the best representation of the tooth-coil EMF waveform, i.e. changes in the magnetic flux passing through the tooth.

Supplement 2

For the magnetic circuit, as shown in Fig. 15, we have:

$$\begin{cases} H_m l_m + H_b l_b = 0 \\ H_g \delta + H_m l_m = 0 \\ \Phi_m = \Phi_b + \Phi_g \end{cases}$$

where:

$$\begin{aligned} \Phi_m &= B_m b_m l_{Fe} \\ \Phi_g &= B_g \alpha_1 R_{sw} l_{Fe} \\ \Phi_b &= B_b b_b l_{Fe} \\ B_m b_m &= B_b b_b + B_g \alpha_1 R_{sw} \\ B_g &= \mu_o H_g \rightarrow H_g = \frac{B_g}{\mu_o} \\ B_b &= B_{bo} + \mu_b H_b \rightarrow H_b = \frac{1}{\mu_b} (B_b - B_{bo}); \mu_b = \frac{dB_b}{dH_b} H_b \\ B_m &= B_r + \mu_m H_m = B_r + \frac{B_r}{-H_C} H_m \rightarrow H_m = \frac{1}{\mu_m} (B_m - B_r) \\ \mu_m &= \frac{B_r}{-H_C}; H_C < H_m \leq 0 \end{aligned}$$

Combining above dependences we get the circuit equation as shown in Fig. 15. Their matrix form is presented below:

$$\begin{bmatrix} \frac{l_b}{\mu_b} B_{bo} + \frac{l_m}{\mu_m} B_r \\ \frac{l_m}{\mu_m} B_r \\ 0 \end{bmatrix} = \begin{bmatrix} \frac{l_b}{\mu_b} & 0 & \frac{l_m}{\mu_m} \\ 0 & \delta & \frac{l_m}{\mu_m} \\ b_b & \alpha_1 R_{sw} & -b_m \end{bmatrix} \begin{bmatrix} B_b \\ B_g \\ B_m \end{bmatrix}$$

Hence:

$$\begin{bmatrix} B_b \\ B_g \\ B_m \end{bmatrix} = \frac{1}{\Delta} \begin{bmatrix} -\frac{\delta b_m}{\mu_o} - \frac{\alpha_1 R_{sw} l_m}{\mu_m} & \frac{\alpha_1 R_{sw} l_m}{\mu_m} & -\frac{\delta}{\mu_o} \frac{l_m}{\mu_m} \\ \frac{l_m b_b}{\mu_m} & -\frac{l_b b_m}{\mu_b} - \frac{l_m b_b}{\mu_m} & -\frac{l_b}{\mu_b} \frac{l_m}{\mu_m} \\ -\frac{\delta b_b}{\mu_o} & -\frac{\alpha_1 R_{sw} l_b}{\mu_b} & \frac{\delta}{\mu_o} \frac{l_b}{\mu_b} \end{bmatrix} \begin{bmatrix} \frac{l_b}{\mu_b} B_{bo} + \frac{l_m}{\mu_m} B_r \\ \frac{l_m}{\mu_m} B_r \\ 0 \end{bmatrix}$$

$$\Delta = -\frac{\delta b_m}{\mu_o} \frac{l_b}{\mu_b} - \frac{\alpha_1 R_{sw} l_m}{\mu_m} \frac{l_b}{\mu_b} - b_b \frac{l_m}{\mu_m} \frac{\delta}{\mu_o} = -\frac{\mu_m \delta b_m l_b + \mu_o \alpha_1 R_{sw} l_m l_b + \mu_b \delta l_m b_b}{\mu_o \mu_b \mu_m}$$

After arranging the equations we obtain:

$$\begin{aligned} B_m &= -\frac{l_m}{\delta} \frac{B_r - \frac{b_b}{b_m} B_{bo}}{\frac{\alpha_1 R_{sw} l_m}{b_m} \frac{l_m}{\delta} + \mu_{mr} + \mu_{br} \frac{l_m}{l_b} \frac{b_b}{b_m}} \\ B_g &= -\frac{l_m}{\delta} \frac{B_r - \frac{b_b}{b_m} B_{bo}}{\frac{\alpha_1 R_{sw} l_m}{b_m} \frac{l_m}{\delta} + \mu_{mr} + \mu_{br} \frac{l_m}{l_b} \frac{b_b}{b_m}} \end{aligned}$$

The B_g induction corresponds to the maximum value of induction in the air gap between the rotor and the stator, according to formula (51). The differences in signs arise from the assumed character of customization. The formulas may be helpful in the selection of substitute parameters of “external” magnetic bridges.

References

1. Hanselman D (2006) Brushless permanent magnet motor design. Magna Physics Publishing, Lebanon
2. Gieras J (2010) Permanent magnet motor technology, design and applications. CRC Press, Boca Raton
3. Bajek M (2012) Property Analysis and synthesis design of a synchronous motor with permanent magnets for direct starting (LSPMSM) using field methods and optimization. The doctoral dissertation, supervisor dr hab. W.Jażdżyński. AGH, Wydz.EAIIIB, Kraków
4. Honsinger VB (1982) The fields and parameters of interior type ac permanent magnet machines. IEEE Trans. Power Appar Syst PAS-101(4):867–876
5. Skwarczyński J (1990) Internal asymmetries synchronous machines with poles. In: Elektrotechnika, zeszyt, vol 16. Wydawnictwa AGH, Kraków, p 1350
6. Drabek T (1999) Determination of parameters of mathematical models of electromechanical, reluctance actuators. The doctoral dissertation, AGH, Kraków

Modeling of Repetitive Ignitions in Switching Devices: Case Studies on Vacuum Circuit Breaker and GIS Disconnecter

Marcin Szewczyk, Tomasz Kuczek, Piotr Oramus
and Wojciech Piasecki

Abstract Repetitive ignitions of electric arc during switching operation may result in generating Fast and Very Fast Transients (FT and VFT) and thus require analyses to ensure reliable system operation. The paper presents a common approach for modeling and simulation of such phenomenon for two types of switching devices: Vacuum Circuit Breakers (VCB) and GIS disconnectors. In each case, the associated (VFT) are modeled with the use of a case-specific Breakdown Voltage Characteristic (BDV), characterizing the switching process, and with the use of case-specific power system conditions. Two case studies are presented. For Vacuum Circuit Breaker, a switching operation of un-loaded transformer is presented. For GIS disconnector, switching of short bus-bar during the disconnector type testing is presented.

1 Introduction

Very steep wavefront transients in power networks characterized by high dU/dt are often a result of switching events using various types of HV and MV switching apparatus. The transients overvoltage is often of a repetitive nature, which means that multiple overvoltages may be generated during a single switching operation. Those repetitive overvoltage characterized by high rate of rise values may pose significant risks as they can destroy motors, transformers, and other electrical equipment due to highly non-uniform potential distribution and internal resonant phenomena resulting in local voltage amplification. Overstressing the insulation system reduces significantly the equipment lifetime and often leads to an internal short-circuit.

M. Szewczyk (✉) · T. Kuczek · P. Oramus · W. Piasecki
ABB Corporate Research Center, Kraków, Poland
e-mail: marcin.szewczyk@pl.abb.com

The existing standards specifying testing procedures for HV and MV equipment do not cover the phenomena mentioned above as the nature of the generated transients depends very strongly not only on the specific parameters of the given piece of equipment, but also on parameters of the network and the physical processes within the switching device. Therefore the analysis of the transients which occur during the switching operation often requires case by case studies, for which are needed.

Two types of Very Fast Transients (VFT) are recognized in power system [1] as requiring high attention to ensure the system reliable operation: (1) VFT originating from operation of Vacuum Circuit Breakers (VCB), and (2) VFT originating from operation of Gas Insulated-Switchgear (GIS) disconnectors.

Despite of the fact that the two types of VFT are associated with physically different switching devices and operating conditions, repetitive ignitions of the electric arc in a contact gap can be analyzed in a similar way. The ignitions occur when voltage across the gap is higher than dielectric withstand characteristics of the gap (Breakdown Voltage Characteristics, BDV). In each case the transients associated with the switching operation are characterized with high frequency and have repetitive character. As such, they can pose a threat to power equipment insulation system, such as when they interact with resonant frequencies of power transformers [2]. In some cases this requires mitigation methods [2, 3], the first evaluation of which being done with the use of modeling and simulation approach.

In this paper a common approach is presented for modeling and simulation of two different types of switching operations: VCB and GIS disconnector. In the two cases a method is used which was initially proposed for modeling of Vacuum Circuit Breakers, as described e.g. in [4, 5].

The paper is organized in the following way. After introduction in Sect. 1, Sect. 2 follows with description of the method originally proposed for modeling of Vacuum Circuit Breakers, with indicated differences between modeling of VCB and GIS disconnector. In Sect. 2.2 and Sect. 2.3, application of the method is presented for typical VFT-related system studies: Sect. 2.2 presents VCB operation when switching of an unloaded transformer and Sect. 2.3 presents GIS disconnector operation when switching of a short bus-bar during the disconnector type testing. Finally, the summing-up section with conclusions is given.

The system studies presented in this paper are typically performed as a part of the system configuration analyses in the course of insulation coordination studies or for the design process related to the insulation system design of the switching device and power equipment. The objective of such analyses is to evaluate reliable power system operation in presence of VFT.

2 Modeling of Repetitive Re-Ignitions in Switching Devices

2.1 General Approach

The approach for modeling of repetitive ignitions was first presented for modeling of Vacuum Circuit Breakers operations, e.g. in [4, 5]. The approach is to use a controlled switch which is switched on and off after specific criteria are checked. This approach is illustrated in Fig. 1. As it can also be used to simulate GIS disconnectors, additional capacitor was applied as indicated in a green frame in Fig. 1.

In this approach, after the opening operation of the breaker’s contacts starts, the dielectric withstand voltage between the contacts increases as a function of time. When the Breakdown Voltage Characteristics is exceeded by Transient Recovery Voltage (TRV), a control signal is generated to close the switch. In this way the ignition is simulated, being called a re-strike for the opening operation and a pre-strike for the closing operation. When quenching capability of the contact gap is high enough, the arc is effectively extinguished, which is simulated by means of a control signal generated to open the switch in Fig. 1. The theme is repeated during the switching device operation until the dielectric strength of the contact gap is higher than the TRV for the opening operation, or until contacts mating for the closing operation.

The model can be further advanced by considering the arc voltage characteristics. This is modeled with the use of a variable resistor which value is changed in each simulation step. This approach is illustrated in Fig. 2 [4]. The variable arc resistance is implemented according to the model assumptions, based on the switch voltage, switch current and other model-specific parameters [5].

The approach presented in Figs. 1 and 2 was used to perform simulations presented further in this paper. The models were implemented in EMTP-ATP software [6].

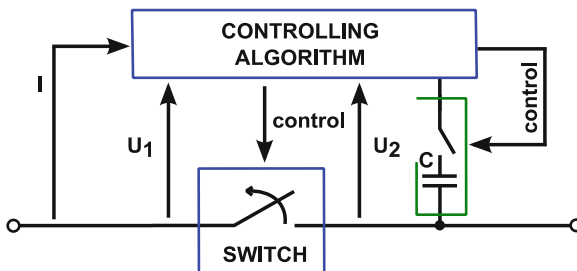
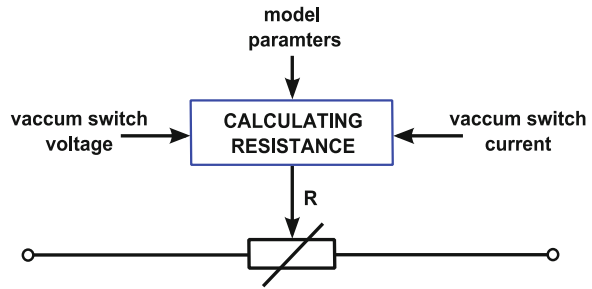


Fig. 1 Model of vacuum circuit breaker based on ideal switch; capacitor for GIS disconnector modeling marked with green frame

Fig. 2 Model of arc ignition based on variable arc resistance



2.2 Modeling of Vacuum Circuit Breaker

Several specific phenomena are implemented in a mathematical model of a Vacuum Circuit Breaker, among which the major ones are: arcing time, current chopping, dielectric strength of the contact gap, and quenching capability of high frequency current.

Arcing time is an interval between the first and the last occurrence of the arc ignition in the process of contacts separation for opening and contacts mating for closing. Typical values of the arcing time are in the range of hundreds microseconds. A Gaussian distribution is used to represent the random nature of this phenomena.

Chopping current is also a random phenomenon. The mean value of the chopping current in the Vacuum Circuit Breaker can be estimated by dependence [4, 5]:

$$I_{ch} = (\omega \cdot i \cdot \alpha \cdot \beta)^q \quad (1)$$

where: $\omega = 2 \cdot \pi \cdot 50$ Hz, i —amplitude of the 50/60 Hz current, α —constant (e.g. $\alpha = 6.2 \cdot e^{-16}$ in [5]), β —constant (e.g. $\beta = 14.3$ in [5]), $q = (1 - \beta) - 1$.

The value of the chopping current depends on the contact material properties, but also on the separation time of the contacts and is lower for the situation when the contacts start to separate in a closer vicinity of a current zero crossing.

For modeling of Breakdown Voltage Characteristics, the two breakdown mechanisms are considered. The first one is the breakdown of a cold gap, which is for when the arc ignites for the first time during an opening or a closing operation process. The second breakdown mechanism is related to the gap which has already ignited. In that case, a residual charge carriers exist near a cathode. The charge causes that the breakdown occurs at lower voltage values. A typical relation of the breakdown voltage for the cold gap is given by the linear formula:

$$U = A \cdot (t - t_{open}) + B \quad (2)$$

where: A , B —values of constants, given e.g. in [4], t_{open} —time of contact separation.

When Transient Recovery Voltage exceeds the dielectric strength of the breaker's contact system, the reignition occurs. The reignition is characterized with the high frequency current related to the arc stability and to the external circuit parameters (inductance and capacitance and associated energy balance).

2.3 Modeling of GIS Disconnectors

In principle the same approach as described above for modeling of Vacuum Circuit Breakers is utilized for modeling of GIS disconnectors. Specific conditions include: (1) Breakdown Voltage Characteristic, being specific to the breakdown in SF6 gas and to the design of the disconnector contact system, and (2) simulated circuit diagram, being specific to a typical disconnector configuration within the test set-up and substation. As the disconnector is installed together with an associated circuit breaker, and during the disconnector operation the circuit breaker has opened contacts, an additional voltage condition at the load side of the disconnector is associated with the Trapped Charge accumulated on the busbar between and disconnector and the circuit breaker, represented by capacitor C in Fig. 1. The capacitor serves to simulate the voltage condition associated with a Trapped Charge in the busbar between the operated disconnector and an open contact system of an associated circuit breaker. Also, the disconnector specific Breakdown Voltage Characteristics is in use, which in its basic form is given by a linear function, having zero value at the time of the contacts mating and the power system withstand voltage at the time of full contact separation.

The breakdown time in SF6 is even shorter than in vacuum, which leads to even higher frequencies of transients when interaction between the disconnector and the system elements occurs. In the presence of very high frequencies, shorter elements have to be considered as lines with distributed parameters.

The arc resistance is modeled by the exponential formula with a time constant leading to the arc duration which is specific to the breakdown time in SF6 gas [7]:

$$R = R_a + R_0 \cdot e^{-t/\tau}, \quad (3)$$

where: R_a —arc static resistance, R_0 —resistance of the gap while disconnector is opened, τ —time constant.

2.3.1 Case Study: Switching of Un-Loaded Transformer with Vacuum Circuit Breaker

In this section an exemplary case study is presented which involves Vacuum Circuit Breaker switching off event in a medium voltage (MV) network. The studied circuit consists of an external grid which supplies the MV/LV distribution transformer

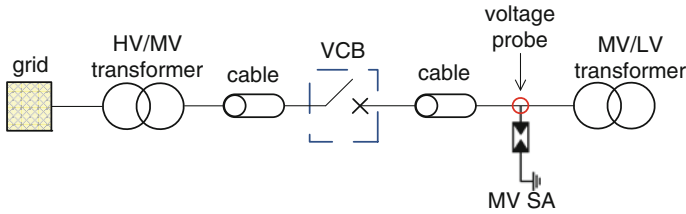


Fig. 3 Vacuum circuit breaker switching study—network diagram

through HV/MV power transformer, as presented in Fig. 3. Medium voltage cables are also considered in the network diagram.

The goal of the study was to illustrate the effect of the Vacuum Circuit Breaker opening operation on transient behavior for the following conditions:

- Breakdown Voltage Characteristic (BDV): simulations performed for 20 and 5 kV/ms
- Cable length between VCB and MV/LV transformer: simulations performed for 15 m and 200 m

The objective was to present the impact of the above listed parameters on transient overvoltages at the MV/LV transformer terminals (see Fig. 3). Based on simulation results it was presented that in order to achieve credible simulation results, detailed input data has to be assumed, both in terms of the system (cables lengths in the case presented) and switching device (BDV of the Vacuum Circuit Breaker in the case presented).

In the studied case the medium voltage network is at 15 kV voltage level. Single-core cables with cross sectional area equals to 95 mm² were modeled by means of surge impedance $Z = 30 \Omega$ and wave propagation speed $v = 200 \text{ m}/\mu\text{s}$ (lossless distributed line). The unloaded MV/LV transformer was modeled according to the data in Table 1.

Four scenarios were simulated. The simulation results are presented in Figs. 4, 5 and 6 in the form of voltage waveforms presenting phase-to-ground voltages at the operated transformer’s primary side according to Fig. 3. The results are presented for the assumed BDV (20 and 5 kV/ms) and for the two cable lengths (15 and 200 m).

Table 1 MV/LV transformer input data

Parameter	Value
Power, S	630 kVA
Voltage ratings, U_{N1}/U_{N2}	15/0.4 kV
Short circuit voltage, $u_k\%$	6 %
No load current, I_0	1 %
Load losses, ΔP_{Cu}	7 kW
No load losses, ΔP_{Fe}	0.8 kW
Primary side capacitance (phase to phase)	0.9 nF
Primary side capacitance (phase to ground)	1.35 nF

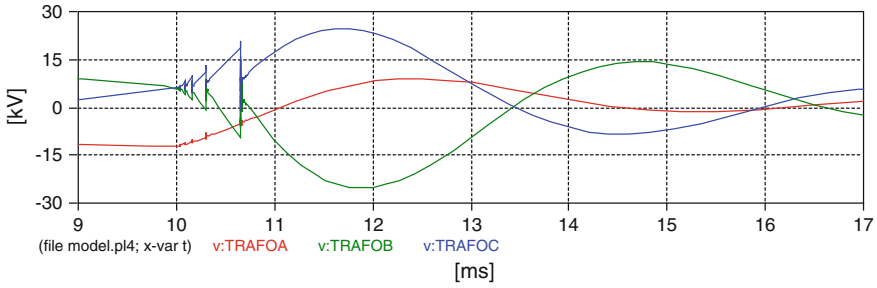


Fig. 4 MV side voltage; BDV = 20 kV/ms, 15 m cable

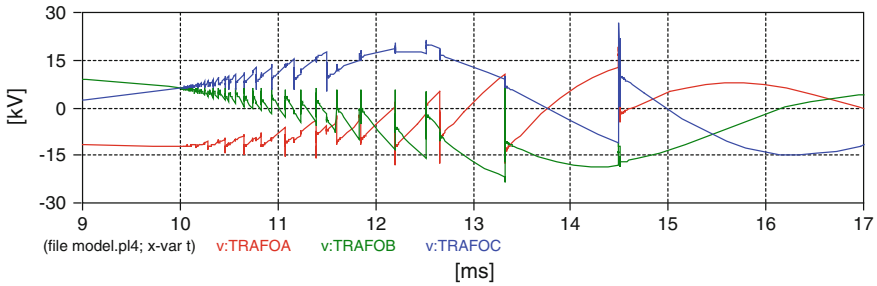


Fig. 5 MV side voltage; BDV = 5 kV/ms, 15 m cable

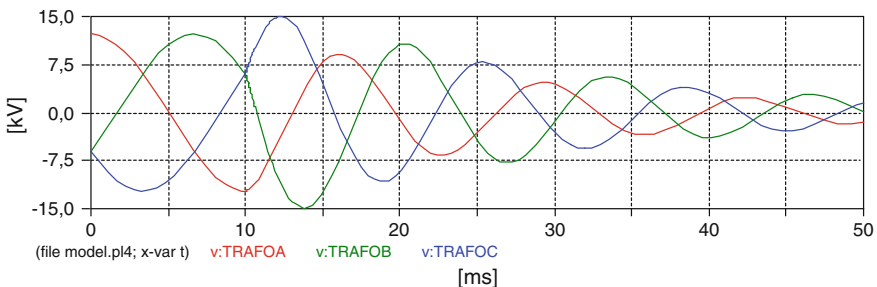


Fig. 6 MV side voltage; BDV = 5, 20 kV/ms, 200 m cable

As it is illustrated in the Figs. 4, 5 and 6, the system configuration as well as the rate of rise of the assumed VCB's dielectric withstand strength have significant influence on the simulation results. At longer cables multiple arc re-ignitions do not occur due to the highly capacitive component of the switched off circuit, which decreases the TRV (see Fig. 6). In the case of short cable connections, for the BDV with lower rate-of-rise value, arc re-strikes last longer and their count number is significantly higher.

2.3.2 Case Study: Switching of Short Bus-Duct with GIS Disconnecter

In this section an exemplary case study is presented which involves GIS disconnector opening operation in type test set-up. The studied circuit, as presented in Fig. 7, consists of an AC 50 Hz voltage source, a DC voltage source, and two disconnectors: DS—disconnector under test, and DA—auxiliary disconnector. The AC voltage rms value is equal to the rated voltage of the disconnector under test, multiplied with factor 1.1. The DC voltage value is -1.0 p.u., where p.u. is the amplitude of the phase-to-ground rated voltage.

The type test procedure according to IEC 62271-102 [8] assumes that initially a short bus-duct d2 is charged to the DC value with the use of auxiliary disconnector DA. During the operation of the disconnector under test DS, the auxiliary disconnector DA remains open.

During the disconnector DS operation, the voltage on the disconnector source side changes with the AC 50/60 Hz frequency, while the voltage on the load side remains at a certain DC level, as presented in Fig. 8. In Figs. 7 and 8, the

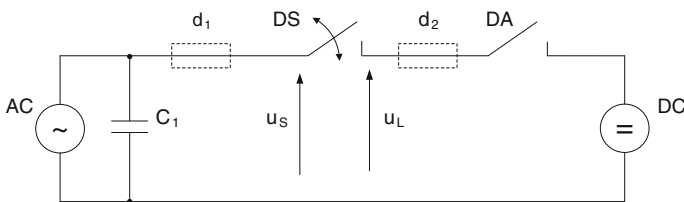


Fig. 7 Test Duty 1 set-up according to IEC 62271-102 [8]

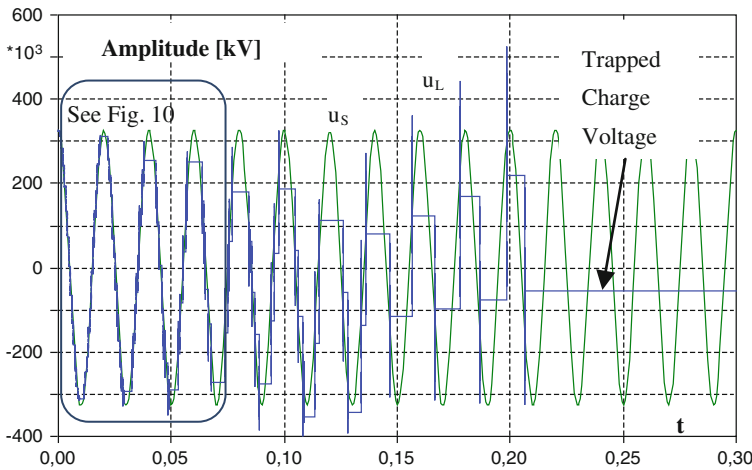


Fig. 8 Very fast transient process during type testing according to Fig. 7; u_S —source side voltage, u_L —load side voltage, for disconnector opening operation

disconnecter source and load side voltages are indicated as: u_S —the source side voltage (sinusoidal waveform in Fig. 8, in green), and u_L —the load side voltage (step-wise waveform in Fig. 8, in blue). A breakdown occurs every time when the voltage between the disconnecter contacts exceeds the breakdown voltage related to the actual contact gap length, as presented in Fig. 8. Due to the very short breakdown time in SF₆ (few ns), transients originating from arc ignitions in GIS have very steep fronts (Very Fast Transients).

When the disconnecter opening operation is completed, after the occurrence of the last re-strike, Trapped Charge Voltage (TCV) remains on the load side of the disconnecter. The Trapped Charge Voltage is an initial condition for the closing operation of the disconnecter, which starts after the opening operation is completed. The relation between the overvoltage and the voltage drop across the contact system at the time of the arc ignition is linear and thus depends on the Trapped Charge Voltage at the time of the arc ignition [9] (Fig. 9).

For design of the disconnecter insulation system, it is thus important that the value of the Trapped Charge Voltage reflects the real conditions during type testing. It is visible in Fig. 8 that none of the re-strikes reaches the most unfavorable condition of -2.0 p.u. voltage drop on the contact system at the time of the arc ignition. Also, for the first arc ignition during the closing operation, the Trapped Charge Voltage is significantly lower than the most severe condition of -1.0 p.u.

In Table 2 the values of Trapped Charge Voltages are calculated for four rates-of-rise of Breakdown Voltage Characteristic assumed for calculation. The BDV are related to the speed of the disconnecter moving contact, which was varied from 0.1 (low speed disconnecter) to 3.0 m/s (high speed disconnecter). It is shown that for low speed disconnecters the Trapped Charge Voltage conditions are lower.

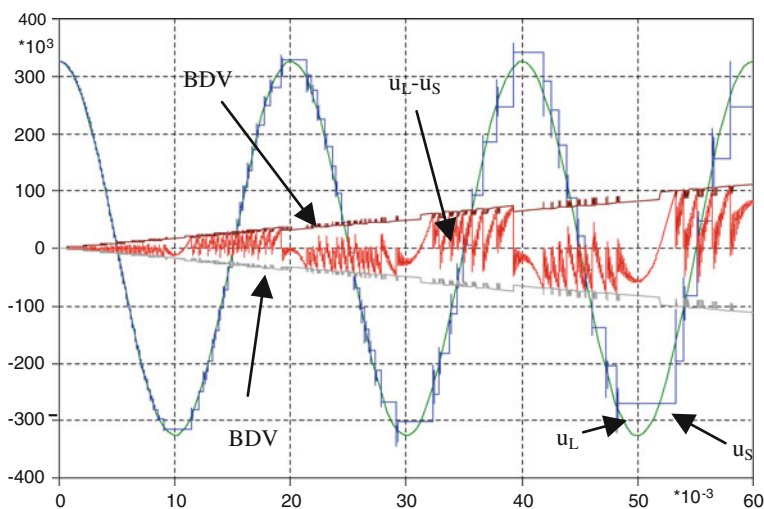


Fig. 9 Breakdown voltage characteristics, source side voltage u_S , load side voltage u_L , voltage across the contacts $u_S - u_L$ during disconnecter opening operation

Table 2 Trapped charge voltage calculated for different speed of disconnector moving contact

Contact speed (m/s)	Trapped charge Voltage (p.u.)
0.1	-0.24
1.0	-0.55
1.5	-0.68
3.0	-1.00

3 Conclusions

Although Vacuum Circuit Breakers (VCB) and GIS disconnectors are governed with different physical principles and are operating in different network conditions, the repetitive process of the arc ignition during operation of both switching devices can be modeled based on a common approach.

In the paper the approach was presented together with two simulation case studies: the VCB operation of an un-loaded transformer, and the GIS disconnector operation during the disconnector type testing.

Parameters associated with the internal switching process can be modeled with the use of Breakdown Voltage Characteristics (BDV). It was presented that the BDV has an impact on time instances when the breakdowns occur. However, for a given breakdown (strike event), the associated voltage waveform depends on the external circuit (here energy oscillation takes place).

References

1. CIGRE JWG A2–A3–B3.21 (2005) Electrical environment of transformers—impact of fast transients. *Electra* 218:25–37
2. IEEE PC57.142/D8.3 (2012) Guide to describe the occurrence and mitigation of switching transients induced by transformer, switching device, and system interaction. IEEE PES Transformers Committee and the Switchgear Committee, WG
3. Riechert U, Bösch M, Smajic J, Shoory A, Szewczyk M, Piasecki W, Burow S, Tenbohlen S (2012) Mitigation of very fast transient overvoltages in gas insulated UHV substations. CIGRE
4. Helmer J, Lindmayer M (1996) Mathematical modeling of the high frequency behavior of vacuum interrupters and comparison with measured transients in power systems. IEEE 17th International Symposium on Discharges and Electrical Insulation in Vacuum, Berkeley
5. Wong SM, Snider LA, Lo EWC (2003) Overvoltages and reignition behaviour of vacuum circuit breaker. International Conference on Power Systems Transients (IPST), New Orleans, USA
6. Dommel HW, Meyer WS (1974) Computation of electromagnetic transients. *Proc IEEE* 62 (7):983–993
7. Povh D, Schmitt H, Volcker O et al. (1996) Modeling and analysis guidelines for very fast transients. *IEEE Power Eng Rev* 17(13)
8. IEC 62271-102 (2013) High-voltage switchgear and controlgear—Part 102: alternating current disconnectors and earthing switches
9. Szewczyk M, Piasecki W, Stosur M, Riechert U, Kostovic J (2011) Impact of disconnector design on very fast transient overvoltages in gas-insulated UHV switchgear. In: Proceedings of 17th International Symposium on High Voltage Engineering (ISH), Hannover, Germany. 22–26 Aug 2011

The Use of Statistical Signatures to Detect Anomalies in Computer Network

Marek Bolanowski and Andrzej Paszkiewicz

Abstract This article presents a new approach for detecting anomalies in the computer network. The approach is based on the determination of the network traffic statistical parameters in case of normal condition. When network anomaly happens, usually more than one statistical parameter is change. A set of parameters that have changed can be used to identify threats. Currently, anomaly detection mechanisms used in the network traffic are computationally complex and cannot be used in case of high speed connection. The presented method does not guarantee the anomaly identification but can be used as one of the indicators used for the isolation of suspicious flows (through ongoing modifications the routing or switching rules). Separated flow is subjected to further analysis with use of classical methods for anomaly detection. With this approach it is possible to make a rough anomaly identification in the core of high speed computer network.

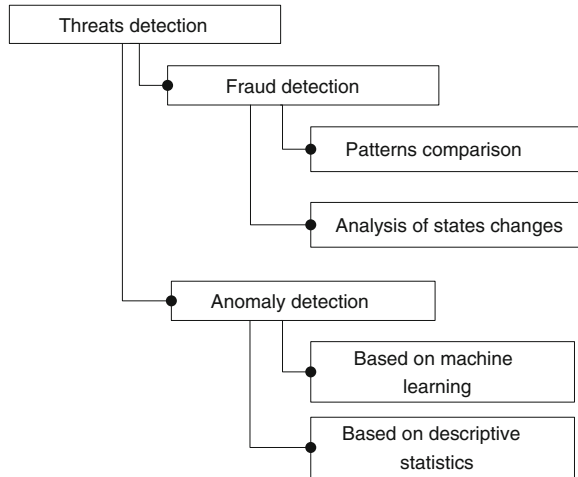
1 Introduction

Today high throughput connection become an immanent component of the computer systems used to support business operation, emergency services, media (television VoD, Radio, VoIP), households, home office. One of the main problems associated with the popularization of network access is to provide users with an appropriate level of security. This is especially important from the point of view of critical infrastructure systems. Modern security systems are based mainly on systems IPS and IDS [1–4] often built in the topology of the demilitarized zone. Their Fig. 1 shows the classification of method used to anomaly detection. This approach

M. Bolanowski (✉) · A. Paszkiewicz
Department of Distributed Systems, Rzeszow University of Technology,
al. Powstańców Warszawy 12, 35-959 Rzeszów, Poland
e-mail: marekb@prz.edu.pl

A. Paszkiewicz
e-mail: andrzejp@prz.edu.pl

Fig. 1 Classification of methods for threats detection



works very well for relatively low bandwidth, but has encountered two main problems:

- Attacks detection based on static signatures, which are updated when new threat is detected, usually with use of non-automatic procedure, allows only to detect existing attacks.
- It is impossible to filter all traffic in the case of high speed links.

In the second case, with use of pseudo automatic or statistical methods, ports, addresses, services etc. are selected and used as a parameter specifying the stream filtered deeply with IDS probe. In effect, only a statically separated fragment of network traffic is filtered, this raises specific risks in the network. Later in this article the authors propose a new model which allows to dynamically define the range of traffic (e.g. set of network flows defined with source and destination address in layer 2) subjected to a extended inspection (up to layer 7 of the OSI model) [4]. In the literature many works can be found describing new methods of real time threat detection, starting from the signature-based methods, through the self-similarity analysis, entropy, or a probability distribution [5–8]. Computer network is an example of a complex system [9], and using non-extensive statistics to analysis some of its parameters (intensity of TCP packets, the ratio of TCP/UDP, the overall volume of traffic, etc.), the abnormal behavior of the system can be identified which is a symptom of an attack on the network assets [6, 7, 10, 11]. Analysis of a traffic parameter or group of its parameters can only identify a transition a communication channel from a state of equilibrium to non-equilibrium and do not specify the exact type of identified attack. It seems appropriate to introduce non-extensive analysis of a group of network parameters and statistical descriptors in order to determine not only the fact of the attack, but also identify its type or accurate identification of danger.

In the second chapter the authors present the results on the sensitivity of selected statistical parameters on the occurrence of specified network threats.

The third chapter will present a model of threat detection using the method of determining the signatures presented in the second chapter.

2 Detection of Network Threats Using Statistical Signatures

In order to examine the traffic the following statistical parameters were selected [12]:

- The arithmetic mean $\bar{x} = \frac{\sum_{i=0}^n x_i}{N}$, where: x —variant of the measured characteristic, N size of the set;
- median: $m_e = x_{\frac{N+1}{2}}$, for even N and $m_e = \frac{1}{2} (x_{\frac{N}{2}} + x_{\frac{N}{2}+1})$, for odd N ;
- variance and standard deviation, described respectively as: $s^2 = \frac{1}{N} \sum_{i=1}^N (x_i - \bar{x})^2$ and $s = \sqrt{s^2}$;
- kurtosis: $K = \frac{m_4}{s^4}$ where: m_4 —central moment of the fourth order, specifying the average size of the fourths powers deviations of features from the arithmetic mean, s^4 —fourth power of the features deviations from the arithmetic mean.
- skewness: $A_m = 3 \frac{\bar{x}-m}{s}$ and range: $R = x_{max} - x_{min}$
- H parameter was estimated using the following methods: residual regression, aggregate variance method, absolute values method and periodogram-based method [13].

Methodology of the research assume two main steps:

1. In the first step, sample of network traffic without anomalies was tested,
2. In the second step, sample of network traffic with anomalies was tested. Anomalies were generated with use of the specialized software dedicated to security and penetration test (e.g. Metasploit).

For both steps the statistical parameters of traffic were determined (for normal traffic as well as disturbed traffic). The following types of time courses were tested: traffic in packets per second (p/s), TCP segments per second (TCP/s), UDP datagrams per second (UDP/s), ICMP/s, the average size of packets (ASP). Scheme of the research shows Fig. 2.

Table 1 summarizes the data for a few selected network attacks in order to present the rules for creating statistical signatures. In the table these parameters that were changed in the case of the attack was shown in bold:

The data presented in Table 1 are only sample data for a number of attacks. A total test was made for more than 30 types of threats. It should be noted that the sensitivity analysis of statistical parameters for the given attack should be done with use of multi-dimensional approaches. For example, at the first level we should

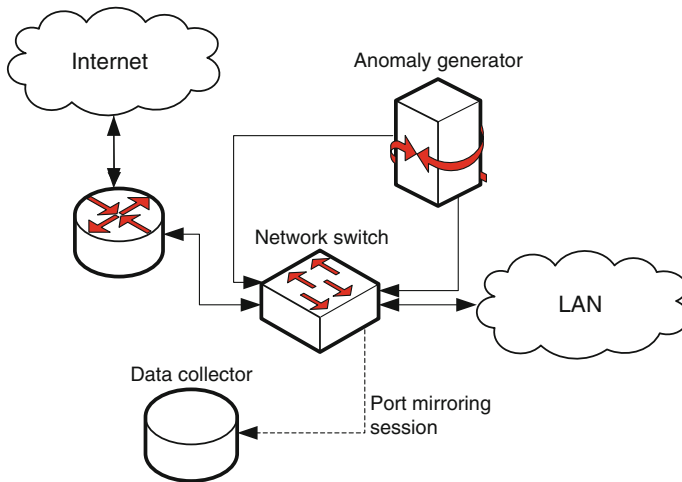


Fig. 2 Diagram of test stand

precisely define the method to create a time series for given anomaly because we can use a different data: p/s, TCP/s, UDP/s, APS.

We can choose one time series or analyze them several at a one time. For each of the time series statistical parameters may show sensitivity for the same anomaly (example: Table 1, the type of attack “Port scanning Nmap”). The graphs from Figs. 3 to 4 time series are presented for the same kind of attack (“Nmap port scan”). As we can see all the time series clearly show the moment of the attack. In case of DoS attack presented in Fig. 5 we can see moment of attack looking at the time series presented in p/s and TCP/s. When we look at the time series presented in UDP/s (Fig. 6) its shows a lack of sensitivity to DoS attack.

The time series present themselves differently depending on the traffic parameters selected for its creation.

The authors also made tests in which the same kind of attack was simulated, and the character of normal traffic was changed (for example, a typical traffic LAN- > WAN, dominance of Video and VoIP traffic, transmission of large files). It showed that, despite the changes in the character of traffic, the same statistical parameters showed a sensitivity for a given attack.

The last type of tests focused on examining linear cross-correlation [14] parameters for normal traffic and traffic test. For example, in case of attack “Port scanning Nmap” correlation UDP/s to p/s, changed from 0.03 to 0.35, as well as the correlation between the APS to p/s from 0.30 to -0.20. Similar changes (other sets of parameters) occurred in the remaining cases.

Multidimensional approach to threat detection in network not only allows for anomaly detection in traffic but also allows you to estimate the type of the threat or even determine a specific type of attack. Another important factor is the possibility of individual tuning of the value of parameter changes for a given groups of attacks, by which it becomes possible to eliminate a greater number of false alarms.

Table 1 Sensitivity of statistical parameters on the occurrence of an attack

Type of attack	The value of the parameters before the attack	The value of the parameters after the attack
Winamp Buffer Overflow p/s	$\bar{x} = 202.56; m_e = 64.00;$ $s = 300.41; K = 5.75; A_m = 2.54;$ $Z = 1472.00; \text{Min} = 42.00;$ $\text{Max} = 1514.00; H = 0.995$	$\bar{x} = \mathbf{79.43}; m_e = 60.00; s = \mathbf{87.10};$ $\mathbf{K} = \mathbf{117.49}; \mathbf{A}_m = \mathbf{9.27};$ $Z = 1454.00; \text{Min} = 60.00;$ $\text{Max} = 1514.00; H = 0.999$
Binary payload p/s	$\bar{x} = 202.56; m_e = 64.00;$ $s = 300.41; K = 5.75; A_m = 2.54;$ $Z = 1472.00; \text{Min} = 42.00;$ $\text{Max} = 1514.00; H = 0.995$	$\bar{x} = \mathbf{94.10}; m_e = 74.00; s = \mathbf{79.85};$ $\mathbf{K} = \mathbf{71.82}; \mathbf{A}_m = \mathbf{6.22};$ $Z = 1454.00; \mathbf{Min} = \mathbf{60.00};$ $\text{Max} = 1514.00; H = 0.999$
Port scanning Nmap p/s	$\bar{x} = 284.09; m_e = 292.50;$ $s = 143.00; K = -0.55; A_m = 0.14;$ $Z = 571.00; \text{Min} = 2.00;$ $\text{Max} = 573.00; H = 0.557$	$\bar{x} = \mathbf{296.38}; m_e = 296.50;$ $s = \mathbf{153.23}; K = -1.61; A_m = 0.60;$ $\mathbf{Z} = \mathbf{982.00}; \text{Min} = \mathbf{4.00};$ $\mathbf{Max} = \mathbf{986.00}; \mathbf{H} = \mathbf{0.622}$
Port scanning Nmap TCP/s	$\bar{x} = 283.75; m_e = 292.50;$ $s = 142.98; K = -0.55$ $A_m = 0.14; Z = 570.00;$ $\text{Min} = 2.00; \text{Max} = 572.00;$ $H = 0.557$	$\bar{x} = 288.11; m_e = 293.50;$ $s = 144.40; K = 0.56; A_m = 0.27;$ $\mathbf{Z} = \mathbf{920.00}; \text{Min} = \mathbf{55.00};$ $\mathbf{Max} = \mathbf{922.00}; \mathbf{H} = \mathbf{0.615}$
Port scanning Nmap UDP/s	$\bar{x} = 0.11 = 0.11; m_e = 0.00;$ $s = 0.39; K = 14.48; A_m = 3.87;$ $Z = 2.00; \text{Min} = 1.00;$ $\text{Max} = 21.00;$	$\bar{x} = \mathbf{7.23}; m_e = 0.00; s = \mathbf{56.24};$ $\mathbf{K} = \mathbf{103.50}; \mathbf{A}_m = \mathbf{9.96};$ $\mathbf{Z} = \mathbf{686.00}; \text{Min} = 1.00;$ $\mathbf{Max} = \mathbf{686.00};$
Port scanning Nmap APS	$\bar{x} = 991.25; m_e = 998.00;$ $s = 26.79; K = 46.76; A_m = -5.84;$ $Z = 295.00; \text{Min} = 732.00;$ $\text{Max} = 1027.00; H = 0.446$	$\bar{x} = 963.23; m_e = 997.00;$ $s = \mathbf{131.94}; \mathbf{K} = \mathbf{27.31};$ $A_m = -5.12; \mathbf{Z} = \mathbf{975.00};$ $\mathbf{Min} = \mathbf{52.00}; \text{Max} = 1027.00;$ $H = 0.540$
DoS (type 1) p/s	$\bar{x} = 460.56; m_e = 513.00;$ $s = 131.40; K = 1.36; A_m = -1.28;$ $Z = 567.00; \text{Min} = 18.00;$ $\text{Max} = 585.00; H = 0.474$	$\bar{x} = \mathbf{676.25}; m_e = \mathbf{567.00};$ $s = \mathbf{305.65}; \mathbf{K} = \mathbf{-0.80};$ $\mathbf{A}_m = \mathbf{0.88}; \mathbf{Z} = \mathbf{1002};$ $\mathbf{Min} = \mathbf{252.00}; \mathbf{Max} = \mathbf{1254.00};$ $H = 0.485$
DoS (type 1) TCP/s	$\bar{x} = 459.63; m_e = 513.00;$ $s = 131.40; K = 1.36; A_m = -1.28;$ $Z = 562.00; \text{Min} = 18.00;$ $\text{Max} = 580.00; H = 0.480$	$\bar{x} = \mathbf{676.25}; m_e = 567.00;$ $s = \mathbf{305.66}; K = -0.80; A_m = 0.88;$ $\mathbf{Z} = \mathbf{1001}; \mathbf{Min} = \mathbf{252.00};$ $\mathbf{Max} = \mathbf{1253.00}; H = 0.485$
DoS (type 1) UDP/s	$\bar{x} = 0.53; m_e = 0.00; s = 1.67;$ $K = 26.58; A_m = 4.83; Z = 12.00;$ $\text{Min} = 1.00; \text{Max} = 12.00;$ $H = 0.480$	$\bar{x} = \mathbf{0.18}; m_e = 0.00; s = \mathbf{1.23};$ $\mathbf{K} = \mathbf{33.41}; \mathbf{A}_m = \mathbf{8.99}; Z = 12;$ $\text{Min} = 1.00; \text{Max} = 12.00;$ $H = 0.485$
DoS (type 1) APS	$\bar{x} = 996.42; m_e = 1002.00;$ $s = 23.11; K = 52.88; A_m = -6.55;$ $Z = 239.00; \text{Min} = 769.00;$ $\text{Max} = 1008.00; H = 0.376$	$\bar{x} = \mathbf{847.12}; m_e = 1001.00;$ $s = \mathbf{249.50}; \mathbf{K} = \mathbf{-0.87};$ $A_m = -1.03; \mathbf{Z} = \mathbf{681};$ $\mathbf{Min} = \mathbf{328.00}; \text{Max} = 1009.00;$ $H = 0.460$
Internet Explorer DHTML attack p/s	$\bar{x} = 629.37; m_e = 352.00;$ $s = 632.88; K = -1.54; A_m = 0.48;$	$\bar{x} = 620.98; m_e = \mathbf{85.00};$ $s = \mathbf{658.00}; K = -1.63; A_m = 0.49;$

(continued)

Table 1 (continued)

Type of attack	The value of the parameters before the attack	The value of the parameters after the attack
	$Z = 1454.00$; $\text{Min} = 60.00$; $\text{Max} = 1514.00$; $H = 0.559$	$Z = 1472.00$; $\text{Min} = 42.00$; $\text{Max} = 1514.00$; $H = 0.539$
AFP “newfunction” p/s	$\bar{x} = 155.31$; $m_e = 60.00$; $s = 243.45$; $K = 11.41$; $A_m = 3.32$; $Z = 1454.00$; $\text{Min} = 60.00$; $\text{Max} = 1514.00$; $H = 0.995$	$\bar{x} = \mathbf{423.93}$; $m_e = 60.00$; $s = \mathbf{458.00}$; $K = \mathbf{-0.93}$; $A_m = \mathbf{0.78}$; $Z = 1454.00$; $\text{Min} = 60.00$; $\text{Max} = 1514.00$; $H = \mathbf{0.863}$
Internet Explorer attack (type 2) p/s	$\bar{x} = 202.56$; $m_e = 64.00$; $s = 300.41$; $K = 5.75$; $A_m = 2.54$; $Z = 1472.00$; $\text{Min} = 42.00$; $\text{Max} = 1514.00$; $H = 0.995$	$\bar{x} = \mathbf{469.83}$; $m_e = 60.00$; $s = \mathbf{505.96}$; $K = \mathbf{-1.38}$; $A_m = \mathbf{0.62}$; $Z = 1460.00$; $\text{Min} = 54.00$; $\text{Max} = 1514.00$; $H = 0.947$

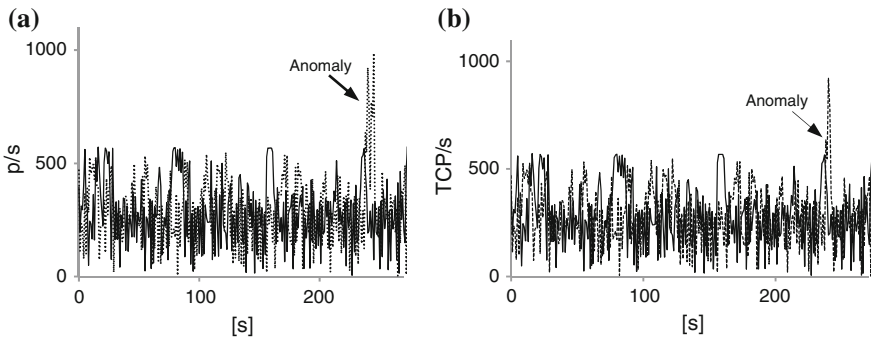
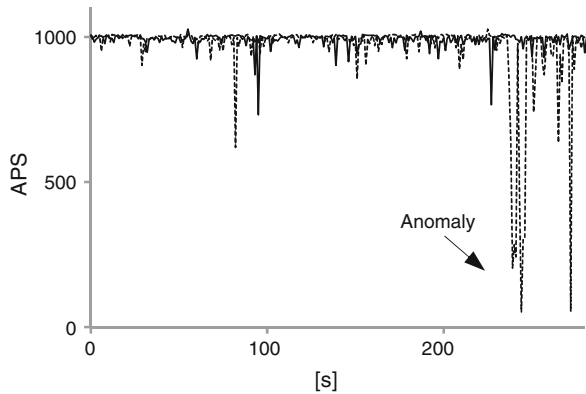


Fig. 3 Port scanning NMAP: **a** traffic without anomaly (*solid line*), with anomaly (*dotted line*) in p/s; **b** in TCP/s

Fig. 4 Scan port NMAP: traffic without anomaly (*solid line*), with anomaly (*dotted line*) in APS



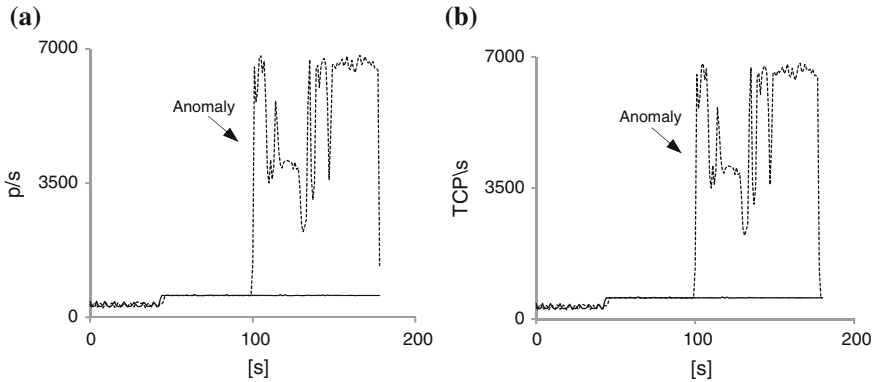


Fig. 5 DoS attack: **a** traffic without anomaly (solid line), with anomaly (dotted line) in p/s; **b** TCP/s

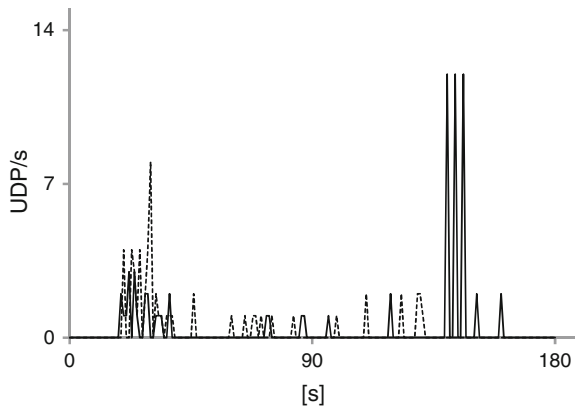


Fig. 6 DoS attack: traffic without anomaly (solid line), with anomaly (dotted line) in UDP/s

3 Detection of Network Threats with Use of Statistical Signatures

Using the previously described methods in systems of threat detection allows for a two-step traffic analysis. Diagram of such a system is presented in Fig. 7.

In the first phase, traffic incoming to the router is sampled using the probe and the sample is sent using a protocol Tprot (e.g. sFlow, NetFlow, RMON) to the network processor which create the corresponding time series and sent them for analysis in the module SA, the results are compared with the data in SD. Then MM module compares the results from AS with set thresholds. If a threat is detected, MM using a communication protocol (e.g. SSH) sends a message to the router and creates a new access list, which redirects suspicious traffic or flow to the module of advanced inspection AFI. In the AIF traffic can be analyzed up to 7th layer of OSI

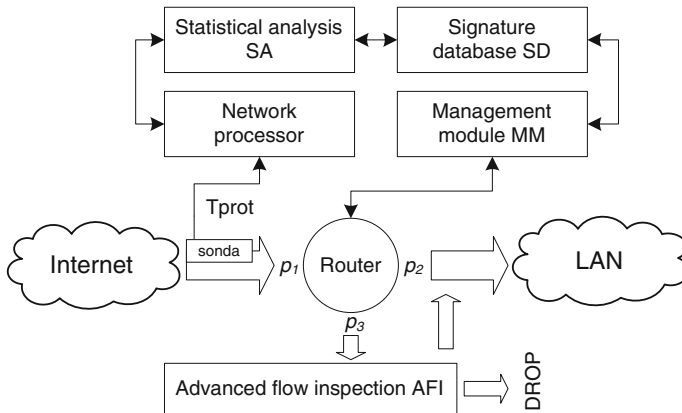


Fig. 7 Diagram of proposed model for anomaly detection in network traffic

model including the use of classical methods of threat analysis. If the alarm turns out a false alarm, traffic is switched back to the LAN, in the other case is dropped.

Especially noteworthy are the following aspects of the model:

- Unlike the classical methods described in the introduction of this article, administrator of the system can set separate sensitivity levels for different groups of attacks which makes proposed model much better to avoid false alarms.
- Commercially available modules of advanced flow inspection are not able to analyze the whole traffic in real time in case of links characterized by high throughput (100 Gb/s and more). Often the types of flows or services are chosen statically to be checked by AFI. Presented model allows for dynamic selection of flow (using the Access List), which are forwarded to the AFI. This improves the security of the system because it can reacts rapidly in case of new threats.
- The present system does not add delay to the network because it works like a normal IDS probe [15] (Intrusion Detection System), and when it detects an attack redirects only selected network flows for the analysis. The slight delay can be provided only in case of flows redirected to AFI.
- This system can be deployed on existing devices using the existing open network protocols.

4 Summary

The article presents a method for the detection of threats in the network based on descriptive statistics. On its basis the sensitivity of specified statistical parameters for selected types of attacks are determined. This approach allows to create database of statistical signatures of threats in computer networks. Study results show the

relationship between sensitivity of statistical parameters and elements describing the network traffic which were taken into consideration when creating a time series. Different types of threats are more easily identifiable (greater changes in certain statistical parameters) from the point of view of different time series. Use of proposed model for network anomaly detection allows for more precise identification of specific attacks. Thanks to this configuration of security system can be made more precise, and allows to avoid false alarms easier.

The implementation model of the intrusion detection system was proposed using the existing commercial hardware and protocols. The main disadvantage currently used statistical intrusion detection system is the difficulty in determining the threshold value of the statistical parameter which trigger actions connected with the given attack type. Incorrect assumptions will result in a large number of false alarms. The authors propose a departure from such threats identification and proposes identification which based on fact of changing the specified set of statistical parameters within a given range.

References

1. García-Teodoro P, Díaz-Verdejo J, Maciá-Fernández G, Vázquez E (2009) Anomaly-based network intrusion detection: techniques, systems and challenges. *Comput Sec* 28(1–2):18–28
2. Kumaravel A, Niraisha M (2013) Multi-classification approach for detecting network attacks. In: Conference on information and communication technologies, IEEE, (ICT 2013)
3. Lee G (2012) The challenges of securing the virtualized environment. *IEEE Comput* 45 (1):17–20
4. Animesh P, Jung-Min P (2007) An overview of anomaly detection techniques: existing solutions and latest technological trends. *Elsevier Comput Net* 51:3448–3470
5. Sastry C, Rawat S, Pujari A (2007) Network traffic analysis using singular value decomposition and multiscale transforms. *Inf Sci* 177(23):5275–5291
6. Han W, Xiong W, Xiao Y et al (2012) A class of non-statistical traffic anomaly detection in complex network systems. In: 32nd International conference on distributed computing systems (ICDCSW), pp 640–646, IEEE
7. Xiong W, Xiong N, Yang Let al (2013) An anomaly-based detection in ubiquitous network using the equilibrium state of the catastrophe theory. *J Supercomputing Springer* 64 (2):274–294
8. Lemes Proença M, Coppelmans C, Bottoli M, Alberti A (2004) The hurst parameter for digital signature of network segment. *Telecommunications and networking—ICT 2004 Springer, Berlin*, pp 772–781
9. Grabowski F (2011) Thermodynamic equilibrium of heterogeneous and distributed components of complex system as basis of effective control and management. In: 4th International conference on advanced computer theory and engineering (ICACTE 2011), pp 461–463
10. Palmieri F (2010) Network anomaly detection through nonlinear analysis. *Comput Secur* 29:737–755
11. Callegari C, Vatou S, Pagano M (2008) A New statistical approach to network anomaly, performance evaluation of computer and telecommunication systems, 2008. *SPECTS*, pp 205–211
12. Sobczyk M (2006) *Statystyka aspekty praktyczne i teoretyczne*. Wydawnictwo Uniwersytetu Marii Curie Skłodowskiej

13. Wroński M (2011) Wybrane narzędzia statystyki nieekstensywnej. Master Thesis,, FE&CE Rzeszow University of Technolog
14. Buda A, Jarynowski Z (2010) Life-time of correlations and its applications. Wydawnictwo Niezależne
15. Grzech A (2008) Optimization of two-level topological structure of distributed, intrusion detection system. Syst Eng ICSENG '08:337–342

Wireless Networks Environment and Complex Networks

Franciszek Grabowski, Andrzej Paszkiewicz and Marek Bolanowski

Abstract Models describing the wireless network environment in most cases are based on the assumption that they are simple systems. However, the parameters describing this type of networks are particularly sensitive to the volatility of the operating conditions. Simple systems take only two operating states into account apart from an overload state, i.e. underload state and a state of equilibrium at the limit of the system. However, the overload state is normal and acceptable by actual natural systems. Wireless networks often operate on the border of a balance between available resources and expectations for the implementation of communication tasks. Therefore, the paper will introduce wireless network especially WLAN in terms of complex systems moving away from the current reductionist paradigm. In addition, there will be presented the method of the dynamic allocation of resources (bandwidth) that is based on properties of complex systems.

1 Introduction

Wireless networks, especially wireless local area networks (WLANs) can be treated as simple systems only from the physical topology point of view, as they are characterized by a little complex topological structure in comparison to interconnection systems used in the design of supercomputers. On the other hand, processes associated with the traffic occurring in them meet conditions imposed complex systems [1] such as non-linearity, thermodynamic disequilibrium, non-extensiveness, nonstationarity of processes, sensitivity to congestion and infection, emergence, dynamic

F. Grabowski (✉) · A. Paszkiewicz · M. Bolanowski
Department of Distributed Systems, Rzeszow University of Technology, al. Powstańców
Warszawy 12, 35-959 Rzeszów, Poland
e-mail: fgrab@prz.edu.pl

A. Paszkiewicz
e-mail: andrzejp@prz.edu.pl

M. Bolanowski
e-mail: marekb@prz.edu.pl

load leveling, fractional Brownian motion, the law power law, small worlds. Processes taking place in these networks are scale free, from short-term to long-term ones. These features enables us to treat real wireless networks as complex systems.

One of the basic and very important characteristics of complex systems is the inclusion of three operating states: underload state, a state of equilibrium at the limit of the system and overload state. In contrast, simple systems take only the first two states into account, apart from an overload state. However, this condition is normal and acceptable by the actual natural systems. Local wireless networks often operate on the border of a balance between available resources and expectations for the implementation of communication tasks. Therefore, during analyzing the performance of WLAN systems, the state of overloading system should be taken into account as an acceptable condition.

Analyzing the available literature we can find publications about analysis or modeling of wireless networks in perspective of complex systems, but mostly in relation to sensor networks [2, 3]. However, these networks are different, and the amount and method of exchanging information is much more limited than in traditional data networks. Therefore, this paper is focused only on wireless networks WLAN (Wireless Local Area Network).

2 WLAN Networks Versus Complex Systems

Beginnings of complex systems science should be found in biology [4]. Mechanisms and processes in natural systems make it impossible to treat them as simple systems. The precursor of this theory was Ludwig von Bertalanffy. The development of systems theory [5] and systems engineering allowed to take into account elements of complex systems in technical sciences and economics. The social sciences such as sociology had active participation in this. At the same time new theories occurred and slowly formed foundations for complex systems. At that moment, the fractal geometry and chaos theory should be mentioned, that were introduced and disseminated by Benoit Mandelbrot and Edward Lorenz. These papers were one of the pillars of dynamic systems theory.

One of the way to describe complex systems is fractal geometry [6]. This geometry is easily reflected in natural systems [7], but it is also used for modeling in computer graphics [8], network design [9], etc. Of course, the WLAN architecture hardly responds to the fractal geometry (Fig. 1). However, traffic statistics, as in wired networks, fit into the formula of the fractal geometry (Fig. 2).

Using e.g. Hurst exponent to the analysis of the traffic, it can be shown that the traffic in WLAN networks is a self-similar [10]. Thanks to that it is possible to analyze the level of self-similarity. This information may be useful in the design and analysis of the computer network operation both in terms of total traffic and its individual components (i.e., selected protocols, conversation, etc.). This phenomenon keeps the statistical similarity regardless of the scale and thus they are part of the further complex system feature, namely the long-term nature [1].

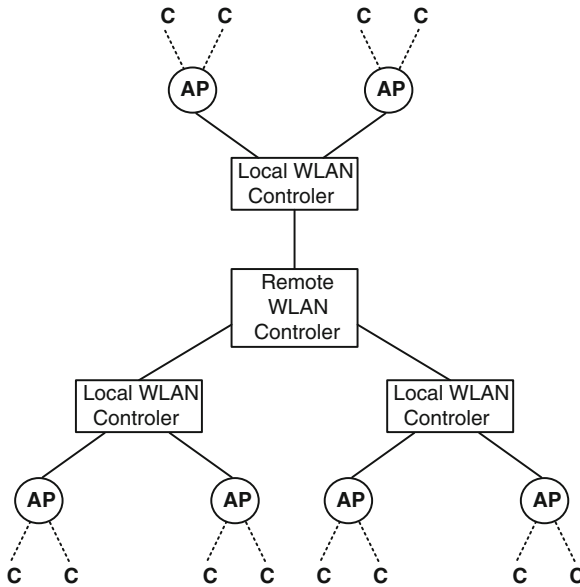


Fig. 1 WLAN in the context of fractal geometry—spatial approach

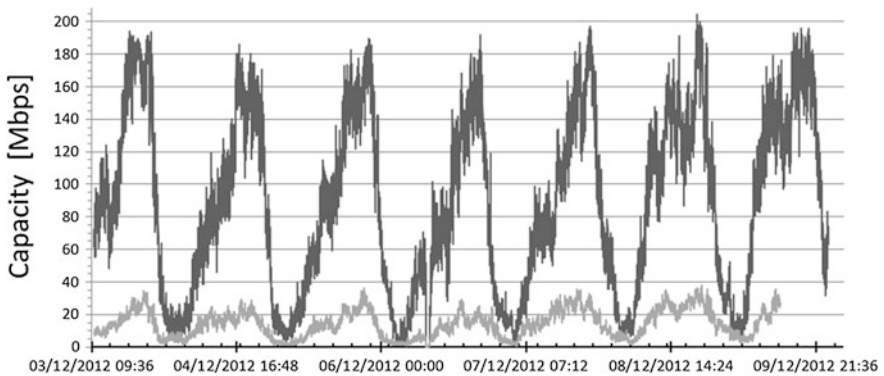
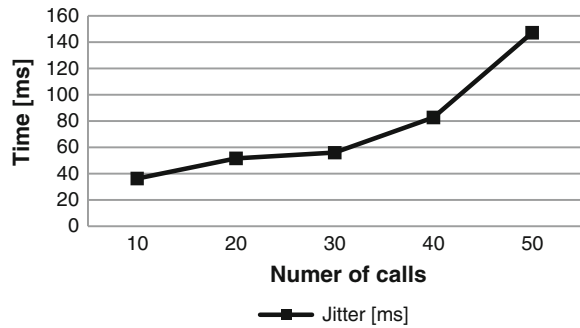


Fig. 2 WLAN in the context of fractal geometry—space-time approach

Another important feature of complex systems, and strictly relating to the WLAN is chaos theory [11]. Edward Lorenz is considered to be the creator of this theory. It assumes the high sensitivity of solutions for arbitrarily small disturbance parameters. Originally it was applied to describe natural phenomena in weather forecasting. However, it soon was found out that other phenomena characteristic of other fields of science similarly run.

Analyzing WLAN it should be remembered that it is especially hostile environment from the point of ensuring the stability of data transmission view. This is

Fig. 3 The maximum jitter in relation to the amount of VoIP calls initiated



because, e.g. interference, high sensitivity to various types of attacks, signal attenuation, problems with steady coverage area, etc. From this perspective, small changes of parameters describing the WLAN operation (e.g. number of users, the amount of transmitted data, roaming, etc.) can lead to a significant deterioration of its operation. Of course, the opposite situation is also possible, i.e. a small change of parameters can result in significant improvement of network performance. For example, for testing WLAN used VoIP traffic. Figure 3 presents the influence of the maximum delay difference (called jitter) in relation to an increase of the number of calls. Of course, these values may vary for different types of used codecs, the amount of transmitted remaining data, interference, etc.

This situation results from the obvious fact that WLANs, like any other natural or artificial system is characterized by limited resources. Therefore, you must change the approach to the analysis of system performance based on reductionist Malthus equation [12] for adaptive.

In the approach proposed by Malthus X_M system performance is expressed by:

$$X_M = \frac{dN}{dt} = rN, \quad (1)$$

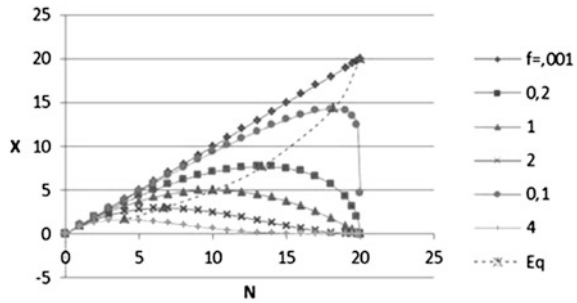
where: r is the growth parameter and N the number of tasks in the system.

This equation refers to a system that has infinite resources, while network traffic is a laminar flow. Such situation in real systems can be treated as an exception to the rule, and not universally applicable rule.

It may be noted that the equation is an integral member of Malthus logistic equation proposed by Verhulst. The condition of limited resources e.g. external conditions is applied to the equation of Malthus by the logistic equation. Therefore, the performance of the system as a whole can be used as proposed by [13] the general logistic equation for the whole family complex systems including computer networks:

$$X = rN \left(1 - \frac{N}{K} \right)^f = X_M (1 - u)^f, \quad (2)$$

Fig. 4 The trajectories of matching points for value of X and N



where K —is the available resources, N —refers to a collection of current data transmission tasks, $u = N/K$, r —is a constant gain factor and f is self-organization parameter of heterogeneous complex system, that describes a trajectory $X(N)$ which are associated with sensitivity of the internal system.

The trajectory of optimal operating points of the system (Fig. 4) can be defined on the set $X(N)$, with r, K, f , as parameters by given Eq. (2).

The results show that it is impossible to determine a single optimal solution, as well as solutions in underload and overload are natural solutions and should be acceptable. It follows that it is necessary to apply adaptive mechanisms, which would allow to react under conditions of limited resources. The above statements are a response to the results obtained and presented in Fig. 4. System, and its performance considered in terms of reductionist does not allow for adaptation to the conditions of overload. This approach is typical for simple systems, and under overload conditions usually leads to degradation of the system expressed by buffer overflow, discarding packets, large delay times. Taking these observations into account, it is important for the wireless networks that are particularly sensitive to the variability of functioning parameters.

The complex system is a fractal structure, where global parameters self-emerge at the local level as a result of feedback. The gain factor of the system with r_f feedback is well known particularly in electronic circuits and control theory and based on the Kirchhoff’s second law in the field amplitude is defined as:

$$r_f = \frac{r}{1 \pm \beta r} \tag{3}$$

where r is the gain factor of the system without feedback, and β is the feedback factor of the system. Comparing Eqs. (2) and (3) we get:

$$(1 - u)^f = \frac{1}{1 \pm \beta r} \tag{4}$$

Above statements explain problems with the performance of the system, which depends not only on the current state but the previous states as well.

Another feature of complex systems applies to a free-scale network. This concept was introduced by Barabási and other authors [14]. This means that the system (in our case WLAN) has scale-free degree distribution characterized by a Poisson distribution whose tail decays according to the power law. The degree distribution often called connectivity indicates the number of connections of a given node to other nodes. On this basis, the probability of a connection between the new node and each node belonging to the network depends very much on the number of edges held by the nodes and for given k -th node is:

$$P(k) \sim k^{-\gamma}. \quad (5)$$

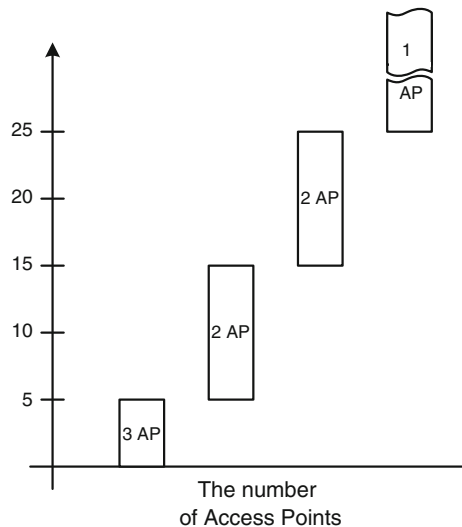
The exponent depends on the type of considered network. The consequence of these assumptions was that most new nodes are connected to nodes that already have many neighbors. Created in this way connections are called preferential connections.

Analyzing selected WLAN networks it can be seen that the load of individual access points is not uniform and depends on their location (Fig. 5). Analysis of the selected WLAN was carried out on local networks.

Figure 5 shows that only certain access points are particularly loaded. You can also find the ones that are largely underload. This property is common in the WLAN infrastructure. Referring to the power law and a free-scale network, the probability of connecting new users to the access point is $P(k)$ and is expressed by Fig. 6a, b.

According to that, network nodes are having one attached element, but also a few nodes that accumulate large part of the traffic from the entire network. These nodes at the same time are characterized by the fact that the probability of

Fig. 5 Examples of the load on each access point



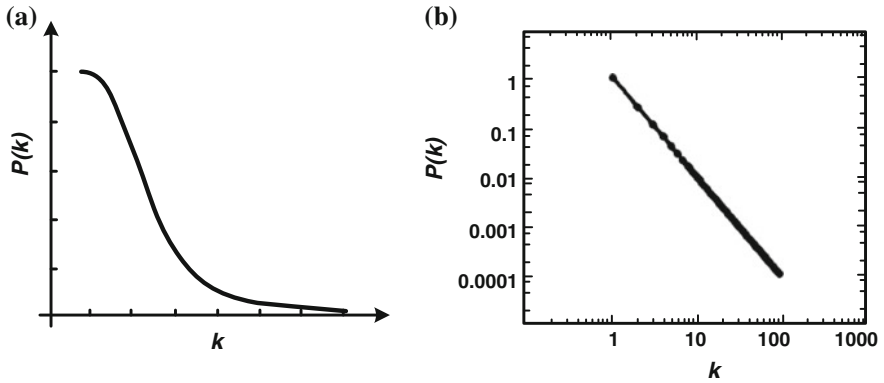


Fig. 6 The probability distribution of connecting to the node: **a** the distribution corresponding to the power law; **b** the distribution corresponding to the power law in a double logarithmic scale

connecting new users e.g. by roaming is greatest. On the other hand, a classic Poisson distribution is characteristic for structure such as the road network. In such structure, there are very rare situations where the majority of connections would pass through the same nodes.

Figure 7 shows the selected graph showing the number of attempts to associate new customers with existing access points. Access points are divided into groups depending on the currently supported number of active users. Obtained results confirm that the behavior of WLAN's users is part of a distribution corresponding to the power law. Thus, this type of network should be treated as a free-scale network.

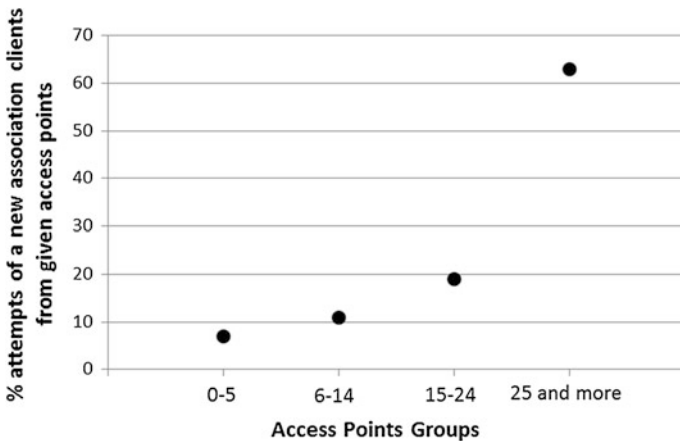


Fig. 7 The request association clients with access points

Based on the above information it seems to be reasonable to use the algorithm of modeling free-scale network for modeling WLANs. Our proposed algorithm is a modification of the classical approach [15] and includes the following activities:

1. Initially, we create the relatively small number of nodes (corresponding APs) m_0 .
2. We introduce another new node (representing a client) m_i . Probability that the new node (client) is connected with the i -th node (access point) depends on the degree of node (k_i):

$$P(k_i) = k_i / \sum_j k_j. \quad (6)$$

3. We continue to add new nodes (clients), until requested quantities.

3 Bandwidth Reservation

Results presented in the paper confirm that local wireless networks are part of the theory of complex systems. This information can be the basis for creating of, among others, new algorithms of designing these networks, load balancing mechanisms in traditional WLANs, mesh networks as well [16], and proposing new solutions to ensure an adequate level of service (QoS).

As an example of such application, we propose a new approach to the management of available bandwidth within the individual access points. The capacity of each node is closely related to the actual, available transmission band. Classical solutions are either associated with a competition mode or guaranteed one. In the first, each of the potential users must compete for access to the medium. However, in the guaranteed mode there is a sequential query of each client and assign them appropriate bandwidth. Both of these approaches, in the case of a large mobile user migration (roaming) or a completely new appearance, are inefficient and consequently may result in the termination of already existing communication sessions. A kind of antidote are indirect mechanisms that statically reserve some bandwidth for new or switched users with other access points [17].

Static resource reservation is not effective enough and in the case of the mis-configuration can lead to degradation of connection quality. Therefore, more complex mechanism should be introduced that will be corresponding to properties of complex networks. Such a mechanism should use, among others, power law, clustering and dynamic resource reservation (bandwidth reservation) on a given transmission path. This solution would be beneficial from the point of video conferences, broadcasts classical VoIP, online games view, etc.

The first element of this system is based on the power law in the context of bandwidth reservation on the access point. Taking the power law into account,

reserved band with C_i (on the i -th node) should be dependent on the probability of connecting new customers to it at a given moment of time t_j :

$$C_i(t_j) \sim P(k_i(t_j)), \quad (7)$$

where: $C_i(t_j) \leq C_i^{\max}$. The limitation on the maximum value of C_i prevents the entire resource reservation. However, such a situation would be beneficial in some cases, for example, in the case of very high mobility of end users. This would require additional research and analysis, which are not the subject of this article.

The above mechanism dynamically reserves bandwidth depending on probability appearance of new users in a given access point. This system does not classify existing and potential users but all of them throws into one bag. In times of creating of community and group profiles, this solution is not sufficient. Therefore, the next step is the further improvement of communications processing through the use of clustering groups based on free-scale networks features. Let define a set of groups $G = \{g_i, i \in N\}$. Each group can be represented by members that communicate together within the group chat, video conferencing, play the game. Therefore, reserving bandwidth for the group should be introduced:

$$C_i^{g_i}(t_j) \sim P_{g_i}(k_i^{g_i}(t_j)), \quad (8)$$

where: g_i denotes i -th group. Thus, $C_i^{g_i}(t_j)$ refers to the capacity for the group g_i -th on i -th node in the time t_j .

Remember to introduce limitations on the maximum bandwidth for each group:

$$C_i^{\max} = \{C_i^k, C_i^d, C_i^{g_1}, \dots, C_i^{g_n}\}, \quad (9)$$

where: C_i^k represents the remaining available bandwidth on a given node that is not participating in the dynamic reservation, C_i^d is associated with dynamic bandwidth reservation for the other users not using the group reservation, $C_i^{g_1}, \dots, C_i^{g_n}$ means the bandwidth reserved for individual groups.

The next step may be the bandwidth reservation on the whole transmission path to ensure proper transmission parameters, for example videoconferences. However, due to the scope of this publication and the complexity of such solution it should be presented in a separate paper.

4 Conclusions

Analyzing the local wireless networks should move away from the reductionist paradigm describing them as simple systems. Phenomena occurring in them clearly indicate that they should be treated as complex systems.

The problem of limited resources applies to all technical systems, and more. It has particular importance in the case of wireless networks, where very often appears a competition for access to bandwidth, interference, etc.

The results are just the beginning of work over the new algorithms bandwidth allocation, traffic prioritization, load balancing, selection of alternative paths, or any other kind of models for network traffic generated for WALN.

References

1. Nicolis G, Nicolis C (2012) Foundations of complex systems: emergence. Information and Prediction. World Scientific Publishing Co., Singapore
2. Chamseddine A, Noura H (2012) Sensor network design for complex systems. *Int J Adapt Control Signal Process* 26(6):496–515
3. Mills KL (2007) A brief survey of self-organization in wireless sensor networks. *Wirel Commun Mobile Comput* 7(7):823–834 (Chichester)
4. Von Bertalanffy L (1969) General system theory: foundations, development, applications. George Braziller, Inc. (1969)
5. Boulding KE (1956) General systems theory—the skeleton of science. *Manage Sci* 2 (3):197–208
6. Song Ch, Havlin S, Makse HA (2006) Origins of fractality in the growth of complex networks. *Nat Phys* 2(4):275–281
7. Mandelbrot BB (1982) The fractal geometry of nature. W. H. Freeman and Company, San Francisco
8. Encarnacao JL, Peitgen HO, Sakas G, Englert G (1992) Fractal geometry and computer graphics. Springer, Berlin
9. Gallos LK, Song Ch, Makse HA (2007) A review of fractality and self-similarity in complex networks. *Physica A*, nr 386:686–691
10. Kaur G, Saxena V, Gupta JP (2010) Characteristics analysis of web traffic with hurst index. In: Proceedings of the world congress on engineering and computer science 2010, vol 1, San Francisco
11. Lorenz EN (1995) The essence of chaos. University of Washington Press, Washington
12. Malthus TR (2007) An essay on the principle of population. Cosimo Classics, New York
13. Grabowski F (2013) Nonextensive model of self-organizing systems. *Complexity*, Wiley 18 (5):28–36
14. Barabási AL (2009) Scale-free networks: a decade and beyond. *Sci Mag* 325:412–413
15. Albert R, Barabási AL (2002) Statistical mechanics of complex networks. *Rev Mod Phys*, 4:47–91 (Notre Dame)
16. Hiertz GR, Denteneer D, Max S, Taori R, Cardona J, Berlemann L, Walke B (2010) IEEE 802.11s: The WLAN mesh standard. *IEEE Wirel Commun* 17(1):104–111 (New York)
17. Perros HG, Elsayed KM (1996) Call admission control schemes: a review. *IEEE Commun Mag* 34(11):82–91 (New York)

Network Anomaly Detection Based on the Statistical Self-similarity Factor

Pawel Dymora and Mirosław Mazurek

Abstract The actual network traffic is self-similar or long-range dependent. Self-similarity analysis and anomaly detection in networks are interesting field of research and scientific work of scientists around the world. Simulation studies have demonstrated that the Hurst parameter estimation can be used to detect traffic anomaly—the Hurst values are compared with confidence intervals of normal values to detect anomaly in few kinds of traffic: TCP, UDP. The dramatic expansion of applications on modern networks gives rise to a fundamental challenge to network security. Therefore, it is important to reduce the burstiness for better network performance, and thereby detect traffic anomalies.

1 Introduction

Statistical analysis of network traffic measurements shows a clear presence of the fractal or self-similar properties in computer network [1, 2]. The statistical characteristics of computer network traffic have been on interests to scientists for many years, not least to obtain a better understanding of the factors that affect the performance and scalability of large systems such as the Internet. Research on network anomaly detection is very challenging and has started many years ago. Network traffic is inherently fractal or long-range dependent (LRD). The normal network behavior is used to detect network anomalies. That fact leads to question the extent to which the results of these studies are applicable in practice. Is it possible to diagnose network traffic and provide congestion risk. At the time being, there is mounting evidence that LRD is of fundamental importance for a number of engineering problems, such as traffic measurements [3, 4] and queuing behavior [5].

P. Dymora (✉) · M. Mazurek
University of Technology, Rzeszow, Poland
e-mail: pawel.dymora@prz.edu.pl

M. Mazurek
e-mail: miroslaw.mazurek@prz.edu.pl

The similar processes have been observed and analyzed in a number of other areas like, for instance hydrology, economics, biophysics. A self-similar phenomenon represents a process displaying structural similarities across a wide range of scales of a specific dimension. Recent measurements of network traffic have shown that traffic exhibits variability at a wide range of scales.

The reference structure is repeating itself over a wide range of scales of diverse dimensions (geometrical, statistical or temporal), and the statistics of the process do not change with the time. In reality, the simple systems don't exist. In the case of real, complex systems, in contradiction to the simple systems, one can indicate the following features of processes: thermodynamic non-equilibrium, heterogeneous topologies, small-worlds phenomenon, long-range dependencies, bursty and self-similar traffic, scale-free (power law) distributions, packet switching, structure hierarchy, percolation, clustering, self-organization, parameters degradation and collapse [2, 6].

The approaches used to address the anomaly detection problem are dependent on the nature of collected data. Network data can be obtained at multiple levels of granularity such as end-user-based or network-based. End-user-based data contains information which characterize the end application (refers to the transmission control protocol TCP and user datagram protocol UDP). Network-based data describe the functioning of the network devices and includes information gathered from network equipment's (routers, switches). Traffic counts obtained from both types of data can be used to generate time series to which statistical signal processing techniques can be applied. Statistical data analysis makes it possible to quantify network behavior and, therefore, describe network anomalies [7].

2 Self-similarity Statistical Factor

Self-similarity and fractals are notions pioneered by Benoit B. Mandelbrot. Self-similarity can be associated with "fractals", which are objects with unchanged appearances over different scales. Estimating the Hurst exponent for a data set provides a measure of whether the data is a pure white noise random process or has underlying trends. Brownian walks can be generated from a defined Hurst exponent. If the Hurst exponent is $0.5 < H < 1.0$, the random process will be a long memory process. Data sets like this are sometimes referred to as fractional Brownian motion. Fractional Brownian motion can be generated by a variety of methods, including spectral synthesis using either the Fourier transform or the wavelet transform. In the case of statistical fractals it is the probability density that repeats itself on every scale. On the other hand a dynamical fractal is generated by a low-dimensional dynamical system with chaotic solutions. Self-similarity means network traffic displays shape similarity in a very wide time scale. Hurst parameter (abbreviated as H) is an important index to measure the similarity which is often used in traffic congestion control and access control. Therefore, to estimate Hurst parameter accurately and rapidly has significance in network management and control.

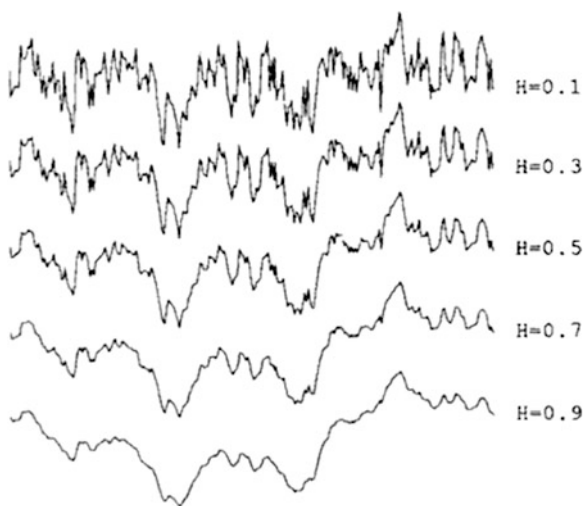
A self-similar time series has the property that when aggregated (leading to a shorter time series in which each point is the sum of multiple original points) the new series have the same autocorrelation function as the original.

That is, given a stationary time series $X = (X_t; t = 0, 1, 2, \dots)$, we define the m -aggregated series $x^{(m)} = (x_k^{(m)} : k = 1, 2, 3, \dots)$ by summing the original series X over no overlapping blocks of size m . Then if X is self-similar, it has the same autocorrelation function $r(k) = R[(x_t - \mu)(x_{t+k} - \mu)]$ as the series $X^{(m)}$ for all m . This means that the series is self-similar: the distribution of the aggregated series is the same (except changes in scale) as that of the original [2, 4].

A process with long-range dependence has an autocorrelation function $r(k) \sim k^{-\beta}$ as $k \rightarrow \infty$ where $0 < \beta < 1$. Thus the autocorrelation function of such a process decays hyperbolically (as compared to the exponential decay exhibited by traditional traffic models). Hyperbolic decay is much slower than exponential decay, and since $\beta < 1$, the sum of tile autocorrelation values of such a series approaches infinity. This has a number of implications. First, the variance of n samples from such a series does not decrease as a function of n (as predicted by basic statistics for uncorrelated datasets) but rather by the value $n^{-\beta}$. Second, the power spectrum of such a series is hyperbolic, rising to infinity at frequency zero—reflecting the “infinite” influence of long-range dependence in the data.

The main advantage of using models of self-similar patterns of the time series is that the degree of self-similarity of the series is expressed by only one parameter. The parameter expresses the speed of decay series autocorrelation function. The fractal dimension is directly related to the Hurst exponent for a statistically self-similar data set. A small Hurst exponent has a higher fractal dimension and a rougher surface. A larger Hurst exponent has a smaller fractional dimension and a smoother surface (Fig. 1). For historical reasons, the parameter used is the Hurst

Fig. 1 Fractional Brownian Motion and the Hurst exponent [8]



parameter $H = 1 - \beta/2$. For self-similar series, $1/2 < H < 1$. As $H \rightarrow 1$ the degree of self-similarity increases. Thus, the main criterion for a series of self-similarity reduces the question of whether H is significantly different from the $1/2$.

There are many ways determine the variance. We can use the variance-time plot, relies on the slowly decaying variance of a self-similar series. The variance of $X(m)$ is plotted against m on a log-log plot; a straight line with slope (β) greater than -1 is indicative of self-similarity, and the parameter H is given by $H = 1 - \beta/2$. We can use R/S method. The R/S plot, uses the fact that for a self-similar dataset, the rescaled range or R/S statistic grows according to a power law with exponent H as a function of the number of points included (n). Thus the plot of R/S against n on a log-log scale has a slope which is an estimation of H . The last approach, the periodogram method, uses the slope of the power spectrum of the series as frequency approaches zero. On a log-log plot the periodogram slope is a straight line with slope $\beta - 1 = 1 - 2H$ close to the origin [9].

These methods are not resistant to faulty assumptions (such as non-stationarity in the dataset) and they do not provide confidence intervals. The fourth method, called the Whittle estimator does provide a confidence interval, but has the drawback that the form of the underlying stochastic process must be supplied.

3 Network Architecture and Subject of Analysis

The scope of this paper is to describe the problem of IP network anomaly detection in a single administrative domain, in a private computer network (small company). The collected data were the result of the normal operation of programming during the work hours. The company has an 8 h working time in two hourly intervals from 7:00 to 15:00 and from 9:00 to 17:00. It is possible that employees remained after hours. At night, all computers should be turned off, but this is not strictly adhered to. Table 1 shows the detailed network traffic parameters.

The network uses 19 computers and network devices. All the computers were located in the same subnet and were connected via a switch to one of the server ports. The Server was connected to the Internet through a router. The analyzed network topology was shown in Fig. 2.

Table 1 Network traffic parameters

Background traffic	One working day
Start time	7:00 am
Duration	24 h
Working time	10 h
Free time	14 h

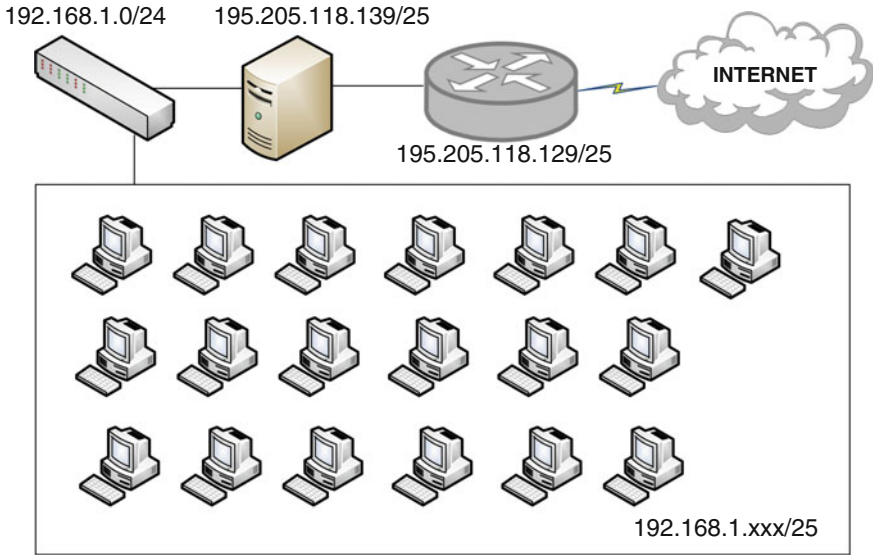


Fig. 2 Analyzed network architecture model

To collect the data we used one of the sniffer programs to capture packets—Wireshark (Fig. 3). This program can save the movement from the level of the data link layer [2]. Captured traffic samples contain information such as the location of the file, its size, format, type of encapsulation and packet size limit, time of the first packet that is the start time of the test procedure and its completion, the total length

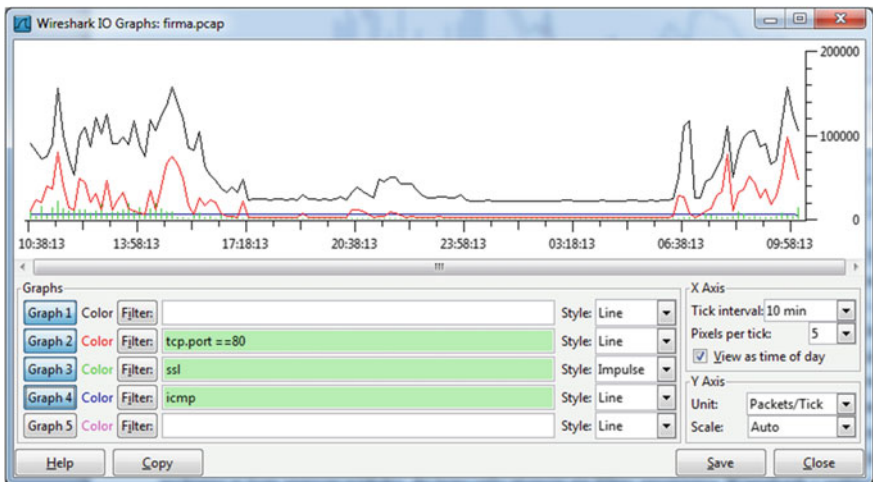


Fig. 3 The sample packets flow in Wireshark sniffer

of the work. In addition, provides information about the number and type of packets. Through 24 h the analyzed network recorded 7 818 848 packets, the average speed was 90.447 packet per second.

4 Framework of Network Traffic Anomaly Detection

The scheme of network traffic anomaly detection based on self-similarity may consist of few modules. We suggest scheme based four modules: traffic collection, statistical analysis, Hurst factor estimation and anomaly detection (Fig. 4).

In order to reduce the impact on normal use of network, when collecting LAN traffic, traffic on router is mirrored to traffic collection server. Packets received from router are processed. We can extract some traffic metrics like number of packets, the total length of the packet. The study aimed to observe network traffic and to determine whether there are long-term dependencies in the all network working time and above-hour intervals. In order to carry out the work of all captured packets we isolated ones that had the greatest impact on the network. They were divided in the terms of services and protocols on five main groups:

- Web—*HTTP*;
- E-mail—*POP3, IMAP, SMTP*;
- *SSL*;
- Unknown—*IPSec, DG Gryphon*;
- *ICMP*;
- *IPv6*.

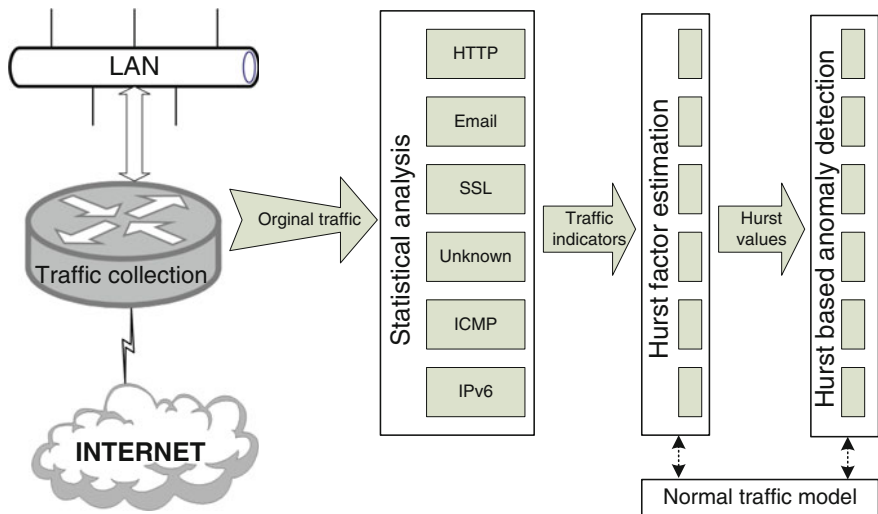


Fig. 4 Network traffic anomaly detection scheme

Next Hurst values of selected traffic metrics are calculated. The values can be used to detect traffic anomaly. The current calculated Hurst value is compared to normal traffic model. If the value deviates from normal model, current traffic is thought to be anomalous and normal otherwise. The assumption is that the Hurst parameter will remain relatively stable.

5 Anomaly Traffic Detection

Network anomalies typically refer to circumstances when network operations deviate from normal network behavior. Network anomalies can rise due to various causes such as network overload, failure network devices, distributed denial of service attacks (DDoS), network intrusions, SYN floods, etc. These anomalous events will disturb the normal behavior of analyzed network [3, 10].

In this paper we propose to identify self-similarity anomalies based on the multi-time scaling nature and heavy-tailed distribution. Multi-time scaling nature means that the time series X and its time scaled version $x^{(m)}$, after normalizing must follow the same distribution. The self-similar process also obeys the heavy-tailed distribution, under which it exhibits extreme variability. In the other word, a heavy-tailed distribution gives rise to very large values with a distribution results in content of the values being small but with a few samples having very large values [7, 9]. We note that each data set in the self-similar aggregated traffic appears to have different burstiness characteristics. Under normal circumstances network traffic shows daily pattern. To reduce the impact on Hurst estimation caused by periodicity of network traffic whole time series is divided into 24 data sets. For each data set, the histogram of 24 equivalent time bins is computed. For each group number of packets, the total length of the packet and the average packet length in hourly intervals was calculated. There were also the largest and the smallest size packet. The next step was to calculate the Hurst factor by earlier estimation of β using the method of Benoit and Power Spectrum.

In practice, firstly a day of normal traffic is collected and traffic metrics mentioned before are extracted. When starting real time detection, the calculated Hurst factor is compared to normal traffic model for each metrics.

Exemplary power-spectrum density for the selected metrics at the same time operation of the network (14:00–5:00) shown in Figs. 5, 6, 7, 8, 9, and 10.

6 Results of Investigations

In the following analysis, we collected a real trace from the private network with duration of 24 h. The remaining flows during network (company) working time are treated as the “normal” traffic. First we studied the HTTP protocol. The HTTP is the most commonly used protocol that supports the Internet. The data are used only

Fig. 5 Power-spectrum density of HTTP traffic for hours 14:00–15:00

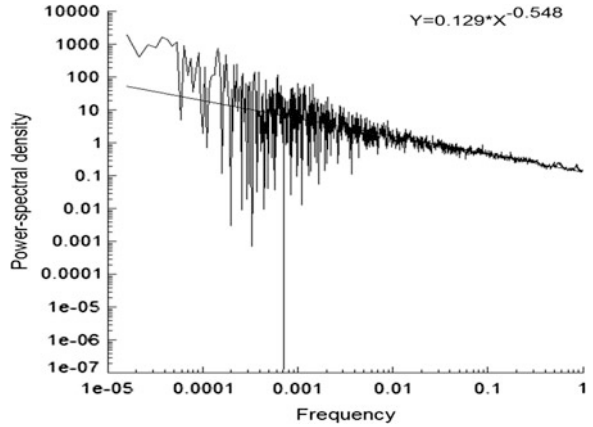


Fig. 6 Power-spectrum density of email packets for hours 14:00–15:00

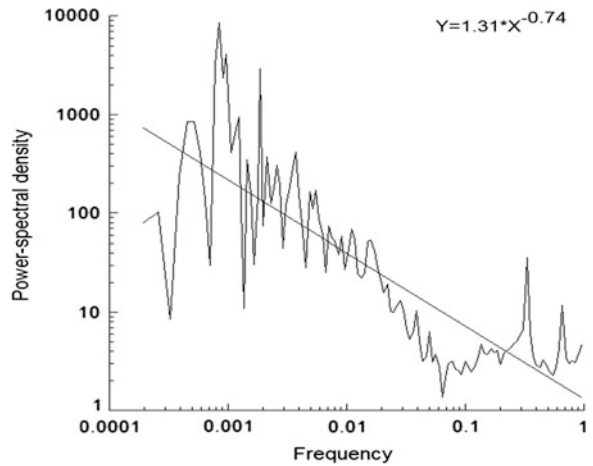


Fig. 7 Power-spectrum density of SSL protocol for hours 14:00–15:00

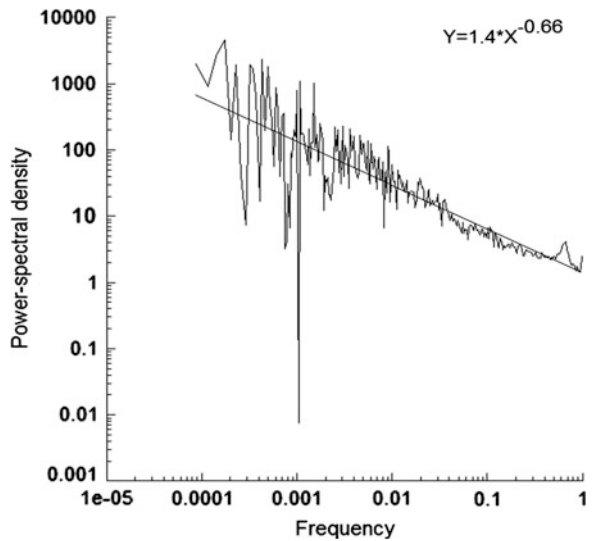


Fig. 8 Power-spectrum density of Unknown traffic for hours 14:00–15:00

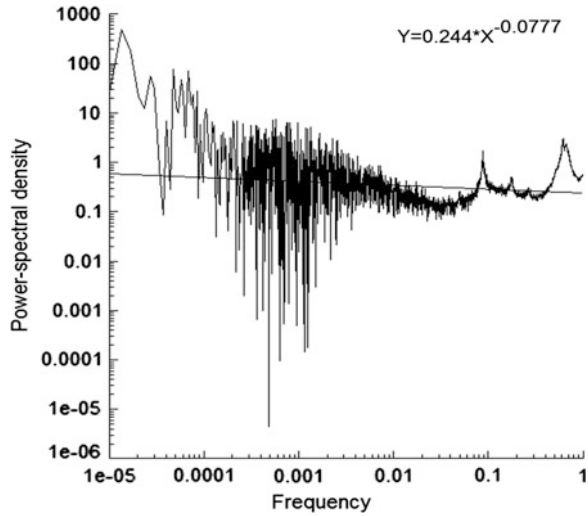
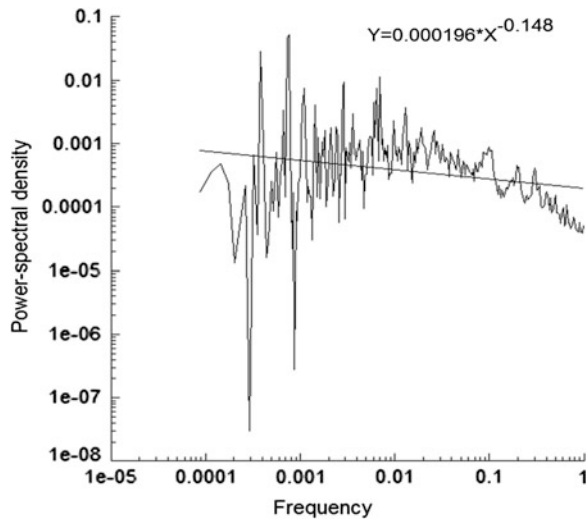


Fig. 9 Power-spectrum density of ICMP packets on hours 14:00–15:00

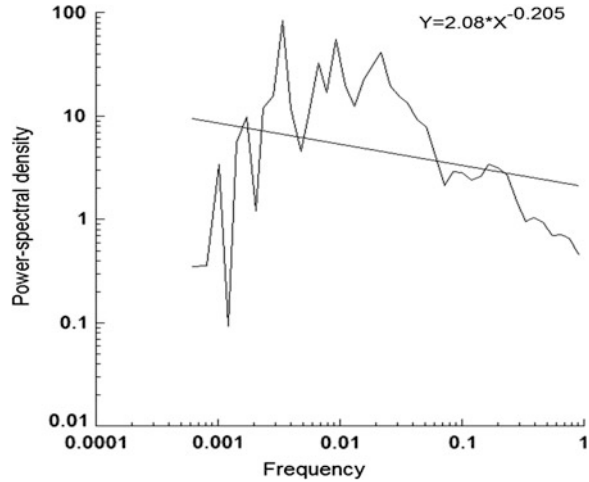


with TCP protocol and the default configuration uses port 80. Each object (e.g. website, video, audio) downloaded from a Web server sends through a single session.

Detailed test results for the HTTP protocol are shown in Table 2. The gray in the table indicates the company’s work time. The average Hurst parameters estimation of HTTP traffic were shown in Fig. 11.

An essential element of communication and business users is the e-mail. Messages that are send may use traffic spam. We send a text messages using standard protocols (POP3 and SMTP) which does not significantly affect network traffic.

Fig. 10 Power-spectrum density of IPv6 traffic for hours 14:00–15:00



However, if the message contains a large attachment, sending and retrieving it may have a significant impact on the operation of the entire network. We analyzed the total traffic generated by the company's employees within 24 h (Fig. 12). With the analyzed samples of traffic packets we estimate the exchange of electronic mail 2.52 % of the total. In total, using protocols responsible for the correspondence sent up to 878.44 MB. The largest increase occurred in the traffic business hours.

The average value of Hurst exponent for e-mail traffic is 0.799, with a maximum value of 0.976 and 0.513 minimum. It can be seen that in the case of reducing the flow in the network (for example, overnight) causes the large fluctuations of Hurst exponent, which tends to a value of 0.5.

The third analyzed service is a Secure Sockets Layer (SSL). SSL technology was originally developed by Netscape Communications to ensure the safety and privacy on the Internet compiled session. Enters data stream encryption. In 1999 the Transport Layer Security (TLS) standard was published, which provides security at the transport layer and solves some of the problems SSL. It is used to encapsulate higher-level applications traffic such as HTTP, Lightweight Directory Access Protocol (LDAP), FTP, SMTP, POP3 and IMAP. It provides authentication and integrity through certificates and digital signatures. Hourly detailed distribution Hurst factor for SSL was shown in Fig. 13.

For SSL average Hurst exponent is 0.721. In the entire traffic range of the test it oscillates in the range of 0.54–0.98. Analysis by Hurst exponent for the flow of packets marked as unknown shows that this traffic does not shows a large variation. Even in the event of fluctuations in the number of packet the results are very similar in each hour. Its nature is self-similar, and the value audited Hurst exponent is in the range of 0.5–0.7.

Programs for the analysis of traffic networks are not always able to recognize all the protocols that exists in the captured files. Groups of such unrecognized packets are described as unknown (Fig. 14). Typically, the data are send by the programs

Table 2 Simulation of the http services

Time clock	Number of packets	The total length of the packets [b]	β	H
7:00–8:00	108370	133943057	-0.575	0.7875
8:00–9:00	100086	121579982	-0.559	0.7795
10:00–11:00	123748	154772543	-0.532	0.766
11:00–12:00	99778	121724775	-0.523	0.7615
12:00–13:00	83546	98390225	-0.593	0.7965
13:00–14:00	78579	41128195	-0.573	0.7865
14:00–15:00	187423	249432486	-0.548	0.774
15:00–16:00	48763	53698411	-0.633	0.8165
16:00–17:00	17940	21589341	-0.743	0.8715
17:00–18:00	6064	3951190	-0.164	0.582
18:00–19:00	8211	6451138	-0.596	0.798
19:00–20:00	10754	9900788	-0.576	0.788
20:00–21:00	17989	18185640	-0.609	0.8045
21:00–22:00	11229	8600740	-0.577	0.7885
22:00–23:00	5430	3136815	-0.327	0.6635
23:00–00:00	4958	3100426	-0.247	0.6235
00:00–1:00	4982	3131088	-0.287	0.6435
1:00–2:00	4933	3086660	-0.178	0.589
2:00–3:00	4990	3151512	-0.021	0.5105
3:00–4:00	4855	2974499	-0.084	0.542
4:00–5:00	4865	3017560	-0.046	0.523
5:00–6:00	21652	27088116	-0.747	0.8735
6:00–7:00	33960	41251848	-0.741	0.8705

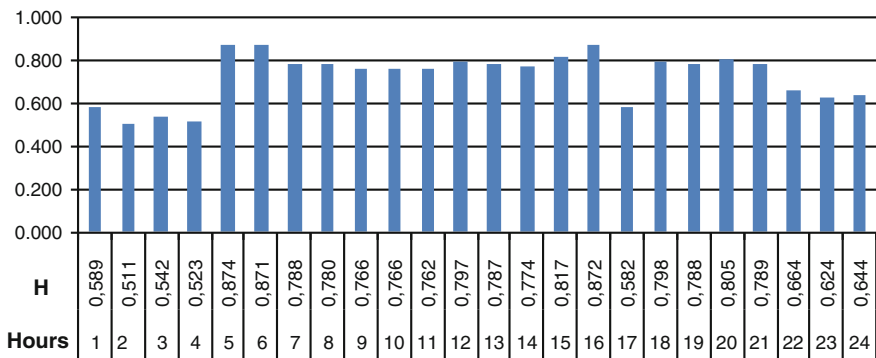


Fig. 11 Hourly detailed distribution of Hurst factor for HTTP protocol

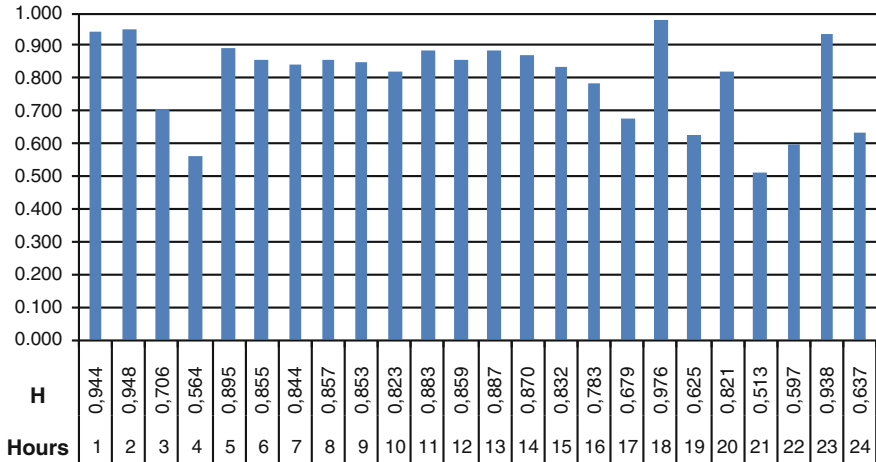


Fig. 12 Hourly detailed distribution of Hurst factor for email service

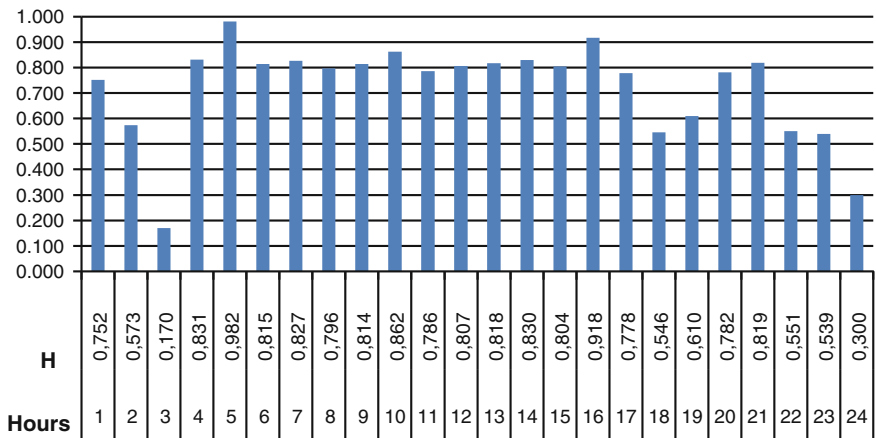


Fig. 13 Hourly detailed distribution of Hurst factor for SSL protocol

that have their copyrights protocols recognized as unknown. But they can also be sent by recognized data protocols, but the port numbers must be changed. In the case of an enterprise network tests packets marked as unknown are the largest share of traffic which is 51.2 % and 17.88 GB of data sent within 24 h.

ICMP test shows high volatility exponent H , in spite of a large number of packets and their length. The average value of Hurst exponent is 0.595 and has a ratio of 0.5–1 (Fig. 15).

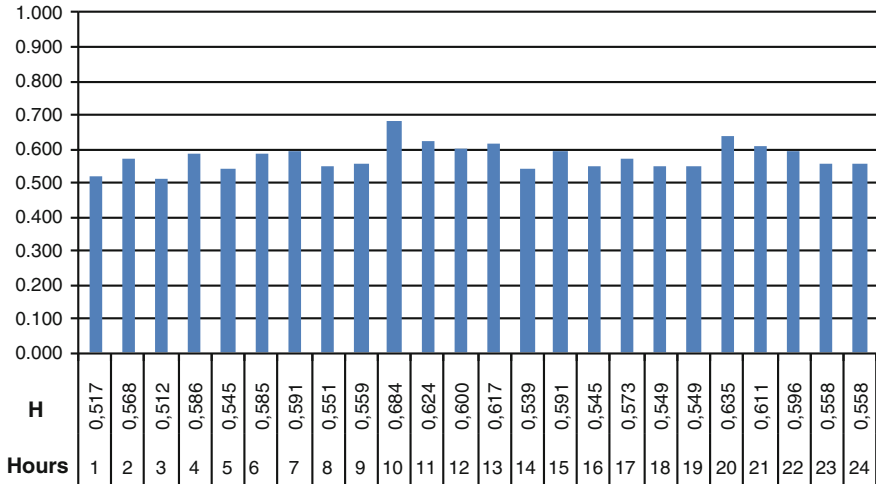


Fig. 14 Hourly detailed distribution of Hurst factor for “Unknown” traffic

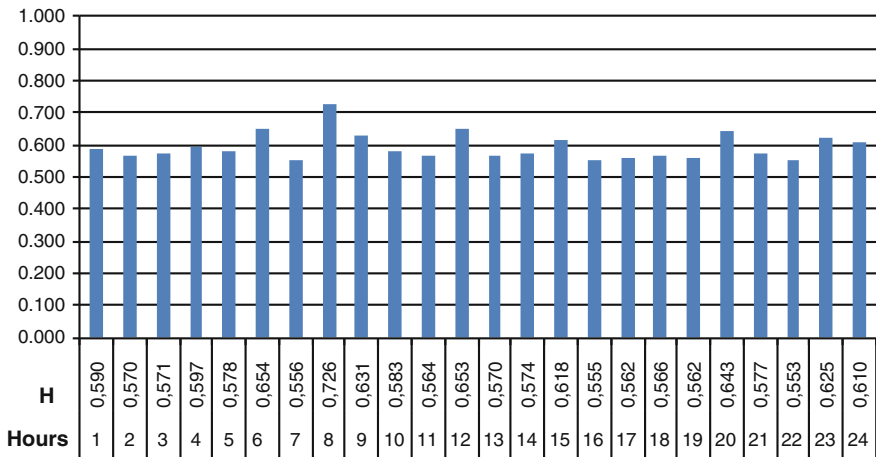


Fig. 15 Hourly detailed distribution of Hurst factor for ICMP protocol

The last analyzed protocol was IPv6. Studies have shown that a new version of the Internet protocol is very good in a LAN environment. Even in the case of large fluctuations in the number of packets, the Hurst exponent does not change much and is stable (Fig. 16).

The analysis for IPv6 traffic presents the calculated value of the Hurst exponent at the level of 0.665 and shows a self-similar nature to the degree of self-similarity in the range of 0.5–1.

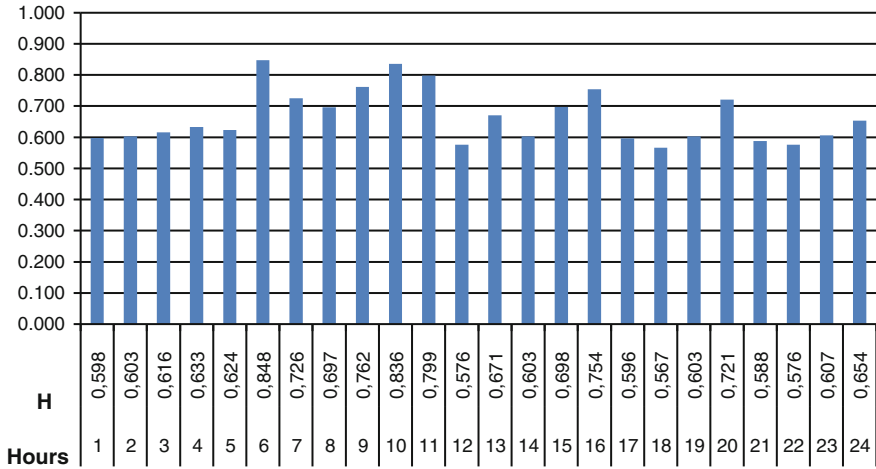


Fig. 16 Hourly detailed distribution of Hurst factor for IPv6 protocol

Table 3 The average values of selected metrics of Network traffic

Traffic metric	The average Hurst value					
	HTTP	Email	SSL	IPsec	ICMP	IPv6
Total H_T	0.729	0.799	0.721	0.577	0.595	0.665
Network busy time H_W	0.791	0.849	0.826	0.589	0.603	0.712
Free time H_F	0.686	0.764	0.646	0.567	0.590	0.631

The obtained results of this experiment show that in contradiction to so far existing belief the traffic can have a self-similar nature. As it can be seen such a property is well visible. Power spectral density can be used not only for proposal of analytical model but also to confirm the validity of proposed model basing on experiment. We compare the Hurst factor estimation of each data set with the Hurst factor of the normal reference model (HT, HW—Table 3).

The analysis of selected protocols shows that network traffic is self-similar. The degree of self-similarity Hurst exponent is specified by the range 0.5–1. The shorter the average length of packet including Hurst exponent tends to 0.5 (white noise).

Any deviation from the mean value demonstrates some anomalies in the operation of the network (equipment failure, collisions) or anomalies in the behavior of users who are responsible for the generation of network traffic (absence of employees, slowness of employees, purposefully running services at night, etc.). The bottom line of the analysis is the value of allowable deviations from the reference value. In this paper we assume a single acceptable percentages, as shown in Table 4.

Table 4 Detailed analysis of variation for HTTP protocol

Hour	HTTP				
	H	H _T -H	% H _T	H _W -H	% H _W
1	0.589	0.140	19.20	0.202	27.71
2	0.511	0.219	29.97	0.281	38.48
3	0.542	0.187	25.65	0.249	34.16
4	0.523	0.206	28.26	0.268	36.76
5	0.874	-0.145	19.82	-0.083	11.32
6	0.871	-0.142	19.41	-0.080	10.91
7	0.788	-0.059	8.02	0.004	0.48
8	0.780	-0.051	6.93	0.012	1.58
9	0.766	-0.037	5.01	0.026	3.50
10	0.766	-0.037	5.08	0.025	3.43
11	0.762	-0.033	4.46	0.030	4.05
12	0.797	-0.068	9.26	-0.005	0.75
13	0.787	-0.058	7.89	0.005	0.62
14	0.774	-0.045	6.17	0.017	2.33
15	0.817	-0.088	12.00	-0.026	3.50
16	0.872	-0.143	19.55	-0.081	11.04
17	0.582	0.147	20.16	0.209	28.67
18	0.798	-0.069	9.47	-0.007	0.96
19	0.788	-0.059	8.09	0.003	0.41
20	0.805	-0.076	10.36	-0.014	1.85
21	0.789	-0.060	8.16	0.003	0.34
22	0.664	0.066	8.98	0.128	17.49
23	0.624	0.106	14.47	0.168	22.98
24	0.644	0.086	11.73	0.148	20.23

The table shows the deviation of the total value and the value in working hours. As we can see in operation time (7:00–18:00) the deviations are of the order of 5–8 %, while outside working hours significantly increased. It can be seen as an anomaly in the operation of the network, but on the other hand the situation is normal because nobody is working after 18:00. Anomaly are increasing factor H during the night, where the network should not work. This may indicate a network intrusion attempts, or other hazards. Aberrance for other traffic metrics are shown in Table 5.

Percentage changes in the Hurst parameter in relation to the reference values in the range of 24 h is shown in Fig. 17.

Examination of the results shows high degree of H parameter stability during operation of the company. Approximately at 10 am we can see a significant increase in the metric labeled Unknown. This can be data sent by well-known protocols, but with changed by the administrator port numbers.

Table 5 Variation for selected traffic metrics

Hours	Email		Unknown		ICMP	
	% H _T	% H _W	% H _T	% H _W	% H _T	% H _W
1	18.15	11.89	10.49	12.56	0.84	2.18
2	18.65	12.39	1.56	3.64	4.29	5.63
3	11.64	17.90	11.27	13.34	4.03	5.38
4	29.47	35.73	1.56	0.52	0.25	1.09
5	12.02	5.76	5.57	7.65	2.86	4.20
6	7.01	0.75	1.30	0.78	9.92	8.57
7	5.57	0.69	2.34	0.26	6.55	7.90
8	7.20	0.94	4.59	6.67	21.93	20.59
9	6.70	0.44	3.12	5.20	6.05	4.71
10	2.94	3.32	18.46	16.38	2.02	3.36
11	10.45	4.19	8.06	5.98	5.29	6.64
12	7.45	1.19	3.99	1.91	9.75	8.40
13	11.01	4.76	6.85	4.77	4.20	5.55
14	8.89	2.63	6.61	8.69	3.53	4.87
15	4.07	2.19	2.43	0.35	3.87	2.52
16	2.07	8.32	5.49	7.57	6.81	8.15
17	15.08	21.34	0.69	2.77	5.63	6.97
18	22.15	15.89	4.82	6.90	4.96	6.30
19	21.84	28.10	4.90	6.98	5.63	6.97
20	2.75	3.50	9.97	7.89	8.07	6.72
21	35.79	42.05	5.81	3.73	3.03	4.37
22	25.34	37.36	3.29	1.21	7.14	8.49
23	17.40	38.74	3.38	5.46	5.04	3.70
24	20.34	68.71	3.38	5.46	2.52	1.18

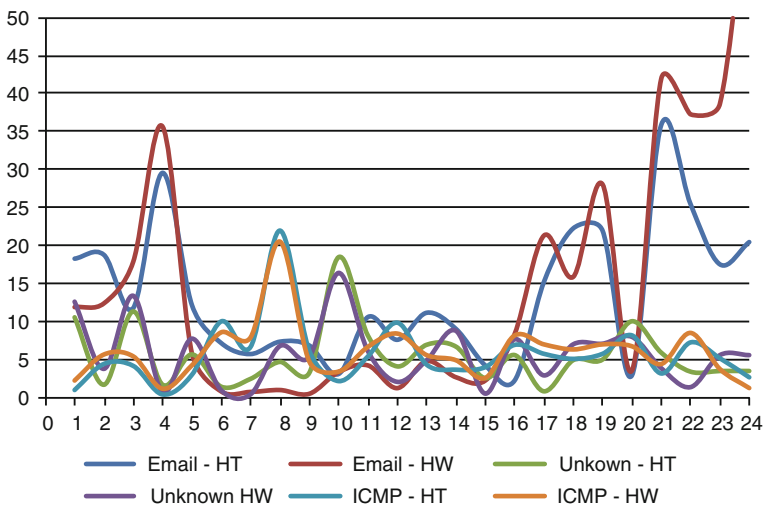


Fig. 17 Percentage changes of the Hurst factor in 24 h period for selected services

7 Conclusion

The objective of presented research was to investigate the potential of using efficient classifier based on approximation function to estimate the Hurst parameter for network traffic self-similarity measurements. The results confirmed that the analyzed traffic has a self-similar nature to the degree of self-similarity in the range of 0.5–1 and can be used to detect the anomaly-behaved traffic efficiently. The parameter H is larger when network utilization is higher. The degree of self-similarity is dependent of the volume of traffic and the type of service. In the case of minor traffic approaching the value of the exponent equal to 0.5 (white noise), is characterized by the complete randomness and lack of correlation between packets. By improving the capability of predicting impending network failures, it is possible to reduce network downtime and increase network reliability. The results of analytical considerations and experiment shows that self-similarity factor can be successfully used in the computer network traffic analysis, and eventually lead to more efficient methods for both failure and intrusion detection.

The future work is to define some parameters for differentiate abnormal communities from normal communities. In addition, we simulate some specific types of network anomalies in a laboratory environment and trace them.

References

1. Strzałka B, Mazurek M, Strzałka D (2012) Queue performance in presence of long-range dependencies—an empirical study. *Int J Inf Sci* 2(4):47–53
2. Dymora P, Mazurek M, Strzałka D (2013) Computer network traffic analysis with the use of statistical self-similarity factor. *Ann UMCS Informatica* 13(2):69–81
3. Yan R, Wang Y (2012) Hurst parameter for security evaluation of LAN traffic. *Inf Technol J* 11(20):269–275
4. Idris MY, Abdullah AH, Maarof MA (2005) Self-similarity measurement methods for network traffic anomaly detection, In: *Proceedings of the postgraduate annual research seminar*, pp 244–248
5. Dymora P, Mazurek M, Strzałka D (2012) Long-range dependencies in memory pages reads during man-compute system interaction. *Ann UMCS Informatica* XII 2:49–58
6. Dymora P, Mazurek M, Strzałka D (2011) Statistical mechanics of memory pages reads during man-computer system interaction. *Metody Informatyki Stosowanej* 1(26):15–21
7. Dymora P, Mazurek M, Strzałka D (2012) Influence of batch structure on cluster computing performance—complex systems approach. *Ann UMCS Informatica* XII 1:57–66
8. Dietmar S (1988) Algorithms for random fractals, chapter 2 of the science of fractal images by Barnsley et al, Springer, New York
9. Cai J, Liu WX (2013) A new Method of detecting network traffic anomalies. In: *Proceedings of the 2nd international conference on computer science and electronics engineering*, pp 2800–2803
10. Thottan M, Ji Ch (2003) Anomaly detection in IP networks. *IEEE Trans Signal Process* 51 (8):2191–2204

Analysis of Static Characteristics of a Switched Reluctance Motor

B. Jankowski, D. Kapelski, M. Karbowski, M. Przybylski
and B. Ślusarek

Abstract Operating parameters of electric motors depend on a type of a magnetic circuit. In this paper, we consider an influence of the type of magnetic circuit on static parameters of switched reluctance motor with power of 450 W. In the research we considered constructions of magnetic circuits made respectively of laminated steel, Fe-based composite and mixed structures. A static electromagnetic torque as function of an angular position of a rotor has been computed based on a finite element method. Experimental measurements have been conducted in order to confirm the result of computations.

1 Introduction

Switched Reluctance Motor (SRM), in recent years, are increasingly used in a broad range of applications because of its features. Among many advantages of the SRM should be mentioned, first of all, a robust construction, a low cost in mass production, reduced maintenance requirements, fault tolerance, a high efficiency and a large torque output over very wide speed range. Furthermore these motors do not need permanent magnets with high price.

B. Jankowski (✉) · D. Kapelski · M. Karbowski · M. Przybylski · B. Ślusarek
Department of Magnetic Materials, Tele and Radio Research Institute, Warsaw, Poland
e-mail: bartosz.jankowski@itr.org.pl

D. Kapelski
e-mail: dariusz.kapelski@itr.org.pl

M. Karbowski
e-mail: marcin.karbowski@itr.org.pl

M. Przybylski
e-mail: marek.przybylski@itr.org.pl

B. Ślusarek
e-mail: barbara.slusarek@itr.org.pl

Switched reluctance motors are more likely to be used in electric and hybrid-electric vehicles [1, 2]. They are also applied in Neptune washing machines produced by Maytag company.

The expanding interest in the introduction of Fe-based composite materials, also called the Soft Magnetic Composite (SMC), in electrical devices, such as electrical motors, is in obvious ways connected with their properties. The principle feature of these materials is that iron particles are insulated by a thin organic or inorganic coating. SMC offers several advantages over laminated steel sheet, e.g. isotropic magnetic properties, the opportunity to tailor their physical properties, very low eddy current loss, relatively high resistivity, high magnetic permeability [3].

Fe-based composite materials are used in the manufacture of electrical devices owing to their physical properties. The most common use of these materials is in various electrical motors, e.g. a high speed permanent magnet motor [4], a synchronous motor [5], an axial-flux permanent magnet synchronous motor [6], a claw pole permanent magnet motor [7]. Furthermore, soft magnetic composites were used in an electromagnetic actuator [8].

An application of soft magnetic composites in switched reluctance motors can be found in scientific literature [9]. Authors in work ([10] *in Polish*) reported comparison of two motors in which the magnetic circuit have been made of the classical laminated silicon steel sheet and Fe-based composite materials. Results confirmed that it is possible to manufacture these kind of motors from magnetic composites. Moreover, it has been presented that the motor made of magnetic composite has a higher efficient compared to the motor with laminated core, especially at high frequencies of magnetic flux in the motor's magnetic circuit. Nonetheless, it seems that it is necessary to undertake further work in order to describe differences and to determine limits of motors.

2 Soft Magnetic Composites

Soft Magnetic Composite (SMC) consist generally of ferromagnetic particles distributed in a matrix of binding agent. Metal powder is produced by atomization techniques; a stream of molten metal is atomized by inert gas or water under high pressure, leading to formation of fine liquid metal droplets which then solidify resulting in fine powder particles. The nature of impact media determines shape of powder particles. Particles of iron powder called Somaloy produced by Swedish company Höganäs for soft magnetic composites are covered chemically by thin inorganic insulation layer-phosphate glass with a thickness of a few nanometers.

Magnetic composites are prepared by compression molding technique; a die is filled with magnetic powder and it is compacted. Then the 'green compact' is cured in a furnace at melting temperature of binding agent. In the case of compression molding techniques frequently an air atmosphere is used during the curing.

Fig. 1 Magnetization curves of Somaloy 700 and Somaloy 700 HR

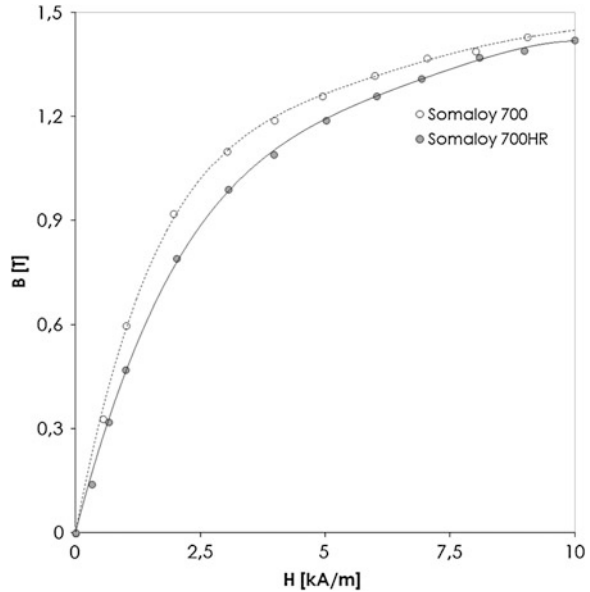


Figure 1 shows magnetization curves of composites made of Somaloy 700 and Somaloy 700 HR (high resistivity) powders manufactured and measured in Tele and Radio Research Institute.

3 Field Model of Switched Reluctance Motor

The structure of the considered motor is shown in Fig. 2. The stator and rotor have respectively 12 and 8 poles. The three-phase concentrated winding has been applied. Each phase consists four coils. Configurations of magnetic circuits of motors and windings are presented in Table 1.

In the paper field models of SRM have been elaborated in FEMM 4.2 software environment. Elaborated models allows us to compute steady state operation. The model is based on the Eq. (1)

$$\nabla \times \left(\frac{1}{\mu(\mathbf{B})} \nabla \times \mathbf{A} \right) = \mathbf{J} \tag{1}$$

where: $\mu(B)$ is the magnetic permeability depended on magnetic induction \mathbf{B} , \mathbf{A} is magnetic vector potential, \mathbf{J} is the current density in windings of a SRM motor. Electromagnetic torque was calculated by an usage of the function torque via weighted stress tensor.

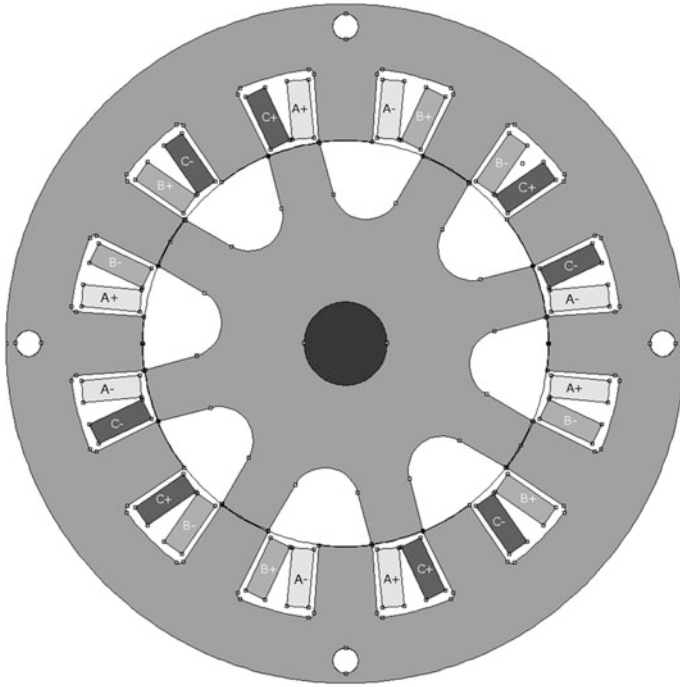


Fig. 2 The structure of switched reluctance motor

4 Experimental Details

This article deals with comparison of measurements of SRM motor with different magnetic circuits. As a motor it was chosen switched reluctance motor produced by Emerson Electric Company model H55BMBJL.

Laboratory test include following models of motors with a different configuration:

- (a) stator and rotor made of the Fe-based composite material,
- (b) stator and rotor made of the laminated silicon steel sheet,
- (c) stator made of the Fe-based composite material and rotor made of the laminated silicon steel sheet,
- (d) stator made of the laminated silicon steel sheet and rotor made of the Fe-based composite material.

The stator and rotor made of the laminated silicon steel sheet come from a commercially available motor H55BMBJL with power of 450 W and rotational speed of 14,000 rpm. In turn, the stator and rotor made of the Fe-based composite material have been manufactured in Tele and Radio Research Institute. Somaloy 700 and Somaloy 700 HR powders have been used to produce an intermediate

Table 1 Parameter of motors and their kinds of stators and rotors

Outer stator's diameter	140 mm
Inner stator's diameter	83.5 mm
Outer rotor's diameter	83 mm
Back iron thickness	13 mm
Length of the air gap	0.25 mm
Axial length of magnetic circuit	46.6 mm
Number of phases	3
Number of stator poles	12
Number of rotor poles	8
Stator's materials	soft magnetic composite—Somaloy 700
Configuration of phases	4 coils in series
Number of turns of a coil	140
Diameter of copper wires	0.60 mm
Resistance of a phase	6.20 Ω
Rotor's material	soft magnetic composite—Somaloy 700 HR
Stator's materials	Non oriented electrotechnical steel
Configuration of phase	2 coils in series connected parallel to 2 coils in series
Number of turns of a coil	170
Diameter of copper wires	0.56 mm
Resistance of a phase	2.16 Ω
Rotor's material	Non oriented electrotechnical steel

product (cylindrical parts and ring segments). Components of motor with given shape have been obtained using an electrical discharge machining (EDS) and a traditional machining. Then, components of motor have been glued using two-component epoxy adhesive Araldite 2014-1 from Huntsman brand.

Basic parameters of the switched reluctance motor are summarized in Table 1, whereas, the stator and rotor made of soft magnetic composites are presented in Fig. 3.

The programmable DC supply to restrict currents in the motor windings has been used to produce electromagnetic torque. Torque characteristics have been conducted for 1-phase control mode ($i_a \neq 0$, $i_b = 0$, $i_c = 0$) and different values of current i_a .

Static torque has been measured using torque sensor MT-3Nm. The AC motor with gearbox generates the rotational speed of 0.8 rpm. The measured data has been transferred to PC using a data acquisition system MW 2006—3 s. Torque sensor and data acquisition system were produced by Pracowania Elektroniki—R. Pomianowski Company.

Fig. 3 The stator and rotor of the switched reluctance motor made of soft magnetic composites



5 Results and Discussion

5.1 Comparison of Experimental Results with Computational Simulations of Switched Reluctance Motor Made of Soft Magnetic Composites

Figures 4, 5 and 6 show some results of simulations conducted for switched reluctance motors with a magnetic circuit made of soft magnetic composites in FEMM 4.2 software.

Figure 4 shows distribution of magnetic flux density in the motor at current in phase A equal 1.7 A. Rotor and stator position is set to be 15° between them. In this position a motor produces maximum electromagnetic torque which derive from computations.

As it can be seen from map of magnetic induction (Fig. 4) in the motor in stator's core average induction is about only 60 mT whereas in stator's pole induction about 200 mT at the time of maximum torque (angle between stator and rotor poles 15°). Magnetic induction in rotor's pole is about 150 mT for the same moment of time. This situation can indicate that cross section of magnetic circuits are too large for these inductions. However during rotation of rotor with nominal rotational speed equal 14,000 revolutions/min frequency of stator's currents is calculated from Eq. (2)

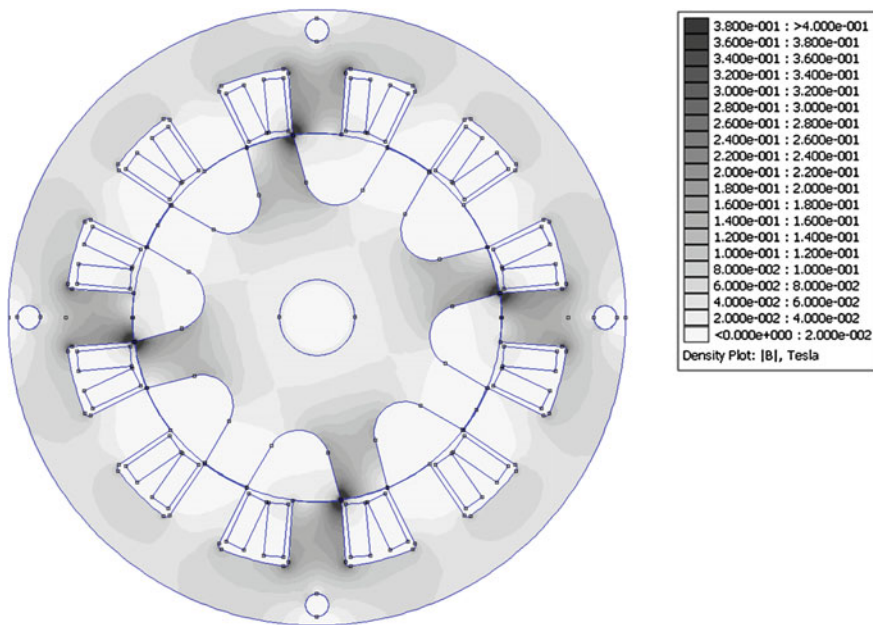
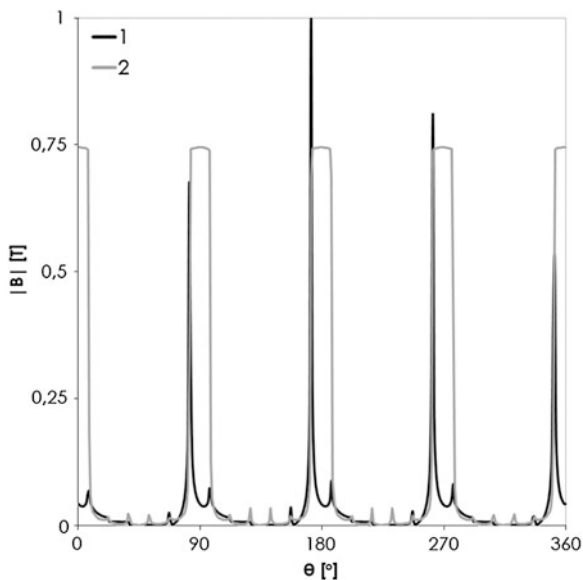


Fig. 4 Magnetic flux density in the motor at the current in phase A $I = 1.7$ A

Fig. 5 Distribution of magnetic flux density in the air gap of motor at the current 1.7 A, 1—poles of stator and rotor displaced by an angle of 15° , 2—poles of stator and rotor aligned



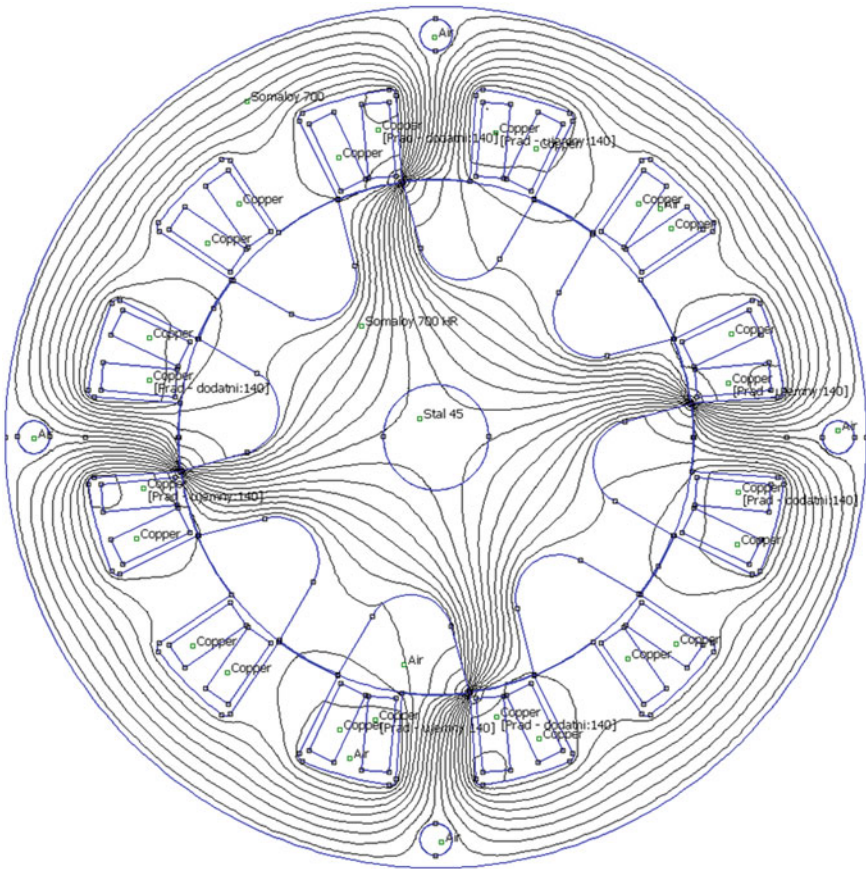


Fig. 6 Distribution of magnetic flux in the switched reluctance motor at the current in phase A $I = 1.7 \text{ A}$

$$f_s = \frac{\omega_{mech}}{2\pi} \cdot P_r \tag{2}$$

where ω_{mech} is angular speed of rotor, P_r is number of poles of a rotor.

Frequency of stator’s current is equal 1,867 Hz and frequency of magnetic flux density in the stator is $f_{flux} = m \cdot f_s = 3 \cdot 1,867 = 5,601 \text{ Hz}$ (m -number of phases of the motor). That’s why the magnetic core loss can be quite large because of frequency of flux density.

During work of a motor it is assumed that the switched reluctance motor is supplied by three phase system. Sequence of supplying currents is as following: phase A for 1/3 of a current period, then phase B for 1/3 of a current period, then phase C for 1/3 of a current period and again phase A and so on. Supply currents are

unipolar and always flow in the same direction. Figure 5 shows distribution of magnetic flux density in the air gap at the current in phase A equal 1.7 A.

Figure 6 shows distribution of magnetic flux in the motor at the current of 1.7 A in phase A.

Experimental and computational results are very similar in shape (Fig. 7). It is confirmed by studies of the higher harmonic content (Fig. 8). Fundamental harmonics have almost the same values, the difference between them is less than 3.5 %. In turn, the second harmonic for computation is almost three times higher than this harmonic for experimental results.

Results in Table 2 also confirmed the concordance between measurements and computations. Average and RMS electromagnetic torque are very similar. Visible are only differences between maximum values of electromagnetic torque.

The electromagnetic torque waveform have been computed in order to determine an influence of a relative magnetic permeability on their shape. Computations have been conducted assuming a constant value of the magnetic permeability—linear relationship between a magnetic flux density B and a magnetic field strength H . Results of these computations are depicted in Fig. 9. Comparison is based on harmonic analysis (Fig. 10). Obviously, with the increase in magnetic permeability also increases the fundamental harmonic. Furthermore, second and fourth harmonic increase significantly, at the same time, third harmonic decrease. With the increase of the magnetic permeability the waveform of electromagnetic torque changes from triangular to rectangular.

Fig. 7 Comparison of measured and computed waveform of electromagnetic torque for currents equal: 1.0, 1.25 and 1.70 A

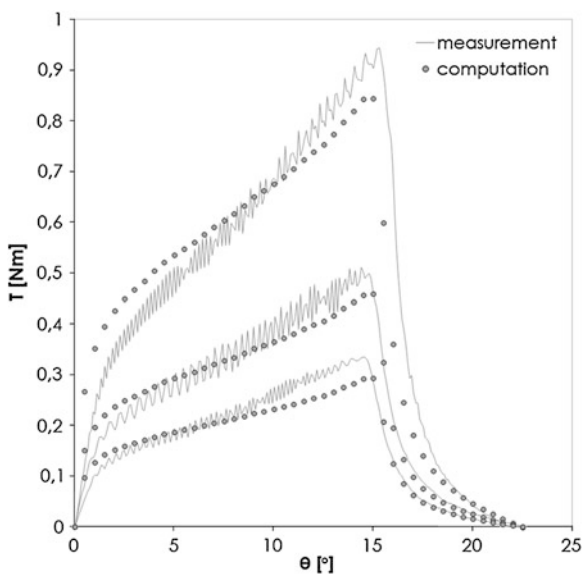


Fig. 8 Comparison of measured and computed higher harmonic distribution of electromagnetic torque at current 1.7 A

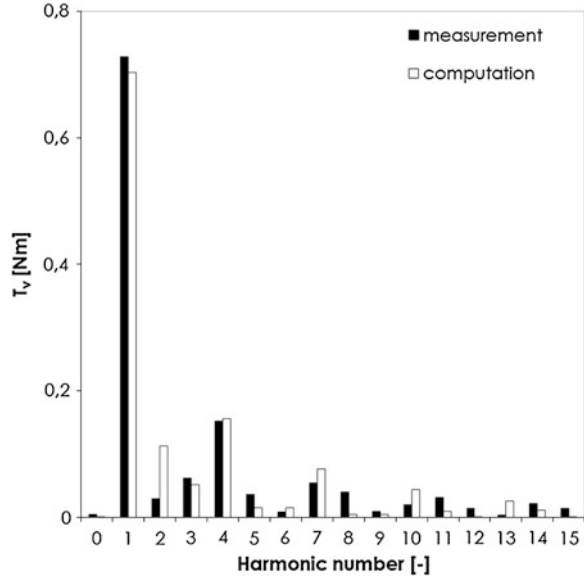


Table 2 Comparison of electromagnetic torque at different currents for SMC stator and SMC rotor

	I = 1 A	I = 1.25 A	I = 1.70 A
<i>Maximum electromagnetic torque</i>			
Measured	0.335	0.511	0.944
Calculated	0.294	0.459	0.846
<i>Average electromagnetic torque</i>			
Measured	0.162	0.250	0.450
Calculated	0.155	0.242	0.445
<i>Root mean square electromagnetic torque</i>			
Measured	0.193	0.297	0.533
Calculated	0.183	0.287	0.522

5.2 Comparison of Experimental Results of Motors with Different Structures

Comparison between laminated and powder magnetic circuits of motors were conducted by assuming the same current linkages Θ . This assumption enables a comparison of torques values and characteristics of switched reluctance motors with different combinations of stator's and rotor's magnetic materials.

Fig. 9 Computed waveform of electromagnetic torque at the $\Theta = 980$ A for relative magnetic permeability equal: 100...2,000

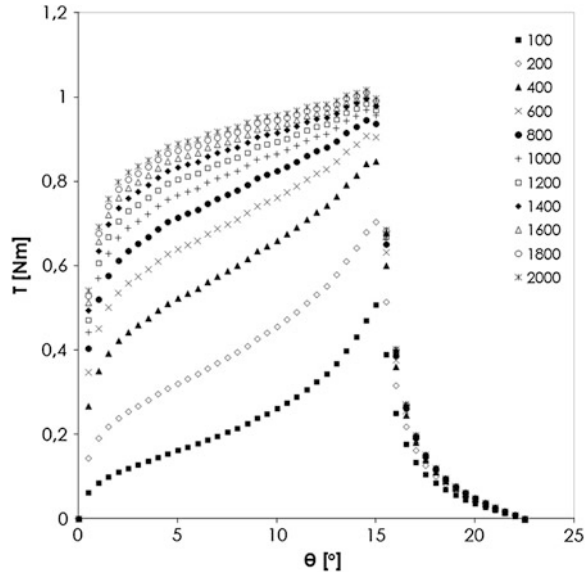
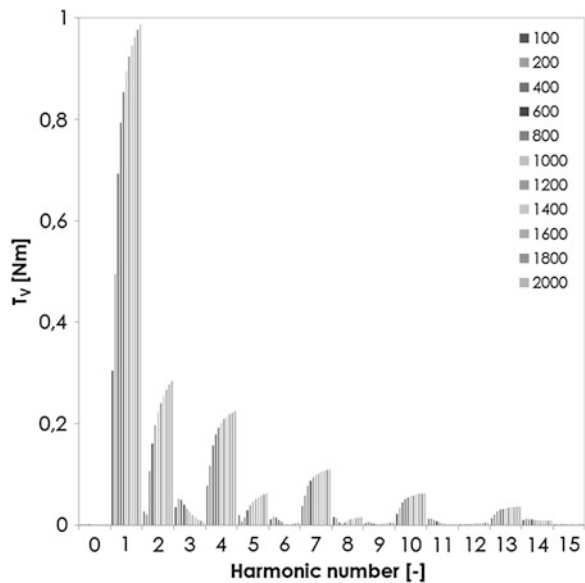
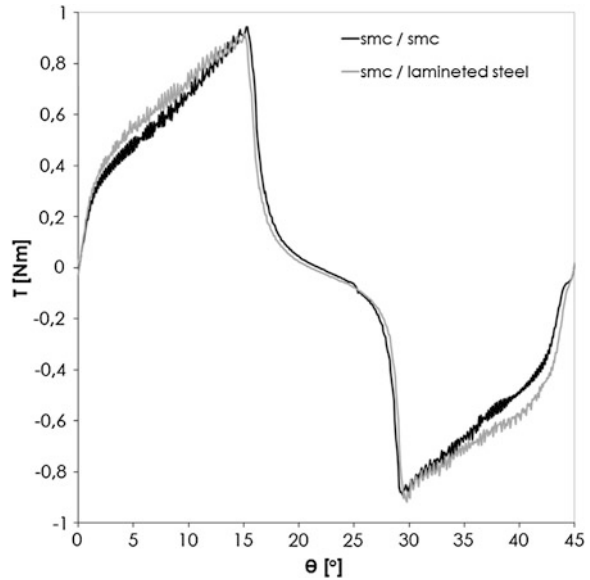


Fig. 10 Comparison of harmonic contents of electromagnetic torques at the $\Theta = 980$ A relative magnetic permeability equal: 100... 2,000



In the first part, the investigation focused on two configurations. First, under consideration it has been the motor with magnetic circuits made entirely of the soft magnetic composite (SMC /SMC). The second configuration under consideration has been the motor with the stator made of the soft magnetic composites and rotor made of the laminated silicon steel sheet (SMC /laminated steel).

Fig. 11 Measured characteristics of two configurations of switched reluctance motors at the current in phase A $I = 1.7$ A



The electromagnetic torque generated by considered motors is very similar in shape as shown in Fig. 11. Presented waveforms, measured at 1,700 mA, have different root mean square (RMS) and average values. The construction made entirely of the soft magnetic composites has the RMS value of the torque less about 4 % and the average less about 4.5 % than the mixed construction. In turn, the difference between the maximum torque in both constructions does not exceed value of 3 %.

Characteristics of root mean square (RMS) and average rectified values (AVG) of electromagnetic torque for different configurations of motors is depicted in Fig. 12.

In the second part of the investigation authors focused on two following configuration: the motor with magnetic circuit made entirely of the laminated steel (laminated steel /laminated steel) and the motor with the stator made of the laminated steel and the rotor made of the soft magnetic composites (laminated steel / SMC).

The electromagnetic torque generated by considered motors is very similar in shape as is shown in Fig. 13. Presented waveforms, measured at 2,500 mA, have different RMS and average values. The construction made entirely of laminated steel has the RMS value of the torque about 1.4 % higher and the average higher about 1.5 % than mixed construction.

Characteristics of root mean square (RMS) and average rectified values (AVG) of electromagnetic torque for different configurations of motors is depicted in Fig. 14.

The distribution of higher harmonics in waveforms of electromagnetic torque of four motors is depicted in Fig. 15. Decisive contribution has following harmonics:

Fig. 12 RMS and AVG characteristics of torque as a function of current linkages for SMC stator and SMC and laminated rotors

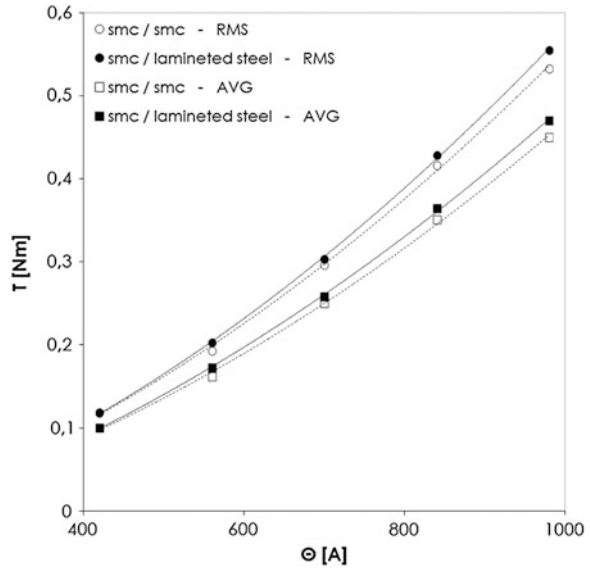
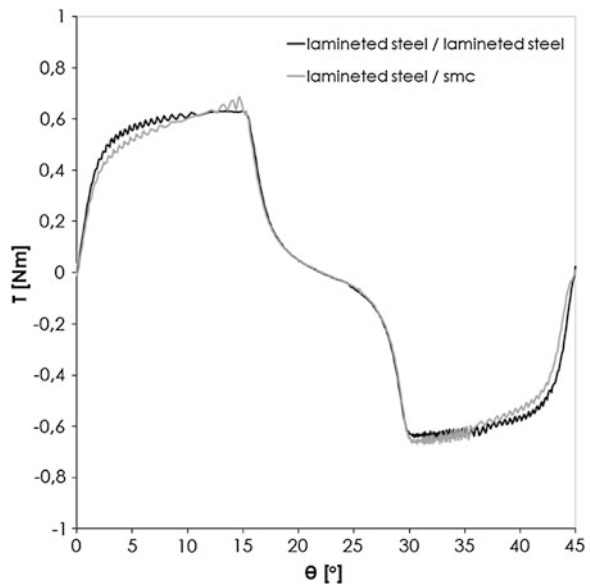


Fig. 13 Measured characteristics of two configurations of switched reluctance motors at the current in phase A $I = 2.5$ A



1, 2, 3, 4, 7 and 8. In case of the motor with magnetic circuits made entirely of the soft magnetic composite (SMC /SMC) are decisive, except the fundamental harmonic, following harmonics: third and fourth. In the motor with magnetic circuits made entirely of the laminated steel (laminated steel /laminated steel), the second harmonic is decisive. In constructions with the stator made of the soft magnetic

Fig. 14 RMS and AVG characteristics of torque as a function of current linkages for laminated stator and laminated and SMC rotors

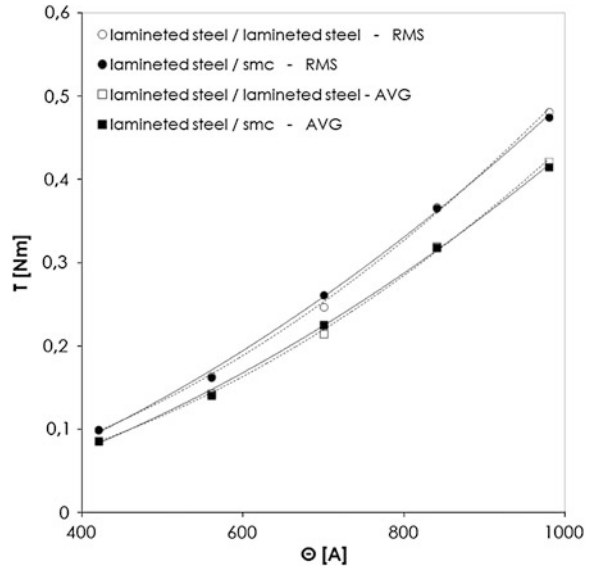
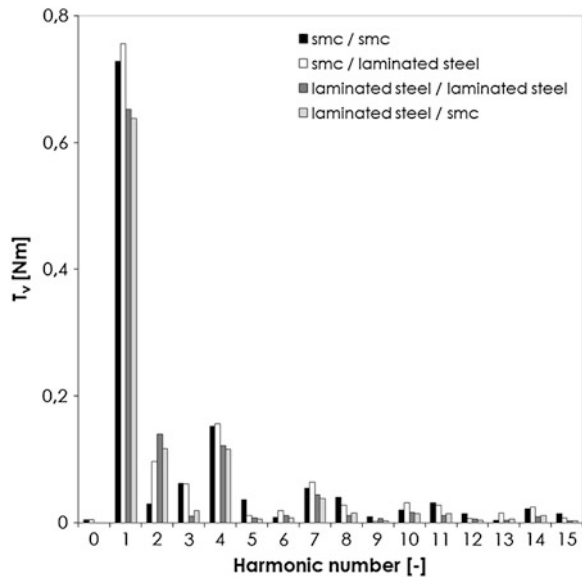


Fig. 15 Comparison of harmonic contents of electromagnetic torques at the $\Theta = 980$ A for all configurations of magnetic circuits



composite visible is constant component of electromagnetic torque. The value of these components is about 0.7 % of relative to the fundamental harmonic. Occurrence of this component is likely related to the practical realization of the magnetic circuit.

6 Conclusion

The research showed that it is possible to build switched reluctance motors with soft magnetic composite magnetic circuit.

The research also shows that soft magnetic composite material is not worse magnetically in static measurements than laminated core. The switched reluctance motor with a magnetic circuit made entirely of soft magnetic composites generates the RMS torque of 0.53 Nm. The motor with the same dimensions but made of a laminated steel generates the RMS torque of 0.48 Nm (assuming the same current linkages). Laminations have better magnetic properties than iron soft magnetic composites but their processing such as cutting, connecting in core significantly decreases magnetic properties. That is why these two kinds of magnetic materials as magnetic circuits are almost the same.

Experimental results and computational simulations showed that the magnetic permeability of the magnetic circuits influences on the shape of electromagnetic torque waveform.

It appears that it is possible to improve parameters of the switched reluctance motor made of soft magnetic composites by applying the compaction in one step of the magnetic circuit instead of gluing it with several elements. This will prevent the occurrence of additional air gap in the magnetic circuit.

Acknowledgments The work has been supported by National Centre for Research and Development, Poland, under Grant no. N R15 0058 06/2009.

References

1. Rahman KM, Schulz SE (2001) Design of high-efficiency and high-torque-density switched reluctance motor for vehicle propulsion. *IEEE Trans Ind Appl* 38:1500–1507
2. Fahimi B, Emadi A, Sepe RB (2004) A switched reluctance machine-based starter/alternator for more electric cars. *IEEE Trans Energy Convers* 19:116–124
3. Shokrollahi H, Janghorban K (2007) Soft magnetic composite materials (SMCs). *J Mater Process Technol* 189:1–12
4. Wojciechowski RM, Jedryczka C, Lukaszewicz P, Kapelski D (2012) Analysis of high speed permanent magnet motor with powder core material. *COMPEL Int J Comput Math Electr Electron Eng* 31:1528–1540
5. Hamlera A, Goricana V, Sustarsic B, Sircc A (2006) The use of soft magnetic composite materials in synchronous electric motor. *J Magn Magn Mater* 304:816–819
6. Di Stefano R, Marignetti F (2012) Electromagnetic analysis of axial-flux permanent magnet synchronous machines with fractional windings with experimental validation. *IEEE Trans Indus Electron* 59:2573–2582
7. Guo Y, Zhu J, Dorrell DG (2009) Design and analysis of a claw pole permanent magnet motor with molded soft magnetic composite core. *IEEE Trans Indus Electron* 45:4582–4585
8. Jack A, Mecrow B, Atkinson G (2009) Current developments in soft magnetic composites for electromagnetic actuators. *Sensor Lett* 7:369–373

9. Vijayakumar K, Karthikeyan R, Rajkumar S, Arumugam R (2008) An investigation into vibration in high speed switched reluctance motor with soft magnetic composite material. In: Proceedings of the IEEE region 10 colloquium and third international conference on industrial and information systems 1–2, Kharagpur, India, pp 330–333
10. Ślusarek B, Jankowski B, Kapelski D, Karbowski M, Przybylski M, Łukaszewicz P (2012) Influence of the application of the powder magnetic core on the performance of the low-power electric motor). In: XV Jubileuszowe Sympozjum “Podstawowe Problemy Energoelektroniki, Elektrotechniki i Mechatroniki” PPEEm, Gliwice, Poland, pp 189–192

Robust Integral Sliding Mode Tracking Control of a Servo Drives with Reference Trajectory Generator

Stefan Brock

Abstract In the paper robust control of speed and position of servo drives is analysed. A modified approach to the design of a robust speed and position controller is proposed, in which the trajectory of motion is invariant to load torque and system parameter variations. The proposed controller structure consists of a reference trajectory generator and a sliding mode controller with output integrator, operating with the reference model. Simple structure of reference signal generator is based on discrete model of an ideal drive system with cascade control. The obtained experimental results verify the proposed method and prove good quality of control.

1 Introduction

High dynamic performance of servomotor drives is required in modern automatically controlled machines to achieve high quality and high productivity in industrial applications. Robustness against parameter variation and load disturbances in accurate trajectory tracking system is a prerequisite to fulfil these requirements. One of the methods to achieve robustness is sliding mode control (SMC). However, SMC creates some problems in practical applications due to chattering effects, such as high frequency oscillation of motor torque, additional mechanical stresses and noise during operation [1].

Many solutions have been proposed to circumvent the chattering problem. The most common is the boundary layer method, which introduces a continuous approximation of the switching characteristic. Also the replace of the saturation function by a linear one, without a limiter, called continuous SMC, is reported. One of the methods that ensures a significant reduction of chattering is based on the

S. Brock (✉)

Institute of Control and Information Engineering, Poznan University
of Technology, Poznan, Poland
e-mail: Stefan.Brock@put.poznan.pl

introduction of an output integral block to SMC. The using of integrator leads to a reduction of both the steady state error and the amplitude of high frequency oscillations in the controller output signal [2]. Similar chattering reduction can be obtained by introducing a first order low-pass output filter instead of an integrator.

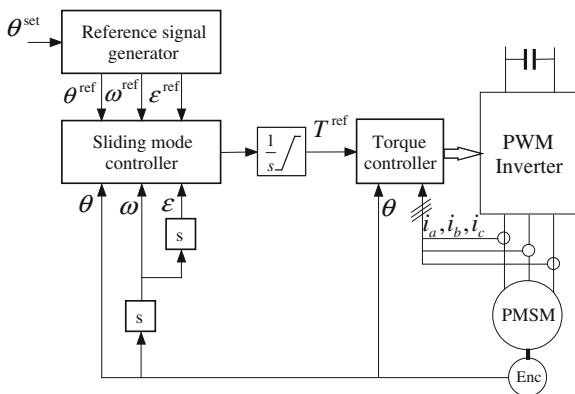
In industrial robots and machine tools it is desired that their speed and acceleration are constrained in certain values for safety, while they should work as fast as possible from the point of working efficiency. Furthermore, from restrictions on hardware, especially maximal current limit, drives cannot speed-up faster than certain acceleration. If step reference is given for such actual systems, high dynamic controller, which gives good performance in some senses, cannot be used for the systems because of safety. The step signal is an unachievable trajectory, therefore, wind-up and overshoot may occur, furthermore, the system becomes unstable in the worst cases [3–5].

A generation of the optimal trajectory for any reference signal is difficult. The minimum time motion of a servo drive along specified path was extensively studied by many researchers. Typical the task can be reduces into calculating the maximum and minimum acceleration along the trajectory in each step, and to find the switching points. Recently developed methods made it possible to compute the maximum and minimum acceleration on-line, but switching points needs off-line computation. This paper presents the original reference signal generator, working on-line, without pre-calculation.

2 Reference Signal Generator

In the paper, a tracking control system of a servo drive shown in Fig. 1 is analyzed. In such a system, a step change of position set values (θ^{set}) can be applied to its input. The response to such an input function should be the drive motion of aperiodic character (without overshoot) with a limited value of acceleration and its

Fig. 1 Block diagram of tracking control system



derivative (jerk) and without the steady state control error. While designing motion trajectories one needs to take into account the existing and introduced limitations as well as the expected range of parameter and load torque variation. This is usually solved by applying a reference signal generator, which produces more or less ideal reference trajectories. The control system must follow the references.

A typical one-axis reference trajectory generator set is shown in Fig. 2. Based on the initial values of position, velocity and acceleration, and given set position switching times for each interval are determined. This part of the calculation is carried out on demand, when it is read the position setpoint change. During motion, on the basis of look up table a reference jerk is determined on-line. The jerk signal is integrated three times, and thus are calculated the reference acceleration, the reference speed and the reference position. Determined reference signals do not exceed the taken limits value. In this way, as quickly as possible the desired position is reached. The disadvantage of this method is the need of the calculation before the move.

The structure of the proposed reference signal generator is presented in Fig. 3. In this generator the discrete model of an ideal drive system with cascade control was used, calculated every sampling time τ_s . Drive model consists of a cascade of two digital integrators forming part of the mechanical model and the model of a closed torque (or motor current) control loop. Model of a closed-loop torque control is replaced with an appropriate delay block with $\tau_d = k \cdot \tau_s$, where τ_d is a total delay time in drive control system. Model of the controllers consists of integrating acceleration controller, proportional speed controller and non-linear static position controller.

The first step in the procedure for selection of the reference signal generator parameters is to determine the cutoff frequency f_s for acceleration control loop. Based on the stability criterion

$$f_s < \frac{1}{4 \cdot \tau_d}, \tag{1}$$

but in order not to excite mechanical vibrations in the drive frequency can be reduced. In order to achieve accepted frequency f_s parameter k_e is defined as

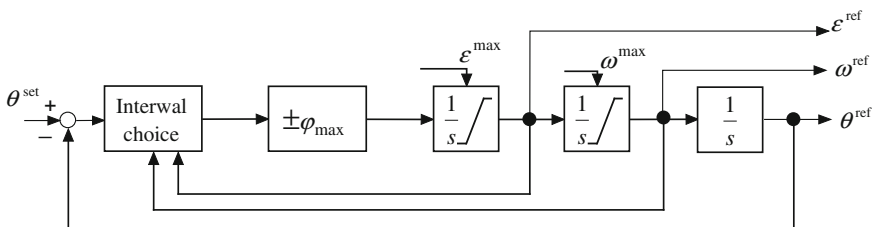


Fig. 2 Block diagram of classical reference signal generator

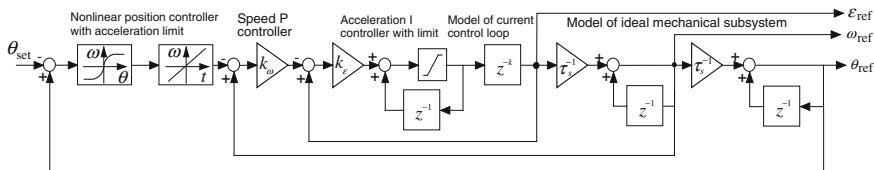


Fig. 3 Block diagram of classical reference signal generator

$$k_e = \pi \cdot f_s. \tag{2}$$

Gain speed controller k_ω was assumed as

$$k_\omega = \frac{f_s \cdot J^{\min}}{2 \cdot J^{\max}}, \tag{3}$$

where values J^{\max} and J^{\min} define the range of variability of the total moment of inertia of the drive. Such gain selection ensures that the damping factor of speed closed-loop is at least equal to $\sqrt{2}$.

Master, non-linear position controller provides near-optimal trajectory, according to the formula

$$\omega = \text{sgn}(\theta^{\text{set}} - \theta^{\text{ref}}) \cdot \sqrt{2 \cdot \varepsilon^{\max} \cdot |\theta^{\text{set}} - \theta^{\text{ref}}|}, \tag{4}$$

where ε^{\max} is the limit of acceleration. For small values of the error $|\theta^{\text{set}} - \theta^{\text{ref}}|$ characteristics (4) leads to a large gain value $d\omega/d(\theta^{\text{set}} - \theta^{\text{ref}})$, therefore, it must be replaced by a block proportional with gain k_θ :

$$\omega = k_\theta \cdot (\theta^{\text{set}} - \theta^{\text{ref}}). \tag{5}$$

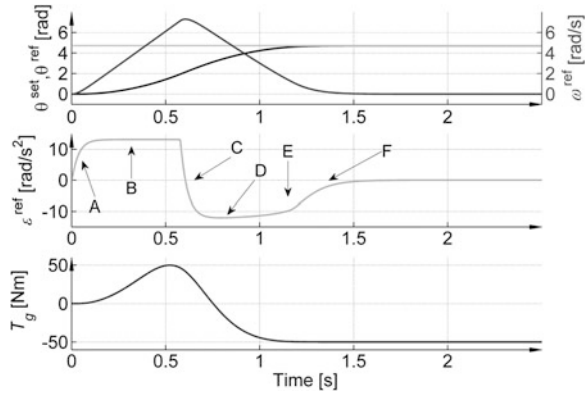
Selecting the value

$$k_\theta = \frac{k_\omega}{4} \tag{6}$$

guarantee, that there will be no reference position overshoot.

Sample waveforms for the case of a slight step change of the desired position are shown in the Fig. 4. Reference waveforms consists of six phases: increase of acceleration with jerk limit (A), constant acceleration (B), continuous change of acceleration to negative value (C), constant negative acceleration (D), time-optimal braking (E) and finally exponential breaking (F) to avoid any overshoot. In case of large desired position change the additional phase with constant speed will be present.

Fig. 4 References signals:
top reference position, set position and reference speed;
middle reference acceleration;
bottom gravitation torque



3 Integral Sliding Mode Controller

Classical sliding mode controller output is discontinuous in nature. Direct use of such signal as reference torque will result in large torque chattering and may excite high frequency mechanical resonance. In order to achieve smooth torque control an integral block is introduced. The 2nd order integral sliding mode control approach is used [6]. The starting point for the synthesis of the sliding controller is to define the sliding surface. The proposed solution surface is specified in the position error e relative to the reference value

$$\begin{aligned} e &= \theta - \theta^{ref}, \\ \dot{e} &= \omega - \omega^{ref}, \\ \ddot{e} &= \epsilon - \epsilon^{ref}. \end{aligned} \tag{7}$$

The generalized error σ on the sliding surface is equal to 0.

$$\sigma = \ddot{e} + 2 \cdot \lambda \cdot \dot{e} + \lambda^2 \cdot e. \tag{8}$$

During the sliding motion generalized error σ disappears with a time constant $1/\lambda$. The control signal v is chosen so that the state vector to bring the switching surface, and then keep it at the surface.

$$\begin{aligned} v_{SMC} &= -K_s \cdot \text{sgn}(\sigma), \\ \text{sgn}(\sigma) &= \begin{cases} -1 & \text{for } \sigma < 0 \\ 0 & \text{for } \sigma = 0. \\ 1 & \text{for } \sigma > 0 \end{cases} \end{aligned} \tag{9}$$

Constant K_s is chosen so as to ensure stable operation the whole range of variation of objects parameters. The output v_{SMC} of the proposed sliding mode controller is not reference current signal, but the first derivative of this current:

$$i_q^{ref} = \int_0^t v_{SMC} d\xi. \tag{10}$$

In this configuration, the sliding mode controller with the output block integrator, chattering phenomenon does not occur. Additionally, the function $\text{sgn}()$ is replaced by a continuous function $\text{sat}()$ of the width Φ .

$$v_{SMC} = -K_s \cdot \text{sat}(\sigma),$$

$$\text{sat}(\sigma) = \begin{cases} \sigma/\Phi & \text{for } |\sigma| < \Phi \\ \text{sgn}(\sigma) & \text{for } |\sigma| \geq \Phi \end{cases} \tag{11}$$

4 Laboratory Stand

Figure 5 presents the structure of the laboratory stand. The system consists of three main parts: the motor with load construction, a PWM converter and the control algorithm implemented in DSP. The data of the investigated drive are presented in the Appendix. A set of metal plates fixed to the arm mounted on the motor shaft enables us to vary the moment of inertia. The disc brake with four adjustable brake

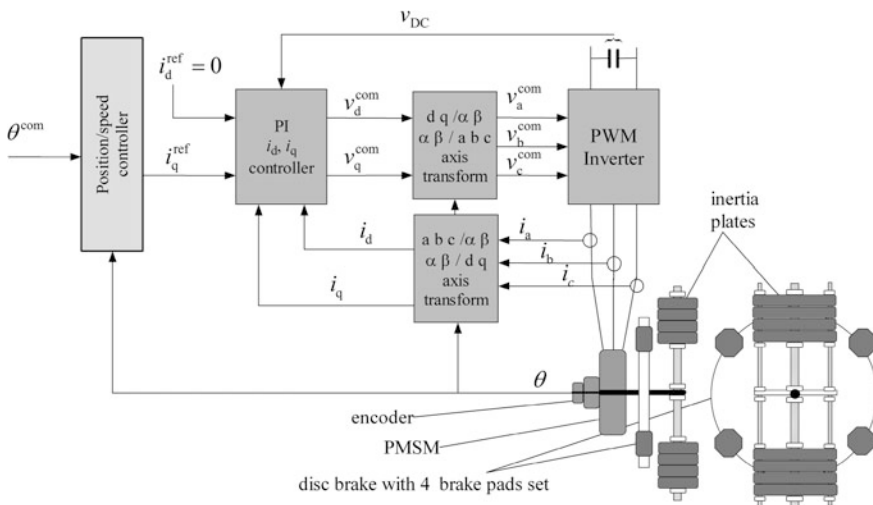


Fig. 5 Block diagram of laboratory stand with and vector controlled PMSM direct drive

pads is fixed to the motor shaft. This adjustable brake can be used to model dry friction, typically for cutting processes [7].

The sampling time of the floating point DSP is set to 100 μ s. An incremental optical encoder tests the rotor position. The speed is calculated by differentiation of rotor position with respect to time. It is very important to filter the speed signal adequately, to exclude the mechanical resonance amplification. The digital biquadratic multi-band filter was designed and tested [8].

Field-oriented control of currents in the axes d and q is performed by applying a robust PI control algorithm. The closed current control loop is much faster than mechanical dynamics.

5 Experimental Results

The research was carried in two phases: simulation and laboratory. Figure 6 presents the results of tests on an accurate simulation model. The reference trajectory, as presented in Fig. 4 was applied. Three cases were tested: small load inertia, middle load inertia with large load torque and big load inertia. The figure shows the reference current and the difference between the reference trajectory and the real signals. The dynamic position error is small then ± 0.012 rad, and the dynamic speed error is small then ± 0.11 rad/s. Reference currents are within the acceptable range ± 5.5 A. There is no chattering in reference current.

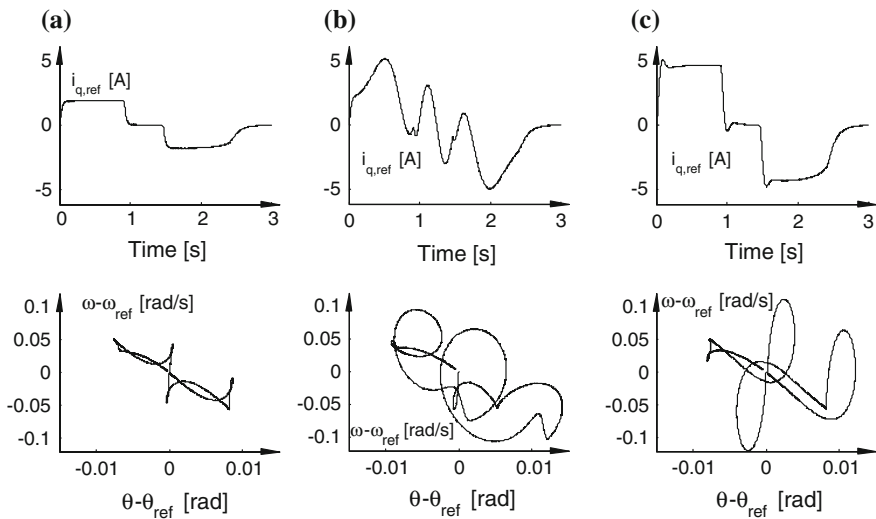


Fig. 6 Simulation results for low, middle and high inertia. *Top* reference current in q-axis. *Bottom* the tracking error of reference trajectory. **a** low inertia **b** middle inertia, active load torque **c** high inertia

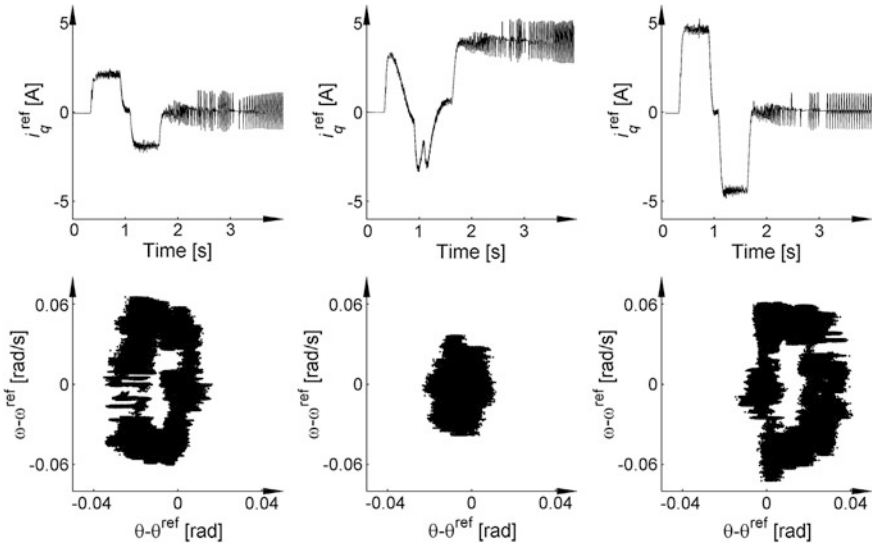


Fig. 7 Experimental results for *low*, *middle* and *high inertia*. *Top* reference current in q-axis. *Bottom* the tracking error of reference trajectory

In the second phase of the study tests were repeated in the laboratory. Collectively the results are shown in Fig. 7. For technical reasons, only position error was registered. Experimental studies confirmed the results of the simulation. The tracking positioning error is less than ± 40 mrad, the tracking speed error is less than ± 70 mrad/s. The final position error in steady state is less than ± 0.25 mrad. There are small oscillations of the current (for the low inertia) due to incomplete suppression of the elastic properties of the load. The oscillations are caused by finite position sensor resolution (0.025 mrad).

6 Conclusions

A modified structure of the robust speed and position controller was proposed. This structure is decomposed into a reference signal generator, based on model of cascade control system and a sliding mode controller with output integrator. The proposed controller ensures good robustness. Filtering the output signal controller by integrator block eliminates chattering phenomena. Simple structure allows easy implementation in real time system. Computer simulation and experimental studies verify the validity of the approach and prove good quality of control for the proposed structure. Further work makes it advisable to use a hybrid control structure that combines the advantages of the sliding mode control and cascade control P-PI [9].

Appendix

Table 1

Table 1 Data of investigated drive

Parameters of PMSM	Unit	Value
Minimum moment of inertia	kg m ²	0.75
Maximum moment of inertia	kg m ²	5.83
Torque constant	Nm/A	17.5
Rated load torque	Nm	50
Rated value of speed	rev/s	2.41
Rated current in q axis	A	2.85
Rated voltage	V	310

References

1. Sabanovic A (2011) Variable structure systems with sliding modes in motion control—a survey. *IEEE Trans Ind Inform* 7(2):212–223
2. Brock S, Deskur J and Zawirski K (1999) Modified sliding-mode speed controller for servo drives. In: *Proceedings of IEEE international symposium on industrial electronics, ISIE*, vol 2, Bled Slovenia, pp 635–640
3. Kroger T (2011) Online trajectory generation: straight-line trajectories. *IEEE Trans Rob* 27 (5):1010–1016
4. Chen G (2009) An online generation of time-optimal trajectories for piecewise step references. In: *Proceedings of IEEE international conference on control and automation, ICCA*, pp 1739–1743
5. Liu S. (2002) An on-line reference-trajectory generator for smooth motion of impulse-controlled industrial manipulators. In: *Proceedings of the 7th international workshop on advanced motion control, AMC*, pp 365–370
6. Bartolini G, Pisano A, Punta E, Usai E (2003) A survey of applications of second-order sliding mode control to mechanical systems. *Int J Control* 76:875–892
7. Brock S (2009) Sliding mode controller for direct drive with dry friction. *Przegląd Elektrotechniczny (Electrical Review)* 85(7):125–129
8. Brock S, Łuczak D (2011) Speed control in direct drive with non-stiff load. In: *Proceedings of IEEE international symposium on industrial electronics (ISIE)*, Gdańsk, Poland, pp 1937–1942
9. Brock S (2013) Hybrid PI sliding mode position and speed controller for direct drive. In: *Mechatronics*. Springer International Publishing, Switzerland, pp 741–748

Dynamic Modeling of the Skin Effect in Rotor Bars with Optimized Ladder Networks

C. Schmülling and A. Conradi

Abstract Modelling of induction machines with deep-bar rotors requires precise consideration of the skin effect. In search for an efficient method to be applied in established transient models based on systems of differential equations, an approach of defining a ladder network by means of optimization on the basis of steady-state characteristics of the inductance and resistance of the rotor bar is presented and compared to other approaches. Transient characteristics are investigated for a representative set of signals and compared to finite-element simulations in order to prove its applicability.

1 Introduction

Consideration of the skin effect in the rotor bars of induction machines within mathematical models can be applied in a variety of ways. Basically most approaches can be divided into two main steps, the determination of the frequency-depending characteristics of the resistance and inductance of the rotor bars and subsequently the implementation into machine models for the calculation of dynamic transients.

Most methods published so far start by solving the differential equation of Ampère's circuital law. Assuming sinusoidal currents and fields, for basic slot geometries gives the well-known formulae first derived by Field [2]. A similar approach [4] can be used in order to derive an electric network containing multiple circuits for the rotor by applying a Taylor series approximation for solving.

C. Schmülling (✉) · A. Conradi
Chair of Electrical Drives and Mechatronics, TU Dortmund University,
Dortmund, Germany
e-mail: christoph.schmuelling@tu-dortmund.de

A. Conradi
e-mail: alexander.conradi@tu-dortmund.de

A method for the analytical calculation of more generally shaped bars can be found in [3]. The rotor bar is therefore separated into several sections which are free of skin effects. Both methods can be illustrated as ladder networks with sets of constant resistances and inductances. The circuits obtained can subsequently also be used in transient models as given in [5].

Still, the number of sub conductors used for dividing the slot is equivalent to the number of additional circuits in the system of differential equations, and therefore having a significant influence on the calculation time, especially for consideration of high frequencies, as the height of the sub conductors is dependent on the skin depth.

As for all methods presented so far the frequency dependency is only calculated under the assumption of sinusoidal fields and currents, there have been approaches [1] to include the simultaneous calculation of eddy currents in the system of differential equations, so that for each rotor circuit there will be two additional equations in the system of differential equations, but being able to account for arbitrary current shapes.

Therefore a different method for setting up a ladder network to be used in transient models is proposed by using an alternative approach, where the network components are not directly linked to a particular sub conductor as the physical approach in [3], but instead determined by using an optimization procedure to fit the frequency-dependant characteristics of the bar resistance and inductance on a given network structure, whereby the number of differential equations can be reduced significantly.

As all methods except [1] are based on the assumption of sinusoidal currents it is further important to show, that modeling the ladder network from precalculated steady-state values also yields correct transients when used in dynamic models.

2 Mathematical Model

To take account of the skin effect in the rotor bars, a ladder network as shown in Fig. 1 is used, giving a set of voltage equations

$$u(t) \cdot [\mathbf{1}] = [\mathbf{R}][\mathbf{i}] + [\mathbf{L}] \frac{d}{dt} [\mathbf{i}] \quad (1)$$

Given known frequency-dependent characteristics $R(f)$ and $L(f)$, which can be calculated by using FEA or one of the methods mentioned in Sect. 1, the network components used in the resistance matrix \mathbf{R} and the inductance matrix \mathbf{L} of (1) can be calculated by solving an optimization problem using the method of least squares:

$$\min_{\vec{R}, \vec{L}} \sum_{i=1}^N \left(\frac{R_{i,ref} - R_i}{R_{i,ref}} \right)^2 + \omega_i \left(\frac{L_{i,ref} - L_i}{L_{i,ref}} \right)^2 \quad (2)$$

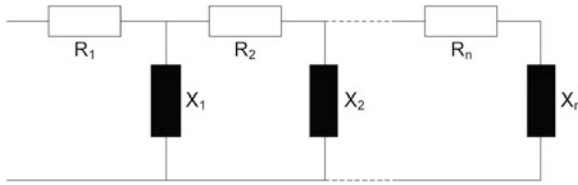
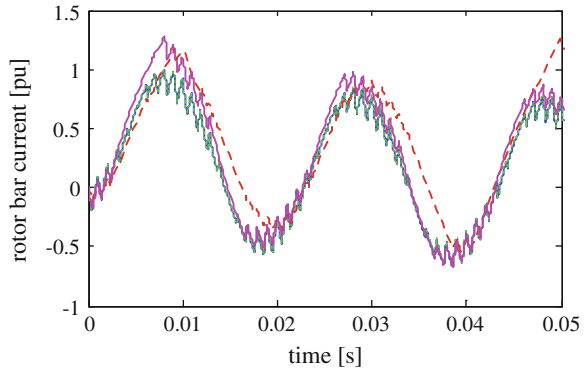


Fig. 1 Ladder network with 2n components

Fig. 2 Comparison of FEA and ladder network simulation for inverter-fed transient operation



For common deep bar shapes using between four to eight constant components (2–4 differential equations) in the ladder network gives good accordance between the equivalent impedance $\underline{Z}(f)$ of the network and the given functions of R and L .

3 Results

In order to test the applicability of the method proposed, a number of typical dynamic sequences which similarly occur in the transient operation of induction machines has been simulated by using FEA and numerically solving the ODE-system in (1), feeding both with the same dynamic voltage.

Figure 2 shows the bar current after switching on a voltage source producing a 50 Hz signal by using a carrier frequency of 1,000 Hz, thus simulating transient inverter-fed operation. It can be seen, that using constant dc-values for R and L (red) as well as ladder network parameters only optimized up to the fundamental frequency of 50 Hz (pink) produce a visible deviation whereas the ladder network with parameters optimized up to carrier frequency (blue) gives exact accordance with FEA results (green).

Figure 3 shows a sudden switch from a voltage frequency of 4–50 Hz, which similarly happens to the induced voltage in the rotor in the case of a three-pole short circuit. Again, the results from FEA and the ladder network show no deviation,

Fig. 3 Transient currents for frequency switch from 4 to 50 Hz

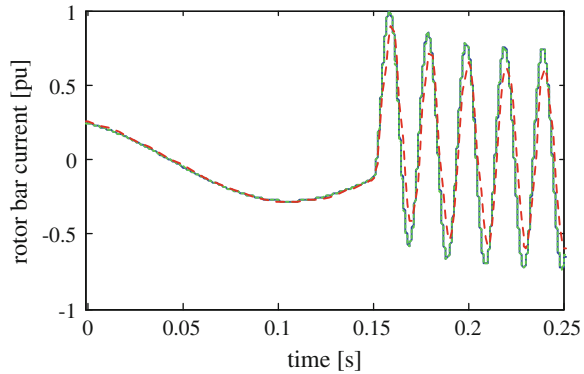
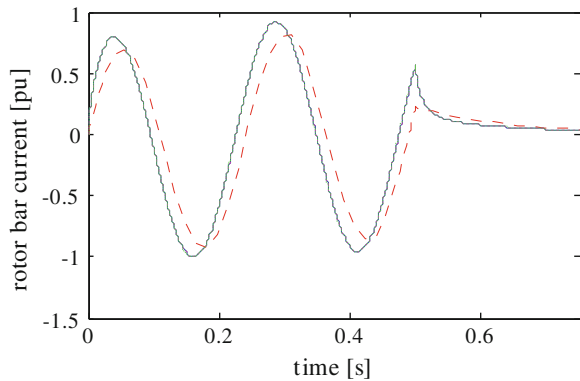


Fig. 4 Transient currents for voltage switch-off



while using constant dc-parameters gives smaller currents due to neglecting the skin effect and $X_{\text{bar}} > R_{\text{bar}}$, so that decrease in inductance dominates increase in resistance on consideration of the skin effect.

As can be seen from the voltage switch-off shown in Fig. 4, it is not necessary to determine the ladder network parameters in the range above the maximum frequency occurring in the feeding voltage, as both optimization up to fundamental frequency as well as to a frequency of 20 times fundamental frequency give according results for the current answer to the step-function of the voltage, even though the time constant was chosen particularly small (deep and thin bar) in order to stress the influence of high frequencies within the exponential decay.

4 Conclusion

Consideration of the skin effect in deep bar rotors of induction machines can be applied in transient machine models based on a system of differential equations by adding additional rotor circuits with constant parameters.

It has been shown, that determination of the parameters by using the assumption of sinusoidal currents gives the same results as transient simulation with FEA. Still, using the model for inverter-fed operation, the optimization used to calculate the parameters of the ladder network with a given number of elements has to be performed up to the carrier frequency in order to give good accordance.

Especially for machines of small power, usually having smaller rotor time-constants, sudden switches in voltage as in the case of motor-startup (cf. Fig. 2) or three-pole short circuit (cf. Fig. 3) will produce a considerable share of current frequencies in the range above 50 Hz during the transients. Nevertheless, simulation results clearly show that optimization up to the maximum frequency occurring in the feeding voltage is sufficient for usage in dynamic models. This observation is of particular importance as optimizing the ladder network over a larger spectrum generally requires more additional circuits.

Another advantage of using optimization for the determination of the ladder network parameters instead of the methods of [4] or [3] is the possibility of using a smaller number of circuits, especially for high frequencies.

By covering these frequencies in the determination of the ladder network, the method proposed can therefore equally replace the method proposed in [1], yet using an approach simpler to be implemented and faster to be calculated on numerically solving the system of differential equations as only one additional equation is used for each rotor circuit instead of two.

References

1. Bolte E (2012) *Electrical machines*. Springer, Berlin/Heidelberg (in German)
2. Field AB (1905) Eddy currents in large-slot-wound conductors. *Proc AIEE* 24:761–788
3. Müller G, Vogt K, Ponick B (2008) *Calculation of electrical machines*. Wiley, Weinheim (in German)
4. Nürnberg W (1976) *The induction machine*. Springer, Berlin/Heidelberg (in German)
5. Puchała A (1977) *Dynamics of machinery and electromechanical systems*. Państwowe Wydawn, Warsaw (in Polish)

Using Balsa Environment for the Asynchronous Microprocessor Design

Dariusz Stachańczyk

Abstract The article discusses selected issues related to the design of complex asynchronous systems. The asynchronous implementation of the complex electronic system can bring potentially several advantages over synchronous circuits like low power consumption, less emission of electromagnetic noise and high operation speed. In a practice however, such systems are not very popular because of the limited choice of an efficient EDA tools supporting asynchronous circuits design. The example of an EDA tool for asynchronous circuits design is the Balsa environment that has been presented and discussed in this paper. This environment was used to design the exemplary microprocessor with an asynchronous architecture. The results and experience obtained during the experiments are presented within this paper.

1 Introduction

The substantial complexity of the synthesis problem and limited selection of EDA tools supporting asynchronous circuit design caused that for many years the vast majority of electronic systems was realized in the synchronous form. However, in the last few years there has been also increasing interest in the digital circuits designed in an asynchronous form. This is due to the potential benefits deriving from the use of asynchronous architecture, which typically are difficult or impossible to achieve in the case of the synchronous system [1]. The most important asynchronous circuit advantages are low power consumption, low emission of electromagnetic noise and high operation speed. Therefore, despite an increased design complexity, more and more research and design groups are interested in asynchronous circuit design nowadays. The results obtained by both research bodies and commercial design centers dealing with asynchronous circuits confirms

D. Stachańczyk (✉)
Silesian University of Technology, Gliwice, Poland
e-mail: dariusz.stachanczyk@polsl.pl

the possibility of obtaining tangible benefits arising from the use of asynchronous technology. The carried out research is focused mainly on the design of asynchronous processors, that could have a performance equal or better than synchronous equivalents and consume much less energy at the same time. The most important, existing implementations of the different asynchronous processors are discussed in [2]. Unfortunately, the limited availability of EDA tools that supports the asynchronous systems design means that the implementation of such systems requires extensive experience designers, and a considerable amount of time. Additionally, to achieve desired results most of described asynchronous circuits had to be designed almost manually, often at transistor level. Thus, despite the potential advantages of asynchronous circuits, the complexity of their design significantly reduces designers' interest in systems of this type. This problem can be solved through the introduction of widely acceptable and efficient hardware description language and appropriate synthesis tools. Although there are already some tools supporting asynchronous circuits design [2] available but in most cases these are commercial tools with limited accessibility. Therefore, there is still a need for affordable tools that would also allow individual engineers or small design centers to design and research asynchronous electronic systems. The one of such tools is a freely available BALSAs environment developed by the APT research group at the University of Manchester [3, 4].

2 BALSAs Design Environment

The traditional design methods based on an asynchronous finite-state machine graph describing the operating cycle of the entire system are quite inefficient for the asynchronous circuits of high complexity. In a case of such circuits the whole system is built rather from asynchronous components that exchange data with use of a selected handshake protocol. The one of most popular solutions for handshake data exchange is so-called *bundled-data* protocol that uses two additional lines *Request (Req)* and *Acknowledge (Ack)* to synchronize data flow. The data flow control system in such system is usually built with use of Muller C-element [1] that controls the enable signal of latch registers storing output and input data of the constituent functional blocks of the system (Fig. 1).

The necessity to implement additional mechanisms for controlling the data flow between particular components of the system complicates the synthesis process and a complete system is usually more complex than its synchronous counterpart. However, designer creating a project in BALSAs does not need to focus on the data transfer details for the selected protocol, because the complete data flow is modeled through abstract channels. The BALSAs hardware description language and synthesis tools allow designers to compile behavioral description of an asynchronous circuit to a form of constituent system components that communicate using the selected handshake protocol. During the design implementation the abstract communication channels are converted to the corresponding logical structures depending of the

(a)	(b)
<pre> procedure async_uP (-- uP Interface input dataIn : 8 bits; output dataOut : 8 bits; output address : 8 bits; output rw : 1 bits) is </pre>	<pre> module processor(clock, reset, rw, datain, dataout, address); input clock, reset; output rw; reg we; input [7:0] datain; output [7:0] dataout; output [7:0] address; reg [7:0] address; reg [7:0] dataout; </pre>

Fig. 2 The CPU interface described in balsa (a) and its synchronous equivalent described in Verilog HDL (b)

equivalent synchronous CPU written in Verilog (Fig. 2b). It should be however noted that, for *bundled-data* protocol, after the implementation *Req* and *Ack* control lines will be added for each I/O channel of asynchronous model. Additionally the 2-wire *activate* control signal will be also added to control operation of microprocessor.

The complete balsa description of a microprocessor consists of several procedures that define phases of the system operation. These procedures can be seen as the equivalent of the “always@” blocks used in Verilog description but obviously there are some differences between them. In a case of microprocessor “always@” Verilog blocks describe usually the parallel working circuit components synchronized by common system clock signal. The balsa procedures also describe the functional hardware blocks but they are not event triggered and they can be invoked sequentially or parallel. The order of procedures invocation depends on the operator separating them within the main procedure describing the circuit. There are two operators specific for a balsa language—the sequence operator (;) and the parallel composition operator (||) [5]. The first one separates operations that have to be invoked one after another while the second composes commands that can be performed in parallel. An example of the use of sequence and parallel operators within asynchronous CPU design is presented in Fig. 3. In the main loop of the CPU description (Fig. 3a) the sequence operator is used to set the order of procedures responsible for fetching data from memory (Fetch()), decoding and executing CPU instructions (DecodeExecute()) and program counter incrementing (incPC()). The Fig. 3b presents the use of parallel composition operator in data fetching procedure. In this case the data transfers on different memory channels can be performed simultaneously since they are then synchronized by appropriate sequence of the *Req* and *Ack* signals.

The CPU instruction set comprises sixteen instructions for the data transfer, typical arithmetic and logic operations as well as some instructions for program execution control. The implementation of particular instructions is made in a similar

(a)	(b)
<pre> -- Main Loop begin Initialize(); loop Fetch(); DecodeExecute(); incPC() end end </pre>	<pre> shared Fetch is begin rw <- 1 address <- pc dataIn -> ireg End </pre>

Fig. 3 The CPU interface described in balsa (a) and its synchronous equivalent described in Verilog HDL (b)

```

shared aluExec is begin
  case (#ireg[7..4] as 4 bits) of
    i_NOTA then acc:=not acc
    | i_INCA then
      aluOut := (acc+1 as 9 bits);
      c_flag:= #aluOut[8] ||
      acc := (#aluOut[7..0] as 8 bits)
    | i_DECA then
      aluOut := (acc-1 as 9 bits);
      c_flag:= #aluOut[8] ||
      acc := (#aluOut[7..0] as 8 bits)
    -- The code for other ALU instructions
    else
      continue
  end ;
  if acc=0 then z_flag:=1 else z_flag:=0 end
end

```

Fig. 4 The procedure describing the ALU operations

way as in a case of synchronous CPU described in Verilog. For example for arithmetic and logic unit (ALU) operations the value of variable representing an accumulator is modified accordingly to instruction code stored in the instruction register (*ireg* variable). The exemplary code describing the ALU operations is presented in Fig. 4.

To verify the designed CPU the inbuilt BALS simulator was used. The included libraries contain also simulation model of a memory that can be use to create a top level architecture and to store a microprocessor program. Although the simulator is quite simple it enables defining required input stimulus and generates a detailed output file with the signals waveform. This allows verifying if the program is executed correctly and the correct values are written to registers and interfaces.

Table 1 FPGA implementation results

CPU model	Asynchronous	Synchronous
Flip-Flops	163	74
LUT	526	174
I/O	36	27

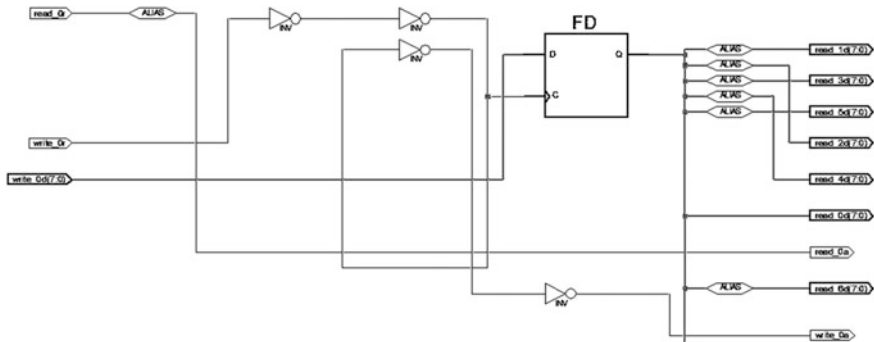


Fig. 5 FPGA implementation of the asynchronous output data buffer

When a more thorough verification is required then the generated by BALSAs compiler netlist can be used to simulate the design in any HDL simulator. In a case of asynchronous CPU design the generated netlist was used to implement the project in the Xilinx FPGA device and the results were compared to the results obtained for the analogous synchronous microprocessor (Table 1).

Comparing the results it can be seen that for the implementation of an asynchronous system twice more flip-flops and a few I/O blocks more were used. This is due to the need to implement additional data buffers and the *Req* and *Ack* signals. Attention should also be paid to significantly greater number of LUT resources used, which results from the fact that the additional data flow control logic has to be implemented in the asynchronous system. This additional logic uses a lot of connected in cascade NOT gates to achieve the desired delays in request and acknowledge lines. The Fig. 5 presents the example of the *Req* and *Ack* signals implementation for the *dataOut* channel.

The circuit generated by BALSAs for FPGA uses flip flops to store data while the delayed by two NOT gates appropriate input *Req* signal is used as a latch clock. The latch clock signal delayed through a further two gates is then passed on as an output *Ack* signal. This NOT gate cascades have to ensure that data on register inputs will be stable before *Req* signal will latch the data. Similarly, the *Ack* signal is delayed to ensure that data have been before properly saved in the registers.

Since there is no clock signal in the asynchronous implementation it is hard to compare the operation speed of both circuits using just data from implementation report. For the objective assessment of the asynchronous circuit speed the further

simulation and signal delays analyse is required. However, it can be assumed that the speed of the asynchronous CPU implemented in FPGA will be much lower due to the delays on *Req* and *Ack* lines of the circuit.

4 Conclusion

Although the implementation of the electronic system in the asynchronous form can bring potential benefits but it should be noted that most of these benefits applies only ASICs implementations. The limitations of available EDA tools as well as the limitations of programmable structure itself prevent effective implementation of asynchronous circuit in CPLDs and FPGAs. Summarizing the experiments in the BALS environment and the results obtained during the CPU implementation it can be seen that asynchronous circuits implemented in FPGA use more resources and are slower than their synchronous counterparts. Of course, the lower operating speed and the greater system complexity should not to be factors determining the validity of the implementation of asynchronous circuits in the programmable structures. It appears that, despite the increased complexity and a lower speed, asynchronous circuits implemented in FPGA and CPLD should generate low EMI noise and have low power consumption like in the ASICs case. Therefore, in the further research the author will continue work on verification the potential advantages of programmable structures use for the asynchronous circuits implementation.

References

1. Sparsø J, Furber S (2001) Principles of asynchronous circuit design—a systems perspective. Kluwer, Academic Publishers, Boston
2. Stachańczyk D (2009) Design of complex electronic systems in the asynchronous form—circuits and tools analyse. PAK 55(7):473–475
3. The balsa asynchronous synthesis system. <http://intranet.cs.man.ac.uk/apt/projects/tools/balsa/>. Accessed 9 Sept 2013
4. Stachańczyk D (2012) Using BALS environment for the asynchronous circuits design. Prz Elektrot R.88(11b):87–89
5. BALS: a tutorial guide. Version V3.5—2006

Random Dynamical Systems of the First Order

J. Walczak and S. Mazurkiewicz

Abstract The article discusses the method of solving random differential equations of the first order. Random factors cause that only some methods for solving stochastic differential equations enable to obtain efficient results. In addition to the differential equation (together with the initial condition) the output equation should be given. If the output equation is not given, solution of the differential equations are not useful from the viewpoint of the moments of the output process (as opposed to stochastic differential equations in which the coefficients are not random variables). It was assumed that the coefficients are functions of two random variables (A and B) and the force does not contain irregular processes (Winner processes, white and colored noise). The considered equations describe electrical dynamical systems of the first order. The expected value of response of the system, cross-correlation function of the force process and response process and the correlation function of the system response have been determined. It was considered RL series circuit as an example of a solution the problem, where the response is the voltage at the resistance. An example of the problem solution has been presented for a series RL circuit assuming that the voltage across the resistor is the response of the system.

1 Introduction

The article discusses the method of solving random differential equations of the first order [1, 2]. The considered equations describe the first order dynamic electrical systems [3]. The expected value of the system response, the cross correlation function of the response and the force and the correlation function of the response

J. Walczak (✉) · S. Mazurkiewicz
Faculty of Electrical Engineering, Silesian University of Technology, Gliwice, Poland
e-mail: janusz.walczak@polsl.pl

S. Mazurkiewicz
e-mail: seweryn.mazurkiewicz@polsl.pl

have been determined [4, 5]. The example of a solution to the problem for a series RL circuit where the response is defined as the voltage across the resistor has been shown. In the same way, other systems of the first order can be considered [6, 7]. The article is a continuation of the previous works on stochastic models of lumped elements RLMC [8, 9] as well as stochastic dynamical systems including these elements [10].

2 Formalization of the Problem

Let us consider be the differential equation [1]:

$$\frac{dX(t)}{dt} + p(A, B)X(t) = q(A, B)F(t), \quad (1)$$

and the output equation:

$$Y(t) = r(A, B)L_t[X(t)], \quad (2)$$

where $X(0) = X_0$, A, B are the random variables, whereas $p(\cdot, \cdot)$, $q(\cdot, \cdot)$ and $r(\cdot, \cdot)$ are the continuous deterministic functions. $L_t[\cdot]$ is the linear operator. $F(t)$ is a stochastic process representing the system excitation.

3 Solution of the Problem

The analytical solution of Eq. (1) is given by the formula [1]:

$$X(t) = \int_0^t q(A, B)F(s) \exp(p(A, B)(s - t))ds + X_0 \exp(-p(A, B)t). \quad (3)$$

It is assumed that the random variables A, B, X_0 and the stochastic process $F(t)$ are mutually independent. Using the expected value operator $E[\cdot]$ to the both sides of Eqs. (2) and (3) the expected value of the output process and the cross-correlation function has been obtained:

$$\begin{aligned} \mu_Y(t) = L_t \left[\int_0^t E[r(A, B)q(A, B) \exp(p(A, B)(s - t))]E[F(s)]ds \right] \\ + L_t[E[X_0]E[r(A, B) \exp(-p(A, B)t)]], \end{aligned} \quad (4)$$

$$R_{FY}(t_1, t_2) = L_{t_2} \left[\int_0^{t_2} W_1(s, t_2) W_2(t_1, s) ds \right] + L_{t_2} [E[X_0^2] E[F(t_2)] W_3(t_2)], \quad (5)$$

where:

$$W_1(s, t_2) = E[r(A, B)q(A, B) \exp(p(A, B)(s - t_2))], \quad (6)$$

$$W_2(s_1, s_2) = E[F(s_1)F(s_2)], \quad (7)$$

$$W_3(t_2) = E[r(A, B) \exp(-p(A, B)(t_2))], \quad (8)$$

In the same way, one can obtain the autocorrelation function:

$$\begin{aligned} R_Y(t_1, t_2) = & L_{t_1} L_{t_2} \left[\int_0^{t_2} \int_0^{t_1} W_4(s_1, s_2, t_1, t_2) W_2(s_1, s_2) ds_1 ds_2 \right] \\ & + L_{t_1} L_{t_2} \left[E[X_0] \int_0^{t_1} W_5(s_1, t_1, t_2) E[F(s_1)] ds_1 \right] \\ & + L_{t_1} L_{t_2} \left[E[X_0] \int_0^{t_2} W_5(s_2, t_1, t_2) E[F(s_2)] ds_2 \right] \\ & + L_{t_1} L_{t_2} [E[X_0^2] W_6(t_1, t_2)], \end{aligned} \quad (9)$$

where:

$$W_4(s_1, s_2, t_1, t_2) = E[r^2(A, B)q^2(A, B) \exp(p(A, B)(s_1 + s_2 - t_1 - t_2))], \quad (10)$$

$$W_5(s, t_1, t_2) = E[r^2(A, B)q(A, B) \exp(p(A, B)(s - t_1 - t_2))], \quad (11)$$

$$W_6(t_1, t_2) = E[r^2(A, B) \exp(-p(A, B)(t_1 + t_2))]. \quad (12)$$

If RL or RC circuits are described by random variables, general equations describing all of the above cases are given by Eqs. (1) and (2). The random variable A becomes the random variable R and the random variable B becomes the random variable C or L . The random functions $p(\cdot, \cdot)$, $q(\cdot, \cdot)$ and $r(\cdot, \cdot)$ depend on the system structure. The operator $L_t[\cdot]$ is the identity or the derivative with respect to time.

The following chapter illustrates the method of determining the expected value and the correlation functions of the voltage across the resistor in the series RL circuit.

4 Example

Let us suppose that a series RL circuit is given and the response of the system is defined as the voltage across the resistor ($X(t) = I_L(t)$). The random variable A represents the resistance ($A = R$) and the random variable B represents the inductance ($B = L$). In this case, the functions $p(\cdot, \cdot)$, $q(\cdot, \cdot)$, $r(\cdot, \cdot)$ and operator $L_r[\cdot]$ have the form:

$$p(A, B) = \frac{A}{B}, \quad q(A, B) = \frac{1}{B}, \quad r(A, B) = A, \quad (13)$$

$$L_r[\cdot] = \text{id}(\cdot). \quad (14)$$

For simplicity of calculations, it has been assumed that the inductance (variable B) and the initial condition $X(0) = X_0$ are the real numbers ($B = 1$, $X_0 = 0$). In contrast, the resistance (variable A) is the random variable with the uniform distribution $A = U(a = 2, b = 4)$. Excitation is equal to $F(t) = D \cdot \mathbf{1}(t)$, where D is the random variable with known moments $E[D] = 2$ and $E[D^2] = 8$ (the variance is equal to $\sigma_D^2 = 4$).

Using Eq. (4) one can determine the expected value of the response:

$$\mu_Y(t) = 2 - \frac{\exp(-2t) - \exp(-4t)}{t}. \quad (15)$$

The zero initial condition causes that after switching the system on at the time $t = 0$ no current flows through the coil, and the voltage across the coil is equal to the supply voltage. Together with increase of the current, the voltage across the coil decreases (increase across the resistor) and reaches the zero value after the end of the current rise (the voltage across the resistor reaches the supply voltage value). The expected value of the system response, which has been shown in Fig. 1 is consistent with the above reasoning.

Using formula (5) the cross-correlation function of the force and the response can be determined:

$$R_{FY}(t_1, t_2) = 8 - \frac{4(\exp(-2t_2) - \exp(-4t_2))}{t_2}. \quad (16)$$

The cross-correlation function (Eq. 16) depends only on the time t_2 . This is caused by the fact that the force (each realization of the process $F(t)$) for the time $t > 0$ is a constant function (change of the time t_1 does not affect the cross-correlation of the force and the response processes).

Using formula (9) the autocorrelation function of the response can be determined:

Fig. 1 The expected value of the response (voltage across the resistor)

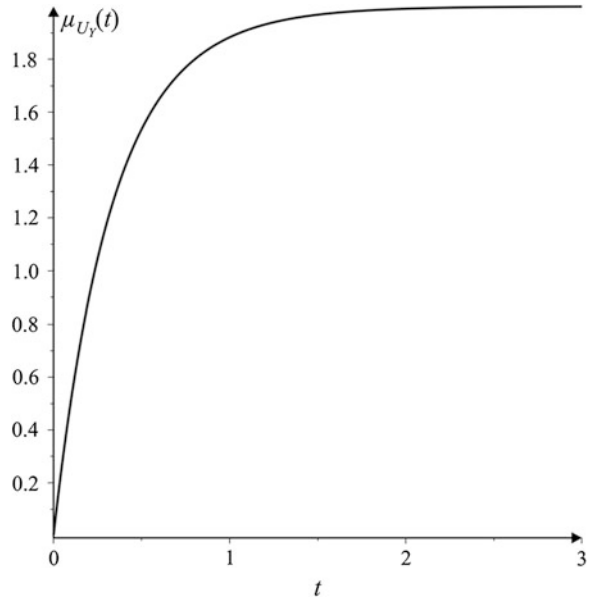
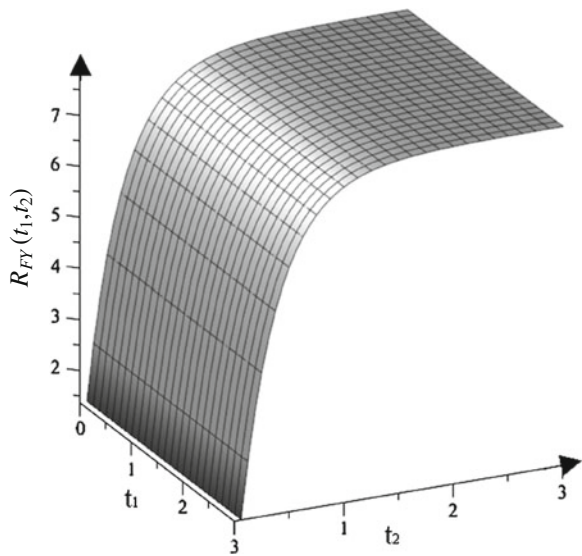
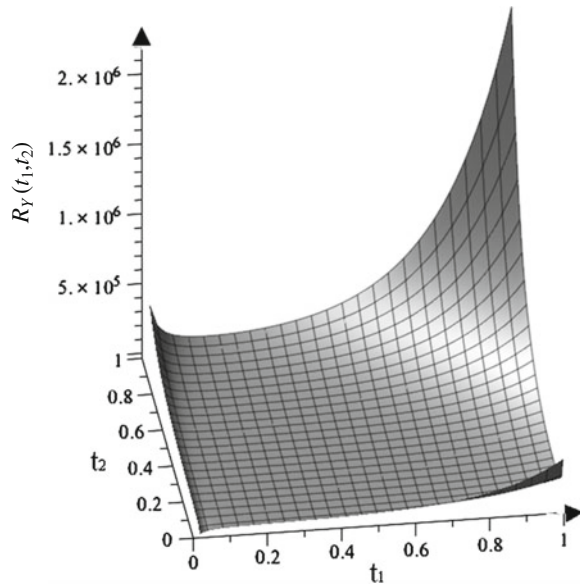


Fig. 2 The cross correlation of the force and the response ($R_{FY}(t_1, t_2)$)



$$\begin{aligned}
 R_Y(t_1, t_2) = & \frac{-8}{(t_1 + t_2)t_1t_2} (-t_1(t_1 + t_2) \exp(6t_1 + 2t_2) + t_1(t_1 + t_2) \exp(6t_1 + 4t_2) \\
 & + ((-t_1 - t_2) \exp(6t_2 + 2t_1) + (t_1 + t_2) \exp(6t_2 + 4t_1) + t_1 - 2(t_1 + t_2) \exp(6t_1 + 6t_2) \\
 & + \exp(2t_1 + 2t_2) - \exp(4t_1 + 4t_2))t_2 \exp(-6t_1 - 6t_2)).
 \end{aligned}
 \tag{17}$$

Fig. 3 The correlation of the response()



The correlation function of the response (Eq. 17) depends in the complex way on the both of the times t_1 and t_2 . Formula (17) cannot be represented as a function of the difference of the times t_1 and t_2 , which means that the output process is not stationary (also the expected value is not constant, see formula (15)).

Figure 2 shows the cross correlation of the force and the response, while Fig. 3 shows the autocorrelation of the response.

5 Conclusions

Equation (1) describes the broad class of electric dynamical systems of the first order with random coefficients. It has been assumed that the equation depends on two random coefficients (A and B). However, the extension to the larger number of the random coefficients is not a problem (using the method analogous to described in the article). The solution of Eq. (1) is given by the Eq. (3). However, the randomness of the coefficients (and the method) causes that it is necessary to know the output Eq. (2). The moments of the solution of the differential equation ($E[X(t)]$ and $E[X^2(t)]$) are useless for the calculation of the moments of the system response as opposed to the stochastic differential equations in which the coefficients are not the random variables. For these equations, usually knowing the moments of the solution, one can calculate the moments of the stochastic process defined by the output equation using the methods of the classical mathematical analysis.

References

1. Soong TT (1973) Random differential equations in science and engineering, mathematics in science and engineering, vol 103. Academic Press, New York
2. Skowronek K (2011) Electrical circuits in the terms of the stochastic. Monograph, Pol. Pozn., Poznan, Wyd
3. Kadlecova E, Kubasek R, Kolarova E (2006) RL circuits modeling with noisy parameters. In: Conference on applied electronics, Pilsen 6–7 Sept 2006, pp 217–220
4. Grabowski D (2009) Moments of stochastic power processes for basic linear elements. In: International conference of fundamentals of electrotechnics and circuit theory, IC-SPETO 2009, pp 83–84
5. Kolarova E (2006) Statistical estimates of stochastic solutions of RL electrical circuit. In: IEEE International conference of industrial technology, ICIT 2006, pp 2546–2550
6. Kolarova E (2008) An application of stochastic integral equations to electrical networks. Acta Electrotechnica et Informatica 8(3):14–17
7. Kolarova E (2005) Modeling RL electrical circuits by stochastic differential equations. In: International conference on EUROCON, 22–24 Nov 2005, Belgrade, Serbia 2005, pp 1236–1238
8. Walczak J, Mazurkiewicz S (2014) Random models of coupled inductors. Computer applications in electrical engineering 2014, chapter in monograph. Polish Academy of Sciences, Wyk, pp 321–327
9. Walczak J, Mazurkiewicz S, Grabowski D (2013) Stochastic models of lumped elements. In: International symposium on theoretical electrical engineering 2013, Pilsen, Czech Republic, pp II-19–II-20
10. Mazurkiewicz S, Walczak J, Jakubowska A (2013) Analysis of linear stochastic dynamic systems of the n -th order of the method of moments. In: Advanced methods of the theory of electrical engineering, pp II-2

Analysis of the Distribution of Air Flow Rate Through Stator End Winding of Turbo Generator

K. Zhao and C. Kreischer

Abstract This paper presents a combined method of FEM and 1-D fluid network theory to model the distribution of the air flow rate in the stator end winding of an air cooled turbine generator. The model of the end winding can be integrated into a 1-D fluid network of the whole cooling system. Thus, the result of simulation can be directly used for further studies of the cooling system.

1 Introduction

In this paper the stator end winding is modeled by the use of fluid mechanics theory. The end winding is analyzed under different boundary conditions and the simulation results are used to derive a simplified model for system simulations using a 1-D fluent network.

Before the mathematical model is set up the geometric structure of the end winding has to be introduced.

2 Geometric Structure

Every stator coil distributes on a conic section. The two-layered coils of the end winding are electrically connected in the front. The inner and outer coils are bent reverse and cross each other.

K. Zhao (✉) · C. Kreischer
Chair of Electrical Drives and Mechatronics, TU Dortmund University,
Dortmund, Germany
e-mail: zhaokaining2002@yahoo.com

C. Kreischer
e-mail: christian.kreischer@tu-dortmund.de

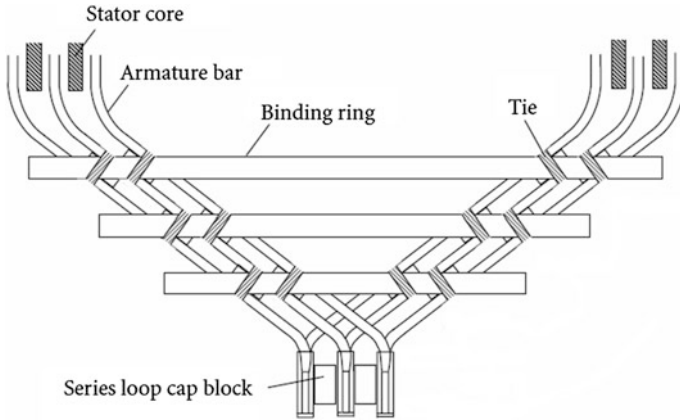


Fig. 1 Coils at end winding with bindings [1]

In order to protect the coils during operation and in the case of a fault the end windings have to be banded. To stiffen the structure additional banding rings are often used (Fig. 1).

In Fig. 1 a piece of the whole binding is shown. The whole end winding forms a complex porous structure. In operation the coolant (in this case air) flows through the porous structure. The coil ends are brazed together to form bar conductors for the electric current. The series loop cap blocks stiffen the front of the end winding to reduce vibrations.

The whole structure of the end winding is shown in Fig. 2.

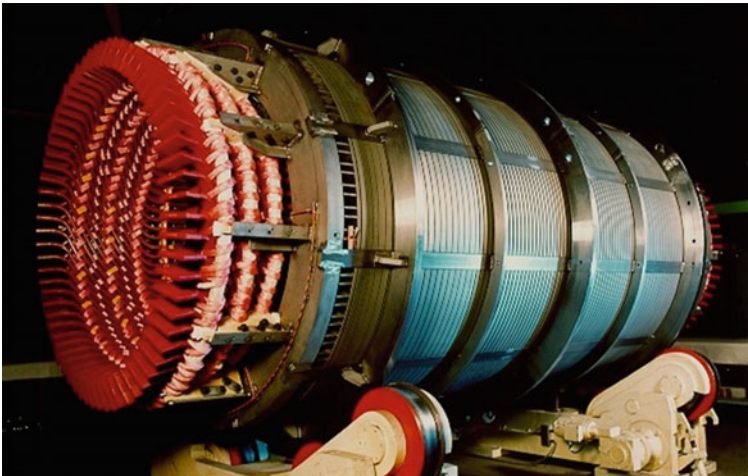
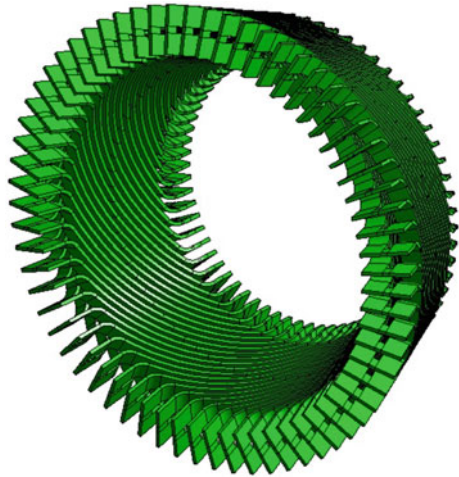


Fig. 2 Assembly of end winding with bandages [2]

Fig. 3 End winding without other components



Besides bandages there are several supports used in order to stiffen the structure. Because of the resulting highly porous structure it is impossible to model the air flow through the end winding directly with a discrete network like the internal flow in pipes. To treat the whole end winding as a compact object, the presented method leads to a simplified model in which the end winding can be treated as a single component to be integrated into the whole fluid network of a turbine generator. For the study the influence of the rotor has to be considered.

The model of the end winding has to be set up from a mechanical CAD model before detailed 3D finite element simulations can be made. As mentioned previously the stator bars are bent and twisted in 3D.

Figure 3 shows the bars of the end winding without support elements. The other components include the stiffening elements, retaining ring of rotor, pressure plate and environment with boundary conditions. In the simulation only 1/6 part is considered under the assumption that the distribution of coolant is regularly.

3 Simulation

In the observed region, the simulation object (coil) is totally inversed with the help of Ansys[®] Workbench. This means the observed object is the coolant, which flows through the meshed region, not the coil. Thus the negative picture is shown in Fig. 4. After setting up the boundary conditions the simulation is implemented as follows:

The distribution of flow rate can be also calculated through the simulation with Ansys[®] Workbench as shown in Fig. 5.

Fig. 4 Pressure distribution of coolant

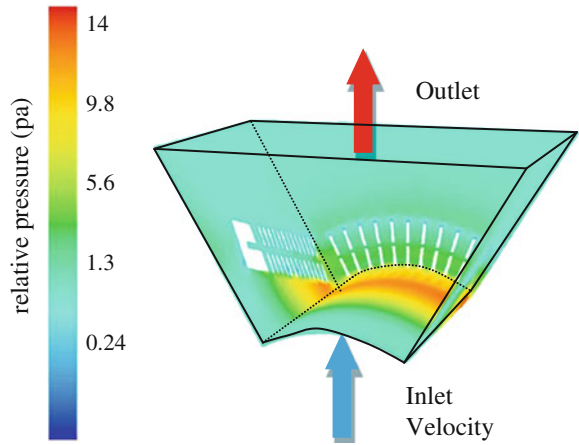
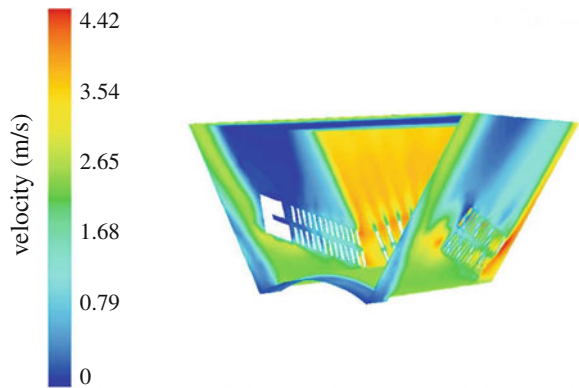


Fig. 5 Velocity distribution of coolant



According to the fluid mechanical theory [3] the following equations hold true:

$$\Delta P_V = \rho \cdot \xi \cdot \frac{1}{2} \left(\frac{\dot{V}}{A} \right)^2 \tag{1}$$

and

$$R = \frac{\rho \cdot \xi}{2 \cdot A} \tag{2}$$

With:

- ΔP_V : Pressure drop
- \dot{V} : flow rate
- A : area
- ρ : density of coolant

ζ : friction coefficient
 R: resistance

The inlet velocity is set as boundary condition for each simulation. Through the simulation the pressure drop and flow rate can be measured. Both results are used to calculate the fluent resistance of the end winding.

After simulation with different inlet velocities the following characteristic curves can be depicted as:

The resistance decreases very slowly as the flow rate increases and can be treated as a constant of 0.088 m^{-4} (Fig. 6).

With the help of the software Flowmaster[®] [4] the complex geometric object is abstracted as one component and can be integrated into the whole cooling network. A part of the resulting network is shown in Fig. 7.

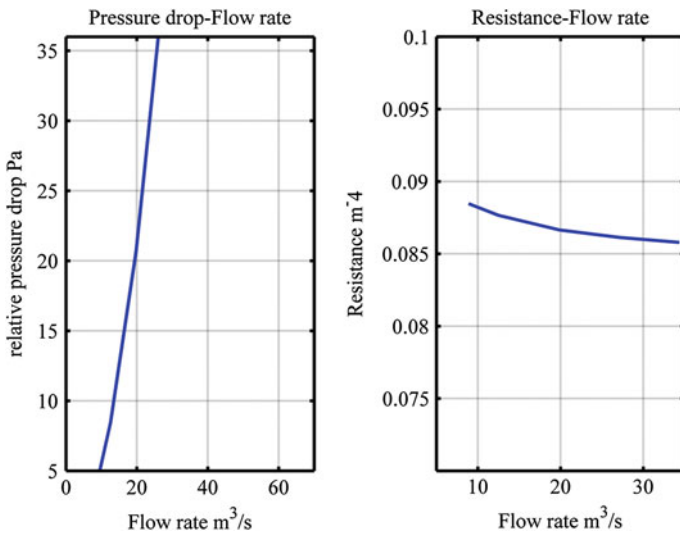
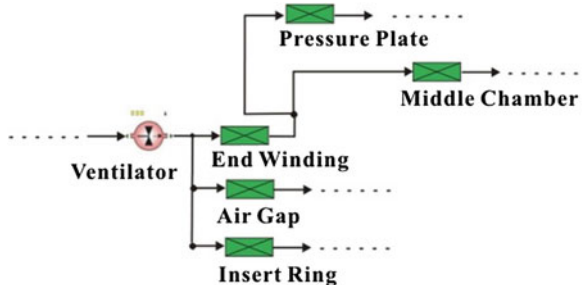


Fig. 6 Nonlinear characteristic curves after simulation

Fig. 7 A part of cooling network built up with Flowmaster[®]



Other complex elements of the cooling system have to be investigated in a similar way to build up the whole network model which allows the prediction of flow rate and pressure drop in each component of the system. This can be used for optimization purposes of the cooling system.

4 Conclusion

The presented combination of two simulation tools (Ansys[®] and Flowmaster[®]) combines the advantages of the finite element method and the network theory. As Flowmaster[®] bases on a flow network, the standard components are not suitable for the modeling of the cooling channel in the generator. But on the other hand the components in the network affect each other. Only utilizing FEM cannot solve the whole variation of flow rate in acceptable time. The network model allows the exploration of the global coolant distribution and additionally is flexible to investigate in different input conditions.

References

1. Tong, W (2008) Numerical analysis of flow field in generator end-winding region. Department of Mechanical Engineering, Virginia Polytechnic Institute and State University, Blacksburg
2. Rosendahl J (2010) Ursachen und Auswirkungen von Windungen und Phasenschlüssen im Stator großer Synchronmaschinen, TU Dortmund University
3. Streeter VL, Wylie EB (1998) Fluid mechanics, 9th edn. McGraw-Hill Companies Inc, Michigan
4. Flowmaster V7 (2010) New user training, Version 10, USA

Two-Directional Two-Pole Single Phase Line Start Permanent Magnet Synchronous Motor

M. Gwoździewicz

Abstract The paper deals with constructions of two-directional two-pole single-phase line start permanent magnet synchronous motor. Circuit-field single-phase line start permanent magnet synchronous motor models were applied in Maxwell ver. 16 program. Various rotor constructions were taken into account. Influence of the rotor construction on the motor properties was examined.

1 Introduction

The norm IEC 60034 part 30 orders the electrical motor producers to produce electrical motors with minimum factor of the efficiency. The goal of this command is to minimize electrical energy consumption by minimization of electrical motor power losses. Nowadays this norm ranges low-voltage electrical motors with rated power $0.75 \text{ kW} \leq P_n \leq 375 \text{ kW}$ and number of pole pairs $2p = 2; 4; 6$. The new project of the norm assumes widening of the electrical motor rated power range up to $0.12 \text{ kW} \leq P_n \leq 1,000 \text{ kW}$, number of pole pairs up to $2p = 2; 4; 6; 8$ and including multi-phase motors (single-phase motors in it).

Producers of electrical motors responded to the norm requirements by designing and producing high-efficiency three-phase motors which fulfil the norm by achieving the minimum factor of the efficiency. The electrical motor producers respond did not include single-phase motors which are not included by the norm yet.

If the new norm project IEC 60034 part 30 were valid no single-phase motor produced nowadays would fulfil the norm requirements.

In articles [2, 8] possibility of building of single-phase line start permanent magnet synchronous motor was proven. The single-phase line start permanent

M. Gwoździewicz (✉)

Institute of Electrical Machines, Drives and Measurements,
Wrocław University of Technology, Wrocław, Poland
e-mail: maciej.gwozdziewicz@pwr.edu.pl

magnet synchronous motor would achieve much better running properties than single-phase induction motor running properties. Taking into account the modern electrical motor development we can suppose that in case of restricted new requirements of producing electrical motors producers of single-phase motors will be forced to design and produce single-phase line start permanent magnet synchronous motors.

The price of permanent magnet is still going up. Due to this reason the goal of modern designing of permanent magnet synchronous machine is to obtain good running performances (efficiency, power factor) with simultaneously minimizing the permanent magnet mass.

2 Construction of Two-Directional Two-Pole Single-Phase Line Start Permanent Magnet Synchronous Motor

In Maxwell version 16 program sixteen circuit-field models of single-phase line start permanent magnet synchronous motor were built. The models are based on the mass production single-phase induction motor type SEh 80-2B with rated power $P_n = 1.1$ kW supplied by the AC voltage $U_n = 230$ V $f_n = 50$ Hz. Neodymium magnet *N38SH* with remanence induction $B_r = 1.24$ T and magnetic field coercivity $H_{cb} = 990$ kA/m was chosen for the excitation. Methodology of single-phase line start permanent magnet synchronous motor designing was revealed in articles [1, 4]. The papers [3, 5–7, 9] were also helpful for the designer. All built models are shown in Fig. 1.

Two-directional single-phase AC motor has the same main and auxiliary winding with the same number of turns. Their endings are connected together in one node to one phase (ground potential). The capacitors (running and starting) are connected in parallel with the windings beginnings. To change direction of motor rotation the supply phase must be reconnected from one winding beginning to one another. Due to that tasks of these two windings changes each other (main↔auxiliary). The schema of this connection is presented in Fig. 2.

3 Investigation

Influence of the number of rotor bars and permanent magnets shapes were investigated. The goal was to obtain the highest magnitude of the 1st harmonic of back EMF and the lowest THD coefficient of the back EMF. Results of this investigation are shown in Fig. 3. According to the obtained results the best solution for two-directional two-pole single-phase line start permanent magnet synchronous motor with number of stator slots $Q_S = 24$ slots are number of rotor slots $Q_R = 17$ slots and W shape of permanent magnets.

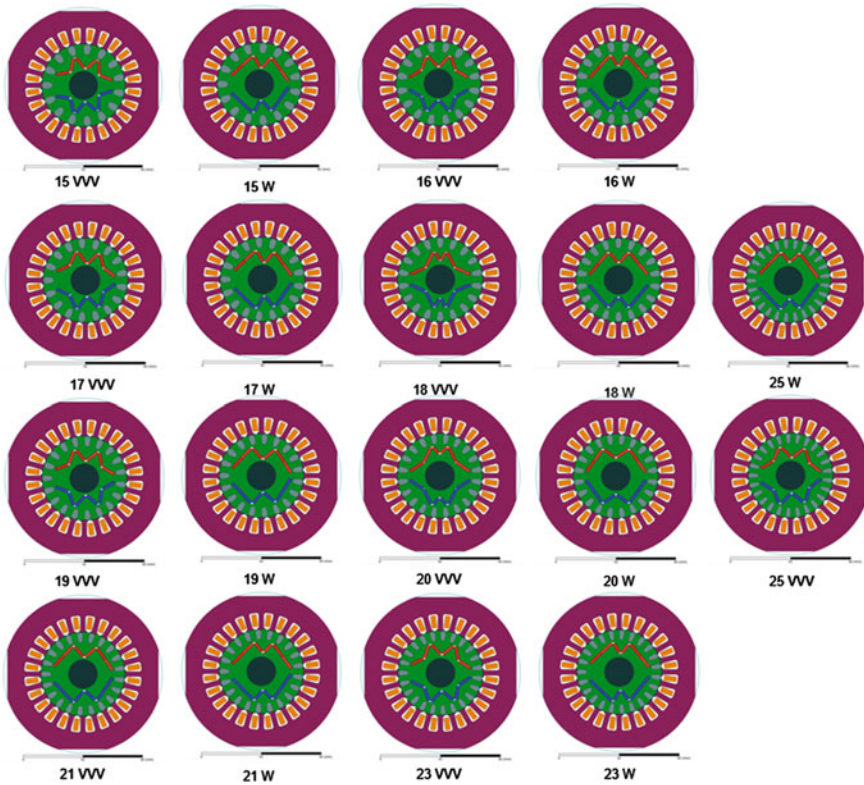
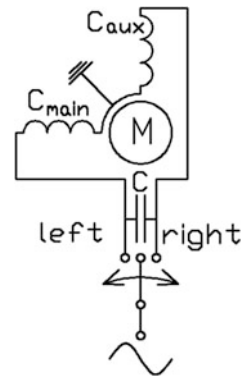


Fig. 1 Models of two-directional two-pole single-phase line start permanent magnet synchronous motor

Fig. 2 Electrical scheme of the two-directional single-phase AC motor



Next step was investigation of influence of the capacitor capacitance on the single-phase permanent magnet synchronous motor on its efficiency curve. Results of this investigation are presented in Fig. 4. For the assumed rated power of the

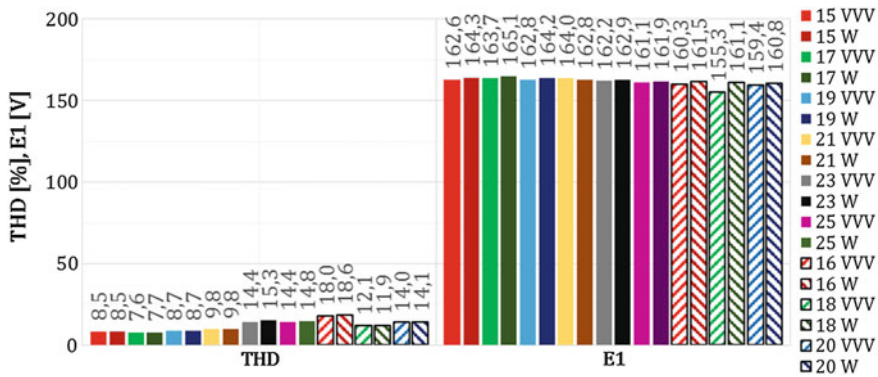
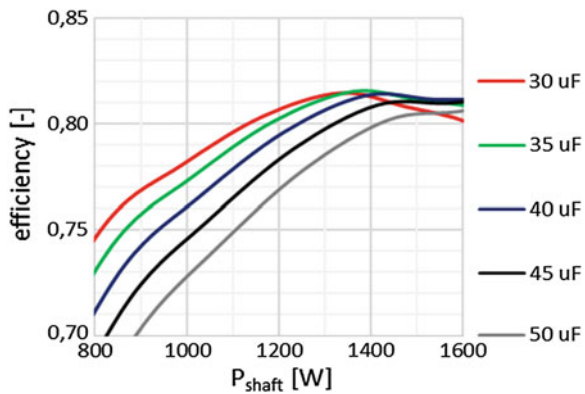


Fig. 3 Influence of the number of rotor bars and permanent magnets shape on the RMS value of the 1st back EMF and its THD factor

Fig. 4 Influence of the number of rotor bars and permanent magnets shape on the RMS value of the 1st back EMF and its THD factor



motor $P_n = 1.5$ kW the best solution is capacitor with capacitance $C = 35 \mu\text{F}$ because of the highest magnitude of the efficiency $\eta_{max} = 81.6 \%$.

The last step was comparison of two-pole single-phase induction motor and two-pole line start permanent magnet synchronous motor. Both motors have the same stator. Results of the comparison is shown in Table 1. PMSM has much better running properties than IM.

Table 1 Comparison of single-phase IM and PMSM

Motor	Type	IM	PMSM
P_n	kW	1.1	1.5
n_n	rpm	2,780	3,000
η_n	%	72.0	81.1
PF	–	0.97	0.95
I_n	A	7.0	8.2

4 Conclusions

Two-directional two-pole single-phase line start permanent magnet synchronous motor has much better properties in comparison with single-phase induction motor. Moreover, rated power of the PMSM motor is higher from the same volume and speed is constant.

To build two-directional single-phase AC motor numbers of stator windings turns must be the same. The proper direction switch must be applied to avoid short-circuit and burning of the motor during changing direction of the motor rotation.

References

1. Aliabad AD, Mirsalim M, Ershad NF (2010) Line-start permanent-magnet motors: significant improvements in starting torque, synchronization, and steady-state performance. *IEEE Trans Magn* 46(12):4066–4072
2. Feng X, Liu L, Kang J, Zhang Y (2010) Super premium efficient line start-up permanent magnet synchronous motor. In: 2010 XIX international conference on electrical machines (ICEM), Rome, Italy, pp 1–6, 6–8 September 2010
3. Guang Y, Jun M, Jian-Xin S, Yu W (2008) Optimal design and experimental verification of a line-start permanent magnet synchronous motor, 2008. In: ICEMS 2008. international conference on electrical machines and systems, p 3232–3236
4. Gwozdziejewicz M, Zawilak J (2013) Single-phase line start permanent magnet synchronous motor rotor designing, *Przegląd Elektrotechniczny*
5. Kurihara K, Wakui G, Kubota T (1994) Steady-state performance analysis of permanent magnet synchronous motors including space harmonics. *IEEE Trans Magn* 30(3):1994
6. Liang F, Lee BH, Jung-Pyo H, Hyuk N (2009) Estimation of magnet reduction in single-phase line-start permanent magnet synchronous motor. In: Annual meeting of the IEEE industry applications society, IAS 2009
7. Lin D, Zhou P, Lambert N (2010) Starting winding optimization in single-phase. In: Electrical machines (ICEM), 2010 XIX international conference
8. Popescu M, Miller TJE, McGilp MI (2006) Torque behavior of 1-phase permanent magnet AC motor. *IEEE Trans Energy Convers* 21
9. Yang G, Ma J, Shen JX, Wang Y (2008) Optimal design and experimental verification of a line-start permanent magnet synchronous motor. 2008. In: International conference on electrical machines and systems ICEMS, p 3232–3236

Overhead Lines in Power System with Wind Power Plants and Photovoltaic Power Plants

M. Zeńczak

Abstract Presented analysis takes into considerations the current carrying-capacity as the function of temperature of the air, sun radiation and wind speed. The wind creates the additional possibility of transmission of energy generated in wind power plants, because the higher wind velocity the higher current-carrying capacity of overhead lines and the higher generated power in wind power plants. On the other hand the higher solar radiation and temperature, the lower current-carrying capacity of overhead lines. The solar radiation and temperature change the level of generation in photovoltaic power plants. The paper presents exact analysis of relation between current-carrying capacity of overhead lines and level of generation in wind power plants and photovoltaic power plants for different conditions.

1 Introduction

The current-carrying capacity is the most important parameter of overhead lines during analysis of possibilities of connection new sources of electrical energy to power system. Among the all renewable energy sources mainly wind and sun can be used for generation of electrical energy. Therefore the development of wind power plants (WPP) and photovoltaic power plants (PPP) is quite high. Very often current-carrying capacity of lines is some obstacle in this development.

The current-carrying capacity is treated by the transmission and distribution operators as the constant parameter, at most dependent on season of the year. In fact the current-carrying capacity is the function of temperature of air, sun radiation and wind speed: the higher sun radiation or temperature the lower current-carrying capacity but the higher wind speed the higher current-carrying capacity [1, 2].

M. Zeńczak (✉)

Chair of Power Engineering and Electrical Drives, West Pomeranian University
of Technology, Szczecin, Poland
e-mail: michal.zenczak@zut.edu.pl

The wind speed is the main quantity which indicates level of generation of electrical energy in WPP: the higher wind speed the higher level of generation of electrical energy. The level of generation in PPP depends on sun radiation and temperature: the higher sun radiation, the higher level of generation, but in single cell the generation is higher, when temperature is lower.

The current-carrying capacity, generation of electrical energy in WPP and PPP are strictly connected with weather conditions: temperature of air, sun radiation and wind.

2 Generation of Electrical Energy in Wind Power Plants

The power in moving air is the flow rate of kinetic energy per time unit. The power coming in the upstream wind is given by relation:

$$P = \frac{1}{2}(\rho Av)v^2 = \frac{1}{2}\rho Av^3 \quad (1)$$

The actual power extracted by the rotor blades is the difference between the upstream and downstream wind powers. Macroscopically, the air speed is discontinuous from v to v_0 at the plane of rotor blades, with an average of v and v_0 . Multiplying the air density ρ by the average speed, gives the mass flow rate of air through the rotating blades. The mechanical power extracted by the rotor, which drives the electrical generator is expressed by the following relationship:

$$P_o = \frac{1}{2} \left[\rho A \frac{v + v_0}{2} \right] (v^2 - v_0^2) \quad (2)$$

Relationship (2) can be expressed in following form:

$$P_o = \frac{1}{2} \rho A C_p v^3 \quad (3)$$

where:

$$C_p = \frac{(1 + \frac{v_0}{v}) \left[1 - (\frac{v_0}{v})^2 \right]}{2} \quad (4)$$

C_p is ratio of mechanical power which can drive the generator to power of wind. For a given upstream wind speed relationship (4) shows that the value of C_p depends on the ratio of downstream to the upstream wind speeds. C_p has maximum value of 59 for v_0/v ration equals to 1/3. In practical designs, the maximum achievable C_p ranges between 0.4 and 0.5 for modern high-speed two blade turbines, and between 0.2 and 0.4 for slow-speed turbines with more blades [3]. Generally the power output of the wind turbine in air, where $\rho = \text{const}$ can be expressed by the simple relationship:

$$P_o = Const \cdot v^3 \tag{5}$$

It means, that power, which can drive the generator is proportional to the third power of wind speed. Wind power plants are equipped in many control systems. These control systems use many different algorithms. But generally the output characteristic of wind power plant has following separate regions:

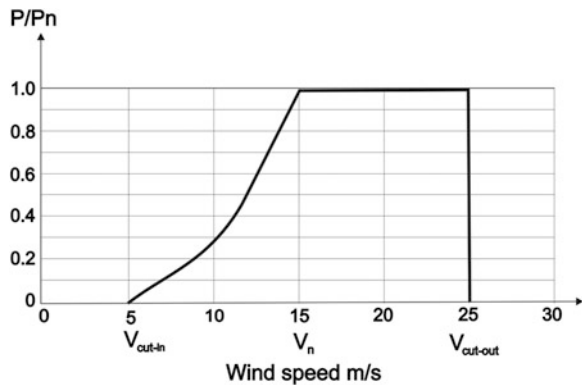
- $v < v_{cut-in}$ —speed of wind lower than speed, at which the turbine starts producing power,
- $v = v_{cut-in}$ —speed, at which the turbine starts producing power,
- $v_{cut-in} < v < v_n$ —region of constant C_p , where rotor speed varies with the wind speed variation to operate at the constant tip speed ratio (TSR) corresponding to the maximum C_p value,
- $v_n < v < v_{cut-out}$ —region of constant power—the C_p is lower than the maximum C_p ,
- $v = v_{cut-out}$ —cut-out speed, at which the rotor is shut off,
- $v > v_{cut-out}$ —standstill of WPP.

The typical value of v_{cut-in} is 5 m/s, while typical value for v_n is 15 m/s and typical value of $v_{cut-out}$ is 25 m/s. In point of view of current-carrying capacity two regions are interesting: the region of constant C_p (increasing power) and region of constant power. These regions are presented in Fig. 1.

Taking into account control systems of power plant, the power of WPP has the form:

$$P_{WPP} = \begin{cases} 0 & \text{for } v < v_{cut-in} \\ K + Lv^3 & \text{for } v_{cut-in} \leq v < v_n \\ P_n & \text{for } v_n \leq v \leq v_{cut-out} \\ 0 & \text{for } v > v_{cut-out} \end{cases} \tag{6}$$

Fig. 1 Approximate output characteristic of typical wind power plant



Currents in power lines connected to wind power farms depend on wind speed only in some ranges. It means, that currents in power lines are increasing function of wind speed for the range: $v_{cut-in} < v < v_n$. For the range $v_n < v < v_{cut-out}$ currents do not change.

3 Generation of Electrical Energy in Photovoltaic Power Plants

The level of generation in photovoltaic plants is defined for the Standard Test Conditions (STC): temperature $t_{STC} = 25$ °C, solar radiation $Q_{SSTC} = 1,000$ W/m², air mass AM1.5. In conditions other than STC the level of generation is different. In point of view of current-carrying capacity the most essential is maximum generated power in weather conditions, which are the basis for estimation of current-carrying capacity.

The level of generation in single photovoltaic cell is the following function of temperature [3]:

$$P = I_0(1 + b_I \Delta \vartheta) U_0(1 + b_U \Delta \vartheta) \quad (7)$$

For typical cells the relative increase of current b_I is much more lower than relative decrease of voltage b_U . Therefore the function (7) is decreasing function of temperature.

For typical photovoltaic plants coefficient of relative power b_P changes in range from -0.005 (for monocrystalline cells) to -0.00268 (for amorphous cells). Relationship (7) can be written in following form:

$$P_{MPP} = P_{MPPSTC}(1 + b_P \Delta \vartheta) \quad (8)$$

where P_{MPP} —power in given temperature, P_{MPPSTC} —power in standard conditions. The level of generation in photovoltaic plants is the rising function of solar radiation. If the efficiency of transformation of solar energy to electrical energy η is constant in range from 0 to 1,100 W/m², then the linear function between maximum power point (MPP) and solar radiation can be assumed:

$$P_{MPP} = P_{MPPSTC} \frac{Q_S}{Q_{SSTC}} \quad (9)$$

$$I_{MPP} = P_{MPPSTC} \frac{Q_S}{\sqrt{3} U_n Q_{SSTC}} \quad (10)$$

Relationships (9) and (10) enable calculation of power in maximum power point P_{MPP} for given value of solar radiation Q_S and the current I_{MPP} flowing from photovoltaic power plant to power system for the nominal voltage U_n .

4 Current-Carrying Capacity of Overhead Lines

The basic criterion of current-carrying capacity of overhead lines is maximum permissible sag, which is connected with minimal distances between conductors and ground or objects crossed by line. The design temperature is basis for estimation of permissible sag and distances between conductors and crossed objects. In Poland lines are designed mainly for 40 °C, although there are lines designed for 60 and 80 °C. Temperature of 80 °C is the highest permissible temperature of common AFL conductors. The highest permissible temperature of new conductors achieves even +250 °C [4]. Such the conductors create new chances of increasing of current-carrying capacity of lines. Besides the high temperature conductors have very profitable mechanical properties. Their sag is low. Therefore high temperature conductors with low sag are called HTLS. They are suited for modernization of old power transmission lines with low pylons and for building new power transmission lines of high transmission capability.

The current-carrying capacity in power transmission or distribution companies is defined for winter and summer. This may cause, that in very hot sunny weather, without wind lines may be overload. On the other hand even in summer the same lines during cold, cloudy days with strong wind have big margin of current-carrying capacity, which can be utilized. Thus instead of application of new HTLS conductor there is possibility of utilization common traditional AFL conductors with monitoring of temperature [1]. The temperature of conductor depends on current, wind speed, temperature of air and sun radiation. Therefore temperature of conductor dependent on weather condition changes in quite wide range. The thermal static balance of conductor can be expressed by following relationship:

$$P_i + P_s = P_c + P_r \quad (11)$$

where: P_i —power produced by current flow, P_s —power absorbed from sun radiation, P_c —power of convection, P_r —power of radiation. The dynamic balance should take into consideration energy used for heating up conductors to their new temperature. Total thermal power absorbed from sun radiation P_s can be calculated from the relationship:

$$P_s = \alpha_s Q_s D_w \quad (12)$$

where: α_s —absorption coefficient of conductor surface, Q_s —solar radiation, D_w —external diameter of conductor.

P_c and P_r are functions of temperature of environment ϑ_{EN} and temperature of conductor ϑ_w :

$$P_c = \pi \lambda (\vartheta_w - \vartheta_{EN}) Nu \quad (13)$$

$$P_r = \pi D_w \varepsilon \delta_B \left[(\vartheta_w + 273)^4 - (\vartheta_{EN} + 273)^4 \right] \quad (14)$$

where: λ —thermal conductivity of air, ε —thermal emission factor, δ_B —Stefan-Boltzmann’s constant.

Nusselts number Nu is related to Reynolds number Re

$$Nu = B(Re)^n \tag{15}$$

where: B, n —coefficients, which are the function of Reynold’s number Re . Reynold’s number is function of wind speed:

$$Re = \frac{\rho v D_w}{\nu} \tag{16}$$

where: ρ —air density, ν —viscosity of air, v —wind speed.

Table 1 presents physical properties of air. The STC are marked in all tables as bold letters. Table 2 presents values of coefficients B and n .

The load capacity as the function of weather conditions can be expressed by the formula:

$$P_i = P_c + P_r - P_s \tag{17}$$

where P_s, P_c and P_r were estimated before.

Relationship (17) enables estimation of current—carrying capacity:

$$I_{cc} = \sqrt{\frac{1}{R}(P_c + P_r - P_s)} \tag{18}$$

where: R —resistance of conductor in given temperature:

$$R = R_{20}(1 + \alpha \Delta\vartheta) \tag{19}$$

where: R_{20} —resistance of conductor in temperature 20 °C.

Table 1 Physical properties of air

T	t	ρ	λ	ν
K	°C	kg/m ³	W/(m·K)	m ² /s
273	0	1.293	0.0244	0.00001328
278	5	1.270	0.0248	0.00001372
283	10	1.247	0.0251	0.00001416
288	15	1.226	0.0255	0.00001461
293	20	1.205	0.0259	0.00001506
298	25	1.185	0.0263	0.00001553
303	30	1.165	0.0267	0.00001600
308	35	1.147	0.0271	0.00001648
313	40	1.128	0.0276	0.00001696

Table 2 Values of coefficient B and n

Roughness R_s	Reynold's number Re		B	n
	from	to		
Any wire	100	2,650	0.641	0.471
$R_s \leq 0.05$	2,650	50,000	0.178	0.633
$R_s \geq 0.05$	2,650	50,000	0.048	0.800

Roughness R_s can be estimated from the expression:

$$R_s = \frac{d_w}{2D_w - 2d_w} \quad (20)$$

where: d_w —diameter of single wire in conductor.

5 Current-Carrying Capacity of Overhead Lines for Different Situations

There are many kinds of conductors, which are used in Poland and other countries. The most important parameter is diameter of conductors. The aim of presented analysis is relation between current carrying capacity, generation of power in wind power plants and photovoltaic plants. Table 3 contains the basic properties of typical conductors.

Taking into consideration real wind power plants and photovoltaic plants, it may be concluded, that nowadays the level of generation of electrical energy in both plants may be quite different: there are big wind power farms with nominal power about hundreds MW, while the highest power of photovoltaic plants is not higher than a few MW.

Considering polish regulations the power of photovoltaic plants perhaps will be not higher than 2 MW, because for the power not higher than 2 MW the connection expertise is not required.

Therefore analysis is presented for two different conductors. The first analysis is done for the overhead line with conductor AFL-6 120 mm². Such the conductors are mainly used for 110 kV line. The current carrying capacity is 415 A (80 MW). It means that the wind power farm and photovoltaic plants are connected to 110 kV grid. Of course in Poland such the situation is typical for wind power farms, because there are many wind power farms with nominal power from range 10–40 MW. For PPP this situation nowadays in Poland is only theoretical.

The second analysis takes into consideration conductor AFL-6 35 mm². Such the lines are mainly used as the lateral of rural network 15 kV. The current carrying capacity is 170 A (4,42 MW). It is typical solutions when there is necessity of connecting new WPP or PPP to power system.

Table 3 Properties of conductors

Conductor AFL	Diameter	Resistance of 1 km for $t = 20\text{ }^{\circ}\text{C}$	Current-carrying capacity
mm^2	mm	Ω/km	A
525	31.50	0.0564	1030
240	21.70	0.1240	630
185	19.20	0.1593	540
120	15.65	0.2388	415
70	12.6	0.3835	255
50	9.6	0.6053	210
35	8.1	0.8522	170

Analyses have been done for the wind speeds: 0.5, 5, 10 and 15 m/s. Values of temperature: 10, 15, 20, 25, 30 and 35 $^{\circ}\text{C}$. Values of solar radiation: 0, 100, 200, 300, 400, 500, 600, 700, 800, 900, 1,000 and 1,100 W/m^2 . Values of α_S (absorption coefficient of conductor surface) and ε (thermal emission factor) are 0.5.

5.1 Calculation for Conductor AFL-6 35 mm^2

The results of calculations for conductor AFL-6 35 mm^2 are presented in Tables 4, 5, 6 and 7.

Table 8 contains results of calculations of current-carrying capacity as the function of α_S and ε in STC

Table 4 Current-carrying capacity of conductor AFL-6 35 mm^2 for wind speed 0.5 m/s

v 0.5 m/s	g_{EN} 10 $^{\circ}\text{C}$	g_{EN} 15 $^{\circ}\text{C}$	g_{EN} 20 $^{\circ}\text{C}$	g_{EN} 25 $^{\circ}\text{C}$	g_{EN} 30 $^{\circ}\text{C}$	g_{EN} 35 $^{\circ}\text{C}$
Q_S (W/m^2)	I_{CC} (A)	I_{CC} (A)	I_C (A)	I_{CC} (A)	I_{CC} (A)	I_{CC} (A)
0	159.3	145.0	129.8	112.0	89.3	64.5
100	158.0	143.8	128.1	110.2	86.8	61.1
200	156.8	142.3	126.4	108.2	84.3	57.4
300	155.4	140.8	124.7	106.2	81.6	53.5
400	154.0	139.2	123.0	104.1	78.9	49.2
500	152.6	137.6	121.1	102.0	76.1	44.6
600	151.1	136.1	119.3	99.8	73.2	39.4
700	149.7	134.5	117.5	97.6	70.2	33.5
800	148.2	132.8	115.6	95.4	67.0	26.2
900	146.7	131.2	113.7	93.1	63.7	15.8
1,000	145.3	129.5	111.8	90.7	60.2	0.0
1,100	143.8	127.8	109.8	88.3	56.4	0.0

Table 5 Current-carrying capacity of conductor AFL-6 35 mm² for wind speed 5 m/s

v 5 m/s	g_{EN} 10 °C	g_{EN} 15 °C	g_{EN} 20 °C	g_{EN} 25 °C	g_{EN} 30 °C	g_{EN} 35 °C
Q_S (W/m ²)	I_{CC} (A)	I_{CC} (A)	I_{CC} (A)	I_{CC} (A)	I_{CC} (A)	I_{CC} (A)
0	267.3	241.6	215.5	186.0	151.6	106.8
100	266.5	240.7	214.4	184.9	150.1	104.8
200	265.7	239.8	213.4	183.7	148.7	102.7
300	264.9	238.9	212.4	182.5	147.2	100.5
400	264.0	237.9	211.3	181.3	145.7	98.4
500	263.2	237.0	210.4	180.1	144.2	96.1
600	262.4	236.0	209.3	178.9	142.7	93.8
700	261.6	235.2	208.3	177.7	141.2	91.5
800	260.7	234.3	207.2	176.4	139.6	89.1
900	259.9	233.3	206.2	175.2	138.1	86.6
1,000	259.0	232.4	205.1	173.9	136.5	84.1
1,100	258.2	231.5	204.1	172.7	134.9	81.4

Table 6 Current-carrying capacity of conductor AFL-6 35 mm² for wind speed 10 m/s

v 10 m/s	g_{EN} 10 °C	g_{EN} 15 °C	g_{EN} 20 °C	g_{EN} 25 °C	g_{EN} 30 °C	g_{EN} 35 °C
Q_S (W/m ²)	I_{CC} (A)	I_{CC} (A)	I_{CC} (A)	I_{CC} (A)	I_{CC} (A)	I_{CC} (A)
0	350.1	316.1	279.7	239.7	193.6	135.5
100	349.5	315.4	279.0	238.8	192.5	133.9
200	348.9	314.8	278.2	237.8	191.3	132.3
300	348.2	314.1	277.4	236.9	190.2	130.6
400	347.6	313.4	276.6	236.0	189.1	129.0
500	347.0	312.7	275.8	235.1	187.9	127.3
600	346.4	312.0	275.0	234.2	186.7	125.5
700	345.7	311.3	274.2	233.2	185.6	123.8
800	345.1	310.6	273.4	232.3	184.4	122.0
900	344.5	309.9	272.6	231.3	183.7	120.2
1,000	343.8	309.2	271.8	230.4	182.0	118.4
1,100	343.2	308.5	271.0	229.5	180.8	116.6

Table 7 Current-carrying capacity of conductor AFL-6 35 mm² for wind speed 15 m/s

v 15 m/s	ϑ_{EN} 10 °C	ϑ_{EN} 15 °C	ϑ_{EN} 20 °C	ϑ_{EN} 25 °C	ϑ_{EN} 30 °C	ϑ_{EN} 35 °C
Q_S (W/m ²)	I_{CC} (A)	I_{CC} (A)	I_{CC} (A)	I_{CC} (A)	I_{CC} (A)	I_{CC} (A)
0	410.6	370.7	328.0	281.0	226.9	158.8
100	410.1	370.1	327.3	280.2	226.0	157.5
200	409.5	396.6	326.7	279.4	225.0	156.1
300	409.0	369.0	326.0	278.6	224.0	154.7
400	408.5	368.4	325.3	277.8	223.1	153.3
500	407.9	367.8	324.7	277.1	222.1	151.8
600	407.4	367.2	324.0	276.3	221.1	150.4
700	406.9	366.6	323.3	275.5	220.1	148.9
800	406.3	366.0	322.6	274.7	219.1	147.5
900	405.8	365.4	322.0	273.9	218.1	146.0
1,000	405.3	364.8	321.3	273.1	217.1	144.5
1,100	404.7	364.5	320.6	272.3	216.1	143.0

5.2 Calculation for Conductor AFL-6 120 mm²

The results of calculations for conductor AFL-6 120 mm² are presented in Tables 9, 10, 11 and 12. Table 13 contains results of calculations of current-carrying capacity as the function of α_S (absorption coefficient of wire surface) and ε (thermal emission factor) in STC.

6 Wind Power Plants, Photovoltaic Power Plants and Current-Carrying Capacity

The most interesting range of wind speed is $v_{cut-in} < v < v_n$. In this range currents (powers) flowing from wind power plants are increasing function of wind speed:

$$P_{WPP} = P_n \frac{v^3 - v_{cut-in}^3}{v_n^3 - v_{cut-in}^3} \quad (21)$$

$$I_{WPP} = \frac{P_n}{\sqrt{3}U_n} \cdot \frac{v^3 - v_{cut-in}^3}{v_n^3 - v_{cut-in}^3} \quad (22)$$

The level of generation in WPP is independent of solar radiation and temperature of air, while the level of generation in PPP depends on solar radiation and temperature of air, but not on wind speed. Of course meteorology knows perhaps

Table 8 Current-carrying capacity of conductor AFL-6 35 mm² as the function of α_s and ε in STC

	$v = 0.5$ m/s	$v = 5$ m/s	$v = 10$ m/s	$v = 15$ m/s
$\alpha_s = \varepsilon$	I_{CC} (A)	I_{CC} (A)	I_{CC} (A)	I_{CC} (A)
0.15	101.7	179.9	235.0	277.0
0.20	100.2	179.0	234.3	276.4
0.25	98.7	178.2	233.7	275.9
0.30	97.1	177.4	233.0	275.3
0.35	95.6	176.5	232.4	274.8
0.40	94.0	175.7	231.7	274.2
0.45	92.3	174.8	231.1	273.7
0.50	90.7	173.9	230.4	273.1
0.55	89.0	173.1	229.7	272.6
0.60	87.3	172.2	229.0	272.0
0.65	85.5	171.3	228.4	271.4
0.70	83.8	170.4	227.8	270.9
0.75	81.9	169.5	227.1	270.3
0.80	80.1	168.6	226.4	269.8
0.85	78.2	167.8	225.8	269.2
0.90	76.2	166.8	225.1	268.6
0.95	74.2	165.9	224.4	268.1

Table 9 Current-carrying capacity of conductor AFL-6 120 mm² for wind speed 0.5 m/s

v 0.5 m/s	g_{EN} 10 °C	g_{EN} 15 °C	g_{EN} 20 °C	g_{EN} 25 °C	g_{EN} 30 °C	g_{EN} 35 °C
Q_s (W/m ²)	I_{CC} (A)	I_{CC} (A)	I_{CC} (A)	I_{CC} (A)	I_{CC} (A)	I_{CC} (A)
0	358.6	327.3	302.9	252.9	206.2	145.7
100	354.4	322.7	297.9	246.9	198.8	135.0
200	350.1	318.0	292.8	240.7	191.1	123.4
300	345.8	309.2	287.6	234.4	183.1	110.6
400	341.5	304.4	282.4	227.9	174.7	96.0
500	337.0	303.6	277.0	221.2	165.9	78.9
600	332.6	298.6	271.5	214.3	156.6	56.8
700	328.0	293.5	265.9	207.2	146.7	14.8
800	323.4	288.4	260.2	200.0	136.1	0.0
900	318.7	283.1	254.4	192.2	124.6	0.0
1,000	314.0	277.7	248.4	184.2	111.9	0.0
1,100	309.2	272.3	242.3	175.9	97.6	0.0

Table 10 Current-carrying capacity of conductor AFL-6 120 mm² for wind speed 5 m/s

v 5 m/s	g_{EN} 10 °C	g_{EN} 15 °C	g_{EN} 20 °C	g_{EN} 25 °C	g_{EN} 30 °C	g_{EN} 35 °C
Q_S (W/m ²)	I_{CC} (A)	I_{CC} (A)	I_{CC} (A)	I_{CC} (A)	I_{CC} (A)	I_{CC} (A)
0	658.9	595.2	527.0	451.7	365.7	252.7
100	656.6	592.7	524.1	448.3	361.5	246.7
200	654.3	590.2	521.2	445.0	357.4	240.5
300	652.0	587.6	518.4	441.6	353.1	234.2
400	649.7	585.1	515.5	438.2	348.9	227.7
500	647.4	582.5	512.5	434.7	344.5	221.0
600	645.1	579.9	509.6	431.3	340.2	214.1
700	642.7	577.3	506.6	427.8	335.7	207.0
800	640.4	574.7	503.7	424.3	331.2	199.6
900	638.1	572.1	500.7	420.7	326.7	191.9
1,000	635.7	569.5	497.7	417.1	322.0	184.0
1,100	633.3	566.8	494.7	413.5	317.3	175.6

Table 11 Current-carrying capacity of conductor AFL-6 120 mm² for wind speed 10 m/s

v 10 m/s	g_{EN} 10 °C	g_{EN} 15 °C	g_{EN} 20 °C	g_{EN} 25 °C	g_{EN} 30 °C	g_{EN} 35 °C
Q_S (W/m ²)	I_{CC} (A)	I_{CC} (A)	I_{CC} (A)	I_{CC} (A)	I_{CC} (A)	I_{CC} (A)
0	862.1	778.5	689.0	590.3	477.7	333.9
100	860.4	776.6	686.8	587.7	474.6	329.3
200	858.6	774.7	684.6	585.2	471.4	324.7
300	856.9	772.7	682.4	582.6	468.2	320.1
400	855.1	770.8	680.2	580.0	465.0	315.4
500	853.4	768.8	678.0	577.4	461.8	310.6
600	851.6	766.9	675.8	574.8	458.5	305.7
700	849.9	764.9	673.5	572.2	455.2	300.8
800	848.1	763.0	671.3	569.6	451.9	295.7
900	846.3	761.0	669.1	566.9	448.6	290.6
1,000	844.5	759.0	666.8	564.3	445.2	285.4
1,100	842.8	757.0	664.6	561.6	441.8	280.1

relationships between wind speed, air temperature and solar radiation, but in point of view of power system all these three weather factors may be independent of each other. It means that in nature all of these weather factors may change in some ranges separately. Therefore the wind speed, solar radiation and temperature of air should be monitored the whole time, if this information is used in power system.

Table 12 Current-carrying capacity of conductor AFL-6 120 mm² for wind speed 15 m/s

v 15 m/s	ϑ_{EN} 10 °C	ϑ_{EN} 15 °C	ϑ_{EN} 20 °C	ϑ_{EN} 25 °C	ϑ_{EN} 30 °C	ϑ_{EN} 35 °C
Q_S (W/m ²)	I_{CC} (A)	I_{CC} (A)	I_{CC} (A)	I_{CC} (A)	I_{CC} (A)	I_{CC} (A)
0	1010.7	912.6	807.5	691.7	559.7	391.1
100	1009.2	910.9	805.6	689.5	557.0	387.2
200	1007.7	909.3	803.7	687.3	554.3	383.3
300	1006.2	907.6	801.9	685.1	551.6	379.4
400	1004.7	906.0	800.0	682.9	548.9	375.4
500	1003.3	904.3	798.1	680.7	546.2	371.4
600	1001.8	902.6	796.2	678.5	543.4	367.3
700	1000.3	901.0	794.3	676.3	540.6	363.2
800	998.8	899.3	792.4	674.1	537.9	359.1
900	997.3	897.6	790.6	671.9	535.1	354.9
1,000	995.7	896.0	788.7	669.6	532.2	350.6
1,100	994.2	894.3	786.7	667.4	529.4	346.3

Table 13 Current-carrying capacity of conductor AFL-6 120 mm² as the function of α_S and ϵ in STC

	$v = 0.5$ m/s	$v = 5$ m/s	$v = 10$ m/s	$v = 15$ m/s
$\alpha_S = \epsilon$	I_{CC} (A)	I_{CC} (A)	I_{CC} (A)	I_{CC} (A)
0.15	220.4	434.3	577.1	680.5
0.20	215.5	431.9	575.3	678.9
0.25	210.6	429.5	573.4	677.4
0.30	205.6	427.0	571.6	675.8
0.35	200.5	424.6	569.8	674.3
0.40	195.2	422.1	568.0	672.7
0.45	189.8	419.6	566.1	671.2
0.50	184.2	417.1	564.3	669.6
0.55	178.5	414.6	562.4	668.1
0.60	172.5	412.1	560.6	666.5
0.65	166.4	409.6	558.7	664.9
0.70	160.0	407.0	556.8	663.4
0.75	153.3	404.4	555.0	661.8
0.80	146.4	401.9	553.1	660.2
0.85	139.1	399.3	551.2	658.6
0.90	131.4	396.6	549.3	657.1
0.95	123.2	394.0	547.4	655.5

If the total change of current-carrying capacity $\Delta I_{cc} = f(v, \vartheta_{EN}, Q_s)$ or power $\Delta P_i = (v, \vartheta_{EN}, Q_s)$ is utilized, then the following equations should be fulfilled:

$$I_{cc} + \Delta I_{cc} \geq I_{gen} + \Delta I_{MPP} + \Delta I_{WPP} \quad (23)$$

$$P_i + \Delta P_i \geq P_{MPP} + \Delta P_{MPP} + P_{WPP} + \Delta P_{WPP} \quad (24)$$

The current-carrying capacity I_{cc} is raising function of wind speed, decreasing function of temperature of air and decreasing function of solar radiation. Power generated by PPP is decreasing function of temperature of air and rising function of solar radiation. Power generated by WPP is raising function of wind speed. In order to estimation the total change of current-carrying capacity and change of current I_{gen} caused by change of level of generation in WPP and PPP the following expressions can be used:

$$\Delta I_{cc} = \frac{\partial I_{cc}}{\partial v} \Delta v + \frac{\partial I_{cc}}{\partial \vartheta_{EN}} \Delta \vartheta_{EN} + \frac{\partial I_{cc}}{\partial Q_s} \Delta Q_s \quad (25)$$

$$\Delta I_{gen} = \frac{\partial I_{WPP}}{\partial v} \Delta v + \frac{\partial I_{MPP}}{\partial \vartheta_{EN}} \Delta \vartheta_{EN} + \frac{\partial I_{MPP}}{\partial Q_s} \Delta Q_s \quad (26)$$

where:

$$\frac{\partial I_{cc}}{\partial v} = \frac{\pi \lambda B n}{2 I_{cc} R} (\vartheta_w - \vartheta_{EN}) \left(\frac{\rho D_w}{v} \right)^n v^{n-1} \quad (27)$$

$$\frac{\partial I_{cc}}{\partial \vartheta_{EN}} = \frac{-\pi}{2 I_{cc} R} \left[\lambda B \left(\frac{\rho v D_w}{v} \right)^n + 4 D_w \varepsilon \delta_B (\vartheta_{EN} + 273)^3 \right] \quad (28)$$

$$\frac{\partial I_{cc}}{\partial Q_s} = \frac{-\alpha_s D_w}{2 I_{cc} R} \quad (29)$$

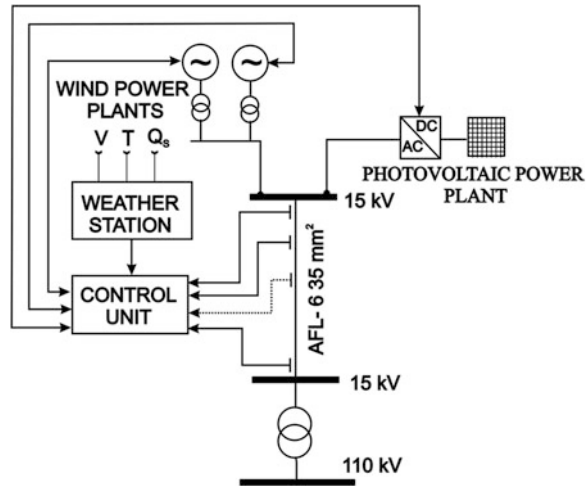
$$\frac{\partial I_{WPP}}{\partial v} = \frac{3 P_n v^2}{\sqrt{3} U_n (v_n^3 - v_{cut-in}^3)} \quad (30)$$

$$\frac{\partial I_{MPP}}{\partial \vartheta_{EN}} = \frac{P_{MPPSTC}}{\sqrt{3} U_n} b_p \quad (31)$$

$$\frac{\partial I_{MPP}}{\partial Q_s} = \frac{P_{MPPSTC}}{\sqrt{3} U_n Q_{SSTC}} \quad (32)$$

For example the current carrying-capacity in STC of conductor AFL-6 35 mm² rises from 173.9 A ($v = 5$ m/s) to 273.1 A ($v = 15$ m/s). It means, that in overhead line 15 kV additional power $\Delta P_i = 2,577$ MW may flow.

Fig. 2 Control system for overhead line connected with wind power plants and photovoltaic power plant



In overhead line 110 kV with conductor AFL-6 120 mm² the current carrying capacity rises in STC from 417.1 A ($v = 5$ m/s) to 669.6 A ($v = 15$ m/s). It means, that in overhead line 110 kV additional power $\Delta P_i = 48,108$ MW may flow.

Information from Tables 8 and 13 shows the influence of state of surface of conductor on current-carrying capacity.

The above analysis assumes, that the temperature of air, solar radiation and wind speed is the same near line, wind power plants and photovoltaic power plants.

If there are many heat sensors on line, then the system is able to control the functioning for places with different weather condition.

Using relationships (23)–(32) the control system for overhead line connected with WPP and PPP can be introduced. The Fig. 2 presents block diagram of this control system.

The algorithm of the system from Fig. 2 should keep the whole time the condition (23) and (24).

7 Discussion and Conclusions

Presented analysis shows, that control of weather conditions creates the possibilities of better utilization of current-carrying capacity of overhead power lines.

Such the solutions may be used in short lateral of rural network 15 kV or in power transmission lines 110, 220 and 400 kV. But the system in long lines will be much more complicated because of necessity of using many sensors in quite different places.

References

1. Kacejko P, Pijarski P (2008) Dynamic fitting of generation level to thermal capacity of overhead lines. *Elect Rev R* 84(5):80–83 (in Polish)
2. Małyszko O, Zeńczak M (2002) Wind power plant and current-carrying capacity of overhead power transmission lines. In: *Proceedings of the XIIth international symposium on heat transfer and renewable sources of energy, Szczecin-Międzyzdroje 2008, Poland*, pp 176–186
3. Patel MR (2006) *Wind and solar power systems*. Taylor and Francis Group, New York
4. Siwy E, Żmuda K (2009) Intensification of the network using in the distribution company. *Elect Rev R* 85(3):243–246 (in Polish)

An Analysis of a Brushless DC Motor with a Cup-Rotor

M.P. Ciurys, I. Dudzikowski and G. Bogusz

Abstract In the paper the designing of a brushless DC motor excited by NdFeB magnets with a cup-rotor, with the driven machine that can be built inside this motor is described. A field-circuit computation model of the motor with a supplying converter was developed. This model takes into account, i.e. the effect of the temperature on the value of the magnetic flux, the winding resistance, and the parameters of the converter semiconductor elements. As a result of the computations the magnetic circuit of the motor was developed in such a way that the magnetic flux did not penetrate the driven device which can be mounted inside the cup-rotor of the motor. The resultant waveforms of the electrical and mechanical parameters of the brushless DC motor are presented in the paper.

1 Introduction

The development of electronic and hard magnetic materials (in particular NdFeB magnets [1]) as well as the tendency to use energy-efficient drive systems makes brushless DC motors (BLDC motors) more and more attractive. These machines, also known as electronically commutated motors, exhibit many advantages in comparison to the other electrical motors. They are characterized by [2–4] high efficiency, high torque and power per mass unit ratio as well as high overload torque, which results in good dynamic properties of these motors. The overload capability of these machines mainly depends on the permissible value of the converter current and the permanent magnets resistance to demagnetization. Another advantage of the internal-rotor motors is a small moment of inertia.

M.P. Ciurys (✉) · I. Dudzikowski · G. Bogusz
Institute of Electrical Machines, Drives and Measurements, Wrocław University
of Technology, Wrocław, Poland
e-mail: marek.ciurys@pwr.wroc.pl

I. Dudzikowski
e-mail: ignacy.dudzikowski@pwr.wroc.pl

Magnetic flux in the rotor of a BLDC motor closes mainly in the area of the surface. As a result, the internal space is not used magnetically. The implementation of a cup-shaped rotor enables the use of this space for a driven machine, e.g. a pump. At present cup-rotors are mainly utilized in motors used in automation, where the small value of the moment of inertia is important. Such a solution is rarely used for permanent magnets machines, which can be found in the double-stator machines designed to operate as an integrated-starter-generator (ISG) [5] or for wind power generation [6].

The aim of this work is to develop a brushless DC motor with a cup-rotor for a driving device (e.g. pump), which can be mounted in the interior of the motor rotor and to determine waveforms of the electrical and mechanical parameters of the motor. The scope of the work is as follows:

- developing a field-circuit model of the BLDC motor with the converter,
- analyzing the impact of the rotor dimensions (angle and height of the magnets as well as rotor yoke thickness) on the cogging torque and the value of magnetic flux,
- determining waveforms of the electrical and mechanical parameters of the brushless DC motor.

2 Field-Circuit Model of the BLDC Motor with the Converter

An analysis was carried out on a designed motor with the following parameters: voltage $U_n = 220$ V, power $P_n = 2$ kW, rotational speed $n_n = 2,650$ rpm, pole pairs $p = 2$.

NdFeB magnets with the coercivity $BH_c = 844$ kA/m and the remanent magnetic flux density $B_r = 1.17$ T were used. A steel sheet typical for an induction three-phase motor was used for the stator. In the Maxwell software a field model of the BLDC motor and a time stepping finite element field-circuit model of the BLDC motor with a converter were developed. A cross-section with flux lines of the motor is shown in Fig. 2. The circuit part of the model (Fig. 1) includes the power supply, the converter and the BLDC motor. The end leakage inductance and resistance of the winding as well as the influence of the temperature on the permanent magnets parameters, the converter diodes and transistors parameters and the armature winding resistance were taken into account.

The circuit model of the BLDC motor with the converter is shown in Fig. 1, where the symbols stand for RA , RB , RC —the resistance of the motor winding phases, while EA , EB , EC are the summary electromotive force induced in the motor winding phases (including the emf of self and mutual induction and the emf of rotation). LAp , LBp , LCp are the end leakage inductance of the motor winding

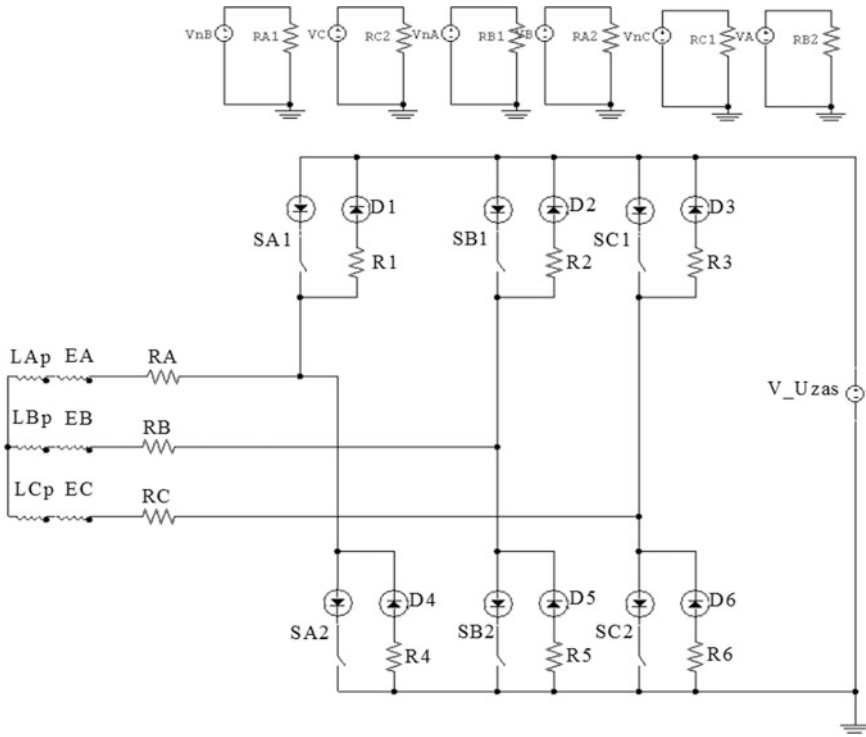


Fig. 1 Circuit model of the BLDC motor with the converter

phases and *SA1, SB1, SC1, SA2, SB2, SC2* stand for transistor switches of the converter; *D1–D6* are feedback diodes (model of an ideal p-n junction) of the converter, and *R1–R6*—the internal resistance of the converter feedback diodes, *V_Uzas*—supply voltage. The circuits with the *VA, VB, VC, VnA, VnB, VnC, RA1, RA2, RB1, RB2, RC1, RC2* elements are used to control the transistor switches operation as a function of the rotor position.

3 An Analysis of the Dimensions of the Magnetic Structure on the Cogging Torque and Magnetic Flux Value

To choose the dimensions of the magnetic structure of the motor that ensures the largest magnetic flux value with a small cogging torque the FEM field computations were performed for the changes of:

Fig. 2 Flux lines of the motor; $\alpha_m = 75^\circ$; $h_m = 4$ mm; $h_j = 12$ mm

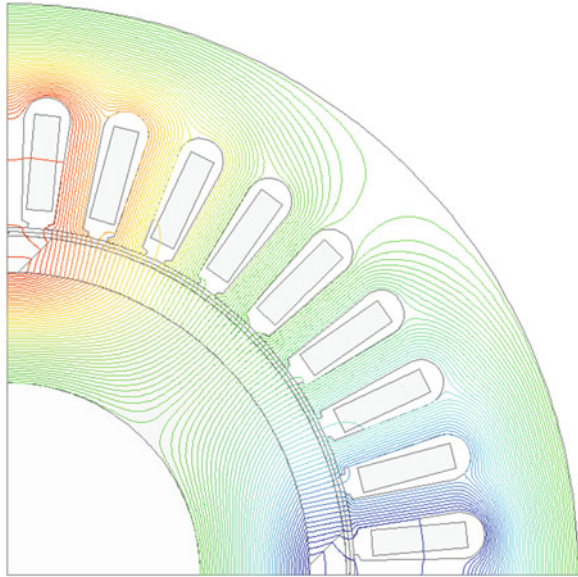
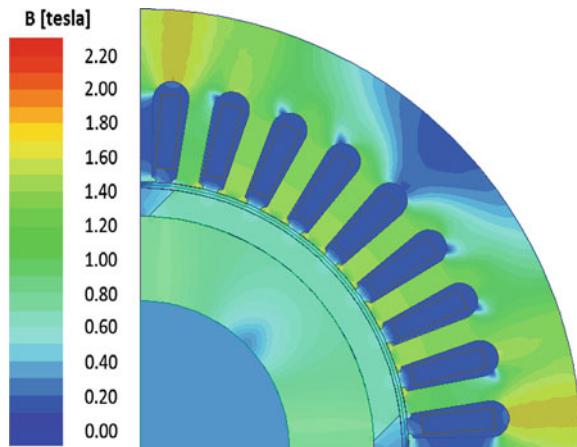


Fig. 3 Flux density distribution in the motor; $\alpha_m = 75^\circ$; $h_m = 4$ mm; $h_j = 12$ mm



- the magnets angle $\alpha_m = 65^\circ\text{--}76^\circ$,
- the magnets height $h_m = 3\text{--}4.5$ mm,
- the rotor yoke thickness $h_j = 4\text{--}12$ mm.

The most important results of the computational analyses are shown in Figs. 2, 3, 4, 5, 6, 7, 8, 9, 10, 11 and 12.

Fig. 4 Magnetic flux versus rotor yoke thickness at the different magnets angle; $h_m = 4$ mm

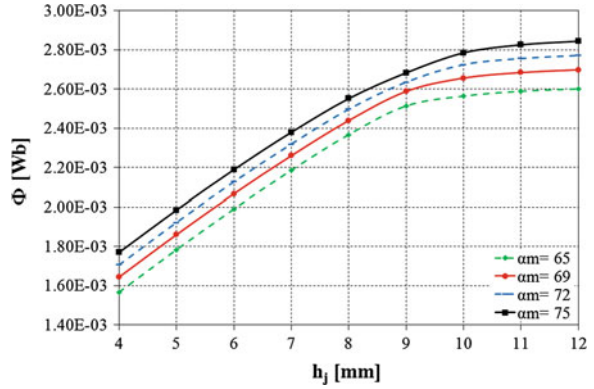


Fig. 5 Magnetic flux versus rotor yoke thickness at the different magnets height; $\alpha_m = 75^\circ$

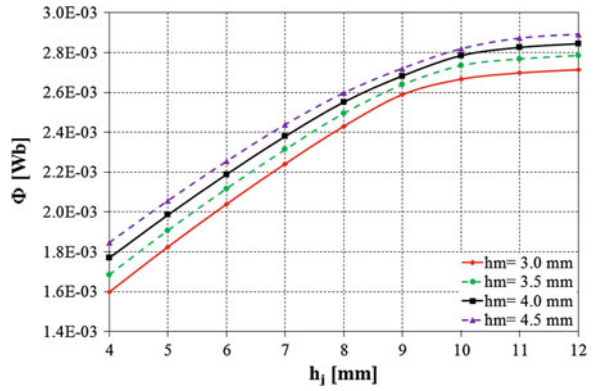


Fig. 6 Magnetic flux versus magnets height at the different magnets angle; $h_j = 12$ mm

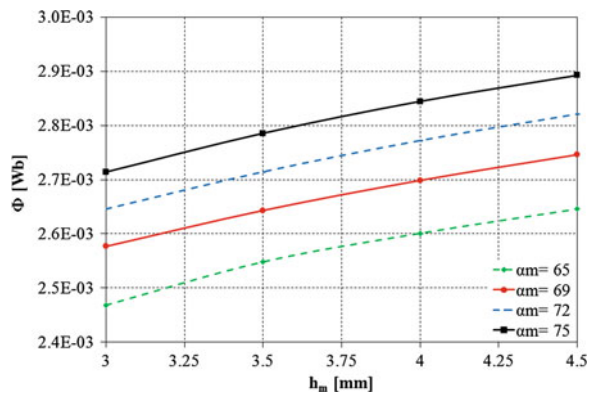


Fig. 7 Magnetic flux versus magnets height at the different rotor yoke thickness; $\alpha_m = 75^\circ$

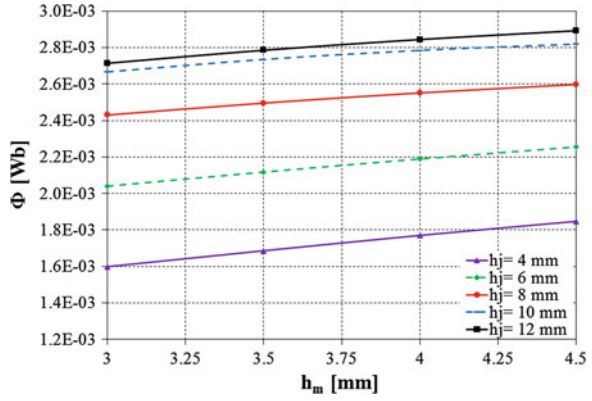


Fig. 8 Magnetic flux versus magnets angle at the different rotor yoke thickness; $h_m = 4$ mm

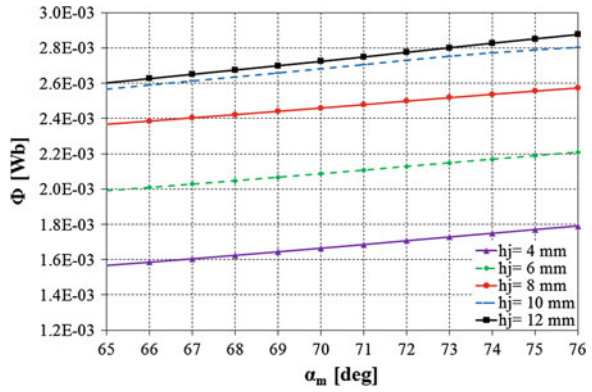


Fig. 9 Magnetic flux versus magnets angle at the different magnets height; $h_j = 12$ mm

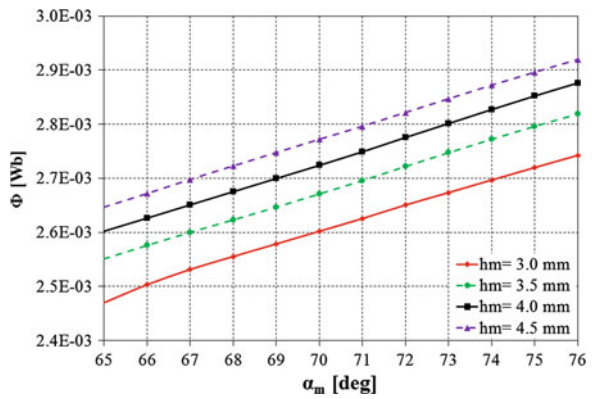


Fig. 10 Cogging torque amplitude versus magnets angle at the different rotor yoke thickness; $h_m = 4$ mm

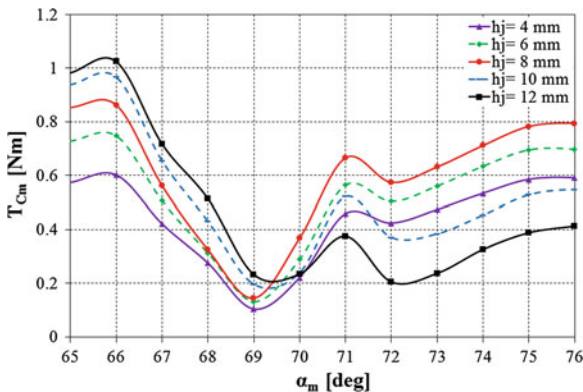


Fig. 11 Cogging torque amplitude versus magnets angle at the different magnets height; $h_j = 12$ mm

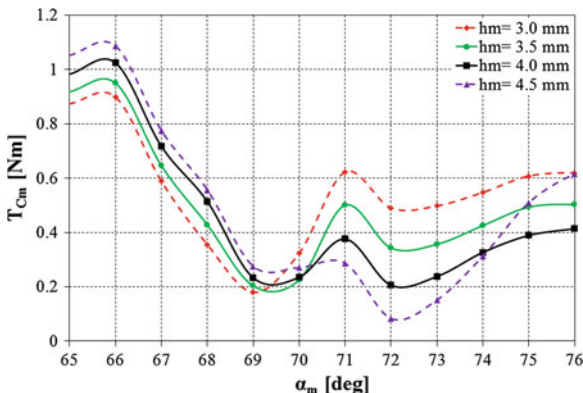
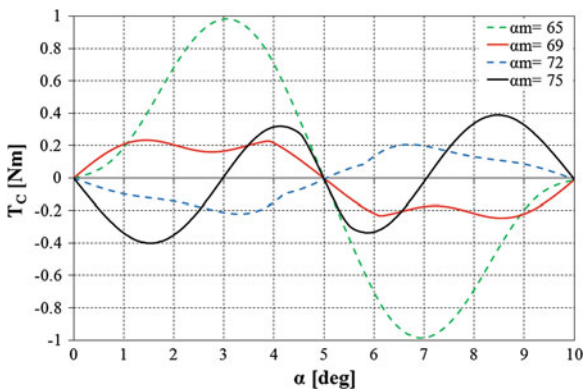


Fig. 12 Cogging torque versus angle of rotation at the different magnets angle; $h_m = 4$ mm; $h_j = 12$ mm



4 Waveforms of the Electrical and Mechanical Parameters of the Motor

By the use of FEM field computations the dimensions of the motor magnetic structure were selected ($h_j = 12$ mm, $\alpha_m = 75^\circ$, $h_m = 4$ mm). The magnetic flux does not penetrate the driven device, which can be mounted in the rotor. Moreover, a high magnetic flux value and resistance to magnets demagnetization are ensured.

For the chosen final magnetic structure dimensions waveforms of the electrical and mechanical parameters of the motor were computed. The computations were performed for a system without a converter current limit and for a system with the limit at $I_{max} = 3I_n$. Examples of the computation results are shown in Figs. 13, 14, 15, 16, 17 and 18.

Fig. 13 Waveforms of the phases currents at the motor start-up; $T_o = T_n$

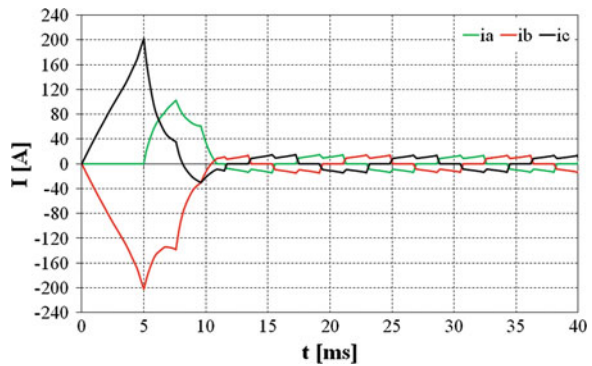


Fig. 14 Waveforms of the phases currents at the motor start-up with the converter current limit at $I_{max} = 3I_n$; $T_o = T_n$

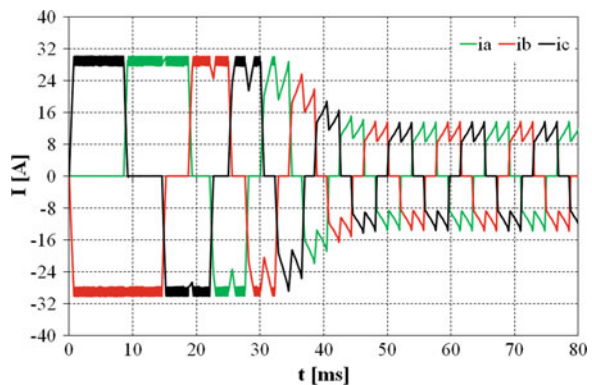


Fig. 15 Transient of the torque at the motor start-up; $T_o = T_n$

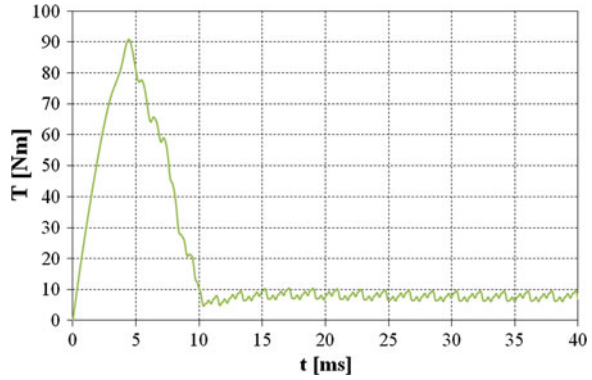


Fig. 16 Transient of the torque at the motor start-up with the converter current limit at $I_{max} = 3I_n$; $T_o = T_n$

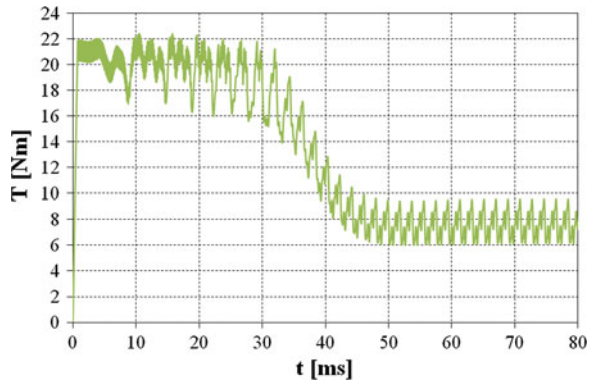


Fig. 17 Rotational speed at the motor start-up; $T_o = T_n$

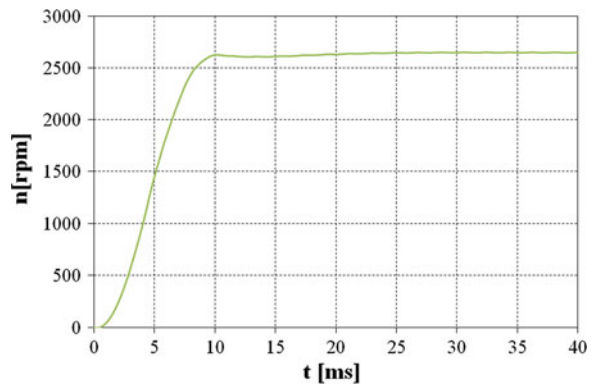
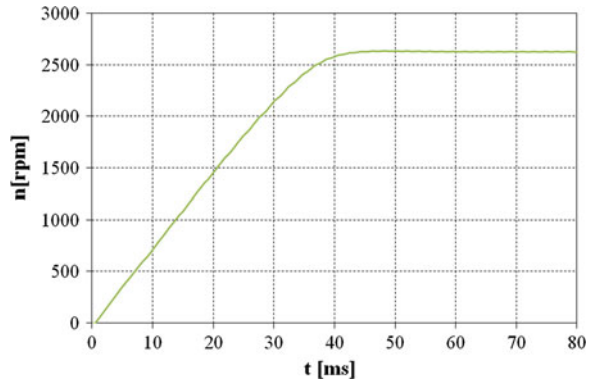


Fig. 18 Rotational speed at the motor start-up with the converter current limit at $I_{max} = 3I_n$; $T_o = T_n$



5 Conclusion

A computational analysis of the impact of magnetic structure dimensions (rotor yoke thickness, magnets angle and height) on the cogging torque and the value of the magnetic flux of the brushless DC motor with a cup-rotor was carried out. The analysis shows that the most important factor during the rotor yoke thickness determination is the value of magnetic flux (Figs. 4, 5, 7 and 8). For the analyzed motor only when the rotor yoke thickness was 12 mm (Figs. 3, 4 and 5) its saturation was small enough for the magnetic flux not to penetrate the driven device, which can be mounted inside the motor. The value of magnetic flux is practically proportional to the magnets angle at different rotor yoke thickness (Figs. 6 and 8). The height of the magnets must provide the resistance to magnets demagnetization at the overcurrent states. It also affects the value of magnetic flux (Figs. 5, 6, 7 and 9). This effect depends on the rotor yoke thickness (on the rotor saturation). The height of the magnets $h_m = 4$ mm was selected to ensure high resistance to magnets demagnetization. The value of the cogging torque at the used rotor yoke thickness ($h_j = 12$ mm) and the magnets height ($h_m = 4$ mm) is the smallest at the magnets angle of $\alpha_m = 72^\circ$ (Figs. 10, 11 and 12). The performed field-circuit computations shows that at $\alpha_m = 72^\circ$ and $\alpha_m = 75^\circ$ the electromagnetic torque pulsations are effectively at the same level ($0.45 T_n$ at the load torque of T_n). In order to achieve a higher value of the magnetic flux, the permanent magnets angle of $\alpha_m = 75^\circ$ was chosen. The performed FEM field-circuit analysis for the final magnetic structure shows that the maximum current during start-up is almost 15 times greater than the maximum value at steady state (Fig. 13) and the maximum torque is 11.5 times greater than the rated torque (Fig. 15). Thus, the high values of the current are not recommended due to the semiconductor elements of the converter. Waveforms of the electrical and mechanical parameters were determined also with the converter current limit (Figs. 14, 16 and 18). For the rated load the start-up process in such a case is four times longer and the maximum torque is limited to the value of $2.8 T_n$. The start-up time of 40 ms and torque overload of $k_T = 2.8$ meet the requirements of the industrial practice.

References

1. Leonowicz M, Wysocki J (2005) Modern magnets—technology, coercivity mechanism, applications. WNT, Warsaw (in Polish)
2. Dudzikowski I, Ciurys M (2011) Commutator and brushless motors excited by permanent magnets. Publishing House of the Wrocław University of Technology, Wrocław (in Polish)
3. Gieras JF (2010) Permanent magnet motor technology—design and applications. CRC Press, Boca Raton
4. Hendershot JR Jr, Miller THE (1994) Design of brushless permanent-magnet motors. Magna Physics Publishing and Clarendon Press, Oxford
5. Chai F, Cui S, Cheng S (2005) Performance analysis of double-stator starter generator for the hybrid electric vehicle. *IEEE Trans Magn* 41(1):484–487
6. Niu S, Chau KT, Jiang JZ, Liu C (2007) Design and control of a new double-stator cup-rotor permanent-magnet machine for wind power generation. *IEEE Trans Mag* 43(6):2501–2503

Description of the Cross Saturation in an IPMSM for Electric Vehicles Using Bicubic Splines

Patrick Seibt and André Fischer

Abstract In this paper an approach to calculate the cross saturation effect in an interior permanent magnet synchronous machine for the use in automotive applications is described. The machine equations for dynamic simulations were modified and the necessary parameters for the flux linkage and inductances are described by bicubic splines, which guarantee consistency for fast simulations.

1 Introduction

The emission standards of motorcars are getting more and more strict [1]. Therefore many automobile manufacturers are offering hybrid cars (HEV), to reduce the fuel consumption of their combustion engines.

The dominating type of electrical machines in the drive chains of electric vehicles (EV) and HEV is the interior permanent magnet synchronous machine (IPMSM), where the permanent magnets are buried inside the rotor iron core. The advantages of this motor type are high efficiency and power density.

Traction motors in automotive applications have to ensure a constant high torque over a wide operating range. Because of the constraint given by the battery voltage the revolution speed is limited [2]. Above a cut-off speed, the machine reaches the field weakening area.

To make objective surveys a model based simulation library of the electric drive chain in Matlab/Simulink was built. For the precision of the simulation, parameter identification for the electrical drive chain is essential. Depending on the operating point, machine parameters are changing.

P. Seibt (✉) · A. Fischer

Chair of Electrical Drives and Mechatronics, Technical University of Dortmund,
Dortmund, Germany
e-mail: patrick.seibt@tu-dortmund.de

A. Fischer

e-mail: andre.fischer@tu-dortmund.de

To describe the dynamics of drive chains, several parameters of the electrical machine have to be known. The dynamic behavior of the IPMSM depends on the distribution of the magnetic flux density. One of the biggest influences is given by the nonlinear saturation effect.

2 Cross Saturation Model

The voltage equations are including the derivatives of the direct- (d) and quadrature- (q) axis flux linkage, which both are dependent on the d-, and q- currents [3]

$$u_d = Ri_d + \frac{d\psi_d(i_d, i_q)}{dt} - p\omega\psi_q(i_d, i_q), \quad (1)$$

$$u_q = Ri_q + \frac{d\psi_q(i_d, i_q)}{dt} + p\omega\psi_d(i_d, i_q). \quad (2)$$

The direct-axis flux linkage is separated into two parts, $\psi_d(i_d, i_q) = L_d i_d + \psi_p$, where L_d is the direct-axis inductance and ψ_p the flux linkage due to the permanent magnets. The quadrature-axis flux linkage can be described as $\psi_q(i_d, i_q) = L_q i_q$. All parts (L_d, L_q, ψ_p) are functions of the d-, and q currents. To take the cross saturation effect into account, differential inductances are defined as [4, 5]

$$\frac{d\psi_d(i_d, i_q)}{dt} = \underbrace{\frac{\psi_d(i_d, i_q)}{i_d}}_{L_{dd}} \frac{di_d}{dt} + \underbrace{\frac{\psi_d(i_d, i_q)}{i_q}}_{L_{dq}} \frac{di_q}{dt}, \quad (3)$$

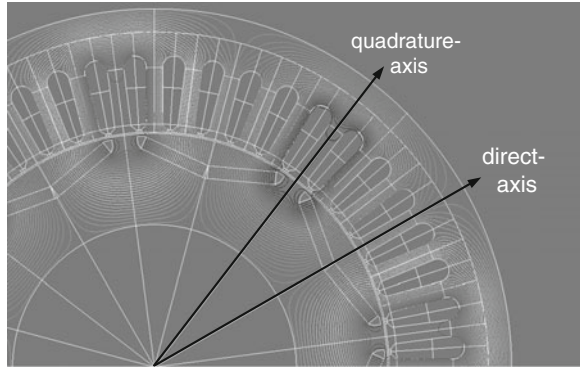
$$\frac{d\psi_q(i_d, i_q)}{dt} = \underbrace{\frac{\psi_q(i_d, i_q)}{i_d}}_{L_{qd}} \frac{di_d}{dt} + \underbrace{\frac{\psi_q(i_d, i_q)}{i_q}}_{L_{qq}} \frac{di_q}{dt}. \quad (4)$$

The voltage equations, containing the cross saturation effect, are given by

$$u_d = Ri_d + L_{dd} \frac{di_d}{dt} + L_{dq} \frac{di_q}{dt} - p\omega\psi_q, \quad (5)$$

$$u_q = Ri_q + L_{qd} \frac{di_d}{dt} + L_{qq} \frac{di_q}{dt} + p\omega\psi_d. \quad (6)$$

Fig. 1 Distribution of magnetic flux in an IPMSM



3 Calculation of the Flux Linkages with FEM

To obtain the flux linkages and differential inductances a Finite-Element-Model of an IPMSM was created in FLUX 2D. The magnetic conditions were solved at different locked-rotor positions and values for the d- and q- currents (Fig. 1).

The nonlinear permeability of the stator and rotor material is expressed as $\mu = B/H$ from the magnetization curve. The results of this multistatic calculation were the phase flux linkages for each pair of (i_d, i_q) , whose fundamental waves had to be transformed with the d, q -transformation into the direct- and quadrature-axis flux linkage.

4 Description of the Flux Linkages with 2D-Splines

For the dynamic simulation of the behavior of the IPMSM the calculated parameters have to be described with an adequate function. It is very difficult to define single functions with coefficients fitting the flux linkages for the whole operating range of the motor. The functions derivatives must also be consistent to avoid numerical errors during simulation. By using the bicubic spline interpolation method a two-dimensional polynomial function for every section is created [6, 7]. Their derivatives are consistent at any of the corner points and border lines. The results are smooth functions for the flux linkages and differential inductances. For example the direct-axis flux linkage is given by

$$\psi_{d,s}(i_d, i_q) = \sum_{n=0}^3 \sum_{m=0}^3 c_{s,n,m} i_d^n i_q^m. \quad (7)$$

Then the differential inductance L_{dd} results of the derivation with respect to i_d

Fig. 2 Direct-axis flux linkage

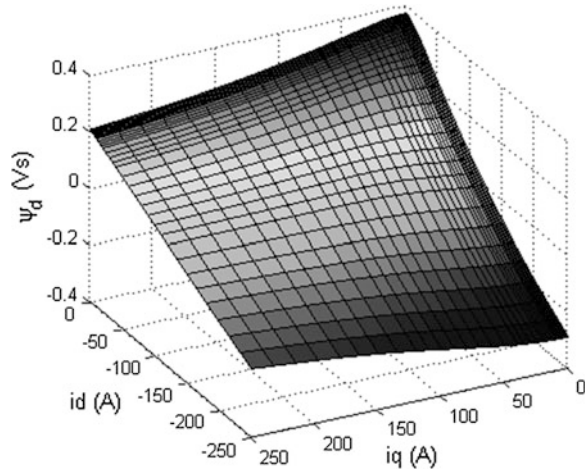
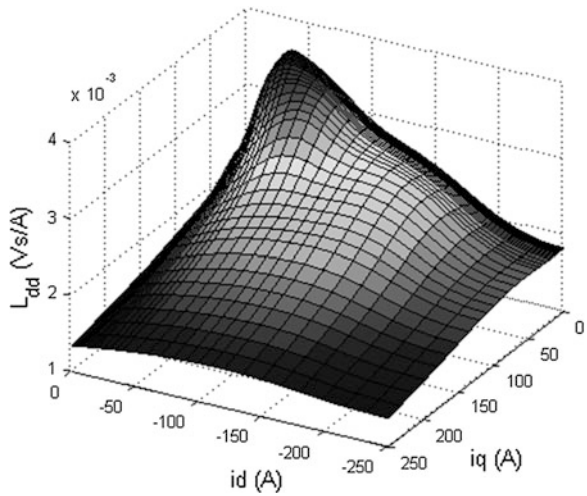


Fig. 3 Differential inductance L_{dd}



$$L_{dd,s} = \frac{\psi_{d,s}(i_d, i_q)}{i_d} = \sum_{n=0}^3 \sum_{m=0}^3 n c_{s,n,m} i_d^{n-1} i_q^m, \tag{8}$$

and L_{dq} of the derivation with respect to i_q (Figs. 2 and 3)

$$L_{dq,s} = \frac{\psi_{d,s}(i_d, i_q)}{i_q} = \sum_{n=0}^3 \sum_{m=0}^3 m c_{s,n,m} i_d^n i_q^{m-1}. \tag{9}$$

The same method is used to describe the quadrature-axis flux linkage ψ_q and the differential inductances L_{qd} and L_{qq} . The equation for the motor torque is approximately the same as in the linear case.

$$T = \frac{3}{2}p(\psi_d i_q - \psi_q i_d). \quad (10)$$

5 Conclusion

To simulate the dynamic behavior of electrical drive chains at the whole operating range, the knowledge of machine parameters, especially the inductances, is indispensable. Describing these parameters in sections through bicubic polynomial functions ensures consistency during simulation. In addition it will be possible to integrate this method into the control algorithm for the drive chain to gain adaptive controllers for high efficiency operations.

References

1. Vollmer U (2012) Design, laying and realization of a loss-optimized electrical drive for hybrid vehicles. Germany (in German), Berlin
2. Meyer M (2010) Efficiency-optimized control of high exploited permanent magnet synchronous machines at the drive trains of automobiles. Hannover, Germany (in German)
3. Müller G, Ponick B (2009) Theorie of electrical machines. Wiley-VCH Verlag, Weinheim, Germany (in German)
4. Chédot L, Friedrich G (2004) A cross saturation model for interior permanent magnet synchronous machine. Application to a starter-generator, Cedex, France
5. Stumberger B, Stumberger G, Dolinar D, Hamler A, Trlep M (2003) Evaluation of saturation and cross-magnetization effects in interior permanent-magnet synchronous motor
6. Kellner S (2012) Identification of parameters at permanent magnet synchronous machines. Erlangen, Germany (in German)
7. Späth H (1991) Two dimensional spline interpolation algorithm. R. Oldenbourg Verlag München Wien, Oldenburg, Germany (in German)

Method for Diagnosing the Vacuum Conditions Using Pulses Voltage Generator

W. Chmielak and Z. Pochanke

Abstract Diagnostic testing of vacuum inside the closed chamber of vacuum circuit breaker is needed to estimate the switching capacity and dielectric strength. It is also extremely difficult because of the inability to direct measurement. This paper presents a preliminary study on a new way to diagnose the state of the vacuum in the vacuum breakers. Presents a proposal of diagnostic system and the results of tests carried out on the model vacuum chamber and several factory vacuum chambers. Initial research gives hope to the possibility of detecting the level of vacuum pressure well below 1 Pa.

1 Introduction

Vacuum switching devices are used worldwide in all kinds of medium-voltage distribution systems. Their obvious advantage is that they have dominated the power distribution market [1]. The development at higher voltages will continue to be driven by the need for environmentally benign interrupting systems [2, 3]. This is supported by more than 8,000 circuit breakers installed in Asia in transmission networks which have excellent operating characteristics [4]. The factor influencing on the dielectric strength and switching capability of the vacuum chambers is the pressure inside the chamber. Treating the vacuum, that is always imperfect, as a special condition of the gas characterized by shifting operating point on the Paschen curve far to the left from the minimum. There the strength of the system is determined by the properties of electrodes—mainly the material and surface condition [1]. From Paschen curve, it appears that the strength of the gas will grow to infinity

W. Chmielak (✉) · Z. Pochanke
Institute of Electrical Power Engineering, Warsaw University of Technology,
Warsaw, Poland
e-mail: chmielak@ee.pw.edu.pl

Z. Pochanke
e-mail: zbpoch@ee.pw.edu.pl

with decreasing pressure to zero. However, even in theory, the residual gas effect ends at the pressure where the free path of electrons exceeds the distance between contacts. In the air, for a distance between electrodes $d = 1$ cm the pressure is approximately 15 Pa (0.15 mbar) [5]. At the lower pressures (product value pd) when the avalanche mechanism practically does not occur, reveal a variety of processes related with emission of charge carriers from the electrodes, their movement and exchange. These processes bring into the space between contacts free charge carriers and neutral particles and cause the avalanche build-up of charge carriers as a result of the collision ionization of neutral particles by free electrons, and (to a lesser extent) ions are accelerated in an electric field. Reducing the level of vacuum inside the circuit breaker carries a risk of deterioration of both the dielectric properties of the insulation system as well as the weakening of the current breaking capacity. Loss of vacuum may be due to outgassing of materials inside the chamber, leaks welded or brazed joints arising as a result of stress or the transfer of gases through the chamber housing materials [1]. Leakage may occur after a large number of operations by fatigue of the metal bellows. The vacuum quality may also be reduced after negligible number of operations by long term diffusion, intercrystalline corrosion or deactivation of the getter material [6].

There are many methods that can be used by producers, mainly Magnetron and Penning methods, but they are not suitable for use in the exploitation [7]. Power supply owners and consumers want to have a simple and accurate method to check the vacuum condition of the vacuum circuit breaker in service. Diagnostic apparatus already exists on the market with a simple indication good-bad, however their effectiveness is poor. They can detect only the fully-sealed chamber, and may indicate that the chamber is bad due to conditioning breakdown. There are many different methods and solutions patents [6, 8–10], which are usually able to catch only a state in which a vacuum breaking mechanism for gas discharge changes, above a few Pascals. The expected detection level is 10^{-4} , or at least 10^{-2} Pa, that is the maximum permissible pressure in the chamber.

It was observed that all voltage studies on vacuum chambers are extremely sensitive to the current state of the contact surface is manifested by a huge dispersion of recorded values. The result is very little plausible interpretation of these results. Therefore to reliably investigate the vacuum chamber it is necessary to have the previous conditioning. Among the methods for conditioning, it appears that the most effective is the pulse spark conditioning.

2 Test Circuit

It was built impulse conditioning set-up capable of vacuum diagnostics inside the vacuum chamber. Proposed testing system, (Fig. 1) generates high voltage pulses in the resonant system of two capacitors connected in parallel with a capacity of $C_1 = 0.1 \mu\text{F}$ each with inductance of pulse transformer TI. Generated signals are attenuated by serial resistance of $R_2 = 780 \Omega$ limiting a capacitor discharge current,

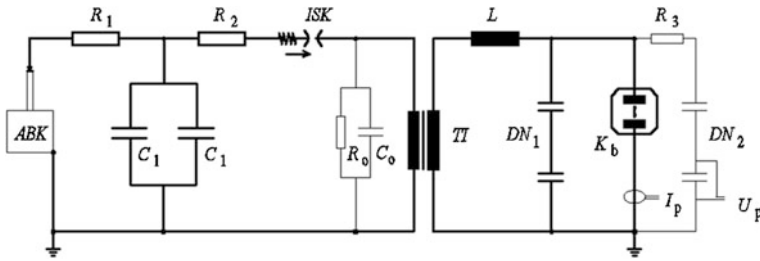
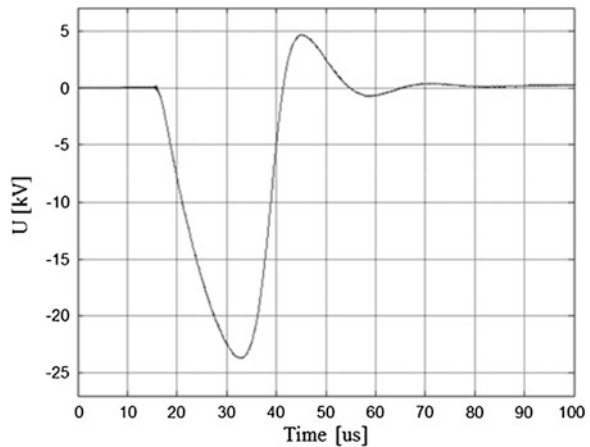


Fig. 1 Impulse conditioning set-up for vacuum chamber diagnostics

so that when a breakdown occurs, it is rapidly disappearing and it does not warming and excessive eroding of the contacts. Rated voltage of capacitors C_1 is equal to 30 kV and with a similar level of transformer isolation TI is a limit on the amount of the allowable generator voltage. Activation of the testing system is done by ISK spark gap. One electrode of spark gap can be approached to a second by stimulating the electromagnet drive, and also has the ability to adjust the distance between the electrodes. During the test the distance between the electrodes was adjusted so that the spark between electrodes followed roughly every 1 s. The time constant of charging capacitor C_1 has been chosen at the level of a few milliseconds. In parallel with the primary winding of a pulse transformer the non-inductive impedance elements $R_0 = 30 \text{ M}\Omega$, $C_0 = 3 \text{ nF}$ are plugged. Along with the inductances of the leads it forms a low pass filter designed to attenuate high frequency noise. A similar function is performed by capacitance voltage divider DN_1 .

On the Fig. 2 the waveform of generated voltage from proposed impulse generator is presented. The voltage pulse is quickly disappearing. Its peak value is about 24 kV and a voltage steepness of $1.6 \text{ kV}/\mu\text{s}$. During the tests the voltage at

Fig. 2 Voltage from impulse generator set-up



the test chamber using a capacitive voltage divider, and the current in the test chamber using a Rogowski coil were measured.

3 Experimental Results of the Model Chamber

The study was carried out on an industrial made vacuum chamber ($U_n = 24$ kV, $I_n = 630$ A) adapted for regulating pressure inside it. Research was carried out at pressures in the range of 10^{-3} – 10^2 Pa. Due to low value of the generated voltage, all tests was performed at a distance between contacts equal to 0.1 mm. The first tests on the test chamber showed well known from the literature conditioning process. Next tests were performed at different pressures inside the chamber. For each pressure series of 100 tests were performed. It has been observed relatively stable level of withstand voltage for each of the test pressures. Tests were carried out for the pressure in the range of 10^{-3} –54 Pa. The average values of breakdown voltage and its standard deviation for the different pressures are shown in Fig. 3. Another form of presentation of the same results shown in Fig. 4.

For the pressure in the chamber equal 9 Pa or higher the breakdown voltage for all 100 samples were practically constant with very small dispersion. With the increase of the pressure the voltage decreased while maintaining a very low dispersion in the individual trials. Moreover, in each of the observed samples (100 samples for pressures 9, 12, 25, 30, 40 and 54 Pa), the same type of high-voltage glow discharge during breakdown (a few hundred volts) providing avalanche mechanism appeared. Below 9 Pa was observed change of discharge mechanism. Under these conditions occurred single and multiple breakdowns, rapidly or long term disappearing, always with negligible voltage. For pressures below 6 Pa the greater dispersion of recorded breakdown voltage but at higher levels was observed. In addition at lower pressures, voltage and current waveforms show the different

Fig. 3 Measured breaking voltage and its standard deviation as a function of pressure

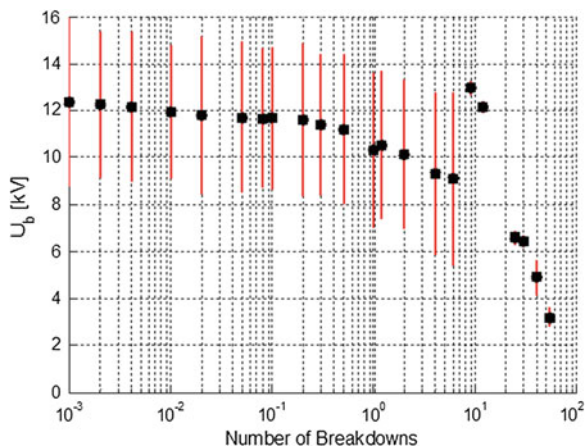
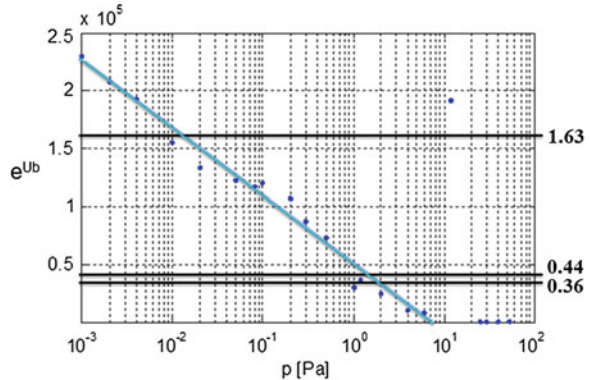


Fig. 4 Measured breaking voltage in different presentation as $e^{Ub} = f(p)$



mechanisms of breakdown—both long-time above 200 μ s and a multiple pulsed fast disappearing. At significantly lower pressures (10^{-3} Pa), it was observed that the long-term breakdown are similar steepness of the current decay that at higher pressures, but much lower discharge voltage of 20 V—characteristic of the discharge in a vacuum. It has been observed also that at pressure range of 10^{-3} –6 Pa breakdown character remains unchanged.

A surprising observation was the increase in value of braking voltage for a pressure of about 10 Pa. Under these conditions, the voltage was even higher than at high vacuum. In addition, the breakdown voltage for pressures above 9 Pa has a very stable value depending on the pressure. This observation was so surprising that the attempts for the pressure around 9 Pa were repeated. A second series of experiments were carried out by changing the pressure in the chamber from high vacuum (10^{-3} Pa) to about 50 Pa and back again in the direction of low pressures. As before, for the pressure of about 10 Pa withstand voltage of chamber was much higher than for the lower and higher pressures. Also, the nature of recorded breakdown was identical to the earlier—for the 10 Pa and higher pressures breakdowns occurred at a specific voltage dependent on the pressure. Dispersion of breakdown voltages were very low ($\ll 10\%$) and always appeared only one type of breakdown—lasting glow discharge with voltage level of several hundred volts—about 300 V for 10 Pa and a little higher voltages for the higher pressures.

4 Experimental Results of Industrial Chambers

Research was carried out on 13 closed vacuum chambers from different manufacturers. Chambers have different stories and were on the resources of a research laboratory. Mostly they were not connected to the voltage and didn't work for many years. Some of them were previously used in the operation, but recently were used only for demonstration purposes, occasionally performing mechanical operations without load. Some of them has completely unknown story. Initially, tests were

performed on first 9 chambers with fully open contacts. For each chamber a series of 30 samples of the impulse voltage with magnitude $U_g = 22$ kV were performed. Under these conditions did not show any breakdowns. Further attempts were made on all chambers at different smaller distances between contacts. Summary of the study is shown on the Table 1.

In most cases, for the distance between contact greater than 0.1 mm breakdowns occurred only in the initial trials. Later withstand voltage of a chamber became higher than the pulse generator voltage. In his early attempts were mostly fast extinguishing breakdowns, which often led to the re-ignition during voltage rebuilding. With the increase in breakdown voltage occurred a rise in the share of individual discharges remaining in the long term. This is probably the more energy discharge leading to ionization of surface contacts.

There were various levels of breakdowns for the individual chambers. Some of them have recovered very quickly high strength in others the process was more time-consuming. The reason for this can be both: state of the contacts and the level of vacuum inside the chamber. The chamber in which the conditioning process took longer studies were performed at distance between contacts $d = 0.1$ mm. The conditioning process of two similar chambers (4 and 5) with identical parameters are shown on Fig. 5.

Table 1 Summary of measurements in real vacuum chambers

Chamber	U_n (kV)	d (mm)	Number of attempts	U_b (kV)	Number of breakdowns
1	24	1.00	10	>22	2
		0.50	30		4
2		0.40	30	>21	18
		0.10	200	>23	180
3		0.10	500	~ 20	600
4	17.5	0.25	180	~ 20	210
		0.10	500	10.5	1,300
5		0.25	350	>23	220
		0.10	400	12	850
6		0.25	130	>23	70
7		0.25	30	>23	15
8	12	0.17	300	>23	420
		0.10	400	~ 12	900
9		2.00	10	>23	0
		0.25	50	>23	2
10	6	0.30	30	3.8	30
		0.50	150	3.8	150
11		0.25	500	14	1,360
12		0.25	500	18	920
13		3.00	500	17	1,200

Comparing the results of the research with the distance between contacts $d = 0.1$ mm, for the chambers 4, 5 and 8 of rated voltage less than 20 kV, it can be concluded a relatively similar characteristics of strength, where the average value of the breakdown voltage at a distance of 0.1 mm is slightly above 10 kV. The highest breakdown voltage has youngest chamber (about 10 years difference), and this may be associated with a higher level of vacuum in its interior but it is at a much larger dispersion. However, given the distance between contacts should be careful with this inference because recorded differences may be due to the inaccuracy of the set distance. Research on such a short distance was also made for 24 kV chambers. Their withstanding voltage values was significantly higher than 20 kV. Such a situation can be explained by a higher quality of contacts performance.

An interesting conditioning process was observed for the chamber 8. Initially proceeded in such a way: there were both single long-term breakdowns with low voltage (~ 20 V) as well as multiple pulse breakdowns. But it happened also a couple of glow discharge, where the discharge voltage was at the level of a few hundred volts. It is probably resulted from the release of larger amounts of adsorbed gas from the cathode (clouds), which was reflected also in the process of conditioning by local weakening of the dielectric strength—between 200 and 300, and 320 and 370 breakdowns (Fig. 6).

Last four chambers had the poorest results. The chamber 10 has been produced in the 70 s of the last century, about 40 years ago and for the last more than 20 years has not been used at all, was used as a demonstration prop. During the trials were registered one type of discharge—they were long lasting with the average breakdown voltage of about 3.8 kV and during the tests the voltage was relatively constant. During discharge the voltage across the chamber had a value of about 200 V, which proves the existence of some form of gas discharge. According to the characteristics shown on Fig. 4 can be calculated that the pressure inside the chamber is about 100 Pa. Chambers 11, 12 and 13 are relatively new and have been

Fig. 5 The conditioning process of the vacuum chambers (4 and 5) at the distance between contacts $d = 0.1$ mm

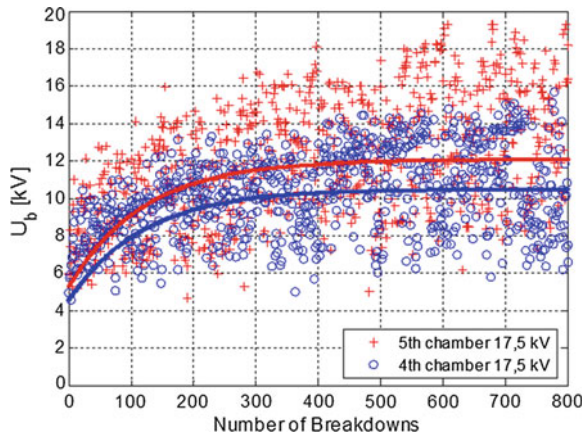
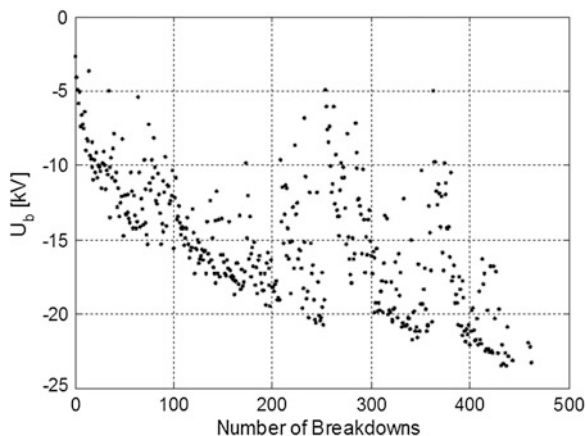


Fig. 6 The conditioning process of 8-th vacuum chamber at the distance between contacts $d = 0.17$ mm



installed on the device that do not have a quality certificate. Studies have shown the voltage range is significantly lower than the other the chambers that have these certificates.

5 Conclusions

Definitely, this method can diagnose the level of vacuum inside the chamber from the pressure level above few Pascal's. Diagnostic testing using a pulsed system have the advantage of quickly and effectively conditioning the test chamber. It makes the recorded withstand voltage of the chamber under study reliable because conditioning the vacuum chambers with the voltage pulse is shown as the most effective method.

Observed increase in breakdown voltage with decreasing pressure in the vacuum chamber to the level 10^{-3} Pa gives hope that this method can be used to diagnose the level of vacuum pressure in a wider range than existing methods applied in operation. From the obtained results it can be set straight relationship between breakdown voltage and the pressure in the pressure range above 10^{-3} Pa.

Table 2 Estimates of pressure inside the chamber on the basis of the reference characteristics plotted in Fig. 4

Chamber	U_n (kV)	d (mm)	Number of attempts	U_b (kV)	e^{U_b}	p (Pa)
2	24	0.10	200	>23	97,000	$\ll 10^{-3}$
3	24	0.10	500	~ 20	5,000	$\ll 10^{-3}$
4	17.5	0.10	500	10.5	0.36	~ 2.0
5	17.5	0.10	400	12	1.63	$\sim 10^{-2}$
8	12	0.10	400	~ 12	0.44	~ 1.5

Ideological example of such a relationship is given on Fig. 4, where the $e^{Ub} = f(p)$. Of course, it can be questionable the credibility of obtained results due to the very small distance between contacts.

However, assuming that the distance between contacts in the test chambers were set precisely, with high accuracy, and that the dielectric characteristics obtained for a model chamber are reference for investigated commercial chambers could be tempted to infer the status of vacuums inside these chambers, by the pressure according to the characteristics shown in Fig. 4. The pressure within the test chamber defined by this method shows Table 2.

Acknowledgments This work is supported by the Polish Ministry of Education of funds for research in 2010–2013.

References

1. Slade PG (2007) The vacuum interrupter theory, design, and application. CRC Press, Boca Raton
2. Ikebe K, Imagawa H, Sato T, Ito H, Kosakada M, Saito H (2010) Present status of high-voltage vacuum circuit breaker application and its technology in Japan. A3_303_2010 Cigre Simp
3. Sibilski H, Dzierżyński A, Berowski P, Błażejczyk T, Hejduk A, Krasuski K, Grodziński A, Szymański A (2012) Testing of medium voltage vacuum circuit breakers contacts. *Electr Rev* 12a:193–196 (in Polish)
4. Ito H (2012) Study Committee A3 Cigre Annual Report 2012, High Voltage Equipment Electra Nr. 266, pp 30–34
5. Chmielak W, Pochanke Z (2012) Diagnostic of vacuum on the basis of the dielectric strength. *Electr Rev* 12b:311–314
6. Frontzek FR, König D (1998) Methods for internal pressure diagnostic of vacuum circuit breakers. In: 18th ISDEIV, Eindhoven, pp 467–472
7. Damstra GC (1995) Pressure estimation in vacuum circuit breakers. *IEEE Trans Dielectr Electr Insul* 2(2):198–201
8. Damstra GC, Merck WFH, Bos PJ, Bouwmeester CE (1998) Diagnostic methods for vacuum state estimation. In: 18th ISDEIV, Eindhoven, pp 443–446
9. Merck WFH, Damstra GC, Gruntjes RJB (1998) Estimation of vacuum condition in vacuum circuit breakers. In: 18th ISDEIV, Eindhoven, pp 506–509
10. Ziyu Z, Shuheng D, Xiuchen J, Naixiang M, Liwen L, Huansheng S, Chongfang L (2008) Measurement of internal pressure of vacuum tubes by micro-discharge and emission current. In: 23rd ISDEIV, Bucharest

The Group and Individual Connection to the Rail System Modelling in a Lightning Discharge Analysis

Zofia Wróbel

Abstract The modelling of group connection to the rail system in an open lay-out and individual connection to the rail system under conditions of surges endangerment of atmospherical origin with the use of numeric methods, demands creations of components elements models: contact line, rail return, tower, insulator, short circuiting switch and surge. In the analysis, one section of a group railed containing 54 fragments was taken into account. In the report an example—results of the modelling of impulse—electromagnetic disturbances caused by statics atmospherical for both railed systems at a current extortion of $5/320 \mu\text{s}$ and $8/20 \mu\text{s}$ and with a voltage of $10/700 \mu\text{s}$ $1.2/50 \mu\text{s}$ were represented.

1 Introduction

The direct surge into the traction wires-net of galvanic coupling causes an increase in the potential of one rail course in relation to another. The connection to the rail system should assure an efficient protection against the shock in the case of short-circuits. The connection to the rail system is a metallic connection of a steel—construction supporting the traction wires-net with a rail. Nowadays two connection to the rail systems are used: group or individual connection to the rail. The group connection to the rail depends on the connection of several supporting constructions by a railing thin line, and then by short circuiting switches the connection of this thin line with track choking-coils or with the rail. The individual railing depends on a metallic connection of the supporting construction with the rail.

Quoad hoc simulatory research with the utilization of computers fulfil an important part helping in the analysis of electromagnetic influences on the given

Z. Wróbel (✉)

PKP Polish Railway Lines JSC, Railway Lines Establishment in Rzeszów,
Rzeszów, Poland

e-mail: zwrobel@prz.edu.pl

device. Using in simulatory programmes checked mathematical models of scheme elements and electric devices as well as physical occurrences can be supplemented or replaced by laboratory research and real lay-out terrain.

2 Damageability of Railway Devices

Analysis of different types of railway devices damages as a resulted from various reasons are performed at the PKP (Polish State Railways). These informations are gathered by different services. It allows the assessment of the repair costs, the frequency of damage occurrence and their distribution in the country. These data supplemented with informations pertaining to the producers of devices and over-voltage precautions, constitute an extremely vital analytical base for PKP Polish Railway Lines JSC. Its compilation involves the work of many researchers.

Table 1 presents a number of unit traction system damage as a result of atmosphere originating surges in the chosen Railway Lines Establishment of PKP Polish Railway Lines JSC on the terrain of the country in the summers of 2007 and 2012. The average numbers of impulse waves per km² in year 2008 were taken from the materials and put in the upper unit of the table [1].

3 The Group Connection to the Rail System in the Open Layout

The connection to the rail system in an open lay-out consists of a section of a length about 2.5 ÷ 3.5 km. The general schema of accepted to calculations of the model of feeding and return network—is represented in Fig. 1 [2]. In this lay-out all constructions supporting of the traction net-wires are electrically joint with a rail. Ends of lines across low-voltage limiters of repeated I-action (Fig. 1: the short circuiting switch) and lines in the isolation are joint to the rail. Supporting constructions of the grouped railed section are earthed severally.

In the state of limiters (short circuiting switch) normal work, they proclaim the isolation among the group connection to the rail line and rails of the railway track. If the carriageable network isolation become damaged, then limiters get down to work, passing into the state of conductivity closing the short-circuit loop [2].

4 The Modelling of the System

In the analysis, one section of the group connection to the rail 54 fragments, was taken into account. The accepted length of fragments (suiting the distance among towers) equals 64 m.

Table 1 Number of damage of unit traction system in the summers of 2007–2012 as a result of atmospheric surges in Railway Lines Establishment of PKP Polish Railway Lines JSC

Atmospheric discharges/ km ²	3.75–7.49	3.75–7.49	1.87–3.74	3.75–7.49	1.87–3.74	3.75–7.49	1.87–3.74	3.75–7.49	1.87–3.74	3.75–7.49	1.87–3.74	>7.5	3.75–7.49
Atmospheric discharges in railway lines establishments	Warszawa	Łódź	Białystok	Siedlce	Lublin	Kielce	Skarżysko Kamienna	Kraków	Rzeszów	Nowy Sącz	Sosnowiec (Katowice)		Częstochowa
Year	Number of atmospheric discharges												
2007	0	0	0	2	4	8	9	6	0	1	2	2	6
2008	1	2	1	0	2	7	8	6	0	0	9	9	9
2009	1	5	0	2	6	6	3	3	1	1	6	6	8
2010	2	1	0	2	4	0	4	7	0	0	7	7	9
2011	1	1	1	0	8	9	7	4	3	0	5	5	10
2012	1	4	0	0	3	8	10	5	0	1	5	5	2
Atmospheric discharges/ km ²	0.46–0.92	0.46–0.92	0.93–1.86	0.93–1.86	0.93–1.86	1.87–3.74	0.93–1.86	0.93–1.86	0.93–1.86	0.93–1.86	0.46–0.92	0.46–0.92	
Atmospheric discharges in railway lines establishments	Tarnowskie Góry	Gdynia	Olsztyn	Bydgoszcz	Wrocław	Opole	Wałbrzych	Poznań	Ostrów Wielkopolski	Zielona Góra	Szczecin		Polish Railway Lines (PLK)
Year	Number of atmospheric discharges												
2007	8	5	1	4	1	3	2	1	2	1	2	2	68
2008	10	4	3	4	1	3	0	1	5	0	1	1	77
2009	7	7	0	4	2	6	2	3	6	0	0	0	80
2010	11	8	3	3	5	5	0	1	3	3	2	2	89
2011	16	7	0	3	0	4	0	3	3	0	1	1	86
2012	21	7	9	15	3	6	1	7	4	1	3	3	116

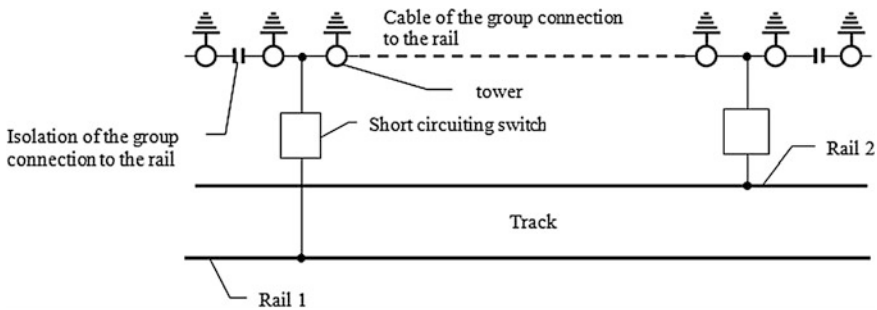


Fig. 1 The schema of the group connection to the rail system in the open lay-out [2]

In the modelling, five lines representing: the line of group connection to the rail, the catenary wire, the traction net-wires and two lines representing rails were taken into account. The cross-tying of rails by around 300 m were also introduced [3, 4].

4.1 The Modelling of Loss-Free Multi-wires Lines

The basic assumption in the analysis of the multi-wires line is the acceptance of the dispersal of the electromagnetic field line in the form of the transverse wave TEM (eng. Transverse Electro-Magnetic) [5]. This means that vectors of electric and magnetical fields intensity are perpendiculars to themselves and lie in the surface (xy) and are perpendiculars to the direction of the dispersal of the wave (z). Losses in the line arise as a result of two mechanisms: of losses in lines (oblong losses) and losses in the circumjacent centre (transverse losses). In the target of parameters delimitation of the inductive and capacitive adjudate, losses in multi-wires long line equalizations formulating (MTL—Multiconductor Transmission Lines) can be skipped. This simplifies the solution and gives bases to the exact delimitation of the coupling parameters. To receive equalizations of the multi-wires long line I marked the individual, equivalent arrangement of the section lay-out about the length Δz , as it is represented in Fig. 2. Mutually conjugate lines (G) and (R) have the same individual parameters: inductances L_G and L_R and the mutual unitary inductance L_m . As assumptions simplifying to the analysis I accepted, that the speed of the dispersal of waves is equal the speed of the light and I did not take into account the reflect current waves.

Longitudinal currents produce a magnetic flux, penetrating every loop formed by the line and the gaining line as well as the inductance arising from the Faraday's law. Voltages among every line and the gaining line produce loads in lines. This generates electric field among every pairs of these lines. This effect mark capacities of the line. Unitary self-capacities of lines (G and R) in relation to the gainings line are defined properly by C_G and C_R and the unitary mutual capacity by C_m . The delimitation of parameters L and C of the long line with the use of unitary

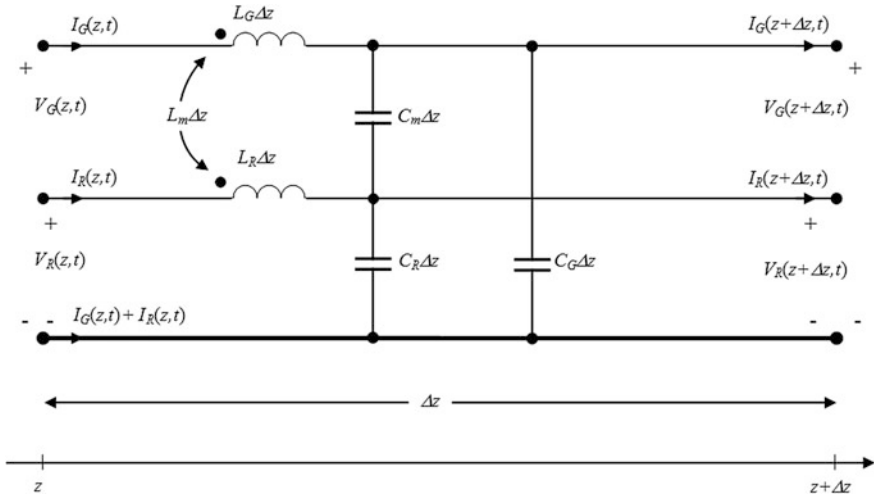


Fig. 2 The individual elementary section of the loss-free two-wire line [5]

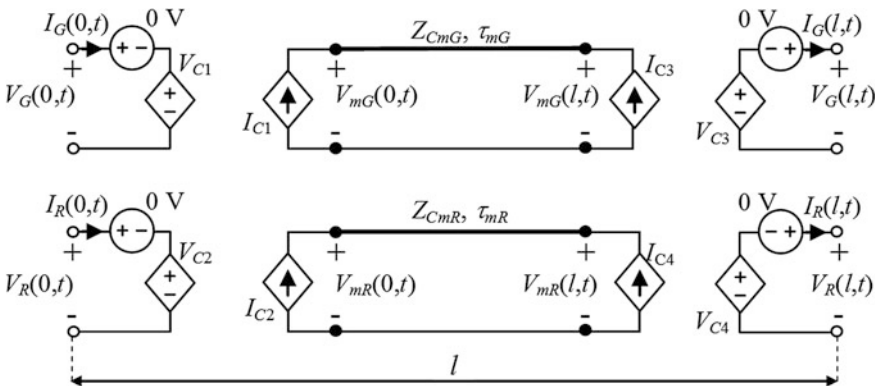


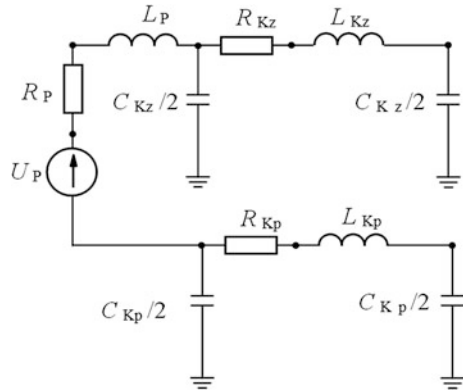
Fig. 3 The complete SPICE model for a two-conductor line with the utilization of controlled source [5]

parameters at the use of equalizations of the electric circuits analysis, as well as to the assumption that $\Delta z > 0$, is presented in [5].

Equalizations MTL in the matrix form have an identical form, as equalizations for two wires of the line. Hence the solution of these equalizations gives similar results, but in a matrix form. This propriety permits the modelling and the solution of the lines system folding of more than two wires [5].

The model of the line section in SPICE for two wires is represented in Fig. 3. Equalizations describing this model of the line section, can be resolved through the elimination of the coupling among lines, what gives the diminution of the pair of

Fig. 4 The Simplified scheme of the traction substation and cable connections [4]



lines to the circuit of two wires, without interplays. Zero-volt voltage sources are necessary in SPICE to sample the controlling current for current-controlled sources [5].

4.2 The Model of the Substation

To the analysis of the model of the substation (Fig. 4) I accepted parameters taking into account: the voltage of the substation $U_p = 3,450$ V, the inductance of the substation and of the power supply system $L_p = 4.774$ mH [4].

Parameters of the cable return—and feeding I presented in compliance with the results of measurements placed in the paper [4] for the frequency 10 kHz and cable lengths 200 m as: $R_{Kz} = R_{Kp} = 3 \Omega$, $L_{Kz} = L_{Kp} = 0.3$ mH, $C_{Kz} = C_{Kp} = 0.4 \mu\text{F}$.

4.3 Towers

For the analysis of atmospheric discharges, model of the tower can be represented by the arranged in rows connection of the inductance and resistance. Accepting the unitary inductance $L_0 = 1.67 \mu\text{H/km}$ calculated from the following formula:

$$L_0 = 0.2 \mu_r \ln \frac{2h}{r} [\mu\text{H/km}] \tag{1}$$

where:

μ_r the relative magnetic permeability (for air $\mu_r = 1$)

h height of the tower

r cable radius

the received inductance of the tower $L = 13.7 \mu\text{H}$.

For the group connection to the rail, the resistance of earthing of the tower carries out $R = 50 \Omega$ [2].

For the individual connection to the rail, the tower inductance was accepted as $L = 13.7 \mu\text{H}$ and tower impedance as $R = 10 \Omega$. As the connection to rail of the tower inductance $L = 5 \mu\text{H}$ was accepted [6].

4.4 Lightning Conductors, Spark Gaps and Short Circuiting Switches

In the analysis as a model of the insulator I took into account in the model of the tower the switch voltage-controlled 90 kV. As a model of short circuiting switches I took into account the switch current-controlled 15 kA and the switch voltage-controlled 120 V [2].

The model of the corner lightning conductor I introduced as a switch voltage-controlled of a jump voltage value 23.8 kV and of brake aerial of the resistance 100 M Ω . Applied to the protection of the trolley wires corner lightning conductors are installed every 1,200 m or 600 m (for terrains of large stormy intensity, more than 30 days in a year). In the analysis I took into account distances 600 m [1, 6]. Applied short circuiting switches in the group connection to the rail can be modelled as properly voltage switch of the voltage 120 V and current of the value 15 kA [2].

5 Surge Currents in the Analysis of the Ground Lightning Discharges

The levels of the resistance on surges of rts (railway traffic system) devices are definite in the norm PN-EN50121-4 (Railway applications—Electromagnetic compatibility. Part 4: Emission and immunity of the signalling and telecommunications apparatus). One of the proposed surges to research for devices in telecommunication and signalling networks in the norm PN-EN 61000-4-5 (2010) (Electromagnetic Compatibility (EMC)—Part 4-5: Testing and measurement techniques- Surge immunity test (IEC 1000-4-5:2005)) is the voltage surge 10/700 μs .

The shape of the voltage surge 10/700 μs which was brought near with the two-exponential course which is appointed in formula [7]:

$$u(t) = 0.10113 U_m [\exp(-0.10068 \times 10^4 t) - \exp(-0.64766 \times 10^6 t)] \quad (2)$$

and the voltage surge 1.2/50 μs in formula:

$$u(t) = 1.0354 U_m [\exp(-1.478 \times 10^4 t) - \exp(-1.635 \times 10^6 t)] \quad (3)$$

In the state of the short-circuit from the voltage surge generator 10/700 μs I received a course of the current 5/320 μs (PN-EN 61000-4-5 (2010), IEC 62305: Protection against lightning Part 1: General principles, Part 2: Risk management, Part 4: Electrical) and electronic systems within structure and for the voltage surge generator 1.2/50 μs I received a course of the current 8/20 μs .

Parameters of the surge current 5/320 μs is definite by the formula [7]:

$$i(t) = 1.012845 I_m [\exp(-2205.969 t) - \exp(-1273948 t)] \quad (4)$$

The waveform 8/20 μs suggested by [8] were assigned by the relationship:

$$i(t) = 2.18 I_m [\exp(-0.065 \times 10^6 t) \sin(0.107 \times 10^6 t)] \quad (5)$$

On LTspice, the model of the surge described by the dependence (3) was written down with the instruction.subckt. The surge as a current source that is controlled by the voltage g.

The modelling of the surge any time, makes possible the remarking of the time decay $T_d = t_0$ [9]. The surge can be brought with the form xudar to any node of the modelled system.

Example 1

```
.subckt UDAR wy Params: t0 = 0.1 us
epior2 1 0 value = 1012.845 * 25 * (exp(-2205.969 * time)-
+exp(-1273948*time))
Top 1 0 1f 0 0 = 100 Td = {t0}
Rc 1f 0 100
g wy 0 1f 0 1
.ENDS UDAR
xudar a UDAR
```

For the surge, the value of an impedance equal 400 Ω was accepted to the analysis. At such value of impedance, the voltage that can act in a given (certain) system may reach the value of 10,000 kV. To the analysis I accepted a surge impedance of 400 Ω .

6 Chosen Results of the Modelling

The represented above elements of the analysed system that grouped in the section form of the type II, creating three models of the section containing a section of the traction wires net and a track of the length 64 m and:

Fig. 5 Current surge 5/320 μs (the *full line*) and 8/20 μs (the *dashed line*) for $I_m = 25 \text{ kA}$

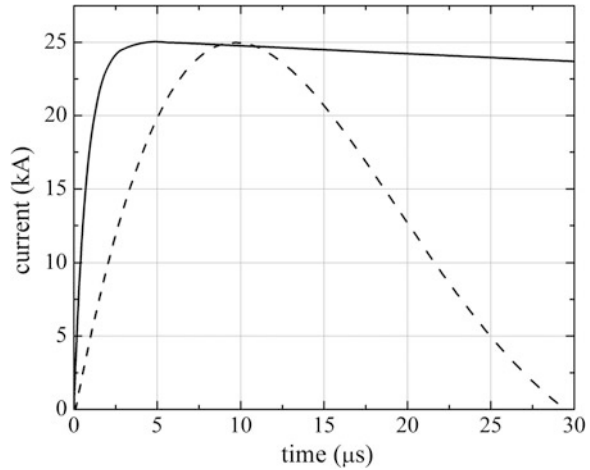
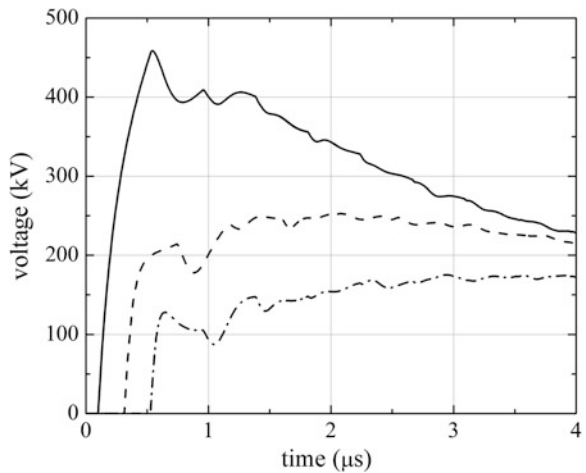


Fig. 6 Group connection to the rail system: Courses of voltages on a catenary wire for tower with a current stroke of 5/320 μs for $I_m = 25 \text{ kA}$ led to the catenary wire (the *full line*) and the following in the distance of 64 m (the *dashed line*) and 128 m (*dotted—dashed line*)



1. the tower with the insulator
2. the tower with corner discharger
3. the tower, from which the surge was brought.

In the analysis, for the reduction I put a metallic short-circuit on the switch of the tower. To the modelling I accepted the sector (fragment) containing 54 sections.

Such written down of the subprogram for the five-wires line model (group connection to the rail lay-out in an open system) and four-wires line model (individual connection to the rail systems) is very complex and because of voluminal considerations cannot be represented here.

The model of the surge that was brought to the node 23 of the catenary wire. To the example—analysis for the current surge model of the shape 5/320 μs and 8/20 μs

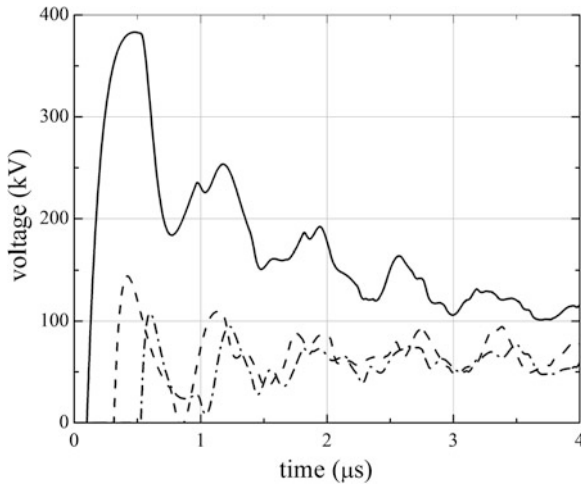


Fig. 7 Individual railed system: Courses of voltages on a catenary wire for tower with a current stroke of $5/320 \mu\text{s}$ for $I_m = 25 \text{ kA}$ led to the catenary wire (the *full line*) and the following in the distance of 64 m (the *dashed line*) and 128 m (*dotted—dashed line*)

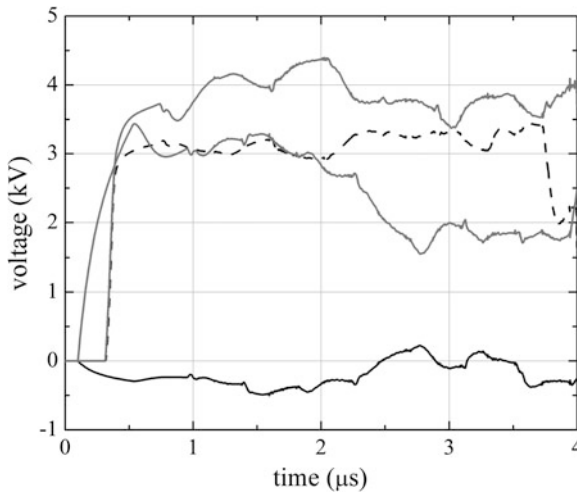


Fig. 8 Group connection to the rail system: Courses of voltages for a tower with a current stroke of $5/320 \mu\text{s}$ for $I_m = 25 \text{ kA}$ led to the catenary wire; the rail 1 (the *black full line*) and the following in the distance of 64 m (the *black dashed line*); the rail 2 (the *grey full line*) and the following in the distance of 64 m (the *grey dotted—dashed line*)

(Fig. 5) I accepted the top—value of the current $I_m = 25 \text{ kA}$. For the voltage surge model of the shape $10/700 \mu\text{s}$ and $1.2/50 \mu\text{s}$ I accepted the maximum value $U_m = 15 \text{ kV}$ (Fig. 22).

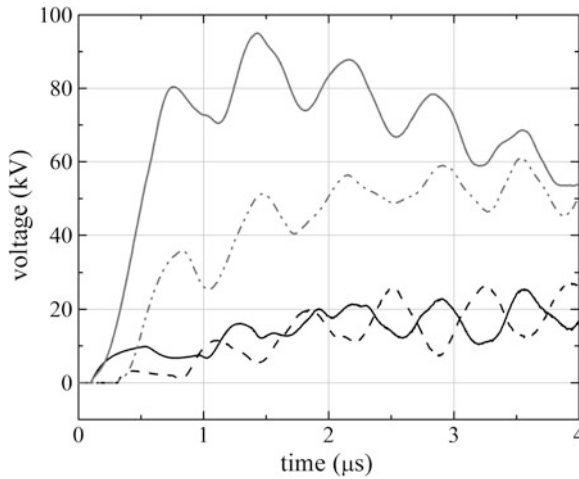
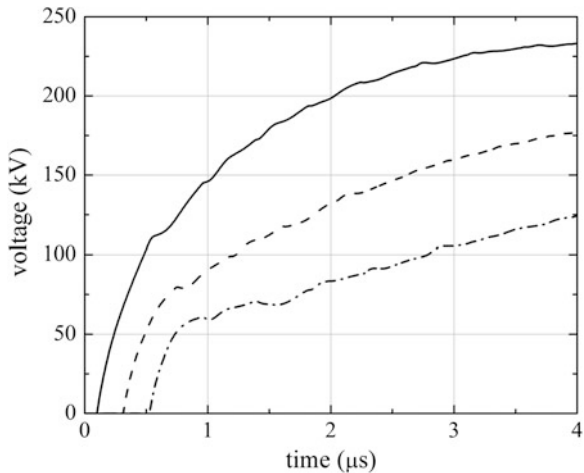


Fig. 9 Individual connection to the rail system: Courses of voltages for a tower with a current stroke of $5/320 \mu\text{s}$ for $I_m = 25 \text{ kA}$ led to the catenary wire; the rail 1 (the *black full line*) and the following in the distance of 64 m (the *black dashed line*); the rail 2 (the *grey full line*) and the following in the distance of 64 m (the *grey dotted—dashed line*)

Fig. 10 Group connection to the rail system: Courses of voltages on a catenary wire for tower with a current stroke of $8/20 \mu\text{s}$ for $I_m = 25 \text{ kA}$ led to the catenary wire (the *full line*) and the following in the distance of 64 m (the *dashed line*) and 128 m (*dotted—dashed line*)



The represented on Fig. 5 shapes of current surges $5/320 \mu\text{s}$ and $8/20 \mu\text{s}$ of the maximum value 25 kV led to the messenger wire on the chosen tower of analysed systems of the catenary wires with group and individual connections to the rail gave interesting results. In the accepted observation time 4 μs for the group connection of the rail, higher maximum voltages values of 460 kV (Fig. 6 for the surge $5/320 \mu\text{s}$)

Fig. 11 Individual railed system: Courses of voltages on a catenary wire for tower with a current stroke of $8/20 \mu\text{s}$ for $I_m = 25 \text{ kA}$ led to the catenary wire (the *full line*) and the following in the distance of 64 m (the *dashed line*) and 128 m (the *dotted—dashed line*)

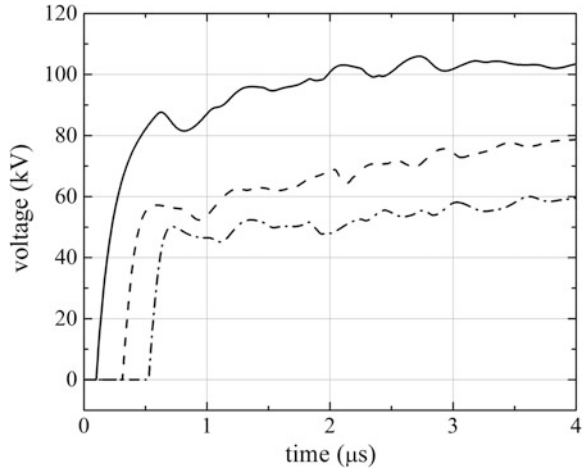
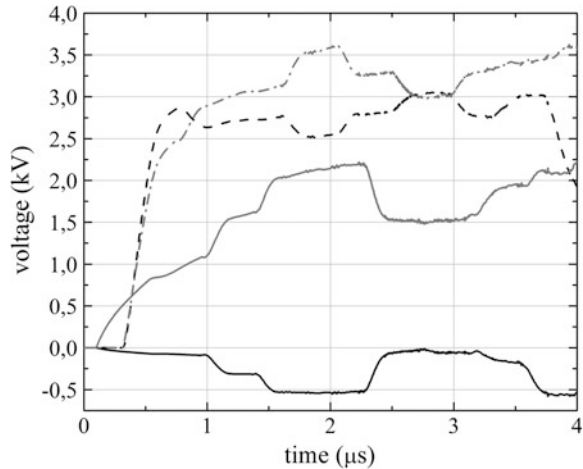


Fig. 12 Group connection to the rail system: Courses of voltages for a tower with a current stroke of $8/20 \mu\text{s}$ for $I_m = 25 \text{ kA}$ led to the catenary wire; the rail 1 (the *black full line*) and the following in the distance of 64 m (the *black dashed line*); the rail 2 (the *grey full line*) and the following in the distance of 64 m (the *grey dotted—dashed line*)



and 240 kV (Fig. 10 for the surge $8/20 \mu\text{s}$) of observed on the messenger wire of three following columns were ascertained. In the case of individual connections to the rail, values of these voltages carried out about 380 and 120 kV (Figs. 7 and 11 properly for surges $5/320 \mu\text{s}$ and $8/20 \mu\text{s}$). Quoad hoc, these results confirm passed {realized} and described on the research [10] measurements. Values of these voltages are significantly lower for group connections of the rail (about 4.5 kV for the surge $5/320 \mu\text{s}$ —Fig. 8 and about 3.7 kV for the surge $8/20 \mu\text{s}$ —Fig. 12) than for individual connections of the rail (about 95 kV for the surge $5/320 \mu\text{s}$ —Fig. 9 and about 7.5 kV for the surge $8/20$ —Fig. 13).

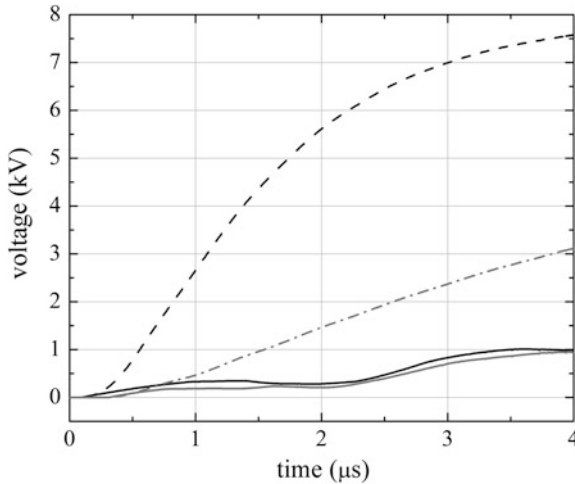
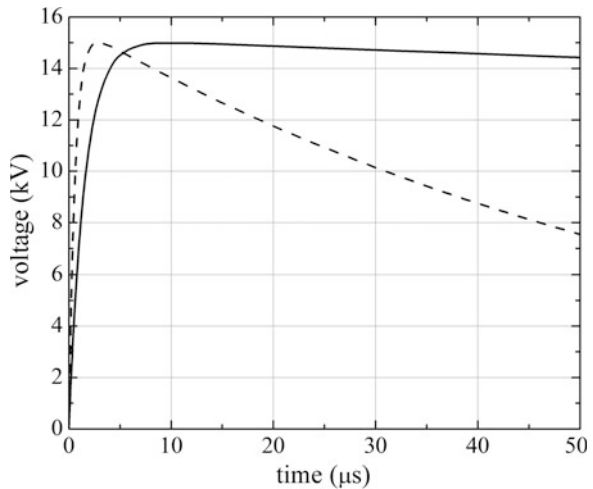


Fig. 13 Individual connection to the rail system: Courses of voltages for a tower with a current stroke of $8/20 \mu\text{s}$ for $I_m = 25 \text{ kA}$ led to the catenary wire; the rail 1 (the *black full line*) and the following in the distance of 64 m (the *black dashed line*); the rail 2 (the *grey full line*) and the following in the distance of 64 m (the *grey dotted—dashed line*)

Fig. 14 Surge voltage of $10/700$ and $1.2/50 \mu\text{s}$ for $U_m = 15 \text{ kV}$



In realized measurements described in the research works [10] to researches the voltage surge $1.2/50 \mu\text{s}$ was also used. For surges of the shapes $10/700$ and $1.2/50 \mu\text{s}$ (Fig. 14) and the maximum value 15 kV , for group and individual connections of the rail properly on Figs. 15 and 16 as well as 19 and 20, voltages courses on the

Fig. 15 Group connection to the rail system: Voltage courses for tower with the surge voltage of $10/700 \mu\text{s}$ for $U_m = 15 \text{ kV}$ led to the catenary wire (the *full line*) and the following in a distance of 64 m (the *dashed line*) and 128 m (the *dotted—dashed line*)

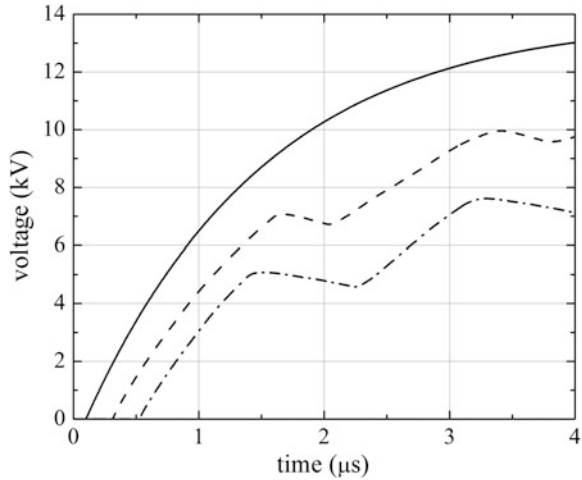
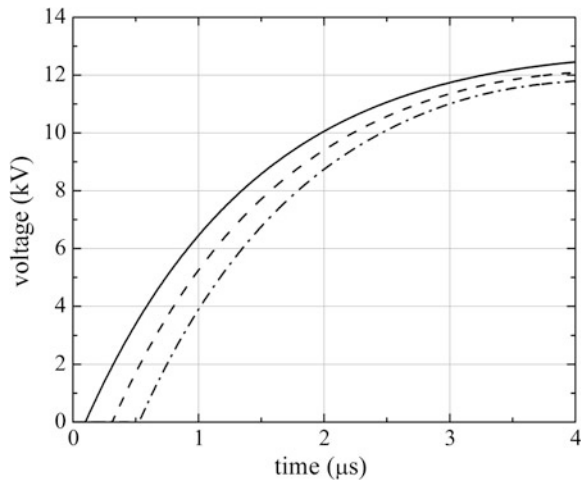


Fig. 16 Individual connection to the rail system: Voltage courses for tower with the surge voltage of $10/700 \mu\text{s}$ for $U_m = 15 \text{ kV}$ led to the catenary wire (the *full line*) and the following in a distance of 64 m (the *dashed line*) and 128 m (the *dotted—dashed line*)



messenger wire for three following columns were represented. On Figs. 17 and 21, results of the modelling for two rails in the case of group connections of the rail were represented. Maximum voltages values are the line 250 V for the surge $10/700 \mu\text{s}$ (Fig. 17) and about 400 V for the surge $1.2/50 \mu\text{s}$ (Fig. 21). For individual connections of the rail, they carry out, about 7.5 kV (Figs. 18 and 21) properly for the surge $10/700 \mu\text{s}$ and $1.2/50 \mu\text{s}$.

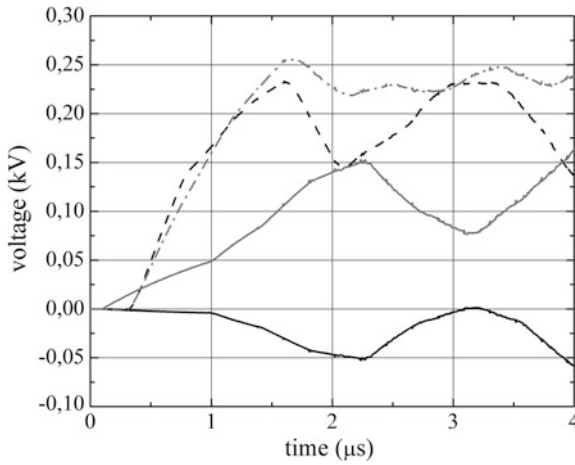


Fig. 17 Group connection to the rail system: Courses of voltages for a tower with the surge voltage of $10/700 \mu s$ for $U_m = 15 \text{ kV}$ led to the catenary wire; the rail 1 (the *black full line*) and the following in the distance of 64 m (the *black dashed line*); the rail 2 (the *grey full line*) and the following in the distance of 64 m (the *grey dotted—dashed line*)

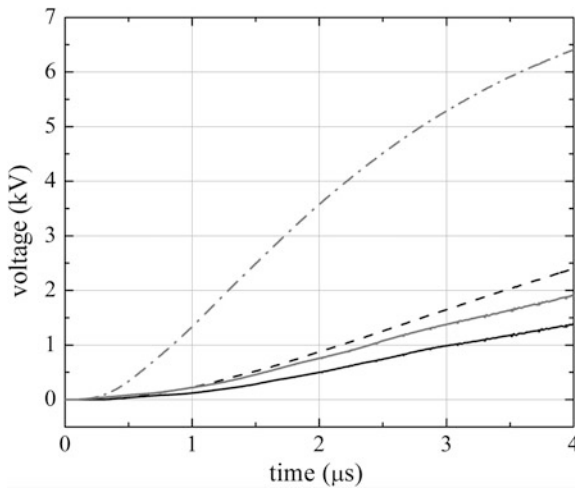


Fig. 18 Individual connection to the rail system: Courses of voltages for a tower with the surge voltage of $10/700 \mu s$ for $U_m = 15 \text{ kV}$ led to the catenary wire; the rail 1 (the *black full line*) and the following in the distance of 64 m (the *black dashed line*); the rail 2 (the *grey full line*) and the following in the distance of 64 m (the *grey dotted—dashed line*)

Fig. 19 Group connection to the rail system: Voltage courses for tower with the surge voltage of $1.2/50 \mu\text{s}$ for $U_m = 15 \text{ kV}$ led to the catenary wire (the *full line*) and the following in a distance of 64 m (the *dashed line*) and 128 m (*dotted—dashed line*)

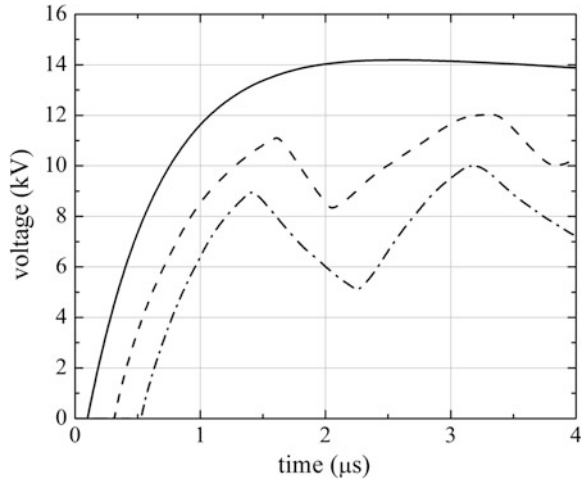
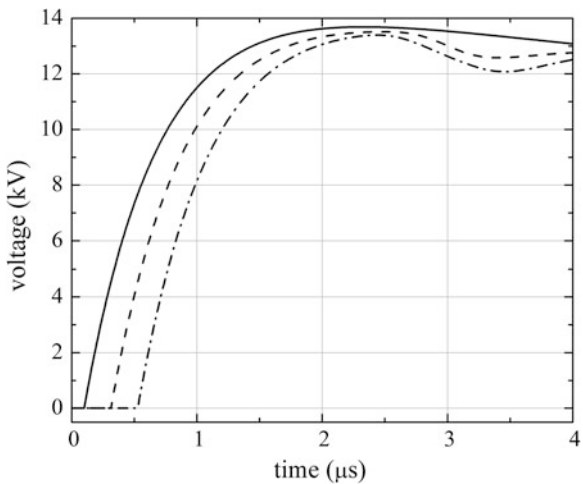


Fig. 20 Individual connection to the rail system: Voltage courses for tower with the surge voltage of $1.2/50 \mu\text{s}$ for $U_m = 15 \text{ kV}$ led to the catenary wire (the *full line*) and the following in a distance of 64 m (the *dashed line*) and 128 m (*dotted—dashed line*)



From realized analysis, it results that a group connections of the rail limit in a greater degree, the voltage that appear in the track. This has a large meaning from the regard on installed in the track railway traffic control device and in the isolation co-ordination.

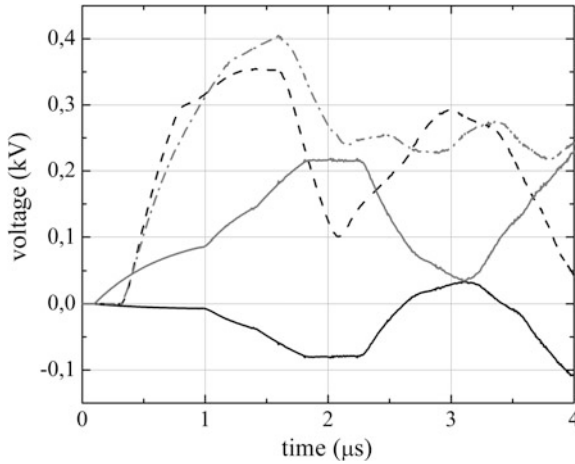


Fig. 21 Group connection to the rail system: Courses of voltages for a tower with the surge voltage of $1.2/50 \mu\text{s}$ for $U_m = 15 \text{ kV}$ led to the catenary wire; the rail 1 (the *black full line*) and the following in the distance of 64 m (the *black dashed line*); the rail 2 (the *grey full line*) and the following in the distance of 64 m (the *grey dotted—dashed line*)

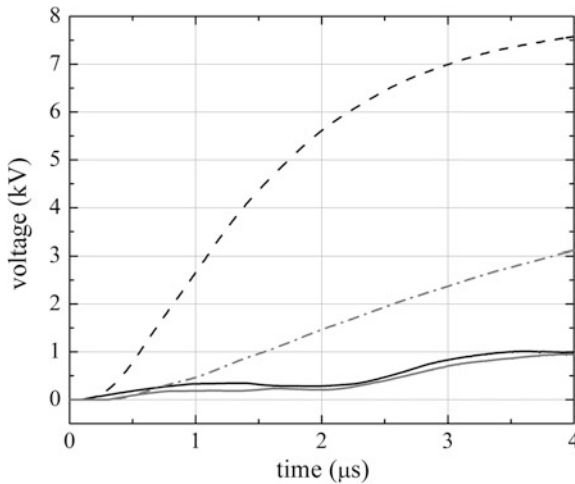


Fig. 22 Individual connection to the rail system: Courses of voltages for a tower with the surge voltage of $1.2/50 \mu\text{s}$ for $U_m = 15 \text{ kV}$ led to the catenary wire; the rail 1 (the *black full line*) and the following in the distance of 64 m (the *black dashed line*); the rail 2 (the *grey full line*) and the following in the distance of 64 m (the *grey dotted—dashed line*)

7 Discussion and Conclusions

In the paper I spoke components of the model describing the accepted to the analysis system of the traction wires net with the group connection to the rail in an open system at an extinction current $5/320 \mu\text{s}$, $8/20 \mu\text{s}$ and voltage's $10/700 \mu\text{s}$, $1.2/50 \mu\text{s}$. I represented possibilities of the simulation at the utilization of the programme LTSpice and I based the necessity of the treat of the problem of the lightning protection efficiency of railways devices.

Analysed possibilities of the programme have the cognitive character and will be put-upon to further analysis and estimations of the threat of feeding parley of the rts devices caused by short-circuits and by surges of the atmospherical origin.

References

1. Łoboda M, Sobolewski K (2009) Lightning deaths and injuries in Poland, European COST action P 18 international symposium on lightning physics and effects. Vienna, Austria
2. Centrum Naukowo-Techniczne Kolejnictwa Zakład Sterowania Ruchem i Teleinformatyki, Doświadczalne badanie systemu uszynień grupowych ze zmodyfikowaną długością ciągłości elektrycznej (zblizoną do długości szlaków tj.: 8–12 km), Etap1 (2008) Badania symulacyjne wyłączalności zwarć izolacji głównej sieci trakcyjnej z układem połączeń uszynień grupowych ze zmodyfikowaną długością sekcji. Zadanie nr 3568/10, Warszawa; Etap 2 (2009) Sprawozdanie z badań wyłączalności zwarć izolacji głównej sieci trakcyjnej do uszynienia grupowego ze zmodyfikowaną długością sekcji. Praca nr 3568/10, Warszawa ©
3. Szelań A (2002) Zagadnienia analizy i projektowania systemu tracji elektrycznej prądu stałego z zastosowaniem technik modelowania i symulacji. Prace Naukowe, Elektryka z. 123, Oficyna Wydawnicza Politechniki Warszawskiej, Warszawa
4. Białoń A, Kaźmierczak A, Zając W (1999) Opracowanie dopuszczalnych parametrów zakłóceń dla urządzeń srk, łączności i pojazdów trakcyjnych. Sprawozdanie końcowe. Praca 6915/23, CNTK, Warszawa
5. Clayton PR (2006) Introduction to electromagnetic compatibility. Wiley, New Jersey. (Published simultaneously in Canada)
6. Głowacki K, Onderka E (2002) Sieci trakcyjne SEMTRAK s.c
7. Safe Engineering Services & Technologies Ltd (1997) FFTSES user's manual, fast fourier transforms. Safe Engineering Services & Technologies Ltd, Montreal, Canada
8. Bajorek J, Knott M, Wyderka S (1992) Efficiency of ZnO arrester models simulation of lightning overvoltages. In: 21st ICLP, Berlin, Germany Pap. No. 5.07
9. Wróbel Z (2010) Possibility of the modelling of combination waves generators. Przegląd Elektrotechniczny, PL ISSN 0033-2097, R. 86 NR 9/2010, pp. 289–292
10. Politechnika Białostocka (2010) Wydział Elektryczny, Poligonowe badania ochrony przeciwprzebieciowej z ogranicznikami warystorowymi. Część I. Sprawozdanie z pomiarów przeprowadzonych w warunkach poligonowych. Białystok ©

Gearless Pedaling Electric Driven Tricycle

K. Zawirski, K. Nowopolski, B. Wicher, D. Janiszewski,
B. Fabiański and K. Siembab

Abstract In the paper the general conception and real construction of a three-wheel bicycle with auxiliary electric propulsion is presented. Each of the vehicle wheels is driven by an electric motor (BLDC) controlled by the central system of power distribution. The generator that charges a battery pack is driven by pedals. The vehicle speed is proportional with adjustable ratio to the pedaling velocity, whereas the power delivered to the motors is appropriately increased to the pedaling power with adjustable degree. Description and analysis of the selected modules of the vehicle are documented with prototype research results.

1 Introduction

The idea of the electric bicycle has been developed for several years, however various countries law legislated exact electrically assisted bicycle. An important feature of them should be natural propel pedal drive system with electric motor (power less than 200 W) regarded only as a support. The formulation of conception and prototype building has been developed. The amount of research work performed under the Polish Agency for Enterprise Development project. The following purposes have been considered:

- construction of eco-tricycle adapted to getting around the city held in accordance definition of an electric bicycle, a fully electric drive mounted in the wheels of the vehicle, without mechanical coupling (i.e. no shaft, chain, gear) between pedals and wheels,
- possibility of charging the power battery pack by pedaling,
- chance to transport 1–3 people or small load carriage.

K. Zawirski (✉) · K. Nowopolski · B. Wicher · D. Janiszewski · B. Fabiański · K. Siembab
Institute of Control and Information Engineering, Poznan University
of Technology, Poznań, Poland
e-mail: krzysztof.zawirski@put.poznan.pl

The paper describes the concept of vehicle, the construction of its main components with results of research and testing of the prototype.

2 Concept of the Drive and Control System

The bike is equipped with three BLDC motors, which individually drive three wheels. The energy conveyed to the motors, which are controlled by the Central Power Distribution system, is proportional to the power of pedaling (with an adjustable ratio, so the motors power may be several times larger). Pedals driven shaft of the generator produces energy, that charges the battery pack. Vehicle velocity is proportional to the angular speed of pedaling with the possibility of different value ratio setting (idea of electronic gear). Generated energy determines the wheels behavior, wherein the level of the power and is controlled by the electronic gearbox without any mechanical coupling. The vehicle drive and control system is divided into modules (subsystems) as follows:

- three independent wheel drives, including BLDC motors power converters and own control systems,
- pedal-driven generator module with inverter and control system that allows to charge batteries,
- Central Control and Power Management Unit,
- Lithium Iron Phosphate battery pack with set of chargers.

Motor drive control system, generator and the central control unit are connected through a communication network interfaces in *Controlled Area Network* (CAN) standard. Figure 1 shows the structure of the system, which consists of the master control unit and power management (PMU), the inverter motor (INVM), the inverter generator driven by the pedals (INVG), the battery charger block (CHA). Proper configuration of the supply lines allows to monitor battery voltage and total current at the branch point. That topology allows to connect subsystem independently to the power network (e.g. disconnection in case of detection any malfunction by switching handling appropriate devices, such as MR, GR, RR, CR, PR). The Power Relay (PR) connector is an electromagnetic relay, in which the coil is connected in series with emergency stop button.

PMU module enables the realization of complex motion control algorithms, such as limiting the centrifugal forces, differentiation of the electromagnetic torque and velocity for each drive. Entire microprocessor system must have regard to the isolating functional sections in high power environment by galvanic isolation system (GI).

The initial vehicle prototype is shown on the Fig. 2.

The unique conception of the gearless tricycle control system (CS) has been developed. Used CAN network gives opportunities of implementing modified algorithms in different CS structures. That approach with CS module, contains problem solutions of vehicle kinematics. The full dynamical model, as described

Fig. 1 Scheme of the power distribution network

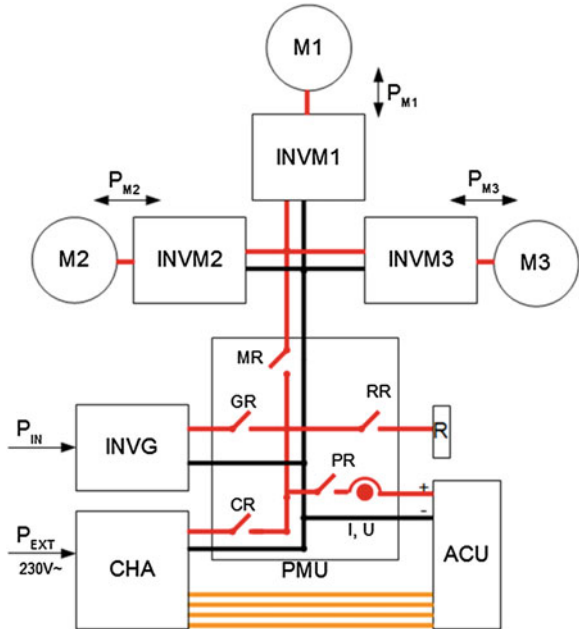


Fig. 2 The view of the vehicle prototype intended for traction tests



[1], has been considered with several basic control schemes. This schemes shown kinematics influences like drives current waveforms and overall system performance.

3 Control and Power Management Central Module

Power Management Unit (PMU) is responsible for the following tasks:

- uninterrupted supervision of system with communication in the distributed network,
- redundant safety algorithm and emergency stop interface,
- interfacing electric drives and visualization unit (VU) in separated CAN networks,
- monitoring the battery status (voltage, current),
- power distribution for low-power electronics.

Above tasks are performed in the two following hardware blocks: a microprocessor one with galvanic isolation and execution block, capable of high power flow. As the control unit, the STM32F407 is used. This is a modern system controller used in all proposed subsystems [2].

Diagram in Fig. 3 shows the central controller (PMU), the master unit of the CAN1 network (drive system core network) and CAN2 as the separated network for interfacing with HMI panel (VU). The possibility of interfering and disturbing high power elements into VU is limited through CAN1 and CAN2 network isolation. It was decided to implement the *CANopen* protocol, often used in automotive, in the ISO/OSI model application layer, characterized in [3, 4]. Adaptation of the *CANopen* specification allows the use of ready-made algorithms for state management of logic nodes, error detection, control or coherence of communication schemes to case and the requirements of application.

Fig. 3 Scheme of the topology of controlled area network and low-current power distribution network

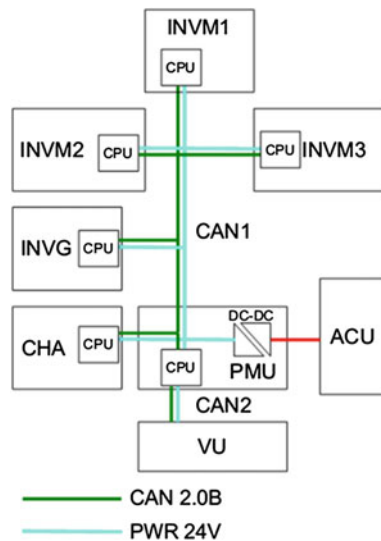


Figure 3 presents also a power bus, a parallel to the CAN network, delivering energy to each of the node controllers. Galvanic isolation of the proposed topology increases the security of the system, due to the decoupling of the power modules failure.

The central unit controls the power management module that conveys the energy to and from the batteries (PMU is only directly connected to the power battery pack).

Assumed functionality allows the implementation of the system safety, as the energy stored in the battery is a potential threat to vehicle. The basic mechanism of the safety system is the coupling of the electromagnetic relay coil with the emergency stop. The emergency shutdown automatically (bypassing the microcontroller) attaches the break resistor to the motor drives power supply nodes. The logic of the power supply switching circuits dedicated for each subsystem (motor drives, generator, charger, power resistor) is next safety system. The logics depending on the condition of the vehicle (e.g. unacceptable is an involuntary movement of the vehicle during stationary battery charging controls solid state power relays (SSR) forming needed energy transfer as well as electromagnetic relay.

4 Wheel Direct Drive

Each of the three wheels are driven by its own direct drive, as mentioned above. The Brushless DC Motor is main element of the proposed solution. There are used standard auxiliary bike motors mounted on a spoked wheel hub. Low rotational speed of the motors allows to apply the drive wheels without any additional mechanical transmission (planar, belt, etc.).

Rated power of each engine, of about 1 kW, is sufficient to ensure that movement of the vehicle along a set of batteries and one or more passengers while maintaining satisfactory dynamic properties compared in classic bike.

During research, it was found, the inductance of the stator windings is very small, of the order of 50 μH . Such a small value causes that even at high carrier PWM frequencies ($f_c = 20 \text{ kHz}$) nature of stator current is interrupted. Interrupted current of the motors necessitates a strong filtering of the measurements. For measurement of the average current, analog and digital filtering is applied. The results shown in Fig. 4.

Used process unfortunately introduces a significant delay, which, makes it impossible to obtain a good dynamic in the loop current in practice, and consequently ensure the proper motion dynamics of the vehicle [5].

Other interesting properties of used motor was observed and taken into account. One of them is not detailed enough, the waveform of electromagnetic force of the stator winding should be trapezoidal as in BLDC but in this case is strictly sinusoidal, as shown in Fig. 5.

In this context it was decided to implement a sine wave inverter control. The idea of forcing control of three-phase sinusoidal voltage is shaping the phase voltage

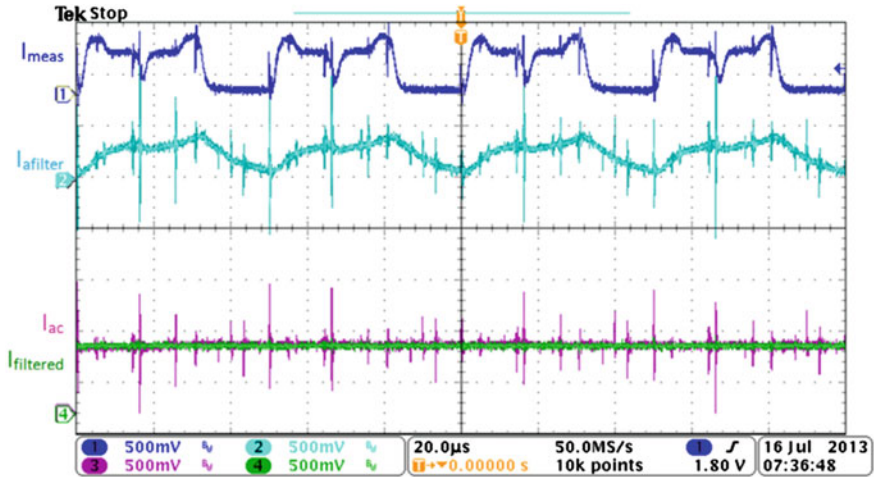


Fig. 4 Illustration of the current measurements: I_{meas} —measured current (scale 500 mV → 16.5 A), $I_{afiltered}$ —current behind analogue filter (scale 500 mV → 16.5 A), I_{ac} —current signal from AC converter (sampled every 50 µs, scale 500 mV → 8 A), $I_{filtered}$ —current signal filtered by an first order IIR digital filter with 400 µs time constant (scale 500 mV → 8 A)

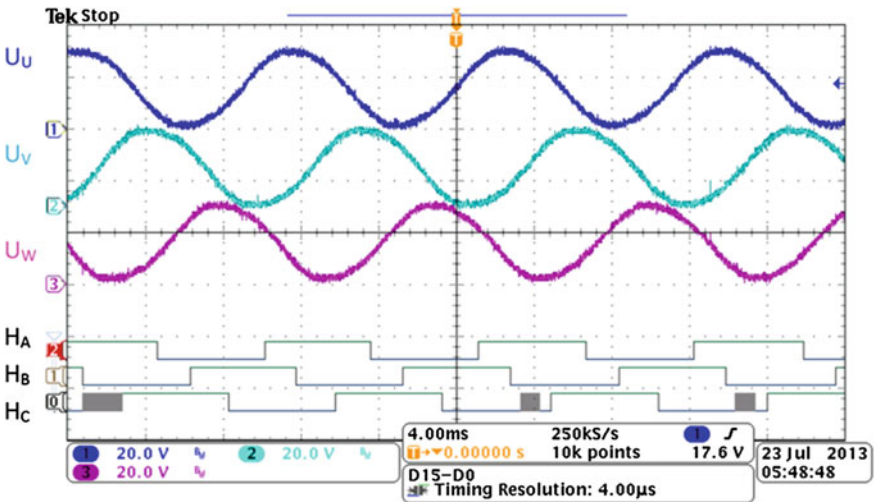


Fig. 5 Examples of EMF of motor stator windings signals and position Hall sensors signals

signals as sinusoidal. Sinusoidal voltage control was successfully tested in the whole range of speed changes. The main advantage of this method is control of electromagnetic torque, smoothing roughness occurring within a single rotation of the motor shaft. This control method has also another important advantage, which is

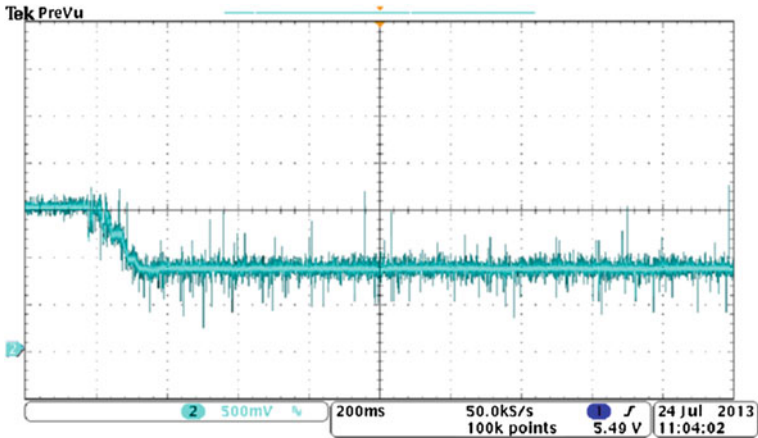


Fig. 6 Motor start to the velocity of 150 rpm with velocity controller

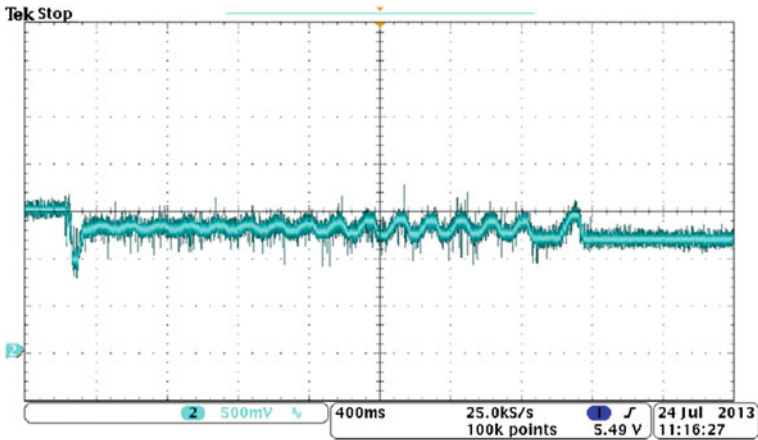


Fig. 7 Motor start to the velocity of 60 rpm with velocity controller—improper controller operation

a significant reduction in the noise level with respect to the classical BLDC trapezoidal control, which revealed especially when torque boost, or working at low speed.

Due to the above-mentioned problems with the design of efficient current controller, an alternative solution without the current loop has been adopted, instead of the typical cascade structure of the control system (described in [5, 6]). The proposed system directly controls the speed by voltage setpoint with current limitation routine. PI speed controller, operating at a frequency of 1 kHz, have been used. Figure 6 shows results during motor start to velocity of 150 rpm.

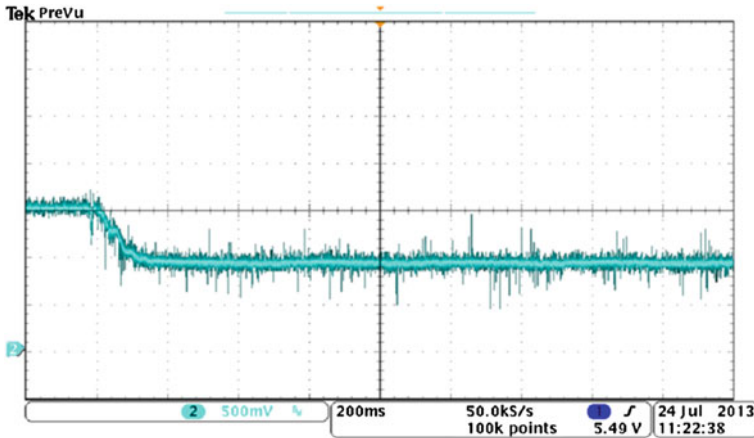


Fig. 8 Motor start with voltage controller to the velocity of 120 rpm

Low resolution of the position measurement signals from the Hall sensors (pulse every 1/6 electrical angular) does not allow for a good computation of small values of speed and consequently the correct velocity of the regulations in this regard. There were difficulties in obtaining a correct operation of the speed controller speed below 70 rpm. Waveforms in Fig. 7 illustrate the incorrect operation (oscillation).

Because of these difficulties, alternative solution assumed, consisting in the adjustment of the motor of the electromotive force (proportional to velocity) with an additional compensation of voltage drop across the resistance of the stator circuit and the circuit. In the control system a limitation of the SEM current supply circuit of each of the DC voltage converter was implemented. Results of them shown in Fig. 8.

Interesting part of investigations was determine the energy efficiency of used electric drive. Figure 9 shows a few representative characteristics, where different torque and speed (75, 150, 200 rpm) was choose as a test variable.

Draws attention to growing together with speed efficiency of the drive. For loads above 20 Nm increase in efficiency is in excess of 20 %, comparing the speed setpoint 75 and 200 rpm, overall observation is thus an increase in efficiency with the power system.

5 Generator Module

One of the BLDC motors, described in Chapter “[Study the Quality of Global Neural Model with Regard to the Local Models of Dynamic Complex System](#)”, was used as the generator. This was the same type of BLDC motor that was used for drive purposes, the only difference was the lower power (250 W) compared to the motors

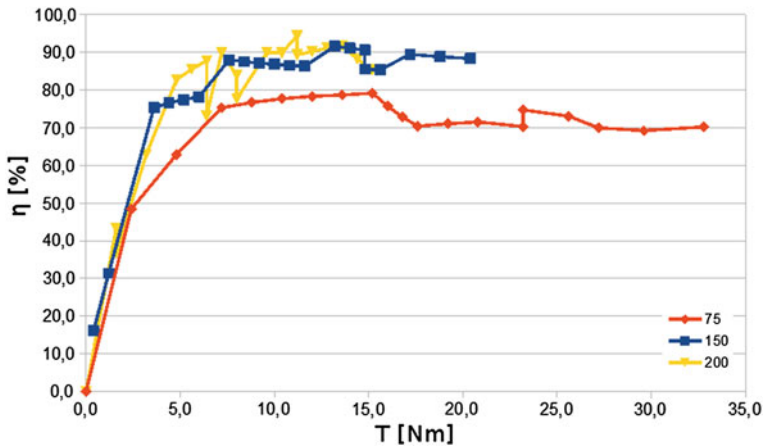


Fig. 9 Efficiency of converter-motor unit versus load torque for various values of reference velocity

installed in wheels. The generator is coupled with the pedals by a chain. The three phases of main windings and three position Hall sensors output are connected to the generator inverter module. The main component of the inverter is also STM32F4 microcontroller that controls all the following functions of the module:

- conversion of the energy generated by the cyclist in order to charge the battery (control of the PWM signal),
- measurement of the generator speed (based on the Hall sensors signals),
- control of the cyclist load torque—motion resistance according to the selected algorithm,
- communication with other modules of the vehicle (including the central control module) by the CAN network,
- acquisition and processing of the measurement signals (voltages and currents both of the generator and the battery side)
- data exchange between the module and a PC during tests.

The scheme of the power section is shown in Fig. 10.

Each of the three phases of the motor is approximated by a serial connection of resistance, inductance and electromotive force. The alternate voltage generated by the motor is rectified by D1–D6 diodes and filtered by the DC capacitor. This DC voltage supplies the high current part of the inverter.

Since for the proper system operation, only increase of the voltage is necessary, the power converter was design in the boost topology. Simple construction and small number of semiconductor power elements, allow to reduce the costs (only one power transistor and one power diode are required), keeping relatively high efficiency of this sort of constructions.

The mentioned torque control takes place through the control of the rectified generator current. In this method a linear relationship between these two variables is

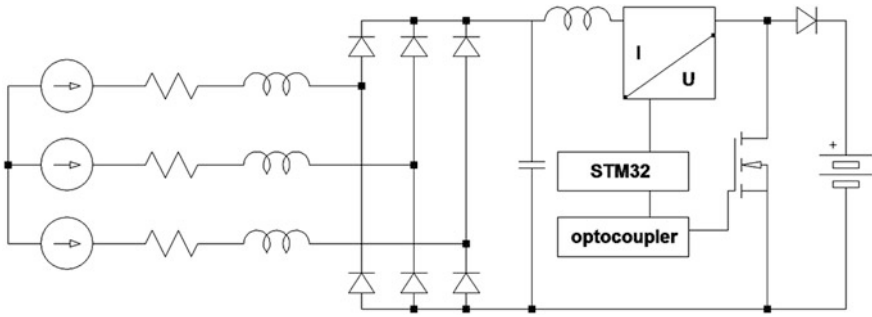
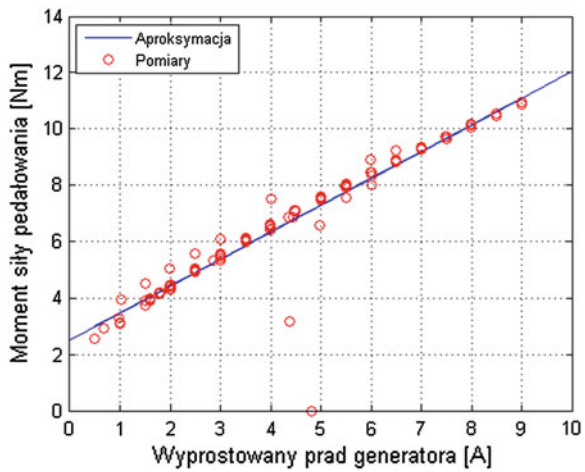


Fig. 10 Scheme of the generator power electronic module

Fig. 11 Pedalling torque versus rectified generator current



assumed, which is proven by the measurements presented in Fig. 11. Due to the variability of the human muscles force in the function of the support angular position, it was necessary to implement ergonomic modifications in the generator current control. The goal of these modifications is smoothness and naturalness of the pedaling process. These methods are described more widely in [7].

6 Conclusions and Summary

During the research, it was shown, that the particular drive modules, the generator system, the system of central control and the power management module operate properly as assumed. The vehicle velocity is proportional to the pedaling speed. The electronic ratio between the pedaling speed and vehicle speed (“gear”) may be changed easily by the driver. The driver feels the resistance of the pedaling,

increasing proportionally to the real resistance of the move, and related to the forced vehicle acceleration. The perceptible resistance of the pedaling depends on the selected ratio (set electronically). The vehicle is equipped with an efficient system of a regenerative brake, allowing to recover some part of the braking energy, and utilized it to charge battery pack.

The assumed solution, based on the galvanic isolation of the microprocessor devices from the power electronics part, allowed to reduce the risk of the potential damages of the central control unit.

References

1. Fabianski B, Wicher B (2014) Dynamic model and analysis of distributed control system algorithms of three wheel vehicle. In: Proceedings of the 19th international conference on methods and models in automation and robotics (MMAR 2014), Miedzyzdroje
2. STM Corp (2007) Software techniques for improving microcontroller EMC performance, AN1015
3. Boterenbrood H (2000) CANopen—high-level protocol for CAN-bus. NIKHEF, Amsterdam
4. Corrigan S (2008) Introduction to the controller area network (CAN), Texas instrument application report
5. Brock S, Zawirski K (2012) New approaches to selected problems of precise speed and position control of drives. In: Proceedings of the IECON 2012—38th annual conference IEEE industrial electronics society, 2012, pp 6291–6296
6. Zawirski K, Janiszewski D, Muszynski R (2013) Unscented and extended Kalman filters study for sensorless control of PM synchronous motors with load torque estimation. Bull Pol Acad Sci Tech Sci, 61(4):793–801
7. Bielak C, Nowopolski K, Wicher B (2013) Static and dynamic ergonomic corrects of torque controlled in bicycle ergometer. In: Proceedings of 18th international conference on methods and models in automation and robotics (MMAR 2013), Miedzyzdroje, Poland

Calculations of Conjugated Fields in the Ferromagnetic Medium

Robert Pękala, Tadeusz Kwater and Bogdan Kwiatkowski

Abstract The article proposes the concept of computations, that allow to examine interaction between the electromagnetic field and the temperature field in an isotropic ferromagnetic environment. Based on the idea of interdisciplinary mathematical modeling, Maxwell's equations and the equations of thermodynamics were used. Mathematical model object in the form of a thin ring, gathering and alternating magnetic flux was considered. The transient processes were numerically solved and the suitable computer simulations were carried out.

1 Introduction

Penetration time-varying magnetic flux to the ferromagnetic material causes the phenomenon of eddy currents, which is associated with power losses and heating of the metal. The increase of material temperature leads to changes of its electromagnetic properties, and it causes changes in the distribution of the electromagnetic field. Therefore, a kind of connection between the electromagnetic and heating phenomena in ferromagnetic material can be considered. The effects of this interaction can be explained through appropriate time-spatial distribution of temperature field of the magnetized material. It should be also denoted that all the qualitative and quantitative estimates are available only by mathematical modeling methods due to the inability to make direct accurate measurements of the temperature inside the object. In this paper authors propose the use of an interdisciplinary mathematical modeling

R. Pękala (✉) · T. Kwater · B. Kwiatkowski
Centre of Innovation and Transfer of Natural Sciences and Engineering Knowledge,
University of Rzeszow, al. Rejtana 16 A, 35-959 Rzeszów, Poland
e-mail: rpekala@ur.edu.pl

T. Kwater
e-mail: tkwater@ur.edu.pl

B. Kwiatkowski
e-mail: bkwiat@ur.edu.pl

to analyze the effect of electromagnetic and temperature field interaction, for the object in the form of electrotechnical steel ring with a rectangular cross-section and the magnetizing winding wound. Taking into account the non-linear phenomena, the appropriate mathematical model—based on the equations of the general theory of the electromagnetic field and the thermodynamic equations—was proposed. Furthermore, an algorithm for the numerical solution of the transient processes was elaborated and suitable computer simulations were carried out in Matlab programming environment.

The issue concerning to heat inside material of objects of different nature was considered in the literature [1, 3, 4, 7]. Proposed solutions there take into account the usual classical equations of eddy current losses or other models, which complexity depends on the specific problem. The exception is the approach presented in [5]—magnetic losses are measured using the indirect method. The mathematical model, presented in this paper, takes also into account the heat equation. In this manner it is possible to obtain space-time distribution of temperature field in the electromagnetic material.

2 Electromagnetic Field Equations

As the object of the research, the ring of electrotechnical steel with magnetizing windings was considered—see Fig. 1.

The electromagnetic field vectors, in the assumed reference system can be described by the following formulas:

$$\mathbf{B} = \alpha_0 \mathbf{B}; \quad \mathbf{H} = \alpha_0 \mathbf{H} \quad \mathbf{E} = \mathbf{r}_0 E_r + \mathbf{z}_0 E_z. \quad (1)$$

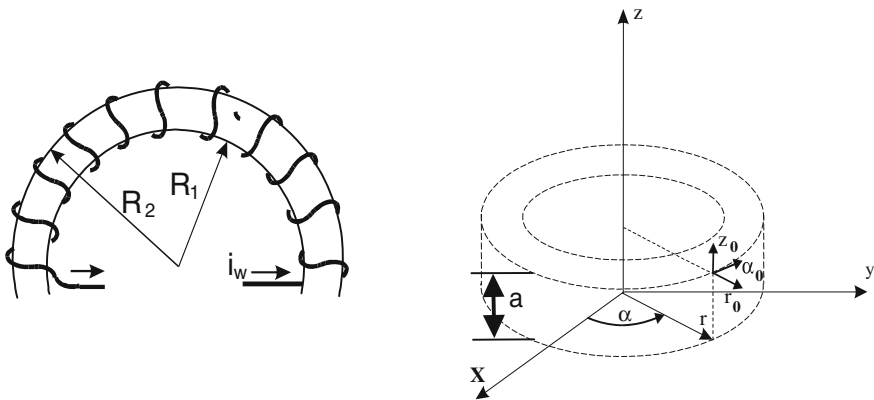


Fig. 1 Ferromagnetic ring with magnetizing windings (a), electromagnetic field vectors in the cylindrical system of coordinates (b)

Considering electromagnetic field equations for this object we used the results of our earlier studies, that were focused on the development of methods for detecting defects in the transformer winding with toroidal core. Taking into account the concept of the electromagnetic field vectors \mathbf{B} , \mathbf{H} and \mathbf{E} described by Eq. (1) and using Maxwell's equations, the electromagnetic field equation for the ferromagnetic ring can be derived in the following form [2]:

$$\frac{\partial B}{\partial t} = \frac{1}{\gamma} \left(\frac{\partial^2 H}{\partial r^2} + \frac{\partial^2 H}{\partial z^2} + \frac{1}{r} \frac{\partial H}{\partial r} - \frac{H}{r^2} \right), \quad (2)$$

where γ denotes electrical conductivity of the electrotechnical steel. The connection between components of vectors \mathbf{B} and \mathbf{H} in (2) can be considered using non-linear magnetization characteristics, taking into account magnetic reluctivity ν of the material:

$$B = H/\nu(B). \quad (3)$$

To solve Eq. (2), it is also necessary to take appropriate boundary conditions for equation. In our case, the Ampere's law was considered, given by the formula:

$$H(r) = wi_w/2\pi r, \quad (4)$$

where i_w —current in magnetizing windings, w —number of turns, $R_1 \leq r \leq R_2$, while R_1, R_2 denotes respectively internal and external radius of the ferromagnetic (Fig. 1a).

Assuming the coil current i_w as the known signal (for example sinusoidal signal), penetrating electromagnetic field in the ring can be calculated. We assumed that there is no leakage flux, so all electromagnetic field is closed in the ferromagnetic.

It should be noted, that in a practice components of vectors \mathbf{B} and \mathbf{H} may reach values from non-linear range of magnetization characteristics (3), and it causes deformation of the magnetizing current. Thus, the assumption of the current windings as the given quantity should be regarded as the simplification of problem.

3 Equations of Conjugated Fields of Electromagnetic Ring

The penetration of the electromagnetic field to the ferromagnetic material will cause formation of heat phenomena, that should be considered in two aspects. At first, as it is well known, the penetration of the field in ferromagnetic environment causes outbreaks of power generation by the eddy-currents. It leads to the formation of temperature gradients and flows of the heat flux. This phenomena may be considered on the basis of the theory of heat conduction, including heat conduction equation.

The second aspect relates to the fact, that heating of the material will transfer heat into the external environment. Thus, convection and radiation may be considered as another form of heat transfer.

It should also be noted, that the inclusion of heat phenomena will cause the modification of the electromagnetic field Eq. (2). In this equation, the conductivity γ will no longer be a constant value, but will decrease non-linearly during increasing temperature T , according to the well known relationship:

$$\gamma = \gamma(T) = \frac{\gamma_0}{1 + \alpha(T - T_0)}, \quad (5)$$

where T_0 —temperature of environment, α —temperature coefficient of the material and $\gamma_0 = \gamma(T_0)$.

Figure 2 shows the changes in conductivity γ of the electrotechnical steel in the temperature range $T = 20/120$ °C.

Based on the above characteristic we can see changes in the conductivity, even at relatively low temperature gradients. It confirms, that Eq. (5) should be considered in electromagnetic field Eq. (2). Taking into account the space inside the ferromagnetic material, thermal phenomena can be described by the equation of heat conductivity in a hyperbolic form [6]:

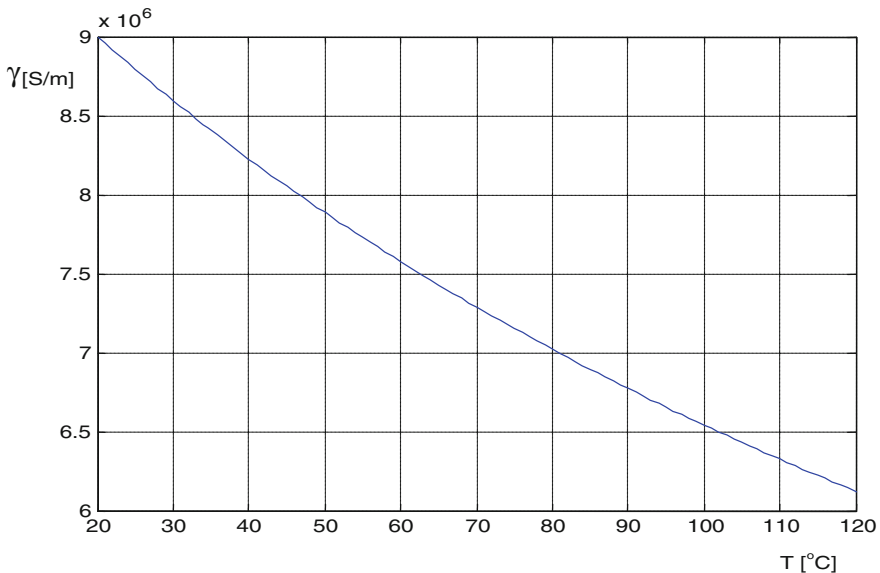


Fig. 2 Characteristic of the electrotechnical steel conductivity γ as a non-linear function of temperature T

$$\frac{\partial T}{\partial t} + \frac{\partial T^2}{\partial t^2} = \frac{\lambda}{\rho c} \nabla^2 \mathbf{T} + \frac{1}{\rho c} \left(P + \tau \frac{\partial P}{\partial t} \right), \quad (6)$$

where λ —thermal conductivity of the ferromagnetic medium, ρ , c means its density and specific heat respectively, P —the power density which is processed to heat, τ —relaxation time. The spread of the heat flux in metal environment can be considered with relaxation time τ of 10^{-11} s. So, it can be assumed simplification, that heat conduction takes place with infinite speed, i.e. $\tau = 0$. In this case Eq. (6) simplifies to the form:

$$\frac{\partial T}{\partial t} = \frac{\lambda \nabla^2 \mathbf{T} + P}{\rho c}. \quad (7)$$

The effect of eddy-currents loses entitles to treat the variable P as a component representing the heat generation source (with “+” in above equation). In particular, the power generated density can be calculated by well known formula $P = \gamma E^2$, where E is a scalar value of the resultant electric field.

Taking into account, that the electromagnetic field Eq. (2) is considered with spatial derivatives along r and z axis, the temperature T should be treated as a function of the space-time coordinates, i.e.: $T = T(r, z, t)$. Thus, laplacian of vector \mathbf{T} in Eq. (7) for the considered cylindrical reference system will have the following form:

$$\nabla^2 \mathbf{T} = \left(\frac{\partial^2 T}{\partial r^2} + \frac{\partial^2 T}{\partial z^2} + \frac{1}{r} \frac{\partial T}{\partial r} \right), \quad (8)$$

so we can finally formulate the equation of thermal conductivity of the test object as follows:

$$\frac{\partial T}{\partial t} = \frac{1}{\rho c} \left[\lambda \left(\frac{\partial^2 T}{\partial r^2} + \frac{\partial^2 T}{\partial z^2} + \frac{1}{r} \frac{\partial T}{\partial r} \right) + \gamma (E_r^2 + E_z^2) \right]. \quad (9)$$

As previously mentioned, changes in temperature will affect the value of the conductivity of the material. Taking into account (8) and (9) it can be assumed, that conductivity γ is a function of variables: $\gamma = \gamma(T, r, z, t)$.

In a cylindrical reference system, which is shown in Fig. 1, the first Maxwell’s equation can be written as:

$$-\frac{\partial H}{\partial z} \mathbf{r}_0 + \left(\frac{\partial H}{\partial r} + \frac{H}{r} \right) \mathbf{z}_0 = \gamma E_r \mathbf{r}_0 + \gamma E_z \mathbf{z}_0, \quad (10)$$

it means, that the components of the vector \mathbf{E} can be calculated according to the following equations:

$$E_r = -\frac{\partial H}{\partial z} \frac{1}{\gamma}; \quad E_z = \left(\frac{\partial H}{\partial r} + \frac{H}{r} \right) \frac{1}{\gamma}. \quad (11)$$

If Eq. (11) will be used in left side of second Maxwell's equation, the equation of electromagnetic field (1) can be obtained under condition that $\gamma = \text{const}$. In our investigation the case, where $\gamma = \gamma(T, r, z, t)$ is considered. Thus, calculation the vector \mathbf{E} rotation leads to the following formulas:

$$\frac{\partial E_r}{\partial z} = \frac{\partial}{\partial z} \left(-\frac{\partial H}{\partial z} \frac{1}{\gamma} \right) = \left(\frac{\partial H}{\partial z} \frac{\partial \gamma}{\partial z} \frac{1}{\gamma} - \frac{\partial^2 H}{\partial z^2} \right), \quad (12)$$

$$\frac{\partial E_z}{\partial r} = \frac{\partial}{\partial r} \left[\left(\frac{\partial H}{\partial r} + \frac{H}{r} \right) \frac{1}{\gamma} \right] = \frac{1}{\gamma} \left(\frac{\partial^2 H}{\partial r^2} + \frac{1}{r} \frac{\partial H}{\partial r} - \frac{H}{r^2} - \frac{\partial H}{\partial r} \frac{\partial \gamma}{\partial r} \frac{1}{\gamma} - \frac{H}{r} \frac{\partial \gamma}{\partial r} \frac{1}{\gamma} \right). \quad (13)$$

Finally, the equation of the electromagnetic field in the ring, taking into account (12) and (13), can be written as follows:

$$\frac{\partial B}{\partial t} = \frac{1}{\gamma} \left[\frac{\partial^2 H}{\partial r^2} + \frac{\partial^2 H}{\partial z^2} + \frac{\partial H}{\partial r} \left(\frac{1}{r} - \frac{\partial \gamma}{\partial r} \frac{1}{\gamma} \right) - \frac{\partial H}{\partial z} \frac{\partial \gamma}{\partial z} \frac{1}{\gamma} - \frac{H}{r} \left(\frac{1}{r} + \frac{\partial \gamma}{\partial r} \frac{1}{\gamma} \right) \right]. \quad (14)$$

It can be seen, that for $\gamma = \text{const}$ appropriate conductivity spatial derivatives assume the values zero, and Eq. (14) is converted to the form of Eq. (1). It confirms the correctness of the assumed approach.

Solving partial differential equations of the conjugated fields (9) and (14) requires appropriate initial and boundary conditions. For electromagnetic field equation zero initial conditions were assumed:

$$B = B(r, z, t)|_{t=0} = B(r, z, 0) = 0, \quad (15)$$

where $R_1 \leq r \leq R_2$, $0 \leq z \leq a$. Boundary condition are defined by using Ampere's law, given by Eq. (4). For heat conduction Eq. (9), the initial condition with uniform temperature distribution in a ferromagnetic material was assumed:

$$T = T(r, z, t)|_{t=0} = T(r, z, 0) = 293, 15^\circ \text{K}. \quad (16)$$

It should be denoted, that ferromagnetic ring will exchange heat with external environment. To simplify the study, only convection phenomena was considered, while radiation was omitted. In this case, phenomenon at the edge can be expressed by Newton equation [6]. It describes the heat transfer in the normal direction to the surface of the ferromagnetic ring as follows:

$$-\lambda \frac{\partial T}{\partial n} = h_c (T - T_0). \quad (17)$$

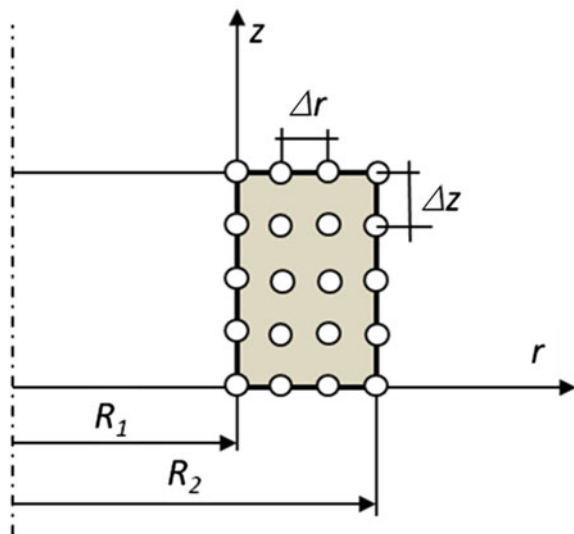
The heat transfer coefficient h_c describes the intensity of convective heat transfer to the environment surrounding and reaches a value between 5 and 500 W/(m² · K).

In general case, h_c may be a function of other quantities (such as the surface temperature of the material). In the investigations the constant value $h_c = \text{const}$ was assumed. Similar assumption has also been made for temperature T_0 in Eq. (17). It means, that the space ring surrounding is unlimited and can absorb any amount of energy, generated by the heating ferromagnetic.

4 Numerical Simulations of He Transient State

The equation of the electromagnetic field (14) and the boundary conditions (4), (15), non-linear magnetization curve Eq. (3) and the heat conduction Eq. (9) with boundary conditions (16), (17) and a non-linear Eq. (5) represent a mathematical model of the considered object in the transient state. Such formulated problem has no analytical solution therefore, required results can be obtained only through numerical calculations. The form of partial differential equations shows, that the relevant calculations should be implemented in two-dimensional space, defined by the variables r and z . Thus, during building a numerical model, the spatial discretization of the partial differential equations has been made, using finite difference method. It leads to the grid of nodes, which is shown on the Fig. 3, where Δy and

Fig. 3 Spatial discretization nodes in the half of the ferromagnetic cross-section



Δz are the discretization steps in the direction of r and z respectively. The symmetry of the object allows to consider only half of the cross-section.

The choice of the number of nodes and hence the increment Δy Δz , should be adjusted to obtain the best possible “resolution” of the mathematical model. But it is strongly connected with the value of the time discretization step in the context of ensuring the stability and accuracy of numerical calculations.

As a method of the time discretization, the implicit Euler method was used considering, that state variables are characterized by a highly diverse dynamics. Thus, the essential calculations was based on the initial conditions problem, given by the following formula:

$$\mathbf{X}_n = \mathbf{X}_{n-1} + \Delta t f(\mathbf{X}_n), \quad (18)$$

where $\mathbf{X} = \begin{bmatrix} B \\ T \end{bmatrix}$ denotes column vector of unknowns.

The appropriate calculations were carried out in the system predictor-corrector, where the task of predictor fulfills the explicit method, while corrector—the simple iterations method. Based on these methods, appropriate algorithm were designed and computer simulations were carried out. For the calculation the electrotechnical steel ET41 was used. Its magnetization characteristic can be approximated by the following spline function:

$$H = \begin{cases} 14.93B & \text{for } B \leq 1.3 \\ 251649B^7 - 2581280B^6 + 11321738B^5 - 27522529B^4 \\ + 40044890B^3 - 34870545B^2 + 16825767B - 3470325 & \text{for } 1.3 < B < 1.85 \\ 5321B - 9565 & \text{for } B \geq 1.85 \end{cases}$$

Conductivity of this material has value $\gamma_0 = 2.0833 \times 10^6$ S/m. The following geometrical dimensions were assumed (Fig. 1): $R_1 = 0.1$ m, $R_2 = 0.12$ m, $a = 0.01$ m. The values of the coefficients were adopted in accordance with the relevant data: $\alpha = 0.0021$ 1/°K, $\lambda = 58$ W/(m · °K), $\rho = 7,800$ kg/m³, $h_c = 10$ W/(m² · K), $c = 400$ J/(kg · °K). Calculations were carried out in equidistant spatial grid of nodes with the number of $M = 55$ and $N = 19$ on r and z axis respectively. To ensure numerical stability, the diffusion Courant number criterion was taken. On the Fig. 4 the spatial distribution of magnetic induction B and the temperature T , obtained for a certain time point, is presented.

Simulation results presented on the Fig. 4a indicate, that the largest concentration of magnetic flux is concentrated on the external space of the ring. It is connected with the presence of the electromagnetic skin effect. The spatial distribution of temperature on the Fig. 4b indicates that the heating in these areas of the material is more intensive. On the Fig. 5 the spatial distribution of the conductivity of the material is shown.

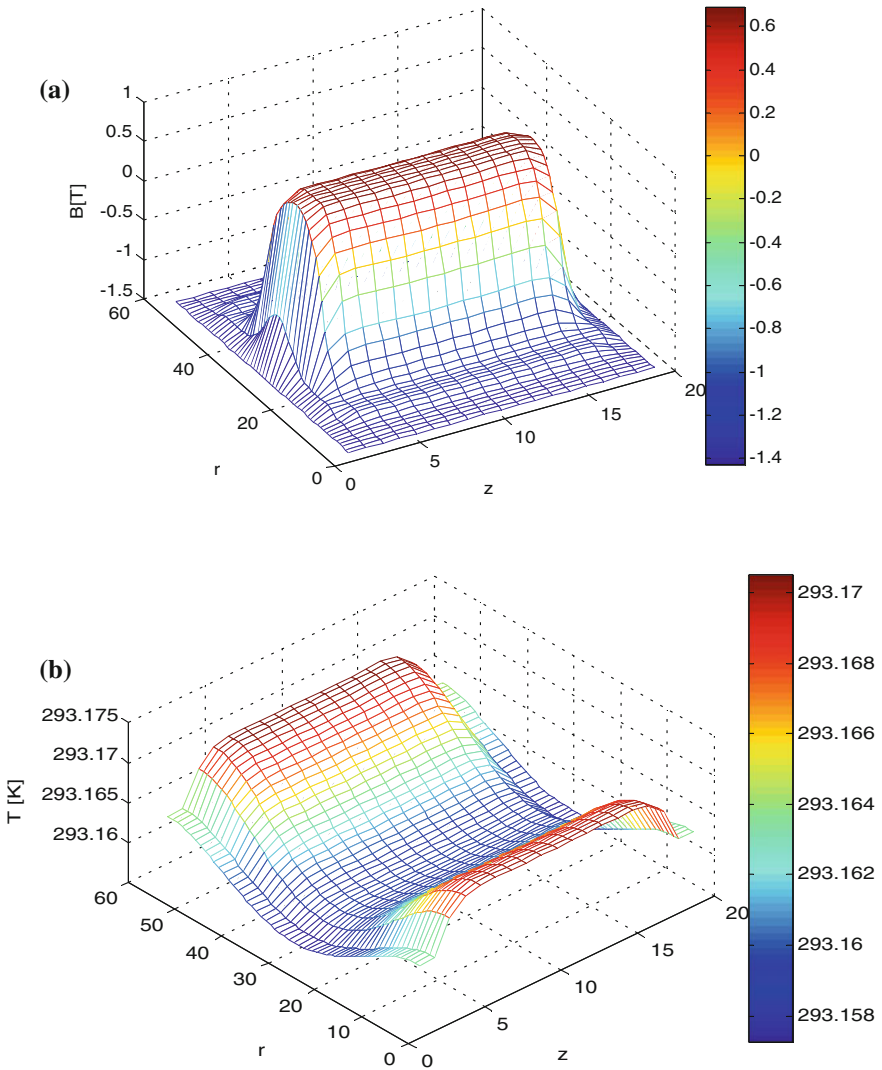


Fig. 4 Spatial distribution of magnetic induction (a) and temperature (b)

Obtained results indicate on decrease in conductivity γ in the areas of higher temperature, which is in accordance with Eq. (5). The model also allows to generate time-courses of any quantity at any node of the spatial grid. Figure 6 shows the time course of the temperature in the node with coordinates of $M = 20, N = 4$.

Presented result above confirms heating phenomenon in the ferromagnetic material, described by adequate theory. The temperature and electromagnetic fields are strongly connected due to conductivity γ variation in the electromagnetic field equation.

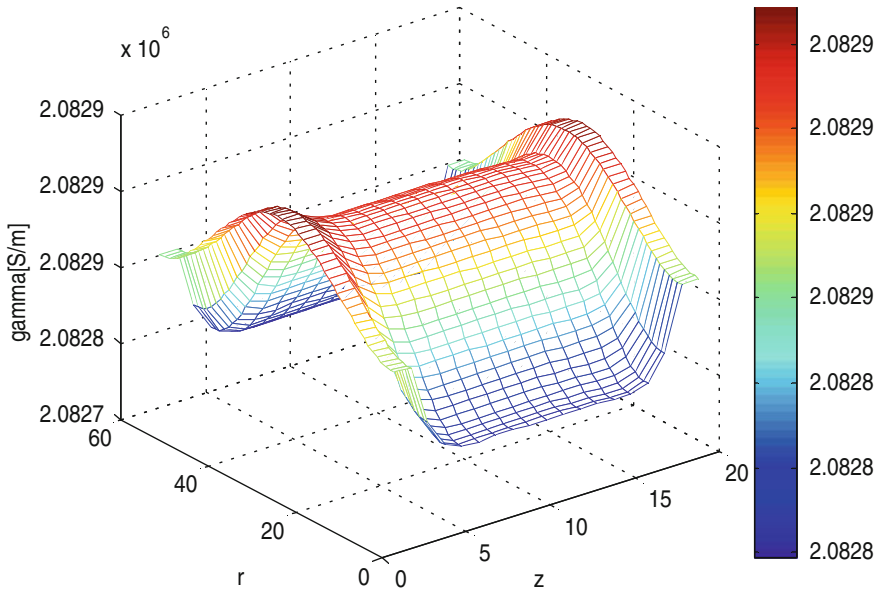


Fig. 5 Spatial distribution of the conductivity γ

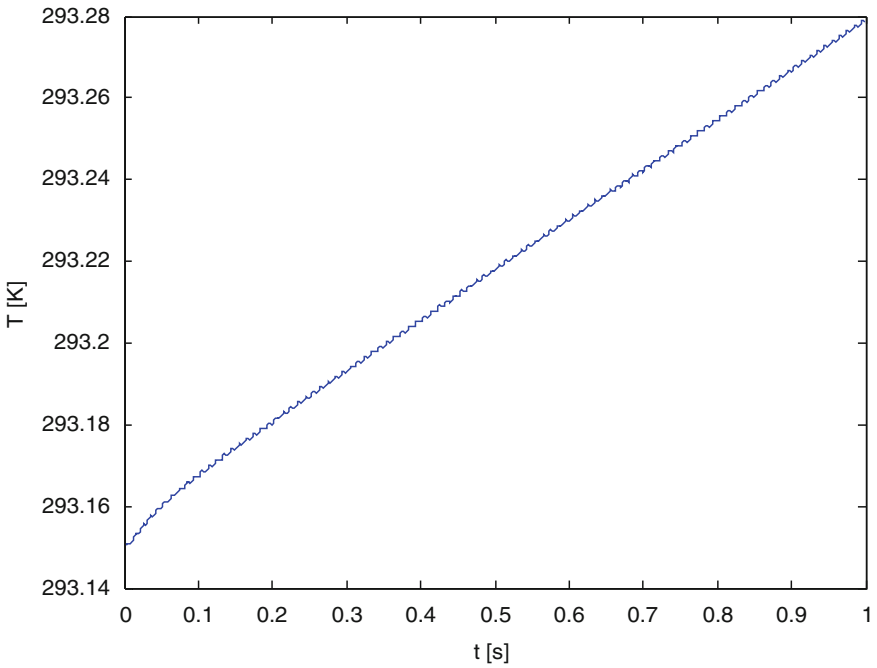


Fig. 6 Temperature time course in the fixed spatial node

5 Conclusions

Proposed idea of calculations can be developed and improved by incorporating omitted aspects of the phenomena. In particular, it will be important to take into account the magnetic hysteresis loop, the phenomenon of deformation of the magnetizing current. It is required to improve description of thermal phenomena and finally try to resolve steady-state problem. The authors also plan to conduct researches for the ferromagnetic cores with laminated structure. It is very interesting and complex task, especially for the case, when the equations of conjugated field will be considered in real core structure.

The implementation of the calculations on a personal computer is not effective due to the high computational complexity of the problem. Therefore, the simulation times and changes of the particular quantities, presented in the article, are relatively small. Long-term simulations will require the use of hardware with the structure of a computer cluster.

References

1. Aime J, Cogitore B, Meunier G, Clavel E, Marechal Y (2011) Numerical methods for eddy currents modeling of planar transformers. *IEEE Trans Magn* 5:1014–1017
2. Gomółka Z, Kwiatkowski B, Pękala R (2011) Non-invasive diagnosis of magnetizing coils using artificial neural networks. *Przegląd Elektrotechniczny* 8:66–69 (in Polish)
3. Mróz J (2011) Distribution of current density in the winding two stairwell for the calculation of heat. *Przegląd Elektrotechniczny* 5:238–241 (in Polish)
4. Pluta W (2011) Core loss models in electrical steel sheets with different orientation. *Przegląd Elektrotechniczny* 9b:37–42
5. Shimoji H, Todaka T, Enokizono M (2011) Core loss distribution measurement of electrical sheets using a thermographic camera. *Przegląd Elektrotechniczny* 9b:65–68
6. Taler J, Duda P (2003) Solving simple and inverse heat conduction problems. WNT, Warszawa (in Polish)
7. Todaka T, Yamamichi D, Enokizono M (2011) Numerical modeling of magnetic properties of ferromagnetic shape memory materials depending on temperature and stress. *IEEE Trans Magn* 5:926–929